CYCLIZATION REACTIONS FOR THE FUNCTIONALIZATION OF FULLERENES: EXPERIMENTAL AND THEORETICAL STUDIES

Albert Artigas Ruf

Per citar o enllaçar aquest document:
Para citar o enlazar este documento:
Use this url to cite or link to this publication:
http://hdl.handle.net/10803/668818

ADVERTIMENT. L'accés als continguts d'aquesta tesi doctoral i la seva utilització ha de respectar els drets de la persona autora. Pot ser utilitzada per a consulta o estudi personal, així com en activitats o materials d'investigació i docència en els termes establerts a l'art. 32 del Text Refós de la Llei de Propietat Intel·lectual (RDL 1/1996). Per altres utilitzacions es requereix l'autorització prèvia i expressa de la persona autora. En qualsevol cas, en la utilització dels seus continguts caldrà indicar de forma clara el nom i cognoms de la persona autora i el títol de la tesi doctoral. No s'autoritza la seva reproducció o altres formes d'explotació efectuades amb finalitats de lucre ni la seva comunicació pública des d'un lloc aliè al servei TDX. Tampoc s'autoritza la presentació del seu contingut en una finestra o marc aliè a TDX (framing). Aquesta reserva de drets afecta tant als continguts de la tesi com als seus resums i índexs.

ADVERTENCIA. El acceso a los contenidos de esta tesis doctoral y su utilización debe respetar los derechos de la persona autora. Puede ser utilizada para consulta o estudio personal, así como en actividades o materiales de investigación y docencia en los términos establecidos en el art. 32 del Texto Refundido de la Ley de Propiedad Intelectual (RDL 1/1996). Para otros usos se requiere la autorización previa y expresa de la persona autora. En cualquier caso, en la utilización de sus contenidos se deberá indicar de forma clara el nombre y apellidos de la persona autora y el título de la tesis doctoral. No se autoriza su reproducción u otras formas de explotación efectuadas con fines lucrativos ni su comunicación pública desde un sitio ajeno al servicio TDR. Tampoco se autoriza la presentación de su contenido en una ventana o marco ajeno a TDR (framing). Esta reserva de derechos afecta tanto al contenido de la tesis como a sus resúmenes e índices.

WARNING. Access to the contents of this doctoral thesis and its use must respect the rights of the author. It can be used for reference or private study, as well as research and learning activities or materials in the terms established by the 32nd article of the Spanish Consolidated Copyright Act (RDL 1/1996). Express and previous authorization of the author is required for any other uses. In any case, when using its content, full name of the author and title of the thesis must be clearly indicated. Reproduction or other forms of for profit use or public communication from outside TDX service is not allowed. Presentation of its content in a window or frame external to TDX (framing) is not authorized either. These rights affect both the content of the thesis and its abstracts and indexes.

Doctoral Thesis

Cyclization reactions for the functionalization of fullerenes: experimental and theoretical studies

Albert Artigas Ruf

2019

Doctoral Programme in Chemistry

Supervised by:

Prof. Anna Roglans Ribas

Prof. Miquel Solà Puig

Dr. Agustí Lledó Ponsati

Tutor:

Prof. Anna Roglans Ribas

Presented in partial fulfilment of the requirements for a doctoral degree from the Universitat de Girona

Universitat de Girona

Prof. Anna Roglans Ribas, Prof. Miquel Solà Puig and Dr. Agustí Lledó Ponsati, from the Universitat de Girona,

WE DECLARE:

That this thesis entitled **“Cyclization reactions for the functionalization of fullerenes: experimental and theoretical studies”** presented by **Albert Artigas Ruf** to obtain the doctoral degree has been completed under our supervision and meets the requirements to opt for an International Doctorate.

.

For all intents and purposes, we hereby sign this document

Prof. Anna Roglans Prof. Miquel Solà Puig Dr. Agustí Lledó Ponsati

Girona, 30th October 2019

Als meus pares.

Aquesta tesi és també el fruit últim del seu treball i la seva inestimable dedicació.

Acknowledgements

This thesis is the result of a cooperative effort. I would like to thank the following people, whose contribution has been indispensable for the realization of this work:

- My supervisors Prof. Anna Roglans, Prof. Miquel Solà and Dr. Agustí Lledó, to trust me to develop the projects contained in this thesis. For their support and advice along this period of my life, and for teaching me almost everything I know about chemistry. My gratitude to them does not fit in these lines. I am certain that if at this point I have acquired some of the knowledge it takes to be a researcher in the field of chemistry, it is largely thanks to them. Of course, I cannot forget the contribution of Dr. Anna Pla Quintana in this regard. Although not stated here as a supervisor, her teachings have been equally valuable.
- Dr Luís Echegoyen, to host me in his laboratories during a predoctoral research stay at the University of Texas at El Paso (UTEP) and to make me feel like a member of the “LE group” from the very first day. I hope our cooperation and friendship will last beyond our first collaboration. Also, I would like to thank Dr. Edison Castro. He was the first to host me in Texas and quickly became a close friend and an invaluable collaborator. I cannot close this paragraph without mentioning the rest of the LE group: Alejandra Torres, Jesse Murillo, Olivia Fernández and Wenting Cai. They all made my days in Texas an unforgettable experience.
- Dr. Lluisa Matas, Dr. Sergio Braulio, Anna Costa, Dr. Laura Gómez and Xavier Fontrodona from the *Serveis Tècnics de Recerca* at the Universitat de Girona for NMR, HPLC, MS and XRD analyses. The researchers in our institution are lucky to count on this team of professionals.
- All my colleagues at the METSO laboratory who have shared with me these four years as a graduate student. First of all, the ones who were already in the lab when I arrived in Girona in autumn 2015: Dr. Anna Soler, Dr. Óscar Torres, Dr. Martí Fernádez and Dr. Daniel Cassú. Also, all the students that came after me, with whom I forged a very special friendship: Álex Díaz, Cristina Castanyer, Dr. David Lozano, Ricard López, Jordi Vila and Rubén Álvarez. The undergraduate students I have mentored also merit recognition here: Màrius Duñach, Marc Castaño, Joel Nadal, Guillem Sasarols and Maria Eugènia López. They all have shown strong dedication and have helped me develop my skills as a mentor.
- All my colleagues in the computational chemistry laboratory: Steven Roldan, Martí Gimferer, Sergio Fernández, Sílvia Escayola, Gerard Pareras, Pau Besalú, Leila Pujals, Marc Montilla and Gerard Riesco. Daniel Masó deserves a special mention. He is the best IT technician the IQCC could ever have, but also an amazing colleague and friend with whom I would like to share office forever. I thank also the secretaries at the IQCC: Carme López, Sílvia Valentí and Ana María Gálvez.
- I am especially happy to dedicate some lines to my dear friend Carles Fuertes. He is an excellent scientist and, more importantly, he has become my closest friend in Girona. I have to thank him for endless hours of conversation, confidences and scientific discussion. I will keep being his friend and most enthusiastic admirer after we graduate.
- All my former colleagues at the medicinal chemistry unit at the University of Barcelona. Very specially, I want to thank Dr. Irene Sola, my first mentor in an organic chemistry laboratory and friend. I would not

be able to set up a single reaction or run a chromatographic column without her patience and dedication when she supervised me as an undergraduate and MSc student. Also I want to thank Prof. Diego Muñoz-Torrero for giving me the opportunity to take my first steps in the field of chemical research within his group.

- Dr. Diana Salazar, also for her help and mentoring at the Royal College of Surgeons in Ireland (RCSI).
- All my friends, comrades and family for their support and for always caring about the progress of my work. Specially my parents, who are always prouder of my achievements than myself.
- My dearest love Anna. She has been there most of the time. I can’t be happier at her side and I know that we will continue to support each other for many more years.

This thesis would have not been possible without financial support by the Spanish Ministry of Economy and Competitivity (Projects CTQ2014-54306-P, CTQ2017-85341-P and CTQ2017-83587-P, and FPI predoctoral grant BES-2015-074124) and the Generalitat de Catalunya (Projects 2014SGR931 and 2017-SGR-39).

Summary

Fullerenes are spherical allotropes of carbon. They present themselves as discrete molecular entities formed by an even number of carbon atoms, organized in twelve pentagons and a variable number of hexagons. The outstanding properties of fullerenes make them interesting compounds in a variety of fields, ranging from medicine to photovoltaics, albeit they have to be functionalized before they can become useful molecules. In this regard, the C–C double bonds found at the junctions between hexagons, the so-called [6,6] bonds, have a reactivity comparable to that of electron-deficient olefins. The most famous and representative member of the fullerene family is the football-shaped fullerene C_{60}. Its discovery in 1985 by Kroto, Smalley and Curl deserved the Nobel Prize in chemistry eleven years later and stimulated the search and development of new allotropic forms of carbon. Three decades after its groundbreaking discovery, organic chemists have managed to attach almost every functional group to the surface of C_{60} by employing a wide variety of synthetic strategies. Specifically, the synthesis of cyclohexadiene-fused fullerene derivatives can be achieved by means of transition metal-promoted [2+2+2] cycloaddition reactions of C_{60} and alkynes. Moreover, the derivatives resulting from such reactions are considered appealing molecules, since they have been employed as synthetic intermediates of open-cage fullerenes. In spite of its synthetic usefulness, methods allowing for the preparation of C_{60}-cyclohexadiene derivatives are still far from optimal. The only two methods described in the literature are either not catalytic or have a very limited reaction scope.

Our group has been involved in the study of Rh(I)-catalyzed [2+2+2] cycloaddition reactions. For many years, we have combined different substrates like alkynes, alkenes, nitriles and allenes in these reactions to efficiently prepare diversified carbo- and heterocyclic reaction products. In some cases, the reaction mechanism has been elucidated by quantum chemical calculations. Regarding the chemistry of fullerenes, we have studied computationally some fundamental aspects of their reactivity like the regioselectivity of certain cycloaddition reactions.

Given the experience demonstrated by our group and the lack of an optimal and catalytic methodology to prepare cyclohexadiene derivatives of C_{60}, the main goal set within the context of this thesis was to develop a new protocol based on Rh(I) catalysis to efficiently access this kind of compounds. As reported in chapters 3 to 5, we have succeeded in reacting C_{60} with a series of diynes. The reactions provide a series of *open-cage* derivatives in a single catalytic step. Additionally, we have thoroughly studied the reaction mechanism behind this chemical transformation by DFT calculations. Also, in collaboration with the group of Dr. Luís Echegoyen, some of the derivatives obtained have been incorporated as electron-transporting layers in perovskite solar cells. Besides, in chapter 6 we report a synthetic method to prepare polycyclic heterocycles from bisallenes and alkenes using again a Rh(I) catalyst. This protocol was also successfully applied to functionalize C_{60}. To end, chapter 7 deals with the computational study of the regioselectivity in the Diels-Alder cycloaddition reaction of cyclopentadiene and the elusive fullerene $^{\#6094}C_{68}$.

Resum

Els ful·lerens són al·lòtrops esfèrics del carboni. Es presenten com a entitats moleculars discretes i estan formats per un nombre parell d’àtoms de carboni, organitzats en dotze pentàgons i un nombre variable d’hexàgons. Els ful·lerens presenten un seguit de propietats que els fa compostos d’especial interès en diversos camps d’aplicació com ara la medicina o l’energia fotovoltaica. No obstant, per tal de convertir-los en molècules útils, els ful·lerens han de ser convenientment funcionalitzats. En aquest sentit, els dobles enllaços presents a les unions entre dos hexàgons, els anomenats enllaços [6,6], reaccionen de forma anàloga a com ho fan les olefines deficients en electrons. L’exemple més representatiu dels ful·lerens és el C_{60}. El seu descobriment l’any 1985 fou reconegut amb el premi Nobel de química, concedit a Kroto, Smalley i Curl onze anys després. Tres dècades d’avenços en el camp de la química dels ful·lerens permeten que, a dia d’avui, pràcticament qualsevol grup funcional pugui ser unit a la superfície del C_{60} mitjançant tècniques de síntesi orgànica. Concretament, la síntesi de derivats de ful·lerè units a anells de tipus ciclohexadiè és possible mitjançant reaccions de cicloaddició [2+2+2] promogudes per metalls de transició entre C_{60} i alquins. Els compostos derivats d’aquestes reaccions, a més, poder ser utilitzats com a intermediaris sintètics dels anomenats ful·lerens *open-cage*. No obstant, malgrat la seva utilitat, cap mètode descrit a la bibliografia científica permet accedir a derivats de tipus C_{60}-ciclohexadiè de forma eficient. Els únics dos exemples que hi trobem no són catalítics i presenten un abast limitat.

Durant els darrers anys, el nostre grup s’ha dedicat a l’estudi de les reaccions de cicloaddició [2+2+2] catalitzades per complexes de Rh(I). Concretament, s’han aconseguit fer reaccionar compostos com ara alquins, alquens, nitrils o al·lens, per donar lloc, eficientment, a diversos compostos carbo- i heterocíclics com a productes de reacció. Pel que fa el camp de la química de ful·lerens, el nostre grup ha estudiat, mitjançant càlculs computacionals, aspectes fonamentals de la seva reactivitat com ara la regioselectivitat de determinades reaccions de cicloaddició.

Atesa l’experiència demostrada pel nostre grup i tenint en compte la manca d’una metodologia eficient que permeti preparar derivats de C_{60} units a anells de tipus ciclohexadiè, l’objectiu principal d’aquesta tesi doctoral consisteix en desenvolupar un nou protocol basat en catàlisi de Rh(I) que en permeti la síntesi de forma efectiva. En aquest sentit, tal i com es recull en els capítols 3 a 5 del present manuscrit, en el transcurs de la tesi s’ha aconseguit fer reaccionar C_{60} amb una sèrie de diïns. La reacció desenvolupada dóna lloc a un seguit de derivats de tipus *open-cage* en un sol pas, el qual té lloc en condicions catalítiques. Així mateix, el mecanisme de la reacció s’ha estudiat acuradament mitjançant càlculs computacionals. En col·laboració amb el grup de recerca del Dr. Luís Echegoyen, hem aconseguit incorporar alguns dels productes resultants d’aquestes reaccions en cel·les solars de tipus perovskite com a materials transportadors d’electrons. Més enllà d’això, en el capítol 6 descrivim un nou mètode sintètic per preparar compostos poliheterocíclics a partir de bisal·lens i alquens mitjançant un procés que, un cop més, es basa en catàlisi de Rh(I). Aquesta metodologia de síntesi també s’ha aconseguit aplicar en la funcionalització de C_{60}. Per acabar, en el capítol 7 hem estudiat computacionalment la regioselectivitat en la reacció de cicloaddició de Diels-Alder entre el ciclopentadiè i el ful·lerè $^{\#6094}C_{68}$.

Resumen

Los fullerenos son alótropos esféricos del carbono. Se presentan como entidades moleculares discretas, formadas por un número par de átomos de carbono, organizados en doce pentágonos y un número variable de hexágonos. Sus particulares propiedades les han convertido en compuestos de gran interés en numerosos campos, como la medicina o la energía fotovoltaica. Pese a ello, para convertirse en moléculas con utilidad práctica, los fullerenos deben ser previamente funcionalizados. En este sentido, los dobles enlaces presentes en las uniones entre dos hexágonos, conocidos como enlaces [6,6], reaccionan de forma análoga a las olefinas deficientes en electrones. El ejemplo más representativo de los fullerenos es el C_{60}, cuyo descubrimiento en el año 1985 fue reconocido con el Premio Nobel de química a Kroto, Smalley y Curl once años más tarde. Tres décadas de avances en el campo de la química de los fullerenos permiten que, hoy en día, prácticamente cualquier grupo funcional pueda ser adherido a la superficie del C_{60} mediante técnicas de síntesis orgánica. Concretamente, la síntesis de derivados de fullereno unidos a anillos de tipo ciclohexadieno es posible mediante reacciones de cicloadición [2+2+2] mediadas por metales de transición entre C_{60} i alquinos. Los compuestos derivados de tales reacciones, además, sirven como intermedios sintéticos de los llamados fullerenos *open-cage*. Sin embargo, pese a su utilidad, no existe ningún método en la bibliografía científica que permita acceder a derivados de tipo C_{60}-ciclohexadieno de forma eficiente. Los únicos ejemplos descritos no son catalíticos y presentan un alcance limitado.

Nuestro grupo de investigación se ha dedicado al estudio de las reacciones de cicloadición [2+2+2] catalizadas por complejos de Rh(I) durante los últimos años. Específicamente, hemos conseguido preparar una gran variedad de compuestos carbo- y heterocíclicos combinando sustratos insaturados como alquinos, alquenos, nitrilos o alenos. Con respecto a la química de fullerenos, nuestro grupo ha estudiado, mediante cálculos computacionales, aspectos fundamentales sobre su reactividad tales como la regioselectividad de determinadas reacciones de cicloadición.

Dada la experiencia demostrada por nuestro grupo y teniendo en cuenta la ausencia de una metodología eficiente para preparar derivados de C_{60} unidos a anillos de tipo ciclohexadieno, el objetivo principal de esta tesis doctoral consiste en desarrollar un nuevo protocolo sintético basado en catálisis de Rh(I) que permita su síntesis de forma efectiva. En este mismo sentido, tal y como se recoge en los capítulos 3 a 5 del presente manuscrito, durante el transcurso de la tesis se ha conseguido hacer reaccionar C_{60} con una serie de diinos. La reacción desarrollada da lugar a una serie de derivados de tipo *open-cage* en un único paso, el cual tiene lugar en condiciones catalíticas. De forma adicional, hemos estudiado el mecanismo de la reacción mediante cálculos DFT. En colaboración con el grupo del Dr. Luís Echegoyen, hemos conseguido utilizar algunos de los derivados sintetizados como materiales transportadores de electrones en celdas solares de tipo pervoskita. Por otra parte, en el capítulo 6 describimos un nuevo método de síntesis para preparar compuestos poliheterocíclicos a partir de bisalenos y alquenos mediante un proceso que, una vez más, está basado en catálisis de Rh(I). Esta metodología se ha conseguido aplicar también en la funcionalización de C_{60}. Por último, en el capítulo 7 hemos estudiado la regioselectividad en la reacción de cicloadición de Diels-Alder entre ciclopentadieno y el fullereno $^{\#6094}C_{68}$.

Full list of publications

This thesis is presented as a compendium of the following publications:

Chapter 3

Artigas, A.; Lledó, A.; Pla-Quintana, A.; Roglans, A.; Solà, M. A Computational Study of the Intermolecular [2+2+2] Cycloaddition of Acetylene and C_{60} Catalyzed by Wilkinson's. Catalyst *Chem. Eur. J.* **2017**, *23*, 15067.

(IF: 5.16; JCR Ranking: 37/172; 1st quartile Multidisciplinary Chemistry)

Contribution: *A.A.R. participated in the design of the project, performed all the calculations, analyzed the results, and co-wrote the manuscript*.

Chapter 4

Artigas, A.; Pla-Quintana, A.; Lledó, A.; Roglans, A.; Solà, M. Expeditious Preparation of Open-Cage Fullerenes by Rhodium(I)-Catalyzed [2+2+2] Cycloaddition of Diynes and C_{60}: An Experimental and Theoretical Study. *Chem. Eur. J.* **2018**, *24*, 10653.

(IF: 5.16; JCR Ranking: 37/172; 1st quartile Multidisciplinary Chemistry).

Contribution: *A.A.R. participated in the design of the project, performed all the experiments and calculations, analyzed the results, and co-wrote the manuscript*.

Chapter 5

Castro, E.; Artigas, A.; Pla-Quintana, A.; Roglans, A.; Liu, F.; Perez, F.; Lledó, A.; Zhu, X.-Y.; Echegoyen, L. Enhanced Open-Circuit Voltage in Perovskite Solar Cells with Open-Cage [60]Fullerene Derivatives as Electron-Transporting Materials. *Materials* **2019**, *12*, 1314.

(IF: 2.97; JCR Ranking: 102/293; 2nd quartile Multidisciplinary Materials Science)

Contribution: *A.A.R. participated in the design of the project, synthesized all the products, contributed to the analysis of the results, and co-wrote the manuscript*.

Chapter 6

Artigas, A.; Vila, J.; Lledó, A.; Solà, M.; Pla-Quintana, A.; Roglans, A. A Rh-Catalyzed Cycloisomerization/Diels–Alder Cascade Reaction of 1,5-Bisallenes for the Synthesis of Polycyclic Heterocycles. *Org. Lett.* **2019**, *21*, 6608.

(IF: 6.56; JCR Ranking: 2/57; 1st quartile Organic Chemistry)

Contribution: *A.A.R. participated in the design of the project, performed part of the experiments, performed all the calculations, analyzed the results, and co-wrote the manuscript*.

Chapter 7

Artigas, A.; Fernández, I.; Solà, M. Regioselectivity in Diels−Alder Cycloadditions of $^{\#6094}C_{68}$ Fullerene with a Triplet Ground State. *J. Org. Chem.* **2019**, *84*, 9017.

Contribution: *A.A.R. participated in the design of the project, performed all the calculations, analyzed the results, and co-wrote the manuscript*.

(IF: 4.75; JCR Ranking: 7/57; 1st quartile Organic Chemistry)

Other publications by the author not included in this thesis:

Artigas, A.; Sola, I.; Taylor, M. C.; Clos, M. V.; Perez, B.; Kelly, J. M.; Munoz-Torrero, D. Synthesis and Biological Evaluation of Heteroarylnonanenitriles as Potential Antitrypanosomal Agents: Serendipitous Discovery of Novel Anticholinesterase Hits. *Lett. Org. Chem.*, **2018**, *15*, 455.
Invited article in special issue dedicated to Prof. Miguel Yus (University of Alicante).

Sola, I.; Artigas, A.; Taylor, M. C.; Pérez-Areales, F. J.; Viayna, E.; Clos, M. V.; Pérez, B.; Wright, C. W.; Kelly, J. M.; Muñoz-Torrero, D. Synthesis and biological evaluation of N-cyanoalkyl-, N-aminoalkyl-, and N-guanidinoalkyl-substituted 4-aminoquinoline derivatives as potent, selective, brain permeable antitrypanosomal agents. *Bioorg. Med. Chem.* **2016**, *24*, 5162.

Sola, I.; Artigas, A.; Taylor, M. C.; Gbedema, S. Y.; Pérez, B.; Clos, M. V.; Wright, C. W.; Kelly, J. M.; Muñoz-Torrero, D. Synthesis and antiprotozoal activity of oligomethylene- and p-phenylene-bis(methylene)-linked bis(+)-huprines. *Bioorg. Med. Chem. Lett.* **2014**, *24*, 5435.

Glossary of Abbreviations

General abbreviations

1D	Monodimensional
1-MeNp	1-Methylnaphtalene
2D	Bidimensional
Å	Angstrom
a.u.	Atomic units
Abs	Absorbance
Ac	Acetyl
ACS	American Chemical Society
AO	Atomic orbitals
Ar	Aryl
ASM	Activation strain model
B3LYP	Becke, three parameter, Lee-Yang-Parr
B88	Exchange functional by Becke
BHJ	Bulk heterojunction
BLYP	Combination of B88 exchange and LYP correlation functionals
BO	Born-Oppenheimer
BPW91	Combination of B88 exchange and PW91 correlation functionals
BQ	Benzoquinone
Bu	Butyl
CAN	Cerium (IV) ammonium nitrate
CCDC	Cambridge Crystallographic Data Centre
cc-pVNZ	Correlation consistent-polarized basis sets by Dunning (N = D, T, Q, 5, 6, 7)
cc-pVNZ-PP	Correlation consistent-polarized basis sets by Dunning (N = D, T, Q, 5, 6, 7) including pseudopotential
cod	1,5-cyclooctadiene
Cp	Cyclopentadiene
CPP	Cycloparaphenylene
CV	Cyclic voltammetry
Cy	Cyclopentadienyl
Δ	Heat
d.r.	Diastereomeric ratio
DA	Diels-Alder
DBU	1,8-Diazabicyclo[5.4.0]undec-7-ene
DCM	Dichloromethane
ΔE	Relative electronic energy
def2-TZVPP	Valence triple-zeta with two sets of polarization functions
DF	Density functional
DFT	Density Functional Theory
DFT-D	Density functional theory including disperison effects
ΔG	Relative Gibbs energy
DMA	9,10-dimethylanthracene
DMF	Dimethylformamide
DNA	Deoxyribonucleic acid
DSSC	Dye-sensitized solar cell
E	Electronic energy

ECP	Effective core potential
EDA	Energy decomposition analysis
ee	Enantiomeric exces
EMF	Endohedral metallofullerene
EPR	Electron paramagnetic ressonance
eq.	Equivalent
Et_2O	Diethyl ether
ETL	Electron-transporting layer
ETM	Electron-transporting material
EtOAc	Ethyl acetate
EtOH	Ethanol
Fc	Ferrocene
FF	Fill factor
FG	Functional group
G	Gibbs energy
g	Grams
GGA	Generalized gradient approximation
GTO	Gaussian-type orbitals
h	Hours
HetAr	Heteroaromatic
HF	Hartree-Fock
HIV	Human immunodeficiency viruses
HOMO	Highest occupied molecular orbital
HPLC	High-performance liquid chromatography
HRMS	High resolution mass spectrometry
HTL	Hole-transporting layer
HTM	Hole-transporting material
Ind	Indenyl
*i*Pr	Isopropyl
IPr	N,N'-bis(2,6-diisopropylphenyl)imidazol-2-ylidene)
IPR	Isolated pentagon rule
IR	Infrared spectroscopy
IRC	Intrinsic reaction coordinate
ISC	Intersystem crossing
ITO	Indium tin oxide
IUPAC	International Union of Pure and Applied Chemistry
J_{sc}	Short circuit current density
K	Kelvin degrees
kcal	Kilocalory
KS	Kohn-Sham
LCAO	Linear combination of atomic orbitals
LDA	Local Density approximation
LUMO	Lowest unoccupied molecular orbital
LYP	Correlation functional by Lee, Yang and Parr
M	Molar
M06	Minessota meta-GGA global hybrid functional including 27% HF exchange
M06-2X	Minessota meta-GGA global hybrid functional including 54% HF exchange
M06-2X-D3	Unrestricted M06-2X functional with D3 Grimme's dispersion

M06L	Minessota meta-GGA local functional including 0% HF exchange
$MAPbI_3$	methylammonium lead iodide
m-CPBA	Metachloroperbenzoic acid
Me	Methyl
mg	Miligrams
mL	milliliters
MM	Molecular mechanics
mM	Milimolar
MO	Molecular orbitals
mol%	mol percentage
MRI	Magnetic ressonance imaging
mV	Milivolts
MW	Microwave
NHC	N-heterocyclic carbene
N-MR	*N*-membered ring (a ring formed by *N* members)
NOCV	Natural orbital for chemical valence
*N*Z	*N*-zeta basis set
ºC	Degrees Celsius
o-DCB	1,2-dichlorobenzene
OPV	Organic photovoltaics
OSC	Organic solar cell
$PC_{61}BM$	Phenyl-C_{61}-butyric acid methyl ester
$PC_{71}BM$	Phenyl-C_{71}-butyric acid methyl ester
PCE	Power conversion efficiency
PCM	Polarizable continuum model
PEDOT:PSS	poly(3,4-ethylenedioxythiophene):polystyrene sulfonate
PES	Potential energy surface
Ph	Phenyl
PivOH	Pivalic acid
PL	Photoluminescence
PNSO	N-phosphino tert-butylsulfinamide (ligands)
PPh_3	Triphenylphosphine
PSC	Perovskite solar cell
PTSA	Paratoluenesulfonic acid
PV	Photovoltaics
PW91	Correlation functional by Perdew and Wang
Py	Pyridyl
QM	Quantum mechanics
QM/MM	Quantum mechanics/molecular mechanics
r.t.	Room temperature
RC	Reactant complex
RSC	Royal Society of Chemistry
S	Slater exchange functional
s	Seconds
SCE	Saturated calomel electrode
SCF	Self-consistent field
SCRF	Self-consistent reaction field
SD	Standard deviation

SIP	P-stereogenic secondary iminophosphorane (ligands)
SMD	Continuum model based on density
S_N2	Bimolecular nucleophilic substitution
SPE	Single-point energy
Spiro-OMeTAD	2,2′,7,7′-Tetrakis[N,N-di(4-methoxyphenyl)amino]-9,9′-spirobifluorene
STO	Slater-type orbitals
SVWN	Slater exchange functional in conjunction wit the correlation functional of Vosko, Wilk and Nusair
T	Temperature
TBS	Tert-butyldimethylsilyl
*t*Bu	Tert-butyl
TDI	TOF determining intermediate
TDTS	TOF determining transition state
THF	Tetrahydrofuran
TLC	Thin layer chromatography
TMS	Trimethylsilyl
TOF	Turnover frequency
Tol	Tolyl
TR-PL	Time-resolved photoluminiscence
TS	Transition state
Ts	Tosyl
UB3LYP	Unrestricted B3LYP
UB3LYP-D3	Unrestricted B3LYP functional with D3 Grimme's dispersion
UCM	Universidad Complutense de Madrid
UM06	Unrestricted M06 functional
UTEP	University of Texas at El Paso
UV	Ultraviolet spectroscopy
V	Voltage/Volts
V_{oc}	Open-circuit voltage
VWN	Correlation functional by Vosko, Wilk and Nusair
WIRES	Wiley interdisciplinary reviews
ZPVE	Zero-point vibrational energy

Compound characterization

^{13}C NMR	13-Carbon nuclear magnetic resonance
^{1}H NMR	Proton nuclear magnetic resonance
$CDCl_3$	Deuterated chloroform
cm^{-1}	Reciprocal centimeters
COSY	Proton-proton correlation spectroscopy
d	Doublet
ddd	Doublet of doublets of doublets
dt	Double triplet
E.A.	Elemental analysis
ESI-HRMS	Electrospray ionization high resolution mass spectrometry
HMBC	Heteronuclear multiple-bond correlation spectroscopy
HSQC	Heteronuclear single-quantum correlation spectroscopy
Hz	Hertz
IR (ATR)	Infrared spectroscopy (attenuated total reflectance)
J	Coupling constant
m	Multiplet
M.p.	Melting point
m/z	Mass to charge ratio
MHz	Mega-hertz
MW	Molecular weight
o-DCB-d4	Deuterated 1,2-dichlorobenzene
ppm	Parts per milion
q	Quadruplet
quint	Quintuplet
Rf	Retention factor
s	Singlet
sept	Heptuplet
t	Triplet
UV-vis	Ultraviolet-visible spectroscopy
δ	Chemical shift
λ	Wavelength
ν	Frequency

Diphosphine ligands

(*R*)-BINAP	2,2’-bis(diphenylphosphino)-1,1’-binaphthyl
(*R*)-Tol-BINAP	2,2’-bis(di-*para*-tolylphosphino)-1,1’-binaphthyl
(*R*)-H_8-BINAP	2,2’-bis(diphenylphosphino)-5,5’,6,6’,7,7’,8,8’-octahydro-1,1’-binaphthyl
(*R*)-DTBM-Segphos	5,5’-bis[di(3,5-di-tert-butyl-4-methoxyphenyl)phosphino]-4,4’-bi-1,3-benzodioxole
BIPHEP	2,2’-bis(diphenylphosphino)biphenyl
(*R*)-Monophos	(R)-(−)-(3,5-dioxa-4-phosphacyclohepta[2,1-*a*:3,4-*a′*]dinaphthalen-4-yl)dimethylamine
dppe	1,2-bis(diphenylphosphino)ethane
dppf	1,1′-ferrocenediyl-bis(diphenylphosphine)
(*S*, *S*)-bdpp	(2*S*,4*S*)-2,4-Bis(diphenylphosphino)pentane

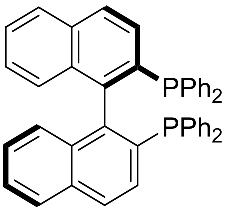

(*R*)-BINAP

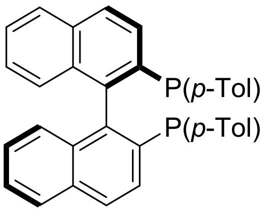
P(p-Tol)
P(p-Tol)

(*R*)-Tol-BINAP

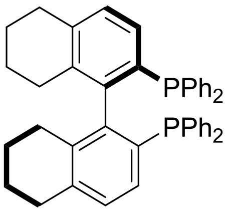

(*R*)-H_8-BINAP

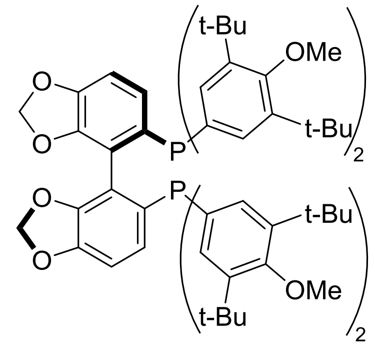
t-Bu
OMe
O
O
t-Bu
2
P
O
O
P
t-Bu
OMe
t-Bu
2

(*R*)-DTBM-Segphos

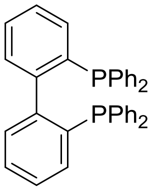

BIPHEP

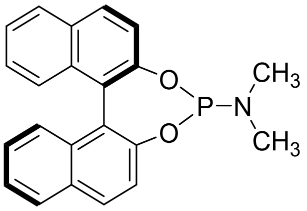
O
P
N
CH3
CH3
O

(*R*)-Monophos

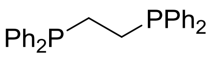

dppe

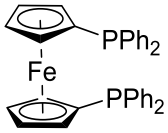
PPh2
Fe
PPh2

dppf

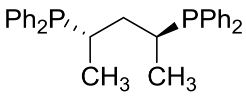
Ph2P
PPh2
CH3
CH3

(*S*, *S*)-bdpp

List of figures

Figure 1.1. Allotropes of carbon and their classification according to dimensionality.. 3

Figure 1.2. Molecular structure of representative EMFs (a) La@C_{82}-C_{2v} (b) Sc_3N@C_{80}-I_h. 6

Figure 1.3. (a) Schematic view of a Krätschmer–Huffman generator. (b) Fullerene production and separation scheme. 6

Figure 1.4. (a) Structures and different classes of bonds present in fullerenes C_{60} and C_{70}. Bond distances taken from X-ray structures [42,43]. (b) ^{13}C NMR spectrum of a mixture of a C_{60} and C_{70} mixture in benzene-d_6... 7

Figure 1.5. Electronic absorption spectra of (a) C_{60} and (b) C_{70} in toluene (data from the author). Insets: 500-700 nm region. 8

Figure 1.6. Cyclic and differential pulse voltammogram of (a) C_{60} and (b) C_{70} 8

Figure 1.7. UV-vis spectra of isolated α, β and γ adducts obtained by 1,3-dipolar cycloaddition with azomethine ylides (Raw experimental data provided by Dr. Edison Castro). 20

Figure 1.8. Simplified working principle of OSCs.. 28

Figure 1.9. Example of a current-voltage (*J*-*V*) curve. 29

Figure 1.10. (a) Common fullerene derivatives used as acceptor materials; (b) donor polymers and molecules used in OSCs; (c) Non-fullerene acceptor molecule. 30

Figure 1.11. Representation of: (a) Planar and bulk heterojunction OSCs; (b) different configurations of BHJ OSCs. 30

Figure 1.12. Three-dimensional crystal structure of $MAPbI_3$ perovskite 31

Figure 1.13. Simplified working principle of PSCs... 32

Figure 1.14. Different structures of PSCs.. 32

Figure 1.15. Gibbs energy profile at 298 K for the [2+2+2] acetylene cyclotrimerization catalyzed by $[RhCl(PPh_3)_3]$ 38

Figure 1.16. Relevant properties of allenes in synthetic organic chemistry. 47

Figure 1.17. Algorithm employed in the SCF approach. 57

Figure 1.18. Graphical representation of Perdew's Jacob's ladder 61

Figure 1.19. Representation of the potential energy as a function of (a) 2 geometric parameters (b) 1 geometric parameter. 62

Figure 1.20. Evolution of the energy vs. optimization steps during a geometry optimization calculation of a transition metal complex. Curly arrows are rough representations of three optimization steps. 63

Figure 1.21. Example of force and displacement values reported by Gaussian's output file after every optimization step. 64

Figure 1.22. Relaxed scan defining the LST between the reacting complex and biradical intermediate in the attack of cyclopentadiene to a carbon atom of $^{\#6094}C_{68}$. 64

Figure 1.23. IRC representation for a DA reaction.. 65

Figure 1.24. Graphical representation of TDI, TDTS and δE according to the energetic span model. 67

Figure 1.25. Schematic representation of the ASM for the DA cycloaddition of cyclopentadiene and C_{60}... 70

Figure 8.1. M06L-D3/cc-pVTZ-PP//B3LYP-D3/cc-pVDZ Gibbs energy profile for the oxidative coupling step (Red = path A; Blue = path B). Energies in parentheses are electronic energies. 138

Figure 8.2. M06L-D3/cc-pVTZ-PP//B3LYP-D3/cc-pVDZ Gibbs energy profile for the insertion steps (Red = path A; Blue = path B). Energies in parentheses are electronic energies. 139

Figure 8.3. M06L-D3/cc-pVTZ-PP//B3LYP-D3/cc-pVDZ Gibbs energy profile for the reductive elimination step and product release. Energies in parentheses are electronic energies. 140

Figure 8.4. M06L-D3/cc-pVTZ-PP//B3LYP-D3 Gibbs energy profiles for the [2+2+2] cycloaddition reaction catalyzed by Wilkinson's complex of (a) C_{60} and to acetylene molecules, and (b) three acetylene molecules. Energies in parentheses are electronic energies. Blue = C_{60} path; Red = acetylene cyclotrimerization path. 140

Figure 8.5. M06L-D3/cc-pVTZ-PP//B3LYP-D3 Gibbs energy profile for the [2+2+2] cycloaddition reaction of C_{60} and to acetylene molecules catalyzed by Wilkinson's complex. Gas phase vs. toluene solution (SMD). Blue = gas phase. Red = solvent = toluene. Energies in parentheses are electronic energies. 141

Figure 8.6. Structure of homocoupled **1a**. 142

Figure 8.7. Structure of a) obtained bis(fulleroid) **2a**, and b) expected 1,3-cyclohexadiene product. Selected ^{1}H and ^{13}C (*in italics*) NMR chemical shifts of **2a**. 143

Figure 8.8. Scope of the Rh(I)-catalyzed [2+2+2] cycloaddition of C_{60} with diynes. Reaction conditions: 0.07 mmol of C_{60}, 5 equivalents of diyne **1**, 10% mol of Rh catalyst in 50 mL of o-dichlorobenzene (*o*-DCB) at 90 °C for 4h. The 10% mol mixture of $[Rh(cod)_2]BF_4$ and Tol-BINAP was treated with hydrogen in dichloromethane (DCM) solution for catalyst activation prior to substrate addition. 144

Figure 8.9. M06-D3/cc-pVTZ-PP//B3LYP-D3/cc-pVDZ Gibbs energy profile for the [2+2+2] cycloaddition of model diyne and C_{60}. Energies in parentheses are electronic energies. 146

Figure 8.10. B3LYP-D3/cc-pVDZ-PP relaxed scan for the [4+4] cycloaddition. Blue = singlet state. Red = triplet state. 147

Figure 8.11. M06/cc-pVTZ-PP//B3LYP-D3/ccpVDZ Gibbs energy profile for the di-p-methane rearrangement. Energies in parentheses are electronic energies. Blue = open-shell singlet. Red = triplet state. Black = singlet state. *Not calculated. We estimate the energy of intermediate C1'' is similar to the one of the triplet state partner C1'. 147

Figure 8.12. M06-D3/cc-pVTZ-PP//B3LYP-D3/cc-pVDZ Gibbs energy profile for the Rh-catalyzed cage-opening di-π-methane rearrangement. Energies in parentheses are electronic energies. 148

Figure 8.13. (a) Representation of HOMO/LUMO energy levels estimated from CV and UV-vis experiments (eV). (b) PL spectra of perovskite and perovskite/ETL films. 150

Figure 8.14. (a) *J-V* curves of devices incorporationg open-cage dicarbonyl derivatives **5a-c** and $PC_{61}BM$. (b) PCE measured for 25 independent cells, average values and representation of the standard deviation (SD). 151

Figure 8.15. Scope of the cycloaddition of 1,5-bisallenes **1** and alkenes **2**. 155

Figure 8.16. HPLC trace of compound **3aa** obtained (a) using (±)-BINAP as a diphosphine ligand and (b) under optimal conditions, using (*R*)-DTBM-Segphos as a phosphine ligand. Conditions: Chiralpak IA column

(4.6 x 250 mm, 5 μm); 1 mL/min flow rate; 100% hexane → 20% 2-propanol in hexane; 40 min.; λ= 254 nm. 156

Figure 8.17. M06L-D3/cc-pVTZ-PP/SMD(76% THF, 24% CH_2Cl_2)//B3LYP-D3/cc-pVDZ-PP Gibbs energy profile for the tandem cycloisomerization/DA cycloaddition leading to product **3aa** (Path A) and cycloisomerization reaction leading to product **4a** (Path B). RC = reactant complex. 157

Figure 8.18. M06L-D3/cc-pVTZ-PP/SMD(76% THF, 24% CH_2Cl_2)//B3LYP-D3/cc-pVDZ-PP Gibbs energy profile for the tandem cycloisomerization/DA cycloaddition leading to product **3aa** (DA cycloaddition involving **A2**). 157

Figure 8.19. M06L-D3/cc-pVTZ-PP/SMD(76% THF, 24% CH_2Cl_2)//B3LYP-D3/cc-pVDZ-PP Gibbs energy profile for the tandem cycloisomerization/DA cycloaddition leading to product **3aa** (DA cycloaddition involving **A3**). 158

Figure 8.20. M06L-D3/cc-pVTZ-PP/SMD(76% THF, 24% CH_2Cl_2)//B3LYP-D3/cc-pVDZ-PP Gibbs energy profile for the tandem cycloisomerization/DA cycloaddition leading to product **3aa** (DA cycloaddition involving **A4**). 158

Figure 8.21. M06L-D3/cc-pVTZ-PP/SMD(76% THF, 24% CH_2Cl_2)//B3LYP-D3/cc-pVDZ-PP Gibbs energy profile for the transformation of intermediate **C1** into intermediate **A2** catalysed by $[Rh(BINAP)]^+$. 159

Figure 8.22. Schlegel diagrams of fullerene $^{\#6094}C_{68}$ showing (a) arbitrary atom numbering and (b) arbitrary bond numbering. 164

Figure 8.23. UB3LYP-D3/6-31G(d,p) Gibbs energy profile for the [5,5] and $[5,6]_F$ paths. Electronic energies given in parentheses. 165

Figure 8.24. Comparative EDA of the $[5,5]/[5,6]_F$ and [6,6] attacks computed at the UM06-2X-D3/TZVP//UB3LYP-D3/6-31G(d,p) level of theory. 166

Supplementary material

Figure S1. M06L-D3/cc-pVTZ//B3LYP/cc-pVDZ Gibbs energy profile for the C_{60} acetylene [2+2+2] cycloaddition catalyzed by Wilkinson's complex. Path A involving [6,6] bond. Electronic energies (Δ*E*) shown in parentheses. Blue: 1 PPh_3; Red = 0 PPh_3. Structures shown for the lowest energy path. S5

Figure S2. M06L-D3/cc-pVTZ//B3LYP/cc-pVDZ Gibbs energy profile for the C_{60} acetylene [2+2+2] cycloaddition catalyzed by Wilkinson's complex. Path A involving [5,6] bond. Electronic energies (Δ*E*) shown in parentheses. Blue: 1 PPh_3; Red = 0 PPh_3. Structures shown for the lowest energy path. S6

Figure S3. M06L-D3/cc-pVTZ//B3LYP/cc-pVDZ Gibbs energy profile for the C_{60} acetylene [2+2+2] cycloaddition catalyzed by Wilkinson's complex. Path B involving [6,6] bond. Electronic energies (Δ*E*) shown in parentheses. Green = 2 PPh_3; Blue: 1 PPh_3; Red = 0 PPh_3. Structures shown for the lowest energy path. . S7

Figure S4. M06L-D3/cc-pVTZ//B3LYP/cc-pVDZ Gibbs energy profile for the C_{60} acetylene [2+2+2] cycloaddition catalyzed by Wilkinson's complex. Path B involving [5,6] bond. Electronic energies (Δ*E*) shown in parentheses. Green = 2 PPh_3 Blue: 1 PPh_3; Red = 0 PPh_3. Structures shown for the lowest energy path. .. S8

Figure S5. M06L-D3/cc-pVTZ//B3LYP/cc-pVDZ Gibbs energy profile for the C_{60} acetylene [2+2+2] cycloaddition catalyzed by Wilkinson's complex. Path C involving [6,6] bond. Electronic energies (ΔE) shown in parentheses. Blue: 1 PPh_3; Red = 0 PPh_3. Structures shown for the lowest energy path. S9

Figure S6. M06L-D3/cc-pVTZ//B3LYP/cc-pVDZ Gibbs energy profile for the C_{60} acetylene [2+2+2] cycloaddition catalyzed by Wilkinson's complex. Path C involving [5,6] bond. Electronic energies (ΔE) shown in parentheses. Blue: 1 PPh_3; Red = 0 PPh_3. Structures shown for the lowest energy path. S10

Figure S7. M06-D3/cc-pVTZ-PP//B3LYP-D3/cc-pVDZ-PP Gibbs energy profile for the transformation of **A1** into **A2** through **TS A1A2**. Comparison between dimethylphosphine vs diphenylphosphine models. S23

Figure S8. M06-D3/cc-pVTZ-PP//B3LYP-D3/cc-pVDZ-PP Gibbs energy profile for alternative Path A. S25

Figure S9. M06-D3/cc-pVTZ-PP//B3LYP-D3/cc-pVDZ-PP Gibbs energy profile for path B................... S26

Figure S10. Absorption spectra of compounds **5a-c** and $PC_{61}BM$. S29

Figure S11. Cyclic voltammetry of compounds **5a-c.** Conditions: 0.1 mM C_{60}/**2a/4b-c/5a** and 0.05 M $Bu_4N^+PF_6$- in o-dichlorobenzene, silver wire pseudo-reference reference electrode, 1 mm glassy carbon disk working electrode, Pt wire auxiliary electrode, scan rate 100 mV.s^{-1}, 25 °C**.** S29

Figure S12. Chlorobenzene solutions (20 mg/ml) of **5a-b** and $PC_{61}BM$. **5c** dissolves only partially in chlorobenzene.. S29

Figure S13. TR-PL of perovskite, perovskite/compounds **2a-c** and perovskite/$PC_{61}BM$ films. S30

Figure S14. Stability of 5a-c and $PC_{61}BM$ devices... S30

Figure S15. *J-V* curves of the inverted PSCs based on **2a,b** with respect to forward and reverse scan directions (the scanning rate was 100 mV/s).. S30

Figure S 16. UB3LYP-D3/6-31G(d,p) Gibbs energy profile for the formation of adduct [6,6]. All energies are relative to infinitely separated reactants and are given in kcal·mol^{-1}. S52

Figure S17. UB3LYP-D3/6-31G(d,p) Gibbs energy profile for the formation of adduct [5,6]F. All energies are relative to infinitely separated reactants and are given in kcal·mol^{-1}. S52

Figure S18. UB3LYP-D3/6-31G(d,p) Gibbs energy profile for the formation of adduct [5,5]. All energies are relative to infinitely separated reactants and are given in kcal·mol^{-1}. S53

Figure S19. UB3LYP-D3/6-31G(d,p) Gibbs energy profile for the formation of adduct [5,6]D. All energies are relative to infinitely separated reactants and are given in kcal·mol^{-1}. S53

Figure S20. UB3LYP-D3/6-31G(d,p) Relaxed scan between biradical intermediate and reaction product (triplet state, path [6,6]). S54

Figure S21. UB3LYP-D3/6-31G(d,p) Relaxed scan between biradical intermediate and reaction product (Open-shell singlet state, path $[5,6]_F$). S54

Figure S22. UB3LYP-D3/6-31G(d,p) Relaxed scan between biradical intermediate and reaction product (Open-shell singlet state, path $[5,6]_D$).. S55

List of schemes

Scheme 1.1. Planar embedding (no crossing edges) for three different fullerenes obtained from a perspective projection. (a) icosahedron C_{20}-I_h; (b) truncated icosahedron C_{60}-I_h; (c) C_{540}-I_h 4

Scheme 1.2. Classification of different bond types that might be present in a fullerene. 5

Scheme 1.3. Common chemical reactions used to functionalize C_{60}. 9

Scheme 1.4. Strain release exemplified with the [4+2] cycloaddition of C_{60} with cyclohexadiene. 10

Scheme 1.5. Functionalization of C_{60} through anionic intermediates. 10

Scheme 1.6. Fullerene functionalization through fullerenyl cation intermediates. 11

Scheme 1.7. (a) Original Bingel cyclopropanation of C_{60}. (b) Hirsch's protocol starting from malonates via *in situ* bromination with CBr_4 and DBU. 12

Scheme 1.8. Transition metal-catalyzed 1,2-hydroarylation of C_{60}. 12

Scheme 1.9. Synthesis of a pentamethyl bucky ferrocene. 13

Scheme 1.10. Synthesis of [6,6] closed and [5,6] open fulleroids formed by reaction of C_{60} with diazo compounds. 14

Scheme 1.11. Synthesis of Phenyl-C_{61}-butyric acid methyl ester ($PC_{61}BM$) from C_{60} and a tosylhydrazone derivative. 14

Scheme 1.12. Transition metal-mediated synthesis of methanofullerenes. 15

Scheme 1.13. 1,3-dipolar cycloaddition of C_{60} and azomethine ylides (Prato Reaction). 15

Scheme 1.14. [2+2] cycloadditions involving C_{60} 16

Scheme 1.15. DA reactions between C_{60} and different dienes or diene precursors. 17

Scheme 1.16. Regioselective Pauson-Khand reaction of a propargylic fulleropyrrolidine adduct. 17

Scheme 1.17. Selected examples of palladium-mediated annulation reactions. 18

Scheme 1.18. Miscellaneous transition metal-mediated radical cyclization reactions. 19

Scheme 1.19. The 8 possible addition patterns for 2-fold addition to C_{60}. Symmetry of the corresponding bisadducts and yields obtained after two successive Bingel additions of diethyl 2-bromomalonate. E = $COOCH_2CH_3$ 21

Scheme 1.20. Use of anthracene and DMA as templates in fullerene functionalization (E = $COOCH_2CH_3$). 22

Scheme 1.21. Tether-controlled multiple functionalization of C_{60}. FG = functional group. 23

Scheme 1.22. Photooxygenative cleavage of azafulleroids. 24

Scheme 1.23. Formation and photooxygenative cleavage of bis(fulleroids). R= CH_3, $C(CH_3)_3$, CH_2CF_3. 24

Scheme 1.24. 19-membered hole open-cage C60 derivative synthetized from a fullerene-mixed peroxide. CAN = cerium (IV) ammonium nitrate. 25

Scheme 1.25. Encapsulation of small molecules in different open-cage fullerene derivatives. 25

Scheme 1.26. Molecular surgery applied to the preparation of $H_2@C_{60}$. 26

Scheme 1.27. Transition metal-catalyzed cyclotrimerization of alkynes (M = transition metal catalyst) 35

Scheme 1.28. Tethered and non-tethered [2+2+2] cycloaddition reactions of alkynes. "M" = metal complex. 36

Scheme 1.29. Simplified representation of the generally accepted mechanism of the transition metal-catalyzed [2+2+2] cycloaddition involving three alkynes. 37

Scheme 1.30. Synthesis of estrone by means of a Co-catalyzed [2+2+2] cycloaddition reaction. 39

Scheme 1.31. Synthesis of (±)-viridin by means of a Rh-catalyzed [2+2+2] cycloaddition reaction. 39

Scheme 1.32. Rh(I)-catalyzed totally intramolecular [2+2+2] cycloaddition reactions of macrocycles reported by our research group. 39

Scheme 1.33. Simplified mechanism for the formation of 1,2.4-substituted and 1,3,5-substituted isomers in alkyne homo-trimerization. 40

Scheme 1.34. Chemo- and regioselective alkyne cyclotrimerizations reported by Tanaka. E = $COOCH_2CH_3$. 40

Scheme 1.35. Rh-catalyzed [2+2+2] cycloadditions towards the synthesis of CPPs and polyaromatic hydrocarbons. 41

Scheme 1.36. Intermolecular transition metal-catalyzed [2+2+2] cycloaddition reactions of alkynes and nitriles. 42

Scheme 1.37. Synthesis of an hexacyclic bipyridine derivative from diynenitriles developed by our group. 42

Scheme 1.38. Generation of central chirality in alkene-involving transition metal-mediated partially intramolecular [2+2+2] cycloadditions. **M*** = chiral catalytic system. 43

Scheme 1.39. Stereoselective enyne-ene and diyne-ene reactions. 44

Scheme 1.40. Rh(I)-catalyzed three component [2+2+2] cycloaddition of two different alkynes and one alkene. 44

Scheme 1.41. Different reaction paths explain differences in enantioselectivity of Rh(I)-catalyzed [2+2+2] cycloadditions of linear enediynes. R and Z groups determine which of two pathways is preferred, as shown by our computational study [298]. 45

Scheme 1.42. Mechanism involved in the Wilkinson's complex-catalyzed [2+2+2] cycloadditions of enediynes with an yne-yne-ene sequence.. 45

Scheme 1.43. Miscellaneous examples of Rh(I)-catalyzed [2+2+2] cycloadditions generating (a) planar, (b) helical and (c) axial chirality. 46

Scheme 1.44. Ni-catalyzed [2+2+2] cycloadditions of 1,2-propadiene. 47

Scheme 1.45. Diastereoselective synthesis of a steroid-like compound from an allene-diyne substrate. 48

Scheme 1.46. Rh-catalyzed **i**ntramolecular [2+2+2] cycloadditions involving allenes developed by our group. 48

Scheme 1.47. [2+2+2] cycloaddition reactions of allene-enes and alkenes or allenes. E = $CO_2CH_2CH_3$ 49

Scheme 1.48. [2+2+2] cycloadditions involving 1,5-bisallenes. 49

Scheme 1.49. Transition metal- catalyzed cycloisomerization reactions of 1,5-bisallenes. 50

Scheme 1.50. Phosphine-catalyzed formal [2+2+2] cycloaddition of alkynes and C_{60} 50

Scheme 1.51. Ni-promored [2+2+2] cycloaddition of diynes and C_{60}**.** 51

Scheme 1.52. Reaction of C_{60} with a palladacylopentadiene complex**.** 51

Scheme 1.53. Unsaturated substrates used in transition metal-catalyzed [2+2+2] cycloaddition reactions. .. 52

Scheme 2.1. Simplified representation of the objectives dealing with C_{60} functionalization.......................... 76
Scheme 2.2. Hypothetic mechanism for the [2+2+2] cycloaddition of 1,5-bisallenes with alkenes. 76
Scheme 2.3. General stepwise mechanism considered for the reaction of $^{6094}C_{68}$ with cyclopentadiene........ 77
Scheme 8.1. Simplified reaction model used to study the [2+2+2] cycloaddition of C_{60} and 2 alkynes....... 138
Scheme 8.2. Further functionalization of bis(fulleroids) **2**. 145
Scheme 8.3. Synthesis of the three open-cage dicarbonyl derivatives incorporated in PSCs...................... 149
Scheme 8.4. Simplified mechanistic pathway for the [2+2+2] cycloaddition of 1,5-bisallenes and an alkene 153
Scheme 8.5. Proposed reaction mechanism for the transformation of bisallene **1** into reaction product **3**... 154
Scheme 8.6. Isolation of **6a** in mechanistic experiments indirectly reveal the formation of a triene intermediate **A5**. 159
Scheme 8.7. General stepwise mechanism for the DA cycloaddition involving $^{\#6094}C_{68}$ and cyclopentadiene. 163

Supplementary material

Scheme S1. Synthesis of diynes **1d** and **1e**. S13
Scheme S2.Synthesis of bis(fulleroids) **2a-h**, **2k** and **2o**. S14
Scheme S3. Synthesis of compounds **4a-c** by Suzuki-Miyaura cross-coupling S20
Scheme S4. Oxidative photocleavage of fulleroid derivative **2a**. S22
Scheme S5. Oxidative photocleavage of compounds **2a**, **2e** and **4b**. S27
Scheme S6. Synthesis of diyne **S4**. S31
Scheme S7. Synthesis of bisallenes **1a-b**. S31
Scheme S8. General procedure for the synthesis of product **3aa**. S34
Scheme S9. Mechanistic experiments using compound **5a** and ethyl acrylate **2a** S42
Scheme S10. Mechanistic experiments using compound **5a**, ethyl acrylate **2a** and Rh(I) catalyst S43
Scheme S11. Synthesis of **7a** S44

List of tables

Table 8.1. Rh(I)-catalyzed [2+2+2] cycloaddition of C_{60} with diyne **1a**: Optimization of reaction parameters. 143

Table 8.2. Redox potentials of fulleroids **2a**, **4b**, **4c**, **5a** and C_{60}. E½ in V vs Fc/Fc+, 0.2 mM C_{60}/**2a/4b-c/5a** and 0.1 M $Bu_4N^+ClO_4$- in o-dichlorobenzene, SCE reference electrode, Pt working electrode, Pt wire auxiliary electrode, scan rate 50 mV.s-1, 25 °C). 146

Table 8.3. Rh(I)-catalyzed cycloaddition of **1a** with ethyl acrylate **2a**. Optimization of reaction parameters. 154

Table 8.4. Rh(I)-catalyzed cycloaddition of **1a** with C_{60}: Optimization of reaction parameters. 160

Supplementary material

Table S1. Optimization of the Rh(I)-catalyzed cycloaddition of bisallene **1a** with alkene **2a**. S33

Table S2. UB3LYP/6-31G(d,p) reaction energies (ΔEr) of all possible $^{\#6094}C_{68}$-Cp adducts. S47

Table of contents

Chapter 1. Introduction 1

Section 1: The chemistry of fullerenes 3

1.1. Carbon nanoallotropes 3
1.2. Fullerenes: spherical allotropes of carbon 4
1.3. Endohedral fullerene complexes 5
1.4. Production of fullerenes 6
1.5. Spectroscopic and physicochemical properties of fullerenes 7
1.6. Exohedral functionalization of fullerenes 9
1.7. “There is a hole in my bucky”: chemistry and applications of open-cage fullerenes 23
1.8. Functional fullerenes: from biomedicine to next-generation photovoltaics 26

Section 2: Transition metal-catalyzed [2+2+2] cycloaddition reactions 35

2.1. General aspects 35
2.2. Mechanism 36
2.3. Transition-metal promoted [2+2+2] cycloadditions in synthetic organic chemistry 38

Section 3: Computational chemistry and molecular modeling 53

3.1. Combining theory and experiments: a powerful approach 53
3.2. Computational numerical techniques 54
3.3. Modeling reaction mechanisms 61
3.4. Computational methods used in this thesis 70

Chapter 2. General objectives 73

Section 1: Rh(I) catalyzed [2+2+2] cycloadditions of fullerenes and alkynes 75

Section 2: A Rh-catalyzed cycloisomerization/Diels-Alder cascade reaction of 1,5-bisallenes for the synthesis of polycyclic heterocycles and the functionalization of fullerenes 76

Section 3: Regioselectivity in Diels–Alder cycloadditions of $^{\#6094}C_{68}$ fullerene with a triplet ground state 77

Chapter 3.

A computational study of the intermolecular [2+2+2] cycloaddition of acetylene and C_{60} catalyzed by Wilkinson's Catalyst 79

Chapter 4.

Expeditious preparation of open-cage fullerenes by rhodium(I)-catalyzed [2+2+2] cycloaddition of diynes and C_{60}: an experimental and theoretical study 89

Chapter 5.

Enhanced open-circuit voltage in perovskite solar cells with open-cage [60]Fullerene derivatives as electron-transporting materials 103

Chapter 6.

A Rh-catalyzed cycloisomerization/Diels-Alder cascade reaction of 1,5-bisallenes for the synthesis of polycyclic heterocycles 115

Chapter 7.

Regioselectivity in Diels–Alder cycloadditions of $^{\#6094}C_{68}$ fullerene with a triplet ground state 125

Chapter 8. Results and Discussion 135

Section 1: Rh(I) catalyzed [2+2+2] cycloadditions of fullerenes and alkynes 137

1.1. A computational study of the intermolecular [2+2+2] cycloaddition of acetylene and C_{60} catalyzed by Wilkinson's complex 137

1.2. Expeditious preparation of open-cage fullerenes by rhodium(I)-catalyzed [2+2+2] cycloaddition of diynes and C_{60}: an experimental and theoretical study 141

1.3. Enhanced open-circuit voltage in perovskite solar cells with open-cage [60]Fullerene derivatives as electron-transporting materials in 148

Section 2: A Rh-catalyzed cycloisomerization/Diels-Alder cascade reaction of 1,5-bisallenes for the synthesis of polycyclic heterocycles and the functionalization of fullerenes 153

Section 3: Regioselectivity in Diels–Alder cycloadditions of $^{\#6094}C_{68}$ fullerene with a triplet ground state 163

Chapter 9. Conclusions 167

Section 1: Rh(I) catalyzed [2+2+2] cycloadditions of fullerenes and alkynes 169

Section 2: A Rh-catalyzed cycloisomerization/Diels-Alder cascade reaction of 1,5-bisallenes for the synthesis of polycyclic heterocycles and the functionalization of fullerenes 170

Section 3: Regioselectivity in Diels–Alder cycloadditions of $^{\#6094}C_{68}$ fullerene with a triplet ground state 170

References 171

Supplementary material S1

Supplementary digital material S3

Supplementary material for chapter 3 .... S5

Supplementary material for chapter 4 .... S13

Supplementary material for chapter 5 .... S27

Supplementary material for chapter 6 .... S31

Supplementary material for chapter 7 .... S47

Chapter 1. Introduction

Section 1: The chemistry of fullerenes

1.1. Carbon nanoallotropes

Only two forms of elemental carbon were known until the end of the 20th century: graphite, which consists of layers of hexagonally arranged sp^2-hybridized carbon atoms in a planar condensed ring system, and diamond, formed by sp^3 carbon atoms tridimensionally organized in a cubic structure [1]. In 1985, an unexpected yet groundbreaking discovery by Kroto, Curl and Smalley completely altered this conception [2]. During a series of experiments directed to understand how long-chain carbon molecules are formed in space, this group of scientists detected C_{60} for the first time and proposed its unique truncated icosahedral structure. The serendipitous discovery of C_{60} deserved the Nobel Prize in chemistry in 1996, and quickly stimulated the discovery and development of many other *carbon nanostructures* [3,4] such as onion-like carbon [5], carbon nanotubes [6], carbon nanohorns [7], graphene [8] and other combined structures like carbon peapods [9] (**Figure 1.1**). All these recently discovered carbon allotropes have one feature in common: they mainly consist of hexagonal networks of sp^2 carbon atoms arranged in different shapes and sizes that determine their electronic and physicochemical properties. Carbon nanostructures have received increasing attention over the last three decades not only because of their fascinating nature, but also because of their potential application as next-generation functional materials in a wide variety of fields, like energy conversion and storage [10], sensing [11], electronics [12], environmental science [13] or biomedicine [14]. In addition to the sp^3 and sp^2 forms of carbon, a new molecular sp-hybridized carbon allotrope, cyclo[18]carbon, has been reported very recently by Anderson [15].

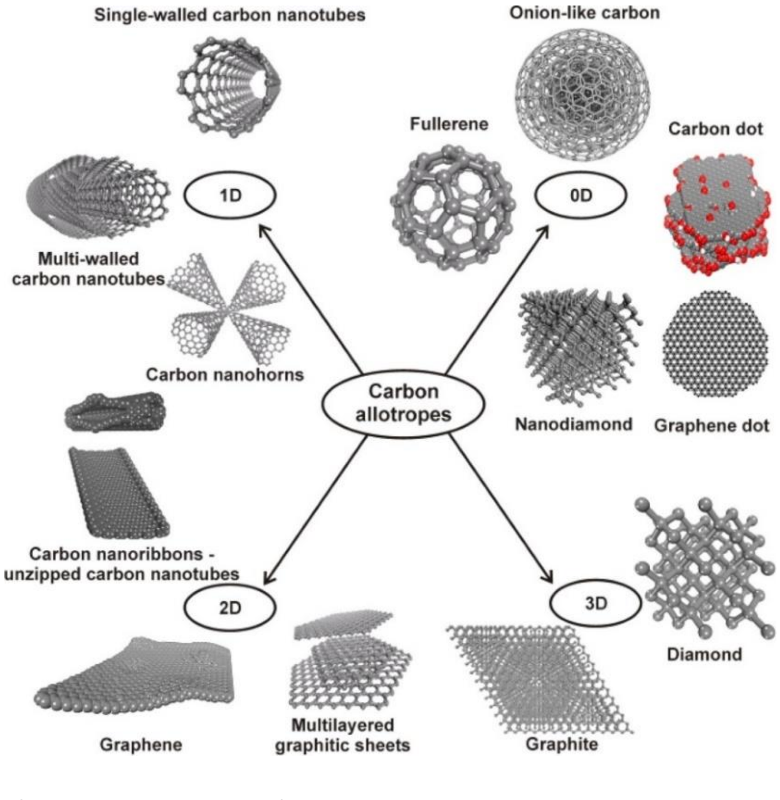
Single-walled carbon nanotubes
Onion-like carbon
Fullerene
Carbon dot
1D
0D
Multi-walled carbon nanotubes
Carbon nanohorns
Carbon allotropes
Nanodiamond
Graphene dot
Carbon nanoribbons - unzipped carbon nanotubes
2D
3D
Diamond
Graphene
Multilayered graphitic sheets
Graphite

Figure 1.1. Allotropes of carbon and their classification according to dimensionality. Reprinted with permission from: Vasilios Georgakilas; Jason A. Perman; Jiri Tucek; Radek Zboril; *Chem. Rev.* **2015**, *115*, 4744. Copyright © 2015 American Chemical Society (ACS) [4].

1.2. Fullerenes: spherical allotropes of carbon

Fullerenes are defined as a family of molecules composed of an even number of carbon atoms forming a cage-like fused-ring polycyclic system of 5-membered rings (5-MR) and 6-MR [1]. They can be regarded as convex *Goldberg polyhedra* [16] with carbon atoms at the vertices, C–C bonds along edges and rings (5 and 6-MRs) forming faces. Therefore, according to Euler's theorem [17], they must satisfy the following properties:

$$\frac{5p + 6h}{3} = n \qquad \text{(Eq. 1.1)}$$

$$p + h = \frac{n}{2} + 2 \qquad \text{(Eq. 1.2)}$$

Where p is the number of pentagonal faces, h is the number of hexagonal faces and n denotes the total number of vertices (carbon atoms, C_n). From these two equations, one can derive that for every fullerene: $p = 12$ and $h = n/2 - 10$. According to these statements, every fullerene with 20 or more carbon atoms ($C_n \geq 20$) could be formed, with the single exception of C_{22}. However, very few cages with $n \leq 40$ have been identified [18].

Obviously, for a given number of vertices, several different polyhedra can be constructed depending on how pentagons and hexagons are arranged. In chemical terms, this means that different isomeric fullerene cages can exist –at least theoretically– with the same C_n value. For clarification purposes, fullerene cages are commonly represented as two-dimensional graphs –*Schlegel diagrams*– that result from "flattening" a fullerene cage onto a plane (**Scheme 1.1**). Furthermore, every fullerene isomer can be systematically numbered and encoded by the *face spiral* algorithm, obtained by unwinding the faces of the Schlegel diagram forming a spiral. As recommended by the IUPAC [19], point group symmetry must be used when naming fullerenes in order to distinguish different isomers (*e.g.* C_{60}-I_h and C_{70}-D_{5h}). A thorough discussion on the topology of fullerenes can be found in Fowler's *An atlas of fullerenes* [20] and also in a more recent review article by Avery [21].

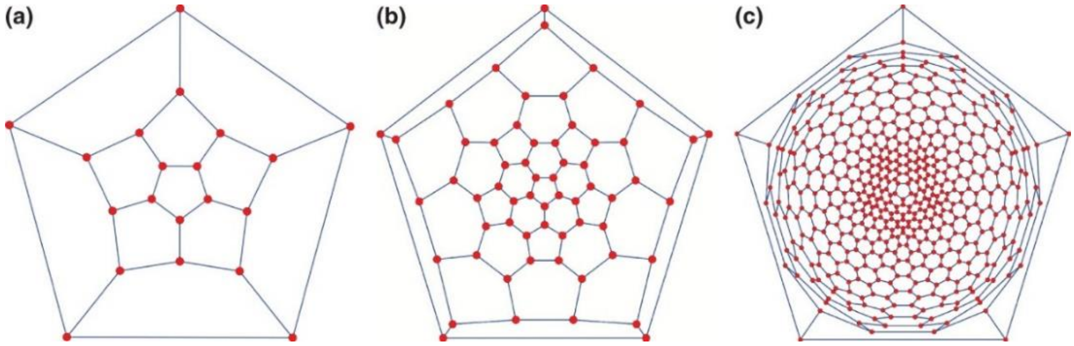

Scheme 1.1. Planar embedding (no crossing edges) for three different fullerenes obtained from a perspective projection. (a) icosahedron C_{20}-I_h; (b) truncated icosahedron C_{60}-I_h; (c) C_{540}-I_h. Reprinted with permission from: Schwerdtfeger, P.; Wirz, L. N.; Avery, J. *WIRES. Comput. Mol. Sci.* **2015**, *5*, 96. Copyright © 2014 The Authors. Wiley & Sons, Ltd [21].

The stability of fullerenes is dictated by the so-called *isolated pentagon rule* (IPR), proposed by Kroto two years after the discovery of fullerenes [22]. This rule states that fullerenes with all pentagons (5-MR) surrounded by hexagons (6-MR) are more stable than those containing contiguous 5-MR. The reason for such preference is that bonds shared by two pentagons increase local strain, giving rise to considerably less stable cages [23]. Stabilization of non-IPR fullerene molecules can be achieved by releasing the strain generated by fused 5-MRs through chemical functionalization or by inclusion of metal clusters [24]. While the vast majority of hollow fullerenes fulfill the IPR, a few examples like $^{\#6094}C_{68}$ contain fused 5-MR in their structure [25,26]. Chapter 7 of this thesis is dedicated to the reactivity of this singular non-IPR fullerene cage, whose chemical reactivity was studied by computational means.

Two different classes of C–C bonds are present in IPR fullerenes. [6,6] Bonds are considered double bonds and form the edges between two 6-MRs. Conversely, [5,6] bonds are considered single bonds and are found at the intersection between 5-MRs and 6-MRs. For non-IPR species, one has to consider also the presence of [5,5] bonds (**Scheme 1.2**).

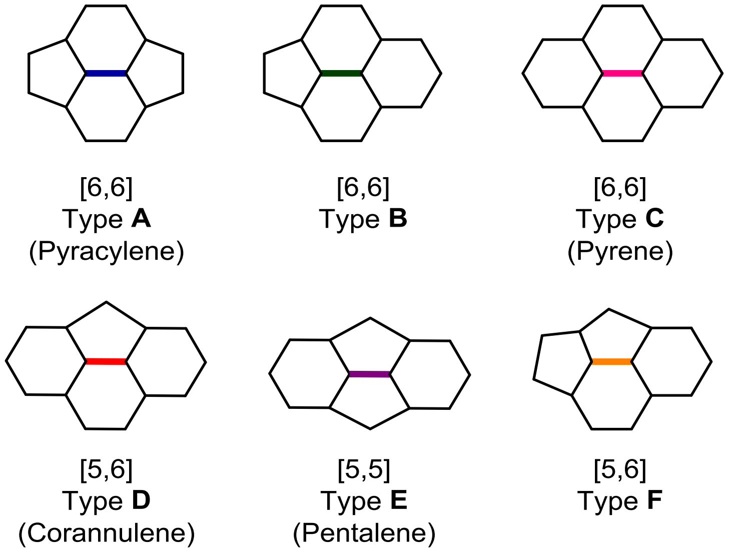

Scheme 1.2. Classification of different bond types that might be present in a fullerene.

1.3. Endohedral fullerene complexes

The hollow nature of fullerenes soon allowed chemists to predict their ability to encapsulate atoms or small molecules in their cavity. In fact, only a few months after the publication of the pioneering work by Kroto, Curl and Smalley [2], the same authors proposed the first *endohedral fullerene-metal complexes* with a C_nLa formula [27]. Such species were observed by mass spectrometry after laser vaporization of graphite in analogous experiments of those performed to detect the first hollow fullerenes. This new class of metal-entrapping fullerene molecules was later called endohedral metallofullerenes (EMF) and given their own naming rules (**Figure 1.2**). EMFs are denoted with the general formula $M_x(A_y)@C_z$, where M_x is a metal, A_y is a nonmetal (that can be present or not), C_z designates a specific fullerene cage and the @ symbol is used to specify that the metal or metal cluster is actually located inside the cavity. $La@C_{82}$ was the first EMF to be isolated and characterized in 1991 [28]. Since then, a plethora of endohedral fullerene complexes –as well as several synthetic derivatives– have been reported. Moreover, the ability of fullerenes to encapsulate species other than metals (*i.e.* nonmetal atoms, small molecules and metal-nonmetal clusters) has been also demonstrated. Gadolinium EMFs are particularly important members of the fullerene family, since some of them may be used in a near future as magnetic resonance imaging contrast agents [29]. Extensive monographies and reviews on the topic have been published over the years [30–33].

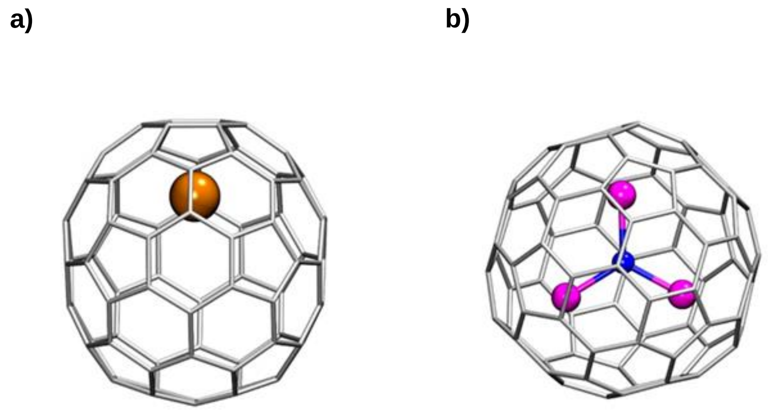

Figure 1.2. Molecular structure of representative EMFs (a) La@C_{82}-C_{2v} (b) Sc_3N@C_{80}-I_h. Adapted with permission from Popov, A. A.; Yang, S.; Dunsch, L. *Chem. Rev.* **2013**, *113*, 5989. Copyright © 2013 American Chemical Society (ACS) [31].

1.4. Production of fullerenes

The highly symmetric icosahedral structure initially proposed for C_{60} remained merely theoretical for 5 years after its discovery. However, in 1990 the field of fullerene chemistry changed forever. In a second remarkable breakthrough, Krätschmer and Huffman managed to produce fullerenes at the gram scale by resistive heating of graphite in an atmosphere of helium [34]. An enhanced version of the Krätschmer-Huffman fullerene generator using an electric arc instead of resistive heating was developed by Smalley [35] soon after. The *arc discharge reactors* still used nowadays for fullerene production are based on this second design (**Figure 1.3a**). The raw material obtained in the Krätschmer-Huffman reactor is a mixture of fullerenes of different sizes, nanotubes and amorphous carbon. Subsequent extraction techniques, neutral alumina chromatography and high-performance liquid chromatography (HPLC) leads to the isolation of fullerenes comprised between C_{60} and C_{100} (**Figure 1.3b)** [36–38].

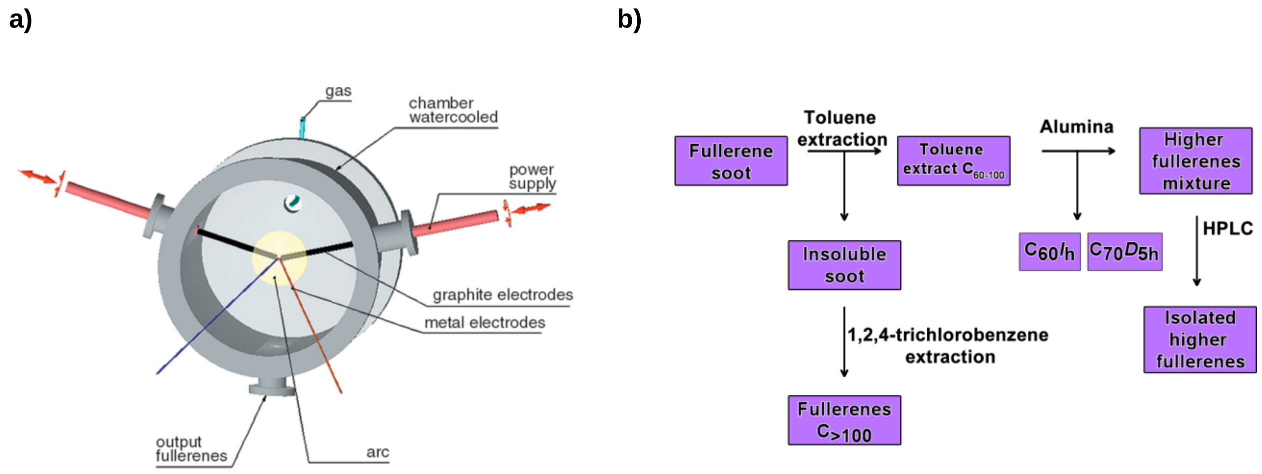
a)
gas
chamber watercooled
power supply
graphite electrodes
metal electrodes
output fullerenes
arc
b)
Fullerene soot
Toluene extraction
Toluene extract C_{60-100}
Alumina
Higher fullerenes mixture
Insoluble soot
C_{60} I_h
C_{70} D_{5h}
HPLC
1,2,4-trichlorobenzene extraction
Isolated higher fullerenes
Fullerenes $C_{>100}$

Figure 1.3. (a) Schematic view of a Krätschmer–Huffman generator. Reprinted with permission from: Popov, A. A.; Yang, S.; Dunsch, L. *Chem. Rev.* **2013**, *113*, 5989. Copyright © 2013 American Chemical Society (ACS) [31]. (b) Fullerene production and separation scheme.

EMFs are generated analogously by using graphite/metal composite rods and replacing helium by reactive atmospheres. The latter applies only for the specific case of *endohedral clusterfullerenes* [39]. In 1991, a completely different approach to generate fullerenes by hydrocarbon flame combustion was reported. This methodology gave access to mass production of fullerenes and commercialization [40].

1.5. Spectroscopic and physicochemical properties of fullerenes

Easy access to macroscopic amounts of fullerenes allowed full spectroscopic and physicochemical characterization of the main cages produced after arc discharge. In many cases, X-ray crystallography allowed confident determination of several cages, thus confirming the predictions made by Fowler, and the general prevalence of the IPR formulated by Kroto [41].

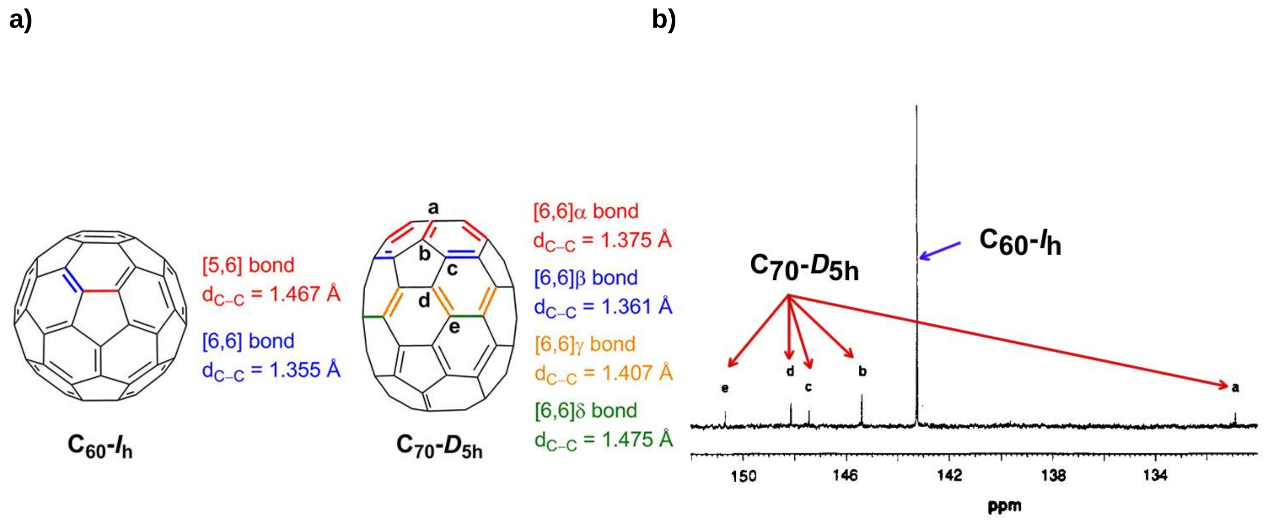

Figure 1.4. (a) Structures and different classes of bonds present in fullerenes C_{60} and C_{70}. Bond distances taken from X-ray structures [42,43]. (b) ^{13}C NMR spectrum of a mixture of a C_{60} and C_{70} mixture in benzene-*d*$_6$. Adapted with permission from: Ajie, H.; Alvarez, M. M.; Anz, S. J.; Beck, R. D.; Diederich. F.; Fostiropoulos, K.; Huffman, D. R.; Krätschmer, W.; Rubin, Y.; Schriver, K. E.; Sensharma, D.; Whetten, R. L. *J. Phys. Chem.* **1990**, *94*, 8630. Copyright © 2013 American Chemical Society (ACS) [44].

In soot, C_{60} is the most abundant fullerene. C_{60}-I_h is its only existing isomer and the smallest one to obey the IPR. Its icosahedral symmetry accounts for the sole signal observable at the ^{13}C NMR spectrum. C_{70}-D_{5h} is the second most abundant fullerene in bulk. It shows an “egg-shaped” geometry and, consequently, five signals attributable to nonequivalent carbon atoms **a-e** are observed in ^{13}C NMR experiments [44]. While C_{60}-I_h has only one kind of [5,6] and [6,6] C–C bonds, C_{70}-D_{5h} has four [5,6] and four [6,6] different C–C bonds (**Figure 1.4**). This feature is of particular relevance from the reactivity point of view, as complex regioisomeric mixtures are usually obtained when functionalizing C_{70}. Both fullerenes are insoluble in polar solvents like methanol, acetone or acetonitrile, poorly soluble in some alkanes and haloalkanes and considerably soluble in aromatic solvents (*e.g.* toluene, 1,2-dicholobenzene, 1-chloronaphtalene) and carbon disulfide.

C_{60}-I_h and C_{70}-D_{5h} have characteristic electronic absorption spectra (**Figure 1.5**). Both show strong absorption bands at the UV region and weaker ones at the visible part (400-700 nm). These latter absorptions correspond to forbidden singlet–singlet transitions and explain the purple and red wine color of C_{60} and C_{70} solutions, respectively [45].

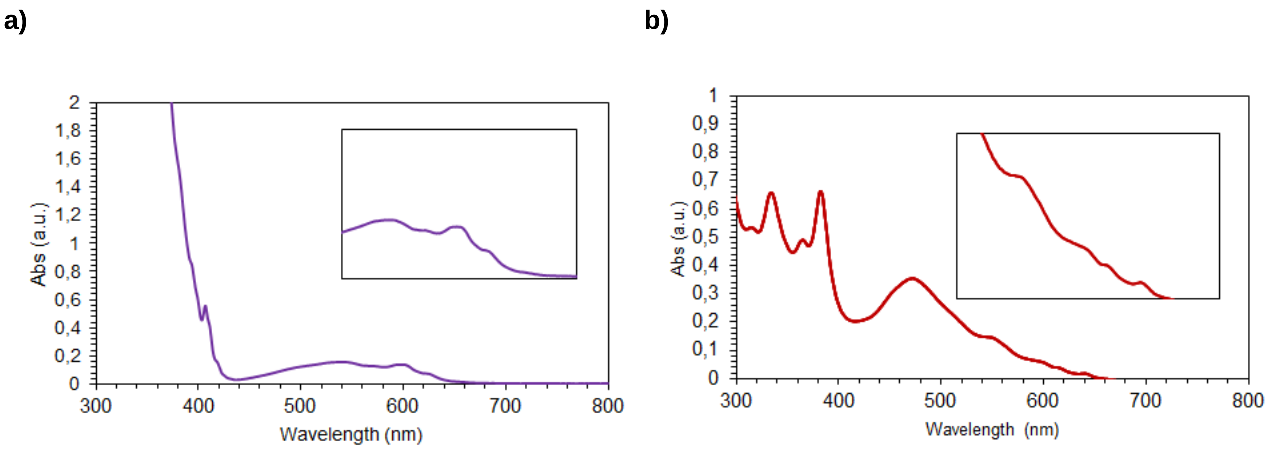

Figure 1.5. Electronic absorption spectra of (a) C_{60} and (b) C_{70} in toluene (data from the author). Insets: 500-700 nm region.

The singlet excited state of C_{60} decays via intersystem crossing (ISC) to the energetically lower-lying triplet excited state with almost quantitative quantum yields (ϕ). $^3C_{60}^*$ can experience a variety of phenomena, such as ground state quenching, singlet oxygen ($^1O_2$) generation or electron transfer from donor molecules with subsequent formation of $C_{60}^{\cdot-}$radical anion which can in turn react with other organic radicals [46,47]. In this sense, fullerenes are often considered *radical sponges* due to their efficiency to undergo these processes [48].

One of the most relevant physical properties of fullerenes is their high electronegativity [49]. Theoretical investigations performed soon after the discovery of C_{60}, anticipated the ability of C_{60} to accommodate up to six electrons, based on the relatively low energy of triply degenerated LUMO and LUMO+1 levels (**Figure 1.6a**). These predictions were confirmed by Echegoyen in 1992, who managed to detect all six consecutive reversible reductions by cyclic voltammetry (CV) and differential pulse polarography experiments (**Figure 1.6b**) [50]. The exceptional photophysical and electrochemical properties of fullerenes, along with their low recombination energy, make them excellent candidates to develop n-type materials for photovoltaic applications.

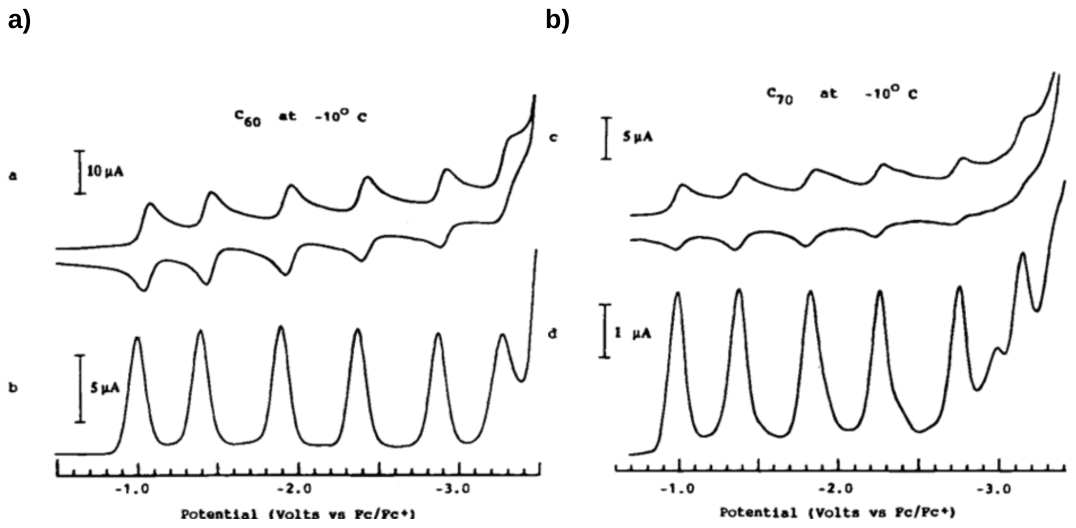

Figure 1.6. Cyclic and differential pulse voltammogram of (a) C_{60} and (b) C_{70}. Adapted with permission from: Reed, C. A.; Bolskar, R. D. *Chem. Rev.* **2000**, *100*, 1075. Copyright © 2000 American Chemical Society (ACS) [49] .

1.6. Exohedral functionalization of fullerenes

Besides characterization and identification of new cages, large-scale availability of fullerenes –mainly C_{60} and, to a lesser degree, C_{70}– opened a whole field of possibilities for synthetic organic chemists. Among all carbon nanostructures, fullerenes are the only *molecular allotropes* of carbon (except for cyclo[18]carbon). They present themselves as discrete entities rather than continuous complex structures, a unique property that make them soluble in a variety of solvents and allow them to be chemically modified in a specific and controlled manner. Thus, a large number of chemical reactions involving covalent derivatization of fullerenes have been developed since the early days of fullerene chemistry at the very beginning of the 1990s [51].

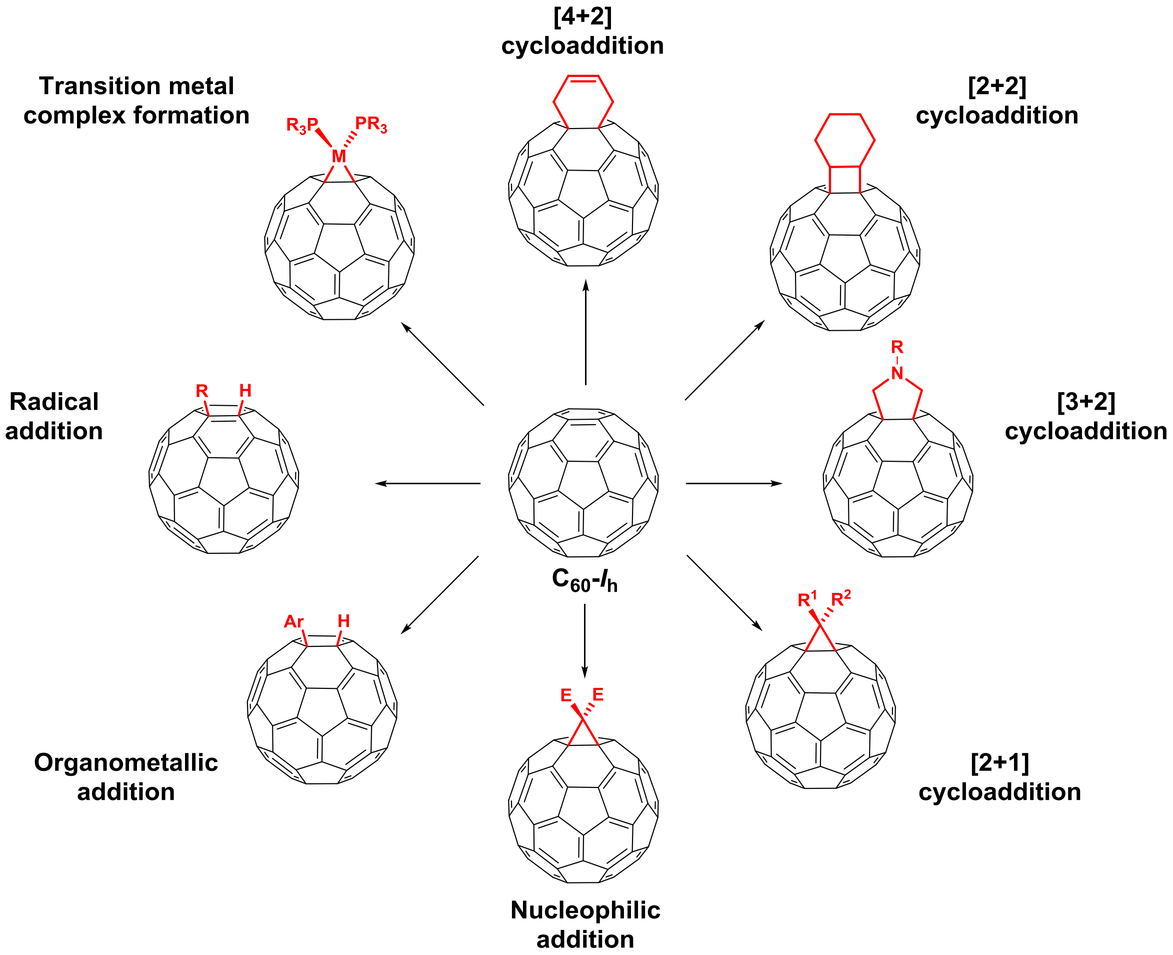
[4+2]
cycloaddition
Transition metal
complex formation
R3P
PR3
M
[2+2]
cycloaddition
R
N
Radical
addition
R
H
[3+2]
cycloaddition
C60-Ih
Ar
H
R1
R2
E
E
Organometallic
addition
[2+1]
cycloaddition
Nucleophilic
addition

Scheme 1.3. Common chemical reactions used to functionalize C_{60}.

Nowadays, almost every functional group can be attached to the fullerene cage by properly choosing a synthetic strategy, and C_{60} has become a common reagent that lies on the benchtops of many synthetic laboratories. From a practical point of view, in general, fullerenes have to be functionalized before they can become useful molecules [52]. This is, to enhance their solubility in common organic solvents, make them soluble in water or tune their photophysical and electrochemical properties, to mention a few examples. A comprehensive monography covering chemical transformations of C_{60} was published by Hirsch some years ago [36] and also several reviews have appeared over the years[52–54]. Some relevant examples are briefly discussed in this section (**Scheme 1.3**).

Although at the beginning C_{60} was considered aromatic, crystallographic data showed that it is more correctly described as a polyene, forming a conjugated π-system that alternates double bonds (*i.e.* pyracylenic [6,6] bonds) and single bonds (*i.e.* corannulenic [5,6] bonds) in a closed spherical network [42]. As a consequence, [6,6] junctions in C_{60} experience analogous reactions to the ones of electron-deficient olefins. Because of its sphere-shaped nature, all 60 sp^2 carbon atoms in C_{60} are considerably strained. The high degree of pyramidalization accounts for the rich reactivity of fullerenes. When reacting with other compounds like dienes or nucleophiles, two involved sp^2 carbon atoms become sp^3-hybridized, causing a release of strain that favors the process to take place [55] (**Scheme 1.4**).

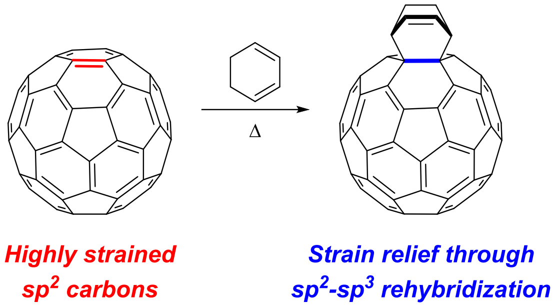
Δ
Highly strained sp^2 carbons
Strain relief through sp^2-sp^3 rehybridization

Scheme 1.4. Strain release exemplified with the [4+2] cycloaddition of C_{60} with cyclohexadiene.

1.6.1. Reductions and oxidations

As anticipated in subsection 1.5, the study of fullerene reactivity began with redox chemistry. Fulleride anions with defined oxidation states can be obtained selectively by applying a given potential, and are isolated as fullerene salts by electrocrystallyzation [56] or reacted *in situ* with organic electrophiles [57,58] (**Scheme 1.5**). Reduction with alkali metals is also possible. This latter example is probably the most significant reduction method of C_{60}, as it can be used to prepare alkali doped superconductive materials with an M_3C_{60} formula [59]. Lastly, fullerenes can also be reduced with alkaline earths, transition metals and organic/organometallic donor molecules [49].

a) K. M. Kadish [57]

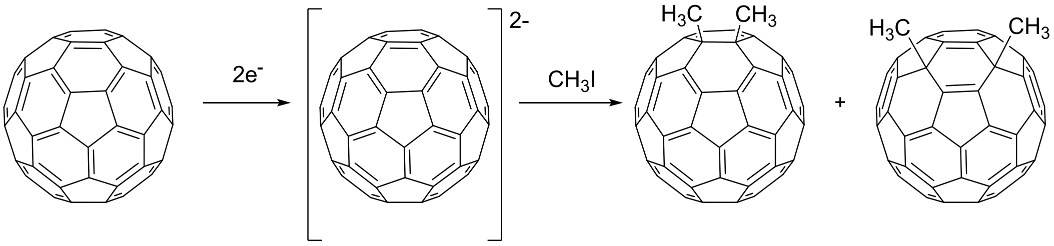

b) G.-W. Wang.[58]

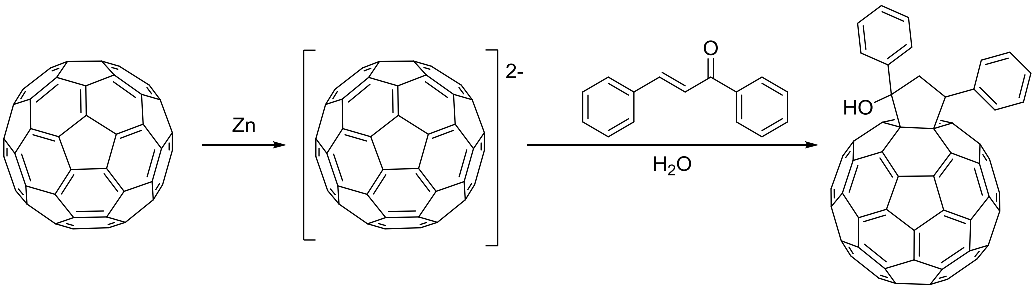

Scheme 1.5. Functionalization of C_{60} through anionic intermediates.

Contrary to reduction processes, removing electrons from HOMO of C_{60} is a rather unfavorable process [60]. Nonetheless, useful and unique strategies have been developed to obtain fullerene derivatives through fullerenyl cationic intermediates [61] (namely $C_{60}^{\bullet +}$ and RC_{60}^{+}) generated by oxidation of C_{60} with $AlCl_3$ [62] and $FeCl_3$ [63], among other oxidizing agents [64] (**Figure 1.6**).

a) E. Nakamura. [62]

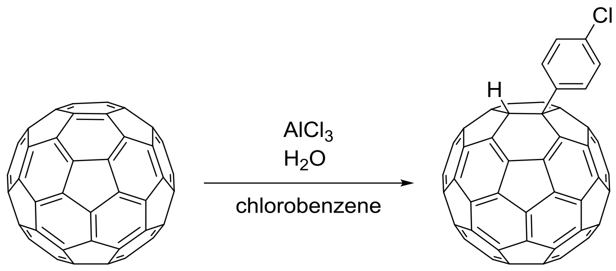

b) Y. Matsuo. [63]

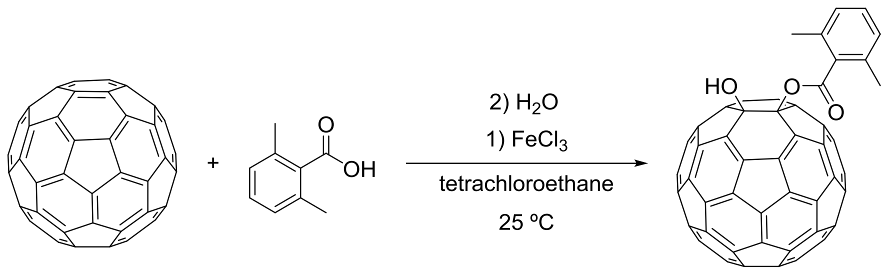

c) Y. Wan Jin [64]

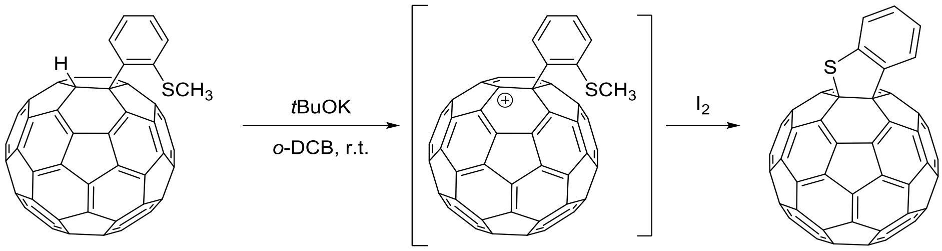

Scheme 1.6. Fullerene functionalization through fullerenyl cation intermediates.

1.6.2. Nucleophilic and organometallic additions

The markedly electronegative character of the C_{60} makes possible the functionalization of [6,6] bonds by nucleophilic additions. The paradigmatic example of this group of transformations is, without any doubt, the Bingel cyclopropanation [65] (**Scheme 1.7a**). This reaction consists in the nucleophilic attack of a carbanion species resulting from abstraction of the acidic proton of an α-bromo ester or an α-bromo ketone. This reaction results in a new carbanion species that ultimately displaces the bromine via a ring-closing intramolecular S_N2 nucleophilic substitution mechanism. The final reaction product is a *methanofullerene* derivative.

An alternative methodology reported by Hirsch consists in the *in situ* formation of the bromo derivative with CBr_4 and DBU [66] (**Scheme 1.7b**). This improved synthetic scheme makes the preparation of methanofullerenes much simpler, as it skips complicated bromination steps and dramatically broadens the scope of potential methanofullerenes. Cyclopropanation reactions are one of the most established synthetic methods in the development of novel functional fullerene-based materials.

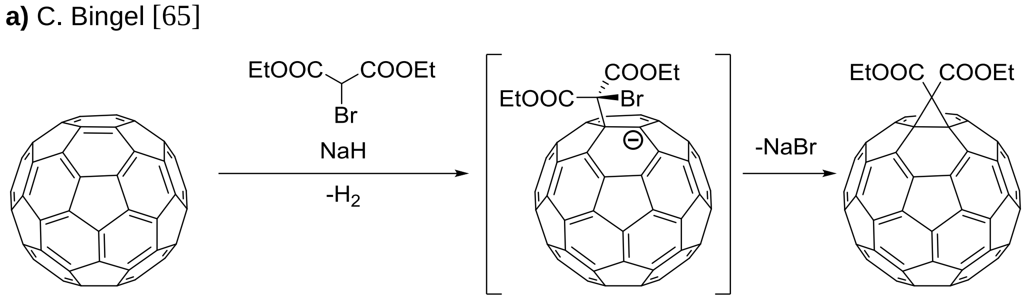
a) C. Bingel [65]
EtOOC
COOEt
Br
NaH
-H2
COOEt
EtOOC
Br
-NaBr
EtOOC COOEt

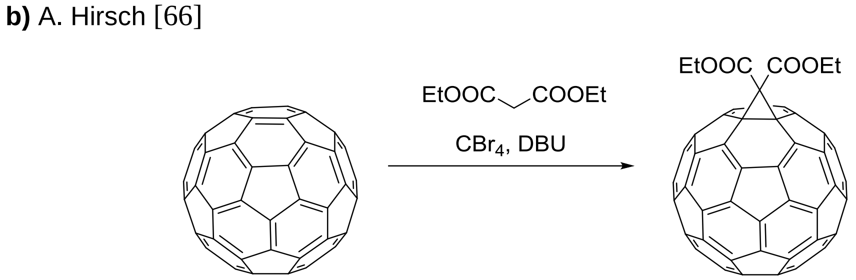
b) A. Hirsch [66]
EtOOC
COOEt
CBr4, DBU
EtOOC COOEt

Scheme 1.7. (a) Original Bingel cyclopropanation of C_{60}. (b) Hirsch's protocol starting from malonates via *in situ* bromination with CBr_4 and DBU.

Nucleophilic additions are not limited to malonates, esters, ketones or ketoesters, since diverse methanofullerene derivatives can be prepared by equivalent synthetic procedures employing other substrates with acidic C–H bonds. In this same sense, other nucleophiles such as organometallic compounds, cyanide anions, amines, phosphorous and silicon organic compounds can be used as the nucleophiles [36].

Hydroarylation and hydroalkenylation reactions with organoboron compounds using rhodium and palladium catalysts have been described [67–69] (**Scheme 1.8**). Our research group recently contributed to the study of these latter reactions with a complete computational study on the mechanism [70].

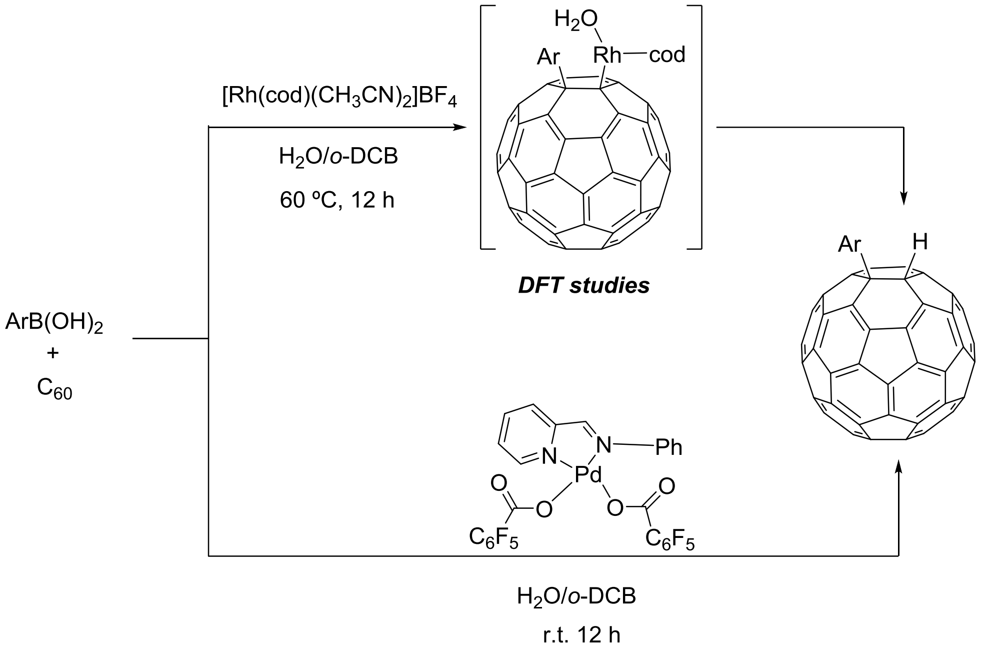
H2O
Ar
Rh
cod
[Rh(cod)(CH3CN)2]BF4
H2O/o-DCB
60 ºC, 12 h
DFT studies
Ar
H
ArB(OH)2
+
C60
N
N
Ph
Pd
O
O
O
O
C6F5
C6F5
H2O/o-DCB
r.t. 12 h

Scheme 1.8. Transition metal-catalyzed 1,2-hydroarylation of C_{60}.

Regioselective 5-fold addition to C_{60} has been achieved using organocopper compounds [71]. Polyadducts resulting from these reactions are the synthetic precursors of the so-called *buckyferrocenes*, a fascinating group of hybrid organometallic complexes in which a fullerene's 5-MR acts as a cyclopentadienyl ligand [72,73].

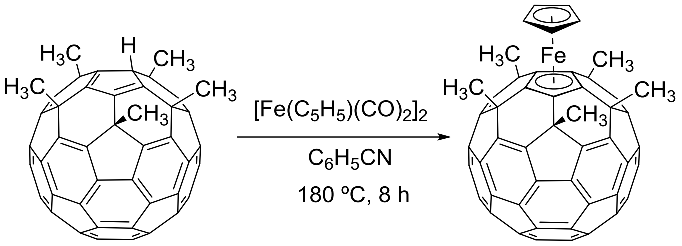

Scheme 1.9. Synthesis of a pentamethyl bucky ferrocene.

1.6.3. Cycloaddition reactions

Fullerenes are involved in a large diversity of cycloaddition reactions that result in fullerene derivatives with fused 3-, 4-, 5-, 6- and 7-MRs [36] (**Scheme 1.3**). For instance, [2+1] cycloadditions take place mainly with carbenes, but also with nitrenes [74] and silylenes [75]. The products formed are fullerene adducts attached to 3-MR, analogous to the ones produced by nucleophilic additions. For the specific case of carbenes, a comprehensive review published by Nagase a few years ago essentially covers all carbene reactions reported with hollow fullerenes and EMFs until 2013 [76].

Although C_{60} reacts with a wide range of carbenes and carbene precursors (e. g. dihalocarbenes, diazirines, vinylcarbenes, heterocyclic carbenes) [76,77], the most common carbene transfer agents to fullerenes are diazo compounds. This chemistry was introduced by Wudl, who has proven the extraordinary versatility of this class of molecules to prepare fullerene derivatives [51].

From a mechanistic point of view, the addition of diazo compounds to fullerenes should be considered a [2+1] cycloaddition only formally, as it proceeds through a [3+2] cycloaddition to a [6,6] bond of C_{60} followed by N_2 extrusion from a generally unstable pyrazoline intermediate. In general, when C_{60} is thermally reacted with diazo compounds, a mixture of [6,6] closed methanofullerenes and [5,6] *open fulleroids* is obtained. For the case of non-symmetrical diazo compounds ($R^1 \neq R^2$), [5,6] open fulleroids appear as a mixture of two diastereomers, being the major product the one with the bulkier group pointing to the former 5-MR of the [5,6] junction (**Scheme 1.10**) Fulleroids tend to transform into their thermodynamically favored [6,6] closed counterparts, although in some cases where the open isomers are particularly stable, this isomerization process does not occur. Like C_{60}, [5,6] open fulleroids are purple in solution, which accounts for the maintenance the original 60 π-conjugated system [77]. Structurally related azafulleroids and azamethanofullerenes can also be prepared by the addition of azides [74,78,79].

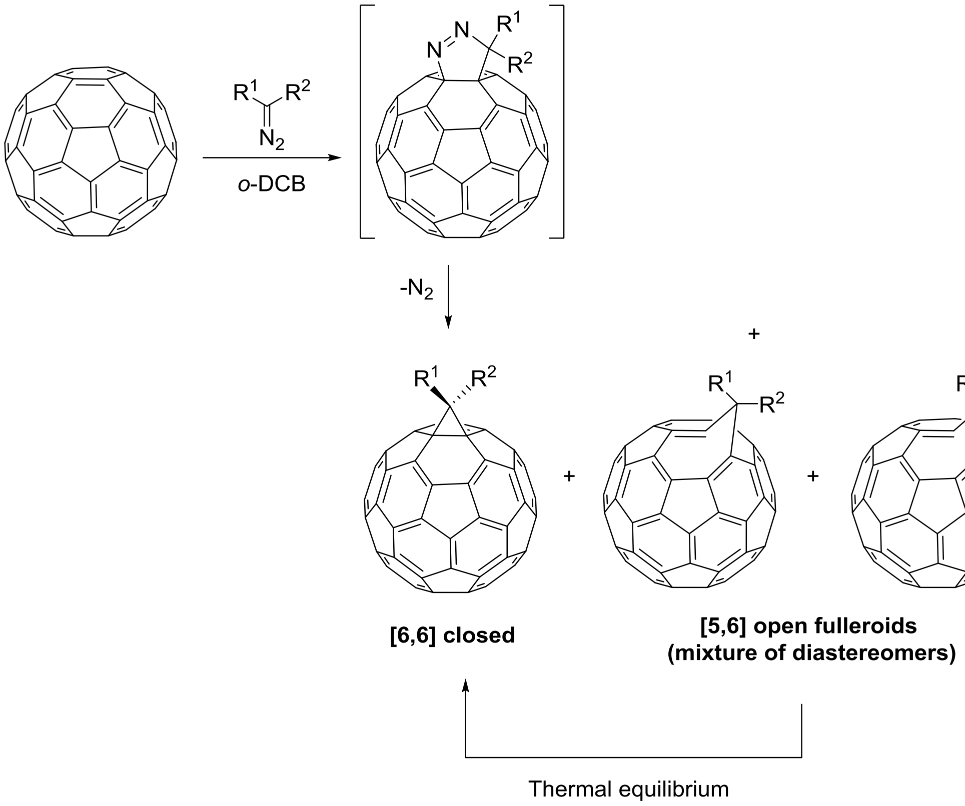
R1 R2
N2
o-DCB
N N R1 R2
-N2
R1 R2
+
[6,6] closed
[5,6] open fulleroids
(mixture of diastereomers)
Thermal equilibrium

Scheme 1.10. Synthesis of [6,6] closed and [5,6] open fulleroids formed by reaction of C_{60} with diazo compounds.

Diazo compounds can be prepared and isolated or, alternatively, generated *in situ* from tosylhydrazones (**Scheme 1.11**). Again, this modified methodologic alternative represents a remarkable improvement with respect to the original procedures in terms of safety and product diversity. Indeed, diazo compounds are considered unstable hazardous materials, often difficult or impossible to isolate. The prominence of this reaction is exemplified by the preparation of [6,6]-phenyl-C_{61}-butyric acid methyl ester ($PC_{61}BM$) [80] and other related compounds, considered nowadays the state-of-the-art n-materials in fullerene-based photovoltaic technology [81].

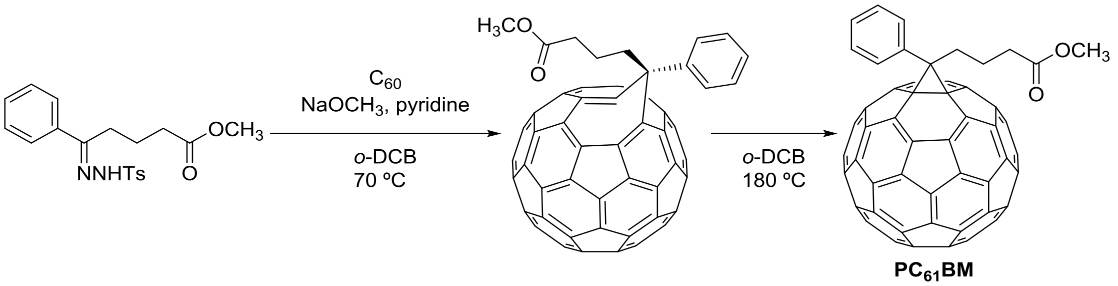
NNHTs O
OCH3
C60
NaOCH3, pyridine
o-DCB
70 ºC
H3CO
O
o-DCB
180 ºC
OCH3
O
PC61BM

Scheme 1.11. Synthesis of phenyl-C_{61}-butyric acid methyl ester ($PC_{61}BM$) from C_{60} and a tosylhydrazone derivative.

Transition metal carbenoids have been employed with the aim of overcoming selectivity issues [82–85]. The reaction of C_{60} with ethyl diazoacetates in the presence of equimolar amounts of dirhodium(II) tetraacetate gave exclusively the [6,6] closed isomer. Similar outcomes were observed with palladium-carbenoid complexes (**Scheme 1.12**).

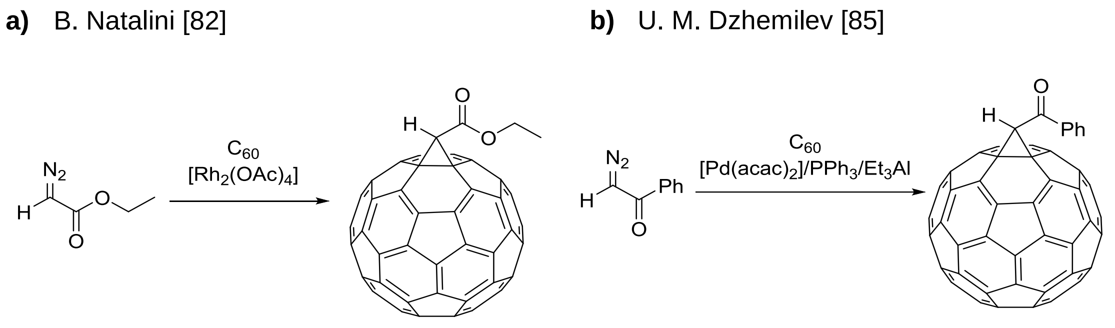

Scheme 1.12. Transition metal-mediated synthesis of methanofullerenes.

Along with cyclopropanations, the reaction of C_{60} with dipoles is often the method of choice when developing new synthetic fullerene derivatives for practical applications. Specifically, 1,3-dipolar cycloadditions of azomethine ylides, also known as *Prato reaction*, afford [6,6] closed fulleropyrrolidine adducts with good yields, good stability and excellent functional group versatility [86,87]. The ylides are formed *in situ* by condensation of α-amino acids and subsequent decarboxylation. Once formed, dipoles add to C_{60} through a [3+2] mechanism (**Scheme 1.13**). Unlike other substrates like diazoalkanes, azides or diazoacetates, N_2 extrusion to give the corresponding [2+1] adducts is not possible after [3+2] cycloaddition with azomethine ylides. Fullerene adducts fused to other 5-membered heterocycles are obtained when similar reactions are performed with nitriles oxides, nitriles imines, sulfinimides, thiocarbonyl ylides, carbonyl ylides, nitrile ylides, isonitriles and disiliranes [36]. Pyrazolino fullerenes obtained by 1,3-dipolar cycloaddition of C_{60} with nitrile imines are of particular interest in the field of organic photovoltaics (OPV) [88].

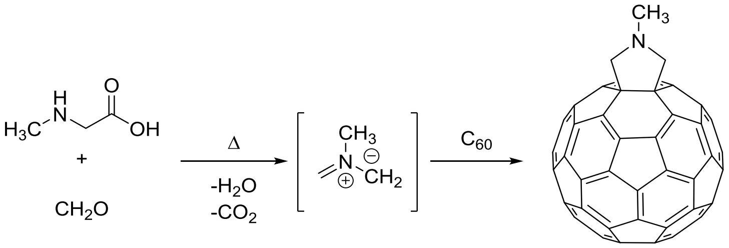

Scheme 1.13. 1,3-dipolar cycloaddition of C_{60} and azomethine ylides (Prato Reaction).

The participation of chiral transition metal complexes and organocatalysts in [3+2] cycloaddition reactions has given access to the enantioselective preparation of 5-MR-fused fullerene derivatives [89]. In 2009, Martín and co-workers reported for the first time an efficient enantioselective synthesis of fulleropyrrolidines [90]. More recently, the same group synthesized optically active pyrrolino fullerene derivatives by both transition-metal catalysis and under organocatalytic conditions employing a series of chiral triazolium salts as *N*-heterocyclic carbene (NHC) precursors [87].

Cyclobutane or cyclobutene rings are linked to C_{60} by [2+2] cycloadditions with unsaturated substrates like electron-rich alkenes and alkynes, enones, allenes and ketenes [3,36]. The [2+2] cycloaddition reaction with arynes is used to attach aromatic moieties to fullerenes [92] (**Scheme 1.14a**). While most cases proceed upon irradiation through a photochemical process, thermal reactions have also been reported. In a recent account, C_{60} was reacted regio- and stereoselectively with allenols generated *in situ* by platinum-catalyzed 1,3-alkoxy migration of propargylic esters [93] (**Scheme 1.14b**). Conversely, with silver catalysts, equivalent compounds isomerized into dienes, affording the corresponding [4+2] adducts after reaction with C_{60} [94] (**Scheme 1.14c**).

a) G. Cooks [92]

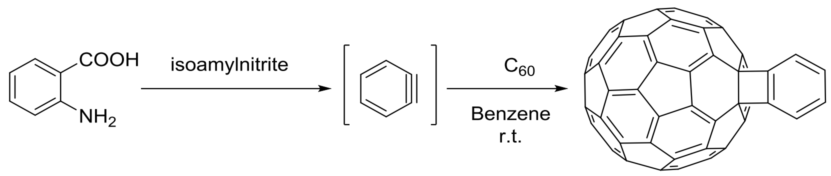
COOH
NH2
isoamylnitrite
C60
Benzene
r.t.

b) I. Ryu [93]

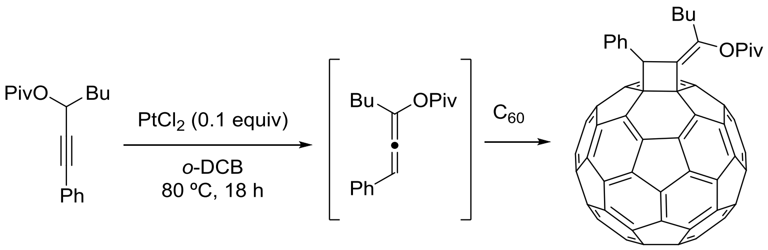
PivO
Bu
Ph
PtCl2 (0.1 equiv)
o-DCB
80 ºC, 18 h
Bu
OPiv
Ph
C60
Bu
Ph
OPiv

c) Y. Maeda [94]

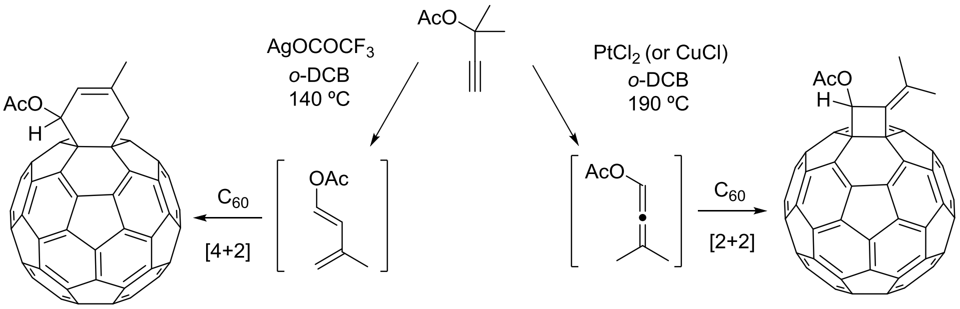
AcO
AgOCOCF3
o-DCB
140 ºC
PtCl2 (or CuCl)
o-DCB
190 ºC
AcO
H
C60
[4+2]
OAc
AcO
C60
[2+2]
AcO
H

Scheme 1.14. [2+2] cycloadditions involving C_{60}

Diels-Alder (DA) reactions are also considered valuable synthetic tools for fullerene functionalization. Since [6,6] bonds exhibit electron-deficient character, C_{60} behaves as a dienophile in [4+2] cycloadditions to yield 6-MR-fused cycloadducts. Indeed, no example of C_{60} acting as the diene has been documented to date. Reactions with common dienes like cyclopentadiene or acenes [95] (**Scheme 1.15a**) proceed efficiently, providing the corresponding 1:1 products, although in some cases retro-DA reactions are operative even at room temperature. This particular feature was wisely employed by Kräutler, who managed to use anthracene addends as "masking" groups in regiocontroled multiple additions to C_{60} [96,97]. Cycloreversion reactions are avoided when *o*-quinidomethane derivatives are used as diene precursors, for which the resulting adducts are stabilized by the aromaticity of the resulting addend [98] (**Scheme 1.15b**). In the presence of a rhodium(I) complex, 1,6-diynes have been used as diene precursors to efficiently yield the corresponding C_{60} [4+2] adducts [99] (**Scheme 1.15c**).

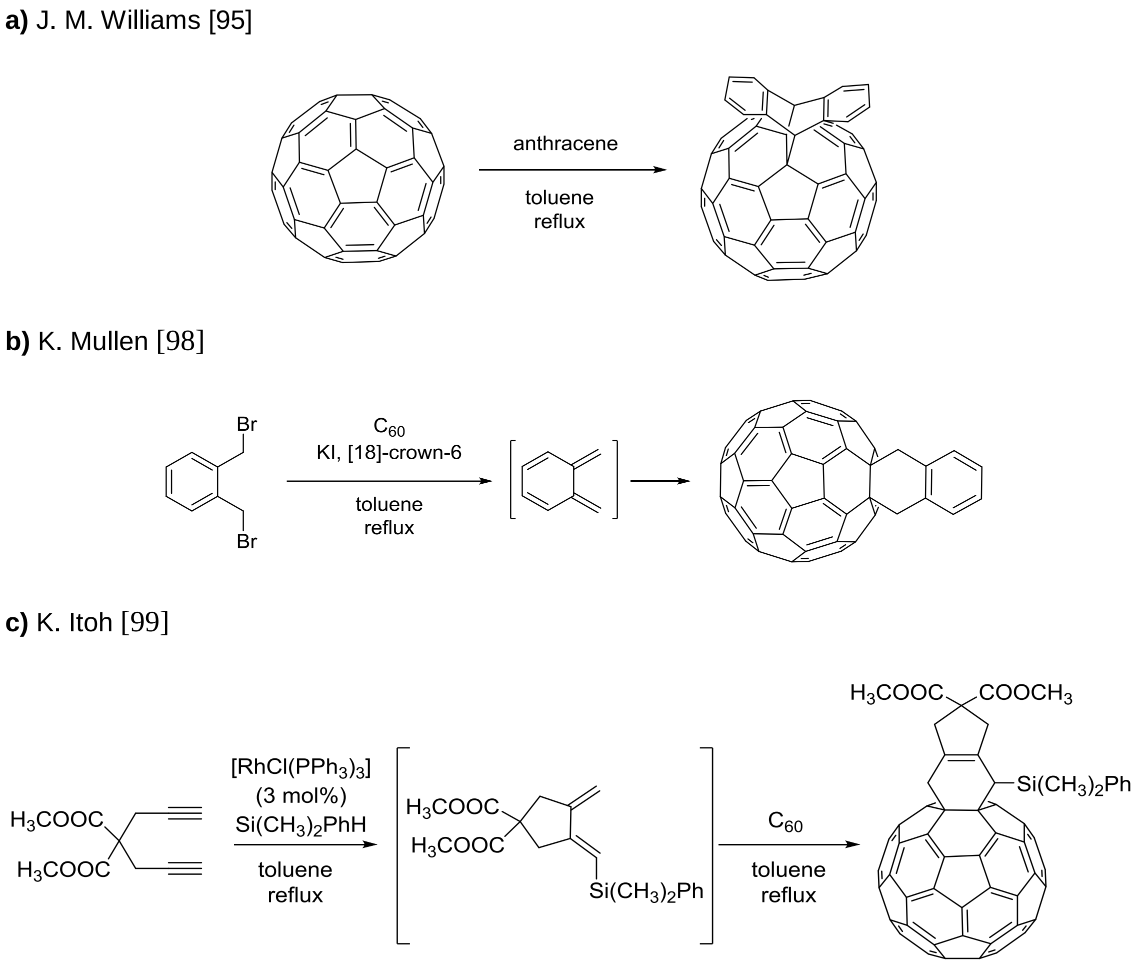
a) J. M. Williams [95]
anthracene
toluene
reflux
b) K. Mullen [98]
Br
Br
C60
KI, [18]-crown-6
toluene
reflux
c) K. Itoh [99]
H3COOC
H3COOC
[RhCl(PPh3)3]
(3 mol%)
Si(CH3)2PhH
toluene
reflux
H3COOC
H3COOC
Si(CH3)2Ph
C60
toluene
reflux
H3COOC
COOCH3
Si(CH3)2Ph

Scheme 1.15. DA reactions between C_{60} and different dienes or diene precursors.

Annulation reactions promoted by transition-metal complexes have further enriched the assortment of fullerene cycloadducts available. For example, regioselective Pauson-Khand/pyrrolidine bisadducts were efficiently prepared by Martín and co-workers using a conventional dicobalt octacarbonyl complex [100,101] (**Scheme 1.16**).

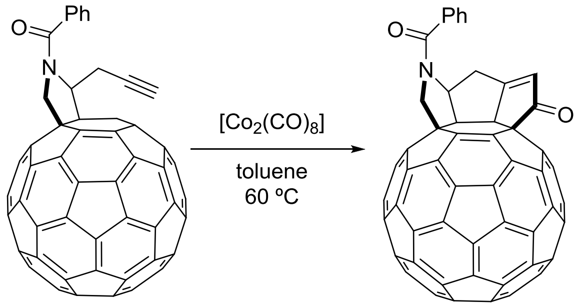
O
Ph
N
[Co2(CO)8]
toluene
60 ºC
O
Ph
N
O

Scheme 1.16. Regioselective Pauson-Khand reaction of a propargylic fulleropyrrolidine adduct.

Recent works have demonstrated that C–H activation is operative in some palladium-catalyzed cyclisations involving C_{60} and a variety of aromatic substrates [102–109] (**Scheme 1.17a-e**). In a similar study, Murata and co-workers recently reported a palladium-catalyzed annulation reaction with aryl halides that takes place through a concerted metalation-deprotonation mechanism [110] (**Scheme 1.17f**).

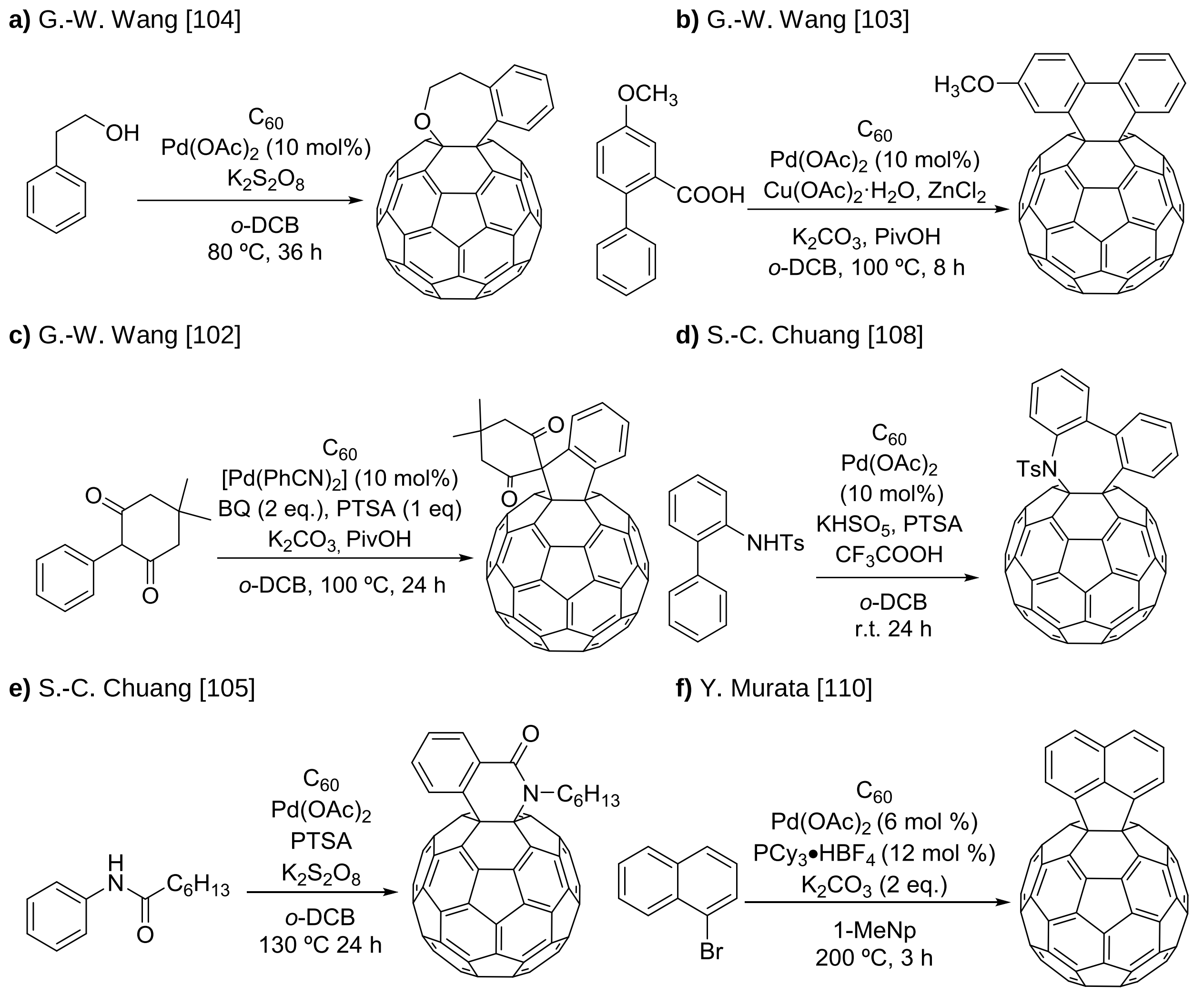
a) G.-W. Wang [104]
OH
C60
Pd(OAc)2 (10 mol%)
K2S2O8
o-DCB
80 °C, 36 h
O
b) G.-W. Wang [103]
OCH3
COOH
C60
Pd(OAc)2 (10 mol%)
Cu(OAc)2·H2O, ZnCl2
K2CO3, PivOH
o-DCB, 100 °C, 8 h
H3CO
c) G.-W. Wang [102]
O
O
C60
[Pd(PhCN)2] (10 mol%)
BQ (2 eq.), PTSA (1 eq)
K2CO3, PivOH
o-DCB, 100 °C, 24 h
O
O
d) S.-C. Chuang [108]
NHTs
C60
Pd(OAc)2
(10 mol%)
KHSO5, PTSA
CF3COOH
o-DCB
r.t. 24 h
TsN
e) S.-C. Chuang [105]
H
N
C6H13
O
C60
Pd(OAc)2
PTSA
K2S2O8
o-DCB
130 °C 24 h
O
N−C6H13
f) Y. Murata [110]
Br
C60
Pd(OAc)2 (6 mol %)
PCy3•HBF4 (12 mol %)
K2CO3 (2 eq.)
1-MeNp
200 °C, 3 h

Scheme 1.17. Selected examples of palladium-mediated annulation reactions.

C_{60} is able to experience transition metal-promoted [2+2+2] cycloadditions. However, this specific reaction will be discussed later on this manuscript, since a whole section (see section 2) is dedicated to cover in detail this kind of chemical processes.

1.6.4. Radical additions

The first examples of radical functionalization appeared during the early stages of fullerene chemistry [111]. However, these reactions were less explored at first than other synthetic methodologies, because the outstanding affinity of C_{60} for free radicals often provides complex mixtures of polyadducts. This particular feature, considered a drawback in synthetic organic chemistry, has aroused great interest among biologists and medicinal chemists, who have shown remarkable interest in fullerene derivatives as potential antioxidant agents that may act against oxidative cell damage produced by free radicals [47,112]. A fully detailed review article covering both fundamental and practical aspects of fullerene radical reactions was published a few years ago by Orfanopoulos and Tzirakis [48]. In spite of the difficulties caused by the inherent promiscuity of fullerenes against radical species, recent progress in the field has led to the development of novel synthetic procedures that allow selective preparation of monoadducts and well-defined polyadducts. As seen previously for the rest of the reactions discussed, the use of transition metals has become decisive.

As a matter of fact, transition metal-mediated radical additions are the most powerful synthetic tools when it comes to fullerene derivatization [48,61,113]. Countless examples of such reactions (mostly cyclizations) have been reported only in the past few years. Though these reactions will not be discussed in detail, some selected examples [114–117] are depicted in **Scheme 1.18**. As a general conclusion, the diversity of carbo- and heterocycles of different sizes attached to C_{60} *via* transition metal-mediated radical cyclization reactions clearly evidences their synthetic utility.

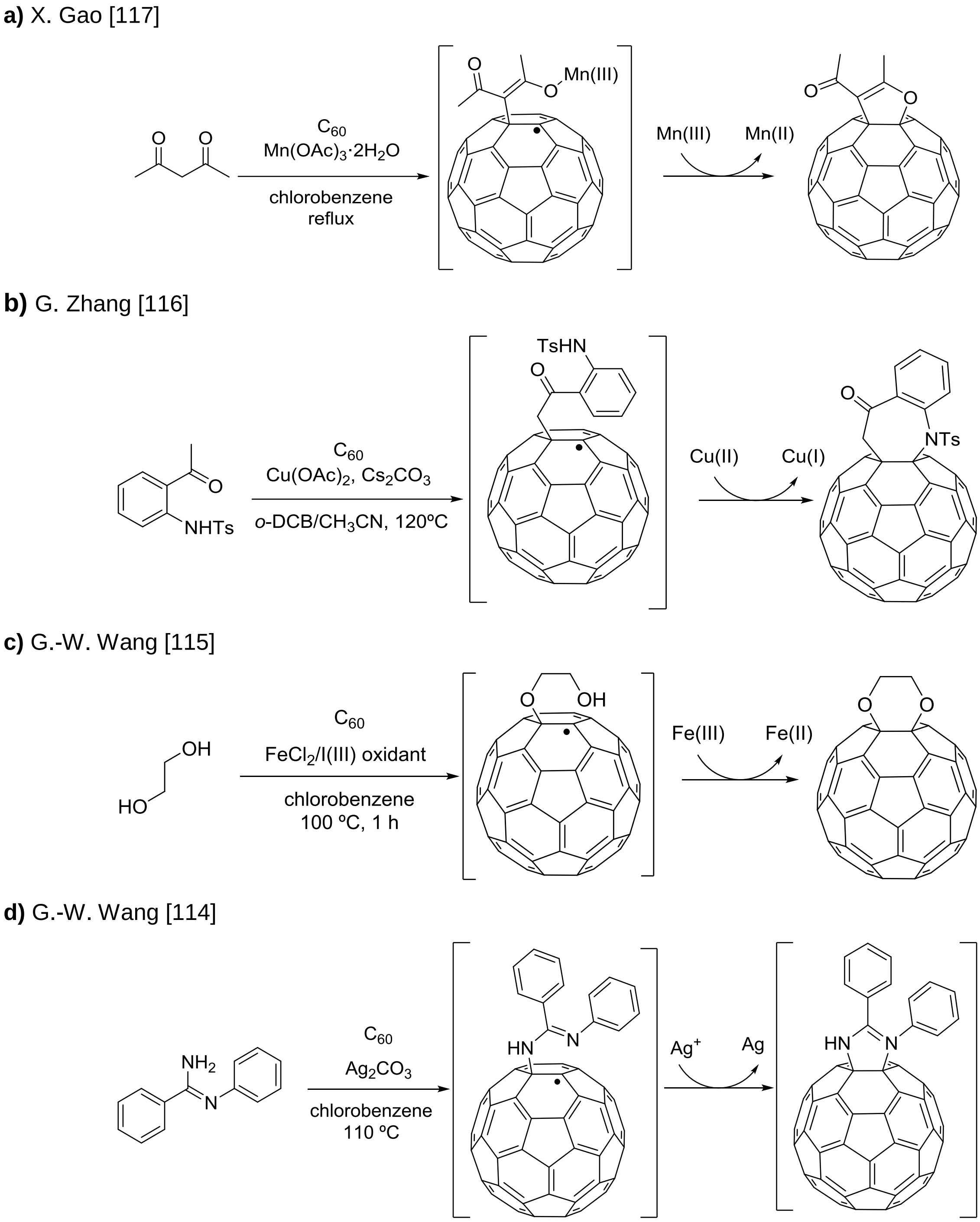
a) X. Gao [117]

b) G. Zhang [116]

c) G.-W. Wang [115]

d) G.-W. Wang [114]

C60
Mn(OAc)3·2H2O
chlorobenzene
reflux
Mn(III)
Mn(III)
Mn(II)
O
C60
Cu(OAc)2, Cs2CO3
o-DCB/CH3CN, 120ºC
NHTs
TsHN
Cu(II)
Cu(I)
NTs
OH
HO
C60
FeCl2/I(III) oxidant
chlorobenzene
100 ºC, 1 h
Fe(III)
Fe(II)
NH2
N
C60
Ag2CO3
chlorobenzene
110 ºC
HN
Ag+
Ag

Scheme 1.18. Miscellaneous transition metal-mediated radical cyclization reactions.

This subsection could be extended with numerous additional examples of chemical reactions such as halogenations, hydrogenations or transition-metal complex formation, to name a few. The supramolecular assembly of fullerenes with other substrates by noncovalent interactions is also a field of increasing interest [118]. The reader is invited to go through the above mentioned monographies and reviews for further insight into reactions that fall behind the scope of this brief summary.

1.6.5. Functionalization of C_{70} and endohedral metallofullerenes

The typical reactivity of C_{60} (see preceding subsections) can in general be applied to higher fullerenes and EMFs [30,36]. However, while in C_{60} all 30 [6,6] double bonds are equivalent, for less symmetrical cages, one has to consider the formation of different isomers upon reaction with nucleophiles, dienophiles, dipoles, *etc.*

For instance, C_{70} exhibits 5 nonequivalent carbon atoms and 4 types of [6,6] bonds (namely α, β, γ and δ bonds) available for addition reactions. More specifically, α and β junctions are type **A** pyracylenic bonds and happen to be the most reactive due to their higher degree of pyramidalization. The γ bonds (type **B**) are considerably less reactive and often require harsher conditions to be functionalized. Finally, δ bonds are rather planar and unreactive pyrene (type **C**) moieties. Regioisomeric mixtures of C_{70} derivatives are difficult to separate and generally preparative HPLC procedures are required in order to isolate pure compounds. The identification of each adduct is generally achieved by analysis of ^{1}H and ^{13}C NMR spectra, which are indicative of the point-group symmetry, and by characteristic patterns of the electronic absorption spectra (**Figure 1.7**).

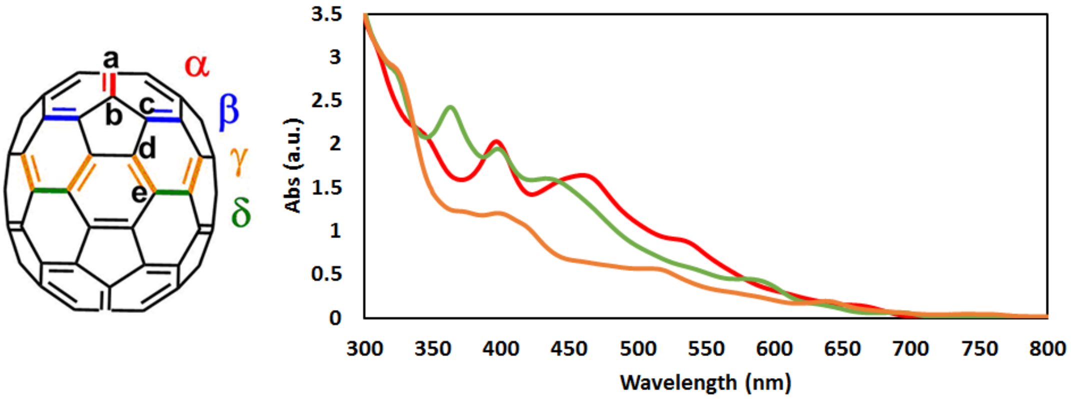

Figure 1.7. UV-vis spectra of isolated α, β and γ adducts obtained by 1,3-dipolar cycloaddition with azomethine ylides (Raw experimental data provided by Dr. Edison Castro).

Cyclopropanations resulting from Bingel-like reactions occur both at the α and β bonds of C_{70}, being α-adducts the major reaction products [65]. However, a recently reported synthetic protocol by Martín consisting in the incorporation of DMF as an additive favors site-selectivity for the β-isomer [119]. Addition of dihalocarbenes and diazo compounds produce extra site-isomers with a fulleroid structure functionalized at the $[5,6]_{d\text{–}d}$ bonds [120]. DA, 1-3-dipolar and [2+2] cycloadditions take place usually at the α, β and γ bonds [121,122], whereas under specific conditions, all these reactions can also provide $[5,6]_{d\text{–}d}$ fulleroids [123–125]. In practical terms, site-selectivity in C_{70} additions has strong implications in fullerene-based photovoltaic devices, as it is generally accepted that isomerically pure fullerene-based materials are better electron acceptors than those consisting of regioisomeric mixtures [122,126,127].

The first chemically modified EMFs consisted of disilylated La@C_{82} derivatives that were reported by Akasaka and co-workers as early as in 1995 [128]. However most of the chemistry involving EMFs has been developed over the last 15 years. The reactivity of EMFs changes significantly as compared with hollow fullerenes, since electron transfer processes from the metals or metal clusters to the carbon cage dramatically disturb their electronic structure. In this regard, our group has made enormous contributions to the fundamental understanding of EMF's reactivity with several computational studies that prove the enormous influence of the encapsulated species on the thermodynamics and kinetics of exohedral additions [128–138].

The exohedral functionalization of EMFs has found remarkable usefulness in structure elucidation of unknown cages when X-Ray crystallography of the pristine species failed. Also, certain EMFs have been isolated from complex mixtures after production by arc discharge using cage-selective carbene additions or halogenation reactions. In medicine, gadolinium endohedral species are transformed into water soluble derivatives before they can be tested as biologically compatible contrast agents. Every aspect regarding the exohedral chemistry of EMFs has been extensively reviewed in many occasions [31–33].

1.6.6. Multiple additions to C_{60} and C_{70}

Controlling the regiochemistry of multiple additions is still a major challenge in today's fullerene chemistry. As discussed above, C_{60} has 30 equivalent [6,6] bonds. As a consequence, from a given monoadduct, 8 different isomers can result by the addition of a second identical and symmetrical addend [140,141] (**Scheme 1.19**). A third addition will potentially form 46 different products. It has been demonstrated that the regiochemistry of successive additions is mainly governed by the frontier molecular orbitals (MOs), whose distribution along the cage is affected by the introduced addends. As discussed previously for C_{70} monoadducts, regioisomeric mixtures of C_{60} bisadducts require tedious chromatographic procedures and subsequent spectroscopic characterization of isolated products. Since pure highly functionalized fullerene derivatives are considered attractive materials for practical applications, many efforts have been devoted to achieve selective formation of the desired bisadducts [36,142].

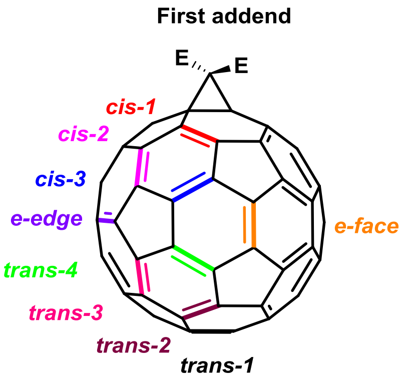

Cis-1	C_s	-
Cis-2	C_s	0.9%
Cis-3	C_2	2.5%
e	C_s	15.5%
Trans-4	C_s	3.7%
Trans-3	C_2	12.0%
Trans-2	C_2	5.3%
Trans-1	D_{2h}	0.8%

Scheme 1.19. The 8 possible addition patterns for 2-fold addition to C_{60}. Symmetry of the corresponding bisadducts and yields obtained after two successive Bingel additions of diethyl 2-bromomalonate. E = $COOCH_2CH_3$.

Examples of inherently regioselective successive additions are scarce [143–145]. For this reason, two main approaches have been developed to overcome this challenging synthetic problem [146]. The use of *removable template addends* was introduced by Hirsch and co-workers in 1995 (**Scheme 1.20a**). The authors used a slightly modified protocol for the Bingel cyclopropanation adding 9,10-dimethyl anthracene (DMA) to the reaction mixture [147]. Reversible [4+2] cycloaddition of DMA moieties acting as labile template agent allows for the efficient production of a T_h symmetric *hexakis*-adduct. A related protocol has been used by Kräutler and co-workers, who took advantage of the selective formation of *trans-1* anthracene bisadducts in the solid state [96] to selectively attach 4 malonate addends at the equator of C_{60} [97]. This elegant synthetic protocol has been used by the group of Prof. Echegoyen to prepare a series of complex fulleropyrrolidine-methanofullerene hexakis adducts in a highly regio- and stereoselective manner [148] (**Scheme 1.20b**). The same group adapted Kraütler's methodology to functionalize C_{70} at the β bonds. In this later case, the anthracene addends act as removable "protecting groups" that selectively blocks the α-positions [149] (**Scheme 1.20c**).

a) A. Hirsch [147]

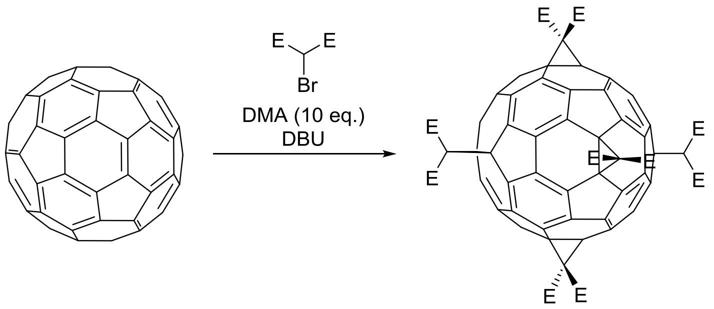

b) L. Echegoyen [148]

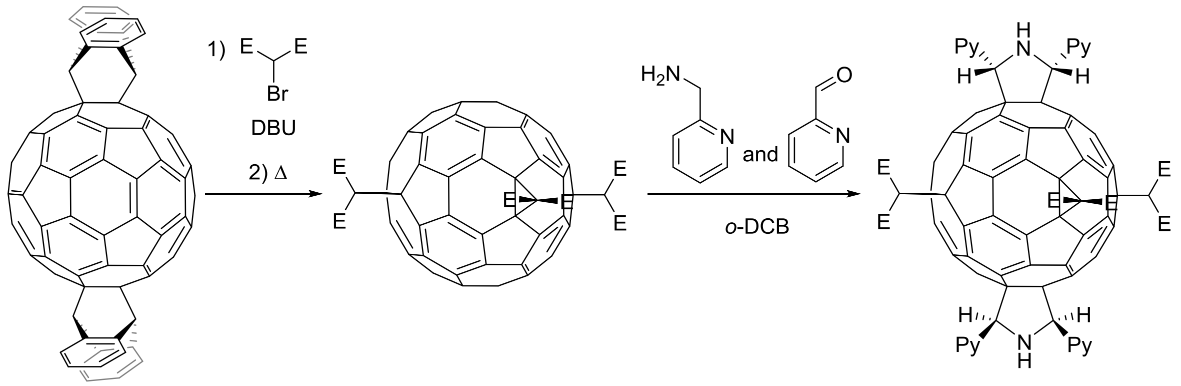

c) L. Echegoyen. [149]

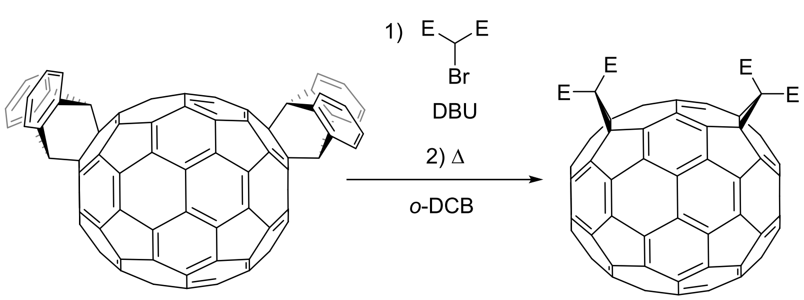

Scheme 1.20. Use of anthracene and DMA as templates in fullerene functionalization (E = $COOCH_2CH_3$).

Another way to control the regiochemistry of multiple additions is the so-called *tether-directed remote functionalization*. This concept was first introduced by Diedrich and co-workers and consists in the addition of multiple addends joined together with a tether functionality. The length and nature of the tether direct the successive additions to a specific [6,6] bond of the fullerene core [150–152]. Selected examples of how this strategy has been used to selectively prepare *cis-1* [153,154], *cis-2* [155] or *trans-1* [156] using diverse reactions are depicted in **Scheme 1.21**.

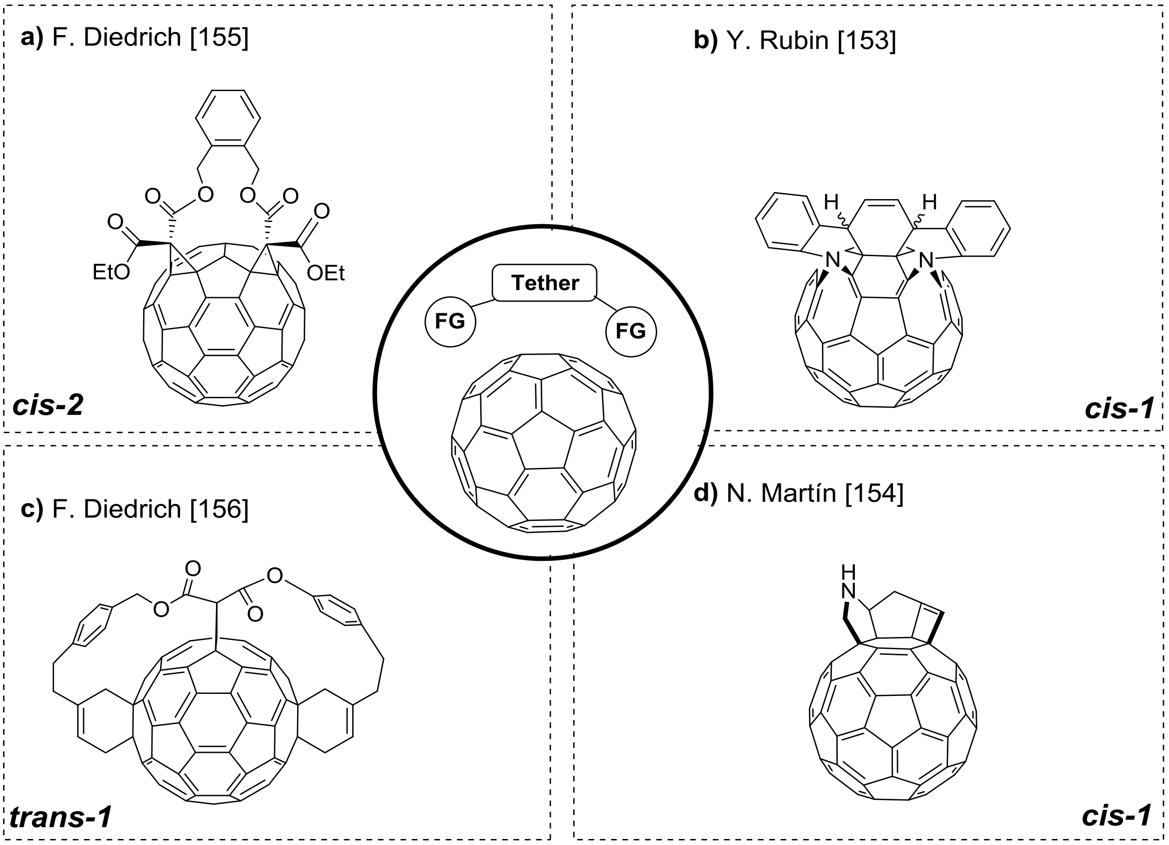

Scheme 1.21. Tether-controlled multiple functionalization of C_{60}. FG = functional group.

1.7. “There is a hole in my bucky”: chemistry and applications of open-cage fullerenes

The exohedral functionalization of fullerenes can result in open-cage structures in which multiple σ and π bonds of a fullerene have been cleaved [157]. As discussed previously in subsection 1.6, the first examples of [5,6] open structures were reported by Wudl as reaction products of C_{60} with certain diazo compounds (*i.e.* diazomethanes, diazoacetates and diazoamides) and azides [158]. This class of derivatives received the names of *fulleroids* and *azafulleroids*. The same research group discovered that azafulleroids experience photooxygenative cleavage when reacting with $^1O_2$ upon light exposure to form a series of ketolactam derivatives with an 11-membered hole on the fullerene surface [159]. These compounds are considered the first *open-cage fullerenes*. Depending on the functional groups attached to the nitrogen atom (**Scheme 1.22**), prolonged exposure to light and atmospheric oxygen triggers a second σ–cleavage leading to a diketo imide fullerene exhibiting a considerably large 15-membered hole [160].

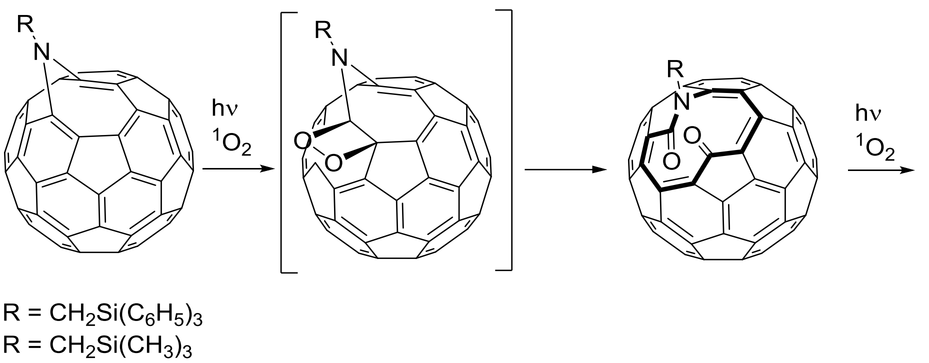
R
N
hν
$^1O_2$
R
N
O
O
R
N
O
O
hν
$^1O_2$
R
O
N
O
O
O
R = $CH_2Si(C_6H_5)_3$
R = $CH_2Si(CH_3)_3$

Scheme 1.22. Photooxygenative cleavage of azafulleroids.

Rubin and co-workers introduced in 1996 a new family of open-cage fullerenes: the so-called *bis(fulleroids)*. These compounds are generally obtained from cyclohexadiene fused C_{60} derivatives *via* a formal [4+4] photocycloaddition that produces a bis(methanofullerene) intermediate. Thermally allowed retro-[2+2+2] cycloaddition ultimately leads to a double bond scission at two opposed [5,6] junctions contiguous to the attached 6-MR [161–170] (**Scheme 1.23a**). Bis(fulleroids) also undergo photooxidative cleavage when reacting with oxygen in the presence of light, forming open-cage derivatives with 2 carbonyl groups at the rim of a 12-membered hole [165,169,171] (**Scheme 1.23b**).

a) S. Murata [164]

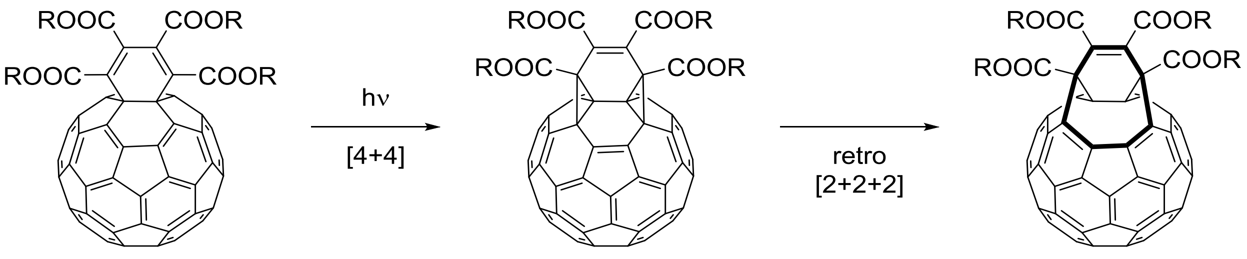
ROOC
COOR
ROOC
COOR
hν
[4+4]
ROOC
COOR
ROOC
COOR
retro
[2+2+2]
ROOC
COOR
ROOC
COOR

b) S. Murata [171]

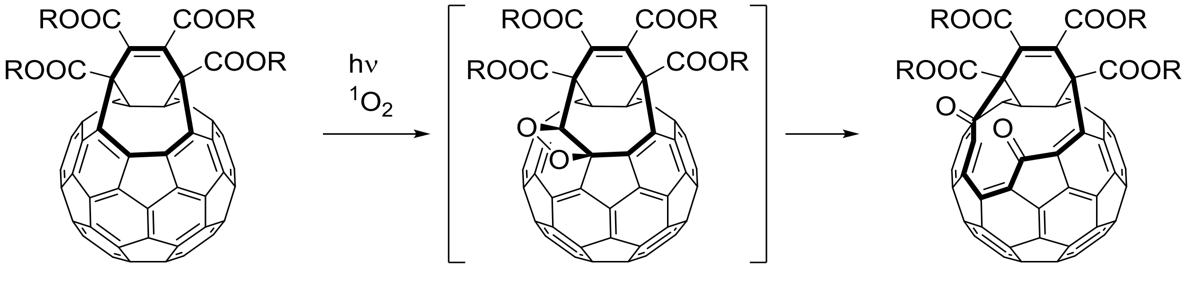
ROOC
COOR
ROOC
COOR
hν
$^1O_2$
ROOC
COOR
ROOC
COOR
O
O
ROOC
COOR
ROOC
COOR
O
O

Scheme 1.23. Formation and photooxygenative cleavage of bis(fulleroids). R= CH_3, $C(CH_3)_3$, CH_2CF_3.

A third approach to disturb the σ-framework of fullerenes was established in 2004 by Gan and Zhang [172] and relies on the synthesis of fullerene-mixed peroxides obtained by regioselective multiple additions of *tert*-butyl peroxy radicals to C_{60} and C_{70}. Preparation of the highly oxidized intermediates was followed by a series of cage-opening and hole-expanding reactions (**Scheme 1.24**). In this latter case, the oxygen-rich peroxo groups attached to the fullerene become the source of carbonyl and ether groups occupying positions at the rim of the orifice [173,174].

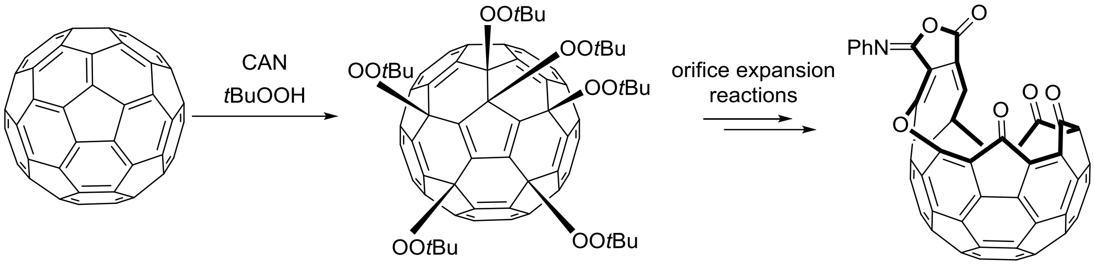
CAN
tBuOOH
OOtBu
OOtBu
OOtBu
OOtBu
OOtBu
OOtBu
orifice expansion
reactions
PhN=
O
O
O
O
O O

Scheme 1.24. 19-membered hole open-cage C_{60} derivative synthetized from a fullerene-mixed peroxide. CAN = cerium (IV) ammonium nitrate.

The ability of fullerenes to host smaller molecules into their cavity had been already extensively studied when in 2001 Rubin and co-workers succeeded to chemically synthetize the first endohedral fullerene complex by means of chemical opening of C_{60} and subsequent encapsulation of H_2 into the resulting open-cage species. Indeed, progressive chemical expansion of fullerene holes has been repeatedly employed with this aim [157]. To date, endohedral complexes encapsulating noble gases or relatively small molecules have been reported with open-cage fullerenes bearing orifices of different sizes. Water, for instance, is easily inserted into a 18-membered hole containing open-cage fullerene by simply heating it in a water containing mixture of solvents [175] (**Scheme 1.25**). Conversely, gases often require high pressure conditions in order to pass through a fullerene's orifice [176] (**Scheme 1.25b**). In some cases where the guest molecule is smaller than the hole radius, a switchable stopper can be installed at the rim in order to avoid scape of the guest molecule from the cavity [177].

a) L. Gan [175]

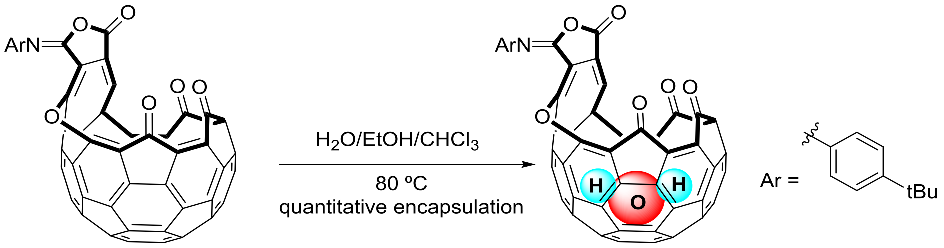
ArN=
O
O
O
O
O O
$H_2O/EtOH/CHCl_3$
80 °C
quantitative encapsulation
ArN=
H
O
H
Ar =
tBu

b) K. Komatsu [176]

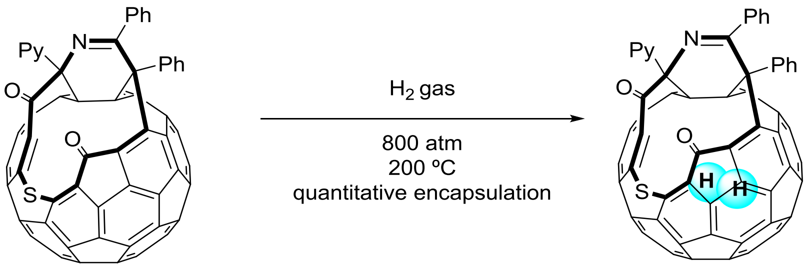
Py
N
Ph
Ph
O
O
S
H_2 gas
800 atm
200 °C
quantitative encapsulation
Py
N
Ph
Ph
O
O
S
H
H

Scheme 1.25. Encapsulation of small molecules in different open-cage fullerene derivatives.

Particularly relevant to the field was the contribution made by Komatsu and co-workers in 2005 [178]. The authors reached the encapsulation of H_2 in a 13-membered hole containing fullerene that was then chemically *sutured* to recover the original C_{60} cage using a four-step synthetic route (**Scheme 1.26**). The elegant usage of organic synthesis towards the selective preparation of endohedral fullerenes established the first example of *molecular surgery*.

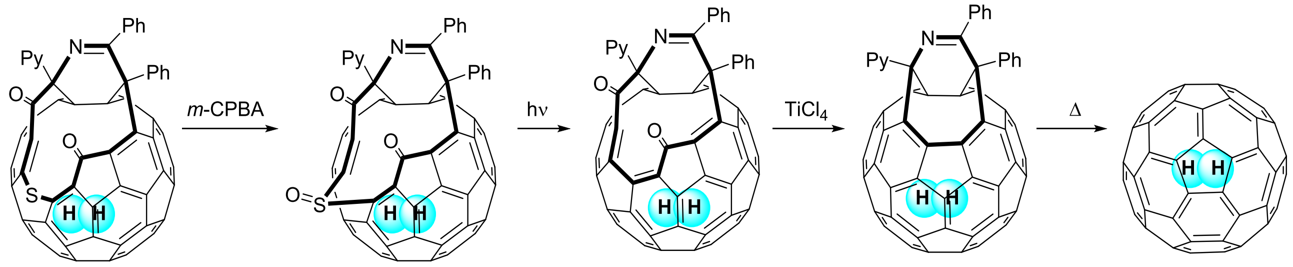

Scheme 1.26. Molecular surgery applied to the preparation of $H_2@C_{60}$.

The same group encapsulated a single molecule of water into C_{60} in 2011 [179] and equivalent approach has been applied more recently to encapsulate two H_2 or H_2O molecules into C_{70} [180,181]. In a very recent work, Whitby and co-workers reported the first synthesis of $CH_4@C_{60}$ following the *molecular surgery* approach [182]. Methane is the first organic molecule and the largest encapsulated so far in $C_{60.}$ Other examples of incarcerated molecules in fullerenes are HF [183] and CO [184].

From the practical point of view, the results obtained with H_2 encapsulation suggest the use of open-cage fullerenes in hydrogen storage technology. In this same sense, O_2/H_2O_2 entrapping fullerene complexes may be used in the field of photodynamic therapy of hypoxia tumors [157,173]. Furthermore, three reports have shown the ability of open-cage fullerenes to behave as efficient electron-accepting materials or as additives in bulk-heterojunction solar cells [185–187]. However, all these applications remain nowadays merely hypothetical or little developed. Beyond medicine and materials science, highly functionalized open-cage fullerene derivatives have been employed as ligands in the synthesis of metal complexes [188]. Regarding functionalization, it has been shown that encapsulated species affect the reactivity of the fullerene cage [189,190].

The chemistry of open-cage fullerene derivatives is of particular relevance in this thesis since chapters 4 and 5 of this manuscript deal with the synthesis and applications of this particular class of compounds.

1.8. Functional fullerenes: from biomedicine to next-generation photovoltaics

The potential practical use of fullerenes was already imagined by Kroto, Smalley and Curl in 1985 in their first report on the discovery of C_{60} [2]. However, it was the later finding of their superior electrochemical, photophysical or semiconducting properties, together with the possibility of preparing manageable materials by covalent functionalization what ultimately stimulated the exploration of possible applications in multiple fields.

1.8.1. Fullerenes for biomedical applications

For their use in medicine, fullerenes –like any other bioactive molecule– have to be solubilized in water. Since fullerenes are completely insoluble in water or any other polar solvent, convenient modification of the pristine cages directed to obtaining hydrophilic derivatives is strictly required. Many successful synthetic strategies have been reported over the years toward this goal and, as a consequence, interesting results have been obtained in the field of medicinal chemistry applied to fullerene derivatives and other carbon nanostructures [191]. Such strategies often rely on the synthesis of fullerene bioconjugates, in which amino acids, sugars, or peptides are attached to a fullerene by taking advantage of conventional fullerene chemistry. Incorporation of hydroxyl groups and other polar functional groups like amides or carboxylic acids has also proven useful. Also, the attachment of ionic functionalities or preparation of fulleropyrrolidine derived quaternary ammonium salts is used to obtain highly water-soluble derivatives. A more complex approach consists in supramolecular encapsulation of fullerenes or fullerene derivatives with polar macromolecules like cyclodextrins. While promising results have been obtained mostly in *in vitro* studies, there are no perspectives of fullerene-based medicines in the near future and part of the scientific community is skeptical about their successful application. Several issues like toxicity, bioavailability, pharmacokinetic behavior, bioaccumulation or environmental impact, to name a few, have to be addressed before realistic biomedical applications of fullerenes derivatives are foreseen [37,191,192].

The first water-soluble fullerene derivative was reported by Wudl in 1993 [193]. It consisted of a methanofullerene derivative bearing amido and carboxylic acid moieties that showed anti-HIV activity, presumably by inhibition of the enzyme HIV-1 protease, whose hydrophobic pocket would efficiently accommodate the hydrocarbon cage. Echegoyen and co-workers have recently proved this hypothesis wrong and proposed a new mechanism of action that would involve impairment of virus maturation promoted by a strong interaction of fullerenes to the virus' immature capsid [194]. Highly functionalized globular fullerene dendrimers displaying carbohydrate moieties have shown potent antibacterial and antiviral activities by inhibiting cell adhesion processes. This approach has been used recently by Martín and co-workers to target the Ebola, dengue and Zika viruses [195,196].

The outstanding ability of fullerenes to act as "radical sponges" has been used to explore the applicability of fullerenols as antioxidant agents acting against free radicals. Paradoxically, the generation of radicals has been exploited in photodynamic therapy. The generation of reactive oxygen species can be promoted by the inherent capacity of fullerenes to act as $^1O_2$ photosensitizer, causing cytotoxic effect against tumor cells and DNA photocleavage [48]. Some fullerene derivatives have demonstrated potent immunomodulatory activity [197]. Finally, fullerenes have been suggested as drug delivery systems [198].

EMFs have shown more realistic applications in biomedicine as compared with hollow fullerene derivatives. Depending on the nature of the metal ion inserted, EMFs may act as nanocarriers for imaging, therapy and microsurgery. The carbon cage provides an isolated environment that protects biological systems from the inherent toxicity of the species entrapped. In this regard, water-soluble Gd-based EMFs have shown very promising results for their potential use as magnetic resonance imaging (MRI) contrast agents [31].

1.8.2. Fullerenes for photovoltaic applications

Fullerene-based photovoltaics represent, by far, the most realistic and developed field in fullerene materials science. Global warming and near depletion of fossil fuels is today one of the greatest concerns of humanity. In this regard, on November 2018, the European Commission presented its long-term strategy for a climate-neutral economy by 2050 [199]. Thus, the emergence of new and better technologies able to satisfy world's energy demands without compromising future generations is crucial.

Photovoltaics (PV), the conversion of sunlight into electricity using semiconducting materials, is the most promising of all technologies directed to the production of clean energy production. In general terms, in a PV device (*i.e.* a solar cell) light-induced charge generation, transport of the charges and collection by two electrodes are the phenomena responsible for the conversion of light into current. Silicon-based solar cells have clearly dominated the PV industry for decades with more than 90% of the total world market. Silicon is the second most abundant element in earth's crust, it has optimal bandgap for PV conversion and is nontoxic [199]. Moreover, crystalline-Si solar cells have achieved power conversion efficiency (PCE) values above 26% [200]. Nonetheless, the high cost associated with large-scale manufacturing of Si-based devices has historically precluded the generalization use of PV as a primary source of energy. Current efforts in this field consist in moving from inorganic to organic-based or hybrid materials. Although still far from industrial use, *organic solar cells* (OSCs) and hybrid *organic-inorganic perovskite solar cells* (PSCs) represent nowadays two promising technologies to replace Si in PV because of their low cost, flexibility and easily manageable nature, suitable for large-scale production. Much progress has been made by the scientific community for almost three decades in this field, and fullerenes have played an essential role in this regard.

In an OSC (**Figure 1.8**), light is absorbed by the so-called active layer, which is in turn constituted by an electron donor (p-type material) and an electron acceptor (n-type material). The sequence of events that leads to current generation can be simplified as follows: 1) absorption of photons by the active layer, 2) formation of an electron-hole pair (exciton) with a positive charge (hole) on the donor and the negative charge on the acceptor, 3) exciton diffusion and splitting, and 4) charge transportation and collection by the electrodes [201].

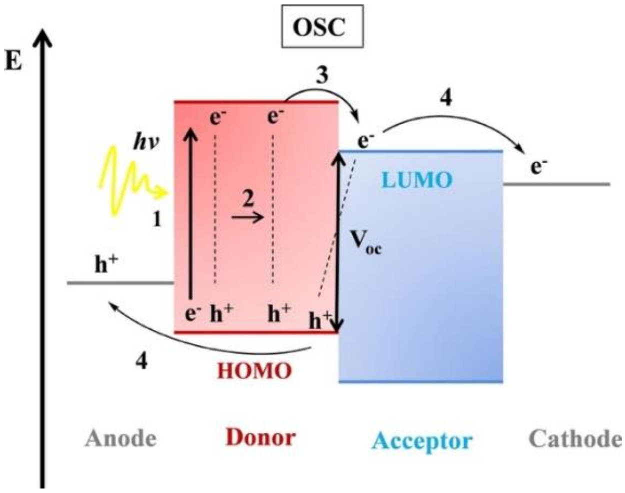

Figure 1.8. Simplified working principle of OSCs. Reprinted from: Marinova, N.; Valero, S.; Delgado, J. L. *J. Colloid Interface Sci.* **2017**, *488*, 373. Copyright © 2018 Elsevier [201].

The performance of a solar cell is determined by the following parameters extracted from the current-voltage (*J*-*V*) curves [202,203] (**Figure 1.9**):

1. **Short circuit current density (J_{sc}):** is the maximum photocurrent density at zero applied potential.
2. **Open-circuit voltage (V_{oc}):** is the voltage value of a given device being open circuited ($J = 0$). It determines the maximum voltage between electrodes. This value is highly determined by the energy difference between the HOMO of the donor and the LUMO of the acceptor.
3. **Fill factor (*FF*):** is the ratio $J\text{max}\cdot V\text{max}/V_{oc}\cdot J\text{sc}$. It can be represented as a rectangle in *J*-*V* curves and represents the ability of carriers to be extracted from a solar cell. In an ideal situation, a *J*-*V* curve would define a perfect rectangle leading to a *FF* value of 100%.
4. **Power conversion efficiency (PCE):** is the most commonly used parameter to evaluate the performance of a solar cell and results from a combination of the previously discussed parameters (Eq.3). It is defined as the proportion of irradiation P_{in} that is converted into actual power $P_{out.}$

$$\eta = \frac{P_{out}}{P_{in}} = \frac{FF(V_{oc} \times J_{sc})}{P_{in}} \qquad \text{(Eq. 1.3)}$$

All this parameters are common for every solar cell regardless of their class.

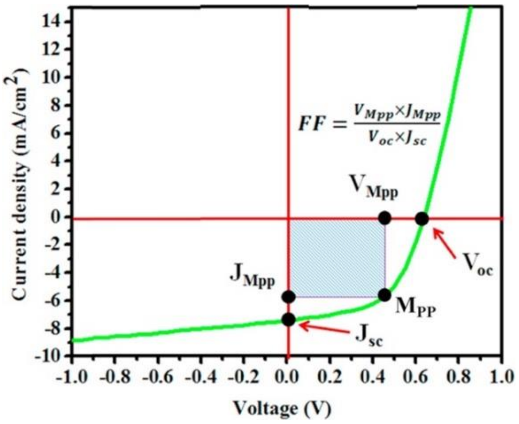

Figure 1.9. Example of a current-voltage (*J*-*V*) curve. Reprinted with permission from: Rafique, S.; Abdullah, S. M.; Sulaiman, K.; Iwamoto, M.. *Renew. Sustain. Energy Rev.* **2018**, *84*, 43-53. Copyright © 2018 Elsevier [203].

In OSCs the donor materials typically involve low bandgap polymers or small donor molecules with high absorption coefficients (**Figure 1.10a**). Fullerene derivatives, by their part, are in general the acceptor molecules of choice (**Figure 1.10b**). The most popular fullerene derivatives used in OSCs are the methanofullerene derivatives $PC_{61}BM$ and $PC_{71}BM$, but a plethora of other fullerene-based molecules have proven useful in many works reported in the literature. While most of them are structurally related to $PC_{61}BM$ and $PC_{71}BM$, efficient derivatives resulting from the use of many synthetic strategies have also been reported [37,204]. Fullerenes have a number of interesting features that make them "the stars of photovoltaics" [205]: they are excellent electron acceptors, have superior electron mobility, low reorganization energy and, unlike other carbon nanostructures, can be functionalized in a controlled manner in order to tune their electronic and physicochemical properties [205]. In spite of all these advantages, fullerene derivatives also present some drawbacks, mostly related with device stability and bandgap tuning. For this reason, many efforts have been devoted in recent years to replace fullerene-based materials by alternative non-fullerene acceptors [206] (**Figure 1.10c**). Outstandingly high PCEs exceeding 16% have obtained very recently with this approach [207]. Some authors have successfully used donor-acceptor hybrid compounds (known as "dyads") as the active layer. These latter compounds consist of donor molecules covalently attached to a fullerene [207,208].

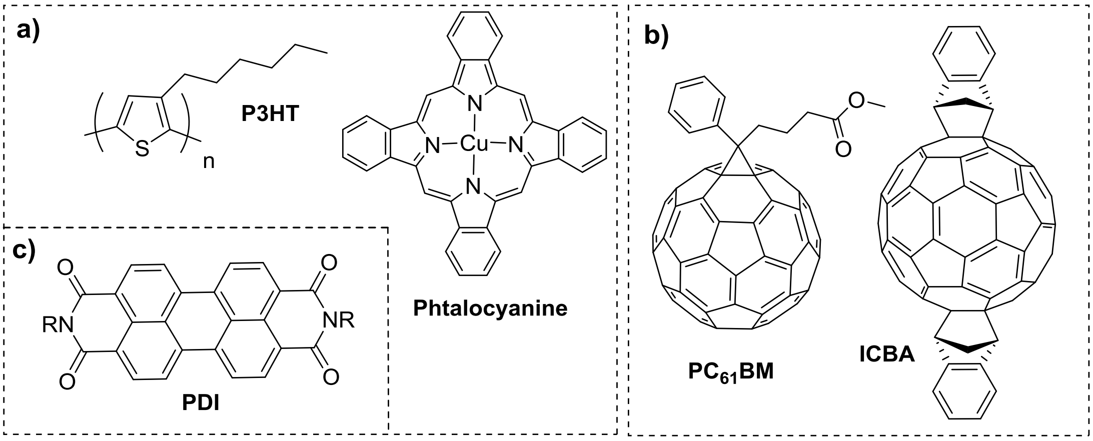
a)
P3HT
S
n
N
N–Cu–N
N
Phtalocyanine
c)
O
RN
O
O
NR
O
PDI
b)
O
O
PC$_{61}$BM
ICBA

Figure 1.10. (a) Common fullerene derivatives used as acceptor materials; (b) donor polymers and molecules used in OSCs; (c) Non-fullerene acceptor molecule.

At their infancy, OSCs were constructed as a planar heterojunction of the donor and the acceptor materials deposited as two different layers and sandwiched between the cathode and the anode. With this device architecture, very low PCE values were obtained. Later, the introduction of the *bulk heterojunction* (BHJ) approach, in which the donor and acceptor materials are blended together in the active layer, remarkably raised the performance of OSCs [209] (**Figure 1.11a**). BHJ is, to date, the state-of-the art architecture in OSCs. Diverse modifications have been introduced in order to circumvent stability issues and to further improve PV performances. That is, design and tuning of alternative acceptor and donor materials, morphology control, introduction of hole- and/or electron-transporting interlayers to avoid charge recombination and the use of enhanced inverted or tandem architectures [203] (**Figure 1.11b**).

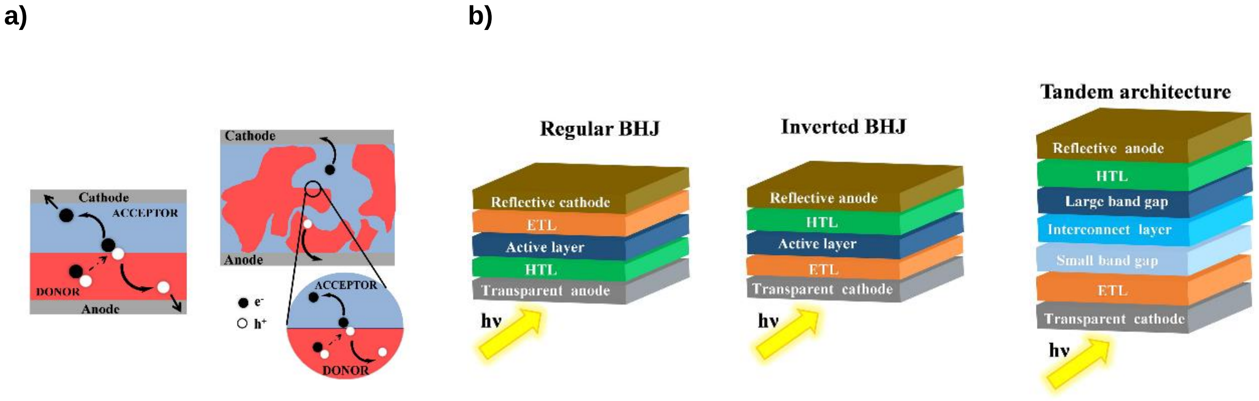
a)
b)
Cathode
ACCEPTOR
DONOR
Anode
Cathode
Anode
ACCEPTOR
DONOR
e⁻
h⁺
Regular BHJ
Reflective cathode
ETL
Active layer
HTL
Transparent anode
hν
Inverted BHJ
Reflective anode
HTL
Active layer
ETL
Transparent cathode
hν
Tandem architecture
Reflective anode
HTL
Large band gap
Interconnect layer
Small band gap
ETL
Transparent cathode
hν

Figure 1.11. Representation of: (a) Planar and BHJ OSCs; (b) different configurations of BHJ OSCs. Reprinted with permission from: Marinova, N.; Valero, S.; Delgado, J. L. *J. Colloid Interface Sci.* **2017**, *488*, 373. Copyright © 2018 Elsevier [201].

1.8.3. Fullerene derivatives as electron-transporting layers in PSCs

In 2009, PSCs emerged as a new class of PV devices [210]. First conceived as a variation of the dye-sensitized solar cells (DSSCs) introduced by Grätzel in the 1980s [211], this new class of hybrid solar cells have experienced an unprecedented efficiency boost in a timespan of less than a decade, raising from 3.8% PCE in their first report to 25.2% in 2019 [212]. While some aspects like stability or upscaling beyond laboratory scale still need to be addressed before industrial production and commercialization, such an exceptional improvement in efficiency make PSCs the most reliable alternative to currently predominant Si-based PV technology [213].

In PSCs, a hybrid organic-inorganic perovskite material with a general formula **ABX_3** adopting a characteristic crystalline structure (**Figure 1.12**) is used as the photoactive layer. **A** is a monovalent cation (i. e. methylammonium or formamidinium), **B** represents a metal (typically Pb) and **X** is a halogen (*i.e.* chlorine, bromine or iodide). The most widespread perovskite material in PV technology is methylammonium lead iodide ($MAPbI_3$). The fabrication techniques and several materials used in PSCs have a lot in common with OSCs. In fact, PSCs technology has taken advantage of most of the acquired experience of chemists and materials scientists working on OPV.

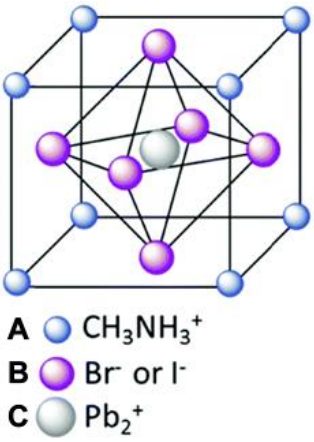

Figure 1.12. Three-dimensional crystal structure of $MAPbI_3$ perovskite. Reprinted with permission from: Castro, E.; Murillo, J.; Fernandez-Delgado, O.; Echegoyen, L. *J. Mater. Chem. C* **2018**, *6*, 2635. Copyright © 2018 Royal Society of Chemistry (RSC) [214].

In spite of the resemblances, the working principle of PSCs differs from OSCs (**Figure 1.13**). The perovskite layer is responsible for light harvesting and charge generation. It is typically sandwiched between a *hole-transporting layer* (HTL) and an *electron-transporting layer* (ETL) which allow for conduction and subsequent collection of holes and electrons on a metallic back contact and a transparent conductive oxide, respectively [201]. Alternatively, HTL and ETL are referred to as *hole-transporting materials* (HTM) and *electron-transporting materials* (ETM), respectively.

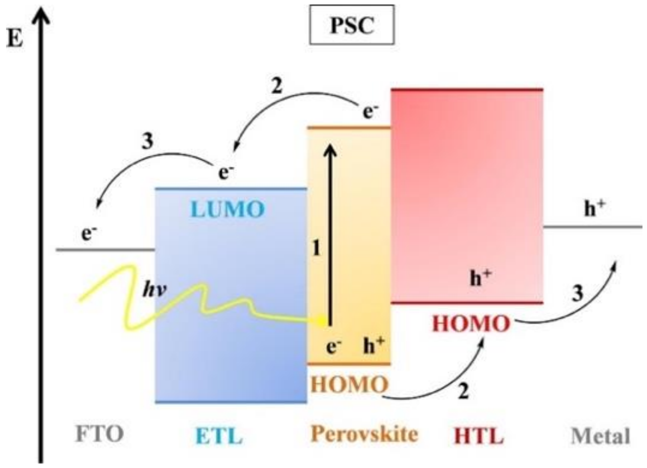
E
PSC
2
e^-
3
e^-
LUMO
e^-
h^+
1
hv
h^+
3
HOMO
e^- h^+
HOMO
2
FTO
ETL
Perovskite
HTL
Metal

Figure 1.13. Simplified working principle of PSCs. Reprinted with permission from: Marinova, N.; Valero, S.; Delgado, J. L. *J. Colloid Interface Sci.* **2017**, *488*, 373. Copyright © 2018 Elsevier [201].

PSCs were initially constructed with a mesoscopic structure resembling DSSCs (**Figure 1.14a**). In this kind of solar cells, a mesoporous metal oxide (TiO_2 or Al_2O_3) acts as the ETL and is infiltrated by the photo-absorbing perovskite layer. Spiro-OMeTAD is commonly used as the HTL. Planar configurations were later introduced (**Figure 1.14b**). They benefit from easier fabrication methods and can be further divided into regular (n-i-p) and inverted (p-i-n) architectures depending on the order of deposition of the ETL and HTL. *Planar inverted PSCs* are structurally related to OSCs and typically involve a fullerene derivative as the ETL and poly(3,4-ethylenedioxythiophene):polystyrene sulfonate (PEDOT:PSS) as the HTL. While record performances have been reported with the mesoscopic device architecture, planar devices have also reached excellent PCE values exceeding 21% [215].

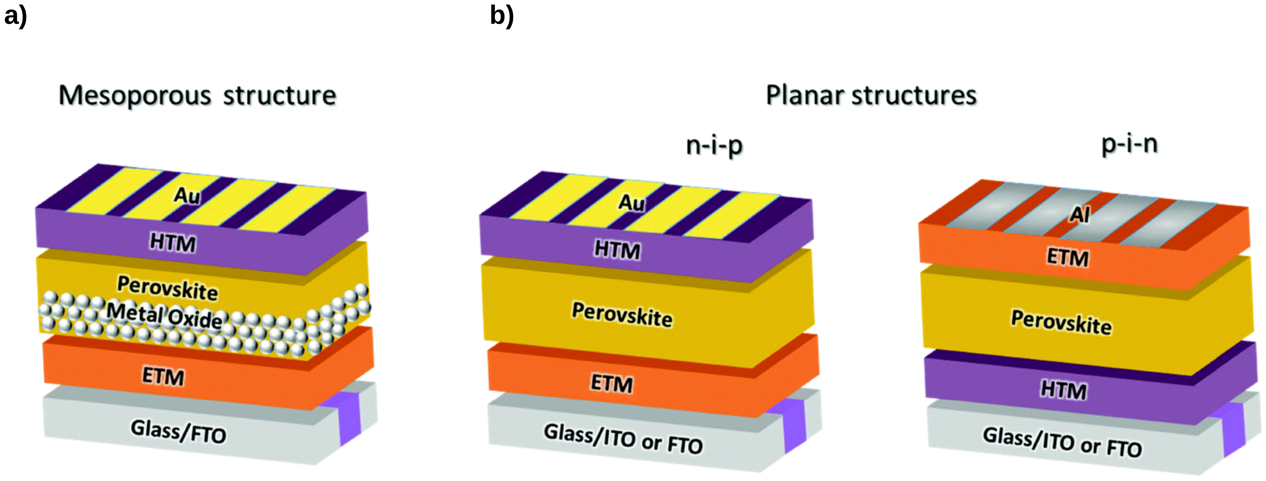
a)
b)
Mesoporous structure
Au
HTM
Perovskite
Metal Oxide
ETM
Glass/FTO
Planar structures
n-i-p
Au
HTM
Perovskite
ETM
Glass/ITO or FTO
p-i-n
Al
ETM
Perovskite
HTM
Glass/ITO or FTO

Figure 1.14. Different structures of PSCs. Reprinted with permission from: Castro, E.; Murillo, J.; Fernandez-Delgado, O.; Echegoyen, L. *J. Mater. Chem. C* **2018**, *6*, 2635. Copyright © 2018 Royal Society of Chemistry (RSC) [214].

The p-i-n structure is the most attractive in terms of manufacturing because the ETL, typically a fullerene derivative, is solution-processed as opposed to the metal oxides employed in the regular planar and mesoporous configurations, which require high-temperature annealing steps. Importantly, p-i-n PSCs can be easily integrated in flexible devices. A downside of the p-i-n configuration is that high V_{oc} values are difficult to achieve. Successful strategies to overcome this limitation rely on the incorporation of dopant materials in both the HTL and ETL, interfacial engineering, morphology control, or the replacement of the HTLs and ETLs [216,217].

Fullerenes were first incorporated in PSCs in 2013. They are used as the ETLs but also provide additional advantages that have helped to circumvent some inherent problems associated with PSCs. Importantly, fullerenes prevent hysteretic behavior of PSCs typically observed in J-V curves by passivating the charge trap states on the surface and ground boundaries of the perovskite layer in both regular and inverted structures. Moreover, when incorporated as additives, fullerenes can improve device stability, act as cathode buffer layers facilitating ohmic contact at the ETL-metal electrode interface, or act as templates for better perovskite crystal growth. In regular devices, fullerenes can replace the metal oxide commonly used as the ETL or can be used as interfacial modification layers [214,218–220].

As in the case of OSCs, $PC_{61}BM$ and $PC_{71}BM$ clearly dominate the field. However, many other synthetic fullerene derivatives have shown excellent performance. The development of new derivatives specifically designed to accomplish one or more of the functions above discussed is indeed a prominent field of research. Recent reports have been focused on interfacial interactions of the perovskite with the neighboring layers. It has been reported that fullerene derivatives displaying specific functional groups in their addends favorably interact with the perovskite layer and lead to a beneficial passivating effect on the latter [221,222]. Synthetic organic chemists working in fullerene chemistry play therefore a central role in the race toward optimal and commercially viable PSCs.

PSCs are of particular relevance in this thesis, since chapter 5 deals with the enhancement of V_{oc} values by incorporating a new class of ETLs (open-cage fullerenes) in devices with a p-i-n structure.

Section 2: Transition metal-catalyzed [2+2+2] cycloaddition reactions

2.1. General aspects

Transition metal-catalyzed reactions represent one of the most powerful synthetic tools to access molecular complexity from simple and readily available substrates [223,224]. Within this context, the development of catalytic methodologies involving the formation of C–C bonds to enable the generation of annulated systems constitutes a field of paramount relevance in synthetic organic chemistry. One paradigmatic process to efficiently accomplish this goal is the *transition metal-catalyzed [2+2+2] cycloaddition reaction*, since it allows for the formation of a wide scope of highly functionalized six-membered carbo- and heterocyclic molecules in a single step with high efficiency and perfect atom economy [225–227].

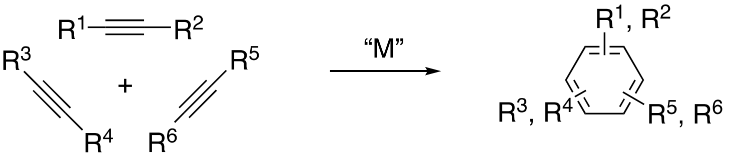

Scheme 1.27. Transition metal-catalyzed cyclotrimerization of alkynes (M = transition metal catalyst)

The first example of *alkyne cyclotrimerization* dates back to more than 150 years ago, when Bertholet discovered the thermal cyclisation of acetylene to produce benzene. Though being exothermic (ΔG = -143 kcal/mol), this process lacks practical usefulness, since extremely high temperatures are required to overcome the large energy barrier of the reaction [228]. Almost one century later, Reppe discovered the first transition-metal-mediated [2+2+2] cycloaddition reaction using a Ni complex [$Ni(PPh_3)_2$ $(CO)_2$] and a series of alkynes. The reaction allowed the synthesis of substituted benzene derivatives under milder conditions [229]. The seminal work by Reppe laid the foundations of a myriad of related reactions reported for more than 7 decades of prolific investigation.

Nowadays, transition metal-catalyzed [2+2+2] cycloaddition reactions are an established instrument of the synthetic toolbox. Several metals have proven useful in promoting or catalyzing the reaction, being Ni, Co, Pd, Rh, Ru, Zr, Ir and Fe the most used ones. Also, diverse groups of molecules other than alkynes, like alkenes, allenes, nitriles or carbonyl compounds have been employed as the unsaturated partners in order to afford a large diversity of families bearing 6-MR.

The reaction proceeds efficiently in its intermolecular version starting from three disconnected unsaturated substrates, but also more complex tethered di- and tri-unsaturated molecules can be used, giving rise to partially or totally intramolecular reactions (**Scheme 1.28**). Notably, for the latter case, up to three rings can be forged in a single reaction step. However, such an efficient process is not free of some inconveniencies, mostly related to chemo- and regioselectivity. When central, axial, planar or helical chirality is generated in reaction products, stereoselectivity has to be considered too. Recent advances in the field have been directed to overcome these difficulties by developing new catalysts and reaction protocols.

The significance of [2+2+2] cycloaddition reactions in synthetic chemistry is clearly evidenced by a large number of reviews published, mainly during the last 15 years. Some cover general aspects [230–233] and other focus on more specific aspects such as the catalytic systems used [234–237], the unsaturated substrates involved [238–245] and the chemo-, regio- and stereoselectivity of the reactions [246–250]. Practical synthetic applications have been reviewed as well [251,252]. A brief summary of this previously reviewed content will be given along this section, together with some uncovered yet relevant recent examples. In line with the projects developed in this thesis, most of the content outlined will be related to rhodium catalysis.

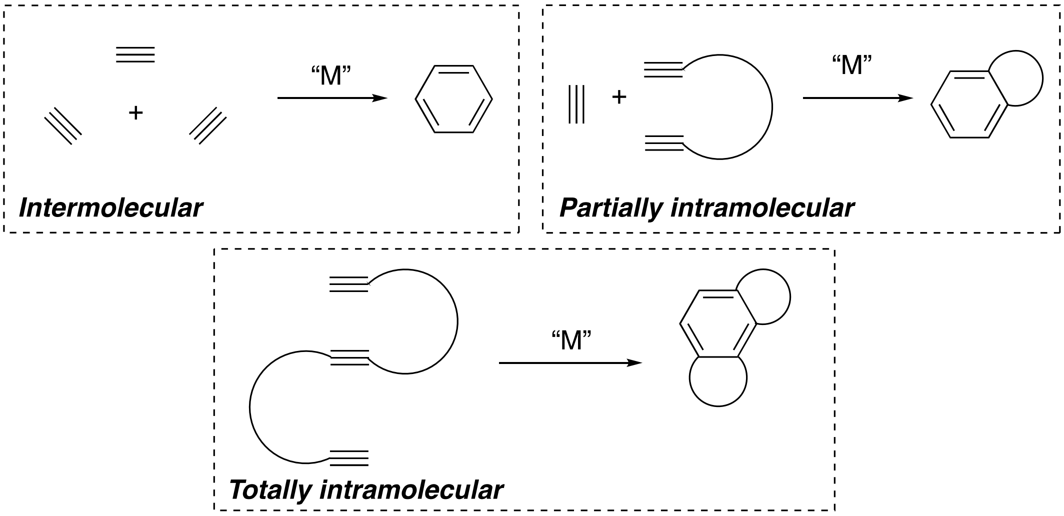

Scheme 1.28. Tethered and non-tethered [2+2+2] cycloaddition reactions of alkynes. "M" = metal complex.

2.2. Mechanism

Several experimental and computational studies have aimed at unraveling the mechanism underlying transition metal-catalyzed [2+2+2] cycloaddition reactions. Although every specific mechanistic pathway is highly affected by the metal, the ligands and substrates considered, the generally accepted mechanism extracted from these works consists of the following steps (**Scheme 1.29**): the reaction starts by coordination of one alkyne to the metal center leading to intermediate **I**. This first step is followed by coordination of the second alkyne to form intermediate **II**, which is transformed into species **IIIa** or **IIIb** through an oxidative coupling mechanism. The concurrence of cyclometallapentadiene **IIIa** or cyclometallaheptatriene **IIIb** in the reaction mechanism has been confirmed experimentally in many occasions [253,254]. With very few exceptions, the oxidative coupling has been found to be rate-determining [255,256]. Coordination of a third alkyne forming intermediate **IV** is subsequently followed by either: 1) insertion by Schore's mechanism [257] leading to homoaromatic cycloheptatriene **V**; 2) [4+2] cycloaddition to form 7-metallanorbornadiene **VI** or 3) [2+2] cycloaddition to form metallabicyclic species **VIII**. Reductive elimination and subsequent complex release ultimately gives the corresponding arene (**P)** as a product. An alternatively concurring mechanism that involves reductive elimination from intermediate **IIIa** leads to a thermodynamic trap of the catalytic cycle by formation of cyclobutadiene metal complex **IX**. The aromaticity acquired by the final reaction product accounts for its easy formation even at mild conditions.

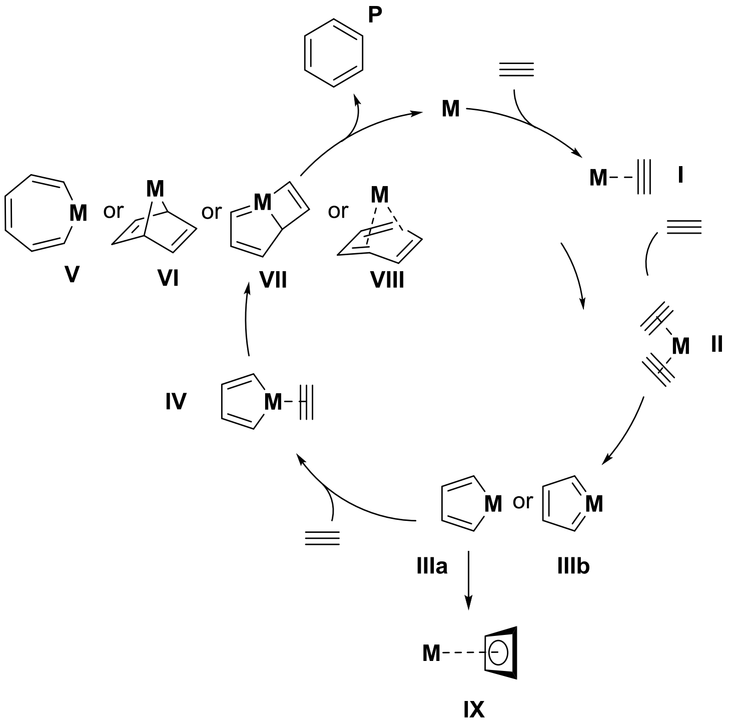

Scheme 1.29. Simplified representation of the generally accepted mechanism of the transition metal-catalyzed [2+2+2] cycloaddition involving three alkynes.

Bickelhaupt reported in 2007 the first computational study of the Rh-catalyzed [2+2+2] cycloaddition reaction [255]. The authors performed DFT calculations to study: 1) the mechanism that transforms three acetylene molecules into benzene, and 2) the mechanism that transforms two acetylenes and one acetonitrile molecule into 2-methylpyridine. Two different Rh(I) half-sandwich complexes (CpRh and IndRh) were used as the model catalysts. The work concluded that both reactions proceed through a rhodacyclopentadiene intermediate (**IIIa**), given that the oxidative coupling step involving acetylene and acetonitrile is thermodynamically disfavored. As above discussed, for both mechanisms this process was found to be the rate-determining step. For the case of benzene formation, coordination of a third molecule and [4+2] cycloaddition leads to a η^4-coordinated Rh–arene intermediate **(VIII**) that releases the final benzene product by coordination of two new acetylene molecules. In the 2-methylpyridine pathway, acetonitrile competes with acetylene to coordinate to the rhodacyclopentadiene intermediate. In this case, a rhodabicyclic complex (**VIII**) forms, which undergoes reductive elimination and release of the product again by coordination of two substrate molecules. As the formation of benzene is thermodynamically favored, an excess of acetonitrile is required in order to obtain good pyridine yields. This latter observation is in good agreement with the experiments.

Our group has also contributed to the computational study of rhodium-catalyzed [2+2+2] cycloaddition reactions. In 2010, we reported a DFT study analyzing the [2+2+2] acetylene cyclotrimerization process catalyzed by Wilkinson's complex [(RhCl(PPh$_3$)$_3$] [256]. The mechanism (**Figure 1.15**) was found to be closely related to the one described by Bickelhaupt. More importantly, this work demonstrated that modeling PPh$_3$ ligands by a simplified version (PH$_3$), resulted in no significant changes in the thermodynamics and the kinetics of the reaction, thus providing a useful simplification to significantly reduce the cost of computational protocols. In 2014, we took advantage of this approximation in a similar work in which the formation of pyridine by the [2+2+2] cycloaddition of two acetylene molecules and hydrogen cyanide was studied [258]. Additionally, we showed in this work that the attachment of an electron withdrawing substituent favors the formation of the pyridine derivative.

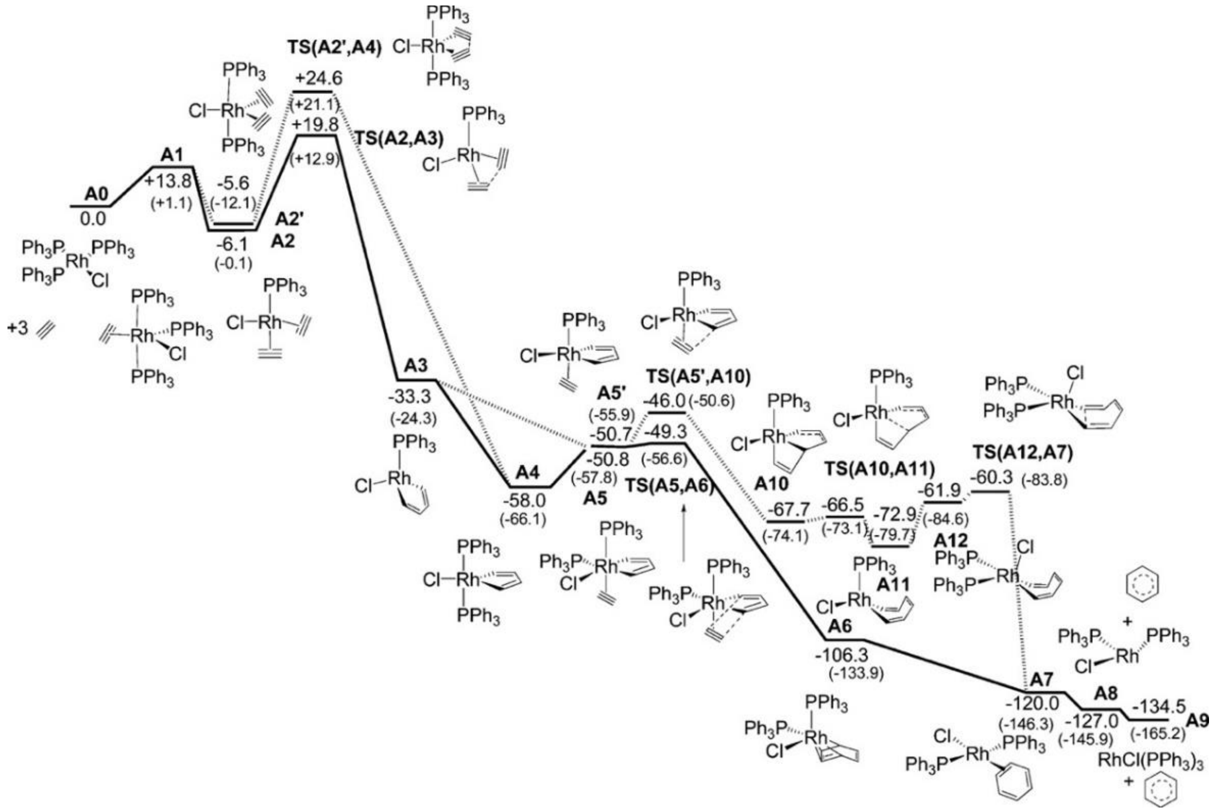

Figure 1.15. Gibbs energy profile at 298 K for the [2+2+2] acetylene cyclotrimerization catalyzed by [RhCl(PPh_3)$_3$]. Reprinted with permission from: Dachs, A.; Osuna, S.; Roglans, A.; Solà, M. *Organometallics* **2010**, *29*, 562. © 2010 American Chemical Society (ACS) [256].

2.3.Transition-metal promoted [2+2+2] cycloadditions in synthetic organic chemistry

2.3.1. Construction of benzene rings

The ubiquitous presence of unsaturated rings in natural products, drugs, functional materials and other classes of compounds of practical interest has made transition metal-catalyzed [2+2+2] cycloadditions an invaluable synthetic alternative for organic chemists as compared to traditional synthetic protocols to functionalize aromatic molecules (*e.g.* electrophilic or nucleophilic aromatic substitutions).

The use of partially or totally intramolecular versions of the transition metal-catalyzed [2+2+2] cycloaddition at late stages of a synthetic sequence has been exploited as a helpful strategy to selectively forge highly substituted arene moieties. The chemo- and regioselectivities are considerably restricted thanks to the position and orientation of the alkyne moieties in tethered substrates. The “intramolecular approach” was used by Volhardt in 1980, who managed to produce the tetracyclic core of the natural product estrone using a Co-catalyzed [2+2+2] cycloaddition reaction of a diyne with an alkyne [259] (**Scheme 1.30**). Volhardt’s synthesis of estrone is of historical relevance, since it represents the first total synthesis employing this reaction.

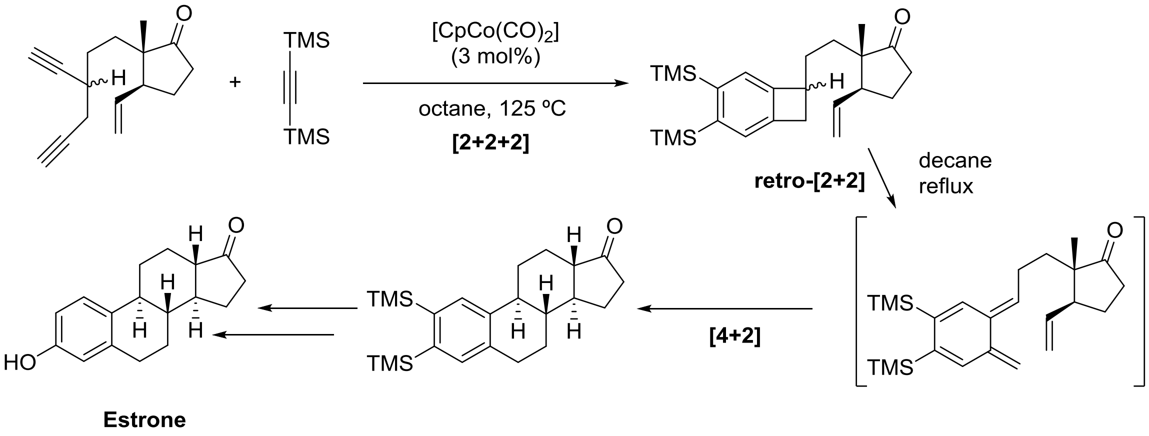
[CpCo(CO)2]
(3 mol%)
octane, 125 °C
[2+2+2]
TMS
TMS
decane
reflux
retro-[2+2]
[4+2]
HO
Estrone

Scheme 1.30. Synthesis of estrone by means of a Co-catalyzed [2+2+2] cycloaddition reaction.

In a more recent report by Sorensen, a totally intramolecular [2+2+2] cycloaddition catalyzed by Wilkinson's complex gave a tricyclic precursor for the total synthesis of the antibiotic compound (±)-viridin [260] (**Scheme 1.31**).

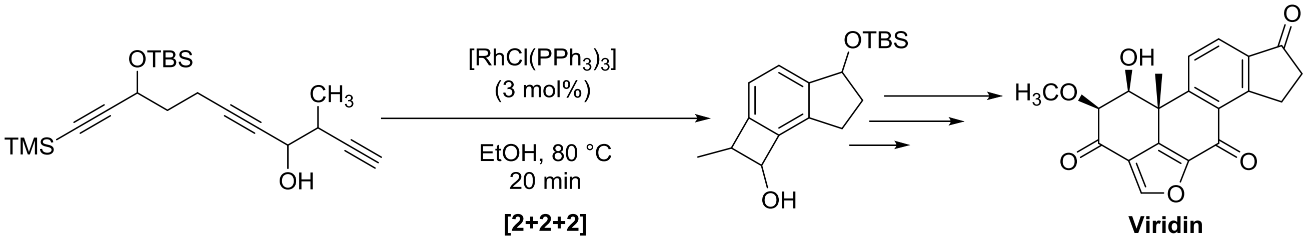
OTBS
TMS
CH3
OH
[RhCl(PPh3)3]
(3 mol%)
EtOH, 80 °C
20 min
[2+2+2]
H3CO
Viridin

Scheme 1.31. Synthesis of (±)-viridin by means of a Rh-catalyzed [2+2+2] cycloaddition reaction.

Our group has reported on several examples of partially and totally intramolecular reactions of three alkynes employing neutral Rh(I) catalysts. Specifically, the reaction of macrocyclic triynes and pentaynes to afford tetracyclic scaffolds bearing central arene moieties was achieved using [RhCl(CO)(PPh$_3$)$_3$] and [RhCl(PPh$_3$)$_3$]-catalyzed reactions [261,262] (**Scheme 1.32**). When the reaction was performed in molten tetra(*n*-butyl)ammonium bromide, the catalyst was recycled and reused [263].

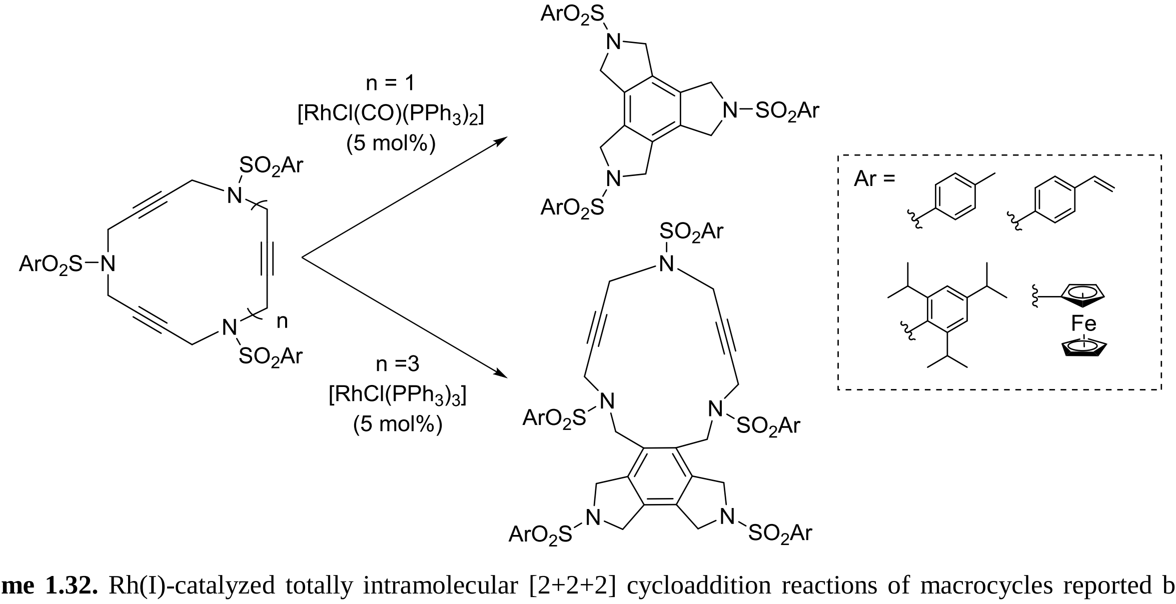
n = 1
[RhCl(CO)(PPh3)2]
(5 mol%)
n =3
[RhCl(PPh3)3]
(5 mol%)
ArO2S
SO2Ar
n
Ar =
Fe

Scheme 1.32. Rh(I)-catalyzed totally intramolecular [2+2+2] cycloaddition reactions of macrocycles reported by our research group.

In 2009, we reported the partially intermolecular reaction of internal diynes with a series of alkynyl-α-amino acids [264]. We have also shown the ability of Rh–NHC complexes to catalyze both totally and partially intramolecular [2+2+2] cycloadditions [265] and of Rh-N-phosphino *tert*-butylsulfinamide (PNSO) complexes to catalyze the partially intramolecular variation of the reaction [266].

The control of chemo- and regioselectivities becomes much more difficult when it comes to intermolecular reactions [248]. As an example, the homo-cyclotrimerization of a terminal alkyne can afford two different isomers, namely 1,2,4-substituted and 1,3,5-substituted benzene derivatives (**Scheme 1.33**). Obviously, when 2 or 3 different alkynes react, the number of possible products dramatically increases.

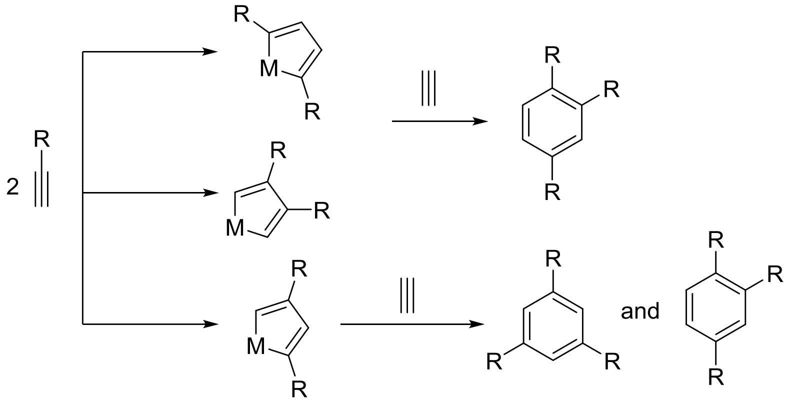

Scheme 1.33. Simplified mechanism for the formation of 1,2.4-substituted and 1,3,5-substituted isomers in alkyne homo-trimerization.

Major advances in controlling this kind of intermolecular reactions of alkynes have been made by the group of Tanaka, who developed in 2003 a method to obtain 1,2,4-substituted isomers selectively by employing cationic Rh(I)–biaryldiphosphine complexes as catalysts [267]. Excellent selectivity for single isomers has been reported for both homo- and hetero-cyclotrimerizations by taking advantage of this versatile catalytic system (**Scheme 1.34**) [268–270]. Our group has reported very recently an exhaustive mechanistic study combining experiments and computational calculations to explain the factors that govern the regioselectivity of these processes [271].

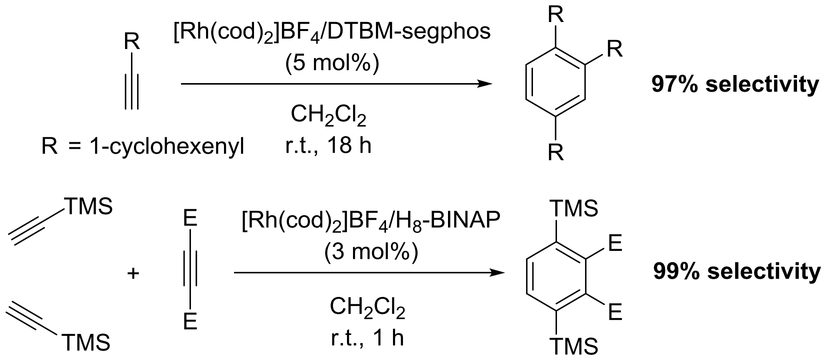

Scheme 1.34. Chemo- and regioselective alkyne cyclotrimerizations reported by Tanaka. E = $COOCH_2CH_3$.

From a practical perspective, [2+2+2] cycloadditions can be used to prepare complex polyaromatic compounds of interest in materials science. By taking advantage of the excellent selectivity provided by Rh(I)–biarylphosphine cationic complexes, Tanaka reported a series of [16], [12], [10], [8] and [6] cycloparaphenylenes (CPPs) which have been synthetized [272–276] (**Scheme 1.35a**). An equivalent protocol was used very recently to chemically construct the smallest carbon nanocage ever reported [277]. Still in the realm of synthetic chemistry applied to materials science, Müllen reported in 2000 a synthetic methodology to prepare large 2D polyaromatic hydrocarbons relying on a straightforward sequence encompassing a Co-catalyzed cyclotrimerization of internal acetylenes substituted with aryl groups, followed by Cu-catalyzed cyclodehydrogenation [278] (**Scheme 1.35b**).

a) K. Tanaka [275]

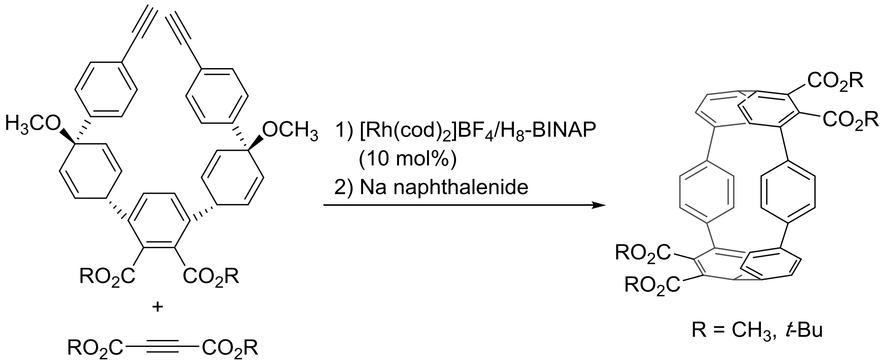

b) K. Müllen [278]

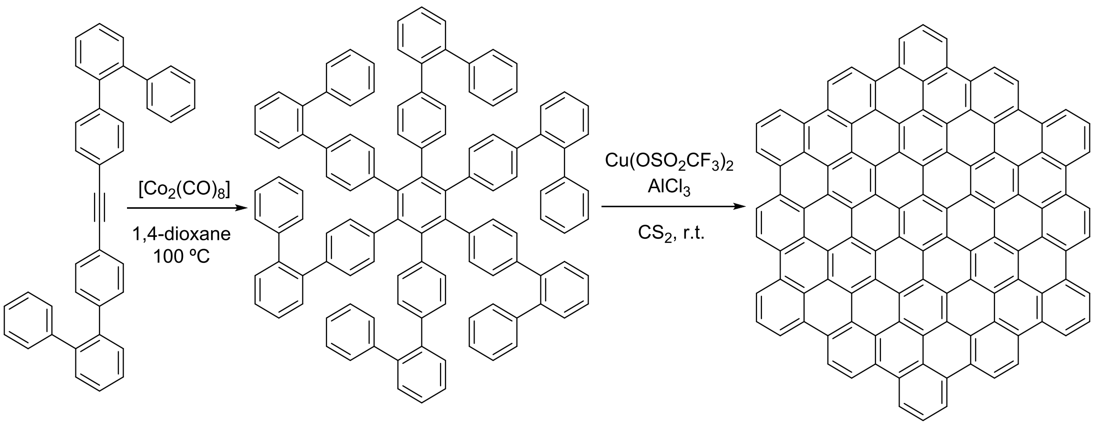

Scheme 1.35. Rh-catalyzed [2+2+2] cycloadditions towards the synthesis of CPPs and polyaromatic hydrocarbons.

2.3.2. Construction of pyridine rings

The participation of nitriles together with alkynes in transition metal-catalyzed [2+2+2] cycloaddition reactions allows for the construction of pyridine rings. While pioneering work mostly involved Co catalysis, it has been demonstrated throughout the years that most of the metals used in alkyne cyclotrimerization also promote pyridine formation [241,243,245]. Indeed, both mechanisms proceed very similarly. Since undesired arenes can be formed as byproducts, the control of chemoselectivity becomes particularly significant in this case.

The first example of a rhodium-catalyzed [2+2+2] cycloaddition of alkynes with nitriles was reported by Ingrosso in 1987 using a cyclopentadienyl rhodium(I) complex $[RhCpL_2]$ as a catalyst [279]. In combination with an excess of nitrile in order to favor the reaction towards pyridine derivatives, the reaction provided a mixture of two pyridine regioisomers together with benzene byproducts (**Scheme 1.36a**). An enhancement in chemo- and regioselectivity was once again achieved by Tanaka in 2006 using cationic rhodium(I)/biarylbisphosphine complexes as catalysts (**Scheme 1.36b**) [270,280–282].

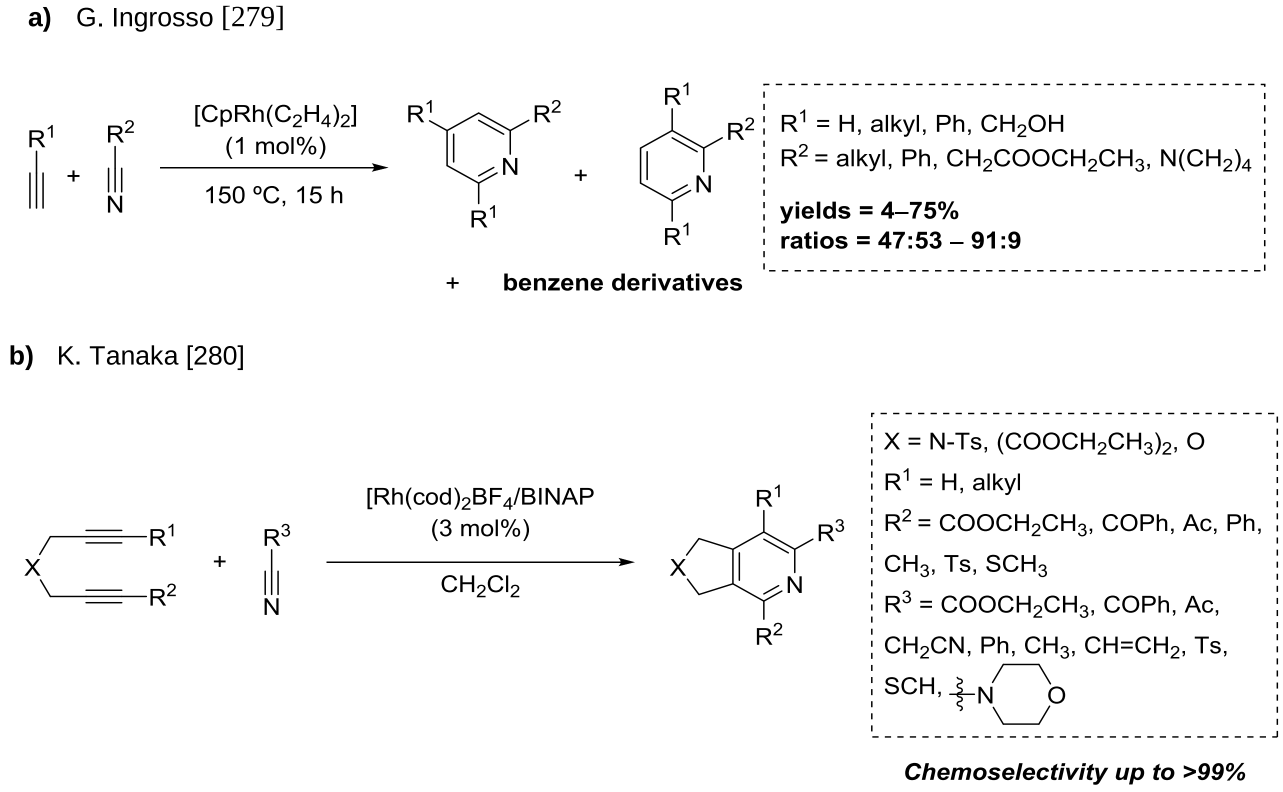
a) G. Ingrosso [279]
R1
R2
N
[CpRh(C2H4)2]
(1 mol%)
150 °C, 15 h
R1
R2
N
R1
+
R1
R2
N
R1
+ benzene derivatives
R1 = H, alkyl, Ph, CH2OH
R2 = alkyl, Ph, CH2COOCH2CH3, N(CH2)4
yields = 4–75%
ratios = 47:53 – 91:9
b) K. Tanaka [280]
X
R1
R2
+
R3
N
[Rh(cod)2BF4/BINAP
(3 mol%)
CH2Cl2
X
R1
R3
N
R2
X = N-Ts, (COOCH2CH3)2, O
R1 = H, alkyl
R2 = COOCH2CH3, COPh, Ac, Ph, CH3, Ts, SCH3
R3 = COOCH2CH3, COPh, Ac, CH2CN, Ph, CH3, CH=CH2, Ts, SCH,
N
O
Chemoselectivity up to >99%

Scheme 1.36. Intermolecular transition metal-catalyzed [2+2+2] cycloaddition reactions of alkynes and nitriles.

Our group described in 2010 the synthesis of tricyclic pyridines *via* a completely intramolecular [2+2+2] cycloaddition of linear diynenitriles catalyzed by [RhCl(PPh$_3$)$_3$] [283]. We observed that microwave (MW) heating dramatically improved catalytic efficiency. Both internal and terminal diynenitriles bearing sulfonamide, oxygen, and malonate tethers were used as substrates. Bipyridine compounds were also prepared by 2-fold cyclisation of linear substrates (**Scheme 1.37**).

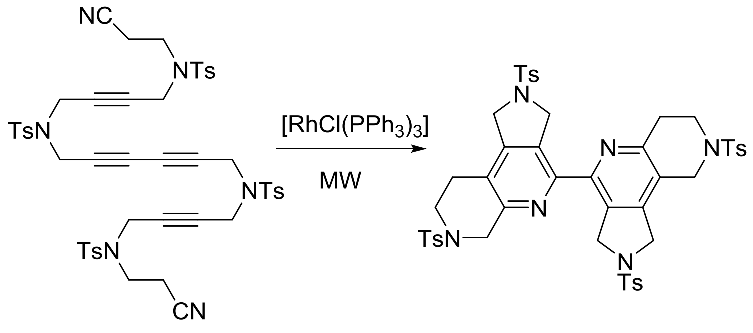
NC
NTs
TsN
NTs
TsN
CN
[RhCl(PPh3)3]
MW
Ts
N
N
NTs
TsN
N
N
Ts

Scheme 1.37. Synthesis of an hexacyclic bipyridine derivative from diynenitriles developed by our group.

The intramolecular variation of the reaction was also used by Tanaka to enantioselectively prepare spiropipyridines using a cationic Rh(I)-(*R*)-Segphos complex as catalyst [284].

2.3.3. Construction of cyclohexadiene rings and the stereoselectivity of Rh(I) catalyzed [2+2+2] cycloadditions

Alkenes are less reactive than alkynes in transition metal-catalyzed [2+2+2] cycloaddition reactions. However, their use is of particular interest, since the 1,3-cyclohexadiene products generated contain two potential stereocenters (**Scheme 1.38**). Therefore, besides common chemo- and regioselectivity issues, controlling the *stereoselectivity* of the process becomes a major synthetic challenge when alkenes are involved [240].

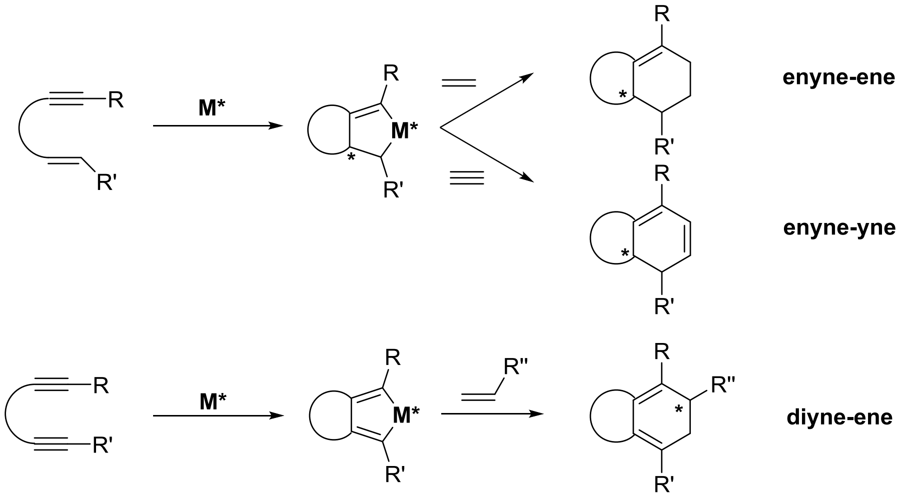

Scheme 1.38. Generation of central chirality in alkene-involving transition metal-mediated partially intramolecular [2+2+2] cycloadditions. **M*** = chiral catalytic system.

Cationic Rh(I)-based catalysts are again an excellent choice. Chiral phosphine ligands in their enantiopure form can be installed in the Rh(I) complex starting from readily available precursors in an easy operational step that is usually performed *in situ* without the need for isolation of the catalytic species. Typically, a CH_2Cl_2 solution of a precursor complex $[Rh(cod)_2]BF_4$ and the desired phosphine ligand are treated with $H_2(g)$ for 30 min. This results in reduction of cyclooctadiene double bonds and subsequent displacement and substitution by the ligand. The obtained catalytic mixture is concentrated to dryness, re-dissolved and added to the reaction. It has been shown that a combination of BINAP and $[Rh(cod)_2]BF_4$ in a 1:1 ratio in CH_2Cl_2 selectively forms $[Rh(cod)(BINAP)]BF_4$ [285,286]. This simple protocol, introduced by the group of Tanaka in early studies on enantioselective [2+2+2] cycloaddition reactions [280], has been widely employed by many groups (including our research group) to survey the activity of dozens of different ligands in short periods of time, thus accelerating the discovery and optimization of a target chemical process. A recent work by Hapke has studied the influence of the diphosphine ligands and the solvent employed in the outcome and time required for catalyst activation [287].

The first example of a Rh-catalyzed enantioselective quaternary center formation was reported by Shibata in 2005 [288]. A partially intramolecular reaction between enynes and alkynes afforded chiral 1,3-cyclohexadienes with excellent yields and enantioselectivities. Soon after, the same group reported the reaction between internal diynes with *exo*-methylene lactones [289]. Several examples of partially intramolecular reactions with both enynes [290,291] (**Scheme 1.39a**) and diynes [292,293] (**Scheme 1.39b**) have followed over the years. As an example, our group reported in 2016 the reaction of sulfonamide-tethered internal diynes with Morita-Baylis-Hillman adducts in a completely diastereoselective and highly enantioselective kinetic resolution process catalyzed by a cationic Rh(I)-(*R*)-BINAP catalyst [294].

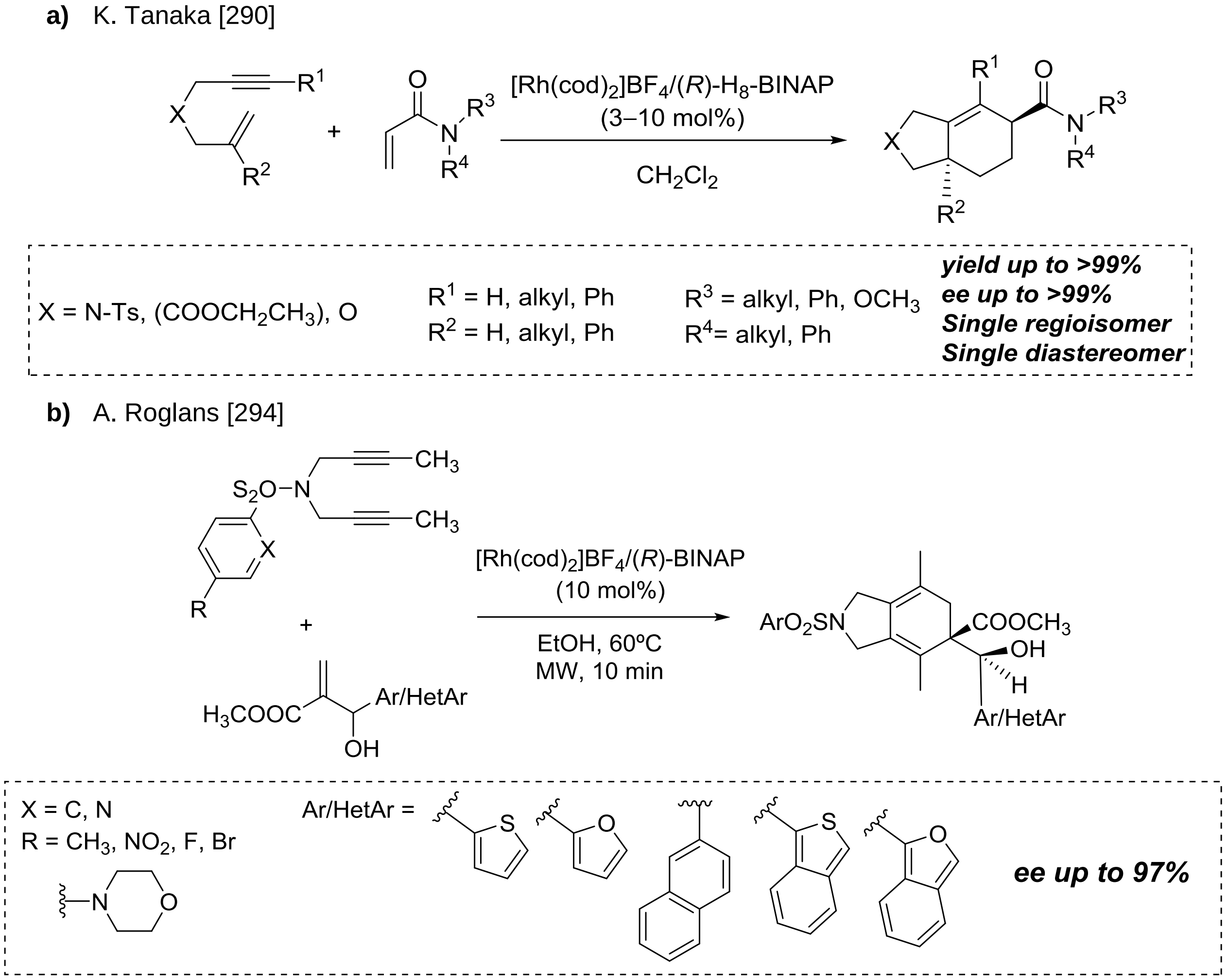
a) K. Tanaka [290]
[Rh(cod)2]BF4/(R)-H8-BINAP
(3–10 mol%)
CH2Cl2
X = N-Ts, (COOCH2CH3), O
R1 = H, alkyl, Ph
R2 = H, alkyl, Ph
R3 = alkyl, Ph, OCH3
R4= alkyl, Ph
yield up to >99%
ee up to >99%
Single regioisomer
Single diastereomer
b) A. Roglans [294]
[Rh(cod)2]BF4/(R)-BINAP
(10 mol%)
EtOH, 60ºC
MW, 10 min
ArO2SN
COOCH3
OH
H
Ar/HetAr
H3COOC
X = C, N
R = CH3, NO2, F, Br
Ar/HetAr =
ee up to 97%

Scheme 1.39. Stereoselective enyne-ene and diyne-ene reactions.

Examples of intermolecular reactions have also been documented [240]. In a remarkable study published in 2014, Tanaka reported highly efficient, chemo-, regio- and enantioselective three component [2+2+2] cycloaddition reaction of two different alkynes with enamides [295].

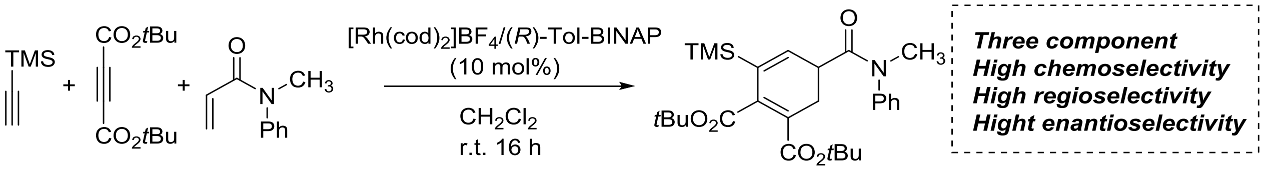
TMS
CO2tBu
CO2tBu
[Rh(cod)2]BF4/(R)-Tol-BINAP
(10 mol%)
CH2Cl2
r.t. 16 h
tBuO2C
Three component
High chemoselectivity
High regioselectivity
Hight enantioselectivity

Scheme 1.40. Rh(I)-catalyzed three component [2+2+2] cycloaddition of two different alkynes and one alkene.

Our group has made important contributions to the field with a series of reports on the intramolecular variation of the reaction. In initial studies, we reported the synthesis of tetracyclic systems bearing a cyclohexadiene core starting from macrocyclic enediynes [261]. When the reaction was carried out using cationic chiral Rh(I)–phosphine catalysts only moderate enantioselectivities were observed [296]. Later, we performed a computational study to fully understand the Rh(I)-diphosphine mechanism of both macrocyclic and linear enediynes [297]. Based on DFT calculations we provided a rationale to the low *ee* values obtained in our work and also to the disparate enantioselectivities obtained in previous studies by Tanaka and Shibata [298] on the [2+2+2] cycloaddition of linear enediynes. We found that while acyclic enediynes with specific substitution patterns prefer the enyne oxidative coupling in some cases, cyclic enediynes always favor the alkyne–alkyne coupling. As depicted in **Scheme 1.41**, following one or the other path is key to the outcome of the reaction in terms of stereoselectivity.

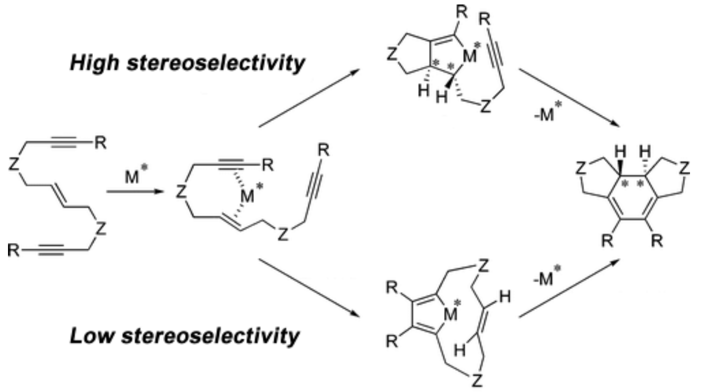

Scheme 1.41. Different reaction paths explain differences in enantioselectivity of Rh(I)-catalyzed [2+2+2] cycloadditions of linear enediynes. R and Z groups determine which of two pathways is preferred, as shown by our computational study [297]. Adapted with permission from: Shibata, T.; Kurokawa, H.; Kanda, K. *J. Org. Chem.* **2007**, *72*, 6521, © 2007 American Chemical Society (ACS) [298].

In a later experimental-computational study, we unveiled the mechanistic differences existing between the Rh(I)–catalyzed [2+2+2] cycloadditions of yne-ene-yne substrates and the ones bearing yne-yne-ene sequences [299]. For the latter ones, a mechanistic pathway involving β-hydride elimination explains the formation of a non-expected tricyclic isomer (**Scheme 1.42**). In collaboration with the groups of Riera and Verdaguer, we reported in 2012 the catalytic activity of Rh(I) complexes with P-stereogenic secondary iminophosphorane (SIP) ligands in the totally intramolecular [2+2+2] cycloadditions with an yne-ene-yne sequence [300]. Remarkably, otherwise difficult to cyclize terminal alkynes gave the corresponding tricyclic products with good yields and enantioselectivities.

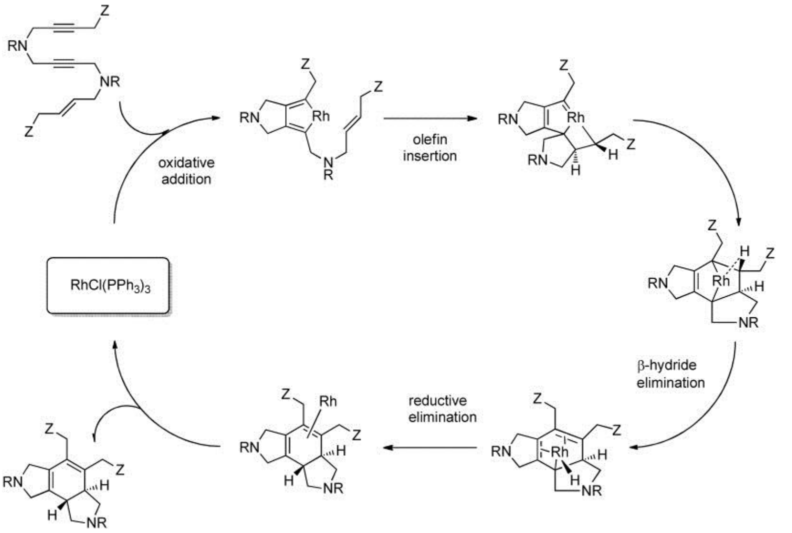

Scheme 1.42. Mechanism involved in the Wilkinson's complex-catalyzed [2+2+2] cycloadditions of enediynes with an yne-yne-ene sequence. Reprinted with permission from: Dachs, A.; Pla-Quintana, A.; Parella, T.; Solà, M.; Roglans, A. *Chem. Eur. J.* **2011**, *17*, 14493. Copyright © 2011 Wiley-VCH Verlag GmbH & Co. KGaA, Weinheim [299].

Besides the introduction of quaternary C-sp^3 stereocenters, chiral transition metal catalysts promoting [2+2+2] cycloaddition reactions can afford optically active products with other kinds of chirality. Planar chirality is present in *para*- and *meta*-cyclophanes obtained by asymmetric partially intramolecular reactions using cyclic diynes with long tether functionalities between the C–C triple bonds [301] (**Scheme 1.43a**). Chiral helical molecules can also be obtained starting from rigid aryl-tethered oligoynes [302] (**Scheme 1.43b**). The enantioselective partially or totally intramolecular reactions of alkynes with properly substituted aryl terminal groups lead to cyclotrimerized compounds with axial chirality [303]. Some years ago, we used Rh-based dendrimeric recyclable systems to obtain axially chiral biaryls with enantioselectivities up to 98% [304] (**Scheme 1.43c**).

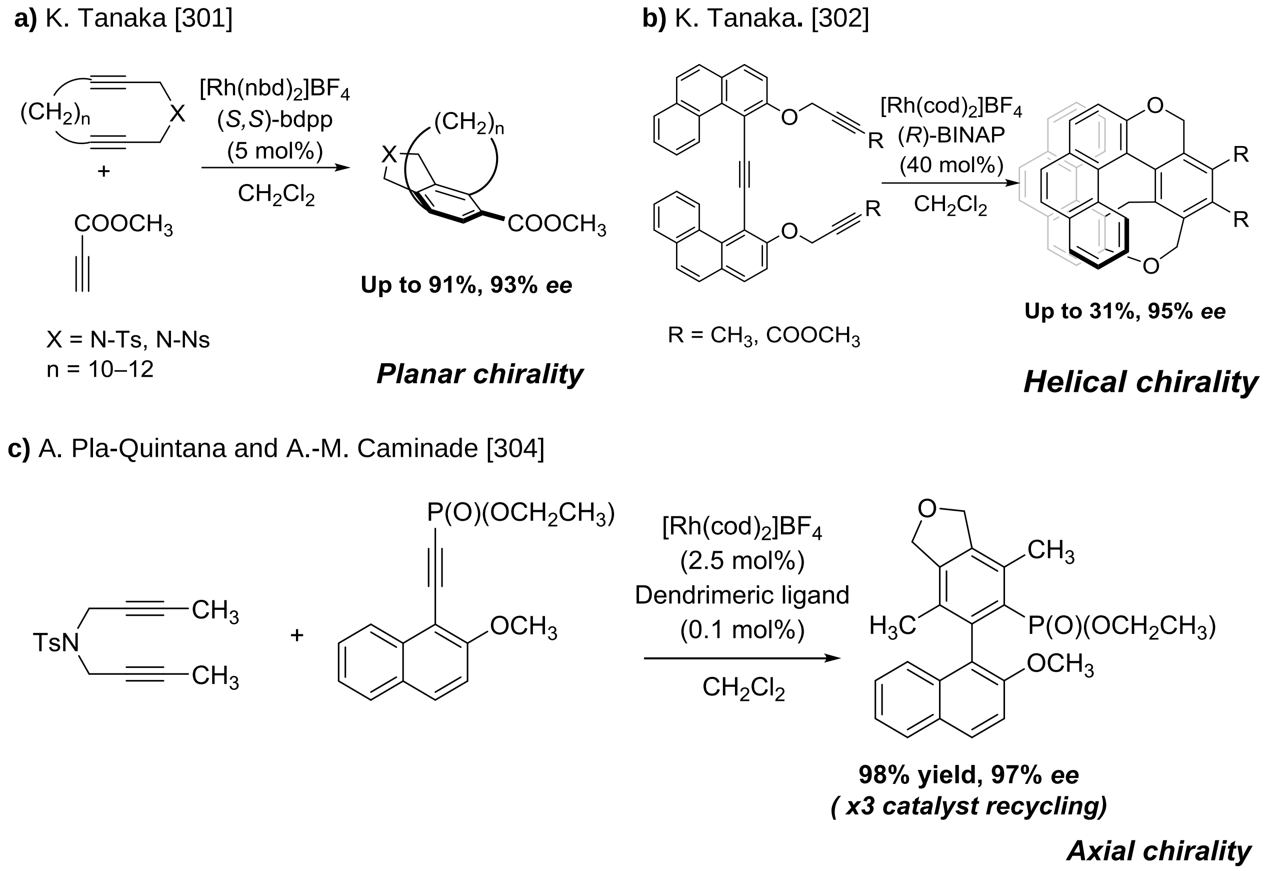
a) K. Tanaka [301]
(CH2)n
X
+
COOCH3
[Rh(nbd)2]BF4
(S,S)-bdpp
(5 mol%)
CH2Cl2
X
(CH2)n
COOCH3
Up to 91%, 93% ee
X = N-Ts, N-Ns
n = 10–12
Planar chirality
b) K. Tanaka. [302]
O
R
O
R
[Rh(cod)2]BF4
(R)-BINAP
(40 mol%)
CH2Cl2
O
R
R
O
R = CH3, COOCH3
Up to 31%, 95% ee
Helical chirality
c) A. Pla-Quintana and A.-M. Caminade [304]
TsN
CH3
CH3
+
P(O)(OCH2CH3)
OCH3
[Rh(cod)2]BF4
(2.5 mol%)
Dendrimeric ligand
(0.1 mol%)
CH2Cl2
O
CH3
H3C
P(O)(OCH2CH3)
OCH3
98% yield, 97% ee
(x3 catalyst recycling)
Axial chirality

Scheme 1.43. Miscellaneous examples of Rh(I)-catalyzed [2+2+2] cycloadditions generating (a) planar, (b) helical and (c) axial chirality.

2.3.4. Allenes in [2+2+2] cycloadditions

Allenes are *cumulated* unsaturated hydrocarbon molecules featuring two contiguous C–C double bonds. Their use in transition metal-catalyzed reactions, and more specifically in [2+2+2] cycloaddition reactions [239], has been of increasing interest in the field of synthetic organic chemistry for many years due to a series of peculiarities (**Figure 1.16**). First, allenes have comparable reactivity to alkynes while maintaining the potential of alkenes and other C-sp^2 unsaturated reaction partners to generate stereocenters in the reaction products. Second, upon a given reaction (take a DA reaction as an example in **Figure 1.16**) both double bonds are likely to react, thus amplifying the number of possible reaction products. Controlling positional selectivity (which of two double bonds reacts) is key when considering allene reactivity. Moreover, the fact that one of the double bonds remains in the reaction product broadens even more the chemical space of hypothetical reaction products. Third, the two π systems in allenes are orthogonal due to the presence of a central C-*sp* atom. This is the cause for allene's inherent axial chirality. Of course, this feature has strong implications in synthetic organic chemistry as well. Progressive advances in the synthesis of allene-containing molecules [305,306] have stimulated their use in the search for new reactivity as well as the synthesis of natural products [307–309]. Our group published a review article in 2016 covering every case of allene-involving transition metal-catalyzed o mediated [2+2+2] cycloaddition reaction published until late 2015.

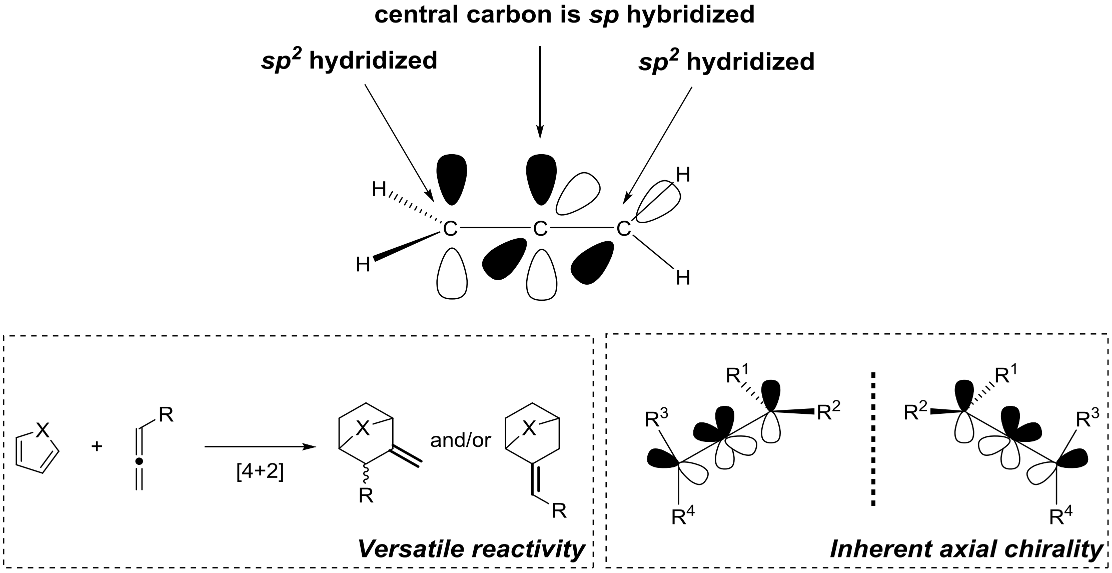
central carbon is sp hybridized
sp2 hydridized
sp2 hydridized
H
H
C
C
C
H
H
X
R
[4+2]
X
R
and/or
X
R
Versatile reactivity
R1
R2
R3
R4
R1
R2
R3
R4
Inherent axial chirality

Figure 1.16. Relevant properties of allenes in synthetic organic chemistry.

Historically, the first example of a transition metal-catalyzed [2+2+2] cycloaddition involving allenes was reported by Benson and Lyndsey in 1959. The Ni(0)-catalyzed intermolecular reaction of propadiene, the simplest member of the allene family, gave a mixture of all possible trimethylenecyclohexanes [310] (**Scheme 1.44a**). In the presence of an alkyne and a Ni(II) catalyst, dimethylenecyclohexene products were formed with good chemo- and regioselectivity [311] (**Scheme 1.44a**). Tetrameric byproducts were obtained together with the [2+2+2] reaction products in both cases.

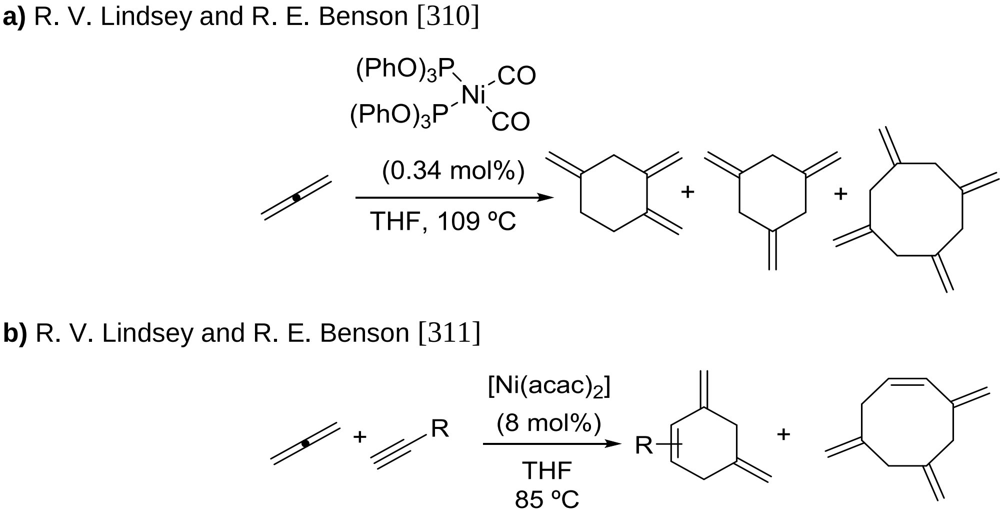
a) R. V. Lindsey and R. E. Benson [310]
(PhO)3P
(PhO)3P
Ni
CO
CO
(0.34 mol%)
THF, 109 °C
+
+
b) R. V. Lindsey and R. E. Benson [311]
+
R
[Ni(acac)2]
(8 mol%)
THF
85 °C
R
+

Scheme 1.44. Ni-catalyzed [2+2+2] cycloadditions of 1,2-propadiene.

Malacria reported several intramolecular cyclisation reactions of linear allene-diyne substrates. Starting from a diastereomerically pure allene-containing substrate, tricyclic steroid analogues were obtained with complete chemo- and diastereoselectivity [312,313] (**Scheme 1.45**).

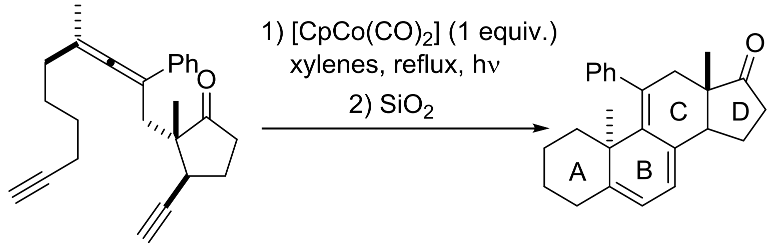

Scheme 1.45. Diastereoselective synthesis of a steroid-like compound from an allene-diyne substrate.

Saito [314] and Mukai [315] have explored the intramolecular reactions of related substrates with allene-yne-ene and ene-allene-yne sequences catalyzed by ruthenium and rhodium complexes, respectively.

The intramolecular Rh(I)-catalyzed [2+2+2] cycloaddition reaction of linear substrates bearing two allene moieties has been mainly developed in our research group. Wilkinson's complex catalyzed cyclization reactions of allene-yne-allene and allene-ene-allene substrates afforded a series of dienes with total chemo- and diastereoselectivity. DFT calculations were carried out to analyze the reaction mechanism in detail [316] (**Scheme 1.46**).

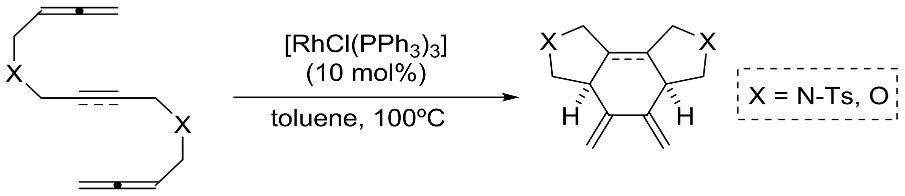

Scheme 1.46. Rh-catalyzed **i**ntramolecular [2+2+2] cycloadditions involving allenes developed by our group.

When the same reactions were performed starting from enantiopure substrates with two stereogenic centers installed at the α-position of the allene moieties, complete chiral induction was observed in the reaction products bearing N-Ts tethers, which were obtained as diastereomerically pure compounds [317]. More recently, we studied the reaction of allene-ene-yne substrates. Disparate diastereoselectivities were observed depending on the catalytic system employed and the mechanism was again rationalized computationally [318]. We have also incorporated nitriles in conjunction with allenes to generate heterocyclic compounds. In this latter example, chemoselective cyclization of allene-ene-nitrile substrates catalyzed by Wilkinson's complex and subsequent treatment with potassium tert-butoxide gave access to interesting 2,6-naphtyridine scaffolds [319].

Some cases of Rh-catalyzed partially intramolecular reactions with allenes have been reported [320,321]. As a representative example, Alexanian showed that ene-allenes react with another allene or an alkene to give bicyclic products with no less than 4 contiguous stereocenters (**Scheme 1.47**).

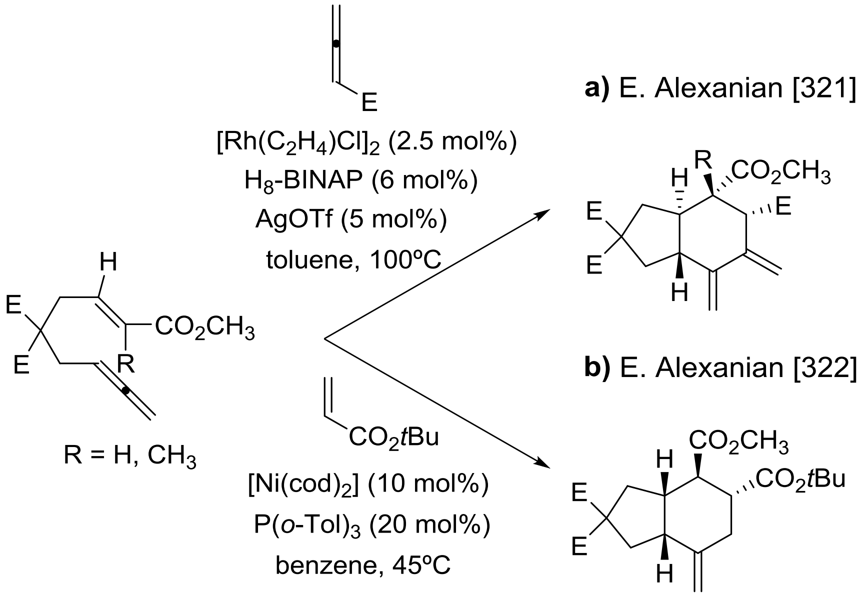
E
[Rh(C2H4)Cl]2 (2.5 mol%)
H8-BINAP (6 mol%)
AgOTf (5 mol%)
toluene, 100ºC
a) E. Alexanian [321]
H
E
E
CO2CH3
R
R = H, CH3
CO2tBu
[Ni(cod)2] (10 mol%)
P(o-Tol)3 (20 mol%)
benzene, 45ºC
b) E. Alexanian [322]
CO2CH3
CO2tBu

Scheme 1.47. [2+2+2] cycloaddition reactions of allene-enes and alkenes or allenes. E = $CO_2CH_2CH_3$

Partially intramolecular reactions of 1,5-bisallenes have been reported by Ma [322–324]. A two-fold cyclization of four different 1,5-bisallenes reacting with themselves catalyzed by $[RhCl(CO)PPh_3)_2]$ allowed access to tetracyclic steroid-like molecules (**Scheme 1.48a**). The same system catalyzed the reaction with an external allene to give a bicyclic product with two exocyclic double bonds (**Scheme 1.48b**) that was further reacted with dienophiles, giving rise again to a series of tetracyclic skeletons. A related yet different example by the same research group involved a three-component cascade reaction of 1,5-bisallenes and an alkyne in the presence of a boronic acid catalyzed by a Pd(0) complex [325].

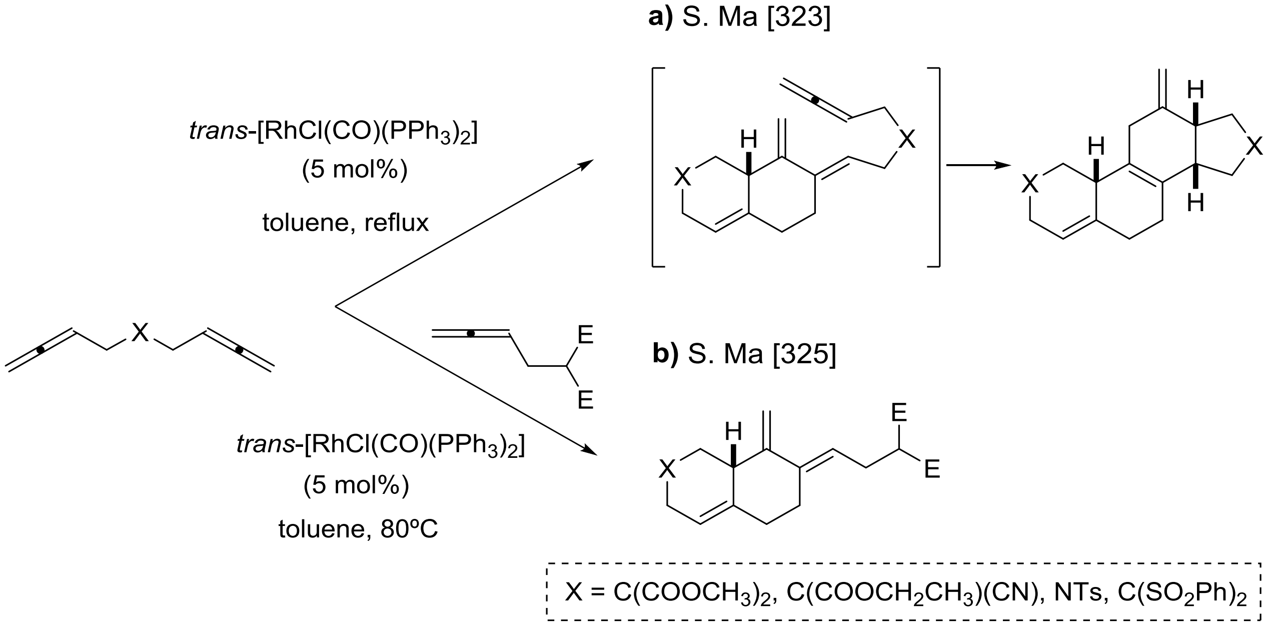
a) S. Ma [323]
trans-[RhCl(CO)(PPh3)2]
(5 mol%)
toluene, reflux
X
H
b) S. Ma [325]
E
trans-[RhCl(CO)(PPh3)2]
(5 mol%)
toluene, 80ºC
X = C(COOCH3)2, C(COOCH2CH3)(CN), NTs, C(SO2Ph)2

Scheme 1.48. [2+2+2] cycloadditions involving 1,5-bisallenes.

While 1,5-bisallenes have a rich chemistry with transition metals [326,327], most studies reported in the literature consist of cycloisomerization reactions that afford assorted reaction products with 5- [328,329], 6- [330] or 7-membered [331,332] rings (**Scheme 1.49**).

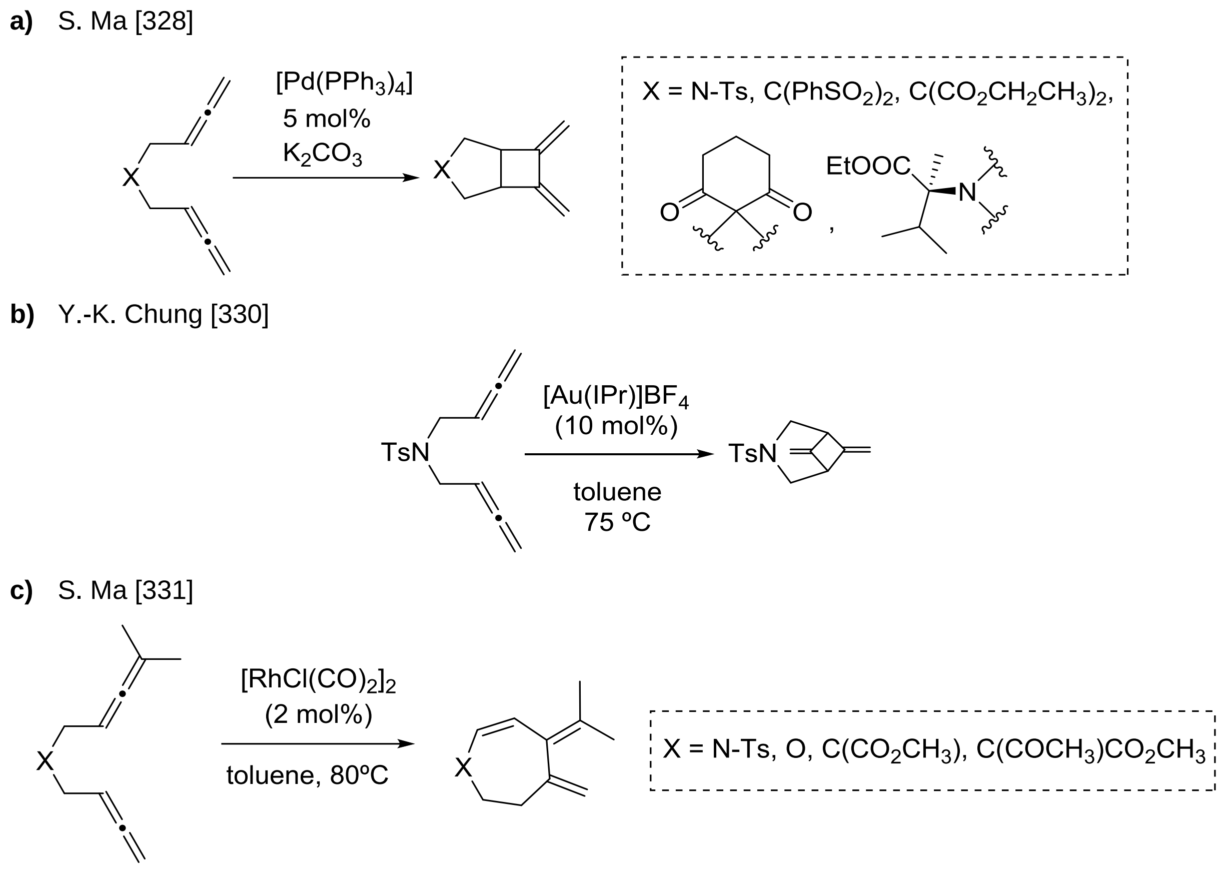
a) S. Ma [328]
[Pd(PPh3)4]
5 mol%
K2CO3
X
X
X = N-Ts, C(PhSO2)2, C(CO2CH2CH3)2,
O
O
EtOOC
N
b) Y.-K. Chung [330]
[Au(IPr)]BF4
(10 mol%)
toluene
75 °C
TsN
TsN
c) S. Ma [331]
[RhCl(CO)2]2
(2 mol%)
toluene, 80°C
X
X
X = N-Ts, O, C(CO2CH3), C(COCH3)CO2CH3

Scheme 1.49. Transition metal- catalyzed cycloisomerization reactions of 1,5-bisallenes.

Cases reporting the incorporation of a third unsaturated partner are limited to the above mentioned by Ma and a [2+2+1] carbonylative cycloaddition reaction reported in 2009 by Mukai [333]. With the aim of expanding the synthetic utility of 1,5-bisallenes in cycloaddition reactions, in the context of this thesis we have investigated the reactivity of 1,5-bisallenes with alkenes and fullerenes using Rh(I)-diphosphine complexes as catalysts. The results of these projects are discussed in chapter 6 of this manuscript.

2.3.5. Fullerenes in [2+2+2] cycloadditions

Fullerenes have comparable reactivity to that exhibited by electron-deficient olefins. In line with this statement, some reports of C_{60} behaving as one of the unsaturated partners in [2+2+2] cycloaddition reactions can be found in the literature. The first example was reported by Cheng in 1995 and consists of a metal-free process promoted by tricyclohexylphosphine in which methyl and ethyl propiolate reacted with C_{60} to afford the corresponding disubstituted 1,3-cyclohexadiene derivatives [334] (**Scheme 1.50**).

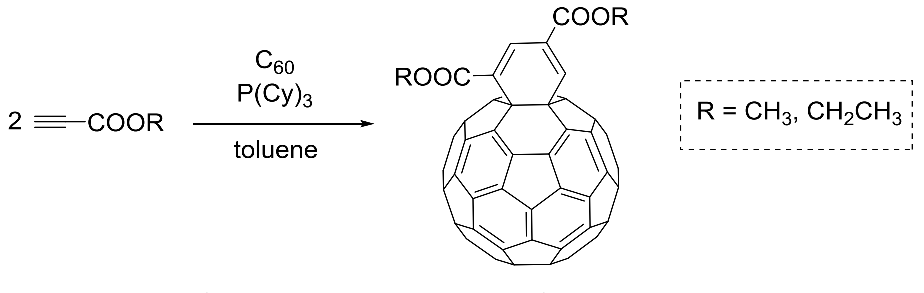
2 ≡—COOR
C60
P(Cy)3
toluene
COOR
ROOC
R = CH3, CH2CH3

Scheme 1.50. Phosphine-catalyzed formal [2+2+2] cycloaddition of alkynes and C_{60}.

In 1998, the same group reported the [2+2+2] cycloaddition reaction of C_{60} and several diynes. The reaction was promoted by stoichiometric amounts of $[NiCl_2(PPh_3)_2]$, excess of triphenylphosphine and Zn as an oxidant [162] (**Scheme 1.51**). The authors observed that the resulting cyclohexadiene products easily reacted with $^1O_2$ at room temperature and under room illumination leading to decomposition products. Conversely, when toluene solutions of the products were exposed to UV light for 2 hours, the corresponding bis(fulleroids) could be isolated.

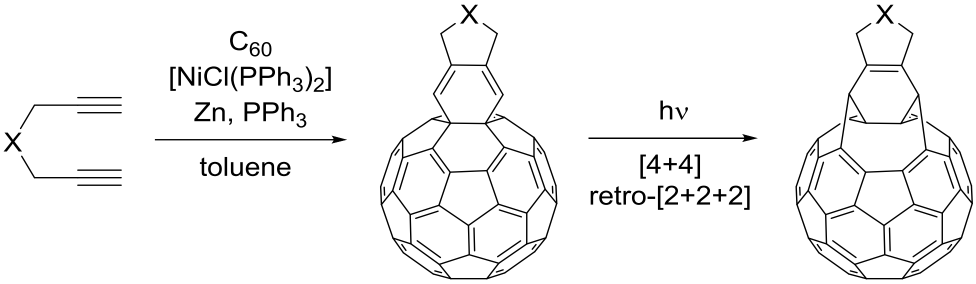

Scheme 1.51. Ni-promored [2+2+2] cycloaddition of diynes and C_{60}.

A later example was reported by Murata in 2000. In this case, a reaction of C_{60} with a palladacyclopentadiene complex, prepared previously by oxidative coupling of two molecules of a dialkyl acetylenedicarboxylate with Pd(0), afforded the corresponding cyclohexadiene-type adducts. The corresponding bis(fulleroids) were again synthetized photochemically [164] (**Scheme 1.52**).

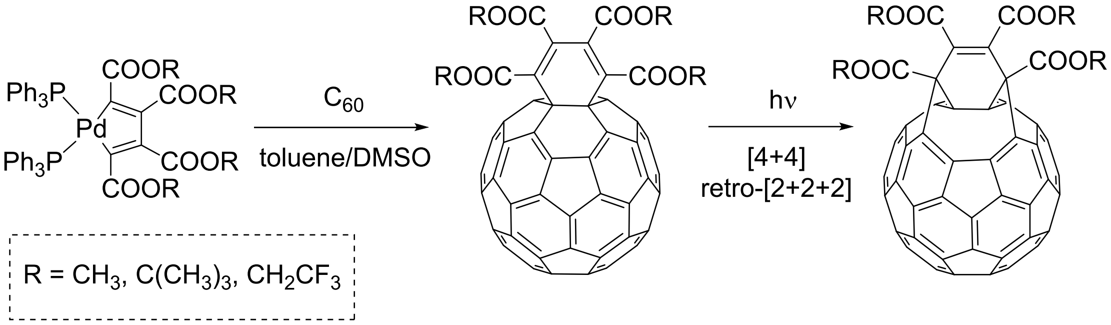

Scheme 1.52. Reaction of C_{60} with a palladacylopentadiene complex.

All in all, these methods are either not catalytic versions of the reaction or are limited to a very reduced substrate scope. Given that 1,3-cyclohexadiene derivatives are precursors of open-cage fullerenes (see for instance **Scheme 1.23** in page 24), the development of efficient catalytic methodologies to access this class of compounds is desirable. The projects developed in chapters 3 and 4 of this thesis were designed with this goal in mind.

2.3.6. Other participating substrates in transition metal-catalyzed [2+2+2] cycloadditions

Previous subsections have covered the reactivity of alkynes, nitriles, alkenes, allenes and fullerenes in [2+2+2] cycloadditions. However, the reaction is not limited to this kind of unsaturated substrates. Many other diverse families of compounds as isocyanates [335], isothiocyanates [336], carbon dioxide [337], carbon disulfide [338], carbonyl compounds [339], phosphaalkynes [340], imines [341] or iminoboranes [342] can afford their corresponding six-membered products when reacted with two unsaturated partners. However, all these cases fall behind the interest of this thesis and will not be further discussed in this section. **Scheme 1.53** shows simplified representations of the products resulting from all these reactions.

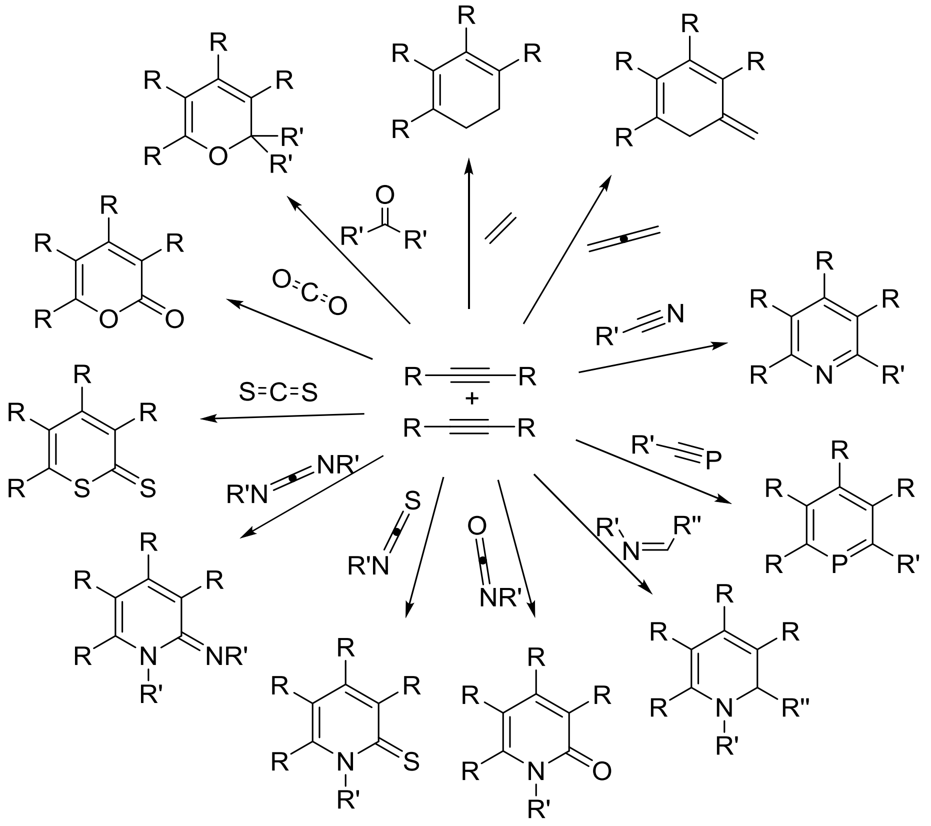

Scheme 1.53. Unsaturated substrates used in transition metal-catalyzed [2+2+2] cycloaddition reactions.

Section 3: Computational chemistry and molecular modeling

3.1. Combining theory and experiments: a powerful approach

The employment of computational chemistry software has become more and more popular among experimental chemists over the last decades. Impressive and fast advances in the *hardware* available, together with the emergence of easy-to-use computational chemistry *software* packages has motivated scientists beyond the field of physical chemistry to make generalized use of computational tools in order to explain (or even predict) reactivity and certain molecular properties. Indeed, since specific calculations can nowadays take shorter times than experiments, especially when performed in modern supercomputers, computational data can be used as a good starting point to guide experimental investigations.

Of course, computational chemistry has limitations. Theoretical methods are based on the use of approximations and, as a consequence, they inherently lack of accuracy to a certain extent. Moreover, the fact that experimentalists often deal with complex problems involving large systems makes calculations alone not sufficient. Within this context, synergistic approaches combining the advantages of both experiments and theory emerge as an excellent alternative to address chemical problems [343–345].

As evidenced by some of the works discussed in section 2 of this introduction, our group has been taking advantage of this approach for many years. Furthermore, the works developed in chapters 3, 4 and 7 of the present manuscript are also good examples of how molecular modeling of reaction mechanisms provides essential information of the chemical processes undertaken in our synthetic laboratories.

Computational calculations can be used for diverse purposes. Starting from a given molecular formula with a particular connectivity, one can compute its “best” structure. That is, in computational terms, the optimized structure at a certain level of theory. Modeling the structure of isolated molecules is a helpful and widely used sort of calculation. However, computational data must be taken with care in this case, since from an experimental point of view, many different structures (*e.g.* conformers, stereoisomers) coexist in solution under a specific set of conditions. More importantly, computational chemistry is used to “explore” the so-called potential energy surface (PES). The PES is the hypersurface defined by the potential energy of a group of atoms over all possible atomic arrangements. Characterization of the PES (or a relevant fragment) results in the finding of local minima and saddle points, which in the case of a specific chemical reaction correspond to its intermediates and transition states (TSs), respectively. The PES is one of the most fundamental models to study chemical transformations. Chemical properties of molecules can also be computed. This includes for example NMR, IR, UV-Vis and EPR spectra. By assuming certain approximations one can also compute properties like equilibrium constants derived from Gibbs energy differences between the minima on a PES, rate constants, and heats of formation or pK_a values. Finally, other properties that do not correspond to physical observables can also be studied by computational means. It is the case of atomic charges, aromaticity and bond order, among other examples.

The following subsections will cover essential key points of quantum and computational chemistry relevant to the content of the computational works included in this thesis. All the contents discussed below are based on recent editions of excellent quantum chemistry, computational chemistry and molecular modeling textbooks [346–353]. Further insight into each one of the topics mentioned is covered in detail in these references. Subsection 3.3 describes the general modeling protocol employed in this thesis. All calculations have been performed using the Gaussian software [354], carefully following the steps described in this subsection.

3.2. Computational numerical techniques

Depending on the accuracy of the models employed, computational numerical techniques fall into three main categories:

1. *Ab initio* (Latin for "from the beginning") quantum chemistry methods are based on solving the Schrödinger equation. Though being the most accurate, *ab initio* calculations are expensive in terms of their computational cost, and its application is limited to relatively small systems. The only input required for to *ab initio* calculations are physical constants.
2. *Semi-empirical* quantum chemistry methods are less accurate since they take advantage of experimental parameters in order to make approximations that reduce the computational cost of calculations. As a result, semi-empirical methods can be applied to larger systems in a cost-effective manner, while scarifying accuracy.
3. *Molecular mechanics* (MM) uses classical mechanics to model chemical systems. The potential energy of a system is calculated as a function of the nuclear coordinates using force fields. MM is used to model large systems like proteins. They can be combined with quantum mechanical methods in hybrid QM/MM calculations in order to treat different areas of a complex system with different degrees of accuracy.

Since only *ab initio* quantum chemistry methods have been used in this thesis, semi-empirical and MM approaches will not be further discussed here.

3.2.1. The Hartree-Fock approximation

The Schrödinger equation in its time-independent version (Eq. 1.4) is central to the study of the properties of a quantum molecular system.

$$\hat{H}\Psi(\vec{r},\vec{R}) = E\Psi(\vec{r},\vec{R}) \qquad \text{(Eq. 1.4)}$$

It takes the form of an eigenvalue equation in which:

- Ψ is the wavefunction.
- The operator $\hat{H}$ is the *Hamiltonian* and its corresponding observable is the total energy of the system (E)
- $\vec{r}$ denotes the coordinates of the particles (electrons and nuclei) that constitute the system.

Likewise, $\hat{H}$ contains the following terms:

$$\hat{H} = -\sum_{i}^{N\,electrons}\frac{\hbar^2}{2m_e}\nabla_i^2 - \sum_{A}^{N\,nuclei}\frac{\hbar^2}{2M_A}\nabla_A^2 - \sum_{i}^{N\,electrons}\sum_{A}^{N\,nuclei}\frac{e^2 Z_A}{r_{iA}} + \sum_{i>j}^{N\,electrons}\frac{e^2}{r_{ij}} + \sum_{A>B}^{N\,nuclei}\frac{e^2 Z_A Z_B}{R_{AB}} \qquad \text{(Eq. 1.5)}$$

The first two terms represent the kinetic energy of electrons and nuclei, respectively. The third, fourth and fifth terms are the potential energy due to electron-nuclei attraction, electron-electron repulsion and nuclear-nuclear repulsion, respectively.

Solving (Eq. 1.4) is only possible for trivial systems like H_2^+ and other related one or few electron systems. If we aim to solve the time-independent Schrödinger equation for a multi-electron molecular system, a series of approximations will be required. In this sense, the Hartree-Fock (HF) approximation relies on reducing the overall problem to a set of one-electron problems. Though the HF method is barely used in nowadays molecular modeling, its discussion in this section is somehow pedagogical, since it represents the starting point of computational chemistry. In this sense, HF theory laid the foundations to more accurate and modern approximations.

The first approximation to take into account towards an estimate solution of the Schrödinger equation for a many-electron system is the *Born-Oppenheimer* (BO) approximation. It relies on the fact that the nuclei are much heavier and move much slower than electrons. According to this statement, nuclei can be "frozen" so that the equation is solved for an energy and wavefunction involving only one set of coordinates (*i.e.* the coordinates of electrons). In this way, the second term in (Eq. 1.5) can be suppressed and the fifth is constant and can be treated independently to provide the nuclear-repulsion energy (E_{NRE}), since it only requires the charges on the nuclei and their distances from one another. This results in a modified *electronic Hamiltonian* that gives E_{BO} upon solving.

$$\hat{H}_{BO}\Psi(\vec{r}_{electrons}) = E_{BO}\Psi(\vec{r}_{electrons}) \quad \text{(Eq. 1.6)}$$

$$E = E_{BO} + E_{NRE} \quad \text{(Eq. 1.7)}$$

The second approximation to simplify (Eq. 1.4 is to construct the wavefunction as a s*ingle determinant* by combining MOs in a way that fulfills the *Pauli principle of antisymmetry*. This mathematical construct is known as the *Slater determinant*.

$$\Psi = \frac{1}{\sqrt{N!}}\begin{bmatrix} \varphi_1\alpha(1) & \varphi_1\beta(1) & \varphi_2\alpha(1) & \cdots & \varphi_{N/2}\beta(1) \\ \vdots & \vdots & \vdots & \ddots & \vdots \\ \varphi_1\alpha(N) & \varphi_1\beta(N) & \varphi_2\alpha(N) & \cdots & \varphi_{N/2}\beta(N) \end{bmatrix} \quad \text{(Eq. 1.8)}$$

$$\langle \varphi_i\alpha | \varphi_j\beta \rangle = \delta_{ij} \quad \text{(Eq. 1.9)}$$

$$\langle \varphi_i | \varphi_j \rangle = \delta_{ij} \quad \text{(Eq. 1.10)}$$

In the Slater determinant:

- α and β are spin-functions for every electron, φ_i represents each MO. $\varphi_i\alpha/\varphi_i\beta$ are *spin orbitals*. Both orbitals and spin orbitals are orthonormal.
- N is the number of electrons.
- Columns correspond to single-electron wavefunctions (spin orbitals) and rows correspond to the electron coordinates.

- The factor in front of the determinant is for normalization.

The third approximation relates to the *molecular orbital theory*. The MOs used to build up a Slater determinant are in turn constructed as a *linear combination of atomic orbitals* (LCAO). In other words, they are obtained by linear combination of a series of functions in a *basis set* (χ_k).

$$\varphi_\mathrm{i} = \sum_{k}^{M} c_{ki}\chi_k \qquad \text{(Eq. 1.11)}$$

Where:

- χ_k are mathematical functions, known as *basis functions*, centred on the nuclei and resembling the eigenfunctions of the hydrogen atom Hamiltonian. A collection of basis functions conforms the *basis set*. The accuracy (and consequently, the computational cost) of a calculation is associated with the number of basis functions in the employed basis set. Basis functions are equivalent to *atomic orbitals* (AO).
- c_{ki} are MO coefficients that indicate to what extent a *basis function* contributes to a given MO.

Two main criteria will guide what mathematical functions to choose when building up a set of MO. First, they should agree with the physics of the problem. Second, they should allow easy *integration* required to calculate the energy (see below). The two main types of basis functions used in electronic structure calculations are the Slater-type orbitals (STO) and Gaussian-type orbitals (GTO). While STOs better describe the actual shape of the AO, integration of GTOs is much easier. According to this, a basis set is often constructed as a linear combination of GTOs, the *primitive functions*, which result in a *contracted function* that better represents the AO. Overall, a specific basis set contains a number of contracted basis functions, which in turn is constituted by the corresponding GTOs and their exponents and contraction coefficients. The smallest possible basis set is called *Single Zeta* (*SZ*) and has the minimum number of functions required to describe all the occupied orbitals of an atom. *Double zeta (DZ)* basis sets have two times the functions required. *Triple Zeta* (*TZ*), *Quadruple Zeta* (*QZ*), *Quintuple Zeta* (5Z), *Hextuple* (6Z) *Zeta* and *Heptuple Zeta* (7Z) contain, of course, 3, 4, 5, 6 and 7 times the minimum required basis functions. Also, polarization and diffuse functions can be added to the basis set. When it comes to molecular modeling, the most commonly used basis sets are the split-valence type developed by Pople (*e.g.* 6-31G) and the correlation consistent polarized basis functions developed by Dunning (*e.g.* cc-pVDZ).

Once the wavefunction has been defined with a proper basis set that define the MO, the next step is to find the “best” values for coefficients c_{ki}. According to the *variational theorem* (Eq. 1.12), an approximate wavefunction has an energy equal or above the exact energy.

$$\frac{\int \Psi^{*}\hat{H}\Psi\partial\tau}{\int \Psi^{*}\Psi\partial\tau} = E_{variational} \geq E_{exact} \qquad \text{(Eq. 1.12)}$$

Hence, starting from a trial wavefunction one can obtain another wavefunction by computing the parameters that minimize the energy. This minimization process results in the Fock equation (Eq. 1.13).

$$\hat{F}\varphi_i = \varepsilon_i\varphi_i \qquad \text{(Eq. 1.13)}$$

Where:

- $\hat{F}$ is the *Fock operator*, an effective one-electron Hamiltonian for an orbital.
- ε_i are the orbital energies.

The Fock operator is expanded as follows:

$$\hat{F}\varphi_i = \hat{T}\varphi_i + \hat{V}_{NE}\varphi_i + \hat{J}\varphi_i - \hat{K}\varphi_i \qquad \text{(Eq. 1.14)}$$

- $\hat{T}$ is the *kinetic energy operator* and $\hat{T}\varphi_i$ accounts for the kinetic energy of one electron in orbital φ_i.
- $\hat{V}_{NE}$ is the *nuclear-electron attraction operator* and $\hat{V}_{NE}\varphi_i$ accounts for the attraction of one electron to the nuclei.
- $\hat{J}$ is the *Coulomb operator* and $\hat{J}\varphi_i$ represents the repulsion of one electron in φ_i and the average charge distribution created by the rest of electrons.
- $\hat{K}$ is the *exchange operator* and it represents a non-local quantity that results from the antisymmetry requirement of the single Slater determinant.

The HF equations are a set of *pseudo-eigenvalue equations* in which $\hat{F}$ depends itself on the MOs. As a consequence, minimization of these equations is only possible by iterative procedures, by using the so-called *self-consistent field* (SCF) approach (**Figure 1.17.**).

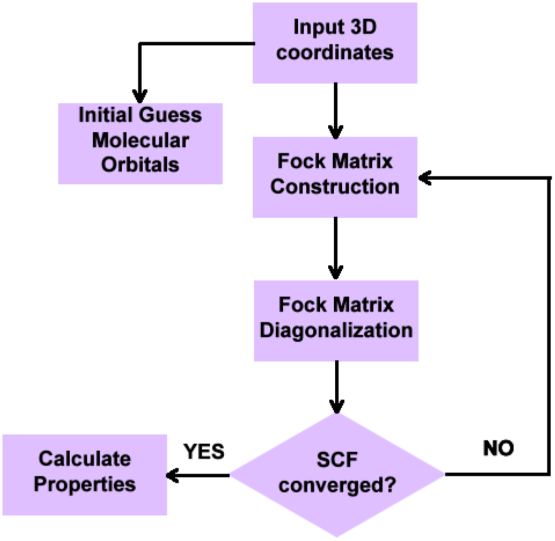
Input 3D coordinates
Initial Guess Molecular Orbitals
Fock Matrix Construction
Fock Matrix Diagonalization
SCF converged?
YES
NO
Calculate Properties

Figure 1.17. Algorithm employed in the SCF approach.

Accurately speaking, the equation to be iteratively solved by quantum chemical programs is actually the *Roothaan-Hall equation*, which has the form of a matrix equation and, consequently, can be solved by standard techniques.

$$FC = \varepsilon SC \qquad \text{(Eq. 1.15)}$$

Where:

- F is the Fock matrix, which includes one-electron integrals involving nuclear-electron attraction operators and two-electron integrals involving electron-electron interaction.
- C is the matrix of coefficients.
- ε is the diagonal matrix of orbital energies.
- S is the overlap matrix.

Probably one of the main weaknesses of the HF method is that, as a consequence of using a single Slater determinant as the trial wavefunction, the electron-electron repulsion is considered only as an average. The correlation energy E_{corr} is thus defined as the difference between the exact non-relativistic BO energy and the energy calculated by the HF method.

$$E_{corr} = E_{exact} - E_{HF} \qquad \text{(Eq. 1.16)}$$

Post-Hartree-Fock methods have been developed in order to overcome the lack of accuracy that emerges as a result of ignoring E_{corr}. Of course, this always comes with an associated (often huge) computational cost.

3.2.2. The Density Functional Theory

Density functional theory (DFT) offers an alternative way of addressing the electron correlation problem. As compared to post-HF methodologies, DFT calculations provide accurate energies at a much lower computational cost, generally equivalent to the one of standard HF calculations. The theoretical foundations of DFT are already more than 50 years old, but it was not until the 1990s –when very efficient and accurate *density functionals* appeared– that its use became generalized. From a computational point of view, the methods used in DFT have much in common with the previously discussed HF theory.

The fundamental premises underlying DFT were postulated by Hohenberg and Kohn in 1964 [355] and state that:

1. *The exact energy of the ground state is a functional of the density*. This is, the ground state electronic energy and any other observable of a molecular system is completely determined by the *electron density* (ρ).

$$E_{exact} = E[\rho_{exact}] \qquad \text{(Eq. 1.17)}$$

2. *The energy of a system in its ground state reaches a minimum value when the exact electronic density is considered*. According to this second theorem, an important property of the *energy density functional* $E[\rho(r)]$ is that it obeys the variational principle.

$$E[\rho] \geq E[\rho_{exact}] \quad \text{(Eq. 1.18)}$$

The use of electron density to calculate the energy has a major advantage over the wavefunction approach: while the latter depends on 4N variables, ρ is only dependent on three spatial variables and is independent of the size of the molecular system considered. Even so, proper use of DFT in computational chemistry is possible thanks to the Kohn-Sham (KS) theory [356], which introduces the use of an auxiliary set of orbitals as a way to calculate the kinetic energy. A downside of such approximation is that the complexity of the problem increases from 3 to 3N variables. Like in HF theory, KS orbitals must fulfill the conditions of orthonormality and maximum double occupancy, and are described by a set of basis functions. An equivalent SCF procedure (KS-SCF) is also used in order to attain a set of orthogonal orbitals that minimize the energy in the DFT-modified Fock equation (Eq. 1.19).

$$\hat{F}^{KS}\varphi_i^{KS} = \varepsilon_i^{KS}\varphi_i^{KS} \quad \text{(Eq. 1.19)}$$

Another fundamental approach of the KS formalism consists in dividing the kinetic energy into two parts: one that can be exactly calculated and another that has to be approximated. The energy as a functional of the density is given by the following expression:

$$E_{DFT}[\rho] = T_S[\rho] + E_{ne}[\rho] + J[\rho] + E_{XC}[\rho] \quad \text{(Eq. 1.20)}$$

- The three first terms are easily recognizable and have been already discussed.
- $E_{XC}[\rho]$ is the *exchange-correlation* term and includes the exchange correlation, the kinetic energy not present in $T_S[\rho]$ and the electron-electron interactions neglected by definition in HF methods.

The KS method allows the exact calculation of the terms with the most important weight in the energy functional. This corresponds to the first three terms in (Eq. 1.20). However, the actual form of the functional corresponding to $E_{XC}[\rho]$ is not known. Hence, one must introduce approximate functionals to describe it. Since $E_{XC}[\rho]$ represents only a small fraction of the total energy, even rough approximations provide with a truthful definition. In this same sense, the accuracy of different DFT-KS approaches directly depends on how accurate is the functional $E_{XC}[\rho]$ we choose. Countless density functionals have been proposed since the early days of DFT-based computational chemistry and new ones keep being published almost every month. Most of them focus on specific molecular properties or are intended for particular applications.

The *Local Density approximation* (LDA), also known as *Local Spin Density Approximation*), assumes that ρ is a slowly varying function that can be treated as a uniform electron gas. By doing so, the *exchange-correlation* *energy* (E_{XC}) is considered to depend only on the electron density value at each point. In LDA E_{XC} is separated in an exchange and a correlation term and each term is treated independently with specific functionals (Eq. 1.21). In Gaussian, the default DFT-LDA method uses the Slater exchange functional (S) [357] in conjunction with the WNV correlation functional developed by Vosko, Wilk and Nusair [358]. LDA is therefore a synonym of SWNV in this program.

$$E_{XC}[\rho] = E_X[\rho] + E_C[\rho] \qquad \text{(Eq. 1.21)}$$

The DFT-LDA approach benefits from simplicity, but poor performance when calculating the energy and other properties of molecules has limited its use to the study of extended systems like metals, where the approximation of a slowly varying ρ is acceptable.

The *Generalized Gradient Approximation* (GGA) considers a non-uniform electron gas by introducing the first derivative (gradient) of ρ as a variable in both $E_X[\rho]$ and $E_c[\rho]$ expressions. The most popular GGA exchange functional is B88, developed by Becke [359]. Regarding GGA correlation functionals, the LYP functional developed by Lee, Yang and Parr [360,361] and the PW91 introduced by Perdew and Wang [362] are among the most widely used. The combination of the abovementioned functionals results in the well-established BLYP and BPW91 methods. Meta-GGA exchange-correlation functionals like the M06L developed by Truhlar [363] additionally consider the second derivative of ρ.

A very useful and generalized approach consists in the use of *hybrid functionals* containing HF exchange energy as part of the exchange functional. A paradigmatic example is the B3LYP exchange-correlation functional [364], which combines B88 and HF exchange together with the LYP correlation functional and three parameters conveniently fitted to reproduce experimental data (Eq. 1.22). Though it was developed in 1993, the B3LYP functional remains nowadays the most used of all density functionals.

$$E_{xc}^{B3LYP} = (1-a)E_{xc}^{LDA} + aE_x^{HF} + b\Delta E_x^{B88} + (1-c)E_c^{LSDA} + cE_c^{LYP} \qquad \text{(Eq. 1.22)}$$

The impossibility of systematic improvement is perhaps the major weakness of DFT. Although additional components have been gradually introduced in order to approach the “exact” exchange-correlation energy, the performance of a new density functional is often uncertain and must rely on comparative benchmarking studies or testing against experimental data or accurate post-HF methods [365]. Perdew’s metaphorical Jacob’s ladder [366] (**Figure 1.18**) represents a way to organize DFT approaches in such a way that, moving up through its rungs, new physical content is added to attain higher levels of *chemical accuracy*.

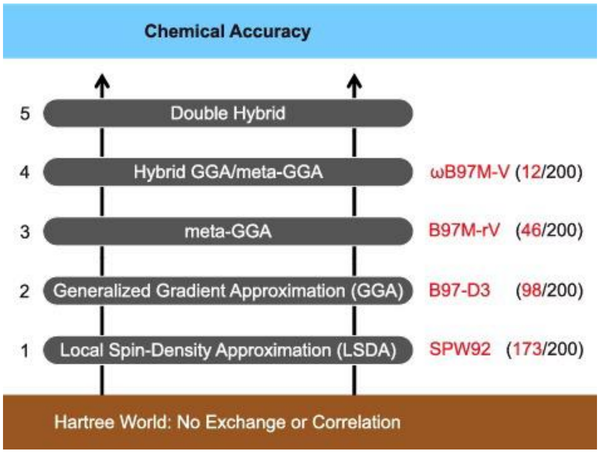
Chemical Accuracy
5
Double Hybrid
4
Hybrid GGA/meta-GGA
ωB97M-V (12/200)
3
meta-GGA
B97M-rV (46/200)
2
Generalized Gradient Approximation (GGA)
B97-D3 (98/200)
1
Local Spin-Density Approximation (LSDA)
SPW92 (173/200)
Hartree World: No Exchange or Correlation

Figure 1.18. Graphical representation of Perdew's Jacob's ladder. Reprinted with permission from: Mardirossian, N.; Head-Gordon, M. *Mol. Phys.* **2017**, *115*, 2315. Copyright © 2017 The Author(s). Published by Informa UK Limited, trading as Taylor & Francis Group

Another important feature of DFT methods is that *numerical integration* is necessary for the evaluation of the exchange-correlation contribution to the density functional. To do so, a *grid of points* in space –specified as a number of radial shells around each atom– must be determined. Since the accuracy of DFT calculations increases with the number of points used to define the grid, the use of large grids is generally recommended [351].

3.3. Modeling reaction mechanisms

3.3.1. Exploration of the PES

The study of reaction mechanisms is amongst the most used applications of computational chemistry. This can be done by studying and characterizing the PES, a mathematical representation of the energy as a function of a set of coordinates that represent the molecular geometries of a given molecular system. Every point in the PES corresponds to a unique combination of bond distances, bond angles and dihedral angles. Consequently, for a hypothetical non-linear molecular system with a number of atoms (N) >2, the PES has 3N -6 dimensions, corresponding to the degrees of freedom of that system. However, the potential energy can be graphically plotted as a function of two geometric parameters, defining a *contour map* (**Figure 1.19a**) or as a function of one single geometric parameter in a 2D representation (**Figure 1.19b**). For the latter case, this geometric parameter corresponds to the *reaction coordinate*.

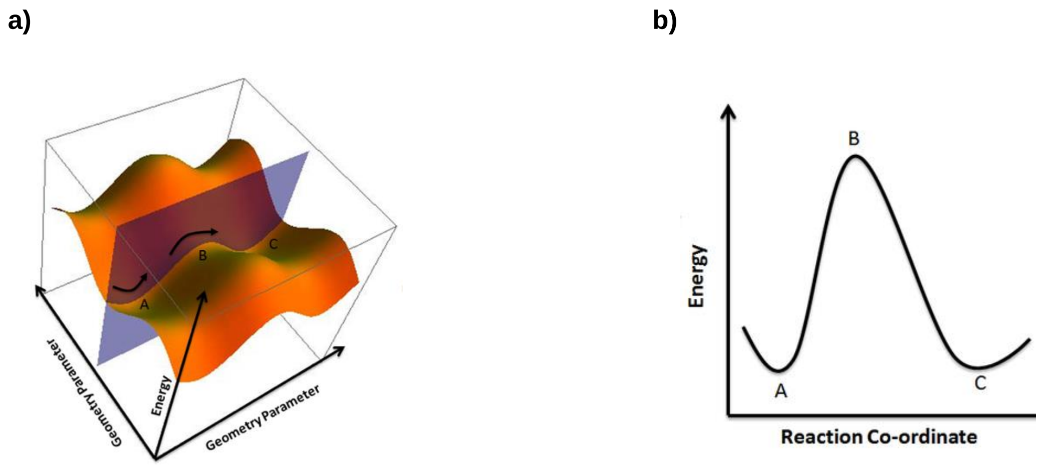

Figure 1.19. Representation of the potential energy as a function of (a) 2 geometric parameters (b) 1 geometric parameter.

Computing the energy for every single point in the PES is unpractical even for the simplest molecular system. Thus, in order to characterize it, one has to focus on its *stationary points*. These key points can in turn be divided into *minima* and *saddle points* and have one shared property: for every stationary point in the PES the first derivative of the potential energy (E) with respect to the Cartesian coordinates of the nuclei ($\vec{R}$), referred as the *gradient*, is equal to zero.

$$\frac{\partial E}{\partial \vec{R}} = 0 \qquad \text{(Eq. 1.23)}$$

For a given chemical reaction, local and global minima (points A and C in **Figure 1.19**) correspond to the reactants, products and intermediates and are located at the deepest point of the "valleys" on the PES. In turn, saddle points (point B in **Figure 1.19**) correspond to the TS and are located at the "mountain passes" connecting 2 minima. Mathematically, a saddle point is a local maximum in one dimension and a minimum in all other dimensions.

Stationary points can be located by performing *geometry optimizations* or *minimizations* [367]. That is, to apply numerical methods to gradually approach a point in the PES for which the gradient is null. Iterative calculation of the energy and the gradient stepping along the PES ultimately leads to a *converged* geometry with a gradient value very close to zero (**Figure 1.20**).

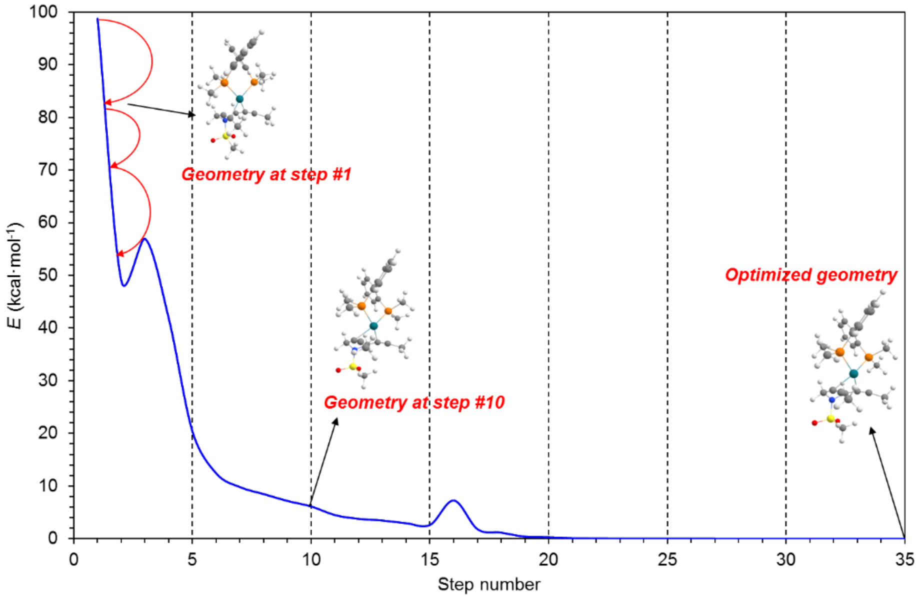

Figure 1.20. Evolution of the energy *vs.* optimization steps during a geometry optimization calculation of a transition metal complex. Curly arrows are rough representations of three optimization steps.

The default method used by Gaussian to accomplish the location of minima and saddle points is based on the so-called *Berny algorithm* [367,368]. This algorithm derives from the so-called *Newton-Raphson method* (Eq. 1.24),which uses the *forces* (the negative of the gradient) together with the *Hessian* (also known as the *second derivative matrix* or *force constants matrix*) to help predicting increasingly more stable (less energetic) structures.

$$\vec{R}_{n+1} = \vec{R}_n - \vec{g}H^{-1} \qquad \text{(Eq. 1.24)}$$

Since calculating the equations for the Hessian has considerable computational cost, an approximate version using semi-empirical electronic structure methods or MM is constructed before the optimization process starts. Methods using this approximation are called *quasi Newton-Raphson* methods. The Hessian is an indication of the curvature at a specific point. The energy and the gradient calculated at each optimization step are used to update the Hessian [369,370]. The data provided by the gradient and the Hessian is then used to determine the size and direction of the next step. For complicated cases, the Hessian has to be calculated explicitly at the beginning of the optimization or even at every optimization step.

An optimization is considered completed when it has *converged*. This is, when the forces and the displacement for the next step are very close to zero. Computational chemistry programs establish default threshold values for the forces and displacement to determine whether an optimization has finished or not. Gaussian also considers the root-mean-square of the forces and the displacement to further ensure correct convergences (**Figure 1.21**).

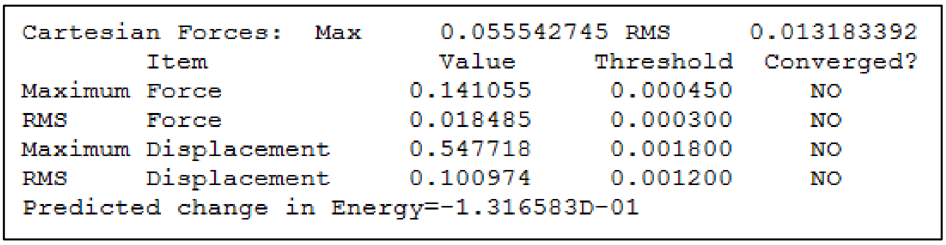

```
Cartesian Forces:  Max     0.055542745 RMS     0.013183392
        Item               Value     Threshold  Converged?
Maximum Force            0.141055     0.000450     NO
RMS     Force            0.018485     0.000300     NO
Maximum Displacement     0.547718     0.001800     NO
RMS     Displacement     0.100974     0.001200     NO
Predicted change in Energy=-1.316583D-01
```

Figure 1.21. Example of force and displacement values reported by Gaussian's output file after every optimization step.

The optimization of equilibrium species (minima) is often performed starting from a rough guess as the *input* geometry because the gradient always has a "downhill" direction along the PES. However, finding the structure of a TS can become a much more involved task that requires an accurate (close to the converged structure) starting guess. This is because the optimization algorithm must perform "uphill" steps (recall that saddle points are maxima in one dimension). In order to attain high quality starting guess geometries, a *relaxed scan* of the PES can be performed. This procedure consists of performing sequential constrained optimization calculations by "freezing" the scan coordinate and optimizing all the other parameters.

A clarifying practical example is depicted in **Figure 1.22** if we aim to locate the TS corresponding to the attack of cyclopentadiene to $^{\#6094}C_{68}$ (see chapter 7), a number of sequential optimization calculations have to be performed by freezing the reaction coordinate (R_{C-C} of the bond being broken) at progressively increasing values. This results in an energy profile corresponding to the *linear synchronous transit* (LST) between "reactant geometries" and "product geometries" [371] that can be used to pick out a "TS-like" structure suitable for a subsequent TS optimization. Gaussian has automated implemented protocols to carry out scan calculations.

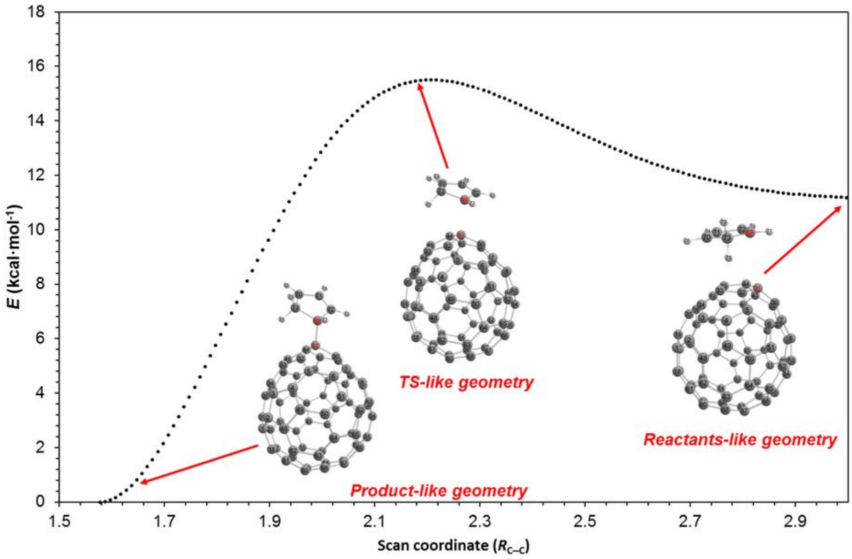

Figure 1.22. Relaxed scan defining the LST between the reacting complex and biradical intermediate in the attack of cyclopentadiene to a carbon atom of $^{\#6094}C_{68}$.

The optimization of TS requires an initial estimate of the Hessian with at least one negative eigenvalue (see below) parallel to the reaction path in order to proceed uphill towards a saddle point by following the Berny algorithm. In this case, approximate semi-empirical estimations are not valid and thus previous explicit calculation of the full Hessian is strictly required.

The next step following the optimization of a stationary point is characterization. In order to distinguish between a minimum from a saddle point one has to look at the *vibrational frequencies*, which are computed from the diagonalized and mass-weighted Hessian of an already optimized geometry. Each eigenvector of the resulting Hessian corresponds to a normal mode of vibration. Therefore, a minimum on the PES will provide all positive eigenvalues and, consequently, all computed frequencies will be real. Given that a saddle point is a maximum along the reaction path and a minimum in all other dimensions, a TS will provide one (and only one) imaginary frequency and all the remaining frequencies will be real. However, the presence of an imaginary frequency does not necessary involve the successful location of the desired TS. Analysis of the vibrational mode is necessary to confirm that the *transition vector* (*i.e.* the vibrational mode associated with the imaginary frequency) matches the desired reaction path. This can be easily done with conventional visualization software.

To conclude, when a TS is located and confirmed by analysis of its vibrational frequencies, it has to be unambiguously connected to the corresponding minima. Intrinsic reaction coordinate (IRC) calculation [372] are generally performed after optimizing a TS structure to verify the structure of minima located downhill from the saddle point. The input geometry of an IRC calculation is the one of a TS. From there, specific numerical methods (Gaussian uses the HPC algorithm [373,374]) are used to follow the reaction path downhill until reactants and products are reached. IRC calculations require force constants to proceed in the correct direction, but this is often not problematic in terms of computational cost, since they can be extracted from the frequency calculation already required to characterize the TS. The exploration of the PES finishes with examination (and confirmation) of the resulting f*orward* and *reverse* optimized geometries.

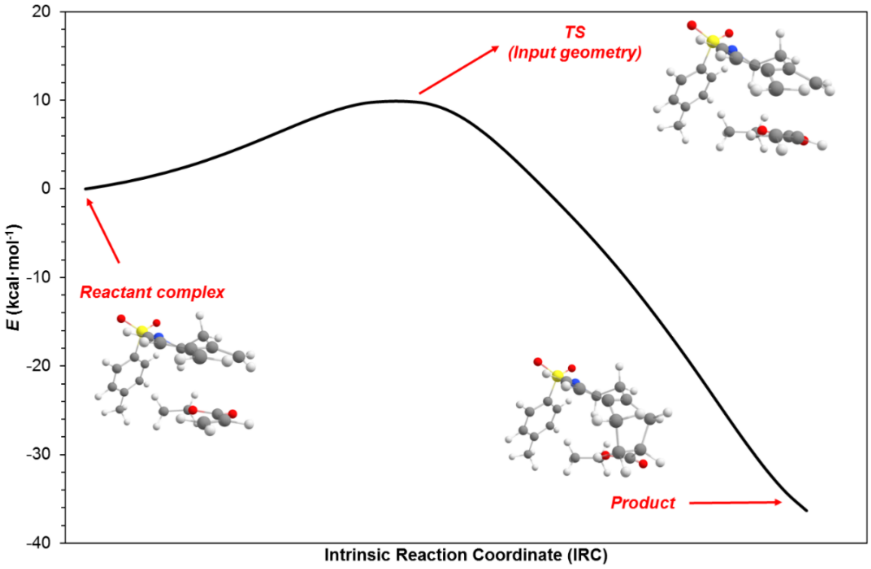

Figure 1.23. IRC representation for a DA reaction.

3.3.2. Thermochemistry

Optimization calculations deliver the electronic energy (E) of a stationary point computed at a certain level of theory. However, the study of chemical reactivity often relies on the use of thermochemical properties like heats of reaction and Gibbs energies of reaction. Such properties can be obtained from Gaussian and other computational chemistry programs by adding approximated corrections to E values based on standard statistical-mechanics and thermodynamic equations for an ideal gas [375,376]. Since different components required for obtaining thermochemical quantities depend on the vibrational normal modes of the molecule (see equations below), analytical Hessians must be computed by performing a frequency calculation. As discussed in the previous subsection, frequency calculations are done routinely to characterize stationary points. Hence, computing thermochemical properties does not involve extra computational effort.

Gaussian prints the following thermochemistry results computed at 298.15 K and 1 atm by default on the output file:

1. The *zero point vibrational energy* (ZPVE) is the energy associated with the vibration of a molecular system at 0 K. Zero-point corrected electronic energy (E_0) is obtained by the sum of E and $E_{ZPVE.}$

- *Zero-point correction* = $E_{ZPVE} = \sum_{i}^{3N-6} \frac{1}{2} h\nu_i$ (Eq. 1.25)
- *Sum of electronic and zero-point Energies* = $E_0 = E + E_{ZVPE}$ (Eq. 1.26)

2. The *thermal correction to internal energy* (E_{tot}) at a given temperature is $C_v T$ and is described as a sum of electronic, vibrational, rotational and translational energies. Gaussian Prints the particular contributions of each component. At conventional temperatures of reaction dE_{vib} is by far the one with a larger contribution to the internal energy. Like $E_{ZPVE,}$ all these contributions are obtained from statistical-mechanical equations.

- *Thermal correction to Energy* = $E_{tot} = dEel + dEvib + dErot + dEtrans$ (Eq. 1.27)
- *Sum of electronic and thermal Energies* = $E_T = E_0 + E_{tot}$ (Eq. 1.28)

3. The thermal correcton to *enthalpy* is then obtained from E_{tot} by simply applying:

- *Thermal correction to Enthalpy* = $H_{corr} = E_{tot} + k_B T$ (Eq. 1.29)
- *Sum of electronic and thermal Enthalpies* = $H = E_0 + H_{corr}$ (Eq. 1.30)

4. The *Gibbs energy* is obtained from the enthalpy and the entropy (S_{tot}), which in turn is calculated analogously to E_{tot} applying statistical mechanical equations.

- *Thermal correction to Gibbs Free Energy* = $G_{corr} = -TS_{tot}$ (Eq. 1.31)
- *Sum of electronic and thermal Free Energies* = $G = H + G_{corr}$ (Eq. 1.32)

In the case at hand, the most relevant thermochemical property is G, as it is used to predict reaction energies (ΔG_r) and energy barriers ($\Delta G^{\ddagger}$) by computing G values associated to optimized reactants, products and transition states. Representation of relative Gibbs free energies with respect to the reactants (ΔG) of a given reaction results in the so-called Gibbs energy profile.

$$\Delta G_r = G_{products} - G_{reactants} \qquad \text{(Eq. 1.33)}$$

$$\Delta G^{\ddagger} = G_{transition\ state} - G_{reactants} \qquad \text{(Eq. 1.34)}$$

For "conventional" chemical reactions, the step with a larger $\Delta G^{\ddagger}$ value in the Gibbs energy profile is considered the *rate-determining step* (rds). However, when modeling catalytic cycles a more accurate terminology based on the *rate-determining states* and the *turnover frequency* (TOF) must be employed. Thereby, according to the *energetic span model* [377]: The *TOF determining intermediate* (TDI), and the *TOF determining TS* (TDTS) are the ones with a larger *energetic span* (δE) in a catalytic cycle. So that:

$$TOF = \frac{k_B T}{h} e^{\frac{-\delta E}{RT}} \qquad \text{(Eq. 1.35)}$$

Accordingly, the activity of a catalyst must be judged not only on its ability to lower the energy of the TDTS, but also on how it modifies the energy of the TDI by stabilizing or destabilizing its structure. In order to identify the TDI and TDTS, two consecutive catalytic cycles must be represented in the Gibbs energy profile (**Figure 1.24**).

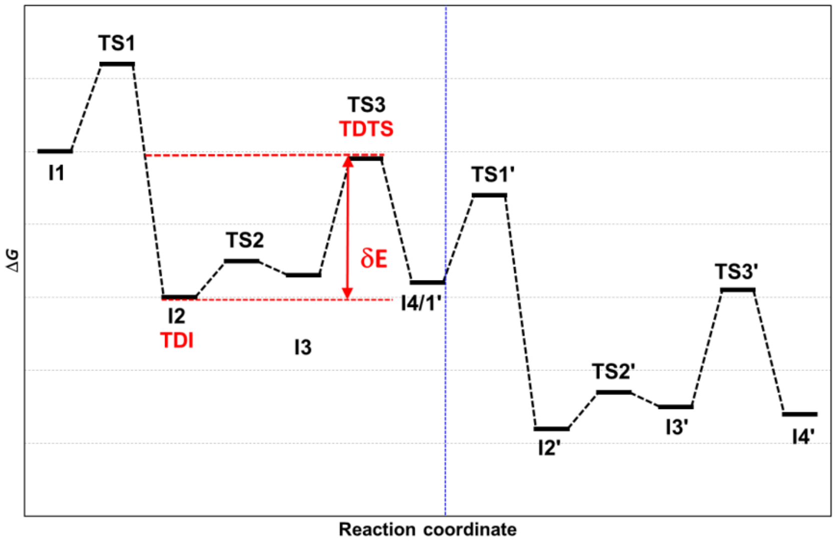

Figure 1.24. Graphical representation of TDI, TDTS and δE according to the energetic span model.

3.3.3. Pseudopotentials

Common electronic structure methods used in computational chemistry ignore relativistic effects. For lighter elements in periods 1-3 in the periodic table this is a valid approximation. However, problems arise with post-third row elements. Hence, when dealing with a chemical problem that involves heavier atoms (*e.g.* transition metals) other approximations have to be introduced in order to attain chemical accuracy.

An *effective core potential* (ECP), also referred to as *pseudopotential*, is used to describe the motion of core electrons, the ones more affected by relativistic effects [378]. It introduces a simplified term that replaces core electrons by a potential function to describe their combined repulsion on valence electrons in the wavefunction. ECPs are used in combination with conventional basis sets and specified in the Gaussian input file.

3.3.4. Modeling chemistry in solution

Calculations in the gas phase are often appropriate for studying chemical reactivity. However, since chemical reactions commonly take place in solution, this approach may fail to reproduce certain chemical phenomena in which the solvation framework plays a critical role. An obvious approach to circumvent this problem is to include explicit solvent molecules around the molecular system of study. However, the consequent computational cost associated with this strategy prevents its generalized use.

An alternative methodology is provided by the so-called *Self-Consistent Reaction Field* (SCRF) methods, by which the solvent in a reaction is treated as a continuous uniform dielectric medium characterized by a dielectric constant (ε). SCRF methods "place" the solute molecule inside a cavity with an associated dielectric medium, so that the effect of the solvent is modeled by simulating an electrostatic interaction.

The *Polarizable Continuum Model* (PCM) is the default SCRF method in Gaussian calculations [379]. However, the model of choice for predicting Gibbs energies in solution ($G_{solvent}$) is the SMD model introduced by Truhlar [380]. This model contains a series of key descriptors other than ε (*i.e.* refractive index, bulk surface tension, and acidity and basicity parameters) that have been parametrized for a large number of solvents. Tailored parameters for mixtures of solvents can also be approximated by a linear combination of the aforementioned parameters (see chapter 7 in this thesis). The SMD model was initially optimized to compute solvation energies (ΔG_{solv}). The values of ΔG_{solv} can be used to predict reaction energies and energy barriers in solution with Truhlar's approximation:

$$\Delta G_{solv} = E_{SMD} - E_{gas\,phase} \qquad \text{(Eq. 1.36)}$$

Combining (Eq. 1.36 and (Eq. 1.32.one can obtain G in solution by simply performing single-point energy calculations (SPE) with the SMD levels adding G_{corr} values computed with gas phase calculations.

$$G_{solvent} = E_{gas\,phase} + \Delta G_{solv} + G^{corr}_{gas\,phase} \qquad \text{(Eq. 1.37)}$$

3.3.5. Dispersion energy

Pure and hybrid density functionals fail to model long-range electronic correlation and thus cannot account for London dispersion interactions. Conversely, it is widely accepted that proper modeling of weak inter- or intramolecular interactions is desirable to reach accurate predictions. When dealing with large molecular systems appropriate modeling of the dispersion energy becomes mandatory.

The most generalized method to include dispersion energy was introduced by Grimme early in the past decade and [381] is based on including an empirical correction term to the KS energy obtained from energy calculations with a given DF. The use of dispersion-corrected DFT (DFT-D) methods like B3LYP-D3 is nowadays generalized.

Although “Minnesota functionals” contain empirical parameters intended to account for dispersion interaction energies, most of them usually fail to reproduce long-range interactions [382]. Grimme’s empirical dispersion in combination with M05 and M06 functionals has proven useful even in this case [382–387]. The DFT-D3(0) [388] version (with the original damping function) is recommended in this case since DFT-D3(BJ) (with the Becke Johnson damping function [389]) double-counts medium-range interactions when applied to *meta*-GGA M06, M06L and M06-2X functionals [384].

Our group demonstrated some years ago that dispersion corrections are essential in the computational study of fullerene reactivity [390]. The model system employed was the DA reaction of C_{60} of cyclopentadiene and other dienes, for which experimental ΔH_r and $\Delta H^{\ddagger}$ were already known. Considerable stabilization of the intermediates and the TS of around 15-20 kcal/mol were observed with respect to the values computed with non-corrected density functionals. Moreover, the values matched much better with the ones found experimentally.

3.3.6. Analysis of the binding energy

The *activation strain model* (ASM) or *distortion/interaction model* [391] allows for the understanding of the factors that determine the nature of activation barriers of chemical reactions. It is a fragment approach in which the barrier of a reaction is described in relation to the original geometry of the reactants. According to the ASM, the PES [$\Delta E(\zeta)$] can be decomposed into two contributions along the reaction coordinate (ζ):

$$\Delta E(\zeta) = \Delta E_{strain}(\zeta) + \Delta E_{int}(\zeta) \qquad \text{(Eq. 1.38)}$$

- The *strain energy* $\Delta E_{strain}(\zeta)$ represents the required energy to deform the reactants from their equilibrium geometry to a particular geometry at a given point (ζ) in the reaction coordinate. It is generally destabilizing and, hence, it is the main cause for the height of an energy barrier.
- The *interaction energy* $\Delta E_{int}(\zeta)$ represents the energy change arising from the combination of the original deformed fragments in a reaction to form a new molecule at a given point (ζ) in the reaction coordinate. It is generally stabilizing and counteracts the strain.

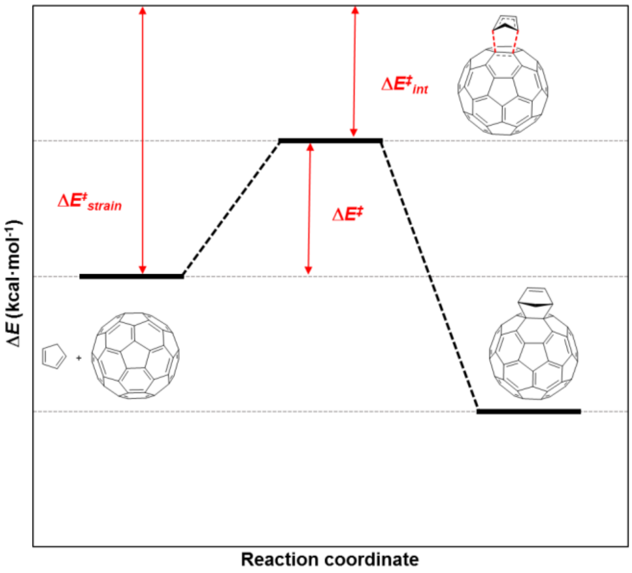

Figure 1.25. Schematic representation of the ASM for the DA cycloaddition of cyclopentadiene and C_{60}.

The second term can be further decomposed on the basis of the *energy decomposition analysis* (EDA) [392,393] method:

$$\Delta E_{int}(\zeta) = \Delta E_{elstat}(\zeta) + \Delta E_{Pauli}(\zeta) + \Delta E_{orb}(\zeta) + \Delta E_{disp}(\zeta) \qquad \text{(Eq. 1.39)}$$

- ΔE_{elstat} represents the classical electrostatic interaction between the unperturbed charge distributions of the deformed reactants. It usually attractive.
- ΔE_{Pauli} represents the destabilizing interactions between occupied orbitals and is responsible for steric repulsion.
- $\Delta E_{orb}(\zeta)$ refers to orbital interaction and accounts for charge transfer, bond formation and polarization.
- $\Delta E_{disp}(\zeta)$ takes into account interactions for which dispersion forces are responsible.

An accurate analysis of each of the different terms that contribute to the energy barrier provides us with valuable information on the factors that determine the performance of a chemical reaction.

3.4. Computational methods used in this thesis

Previous subsections have covered fundamental aspects of computational chemistry and molecular modeling that constitute a general approximation to understand the computational methods used to carry out the projects developed within the framework of this doctoral thesis. This last subsection summarizes the methods used on the basis of what has been previously discussed:

- Geometries of all stationary points were optimized without symmetry constraints with the *Gaussian 09 program* [354] using the DFT B3LYP hybrid exchange-correlation functional [364].
- SPE calculations were performed in order to improve the electronic energy of previously optimized geometries in chapters 3, 4, and 7 using either the M06 [394] or M06L [363] functional.
- The D3 Grimme energy corrections for dispersion with the original damping function were added in all geometry optimizations and SPE calculations [388].

- Solvent corrections were computed with the solvation model based on density (SMD) [380].
- Analytical Hessians were computed to determine the nature of stationary points (one and zero imaginary frequencies for TSs and minima, respectively) and to calculate unscaled zero-point energies (ZPEs) as well as thermal corrections and entropy effects using the standard statistical-mechanics relationships for an ideal gas. These two latter terms were computed at the designated temperature and 1 atm to provide the reported relative Gibbs energies.
- All-electron *double zeta* cc-pVDZ [395] or 6-31G(d,p) [396] basis sets were employed for non-metal atoms and the cc-pVDZ-PP [397] basis set containing an ECP was used for Rh in optimization and frequency calculations. The *triple zeta* cc-pVTZ and cc-pVTZ-PP basis sets were used in M06 and M06L SPE calculations.
- For the projects developed in chapters 3, 4 and 7 the reported Gibbs energies contain electronic energies calculated at the M06L-D3/cc-pVTZ-PP//B3LYP-D3/cc-pVDZ-PP or M06-D3/cc-pVTZ-PP//B3LYP-D3/cc-pVDZ-PP level together with gas phase thermal and entropic contributions computed with the B3LYP-D3/cc-pVDZ-PP method. In chapter 6, the reported Gibbs energies were computed at the UB3LYP-D3/6-31G(d,p) level of theory.
- In chapter 6, the results were discussed by means of the ASM of reactivity at the UM06-2X-D3/def2-TZVPP//UB3LYP-D3/6-31G(d,p). The origins of the orbital interactions were analyzed quantitatively by using the natural orbital for chemical valence (NOCV) extension of the EDA method. All the EDA–NOCV calculations were performed with the ADF program [398]. ASM/EDA calculations were performed and analyzed by Dr. Israel Fernández at the Universidad Complutense de Madrid (UCM).
- When required, catalytic species employed for computational modelling were simplified in order to reduce the computational cost of the calculations.
- Stationary points were unambiguously confirmed by IRC calculations.

Chapter 2. General objectives

Preceding pages of this manuscript have covered some aspects of the chemistry of fullerenes, from their properties to functionalization methods and practical applications. From a synthetic perspective, we have seen that fullerenes behave as electron deficient alkenes in numerous chemical reactions. This particular feature has prominent relevance when it comes to developing new synthetic derivatives with enhanced applicability. We have also discussed in detail the versatility of Rh(I)-catalyzed [2+2+2] cycloaddition reactions in synthetic organic chemistry and how the combination of experiments and theory can be used as a powerful approach to discover and improve chemical processes.

Fullerenes can participate as unsaturated partners in transition metal-promoted [2+2+2] cycloaddition reactions with two alkynes, as demonstrated by previous studies in the literature [162,164]. Moreover, the resulting cyclohexadiene-fused products can be used as synthetic intermediates for the preparation of the so-called open-cage fullerenes. However, previously reported methodologies are not catalytic and/or have a very limited substrate scope. Therefore, developing new synthetic protocols to efficiently prepare cyclohexadiene-C_{60} derivatives by catalytic means is desirable. Beyond that, further exploration of the process, both by experimental and theoretical means, may allow the participation of other unsaturated substrates like allenes.

In view of the precedents exposed, and considering the experience of our group in the fields of fullerene chemistry and Rh(I)-catalyzed [2+2+2] cycloaddition reactions, we set the objectives of the present thesis.

From a general point of view, we aimed to develop and study in detail a series of novel cyclisation reactions directed to the functionalization of fullerenes through the formation of new C–C bonds. More specifically, experimental studies were directed to obtaining novel C_{60} derivatives by employing Rh(I)-catalyzed [2+2+2] cycloaddition reactions starting from C_{60} and diynes or 1,5-bisallenes. Theoretical studies were focused on the thorough study of the mechanism underlying these chemical processes. Additionally, we aimed to expand the fundamental understanding on the reactivity of fullerenes by computationally studying the regioselectivity of DA cycloadditions involving elusive $^{\#6094}C_{68}$ fullerene. The application of fullerene derivatives in the field of photovoltaic technology has also been envisaged.

For clarification purposes, the projects developed are divided into three sections:

Section 1: Rh(I) catalyzed [2+2+2] cycloadditions of fullerenes and alkynes

Chapters 3, 4 and 5 deal with fullerene functionalization by the Rh(I)-catalyzed [2+2+2] cycloaddition of C_{60} and alkynes. Though some examples of transition metal-promoted [2+2+2] cycloaddition reactions involving C_{60} had been reported, the ability of Rh to promote or catalyze the reaction had not been disclosed at the moment of starting this doctoral thesis. Furthermore, the reaction mechanism had never been studied by computational means in any of the examples reported.

Taking into account all these considerations, the first objective was to study computationally the intermolecular [2+2+2] cycloaddition reaction of C_{60} and two acetylene molecules catalyzed by Wilkinson's complex. The results obtained in this first analysis of the reaction were expected to guide further experimental studies.

Once the reaction was considered from a theoretical point of view, our aim in the second project of the thesis was to develop a catalytic protocol to achieve the preparation of cyclohexadiene-fused C_{60} derivatives thus providing a better synthetic alternative involving mild catalytic conditions and wide reaction scope.

The third and last objective in this section was carried out in collaboration with the research group of Dr. Luís Echegoyen, within the framework of a predoctoral stay in his laboratories at the University of Texas at El Paso (UTEP). We aimed to incorporate the fullerene derivatives prepared according to our synthetic protocol as the ETMs in PSCs.

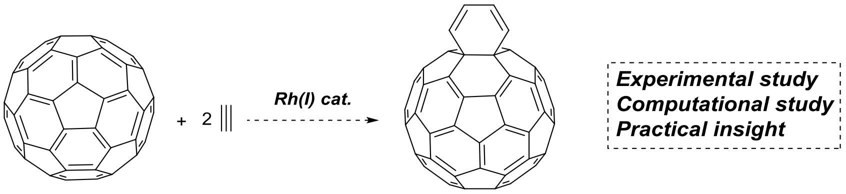

Scheme 2.1. Simplified representation of the objectives dealing with C_{60} functionalization.

Section 2: A Rh-catalyzed cycloisomerization/Diels-Alder cascade reaction of 1,5-bisallenes for the synthesis of polycyclic heterocycles and the functionalization of fullerenes

Within our program directed to the functionalization of fullerenes by Rh(I)-catalyzed [2+2+2] cycloaddition reactions, the second objective of this thesis consisted in developing a new partially intramolecular variation of the reaction involving 1,5-bisallenes and C_{60} as the unsaturated partners.

Since the transition metal-catalyzed [2+2+2] cycloaddition reaction of 1,5-bisallenes with alkenes has been so far elusive, we first envisaged to develop this reaction with simple alkenes. We hypothesized that after oxidative coupling of two double C–C bonds 1,5-bisallenes would yield one two or three of rhodacyclopentane intermediates **I**, **II** and **III**. Subsequently, insertion of the alkene and reductive elimination would afford products **A**, **B** and **C,** respectively. Considering this, we aimed to direct the reaction towards the formation of fused 7-membered carbo- and heterocycles, whose synthesis is considered a more challenging task.

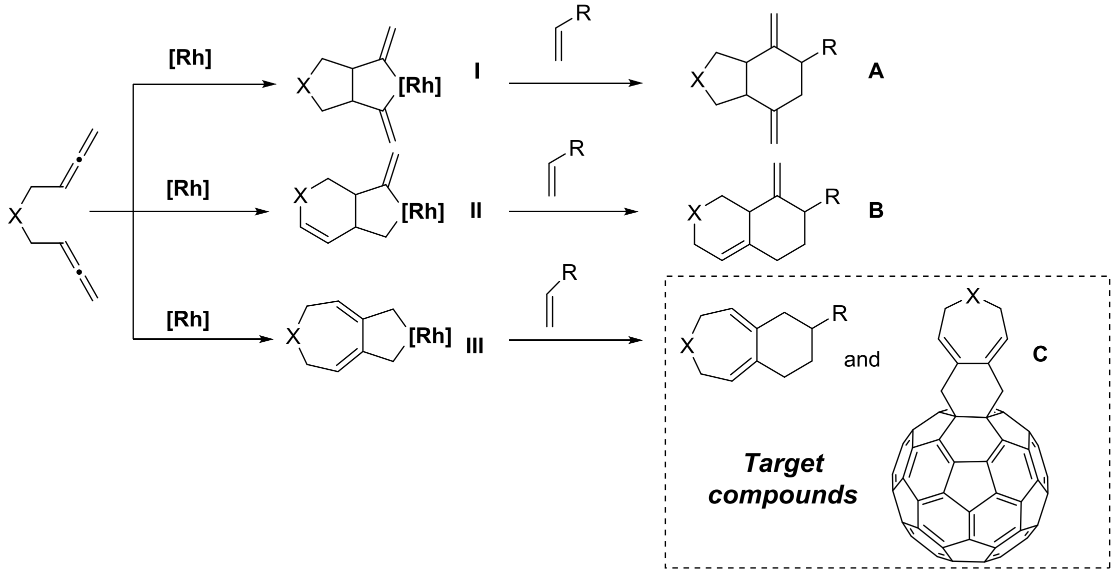

Scheme 2.2. Hypothetic mechanism for the [2+2+2] cycloaddition of 1,5-bisallenes with alkenes.

The results obtained with simple alkene substrates were ultimately intended to be applied to the functionalization of fullerenes.

Section 3: Regioselectivity in Diels–Alder cycloadditions of $^{\#6094}C_{68}$ fullerene with a triplet ground state

Still in the field of fullerene chemistry, another objective set within the context of this thesis was to study the regioselectivity of DA cycloaddition of $^{\#6094}C_{68}$ and cyclopentadiene. This peculiar and highly reactive fullerene cage cannot be isolated, but indirect evidence of its formation was obtained for the first time in 2012 by trapping it as the octachloride derivative $C_{68}Cl_8$. Exploration of its chemical reactivity was considered of great interest because of two particular features: it is one of the few hollow fullerenes not fulfilling the IPR rule and one of the few non-functionalized fullerenes with a triplet ground state. The study of its reactivity by computational means was expected to provide fundamental information on the different factors that govern the regioselectivity in fullerene-involving cyclization reactions.

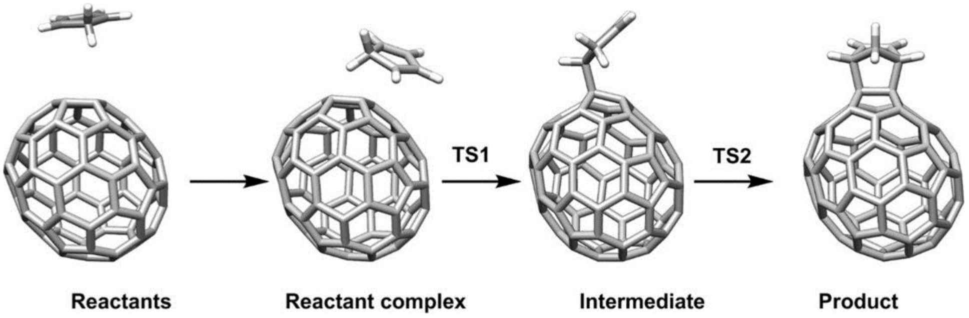

Scheme 2.3. General stepwise mechanism considered for the reaction of $^{6094}C_{68}$ with cyclopentadiene.

Chapter 3. A computational study of the intermolecular [2+2+2] cycloaddition of acetylene and C_{60} catalyzed by Wilkinson's Catalyst

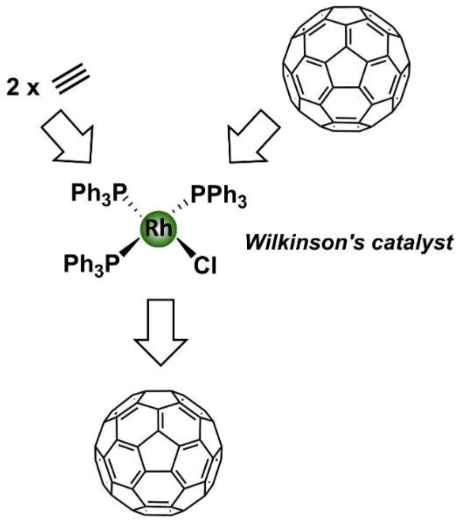

Published in: *Chem. Eur. J.* **2017**, *23*, 15067.

Abstract: The functionalization of fullerenes helps to modulate their electronic and physicochemical properties, generating fullerene derivatives with promising features for practical applications. Herein, DFT is used to explore the attachment of a cyclohexadiene ring to C_{60} through a rhodium-catalyzed intermolecular [2+2+2] cycloaddition of C_{60} and acetylene. All potential reaction paths are analyzed and it can be concluded that the [2+2+2] cycloaddition of C_{60} and two acetylene molecules catalyzed by $[RhCl(PPh_3)_3]$, yielding a cyclohexadiene ring fused to a [6,6] bond of C_{60}, is energetically feasible.

Reproduced with permission from:

Artigas, A.; Lledó, A.; Pla-Quintana, A.; Roglans, A.; Solà, M. A Computational Study of the Intermolecular [2+2+2] Cycloaddition of Acetylene and C_{60} Catalyzed by Wilkinson's Catalyst. *Chem. Eur. J.* **2017**, *23*, 15067. © 2018 Wiley-VCH Verlag GmbH & Co. KGaA, Weinheim.

ChemPubSoc Europe
DOI: 10.1002/chem.201702494
CHEMISTRY
A European Journal
Full Paper

Reaction Mechanisms

A Computational Study of the Intermolecular [2+2+2] Cycloaddition of Acetylene and C_{60} Catalyzed by Wilkinson's Catalyst

Albert Artigas, Agustí Lledó, Anna Pla-Quintana, Anna Roglans, and Miquel Solà*[a]

Abstract: The functionalization of fullerenes helps to modulate their electronic and physicochemical properties, generating fullerene derivatives with promising features for practical applications. Herein, DFT is used to explore the attachment of a cyclohexadiene ring to C_{60} through a rhodium-catalyzed intermolecular [2+2+2] cycloaddition of C_{60} and acetylene. All potential reaction paths are analyzed and it can be concluded that the [2+2+2] cycloaddition of C_{60} and two acetylene molecules catalyzed by $[RhCl(PPh_3)_3]$, yielding a cyclohexadiene ring fused to a [6,6] bond of C_{60}, is energetically feasible.

Introduction

Organic materials are appealing for photovoltaic devices due to the advantages these materials have in comparison with the most commonly used silicon-based systems, such as low-cost synthesis, easy manufacture, and the possibility to generate flexible, light, and cheap devices.[1] In this regard, fullerenes are attractive organic materials that can efficiently harvest sunlight and transform it into other useful forms of energy. The production of dye-sensitized solar cells (DSSCs) is currently among the most realistic application of fullerene derivatives.[2] In the design of DSSCs manufactured by using the molecular heterojunction (mHJ) technique,[3] a fullerene, commonly [60]fullerene (C_{60}), is covalently linked to an electron-donating group. The use of mHJs allows better control of the structure of donor and acceptor units and charge mobility between them.[4] The charge-transfer (charge separation and recombination) properties of the donor–C_{60} dyad critically depend on the connection between donor and acceptor.[5] Most typical chemical reactions of fullerenes (Diels–Alder, 1,3-dipolar, and Bingel–Hirsch cycloadditions)[6] attach an electron-donating group to the fullerenic cages through two C_{sp^3}–C_{sp^3} bonds. We hypothesize that communication between donor and acceptor groups could be improved by connecting donor and acceptor units through C_{sp^3}–C_{sp^2} bonds. In this way, the π system of the cage and electron-donor group could interact more effectively through periconjugation[7] and facilitate charge-transfer separation. The transition-metal-catalyzed [2+2+2] cycloaddition of C_{60} and two alkynes or a diyne represents a potential way to generate this kind of link between the fullerenic cage and the donor. So far, from a practical point of view, cyclohexadiene-fused fullerene derivatives have been used as synthetic intermediates of open-cage fullerenes.[8]

The [2+2+2] cycloaddition of three alkynes is an elegant preparative route to polysubstituted benzenes.[9] Scheme 1 shows the widely accepted reaction mechanism for the [2+2+2] cycloaddition of three acetylenes. The reaction begins with a pair of ligand–alkyne substitution reactions. Oxidative addition of the two alkyne ligands in **II** generates a metalla cyclopentadiene (**IIIa**) or a metallacyclopentatriene (**IIIb**) intermediate. This is commonly the rate-determining step (rds). Subsequent coordination of a third alkyne ligand to **IIIa** or **IIIb** intermediates is followed by alkyne insertion to form a metallacycloheptatriene (**V**; the Schore mechanism),[10] metal-mediated [4+2] cycloaddition to yield a metallanorbornadiene (**VI**), or [2+2] cycloaddition to give a metallabicyclo[3.2.0]heptatriene

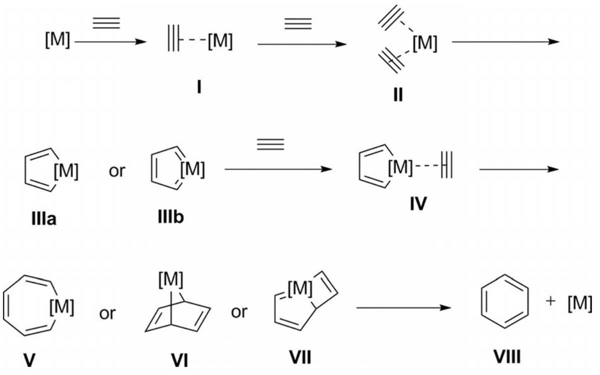

Scheme 1. Most widely accepted reaction mechanisms for the transition-metal-catalyzed [2+2+2] cycloaddition of three acetylenes ([M] = transition-metal catalyst).

---

[a] A. Artigas, Dr. A. Lledó, Dr. A. Pla-Quintana, Prof. Dr. A. Roglans, Prof. Dr. M. Solà
Institut de Química Computacional i Catàlisi (IQCC)
and Departament de Química, Universitat de Girona
C/ Maria Aurèlia Capmany, 69, 17003, Girona, Catalonia (Spain)
E-mail: miquel.sola@udg.edu

Supporting information and the ORCID identification number(s) for the author(s) of this article can be found under https://doi.org/10.1002/chem.201702494.

© 2017 Wiley-VCH Verlag GmbH & Co. KGaA, Weinheim

(**VII**). Finally, reductive elimination of the metal leads to arene **VIII** and recovery of the catalyst. Such [2+2+2] cycloaddition has been also reported between an ene group (or an allene group[11]) and two alkynes or a diyne to yield cyclohexadiene species.[12] Therefore, one can expect that two acetylene molecules could react with C_{60} to generate a six-membered ring attached to C_{60} through two $C_{sp^3}-C_{sp^2}$ bonds.

Murata et al. already formed such a link through the reaction of C_{60} with palladacyclopentadiene complexes to provide cyclohexadiene-type adducts.[13] Moreover, some years ago, Cheng et al. reported a nickel-promoted ene–diyne [2+2+2] cycloaddition reaction on C_{60}.[14] Typically for cycloadditions to C_{60},[15] addition took place at a [6,6] bond. More than stoichiometric amounts of $[NiCl_2(PPh_3)_2]$ and excess PPh_3 were required to obtain a high yield of cycloadduct. In our group, we have been working on [2+2+2] cycloadditions catalyzed by rhodium for many years.[9d,11a] It is known that rhodium catalysts are very efficient in [2+2+2] cycloadditions.[9] Herein, the main goal is to explore the rhodium-catalyzed [2+2+2] cycloaddition of two acetylene molecules and C_{60} by using Wilkinson's catalyst computationally. All possible routes to cycloaddition products are explored by means of DFT calculations, to ascertain whether it is possible to reach the cycloadducts of the reaction under catalytic conditions. We also aim to gain an insight into the regioselectivity of this [2+2+2] cycloaddition reaction and to have a deeper knowledge of the reaction mechanism; in particular, we seek to uncover the intermediates present in the process. The results obtained will guide future experimental attempts in our group to carry out [2+2+2] cycloadditions on C_{60}, higher fullerenes, and endohedral metallofullerenes.

Computational Details

Geometries of the reactants, intermediates, transition states (TSs), and products were optimized with the Gaussian 09 program[16] by using the DFT B3LYP[17] hybrid exchange-correlation functional. All geometry optimizations were performed without symmetry constraints. The all-electron cc-pVDZ basis set[18] was employed for non-metal atoms and the cc-pVDZ-PP basis set containing an effective core relativistic pseudopotential was used for Rh.[19] The electronic energy was improved by performing single-point calculations with the cc-pVTZ (cc-pVTZ-PP for Rh) basis set and the M06L functional. Analytical Hessians were computed to determine the nature of stationary points (one and zero imaginary frequencies for TSs and minima, respectively) and to calculate unscaled zero-point energies (ZPEs), as well as thermal corrections and entropy effects by using the standard statistical-mechanics relationships for an ideal gas.[20] These last two terms were computed at 298.15 K and 1 atm to provide the reported relative Gibbs energies (ΔG). The D3 Grimme energy corrections[21] for dispersion, with its original damping function, were added in all B3LYP/cc-pVDZ-PP and M06L/cc-pVTZ-PP calculations. Gibbs energies of solvation were not included because they were reported to have minor effects in these kinds of transformations, usually carried out in rather nonpolar solvents.[22] However, to assess the importance of solvent effects, we recomputed the reaction profile of the most favorable reaction path in Scheme 3 by adding solvent corrections computed with the solvent model based on density (SMD) continuum solvation model,[23] considering toluene as the solvent with the M06L-D3/cc-pVTZ-PP//B3LYP-D3/cc-pVDZ-PP method. As expected, the results showed that changes in Gibbs energy barriers were not larger than 1.5 kcal mol^{-1} (see Scheme S9 in the Supporting Information). The most important differences corresponded to the dissociation (coordination) of a PPh_3 ligand, which was favored (disfavored) by about 5 kcal mol^{-1} in solution. These energetic changes, however, did not modify the conclusions reached with the gas-phase profiles. In summary, the hereafter reported Gibbs energies contained electronic energies calculated at the M06L-D3/cc-pVTZ-PP//B3LYP-D3/cc-pVDZ-PP level, together with gas-phase thermal corrections and entropic contributions computed at 298.15 K and 1 atm with the B3LYP-D3/cc-pVDZ-PP method.

Abstract in Catalan: La funcionalització dels ful·lerens permet modular les seves propietats electròniques i fisicoquímiques, generant derivats de ful·lerè amb característiques prometedores per a potencials aplicacions pràctiques. En aquest treball, mitjançant la teoria del funcional de la densitat s'ha explorat la unió d'un anell de ciclohexadiè al C_{60} a través d'una cicloaddició intermolecular [2+2+2] de C_{60} i acetilè catalitzada per rodi. L'anàlisi de tots els possibles camins de reacció ens permet concloure que la cicloaddició [2+2+2] de C_{60} i dues molècules d'acetilè catalitzada per $[RhCl(PPh_3)_3]$ per generar un anell de ciclohexadiè fusionat a un enllaç [6,6] del C_{60} és un procés energèticament viable.

Results and Discussion

We have analyzed all potential reaction pathways that transform a C_{60} molecule and two acetylenes into the final cyclohexadiene derivative of C_{60}. First, we have considered two possible initial oxidative additions, namely, path A, involving the addition of two acetylenes to yield the rhodacyclopentadiene intermediate **A4** (Scheme 2) followed by C_{60} insertion or [4+2] cycloaddition, and path B, in which oxidative addition takes place between an acetylene and C_{60} to generate intermediate **B4** that subsequently adds a second acetylene molecule. In the C_{60} insertion/[4+2] cycloaddition in path A and the oxidative addition in path B, we have analyzed the attack on the [6,6] and [5,6] bonds of C_{60}. As usual for C_{60},[15a,c] in all cases, the [6,6] bond is more reactive than the [5,6] bond. Moreover, all reaction pathways have been studied with three possible active catalysts: $[RhCl(PPh_3)_2]$, $[RhCl(PPh_3)]$, and RhCl. This is relevant because, for instance, the preferred oxidative addition between two acetylenes takes place with two phosphines coordinated to rhodium, whereas Rh–C insertion occurs with one coordinated phosphine. It is also worth mentioning that, after oxidative addition, we analyzed the three different possibilities, namely, insertion to form a rhodacycloheptadiene intermediate (analogous to **V** in Scheme 1), rhodium-mediated [4+2] cycloaddition to yield a rhodanorbornene complex (**VI** in Scheme 1), and [2+2] cycloaddition to give a rhodabicyclo[3.2.0]heptadiene species (**VII** in Scheme 1). The most favorable reaction paths go through a rhodacycloheptadiene intermediate, but we also found some reaction pathways involving

© 2017 Wiley-VCH Verlag GmbH & Co. KGaA, Weinheim

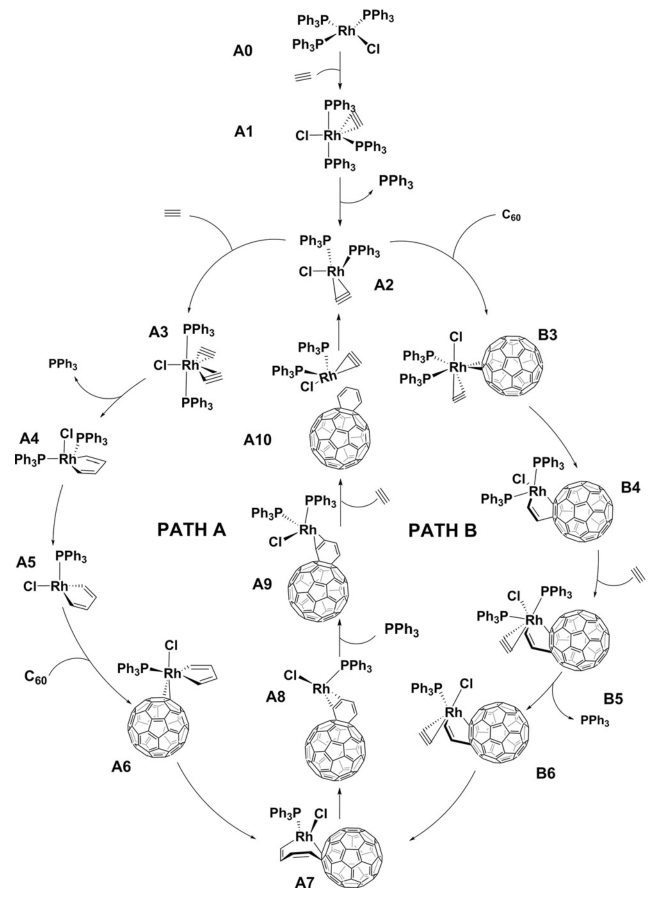

Scheme 2. The two energetically most favorable catalytic cycles for the [2+2+2] cycloaddition reaction of C_{60} and two acetylenes catalyzed by $[RhCl(PPh_3)_3]$: path A corresponds to the initial oxidative addition between two acetylenes, and path B considers the initial oxidative addition between C_{60} and an acetylene molecule.

rhodanorbornene and rhodabicyclo[3.2.0]heptadiene intermediates. Finally, for comparison purposes, we also computed the reaction mechanism of the [2+2+2] cycloaddition of three acetylenes catalyzed by Wilkinson's catalyst. This reaction was already studied by some of us some years ago,[24] but herein we recomputed the Gibbs energy profile to take into consideration dispersion effects in both the geometry and energy of all stationary points. All studied Gibbs reaction profiles are given in the Supporting Information. In the coming paragraphs, we discuss only the two energetically most favorable reaction paths.

As shown in Scheme 2, there is preactivation of the catalysts before entering the catalytic cycle as the 16-electron species **A2**. To reach **A2**, the initial Wilkinson's catalyst coordinates an incoming acetylene molecule and loses a phosphine, in a process that is endergonic by 15.0 kcal mol^{-1}. The PPh_3 ligand in **A1** that is removed to form **A2** occupies a site *cis* to Cl[25] in the equatorial position of the trigonal bipyramid (tbp).

The Gibbs energy profile of the transformation from **A2** to **A11** through paths A and B is given in Scheme 3. Intermediate **A2** adds an acetylene molecule to generate the 18-electron species **A3**, in which the two PPh_3 ligands occupy axial positions of the tbp. We checked that this was the most stable disposition of the ligands. The conversion from **A2** to **A3** is exergonic by merely 2.2 kcal mol^{-1}. Oxidative addition from **A3**, with two equatorial acetylene ligands, has a large Gibbs energy barrier of 37.5 kcal mol^{-1}. Thus, this oxidative addition takes place through its less stable isomer **A3**′ (Scheme 3 and Scheme S1 in the Supporting information), in which the acetylene ligands occupy axial and equatorial positions. Intermediates **A3** and **A3**′ are in equilibrium and easily interconvert through a Berry pseudorotation of the tbp.[26] The approach of the two acetylene ligands during oxidative addition is easier when they occupy axial and equatorial coordination sites.[24,27] The energetic span[28] between the turnover frequency (TOF)-determining intermediate (TDI; **A3**) and TOF-determining TS (TDTS; **TS A3′A4**) is 22.4 kcal mol^{-1}. The molecular structure of **TS A3′A4** is depicted in Figure 1 a. As it can be seen, the C–C bond to be formed in this step has a bond length of 2.008 Å. This is the highest energy barrier throughout the catalytic cycle through path A and, therefore, oxidative addition is the rds for this path, similar to some other [2+2+2] cycloadditions.[12b,22c,27a,29] Oxidative addition affords the rhodacyclopentadiene species **A4** by releasing 11.0 kcal mol^{-1}. In a subsequent step, this intermediate loses a PPh_3 ligand to form **A5** with a cost of 14.6 kcal mol^{-1}. Coordination of **A5** to C_{60} to yield **A6** is an exergonic process by 21.6 kcal mol^{-1}. Alternatively, species **A4** coordinates to a third acetylene molecule (Scheme S1 in the Supporting information) to progress through the benzene-formation pathway (see below). The π localization[29b,30] in **A4** and **A5**, as denoted by the large difference between double C=C (1.35 Å) and single C–C (1.47 Å) bond lengths, shows that these intermediates are not stabilized by the aromaticity of the rhodacyclopentadiene ring. In **A6**, C_{60} is η^2-coordinated to Rh, occupying an axial position of a distorted tbp *trans* to Cl. The structure of **A6** resembles that of the first X-ray crystal structure of cobaltacyclopentadiene(alkyne) complex reported.[31] The Schore mechanism[10] is operative in the insertion of the [6,6] bond of C_{60} into the Rh–C bond through **TS A6A7** to yield rhodacycloheptadiene intermediate **A7**. Transformation of **A6** into **A7** is exergonic by 12.4 kcal mol^{-1} and takes place through a Gibbs energy barrier of only 6.7 kcal mol^{-1}. The [4+2] cycloaddition in **A6** leading to intermediate **C7** has also been considered, but this alternative pathway has a much larger barrier of 24.7 kcal mol^{-1}.

Paths A and B merge in **A7** and share the same reaction path until **A11**, which is the final cyclohexadiene derivative of C_{60}. All attempts to locate the rhodanorbornene and rhodabicyclo[3.2.0]heptadiene intermediates failed and led to complex **A7**. Reductive elimination occurs in **A7** to generate intermediate **A8**, in which the $[Rh^{I}Cl(PPh_3)]$ complex is η^2-coordinated to the cyclohexadiene ring attached to C_{60}. The conversion of **A7** into **A8** is exergonic by just 1.6 kcal mol^{-1} and takes place through a Gibbs energy barrier of 15.2 kcal mol^{-1}. Complex **A8** is a 14-electron species that can accept an incoming PPh_3 ligand to generate the 16-electron species **A9** in an exergonic process by 23.0 kcal mol^{-1}. Finally, release of the product and recovery of **A2** is endergonic by 5.6 kcal mol^{-1}. As a whole, the transformation from reactants to products through path A occurs with a Gibbs energy barrier of 22.4 kcal

© 2017 Wiley-VCH Verlag GmbH & Co. KGaA, Weinheim

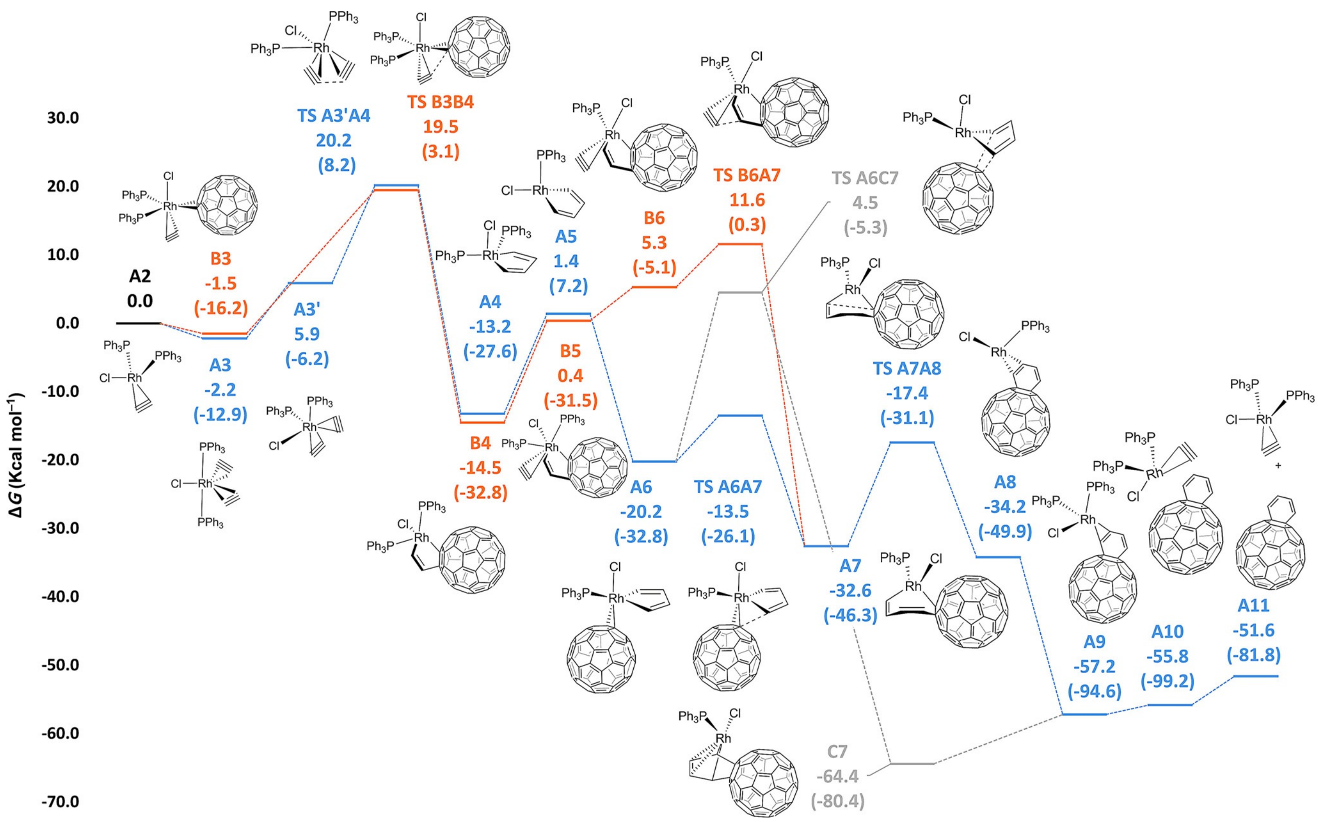

Scheme 3. M06L-D3/cc-pVTZ-PP//B3LYP-D3/cc-pVDZ-PP Gibbs energy profile for paths A (blue) and B (orange) of the [2+2+2] cycloaddition reaction of C_{60} and two acetylenes catalyzed by $[RhCl(PPh_3)_3]$. Energies given in parentheses are electronic energies. All energies are relative energies with reference to **A2** and are given in $kcal\,mol^{-1}$.

mol^{-1} and a Gibbs reaction energy of $-51.6\,kcal\,mol^{-1}$. The fact that **A5** can add C_{60} to give cyclohexadiene-type adducts is in agreement with the experimental reaction reported by Murata et al. of C_{60} with palladacyclopentadiene complexes to generate an adduct with the cyclohexadiene ring attached to C_{60}.[13]

On the other hand, path B starts with the formation of 18-electron complex **B3** by coordination of C_{60} to $[RhCl(PPh_3)_2(C_2H_2)]$. The Gibbs reaction energy of this process is $-1.5\,kcal\,mol^{-1}$. The axial coordination sites of the tbp in complex **B3** are occupied by Cl and acetylene. This is the most stable disposition of the ligands. We have also analyzed the possibility of generating **B2** from **A0** through loss of a PPh_3 ligand and then coordination of C_{60}. Subsequent coordination of acetylene to **B2** forms **B3**. Dissociation of PPh_3 from **A0** and coordination to C_{60} to yield **B2** has a cost of $19.8\,kcal\,mol^{-1}$. This energetic cost is higher than the cost to generate **A2** from **A0** by $4.8\,kcal\,mol^{-1}$, and, therefore, species **B2** is not expected to play a major role in the reaction mechanism. Oxidative addition in **B3** takes places through **TS B3B4** to yield **B4** with a Gibbs energy barrier of $21.0\,kcal\,mol^{-1}$ and releasing $13.0\,kcal\,mol^{-1}$. Interestingly, the oxidative addition of an acetylene and C_{60} has almost the same barrier as that between two acetylenes. Similarly, it was found that the oxidative addition of a nitrile and an acetylene molecules catalyzed by RhCp (Cp = cyclopentadienyl) has a similar barrier to that of two acetylenes.[32] In 16-electron intermediate **B4**, C_{60} is fused to a rhodacyclopentene species. This intermediate is moderately stable and we postulate that it could be isolated at relatively low temperatures. Subsequent coordination of acetylene to **B4** gives the 18-electron **B5** intermediate, which is destabilized by $15.9\,kcal\,mol^{-1}$ relative to **B4**. All attempts to locate the TS of Rh–C insertion in **B5** failed. On the other hand, if **B5** loses PPh_3 to give **B6**, insertion goes through **TS B6A7** (see Figure 1 b) with a Gibbs energy barrier of only $6.3\,kcal\,mol^{-1}$. The energetic span from the TDI **B4** to the TDTS **TS B6A7** is $26.1\,kcal\,mol^{-1}$. Interestingly, the rds in path B is the insertion of the second acetylene molecule. Despite oxidative addition generally being the rds, there are also some examples in which oxidative addition is not rate determining.[32,33] The energetic span of path B ($26.1\,kcal\,mol^{-1}$) is somewhat higher than that found for path A ($22.4\,kcal\,mol^{-1}$). Therefore, although path A is clearly the most favorable, path B cannot be completely ruled out and both paths could be operative to provide the cyclohexadiene ring attached to C_{60} product. Finally, the reaction pathway from **A7** to **A11** is shared by reaction paths A and B, as discussed above.

As mentioned previously, we have studied the oxidative addition of three acetylene molecules catalyzed by $[RhCl(PPh_3)_3]$ to generate benzene (see the Supporting Information). The reaction mechanism from **A0** to **A4** is the same as path A discussed above. In both reaction pathways, oxidative addition is the rds. The two main differences are 1) path A of Scheme 3 involves loss of a PPh_3 ligand in **A4** to form **A5** before insertion;

© 2017 Wiley-VCH Verlag GmbH & Co. KGaA, Weinheim

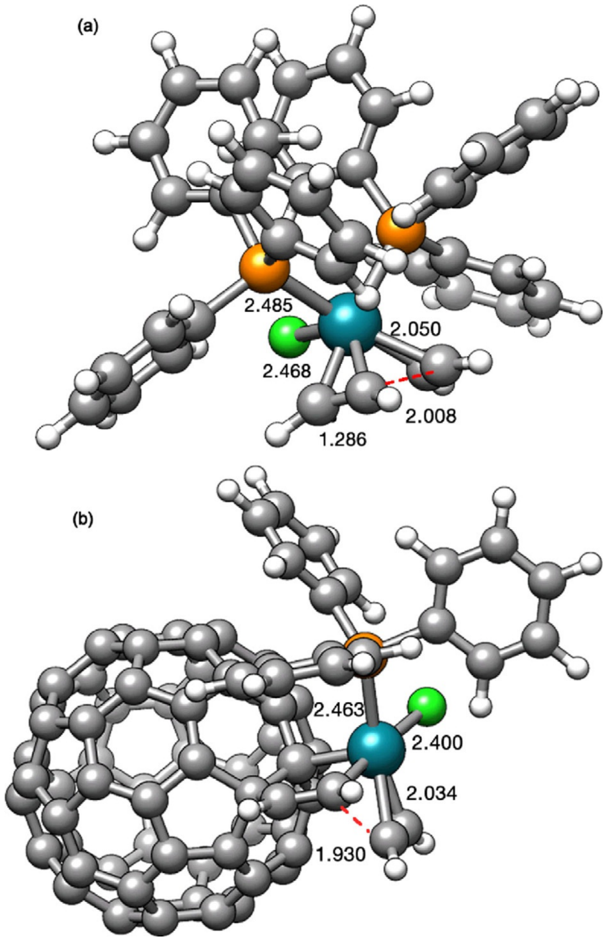

Figure 1. Molecular structure of the rate-determining TSs of a) the oxidative addition step in path A (**TS A3′A4**), and b) the Rh–C insertion step in path B (**TS B6A7**). Bond lengths in Å.

this dissociation costs 14.6 kcal mol^{-1}, whereas PPh_3 in **A4** is not released in the cycloaddition of three acetylene molecules; and 2) Rh–C insertion has an energy barrier of 13.0 kcal mol^{-1} when acetylene is inserted and only 6.7 kcal mol^{-1} when C_{60} is inserted into **A6**. Subsequent steps are almost barrierless in the [2+2+2] cycloaddition of three acetylenes, whereas a barrier of 15.2 kcal mol^{-1} is found in the transformation of **A7** to **A8** (Scheme 3). We conclude that insertion of C_{60} and acetylene can compete and, therefore, to avoid benzene formation, which is somewhat easier, it would be advisable to work with an excess of C_{60}.

Finally, we have analyzed a possible attack on the [5,6] bond of C_{60} (see the Supporting Information). Again, paths A and B have been considered. The reaction pathway lowest in energy for attack on a [5,6] bond is kinetically and thermodynamically less favored than addition to a [6,6] bond. The product of [5,6] addition is 15.3 kcal mol^{-1} less stable in Gibbs energy than that of the [6,6] attack. From a kinetic point of view, for path A, the main difference corresponds to the insertion of C_{60} into the Rh–C bond. In [5,6] addition, the Gibbs energy barrier is 21.9 kcal mol^{-1}, whereas for [6,6] attack it is 15.2 kcal mol^{-1}. For path B, the energetic span in [5,6] attack is 29.7 kcal mol^{-1} and that of [6,6] attack is 26.1 kcal mol^{-1}. Our conclusion is that the major (or the only) product of [2+2+2] cycloaddition will be that generated in [6,6] attack, although the presence of traces of [5,6] addition cannot be completely ruled out.

Conclusion

We have shown that [2+2+2] cycloaddition of C_{60} and two acetylene molecules, to form a cyclohexadiene ring fused to a [6,6] bond of C_{60}, catalyzed by Wilkinson's complex is possible. The most likely reaction pathway involves oxidative addition of the two acetylene molecules followed by insertion of C_{60} into a Rh–C bond of the rhodacyclopentadiene intermediate formed. The reaction yield can be improved by using an excess of C_{60} to avoid side reactions, such as the formation of benzene. Moreover, the energy barriers could be entropically reduced by using diynes instead of acetylene molecules.[34] Capitalizing on all of this information, work is underway in our laboratories to develop a rhodium-catalyzed [2+2+2] cycloaddition involving fullerene. Results will be reported in due course.

Acknowledgements

Financial support from the Spanish Ministry of Economy and Competitivity (MINECO) and European Social Fund (ESF) (Project No. CTQ2014-54306-P, FPI fellowship to A.A., and RyC contract RYC2012-11112 to A.L.) and the DIUE of the Generalitat de Catalunya (Project No. 2014SGR931 and ICREA Academia 2014 to M.S.) are acknowledged. The EU, under the FEDER grant UNGI10-4E-801, has also funded this research.

Conflict of interest

The authors declare no conflict of interest.

Keywords: cycloaddition · density functional theory · fullerenes · reaction mechanisms · rhodium

[1] a) A. J. Heeger, *Adv. Mater.* **2014**, *26*, 10–28; b) D. Jariwala, V. K. Sangwan, L. J. Lauhon, T. J. Marks, M. C. Hersam, *Chem. Soc. Rev.* **2013**, *42*, 2824–2860; c) S. Günes, H. Neugebauer, N. S. Sariciftci, *Chem. Rev.* **2007**, *107*, 1324–1338.

[2] a) D. M. Guldi, B. M. Illescas, C. M. Atienza, M. Wielopolski, N. Martín, *Chem. Soc. Rev.* **2009**, *38*, 1587–1597; b) N. Martín, *Adv. Energy Mater.* **2017**, *2*, 1601102; c) K. Wojciechowski, T. Leijtens, S. Siprova, C. Schlueter, M. T. Hörantner, J. T.-W. Wang, C.-Z. Li, A. K. Y. Jen, T.-L. Lee, H. J. Snaith, *J. Phys. Chem. Lett.* **2015**, *6*, 2399–2405.

[3] J. L. Segura, N. Martin, D. M. Guldi, *Chem. Soc. Rev.* **2005**, *34*, 31–47.

[4] a) J. P. Martínez, M. Solà, A. A. Voityuk, *J. Comput. Chem.* **2016**, *37*, 1396–1405; b) J. P. Martínez, M. Solà, A. A. Voityuk, *Chem. Eur. J.* **2016**, *22*, 17305–17310.

[5] G. Sauvé, R. Fernando, *J. Phys. Chem. Lett.* **2015**, *6*, 3770–3780.

[6] a) A. Hirsch, *Angew. Chem. Int. Ed. Engl.* **1993**, *32*, 1138–1141; *Angew. Chem.* **1993**, *105*, 1189–1192; b) A. Hirsch, *The Chemistry of Fullerenes*, Thieme, Stuttgart, **1994**; c) A. Hirsch, M. Brettreich, *Fullerenes: Chemistry and Reactions*, Wiley-VCH, Weinheim, **2004**; d) N. Martín, *Chem. Commun.* **2006**, 2093–2104; e) S. Osuna, M. Swart, M. Solà, *Phys. Chem. Chem. Phys.* **2011**, *13*, 3585–3603.

[7] T. Ohno, N. Martín, B. Knight, F. Wudl, T. Suzuki, H. Yu, *J. Org. Chem.* **1996**, *61*, 1306–1309.

© 2017 Wiley-VCH Verlag GmbH & Co. KGaA, Weinheim

[8] G. C. Vougioukalakis, M. M. Roubelakis, M. Orfanopoulos, *Chem. Soc. Rev.* **2010**, *39*, 817 – 844.

[9] For selected reviews, see: a) S. Saito, Y. Yamamoto, *Chem. Rev.* **2000**, *100*, 2901 – 2916; b) Y. Yamamoto, *Curr. Org. Chem.* **2005**, *9*, 503 – 519; c) B. R. Galan, T. Rovis, *Angew. Chem. Int. Ed.* **2009**, *48*, 2830 – 2834; *Angew. Chem.* **2009**, *121*, 2870 – 2874; d) A. Pla-Quintana, A. Roglans, *Molecules* **2010**, *15*, 9230 – 9251; e) Y. Shibata, K. Tanaka, *Synthesis* **2012**, *44*, 323 – 350; f) D. L. J. Broere, E. Ruijter, *Synthesis* **2012**, *44*, 2639 – 2672; g) G. Dominguez, J. Perez-Castells, *Chem. Soc. Rev.* **2011**, *40*, 3430 – 3444; for a monograph, see: h) K. Tanaka, *Transition-Metal-Mediated Aromatic Ring Construction* (Ed. K. Tanaka), John Wiley & Sons, Hoboken, **2013**.

[10] N. E. Schore, *Chem. Rev.* **1988**, *88*, 1081 – 1119.

[11] For a review, see: a) A. Lledó, A. Pla-Quintana, A. Roglans, *Chem. Soc. Rev.* **2016**, *45*, 2010 – 2023 and references cited therein; for contributions from our group, see: b) E. Haraburda, M. Fernández, A. Gifreu, J. Garcia, T. Parella, A. Pla-Quintana, A. Roglans, *Adv. Synth. Catal.* **2017**, *359*, 506 – 512; c) E. Haraburda, A. Lledó, A. Roglans, A. Pla-Quintana, *Org. Lett.* **2015**, *17*, 2882 – 2885; d) E. Haraburda, O. Torres, T. Parella, M. Solà, A. Pla-Quintana, *Chem. Eur. J.* **2014**, *20*, 5034 – 5045.

[12] For a review, see: a) G. Domínguez, J. Pérez-Castells, *Chem. Eur. J.* **2016**, *22*, 6720 – 6739 and references cited therein; for selected examples, see: b) A. Dachs, A. Pla-Quintana, T. Parella, M. Solà, A. Roglans, *Chem. Eur. J.* **2011**, *17*, 14493 – 14507; c) A. Torrent, I. González, A. Pla-Quintana, A. Roglans, M. Moreno-Mañas, T. Parella, J. Bene *t*Buchholz, *J. Org. Chem.* **2005**, 70, 2033 – 2041; d) S. Brun, L. Garcia, I. González, A. Torrent, A. Dachs, A. Pla-Quintana, T. Parella, A. Roglans, *Chem. Commun.* **2008**, 4339 – 4341; e) J. A. Varela, S. G. Rubín, L. Castedo, C. Saá, *J. Org. Chem.* **2008**, *73*, 1320 – 1332; f) J. A. Varela, S. G. Rubín, C. González-Rodríguez, L. Castedo, C. Saá, *J. Am. Chem. Soc.* **2006**, *128*, 9262 – 9263; g) T. Shibata, H. Kurokawa, K. Kanda, *J. Org. Chem.* **2007**, *72*, 6521 – 6525; h) S. García-Rubín, J. A. Varela, L. Castedo, C. Saá, *Chem. Eur. J.* **2008**, *14*, 9772 – 9778; i) M. Fernández, M. Parera, T. Parella, A. Lledó, J. Le Bras, J. Muzart, A. Pla-Quintana, A. Roglans, *Adv. Synth. Catal.* **2016**, *358*, 1848 – 1853.

[13] H. Inoue, H. Yamaguchi, T. Suzuki, T. Akasaka, S. Murata, *Synlett* **2000**, *2000*, 1178 – 1180.

[14] T.-Y. Hsiao, K. C. Santhosh, K.-F. Liou, C.-H. Cheng, *J. Am. Chem. Soc.* **1998**, *120*, 12232 – 12236.

[15] a) M. Solá, J. Mestres, J. Martí, M. Duran, *Chem. Phys. Lett.* **1994**, *231*, 325 – 330; b) S. Osuna, J. Morera, M. Cases, K. Morokuma, M. Solà, *J. Phys. Chem. A* **2009**, *113*, 9721 – 9726; c) I. Fernández, M. Solà, F. M. Bickelhaupt, *Chem. Eur. J.* **2013**, *19*, 7416 – 7422.

[16] M. J. Frisch, G. W. Trucks, H. B. Schlegel, G. E. Scuseria, M. A. Robb, J. R. Cheeseman, G. Scalmani, V. Barone, B. Mennucci, G. A. Petersson, H. Nakatsuji, M. Caricato, X. Li, H. P. Hratchian, A. F. Izmaylov, J. Bloino, G. Zheng, J. L. Sonnenberg, M. Hada, M. Ehara, K. Toyota, R. Fukuda, J. Hasegawa, M. Ishida, T. Nakajima, Y. Honda, O. Kitao, H. Nakai, T. Vreven, J. A. Montgomery, Jr., J. E. Peralta, F. Ogliaro, M. Bearpark, J. J. Heyd, E. Brothers, K. N. Kudin, V. N. Staroverov, R. Kobayashi, J. Normand, K. Raghavachari, A. Rendell, J. C. Burant, S. S. Iyengar, J. Tomasi, M. Cossi, N. Rega, J. M. Millam, M. Klene, J. E. Knox, J. B. Cross, V. Bakken, C. Adamo, J. Jaramillo, R. Gomperts, R. E. Stratmann, O. Yazyev, A. J. Austin, R. Cammi, C. Pomelli, J. W. Ochterski, R. L. Martin, K. Morokuma, V. G. Zakrzewski, G. A. Voth, P. Salvador, J. J. Dannenberg, S. Dapprich, A. D. Daniels, Ö. Farkas, J. B. Foresman, J. V. Ortiz, J. Cioslowski, D. J. Fox in *Gaussian 09*, *Revision D.1*, Gaussian, Inc., Wallingford CT, **2009**.

[17] a) A. D. Becke, *J. Chem. Phys.* **1993**, *98*, 5648 – 5652; b) C. Lee, W. Yang, R. G. Parr, *Phys. Rev. B* **1988**, *37*, 785 – 789; c) P. J. Stephens, F. J. Devlin, C. F. Chabalowski, M. J. Frisch, *J. Phys. Chem.* **1994**, *98*, 11623 – 11627.

[18] a) T. H. Dunning Jr., *J. Chem. Phys.* **1989**, *90*, 1007 – 1023; b) D. E. Woon, T. H. Dunning, Jr., *J. Chem. Phys.* **1993**, *98*, 1358 – 1371.

[19] K. A. Peterson, D. Figgen, M. Dolg, H. Stoll, *J. Chem. Phys.* **2007**, *126*, 124101.

[20] P. Atkins, J. De Paula in *Physical Chemistry*, Oxford University Press, Oxford, **2006**.

[21] S. Grimme, J. Antony, S. Ehrlich, H. Krieg, *J. Chem. Phys.* **2010**, *132*, 154104.

[22] a) L. Orian, J. N. P. van Stralen, F. M. Bickelhaupt, *Organometallics* **2007**, *26*, 3816 – 3830; b) L. Orian, L. P. Wolters, F. M. Bickelhaupt, *Chem. Eur. J.* **2013**, *19*, 13337 – 13347; c) C.-H. Guo, H.-S. Wu, M. Hapke, H. Jiao, *J. Organomet. Chem.* **2013**, *748*, 29 – 35.

[23] A. V. Marenich, C. J. Cramer, D. G. Truhlar, *J. Phys. Chem. B* **2009**, *113*, 6378 – 6396.

[24] A. Dachs, S. Osuna, A. Roglans, M. Solà, *Organometallics* **2010**, *29*, 562 – 569.

[25] J. Goodman, V. V. Grushin, R. B. Larichev, S. A. Macgregor, W. J. Marshall, D. C. Roe, *J. Am. Chem. Soc.* **2010**, *132*, 12013 – 12026.

[26] a) J. M. Brown, A. G. Kent, *J. Chem. Soc. Perkin Trans. 2* **1987**, 1597 – 1607; b) N. Koga, S. Q. Jin, K. Morokuma, *J. Am. Chem. Soc.* **1988**, *110*, 3417 – 3425; c) L. A. van der Veen, M. D. K. Boele, F. R. Bregman, P. C. J. Kamer, P. W. N. M. van Leeuwen, K. Goubitz, J. Fraanje, H. Schenk, C. Bo, *J. Am. Chem. Soc.* **1998**, *120*, 11616 – 11626.

[27] a) A. Dachs, A. Roglans, M. Solà, *Organometallics* **2011**, *30*, 3151 – 3159; b) Ò. Torres, A. Roglans, A. Pla-Quintana, J. M. Luis, M. Solà, *J. Organomet. Chem.* **2014**, *768*, 15 – 22.

[28] a) S. Kozuch, S. Shaik, *J. Phys. Chem. A* **2008**, *112*, 6032 – 6041; b) S. Kozuch, S. Shaik, *Acc. Chem. Res.* **2010**, *43*, 101 – 110.

[29] a) K. Kirchner, M. J. Calhorda, R. Schmid, L. F. Veiros, *J. Am. Chem. Soc.* **2003**, *125*, 11721 – 11729; b) J. H. Hardesty, J. B. Koerner, T. A. Albright, G.-Y. Lee, *J. Am. Chem. Soc.* **1999**, *121*, 6055 – 6067; c) A. Dachs, A. Torrent, A. Roglans, T. Parella, S. Osuna, M. Solà, *Chem. Eur. J.* **2009**, *15*, 5289 – 5300.

[30] A. A. Dahy, N. Koga, *Organometallics* **2015**, *34*, 4965 – 4974.

[31] P. I. Dosa, G. D. Whitener, K. P. C. Vollhardt, A. D. Bond, S. J. Teat, *Org. Lett.* **2002**, *4*, 2075 – 2078.

[32] G. Dazinger, M. Torres-Rodrigues, K. Kirchner, M. J. Calhorda, P. J. Costa, *J. Organomet. Chem.* **2006**, *691*, 4434 – 4445.

[33] a) H. Zhou, J. Liu, S. Du, L. Zhang, G. Li, Y. Zhang, B. Z. Tang, H.-J. Gao, *J. Am. Chem. Soc.* **2014**, *136*, 5567 – 5570; b) A. Dachs, A. Torrent, A. Pla-Quintana, A. Roglans, A. Jutand, *Organometallics* **2009**, *28*, 6036 – 6043.

[34] Y. Yamamoto, T. Arakawa, R. Ogawa, K. Itoh, *J. Am. Chem. Soc.* **2003**, *125*, 12143 – 12160.

Manuscript received: May 31, 2017

Accepted manuscript online: July 20, 2017

Version of record online: August 30, 2017

Chapter 4. Expeditious preparation of open-cage fullerenes by rhodium(I)-catalyzed [2+2+2] cycloaddition of diynes and C_{60}: an experimental and theoretical study

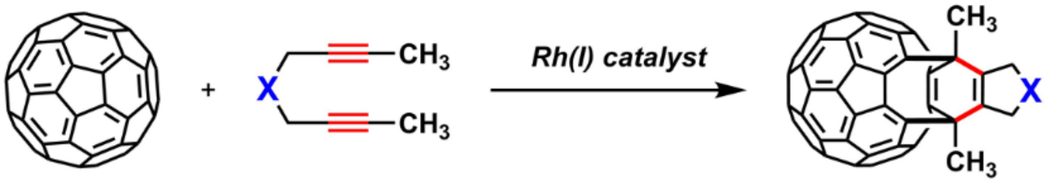

■ *Catalytic conditions* ■ *Direct access to bis(fulleroids)* ■ *Yields up to 60%*
■ *Further functionalization* ■ *Mechanism elucidation* ■ *Rh(I)-catalyzed ring opening*

Published in: *Chem. Eur. J.* **2018**, *24*, 10653.

Abstract: A novel methodology to transform C_{60} into a variety of open-cage fullerene derivatives by employing rhodium(I) catalysis has been developed. This transformation encompasses a partially intermolecular [2+2+2] cycloaddition reaction between diynes **1** and C_{60} to deliver a cyclohexadiene-fused fullerene, which concomitantly undergoes a formal [4+4]/retro-[2+2+2] rearrangement to deliver open-cage fullerenes 2. Most notably, this process occurs without the need of photoexcitation. The complete mechanism of this transformation has been rationalized by DFT calculations, which indicate that, after [2+2+2] cycloaddition, the cyclohexadiene-fused intermediate evolves into the final product through a Rh-catalyzed di-π-methane rearrangement followed by a retro-[2+2+2] cycloaddition. The obtained open-cage fullerenes can be derivatized by Suzuki-Miyaura cross-coupling or subjected to ring expansion to deliver a 12-membered ring orifice in the fullerene structure. Overall, the methodology presented constitutes a straightforward entry to functional open-cage C_{60} fullerene derivatives by employing catalytic methods.

Reproduced with permission from:

Artigas, A.; Pla-Quintana, A.; Lledó, A.; Roglans, A.; Solà, M. Expeditious Preparation of Open-Cage Fullerenes by Rhodium(I)-Catalyzed [2+2+2] Cycloaddition of Diynes and C_{60}: An Experimental and Theoretical Study. *Chem. Eur. J.* **2018**, *24*, 10653. © Wiley-VCH Verlag GmbH & Co. KGaA, Weinheim.

ChemPubSoc
Europe

DOI: 10.1002/chem.201802298

CHEMISTRY
A European Journal
Full Paper

Check for updates

Open-Cage Fullerenes | *Hot Paper* |

Expeditious Preparation of Open-Cage Fullerenes by Rhodium(I)-Catalyzed [2+2+2] Cycloaddition of Diynes and C_{60}: An Experimental and Theoretical Study

Albert Artigas, Anna Pla-Quintana, Agustí Lledó,* Anna Roglans,* and Miquel Solà*[a]

Abstract: A novel methodology to transform C_{60} into a variety of open-cage fullerene derivatives by employing rhodium(I) catalysis has been developed. This transformation encompasses a partially intermolecular [2+2+2] cycloaddition reaction between diynes **1** and C_{60} to deliver a cyclohexadiene-fused fullerene, which concomitantly undergoes a formal [4+4]/retro-[2+2+2] rearrangement to deliver open-cage fullerenes **2**. Most notably, this process occurs without the need of photoexcitation. The complete mechanism of this transformation has been rationalized by DFT calculations, which indicate that, after [2+2+2] cycloaddition, the cyclohexadiene-fused intermediate evolves into the final product through a Rh-catalyzed di-π-methane rearrangement followed by a retro-[2+2+2] cycloaddition. The obtained open-cage fullerenes can be derivatized by Suzuki–Miyaura cross-coupling or subjected to ring expansion to deliver a 12-membered ring orifice in the fullerene structure. Overall, the methodology presented constitutes a straightforward entry to functional open-cage C_{60} fullerene derivatives by employing catalytic methods.

Introduction

Functionalized C_{60} fullerenes, in which the properties of C_{60} can be combined with those of other classes of materials, are an important type of scaffolds with relevant applications in several fields, such as material science, nanotechnology, and medicinal chemistry among others.[1] In particular, carbocyclic fullerene adducts with fused-ring systems have been studied in the field of organic photovoltaic solar cells.[2] Open-cage fullerenes, which result from selective cleavage of one or more fullerene carbon–carbon bond, are particularly interesting structures as they can act as host molecules, encapsulating guests within their cavity, thereby forming endohedral complexes with emerging properties and particular reactivity.[3] From the practical point of view, open-cage derivatives of C_{60} have proven useful as electron accepting materials in organic solar cells[4] and as ligands for the synthesis of metal complexes.[5] The photoinduced ring-opening reaction of cyclohexadiene-fused C_{60} derivatives by tandem [4+4]/retro-[2+2+2] rearrangement is one of the most well-established synthetic entries to open-cage fullerenes.[6] For all these reasons, the development of efficient synthetic routes to fullerene derivatives is still an appealing goal in organic synthesis. On the other hand, transition-metal-catalyzed [2+2+2] cycloaddition reactions appear as the method of choice for the synthesis of six-membered rings and enable the construction of cyclohexadiene scaffolds when the reaction takes place between two alkynes and one alkene.[7] Given that the chemical reactivity of C_{60} is typical of an electron-deficient olefin, it acts as a valuable candidate as a co-substrate in [2+2+2] cycloadditions with alkynes.[7a] Furthermore, cycloaddition reactions with empty fullerenes show a remarkable preference for the [6,6] ring junction over [5,6] bonds.[1c,8]

To the best of our knowledge, only two previous studies have reported transition-metal-promoted [2+2+2] cycloaddition reactions of two alkynes with C_{60} by using stoichiometric amounts of the transition metal species (Scheme 1). The first, published in 1998 by Cheng et al.,[9] described the cycloaddition of terminal diynes with C_{60} by using excess amounts of a nickel precursor to avoid the gradual decomposition of the complex. In this study, the corresponding cyclohexadiene-fused derivatives were isolated and characterized. After irradiation with a 350 nm UV lamp, these compounds rearranged into the corresponding bis(fulleroids) (i.e., compounds in which two C–C bonds of the original C_{60} cage have been broken). The authors found that these fulleroids were thermally and photochemically more stable than their cyclohexadiene counterparts. The second, by Murata et al. in 2000,[10] described the reaction of fullerene with a palladacyclopentadiene—previously prepared by oxidative coupling of two molecules of a dialkyl acetylenedicarboxylate with Pd^0—affording the corresponding cyclohexadiene-type adducts. In an early study by Cheng et al.,[11] a metal-free cyclotrimerization of ethyl propiolate with fullerene promoted by PCy_3 was described

---

[a] A. Artigas, Dr. A. Pla-Quintana, Dr. A. Lledó, Prof. Dr. A. Roglans, Prof. Dr. M. Solà
Institut de Química Computacional i Catàlisi (IQCC)
Departament de Química, Universitat de Girona
C/ Maria Aurèlia Capmany, 69, 17003, Girona, Catalonia (Spain)
E-mail: agusti.lledo@udg.edu
anna.roglans@udg.edu
miquel.sola@udg.edu

Supporting information and the ORCID number(s) for the author(s) of this article can be found under https://doi.org/10.1002/chem.201802298.

© 2018 Wiley-VCH Verlag GmbH & Co. KGaA, Weinheim

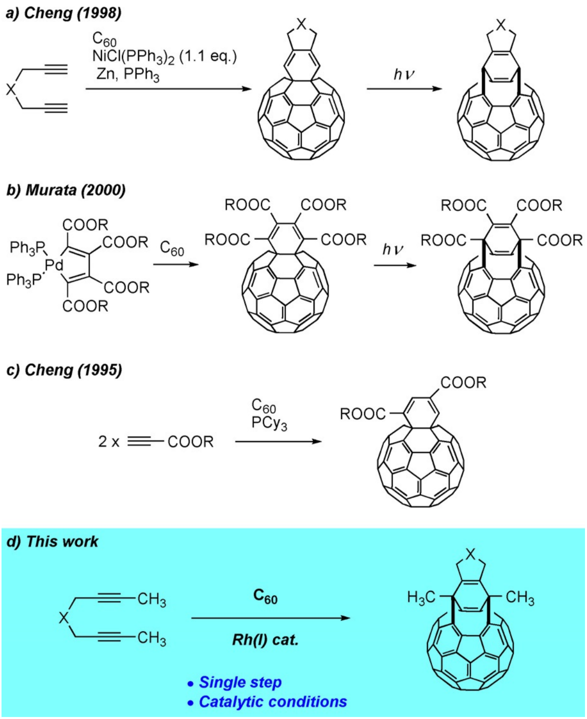
a) Cheng (1998)
C60
NiCl(PPh3)2 (1.1 eq.)
Zn, PPh3
hν
X
b) Murata (2000)
Ph3P
Pd
Ph3P
COOR
C60
ROOC
hν
c) Cheng (1995)
2 x ≡—COOR
C60
PCy3
d) This work
CH3
C60
Rh(I) cat.
H3C
• Single step
• Catalytic conditions

Scheme 1. Approaches to cyclohexadiene-fused and open-cage fullerene derivatives.

(Scheme 1). However, this transformation operates on a different reaction manifold, which is limited to Michael acceptors. Based on our previous experience in Rh-catalyzed [2+2+2] cycloaddition reactions between alkynes and both alkenes and allenes,[12,7] we envisaged the development of a catalytic version of the [2+2+2] cycloaddition reaction between diynes and fullerene. Subsequent [4+4] photocycloaddition and retro-[2+2+2] reaction of the cyclohexadiene derivatives would provide, overall, a versatile and efficient entry to open-cage fullerenes. Based on our previous theoretical DFT study that showed the viability of a rhodium-catalyzed [2+2+2] cycloaddition reaction of two alkynes and C_{60},[13] we present here a successful implementation of this methodology, which affords open-cage fullerenes in a single reaction step.

Abstract in Catalan: *En el present estudi es descriu un nou mètode que permet la transformació del ful·lerè C_{60} en derivats de tipus* open-cage, *fent servir un complex de rodi(I) com a catalitzador. El procés transcorre a través d'una reacció de cicloaddició [2+2+2] entre els diïns* **1** *i el C_{60}, donant lloc a un conjunt de derivats C_{60}-ciclohexadiè que experimenten formalment una transposició de tipus [4+4]/retro-[2+2+2] que finalment resulta en els derivats open-cage* **2**. *Cal destacar que la reacció té lloc en absència de fotoexcitació. El mecanisme complet d'aquest procés s'ha racionalitzat mitjançant càlculs DFT, els quals indiquen que, després de la reacció de cicloaddició [2+2+2], els derivats C_{60}-ciclohexadiè evolucionen fins el producte final a través d'un mecanisme de transposició di-π-metà seguit de cicloaddició retro-[2+2+2]. Els productes obtinguts s'han funcionalitzat emprant reaccions d'acoblament creuat de Suzuki-Miyaura. Finalment, s'ha pogut preparar mitjançant reaccions de foto-oxidació un derivat de C_{60} que conté un orifici de 12 membres en la seva estructura. Així doncs, la metodologia presentada proporciona una accés directe a derivats open-cage de C_{60} fent servir mètodes catalítics.*

Results and Discussion

At the onset, a variety of reaction conditions for the model cycloaddition between fullerene C_{60} and non-terminal *N*-tosyl tethered diyne **1a** were explored (Table 1). Eventually, we

Table 1. Rhodium(I)-catalyzed cycloaddition of C_{60} with diyne **1a**: effect of reaction parameters.

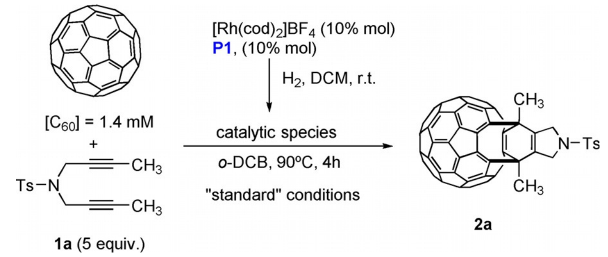
[C60] = 1.4 mM
+
Ts−N
CH3
1a (5 equiv.)
[Rh(cod)2]BF4 (10% mol)
P1, (10% mol)
H2, DCM, r.t.
catalytic species
o-DCB, 90ºC, 4h
"standard" conditions
N−Ts
2a

Entry	Deviation from standard conditions	Yield of **2a**[a]
1	$[RhCl(PPh_3)_3]$, $[C_{60}] = 7$ mM, 1 equiv **1a**, 16 h	0
2	1 equiv $[RhCl(PPh_3)_3]$, $[C_{60}] = 7$ mM, 1 equiv **1a**, 16 h	0
3	**P2** instead of **P1**, $[C_{60}] = 7$ mM, 1 equiv **1a**	20
4	**P2** instead of **P1**, $[C_{60}] = 7$ mM, 1 equiv **1a**, 16 h	20
5	No phosphine, $[C_{60}] = 7$ mM, 1 equiv **1a**, 16 h	0
6	No Rh, **P2** instead of **P1**, $[C_{60}] = 7$ mM, 1 equiv **1a**, 16 h	0
7	**P2** instead of **P1**, $[C_{60}] = 7$ mM, 1 equiv **1a**, 120 °C	20
8	**P2** instead of **P1**, $[C_{60}] = 7$ mM, 1 equiv **1a**, 80 °C MW heating, 40 min	10
9	**P2** instead of **P1**, $[C_{60}] = 7$ mM, slow addition of **1a** (1 equiv) over 4 h	20
10	**P3** instead of **P1**, $[C_{60}] = 7$ mM, 1 equiv **1a**	20
11	**P4** instead of **P1**, $[C_{60}] = 7$ mM, 1 equiv **1a**	traces
12	**P5** instead of **P1**, $[C_{60}] = 7$ mM, 1 equiv **1a**	20
13	**P6** instead of **P1**, $[C_{60}] = 7$ mM, 1 equiv **1a**	10
14	**P7** instead of **P1**, $[C_{60}] = 7$ mM, 1 equiv **1a**	traces
15	**P8** instead of **P1**, $[C_{60}] = 7$ mM, 1 equiv **1a**	traces
16	$[C_{60}] = 7$ mM, 1 equiv **1a**	28
17	1 equiv **1a**	36
18	$[C_{60}] = 7$ mM	43
19	**None**	**52**[b]

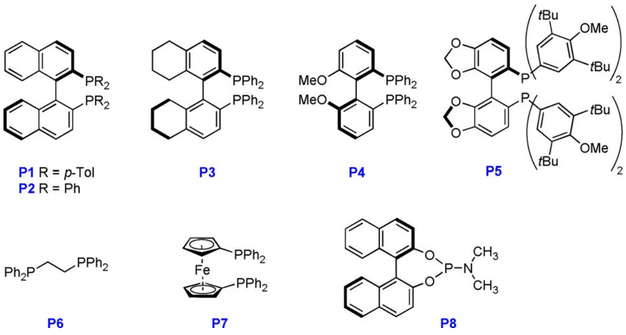
PR2
PR2
P1 R = p-Tol
P2 R = Ph
PPh2
PPh2
P3
MeO
MeO
PPh2
PPh2
P4
P
P
tBu
OMe
tBu
2
P5
Ph2P
PPh2
P6
PPh2
Fe
PPh2
P7
O
P−N
CH3
CH3
P8

[a] Isolated yield. [b] The yield based on consumed C_{60} was 98 %.

found that 10 % mol of a mixture of a cationic rhodium complex with Tol-BINAP (**P1**) as a diphosphine in *o*-dichlorobenzene at 90 °C for 4 h afforded 52 % isolated yield of a dark-brown solid. The mixture of $[Rh(cod)_2]BF_4$ (cod = cyclooctadiene) and Tol-BINAP was treated with hydrogen in dichloromethane solution for catalyst activation prior to substrate addition. The molecular formula of the new compound was determined by HRMS to be $C_{75}H_{17}NO_2S$, indicating that the cycloaddition had taken place. 1D and 2D NMR spectroscopic experiments were used to ascertain the structure of the product formed. Both the ^1H and ^{13}C NMR spectra show that the new compound has C_s rather than C_{2v} symmetry, the latter resulting from a cycloaddition reaction at the [6,6] bond. A careful analysis of the NMR data revealed an unanticipated but desirable outcome: the compound formed was not the expected cycloadduct, but rather the corresponding open-cage bis(fulleroid) structure (Figure 1). The ^1H NMR exhibits a singlet at $\delta =$ 2.79 ppm, corresponding to the two methyl groups originating from the starting diyne, and, importantly, two multiplets centered at 4.46 ppm and 4.59 ppm. The latter correspond to two pairs of diastereotopic protons, H3 and H3′, respectively, a key feature to identification of the symmetry point group. The ^{13}C NMR showed 35 signals in the sp^2 carbon region (30 from the fullerene core, partially overlapped, four from the tosyl group, and one from the fused double bond) and four signals in the sp^3 carbon region at $\delta = 21.8$, 27.7, 43.4, and 55.0 ppm. An HMBC experiment was conducted to confirm the open-cage structure. The 2D spectrum displays a two-bond correlation between the protons of the methyl group and the $C(sp^3)$ at 43.4 ppm and a three-bond correlation between the same protons and three $C(sp^2)$ quaternary carbon atoms (134.9, 137.4, and 150.2 ppm), proving the accuracy of our earlier observation. The assignment of the most characteristic signals in the ^1H and ^{13}C NMR spectra is shown in Figure 1.

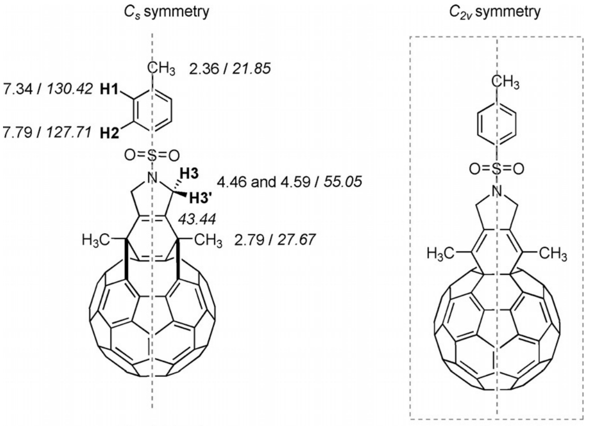

2a, obtained

not isolated

Figure 1. Selected ^1H and ^{13}C (in italics) NMR chemical shifts of **2a**.

Having established a straightforward entry to open-cage fullerenes based on a cascade process triggered by the Rh-catalyzed [2+2+2] cycloaddition and followed by fullerene-cage opening, we next examined the effect that altering various reaction parameters had on the efficiency of the process (Table 1). The Wilkinson catalyst—$[RhCl(PPh_3)_3]$, a neutral rhodium complex—did not promote the reaction even when stoichiometric amounts of catalyst were used (entries 1 and 2, Table 1). We then moved to a combination of a cationic rhodium complex $[Rh(cod)_2]BF_4$ with several phosphines as ligands. BINAP (**P2**) was initially used as a benchmark ligand. When the reaction mixture was heated at 90 °C for 4 h, 20 % yield of cycloadduct **2a** was obtained (entry 3, Table 1). Extending the reaction time to 16 h did not result in any significant improvement (entry 4, Table 1). Two control experiments were then run, one in the absence of BINAP (entry 5, Table 1) and the other in the absence of Rh complex (entry 6, Table 1), which revealed the essential role of the two components in this transformation. Increasing the reaction temperature to 120 °C (entry 7, Table 1) or using microwave heating at 80 °C for 40 min (entry 8, Table 1) did not improve the results. We reasoned that homocoupling reactions of **1a** might effectively compete with the desired cycloaddition pathway, and we ran a reaction slowly adding **1a** to a mixture of fullerene and the catalytic system at 90 °C. However, again only a 20 % yield of **2a** was obtained (entry 9, Table 1). We then turned our attention to other bidentate phosphines: H_8-BINAP (**P3**, entry 10, Table 1), BIPHEP (**P4**, entry 11, Table 1), DTBM-SEGPHOS (**P5**, entry 12, Table 1), DPPE (**P6**, entry 13, Table 1), DPPF (**P7**, entry 14, Table 1), and Tol-BINAP (**P1**, entry 16, Table 1). Among these, **P1** gave the best results. Finally, MonoPhos (**P8**)—a monodentate phosphoramidite—was also tested, but only traces of **2a** were obtained (entry 15, Table 1). At this point and with the optimal ligand of choice, Tol-BINAP, we proceeded to evaluate the effect of fullerene concentration and diyne excess. We found that both the reduction of fullerene concentration (entry 17, Table 1) and the use of diyne **1a** in excess with respect to fullerene (entry 18, Table 1) improved the yield of the reaction (from 28 % to 36 % and 43 %, respectively). An additive effect was observed when the two factors were combined ($[C_{60}] = 1.4$ mM and 5 equiv of **1a**), resulting in our optimized set of conditions (entry 19, Table 1).

Having established the optimum reaction conditions, the scope of the reaction was then evaluated, as shown in Figure 2. In a first step, the nature of the substituents of the phenyl ring at the sulfonamide tether in diyne **1** was evaluated. The corresponding cycloadducts **2b**–**e** were obtained in excellent yields in all cases, including bromo- and iodobenzene derivatives (**2c**,**d**), which have the potential for further functionalization (see below). A diyne bearing the 5-methyl-2-pyridinesulfonyl group provided **2f** in 52 % isolated yield, indicating that the presence of a potentially coordinating nitrogen atom did not poison or interfere with the catalyst. A sulfonamide tether with aliphatic substitution (trimethylsilylethane) was also efficient, delivering the fulleroadduct **2g** in 35 % isolated yield. Other diynes with diethyl malonate, methylene, and oxygen tethers were also tested. However, only the malonate provided good yields of cycloadduct **2h**, whereas the other two did not furnish any product at all (**2i** and **2j**). Several terminal diynes and others with different substitution at the two termini were then evaluated. The results indicate that

© 2018 Wiley-VCH Verlag GmbH & Co. KGaA, Weinheim

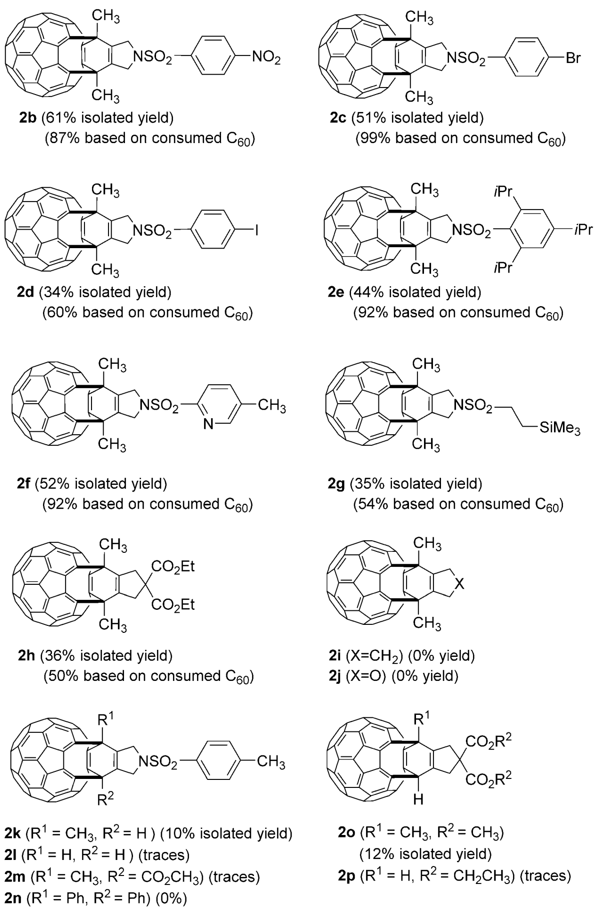

2b (61% isolated yield) (87% based on consumed C_{60})

2c (51% isolated yield) (99% based on consumed C_{60})

2d (34% isolated yield) (60% based on consumed C_{60})

2e (44% isolated yield) (92% based on consumed C_{60})

2f (52% isolated yield) (92% based on consumed C_{60})

2g (35% isolated yield) (54% based on consumed C_{60})

2h (36% isolated yield) (50% based on consumed C_{60})

2i (X=CH_2) (0% yield)
2j (X=O) (0% yield)

2k (R^1 = CH_3, R^2 = H) (10% isolated yield)
2l (R^1 = H, R^2 = H) (traces)
2m (R^1 = CH_3, R^2 = CO_2CH_3) (traces)
2n (R^1 = Ph, R^2 = Ph) (0%)

2o (R^1 = CH_3, R^2 = CH_3) (12% isolated yield)
2p (R^1 = H, R^2 = CH_2CH_3) (traces)

Figure 2. Scope of the [2+2+2] cycloaddition of C_{60} with diynes **1**. Reaction conditions: 0.07 mmol of fullerene, 5 equivalents of diyne **1**, 10% mol of Rh catalyst in 50 mL of *o*-dichlorobenzene (*o*-DCB) at 90 °C for 4 h. The 10% mol mixture of $[Rh(cod)_2]BF_4$ and Tol-BINAP was treated with hydrogen in dichloromethane solution for catalyst activation prior to substrate addition.

alkyne substitution has a dramatic effect on the reaction outcome: only the substrates with at least one internal alkyne gave the corresponding cycloadduct (**2k** and **2o**), albeit in low yields. In the cases of the cycloaddition of diynes **2k**–**p**, homocoupling of the diyne competes with the cross-coupling with fullerene, especially in the cases where the diynes have terminal alkynes, such as **2k**, **2l**, **2o**, and **2p**.

Further functionalization of cycloadducts 2

The halogen atom in derivatives **2c** and **2d** opens the door to further functionalizing the fulleroid adducts. Therefore, iodo derivative **2d** was submitted to a Suzuki–Miyaura cross-coupling reaction with *p*-methoxyphenyl boronic acid. After some experimentation, we found that a 10% mol loading of $[Pd(PPh_3)_4]$ in a mixture of *o*-dichlorobenzene/water 9:1 at 100 °C in the presence of cesium carbonate as a base provided the best reaction conditions (Scheme 2). Biphenyl derivative **4a** was obtained with a 63% yield.

Fullerenes and fulleroids can act as mild electron acceptors, forming charge-transfer dyads with electron-releasing moieties, such as ferrocene.[14] Moreover, fullerenes appended with photoactive moieties, for example, pyrene,[15] can operate as light-harvesting antennas through intramolecular energy transfer processes. All these fullerene derivatives constitute promising scaffolds for photovoltaic materials. In this scenario, our Suzuki–Miyaura cross-coupling derivatization appears as an ideal method to append such electron-donor or photoactive moieties to fulleroid derivatives. By using the same reaction conditions as for *p*-methoxyphenylboronic acid, 1-pyrenylboronic acid was coupled with cycloadduct **2d** under palladium catalysis to afford derivative **4b** in excellent yield. However, in the case of ferrocene boronic acid, competitive dehalogenation took place, delivering **4c** in a modest 14% yield (Scheme 2).

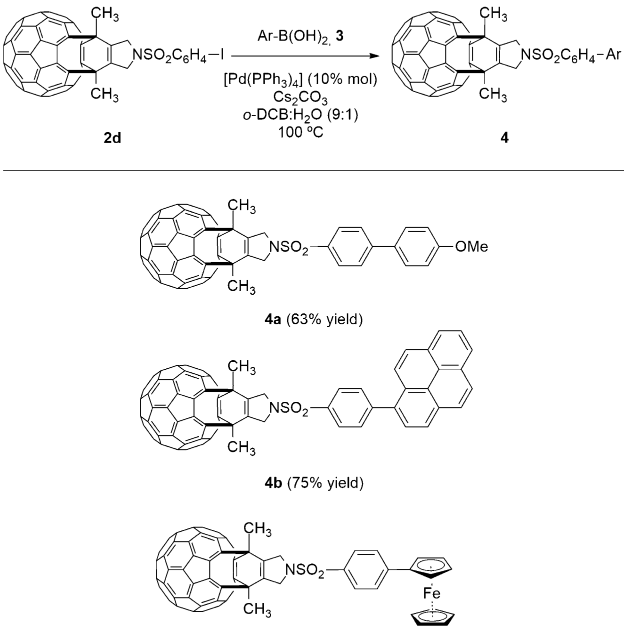

4a (63% yield)

4b (75% yield)

4c (14% yield)

Scheme 2. Suzuki–Miyaura cross-coupling reaction between iodo-fulleroid derivative **2d** with several boronic acids **3a**–**c**. Reaction conditions: 0.054 mmol of **2d**, 2 equivalents of boronic acid **3**, 2.5 equivalents of Cs_2CO_3, 10% mol of $Pd(PPh_3)_4$ in 10 mL of a mixture of *o*-dichlorobenzene:water (9:1) at 100 °C for 4 h.

Oxidative cleavage of fulleroid derivative 2a

As previously described for other open-cage fullerene derivatives,[16] one of the double bonds in the eight-membered ring orifice in **2a** can undergo oxidative cleavage through a photooxygenation process that affords an open-cage fullerene with a 12-membered ring-opening containing two carbonyl carbon atoms, **5**. Upon exposure of a $CDCl_3$ solution of **2a** in an NMR tube to sunlight and air for 5 h, only compound **5** was observed by NMR and HRMS analyses (Scheme 3). The molecular formula of **5** was determined to be $C_{75}H_{17}NO_4S$ by HRMS, indicating the addition of O_2 to **2a**. The color of a solution of compound **5** in chloroform is brown-yellow and the UV/Vis spectrum showed maximum absorptions at 254 and 322 nm, whereas the starting compound **2a** is purple in chloroform solution, displaying maxima at 262, 326, and 520 nm. The two

© 2018 Wiley-VCH Verlag GmbH & Co. KGaA, Weinheim

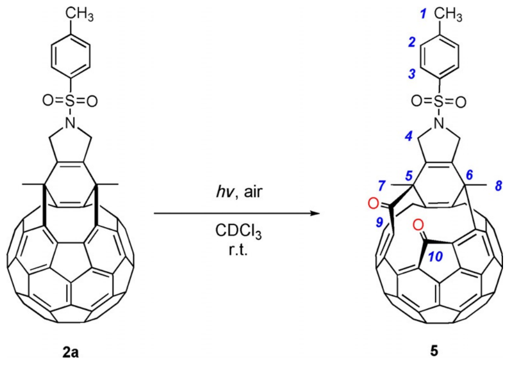

Scheme 3. Oxidative cleavage of bis(fulleroid) derivative **2a**. Arbitrary numbering shown in blue.

UV/Vis spectra were similar, but the lack of absorption at 520 nm in **5** indicates the cleavage of one of the aromatic double bonds of the C_{60} and its replacement by two carbonyl groups, disrupting the π-conjugated system of the C_{60} core. NMR analysis revealed the loss of molecular symmetry in the process. The ^{1}H NMR exhibited two different methyl groups at $\delta = 2.21$ ppm (C7) and 2.57 ppm (C8), and the ^{13}C NMR displayed two signals corresponding to two different carbonyl groups at 191.5 ppm (C10) and 201.5 ppm (C9). In addition, the two quaternary sp^3 carbons, C6 and C5, appeared at 42.7 and 51.7 ppm, respectively. Furthermore, two bands at 1682 cm^{-1} and 1734 cm^{-1}, corresponding to the carbonyl groups, can be observed in the IR spectrum.

Electrochemical behavior of fulleroid derivatives 4b, 4c, and 5

The electrochemical behavior of compounds **4b**, **4c**, and **5** was studied by cyclic voltammetry to complete their characterization, and to ascertain the effect of the structural modifications introducing electron-accepting properties of the resulting fulleroadducts with respect to C_{60} (Table 2).

All the compounds studied showed two fully reversible reduction waves under the experimental settings employed, corresponding to sequential one-electron reductions of the fullerenic core. As expected, the partial disruption of conjugation in bis(fulleroids) **2a**, **4b**, and **4c** results in a cathodic shift with respect to C_{60}. The obtained potentials compare favorably with structurally analogous bis(fulleroids).[4a] Moreover, the introduction of electro- or photoactive moieties as in **4b**/**c** does not significantly alter the overall redox properties (compare entries 2–4 in Table 2), indicating that our synthetic scheme is a reliable entry into such fullerene dyads. Conversely, dicarbonyl derivative **5** is more easily reduced than C_{60}, and displays a redox behavior akin to that of previously obtained open-cage fullerenes with homologous π structures.[4a]

Table 2. Redox potentials of fulleroids **2a**, **4b**, **4c**, **5**, and C_{60}.[a]

Entry	Compound	E^1_{red}	E^2_{red}	E^3_{red}
1	C_{60}	−1.109	−1.514	−2.009
2	**2a**	−1.213	−1.626	
3	**4b**	−1.228	−1.633	
4	**4c**	−1.211	−1.594	
5	**5**	−0.987	−1.370	

[a] $E_{1/2}$ in V vs. ferrocene/ferrocenium (Fc/Fc^+), 0.2 mM C_{60}/**2a**/**4b**,**c**/**5** and 0.1 M $Bu_4N^+ClO_4^-$ in o-dichlorobenzene, saturated calomel reference electrode, Pt working electrode, Pt wire auxiliary electrode, scan rate 50 $mV\,s^{-1}$, 25 °C.

Computational study of the reaction mechanism

We completed our study by evaluating computationally the reaction mechanism that transforms **1a** into **2a**, in a process catalyzed by Rh(Tol-BINAP)$^+$ (**P1** = Tol-BINAP in Table 1). The calculated Gibbs reaction profile at the M06-D3/cc-pVTZ-PP//B3LYP-D3/cc-pVDZ-PP level of theory (see Computational Methods for a detailed description) of the determined reaction mechanism is depicted in Figure 3. To reduce the computational effort required, the tosyl group present in the experimental diyne was substituted by a mesyl group. Moreover, the tolyl groups of the catalyst were substituted by methyl groups, as it is generally accepted that PMe_3 is a better model of PPh_3 than PH_3.[17] Finally, the naphthalene moieties were modeled by benzene units (ligand **P9**, see inset of Figure 2). Because it is likely that the reduction considered in our models does not affect critically their chemical behavior, we are confident that the conclusions reached with our model systems should be still valid for the real systems.

The steps of the first part of the reaction (from **A0** to **A5**) correspond to the classic [2+2+2] reaction mechanism. The reaction starts with the coordination of the two triple bonds of diyne of **1a** with Rh(**P9**)$^+$ to form the 16-electron **A1** intermediate and release 15.9 kcal mol^{-1}. Then, oxidative coupling takes place through **TS A1A2** with a Gibbs energy barrier of 25.7 kcal mol^{-1} to form rhodacyclopentadiene intermediate **A2** in an exergonic process (by 5.1 kcal mol^{-1}). The large difference between the double C=C (1.345 Å) and single C–C (1.481 Å) bond lengths in intermediate **A2** indicates localization of the π-electron density and lack of aromaticity.[18] For this transformation (**A1** to **A2**), which is the rate-determining step in the catalytic cycle, we have explored the influence of using a more realistic model of our catalyst (see Figure S5 in the Supporting Information). In particular, we have substituted the methyl groups of our Rh(**P9**)$^+$ model, shown in Figure 3, with phenyl groups. The changes in the Gibbs energy barrier and Gibbs reaction energies for this oxidative coupling process, when going from the Rh(**P9**)$^+$ model to the more realistic model, are less than 2 kcal mol^{-1}. This is an indication that our model catalyst is appropriate for the present study.

Coordination of **A2** to a [6,6] bond of C_{60} to yield **A3** is an endergonic process that requires 10.0 kcal mol^{-1}. In **A3**, C_{60} is coordinated to Rh by occupying an axial position of the distorted trigonal bipyramid. The insertion of C_{60} into the Rh–C(sp^2) bond results in the formation of the rhodabicyclo[3.2.0]-heptadiene intermediate **A4** in a step that has a Gibbs barrier of 5.9 kcal mol^{-1} and releases 1.8 kcal mol^{-1}. The next step corresponds to the formation of intermediate **A5**, which is formed by a reductive elimination process that has to overcome a very

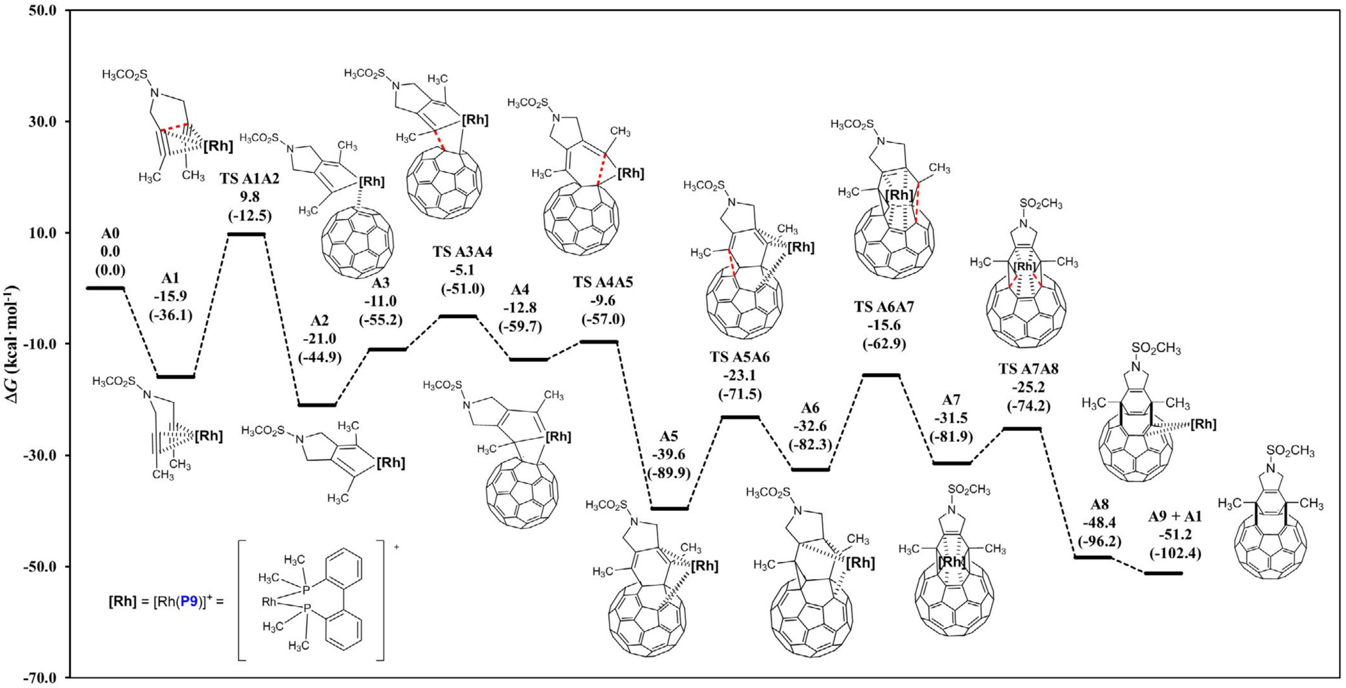

Figure 3. M06-D3/cc-pVTZ-PP//B3LYP-D3/cc-pVDZ-PP Gibbs energy profile of the [2+2+2] cycloaddition reaction of C_{60} and a model of non-terminal tethered diyne **1a** to yield the cyclohexadiene-fused C_{60} derivative **A5** followed by fullerene cage opening to form **A9**. Energies in parenthesis are electronic energies. All relative energies in kcal mol^{-1} are given relative to **A0** (C_{60} + catalyst + **1a**).

low Gibbs energy barrier of 3.2 kcal mol^{-1} and is exergonic by 26.8 kcal mol^{-1}. In **A5**, Rh is coordinated to both the cyclohexadiene and C_{60} moieties. We also explored the formation of **A5** through rhodacycloheptadiene intermediate **A5′** (Figure S1 in the Supporting Information) followed by reductive elimination through **TS A5′A5**. This transformation has to surmount a Gibbs energy barrier of 21.2 kcal mol^{-1} and it is slightly exergonic by 2.7 kcal mol^{-1}, and, consequently, this alternative route through intermediate **A5′** is not competitive and was ruled out. Finally, we also analyzed the possible formation of a rhodanorbornene complex through a rhodium-mediated [4+2] cycloaddition, but all our attempts to find this intermediate failed. It is worth noting that with the Wilkinson catalyst, the same reaction mechanism was found, except for the insertion step, which leads in this case to a rhodacycloheptadiene intermediate analogous to **A5′** (Schore's mechanism)[19] without formation of a rhodabicyclo[3.2.0]heptadiene intermediate **A4**.[13]

In summary, the [2+2+2] cycloaddition that produces **A5** from **A0** has an energetic span[20] between the turnover frequency (TOF) determining intermediate (TDI, **A1**) and TOF determining transition state (TDTS, **TS A1A2**) of 25.7 kcal mol^{-1}. This is in accordance with most [2+2+2] cycloadditions in which the rate-determining step (rds) is the oxidative coupling.

We also analyzed another reaction path that transforms **A0** into **A4**. In this alternative pathway (Figure S2 in the Supporting Information), the oxidative coupling occurs between one alkyne group of **1a** and C_{60} to form a rhodacyclopentene intermediate. Then, the insertion of the second alkyne takes place into a Rh–C(sp^2) bond to form rhodabicyclo[3.2.0]heptadiene **A4**. This alternative pathway has an energetic span between the TDI (**A5**) and TDTS (**TS B1B2**) of 36.5 kcal mol^{-1} and, therefore, has been discarded as a possible reaction pathway.

Release of the cyclohexadiene-fused C_{60} from **A5** allows recovery of **A1** to restart the catalytic cycle. The dissociation process releases 8.9 kcal mol^{-1}. However, the cyclohexadiene-fused C_{60} adduct is not the final product of the reaction, and it evolves to generate the corresponding bis(fulleroid). We explored different scenarios for the formation of this open-cage fullerene product. First, we considered a [4+4]/retro-[2+2+2] sequence of cycloadditions in the isolated cyclohexadiene-fused C_{60} adduct. The linear transit of the [4+4] cycloaddition in the singlet state shows that this process has a barrier of about 50 kcal mol^{-1} (Figure S3 in the Supporting Information). This result is not unexpected as it is well-known that [4+4] cycloadditions are thermally forbidden by the Woodward–Hoffmann rules.[21] In the triplet state, this barrier is reduced to approximately 13 kcal mol^{-1}. Therefore, the combination of [4+4] and retro-[2+2+2] cycloadditions would be possible under photoexcitation of the cyclohexadiene derivative. A similar scenario occurs when a stepwise di-π-methane rearrangement is considered,[22] with formation of a singlet biradical **C2** (Figure S4 in the Supporting Information). For this di-π-methane rearrangement mechanism, we also analyzed the reaction in both the open-shell singlet and triplet excited states. In fact, a bis(fulleroid) species was photochemically synthesized for the first time by Rubin et al. in 1996 from a cyclohexadiene derivative of C_{60}.[6c, 23] The singlet excited state of the cyclohexadiene-fused C_{60} adduct is readily populated by photoexcitation. The triplet state can be populated from the singlet excited state followed by intersystem crossing (ISC). It has been reported that the ISC from the first singlet excited state to the first triplet excited state (S_1 to T_1) occurs with high efficiency in C_{60}, mainly owing to the small splitting between these two states as well as the large spin-orbit interaction in the spherical cage.[24] As shown in Figure S4 (in the Supporting Information), the di-π-methane rearrangement mechanism in both the singlet and triplet excited states is possible with relatively low barriers. In the triplet state, the rds is the formation of the first biradical intermediate with a closed cyclopropane ring, and has a barrier of 22.3 kcal mol^{-1}. Once this intermediate is formed, an ISC brings it to the singlet ground state. From here, the closed-shell singlet [5,6] (bis)methanofullerene species containing two cyclopropane rings is formed with a barrier of only 3.3 kcal mol^{-1}. Finally, a thermally allowed retro-[2+2+2] cycloaddition takes place with a barrier of 2.0 kcal mol^{-1} to yield the final [5,6] open bis(fulleroid)product. The greater stability of the bis(fulleroid)product compared with the (bis)methanofullerene intermediate can be attributed to a) release of ring strain upon opening of the two cyclopropyl rings that are fused to C_{60} pentagons, and b) retention of the 60π electron spherical conjugation and homoaromaticity.[22] The latter relates to the fact that open [5,6] isomers avoid localization of double bonds in pentagonal rings.[25]

Taken together, this data shows that neither the di-π-methane rearrangement pathway nor the [4+4]/retro-[2+2+2] reaction mechanism can explain the formation of the final bis(fulleroid) product without photoexcitation. Furthermore, it is noteworthy that very similar cyclohexadiene derivatives of C_{60} previously reported by Cheng et al. required UV ($\lambda = 350$ nm) irradiation for 2 h to rearrange into the corresponding bis(fulleroids).[9] As we have not employed photoexcitation in our system, a reaction path taking place in the ground state must be operative. At this point, it is convenient to remember that the presence of metals in a formal cycloaddition can (i) transform pericyclic reactions into stepwise processes,[26] or (ii) within a concerted pathway, modify the formal topology of orbital symmetry-allowed mechanisms by means of the participation of the orbitals provided by the metallic center.[27] With these ideas in mind, we investigated the transformation of **A5** to **A9** catalyzed by Rh(**P9**)$^{+}$. As shown in Figure 3, the reaction mechanism that we found follows a Rh-catalyzed di-π-methane rearrangement pathway. Thus, conversion of the cyclohexadiene-fused C_{60} intermediate **A5** to the [5,6] (bis)methanofullerene intermediate **A7** is a stepwise process in which, first, a cyclopropane ring is formed to yield **A6** (Gibbs barrier of 16.5 kcal mol^{-1}, Gibbs reaction energy of 7.0 kcal mol^{-1}). In **A6**, Rh is η^4-coordinated to the methanofullerene (Figure 4), thus stabilizing the allyl radical formed. The second cyclopropane ring formation has to surmount a Gibbs energy barrier of 17.0 kcal mol^{-1} and is endergonic by 1.1 kcal mol^{-1}. Therefore, conversion of **A5** into [5,6] (bis)methanofullerene intermediate **A7** has an overall Gibbs energy barrier of 24.0 kcal mol^{-1} (**TS A6A7** with respect to **A5**) and is endergonic by 8.1 kcal mol^{-1}. **A7** is a [5,6] (bis)methanofullerene that is η^4-coordinated to Rh by one [5,6] bond of the fullerene cage and by the double bond of the cyclohexene addend. Opening of the two fullerene C–C bonds of the cyclopropane moieties to form the bis(fulleroid)product **A8** coordinated to Rh(**P9**)$^{+}$ takes place concertedly in a process that is required to surpass a barrier of 6.3 kcal mol^{-1} and releases 16.9 kcal mol^{-1}. Intermediate **A8** is η^2-coordinated to one of the double bonds at the rim of the eight-membered hole of the fullerene. This structure is analogous to the X-ray structure reported by Rubin et al. for a similar complex. In the latter case, a Co(Cp) (Cp = cyclopentadiene) fragment is η^4-coordinated to the (bis)fulleroid.[6c] Final liberation of product **A9** and recovery of **A1** is slightly exergonic by −2.8 kcal mol^{-1}. Overall, once a Rh(**P9**)$^{+}$-catalyzed di-π-methane rearrangement pathway is considered, the barriers become relatively low and the full process is exergonic. Therefore, we demonstrate that the evolution from cyclohexadiene-fused C_{60} intermediate to the bis(fulleroid) product is possible without irradiation as long as the catalyst is present in the reaction. This conversion occurs through a di-π-methane rearrangement pathway followed by a retro-[2+2+2] cycloaddition. This last step is thermally allowed and can be performed either in the presence or in the absence of catalyst (Figure S4 in the Supporting Information).

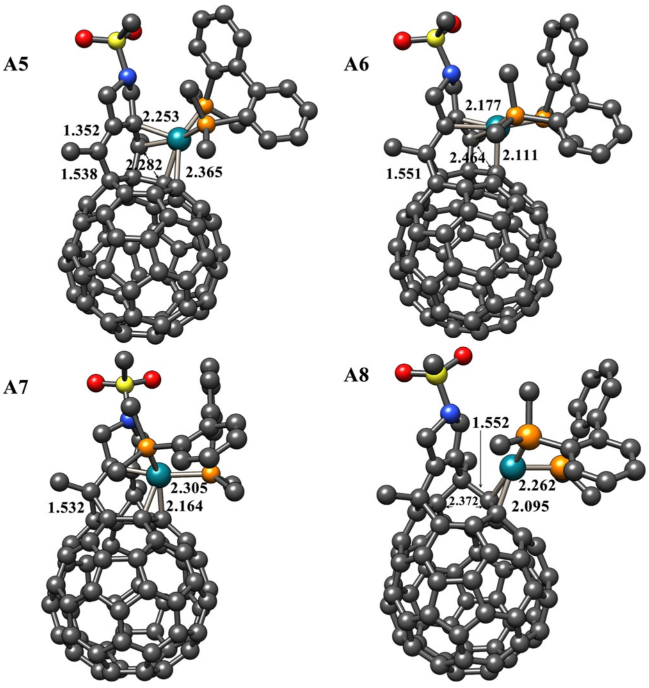

Figure 4. Structure of intermediates **A5**, **A6**, **A7**, and **A8**. Hydrogen atoms have been omitted for clarity. Bond lengths reported in Å.

Conclusion

We have developed an efficient cascade process leading to functionalized open-cage fullerene derivatives. The method is modular and catalytic in rhodium, providing the corresponding fulleroadducts in good to moderate yields starting from simple diyne precursors. The resulting fulleroadducts can be decorated with varied functionalities, including haloarene handles for further functionalization through Pd-catalyzed cross-coupling reactions. Overall, this reaction sequence provides a versatile

© 2018 Wiley-VCH Verlag GmbH & Co. KGaA, Weinheim

entry to donor–acceptor fulleroid dyads based on catalytic methods. DFT calculations show that the reaction takes place through a Rh-catalyzed [2+2+2] cycloaddition via a rhodabicyclo[3.2.0]heptadiene intermediate to yield a cyclohexadiene-fused C_{60} intermediate. This intermediate evolves to the final bis(fulleroid) product via a Rh-catalyzed di-π-methane rearrangement pathway followed by a retro-[2+2+2] cycloaddition. The initial oxidative coupling step of the Rh-catalyzed [2+2+2] cycloaddition is the rate-determining step of the whole reaction pathway.

Experimental Section

Representative procedure for the preparation of 2a

In a 10 mL capped vial, a mixture of $[Rh(cod)_2]BF_4$ (2.8 mg, 0.007 mmol, 0.1 equiv) and Tol-BINAP (4.8 mg, 0.007 mmol, 0.1 equiv) was purged with nitrogen and dissolved in anhydrous CH_2Cl_2 (4 mL). Hydrogen gas was bubbled into the catalyst solution and the mixture was stirred for 30 min. The resulting mixture was concentrated to dryness. Anhydrous *o*-dichlorobenzene (10 mL) was added and the resulting solution was then transferred via syringe into a solution of C_{60} (50 mg, 0.07 mmol, 1 equiv) and diyne **1a** (96 mg, 0.35 mmol, 5 equiv) in anhydrous *o*-dichlorobenzene (40 mL, final $[C_{60}] = 1.4$ mM) preheated to 90 °C. The resulting mixture was heated to 90 °C and stirred for 4 h. The solvent was removed under reduced pressure and the crude reaction mixture was purified by column chromatography on silica gel by using toluene as the eluent, affording unreacted C_{60} (25 mg) and **2a** (36 mg, 52 % yield, 98 % yield based on consumed C_{60}) as a dark-brown solid. Analytical samples were prepared by washing **2a** with *n*-pentane (3×2 mL).

Computational Methods

Geometries of all stationary points were optimized without symmetry constraints with the Gaussian 09 program[28] by using the DFT B3LYP hybrid exchange-correlation functional.[29] The all-electron cc-pVDZ basis set[30] was employed for non-metal atoms and the cc-pVDZ-PP basis set[31] containing an effective core relativistic pseudopotential was used for Rh. The electronic energy was improved by performing single-point energy calculations with the cc-pVTZ (cc-pVTZ-PP for Rh) basis set and the M06 functional[32] and including solvent effect corrections of a *o*-dichlorobenzene solution computed with the solvent model based on density (SMD) continuum solvation model.[33] The D3 Grimme energy corrections for dispersion[34] with the original damping function were added in all B3LYP/cc-pVDZ-PP and M06/cc-pVTZ-PP calculations. Analytical Hessians were computed to determine the nature of the stationary points (one and zero imaginary frequencies for TSs and minima, respectively) and to calculate unscaled zero-point energies (ZPEs) as well as thermal corrections and entropy effects by using the standard statistical mechanics relationships for an ideal gas.[35] These two latter terms were computed at 363.15 K and 1 atm to provide the reported relative Gibbs energies. As a summary, the reported Gibbs energies contain electronic energies including solvent effects calculated at the M06-D3/cc-pVTZ-PP//B3LYP-D3/cc-pVDZ-PP level together with gas-phase thermal and entropic contributions computed at 363.15 K and 1 atm with the B3LYP-D3/cc-pVDZ-PP method. To reduce the computational cost of the calculations, the tosyl group present in model compound **2a** was substituted with a mesyl group, the four tolyl groups present in the Rh^I-Tol-BINAP catalyst were substituted with methyl groups, and the binaphthyl core was substituted with biphenyl (ligand **P9**, see Figure 2).

Acknowledgments

We are grateful for the financial support from the Spanish Ministry of Economy and Competitivity (MINECO, Projects CTQ2017-85341-P and CTQ2017-83587-P, FPI predoctoral grant to A.A., RyC contract RYC2012-11112 to A.L.) and the Generalitat de Catalunya (Project 2017-SGR-39, Xarxa de Referència en Química Teòrica i Computacional, ICREA Academia 2014 prize for M.S.). The EU under the FEDER grant UNGI10-4E-801 has also funded this research.

Conflict of interest

The authors declare no conflict of interest.

Keywords: catalysis · cycloaddition reactions · DFT calculations · open-cage fullerenes · rhodium

[1] For monographies, see: a) F. Langa, J. F. Nierengarten, *Fullerenes: Principles and Applications*, 2nd Ed., The Royal Society of Chemistry, Cambridge, **2012**; b) F. Cataldo, T. da Ros, *Medicinal Chemistry and Pharmacological Potential of Fullerenes and Carbon Nanotubes*, 1st ed., Springer, Berlin, **2008**; c) A. Hirsch, M. Brettreich, *Fullerenes: Chemistry and Reactions*, Wiley-VCH, Weinheim, **2005**. For selected reviews, see: d) S.-E. Zhu, F. Li, G.-W. Wang, *Chem. Soc. Rev.* **2013**, *42*, 7535–7570; e) M. D. Tzirakis, M. Orfanopoulos, *Chem. Rev.* **2013**, *113*, 5262–5321; f) K. Itami, *Chem. Rec.* **2011**, *11*, 226–235; g) F. Giacalone, N. Martín, *Adv. Mater.* **2010**, *22*, 4220–4248; h) Y. Matsuo, E. Nakamura, *Chem. Rev.* **2008**, *108*, 3016–3028; i) C. Thilgen, F. Diederich, *Chem. Rev.* **2006**, *106*, 5049–5135; j) F. Giacalone, N. Martín, *Chem. Rev.* **2006**, *106*, 5136–5190; k) M. Bendikov, F. Wudl, D. F. Perepichka, *Chem. Rev.* **2004**, *104*, 4891–4946; l) E. Nakamura, H. Isobe, *Acc. Chem. Res.* **2003**, *36*, 807–815; m) L. Echegoyen, L. E. Echegoyen, *Acc. Chem. Res.* **1998**, *31*, 593–601; n) M. Prato, *J. Mater. Chem.* **1997**, *7*, 1097–1109.

[2] For selected reviews, see: a) E. Castro, J. Murillo, O. Fernandez-Delgado, L. Echegoyen, *J. Mater. Chem. C* **2018**, *6*, 2635–2651; b) R. Ganesamoorthy, G. Sathiyan, P. Sakthivel, *Solar Energy Mater. Sol. Cells* **2017**, *161*, 102–148; c) M. Rudolf, S. V. Kirner, D. M. Guldi, *Chem. Soc. Rev.* **2016**, *45*, 612–630; d) M. Rudolf, S. Wolfrum, D. M. Guldi, L. Feng, T. Tsuchiya, T. Akasaka, L. Echegoyen, *Chem. Eur. J.* **2012**, *18*, 5136–5148; e) Y. Matsuo, *Chem. Lett.* **2012**, *41*, 754–759; f) Y. Li, *Acc. Chem. Res.* **2012**, *45*, 723–733; g) C.-Z. Li, H.-L. Yip, A. K. Y. Jen, *J. Mater. Chem.* **2012**, *22*, 4161–4177; h) Y. He, Y. Li, *Phys. Chem. Chem. Phys.* **2011**, *13*, 1970–1983; i) J. L. Delgado, N. Martin, P. de la Cruz, F. Langa, *Chem. Soc. Rev.* **2011**, *40*, 5232–5241; j) J. L. Delgado, P.-A. Bouit, S. Filippone, M. A. Herranz, N. Martin, *Chem. Commun.* **2010**, *46*, 4853–4865; k) J. Roncali, *Acc. Chem. Res.* **2009**, *42*, 1719–1730; l) D. M. Guldi, B. M. Illescas, C. M. Atienza, M. Wielopolski, N. Martin, *Chem. Soc. Rev.* **2009**, *38*, 1587–1597; m) J. Chen, Y. Cao, *Acc. Chem. Res.* **2009**, *42*, 1709–1718; n) B. M. Illescas, N. Martín, *C. R. Chimie* **2006**, *9*, 1038–1050.

[3] a) S. Vidal, M. Izquierdo, S. Alom, M. Garcia-Borràs, S. Filippone, S. Osuna, M. Solà, R. J. Whitby, N. Martin, *Chem. Commun.* **2017**, *53*, 10993–10996; b) Y. Hashikawa, M. Murata, A. Wakamiya, Y. Murata, *J. Am. Chem. Soc.* **2016**, *138*, 4096–4104; c) E. E. Maroto, J. Mateos, M. Garcia-Borràs, S. Osuna, S. Filippone, M. Á. Herranz, Y. Murata, M. Solà, N. Martín, *J. Am. Chem. Soc.* **2015**, *137*, 1190–1197; d) L. Shi, L. Gan, *J. Phys. Org. Chem.* **2013**, *26*, 766–772; e) G. C. Vougioukalakis, M. M. Roubelakis, M. Orfanopoulos, *Chem. Soc. Rev.* **2010**, *39*, 817–844; f) N. J. Turro, J. Y. C. Chen, E. Sartori, M. Ruzzi, A. Marti, R. Lawler, S. Jockusch, J. López-Gejo, K. Komatsu, Y. Murata, *Acc. Chem. Res.* **2010**, *43*, 335–345; g) L. Gan, D. Yang, Q. Zhang, H. Huang, *Adv. Mater.* **2010**, *22*, 1498–

© 2018 Wiley-VCH Verlag GmbH & Co. KGaA, Weinheim

1507; h) M. Murata, Y. Murata, K. Komatsu, *Chem. Commun.* **2008**, 6083–6094.

[4] a) M. Murata, Y. Morinaka, Y. Murata, O. Yoshikawa, T. Sagawa, S. Yoshikawa, *Chem. Commun.* **2011**, *47*, 7335–7337; b) C.-P. Chen, Y.-W. Lin, J.-C. Horng, S.-C. Chuang, *Adv. Energy Mater.* **2011**, *1*, 776–780; c) S. H. Park, C. Yang, S. Cowan, J. K. Lee, F. Wudl, K. Lee, A. J. Heeger, *J. Mater. Chem.* **2009**, *19*, 5624–5628.

[5] a) Z. Zhou, N. Xin, L. Gan, *Chem. Eur. J.* **2018**, *24*, 451–457; b) Y. Li, L. Gan, *Chem. Eur. J.* **2017**, *23*, 10485–10490.

[6] Selected references: a) S.-i. Iwamatsu, P. S. Vijayalakshmi, M. Hamajima, C. H. Suresh, N. Koga, T. Suzuki, S. Murata, *Org. Lett.* **2002**, *4*, 1217–1220; b) Y. Murata, N. Kato, K. Komatsu, *J. Org. Chem.* **2001**, *66*, 7235–7239; c) M.-J. Arce, A. L. Viado, Y.-Z. An, S. I. Khan, Y. Rubin, *J. Am. Chem. Soc.* **1996**, *118*, 3775–3776.

[7] For reviews involving alkenes and allenes in transition-metal-catalyzed [2+2+2] cycloaddition reactions, see: a) A. Lledó, A. Pla-Quintana, A. Roglans, *Chem. Soc. Rev.* **2016**, *45*, 2010–2023; b) G. Domínguez, J. Pérez-Castells, *Chem. Eur. J.* **2016**, *22*, 6720–6739; for a monography covering the whole of [2+2+2] cycloaddition chemistry, see: c) K. Tanaka, *Transition-Metal-Mediated Aromatic Ring Construction*, 1st Ed., John Wiley & Sons, Inc., Hoboken, **2013**.

[8] a) I. Fernández, M. Solà, F. M. Bickelhaupt, *Chem. Eur. J.* **2013**, *19*, 7416–7422; b) W. Śliwa, *Fullerene Sci. Technol.* **1995**, *3*, 243–281; c) M. Solá, J. Mestres, J. Martí, M. Duran, *Chem. Phys. Lett.* **1994**, *231*, 325–330.

[9] T.-Y. Hsiao, K. C. Santhosh, K.-F. Liou, C.-H. Cheng, *J. Am. Chem. Soc.* **1998**, *120*, 12232–12236.

[10] H. Inoue, H. Yamaguchi, T. Suzuki, T. Akasaka, S. Murata, *Synlett* **2000**, *2000*, 1178–1180.

[11] K.-F. Liou, C.-H. Cheng, *J. Chem. Soc. Chem. Commun.* **1995**, 1603–1604.

[12] a) E. Haraburda, M. Fernández, A. Gifreu, J. Garcia, T. Parella, A. Pla-Quintana, A. Roglans, *Adv. Synth. Catal.* **2017**, *359*, 506–512; b) D. Cassú, T. Parella, M. Solà, A. Pla-Quintana, A. Roglans, *Chem. Eur. J.* **2017**, *23*, 14889–14899; c) M. Fernández, M. Parera, T. Parella, A. Lledó, J. Le Bras, J. Muzart, A. Pla-Quintana, A. Roglans, *Adv. Synth. Catal.* **2016**, *358*, 1848–1853; d) E. Haraburda, A. Lledó, A. Roglans, A. Pla-Quintana, *Org. Lett.* **2015**, *17*, 2882–2885; e) E. Haraburda, Ò. Torres, T. Parella, M. Solà, A. Pla-Quintana, *Chem. Eur. J.* **2014**, *20*, 5034–5045; f) T. León, M. Parera, A. Roglans, A. Riera, X. Verdaguer, *Angew. Chem. Int. Ed.* **2012**, *51*, 6951–6955; *Angew. Chem.* **2012**, *124*, 7057–7061; g) A. Dachs, A. Roglans, M. Solà, *Organometallics* **2011**, *30*, 3151–3159; h) A. Dachs, A. Pla-Quintana, T. Parella, M. Solà, A. Roglans, *Chem. Eur. J.* **2011**, *17*, 14493–14507; i) S. Brun, L. Garcia, I. Gonzalez, A. Torrent, A. Dachs, A. Pla-Quintana, T. Parella, A. Roglans, *Chem. Commun.* **2008**, 4339–4341; j) A. Torrent, I. González, A. Pla-Quintana, A. Roglans, M. Moreno-Mañas, T. Parella, J. Benet-Buchholz, *J. Org. Chem.* **2005**, *70*, 2033–2041.

[13] A. Artigas, A. Lledó, A. Pla-Quintana, A. Roglans, M. Solà, *Chem. Eur. J.* **2017**, *23*, 15067–15072.

[14] Selected references: a) Z.-Y. Wu, R. Zhong, F.-Z. Yang, *J. Organomet. Chem.* **2017**, *840*, 75–81; b) C.-H. Andersson, L. Nyholm, H. Grennberg, *Dalton Trans.* **2012**, *41*, 2374–2381; c) M. Á. Herranz, B. Illescas, N. Martín, C. Luo, D. M. Guldi, *J. Org. Chem.* **2000**, *65*, 5728–5738; d) D. M. Guldi, M. Maggini, G. Scorrano, M. Prato, *J. Am. Chem. Soc.* **1997**, *119*, 974–980.

[15] Selected references: a) G. Zaragoza-Galán, J. Ortíz-Palacios, B. Valderrama, A. Camacho-Dávila, D. Chávez-Flores, V. Ramos-Sánchez, E. Rivera, *Molecules* **2014**, *19*, 352; b) Y. Matsuo, K. Morita, E. Nakamura, *Chem. Asian J.* **2008**, *3*, 1350–1357; c) F. Hauke, A. Hirsch, S. Atalick, D. Guldi, *Eur. J. Org. Chem.* **2005**, *2005*, 1741–1751.

[16] a) Y. Murata, M. Murata, K. Komatsu, *Chem. Eur. J.* **2003**, *9*, 1600–1609; b) Y. Murata, K. Komatsu, *Chem. Lett.* **2001**, *30*, 896–897; c) Y. Murata, M. Murata, K. Komatsu, *J. Org. Chem.* **2001**, *66*, 8187–8191; d) H. Inoue, H. Yamaguchi, S.-i. Iwamatsu, T. Uozaki, T. Suzuki, T. Akasaka, S. Nagase, S. Murata, *Tetrahedron Lett.* **2001**, *42*, 895–897.

[17] a) T. Kegl, *RSC Adv.* **2015**, *5*, 4304–4327; b) H. Xie, Q. Sun, G. Ren, Z. Cao, *J. Org. Chem.* **2014**, *79*, 11911–11921; c) C. Flener Lovitt, G. Frenking, G. S. Girolami, *Organometallics* **2012**, *31*, 4122–4132.

[18] a) A. A. Dahy, N. Koga, *Organometallics* **2015**, *34*, 4965–4974; b) J. H. Hardesty, J. B. Koerner, T. A. Albright, G.-Y. Lee, *J. Am. Chem. Soc.* **1999**, *121*, 6055–6067.

[19] N. E. Schore, *Chem. Rev.* **1988**, *88*, 1081–1119.

[20] a) S. Kozuch, S. Shaik, *Acc. Chem. Res.* **2011**, *44*, 101–110; b) S. Kozuch, S. Shaik, *J. Phys. Chem. A* **2008**, *112*, 6032–6041.

[21] a) R. B. Woodward, R. Hoffmann, *The Conservation of Orbital Symmetry*, Academic Press, New York, **1970**; b) R. Hoffmann, R. B. Woodward, *Acc. Chem. Res.* **1968**, *1*, 17–22; c) R. B. Woodward, R. Hoffmann, *J. Am. Chem. Soc.* **1965**, *87*, 395–397.

[22] C. H. Suresh, P. S. Vijayalakshmi, S.-i. Iwamatsu, S. Murata, N. Koga, *J. Org. Chem.* **2003**, *68*, 3522–3531.

[23] Y. Rubin, *Chem. Eur. J.* **1997**, *3*, 1009–1016.

[24] R. R. Hung, J. J. Grabowski, *J. Phys. Chem.* **1991**, *95*, 6073–6075.

[25] M. Cases, M. Duran, J. Mestres, N. Martín, M. Solà, *Fullerenes for the New Millennium*, (Eds.: P. V. Kamat, D. M. Guldi, K. M. Kadish), The Electrochemical Society, Inc., Pennigton, vol 11, **2001**.

[26] J. M. Hoyt, V. A. Schmidt, A. M. Tondreau, P. J. Chirik, *Science* **2015**, *349*, 960–963.

[27] M. Mauksch, S. B. Tsogoeva, *Chem. Eur. J.* **2016**, *22*, 13916–13926.

[28] Gaussian 09 (Revision E.01), M. J. Frisch, G. W. Trucks, H. B. Schlegel, G. E. Scuseria, M. A. Robb, J. R. Cheeseman, G. Scalmani, V. Barone, G. A. Petersson, H. Nakatsuji, X. Li, M. Caricato, A. V. Marenich, J. Bloino, B. G. Janesko, R. Gomperts, B. Mennucci, H. P. Hratchian, J. V. Ortiz, A. F. Izmaylov, J. L. Sonnenberg, Williams, F. Ding, F. Lipparini, F. Egidi, J. Goings, B. Peng, A. Petrone, T. Henderson, D. Ranasinghe, V. G. Zakrzewski, J. Gao, N. Rega, G. Zheng, W. Liang, M. Hada, M. Ehara, K. Toyota, R. Fukuda, J. Hasegawa, M. Ishida, T. Nakajima, Y. Honda, O. Kitao, H. Nakai, T. Vreven, K. Throssell, J. A. Montgomery, Jr., J. E. Peralta, F. Ogliaro, M. J. Bearpark, J. J. Heyd, E. N. Brothers, K. N. Kudin, V. N. Staroverov, T. A. Keith, R. Kobayashi, J. Normand, K. Raghavachari, A. P. Rendell, J. C. Burant, S. S. Iyengar, J. Tomasi, M. Cossi, J. M. Millam, M. Klene, C. Adamo, R. Cammi, J. W. Ochterski, R. L. Martin, K. Morokuma, O. Farkas, J. B. Foresman, D. J. Fox, Gaussian, Inc., Wallingford, CT, **2009**.

[29] a) P. J. Stephens, F. J. Devlin, C. F. Chabalowski, M. J. Frisch, *J. Phys. Chem.* **1994**, *98*, 11623–11627; b) A. D. Becke, *J. Chem. Phys.* **1993**, *98*, 5648–5652; c) C. Lee, W. Yang, R. G. Parr, *Phys. Rev.* **1988**, *37*, 785–789.

[30] a) D. E. Woon, T. H. Dunning, Jr., *J. Chem. Phys.* **1993**, *98*, 1358–1371; b) T. H. Dunning, Jr., *J. Chem. Phys.* **1989**, *90*, 1007–1023.

[31] K. A. Peterson, D. Figgen, M. Dolg, H. Stoll, *J. Chem. Phys.* **2007**, *126*, 124101.

[32] Y. Zhao, D. G. Truhlar, *J. Chem. Phys.* **2006**, *125*, 194101.

[33] A. V. Marenich, C. J. Cramer, D. G. Truhlar, *J. Phys. Chem. B* **2009**, *113*, 6378–6396.

[34] S. Grimme, J. Antony, S. Ehrlich, H. Krieg, *J. Chem. Phys.* **2010**, *132*, 154104.

[35] P. Atkins, J. De Paula, *Physical Chemistry*, Oxford University Press, Oxford, **2006**.

Manuscript received: May 8, 2018
Accepted manuscript online: June 4, 2018
Version of record online: July 5, 2018

© 2018 Wiley-VCH Verlag GmbH & Co. KGaA, Weinheim

Chapter 5. Enhanced open-circuit voltage in perovskite solar cells with open-cage [60]Fullerene derivatives as electron-transporting materials

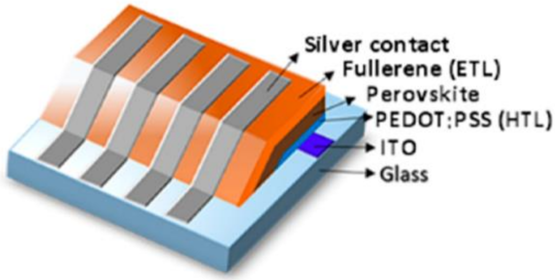

Published in: *Materials* **2019**, *12*, 1314.

Abstract: The synthesis, characterization, and incorporation of open-cage [60]fullerene derivatives as electron-transporting materials (ETMs) in perovskite solar cells (PSCs) with an inverted planar (p-i-n) structure is reported. Following optical and electrochemical characterization of the open-cage fullerenes **2a**–**c**, p-i-n PSCs with a indium tin oxide (ITO)/poly(3,4-ethylenedioxythiophene)-polystyrene sulfonate (PEDOT:PSS)/perovskite/fullerene/Ag structure were prepared. The devices obtained from **2a**–**b** exhibit competitive power conversion efficiencies (PCEs) and improved open-circuit voltage (V_{oc}) values (>1.0 V) in comparison to a reference cell based on phenyl-C_{61}-butyric-acid methyl-ester ($PC_{61}BM$). These results are rationalized in terms of a) the higher passivation ability of the open-cage fullerenes with respect to the other fullerenes, and b) a good overlap between the highest occupied molecular orbital/lowest unoccupied molecular orbital (HOMO/LUMO) levels of **2a**–**b** and the conduction band of the perovskite.

materials

Communication

Enhanced Open-Circuit Voltage in Perovskite Solar Cells with Open-Cage [60]Fullerene Derivatives as Electron-Transporting Materials

Edison Castro [1,†,*], Albert Artigas [2,†], Anna Pla-Quintana [2], Anna Roglans [2], Fang Liu [3], Frank Perez [1], Agustí Lledó [2], X.-Y. Zhu [3] and Luis Echegoyen [1,*]

[1] Department of Chemistry, University of Texas at El Paso El Paso, TX 79968, USA; faperez2@miners.utep.edu
[2] Institut de Química Computacional i Catàlisi (IQCC), Department de Química, Universitat de Girona, 17003 Girona, Catalonia Spain; albert.artigas@udg.edu (A.A.); anna.plaq@udg.edu (A.P.-Q.); anna.roglans@udg.edu (A.R.); agusti.lledo@udg.edu (A.L.)
[3] Department of Chemistry, Columbia University, New York, NY 10027, USA; fl2454@columbia.edu (F.L.); xz2324@columbia.edu (X.-Y.Z.)
* Correspondence: edisoncastro2004@hotmail.com (E.C.); echegoyen@utep.edu (L.E.)
† These authors contributed equally.

Received: 25 March 2019; Accepted: 18 April 2019; Published: 23 April 2019

Abstract: The synthesis, characterization, and incorporation of open-cage [60]fullerene derivatives as electron-transporting materials (ETMs) in perovskite solar cells (PSCs) with an inverted planar (p-i-n) structure is reported. Following optical and electrochemical characterization of the open-cage fullerenes **2a–c**, p-i-n PSCs with a indium tin oxide (ITO)/poly(3,4-ethylenedioxythiophene)-polystyrene sulfonate (PEDOT:PSS)/perovskite/fullerene/Ag structure were prepared. The devices obtained from **2a–b** exhibit competitive power conversion efficiencies (PCEs) and improved open-circuit voltage (V_{oc}) values (>1.0 V) in comparison to a reference cell based on phenyl-C_{61}-butyric-acid methyl-ester ($PC_{61}BM$). These results are rationalized in terms of a) the higher passivation ability of the open-cage fullerenes with respect to the other fullerenes, and b) a good overlap between the highest occupied molecular orbital/lowest unoccupied molecular orbital (HOMO/LUMO) levels of **2a–b** and the conduction band of the perovskite.

Keywords: open-cage fullerenes; perovskite solar cells; improving open circuit voltage

---

1. Introduction

Perovskite solar cells (PSCs) are an emerging class of photovoltaic devices, which promise to rival the performance of state-of-the-art cells, with current record power conversion efficiencies (PCEs) recently reaching 24.2% [1] A major advantage of PSCs is their facile manufacturing process, which is mostly based on solution processing. However, a number of challenges need to be addressed before a marketable technology is available, including (a) cell performance, (b) cell stability, and (c) upscaling beyond laboratory scale toward the industrial production of commercially viable photovoltaic devices [2–7]. Another desirable yet unmet objective is the replacement of Pb by less toxic metals in the perovskite structure [8].

A PSC consists of a sandwiched structure containing a transparent conductive oxide, a hole transport layer (HTL), a perovskite photo-absorber layer, an electron-transport layer (ETL), and a back-contact electrode [9–15]. Among the various cell configurations available for PSCs, the inverted planar structure (p-i-n) (Figure 1) is the most attractive in terms of manufacturing, because the ETL, which is typically a fullerene derivative, is solution-processed [16], as opposed to the metal oxides employed in the regular planar and mesoscopic configurations, which require high-temperature annealing steps [17–19]. Importantly, p-i-n PSCs can be easily integrated in flexible devices [20]. A downside of the p-i-n configuration is that high open circuit voltage (V_{oc}) values are difficult to achieve. Successful strategies to overcome this limitation rely on the incorporation of dopant materials [21–23], interfacial engineering [24–26], morphology control [27,28], or the replacement of the HTL [29,30].

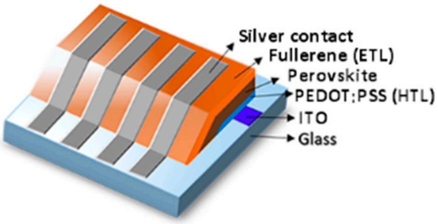

Figure 1. Inverted planar perovskite solar cell (PSC) representation with the structure of indium tin oxide (ITO)/poly(3,4-ethylenedioxythiophene)-polystyrene sulfonate (PEDOT:PSS)/perovskite/electron-transport layer (ETL)/silver.

On the other hand, the replacement of phenyl-C_{61}-butyric-acid methyl-ester ($PC_{61}BM$) by other fullerenes as the ETL has found limited success, with only a few reports of V_{oc} values beyond the 1.0 V threshold [31,32]. For the specific case of poly(3,4-ethylenedioxythiophene)-polystyrene sulfonate (PEDOT:PSS)-based devices, examples are even scarcer [11,33,34]. The development of PSCs with $PC_{61}BM$ surrogates relies mostly on the incorporation of highly crystalline ETLs. The resulting cells benefit from reduced energy disorder and improved charge trap passivation [35,36]. While this approach has been implemented with a variety of fullerenes, the vast majority of them consist of [3+2], [4+2], or cyclopropane adducts [15]. Thus, the introduction of structurally novel fullerene scaffolds that can expand the ETL repertoire is highly desirable.

Overall, the highest certified PCE value reported for PSCs with p-i-n configurations is 20.9% [37]. The development of efficient ETMs that can increase the efficiency of PSCs without the need of additives or complex manufacturing techniques is a major challenge in the field of inverted planar PSCs.

Open-cage fullerenes are a family of synthetic derivatives in which the three-dimensional backbone of the fullerene cage is distorted by the scission of one or more C–C bonds. Open-cage fullerenes have been successfully used as electron-accepting materials or as additives in bulk-heterojunction solar cells [38–40]. However, their use as ETLs in PSCs remains unexplored. Some of us recently reported a straightforward methodology for the synthesis of open-cage fullerene derivatives (Scheme 1) [41,42]. The promising electrochemical properties and remarkable stability of these compounds, together with the fact that fullerene derivatives are so far the materials of choice as the ETL for p-i-n PSCs, prompted us to study the use of these compounds for PSCs.

Herein, we report for the first time the incorporation of open-cage fullerenes in p-i-n PSCs. The cells have been thoroughly characterized, and their photovoltaic performance has been studied. We demonstrate that open-cage fullerenes exhibit improved performances with respect to $PC_{61}BM$-based devices.

2. Results

The open-cage derivatives used in this study, **2a–c**, were prepared by the photochemical oxidation of bis(fulleroids) **1a–c**, which can be obtained from [60]fullerene in one step using our Rh(I)-catalyzed cycloaddition protocol (Scheme 1) [41]. Importantly, unlike precursors **1a-c**, open-cage derivatives **2a–c** do not suffer further degradation upon exposure to light and air. In addition to the parent open-cage derivative **2a**, we selected compounds possessing desirable features for PSC manufacturing, such as the improved solubility of **2b** or the light-harvesting ability of **2c**. With **2a–c** in hand, we first assessed their optical and electrochemical properties. In solution, **2a–c** display remarkable absorption maxima in the visible region (λ_{max} = 705–710 nm, Figure S12). The electrochemical properties of **2a–c** (Figure S13) and

$PC_{61}BM$ (**3**) were determined by cyclic voltammetry (CV) in ortho-dichlorobenzene (*o*-DCB) (see the Supporting Information).

Compounds **2a–c** exhibit three fully reversible cathodic electrochemical behaviors between −0.8 and −2.3 V at a scan rate of 100 mV s^{-1}. The highest occupied molecular orbital/lowest unoccupied molecular orbital (HOMO/LUMO) values were estimated from the ultraviolet (UV) and CV measurements [43].

The optical properties of compounds **2a–c** are summarized in Table 1. Overall, the photophysical and electrochemical properties of the open-cage fullerenes **2a–c** are very similar to those of $PC_{61}BM$, even though the C_{60} cage skeleton is significantly altered with respect to the latter. These results encouraged us to incorporate **2a–c** as the electron-transporting materials (ETMs) in PSCs.

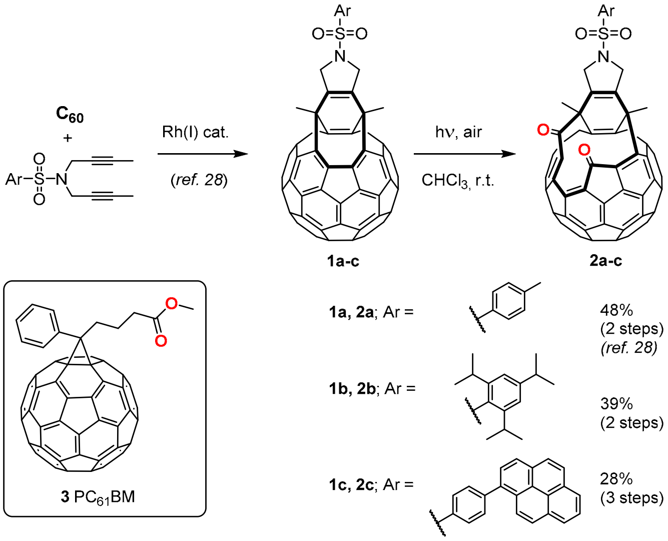

Scheme 1. Synthesis of open-cage fullerene derivatives **2a–c**, and (inset) reference compound used in this study ((**3**, $PC_{61}BM$), See Supporting Information for the synthesis of **1c**).

Table 1. Optical bandgap, onset reduction, and lowest unoccupied molecular orbital/highest occupied molecular orbital (LUMO/HOMO) energy levels of the open-cage **2a–c** and compound **3**.

Comp	λ_{max} (nm)	E_g (ev)	E_{red} (V)	LUMO (ev)	HOMO (ev)
2a	709	1.75	0.94	−3.86	−5.61
2b	705	1.76	0.99	−3.81	−5.57
2c	705	1.76	0.85	−3.95	−5.71
$PC_{61}BM$	718	1.73	0.87	−3.93	−5.66

Figure 2a shows the energy level diagram estimated from the onset potential of the first reductions and the maximum onset absorption from UV-vis spectra for all the compounds [44]. The electrical conductivities for $PC_{61}BM$ and compounds **2a–c** films were compared by recording current–voltage (*J-V*) curves for electron-only devices with a structure of ITO/Al/ETM/Al. All the ETLs showed similar electron conductivities (4.8, 3.5, 2.8 and 3.7 × 10^{-4} cm^2 V^{-1}·s^{-1} for **2a**, **2b**, **2c**, and $PC_{61}BM$, respectively).

To probe the passivation ability of compounds **2a–c**, we studied the photoluminescence (PL) and time-resolved (TR) PL of the photoactive layer (perovskite) with and without **2a–c**, using $PC_{61}BM$ as the control (Figure 2b and Figure S14). A significant PL quenching effect was observed for the perovskite layer coated with the open-cage fullerenes **2a**, **2b**, and $PC_{61}BM$ (Figure 2b). Meanwhile, the PL intensity of the perovskite increases when using **2c**, which is an effect that can be attributed to the lower solubility of **2c** in chlorobenzene (CB) (Figure S15). Compound **2a** exhibits a higher passivation ability than the other fullerenes, resulting in a more pronounced inhibition of the electron–hole recombination processes [45].

Figure S14 shows the TR-PL decay measurements, monitoring the emission peak of $PC_{61}BM$ and **2a–c** coated perovskite layers as a function of time. The pristine perovskite layer exhibits a PL lifetime of about 25.6 ns, whereas perovskite/**2a**, perovskite/**2b**, perovskite/**2c**, and perovskite/$PC_{61}BM$ exhibit PL lifetimes of 3.8 ns, 4.7 ns, 9.2 ns, and 14.1 ns, respectively. Faster decays are measured for the samples coated with **2a** and **2b**, indicating that the charge transfer processes are faster than the charge recombination in the perovskite layer [46].

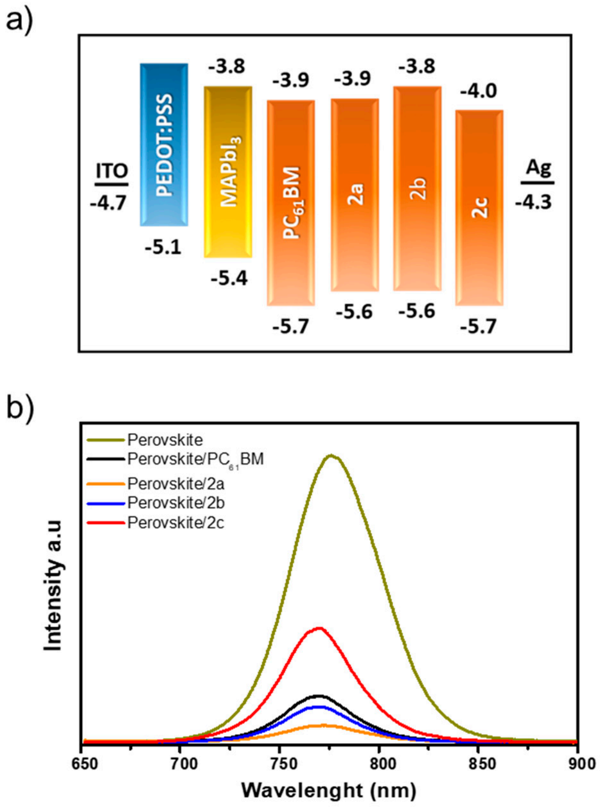

Figure 2. (**a**) Schematic illustration of the estimated HOMO and LUMO energy levels, estimated from cyclic voltammetry (CV) and UV-vis. (**b**) Steady-state photoluminescence (PL) spectra of the perovskite and perovskite/ETM films.

Compounds **2a–c** were incorporated in PSCs with an ITO/PEDOT:PSS/perovskite/fullerene/Ag structure (Figure 1, see Supporting Information for details). The **2a** (1.01 V) and **2b** (0.97 V)-based devices showed a significant enhancement of V_{oc} values compared to the $PC_{61}BM$ (0.92 V)-based devices.

On the other hand, the lower solubility of **2c** led to low-quality films, resulting in lower photovoltaic performances for the **2c**-based devices (Figure 3). Table 2 summarizes the performances of the PSC devices incorporating $PC_{61}BM$ and compounds **2a–c**. The work functions of the charge transport materials affect the V_{oc} of PSCs significantly, so the higher V_{oc} values obtained from **2a** and **2b**-based devices can be attributed to their higher LUMO values, when compared with $PC_{61}BM$ [25,26,46,47]. Commonly, the V_{oc} values are improved by inserting a work-function interlayer between the perovskite and the ETL [26].

PSCs based on all the fullerene derivatives showed negligible hysteretic behavior (Figure S16). Device performance reproducibilities were calculated from the PCE distributions measured for 25 independent cells (Figure 3b). Figure S17 shows the external quantum efficiency (EQE) of the PSCs based on $PC_{61}BM$ and **2a–c**; the devices based on **2a** show higher photoresponse around 600 nm and 750 nm. The integrated photocurrent densities based on EQE measurements (Figure S17) are consistent with those from *J-V* measurements (Table 2). $PC_{61}BM$ devices exhibited a PCE value of 16.22% with a V_{oc} value of 0.92 V, a short circuit current (J_{sc}) value of 21.77 mA·cm^{-2}, and a fill factor (FF) value of

0.80. In contrast, **2a** devices exhibited a PCE value of 16.92% with a V_{oc} value of 1.01 V, a J_{sc} value of 21.21 mA·cm^{-2}, and a FF value of 0.79. The improved device performance was attributed to the better passivation ability of compounds **2a** and **2b**, because of their higher work function, which matches well with the conduction band of the perovskite [25,26,46,47].

The stabilities of PSCs fabricated with PC$_{61}$BM, **2a**, and **2b** were monitored under ca. 25% humidity in air at room temperature without encapsulation for 10 days. The normalized PCEs against time are shown in Figure S18. PC$_{61}$BM-based devices lost 67% of their initial PCE; this was similar to the PC$_{61}$BM-based devices **2a** and **2b**-based devices, which lost 65% and 63% of their initial PCE, respectively. Meanwhile, the devices based on **2c** lost 71% of their initial PCE. Thus, the open-cage compounds are comparable to PC$_{61}$BM in terms of cell stability.

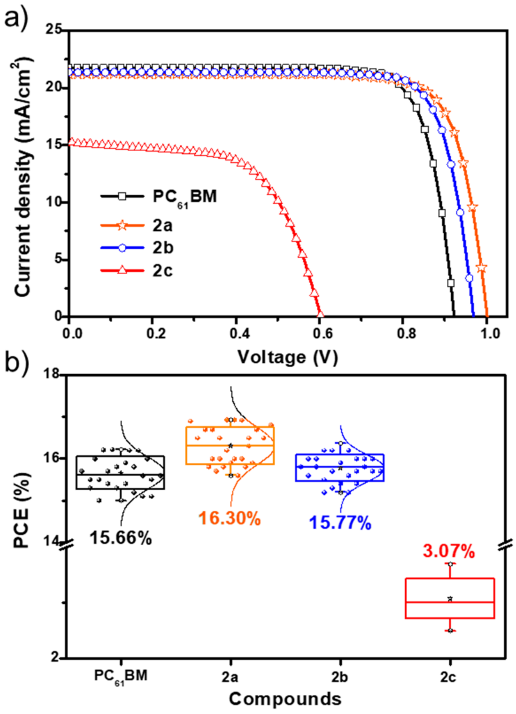

Figure 3. (**a**) Current–voltage (*J*-*V*) curves under 1 sun of illumination (100 mW/cm^2) in forward voltage scans. (**b**) The power conversion efficiency (PCE) histograms measured for 25 independent cells.

Table 2. Summary of device performance. The calculated short circuit current (J_{sc}) values were obtained from the external quantum efficiency (EQE) curves. Values in parentheses represent the best values measured, ^{a} are the average values, and * are the calculated values. PC$_{61}$BM: phenyl-C$_{61}$-butyric-acid methyl-ester.

Compound	J_{sc}* (mA cm^{-2})	J_{sc} (mA cm^{-2})	V_{oc} (V)	FF (%)	PCE (%)
2a	21.05	21.17 ^{a} (21.21)	0.99 ^{a} (1.01)	0.79	16.30 ± 0.62 (16.92)
2b	21.11	20.98 ^{a} (21.37)	0.96 ^{a} (0.97)	0.79	15.77 ± 0.60 (16.37)
2c	14.87	15.01 ^{a} (15.20)	0.53 ^{a} (0.60)	0.41	3.07 ± 0.67 (3.74)
PC$_{61}$BM	21.22	21. 56 ^{a} (21.77)	0.88 ^{a} (0.92)	0.80	15.66 ± 0.56 (16.22)

3. Conclusions

In conclusion, we have successfully prepared a series of p-i-n type PSCs incorporating dicarbonylic open-cage [60]fullerene derivatives **2a–c** as the ETL. For those compounds with appropriate solubility, the resulting PSCs offer performances rivaling or even superior to those of analogous cells employing the $PC_{61}BM$ reference. These results are commensurate with a good overlap between the HOMO/LUMO levels of fulleroids **2a–b** and the conduction band of the perovskite. The modularity of our synthetic approach to open-cage fullerene derivatives **2a–c** offers a promising opportunity to develop superior PSCs beyond this preliminary account.

Supplementary Materials: The following are available online at http://www.mdpi.com/1996-1944/12/8/1314/s1, Figure S-1. ^1H NMR (400 MHz, $CDCl_3$) of compound **3a**. Figure S-2. ^1H NMR (400 MHz, $CDCl_3$) of compound **3b**. Figure S-3. ^1H NMR (400 MHz, $CDCl_3$) of compound **3c**. Figure S-4. ^1H NMR (400 MHz, $CDCl_3$) of compound **1a**. Figure S-5. ^1H NMR (400 MHz, $CDCl_3$) of compound **1b**. Figure S-6. ^1H NMR (400 MHz, o-DCB-$_{d4}$/CS_2) of compound S-5. Figure S-7. ^1H NMR (400 MHz, $CDCl_3$) of compound **1c**. Figure S-8. ^1H NMR (400 MHz, $CDCl_3$) of compound **2a**. Figure S-9. ^1H NMR (400 MHz, $CDCl_3$) of compound **2b**. Figure S-10. ^{13}C NMR (100 MHz, $CDCl_3$) of compound **2b**. Figure S-11. ^1H NMR (400 MHz, $CDCl_3$) of compound **2c**. Figure S-12. UV-vis spectra of compounds **2a-c** and $PC_{61}BM$. Figure S-13. Cyclic voltammetry of compounds **2a-c**. Figure S-14. Time-resolved photoluminescence of perovskite, perovskite/compounds **2a-c** and perovskite/$PC_{61}BM$ films. Figure S-15. Fullerene derivatives **2a-c** and $PC_{61}BM$ in *o*-dichlorobezene (20 mg/mL). Figure S-16. *J-V* curves of the inverted PSCs based on $PC_{61}BM$ (a) and **2a,b** (b and c, respectively) with respect to forward and reverse scan directions (the scanning rate was 100 mV/s). Figure S-17. EQE measurements for **2a-c** and $PC_{61}BM$-based devices. Figure S-18. Stability studies of **2a-c** and $PC_{61}BM$-based devices. Figure S-19. Top-view SEM image of the perovskite film.

Author Contributions: E.C., A.A, F.L. and F.P.: synthesis, characterization, and cells fabrication: E.C., A.A., F.L., F.P., A.P.-Q., A.R., A.L., X.-Y.Z. and L.E.: writing–original draft, review, and editing: L.E. overall supervision of the final work.

Funding: The authors thank the US National Science Foundation (NSF) for its generous support of this work under the NSF-PREM program (DMR 1205302, and CHE-1801317 to L. E.). The Robert A. Welch Foundation is also gratefully acknowledged for an endowed chair to L. E. (Grant AH-0033). Financial support by the Spanish Ministry of Economy and Competitivity (MINECO), European Social Fund (ESF) (Projects CTQ2017-85341-P and CTQ2017-83587-P, FPI predoctoral grant to A. A., RyC contract RYC2012-11112 to A. L.), and the Generalitat de Catalunya (Project 2017-SGR-39) is gratefully acknowledged. The EU has also funded this research under FEDER grant UNGI10-4E-801. X.-Y.Z thanks the Office of Naval Research for support under award no. N00014-16-1-2921. This research was supported in part by the Department of Energy (DOE) Office of Energy Efficiency and Renewable Energy (EERE) Postdoctoral Research Award under the EERE Solar Energy Technologies Office administered by the Oak Ridge Institute for Science and Education (ORISE) for the DOE. ORISE is managed by Oak Ridge Associated Universities (ORAU) under DOE contract number DE-SC00014664. All of the opinions expressed in this paper are the authors' and do not necessarily reflect the policies and views of DOE, ORAU, or ORISE.

Conflicts of Interest: There are no conflicts to declare.

References

1. NREL Best Research-Cell Efficiencies. Available online: https://www.nrel.gov/pv/assets/pdfs/best-research-cell-efficiencies-190416.pdf (accessed on 1 April 2019).
2. Rong, Y.; Hu, Y.; Mei, A.; Tan, H.; Saidaminov, M.I.; Seok, S.I.; McGehee, M.D.; Sargent, E.H.; Han, H. Challenges for commercializing perovskite solar cells. *Science* **2018**, *361*, eaat8235. [CrossRef]
3. Li, Z.; Klein, T.R.; Kim, D.H.; Yang, M.; Berry, J.J.; van Hest, M.F.A.M.; Zhu, K. Scalable fabrication of perovskite solar cells. *Nat. Rev. Mater.* **2018**, *3*, 18017. [CrossRef]
4. Galagan, Y. Perovskite Solar Cells: Toward Industrial-Scale Methods. *J. Phys. Chem. Lett.* **2018**, *9*, 4326–4335. [CrossRef]
5. Wang, F.; Cao, Y.; Chen, C.; Chen, Q.; Wu, X.; Li, X.; Qin, T.; Huang, W. Materials toward the upscaling of perovskite solar cells: progress, challenges, and strategies. *Adv. Funct. Mater.* **2018**, *28*, 1803753. [CrossRef]
6. Abate, A.; Correa-Baena, J.-P.; Saliba, M.; Su'ait, M.S.; Bella, F. Perovskite Solar Cells: From the laboratory to the assembly line. *Chem. Eur. J.* **2018**, *24*, 3083–3100. [CrossRef] [PubMed]
7. Bella, F.; Renzi, P.; Cavallo, C.; Gerbaldi, C. Caesium for perovskite solar cells: An overview. *Chem. Eur. J.* **2018**, *24*, 12183–12205. [CrossRef] [PubMed]
8. Giustino, F.; Snaith, H.J. Toward Lead-free perovskite solar cells. *ACS Energy Lett.* **2016**, *1*, 1233–1240. [CrossRef]

9. Castro, E.; Fernandez-Delgado, O.; Arslan, F.; Zavala, G.; Yang, T.; Seetharaman, S.; Dsouza, F.; Echegoyen, L. New thiophene-based C60 fullerene derivatives as efficient electron transporting materials for perovskite solar cells. *New J. Chem.* **2018**, *42*, 14551–14558. [CrossRef] [PubMed]
10. Castro, E.; Sisto, T.J.; Romero, E.L.; Liu, F.; Peurifoy, S.R.; Wang, J.; Zhu, X.; Nuckolls, C.; Echegoyen, L. Cove-Edge Nanoribbon materials for efficient inverted halide perovskite solar cells. *Angew. Chem. Int. Ed.* **2017**, *129*, 14840–14844. [CrossRef]
11. Castro, E.; Zavala, G.; Seetharaman, S.; D'Souza, F.; Echegoyen, L. Impact of fullerene derivative isomeric purity on the performance of inverted planar perovskite solar cells. *J. Mater. Chem. A.* **2017**, *5*, 19485–19490. [CrossRef]
12. Peurifoy, S.R.; Castro, E.; Liu, F.; Zhu, X.Y.; Ng, F.; Jockusch, S.; Steigerwald, M.L.; Echegoyen, L.; Nuckolls, C.; Sisto, T.J. Three-dimensional graphene nanostructures. *J. Am. Chem. Soc.* **2018**, *140*, 9341–9345. [CrossRef] [PubMed]
13. Tian, C.; Castro, E.; Betancourt-Solis, G.; Nan, Z.-A.; Fernandez-Delgado, O.; Jankuru, S.; Echegoyen, L. Fullerene derivative with a branched alkyl chain exhibits enhanced charge extraction and stability in inverted planar perovskite solar cells. *New J. Chem.* **2018**, *42*, 2896–2902. [CrossRef]
14. Tian, C.; Castro, E.; Wang, T.; Betancourt-Solis, G.; Rodriguez, G.; Echegoyen, L. Improved performance and stability of inverted planar perovskite solar cells using fulleropyrrolidine layers. *ACS Appl. Mater. Interfaces.* **2016**, *8*, 31426–31432. [CrossRef]
15. Tian, C.; Kochiss, K.; Castro, E.; Betancourt-Solis, G.; Han, H.; Echegoyen, L. A dimeric fullerene derivative for efficient inverted planar perovskite solar cells with improved stability. *J. Mater. Chem. A.* **2017**, *5*, 7326–7332. [CrossRef]
16. Khadka, D.B.; Shirai, Y.; Yanagida, M.; Miyano, K. Unraveling the impacts induced by organic and inorganic hole transport layers in inverted halide perovskite solar cells. *ACS Appl. Mater. Interfaces.* **2019**, *11*, 7055–7065. [CrossRef]
17. Castro, E.; Murillo, J.; Fernandez-Delgado, O.; Echegoyen, L. Progress in fullerene-based hybrid perovskite solar cells. *J. Mater. Chem. C.* **2018**, *6*, 2635–2651. [CrossRef]
18. Fang, Y.; Bi, C.; Wang, D.; Huang, J. The functions of fullerenes in hybrid perovskite solar cells. *ACS Energy Lett.* **2017**, *2*, 782–794. [CrossRef]
19. Liu, T.; Chen, K.; Hu, Q.; Zhu, R.; Gong, Q. Inverted perovskite solar cells: Progresses and perspectives. *Adv. Energy Mater.* **2016**, *6*, 1600457. [CrossRef]
20. Wang, Y.-C.; Li, X.; Zhu, L.; Liu, X.; Zhang, W.; Fang, J. Efficient and hysteresis-free perovskite solar cells based on a solution processable polar fullerene electron transport layer. *Adv. Energy Mater.* **2017**, *7*, 1701144. [CrossRef]
21. Xia, X.; Jiang, Y.; Wan, Q.; Wang, X.; Wang, L.; Li, F. Lithium and silver co-doped nickel oxide hole-transporting layer boosting the efficiency and stability of inverted planar perovskite solar cells. *ACS Appl. Mater. Interfaces* **2018**, *10*, 44501–44510. [CrossRef] [PubMed]
22. Wang, Y.; Wang, S.; Chen, X.; Li, Z.; Wang, J.; Li, T.; Deng, X. Largely enhanced VOC and stability in perovskite solar cells with modified energy match by coupled 2D interlayers. *J. Mater. Chem. A.* **2018**, *6*, 4860–4867. [CrossRef]
23. Chen, W.; Zhou, Y.; Wang, L.; Wu, Y.; Tu, B.; Yu, B.; Liu, F.; Tam, H.-W.; Wang, G.; Djurišić, A.B.; Huang, L.; He, Z. Molecule-doped nickel oxide: Verified charge transfer and planar inverted mixed cation perovskite solar cell. *Adv. Mater.* **2018**, *30*, 1800515. [CrossRef] [PubMed]
24. Chen, J.; Lian, X.; Zhang, Y.; Yang, W.; Li, J.; Qin, M.; Lu, X.; Wu, G.; Chen, H. Interfacial engineering enables high efficiency with a high open-circuit voltage above 1.23 V in 2D perovskite solar cells. *J. Mater. Chem. A.* **2018**, *6*, 18010–18017. [CrossRef]
25. Xue, Q.; Bai, Y.; Liu, M.; Xia, R.; Hu, Z.; Chen, Z.; Jiang, X.-F.; Huang, F.; Yang, S.; Matsuo, Y.; Yip, H.-L.; Cao, Y. Dual interfacial modifications enable high performance semitransparent perovskite solar cells with large open circuit voltage and fill factor. *Adv. Energy Mater.* **2017**, *7*, 1602333. [CrossRef]
26. Bai, Y.; Yu, H.; Zhu, Z.; Jiang, K.; Zhang, T.; Zhao, N.; Yang, S.; Yan, H. High performance inverted structure perovskite solar cells based on a PCBM:polystyrene blend electron transport layer. *J. Mater. Chem. A.* **2015**, *3*, 9098–9102. [CrossRef]

27. Cheng, J.; Zhang, H.; Zhang, S.; Ouyang, D.; Huang, Z.; Nazeeruddin, M.K.; Hou, J.; Choy, W.C.H. Highly efficient planar perovskite solar cells achieved by simultaneous defect engineering and formation kinetic control. *J. Mater. Chem. A.* **2018**, *6*, 23865–23874. [CrossRef]
28. Li, W.; Wu, X.; Qin, H.; Zhao, Z.; Liu, H. Light-Driven and Light-Guided Microswimmers. *Adv. Funct. Mater.* **2016**, *26*, 3164–3171. [CrossRef]
29. Zhang, H.; Wang, H.; Zhu, H.; Chueh, C.-C.; Chen, W.; Yang, S.; Jen, A.K.-Y. Low-temperature solution-processed $CuCrO_2$ hole-transporting layer for efficient and photostable perovskite solar cells. *Adv. Energy Mater.* **2018**, *8*, 1702762. [CrossRef]
30. Wang, H.; Yu, Z.; Lai, J.; Song, X.; Yang, X.; Hagfeldt, A.; Sun, L. One plus one greater than two: High-performance inverted planar perovskite solar cells based on a composite CuI/CuSCN hole-transporting layer. *J. Mater. Chem. A.* **2018**, *6*, 21435–21444. [CrossRef]
31. Yan, K.; Chen, J.; Ju, H.; Ding, F.; Chen, H.; Li, C.-Z. Achieving high-performance thick-film perovskite solar cells with electron transporting Bingel fullerenes. *J. Mater. Chem. A.* **2018**, *6*, 15495–15503. [CrossRef]
32. Meng, X.; Bai, Y.; Xiao, S.; Zhang, T.; Hu, C.; Yang, Y.; Zheng, X.; Yang, S. Designing new fullerene derivatives as electron transporting materials for efficient perovskite solar cells with improved moisture resistance. *Nano Energy.* **2016**, *30*, 341–346. [CrossRef]
33. Gil-Escrig, L.; Momblona, C.; Sessolo, M.; Bolink, H.J. Fullerene imposed high open-circuit voltage in efficient perovskite based solar cells. *J. Mater. Chem. A.* **2016**, *4*, 3667–3672. [CrossRef]
34. Chiang, C.-H.; Tseng, Z.-L.; Wu, C.-G. Planar heterojunction perovskite/PC71BM solar cells with enhanced open-circuit voltage via a (2/1)-step spin-coating process. *J. Mater. Chem. A.* **2014**, *2*, 15897–15903. [CrossRef]
35. Xie, F.; Zhang, L.; Su, D.; Jaroniec, M.; Qiao, S.-Z. $Na_2Ti_3O_7$@N-Doped carbon hollow spheres for sodium-ion batteries with excellent rate performance. *Adv. Mater.* **2017**, *29*, 1700989. [CrossRef] [PubMed]
36. Khadka, D.B.; Shirai, Y.; Yanagida, M.; Noda, T.; Miyano, K. Tailoring the open-circuit voltage deficit of wide-band-gap perovskite solar cells using alkyl chain-substituted fullerene derivatives. *ACS Appl. Mater. interfaces.* **2018**, *10*, 22074–22082. [CrossRef]
37. Luo, D.; Yang, W.; Wang, Z.; Sadhanala, A.; Hu, Q.; Su, R.; Shivanna, R.; Trindade, G.F.; Watts, J.F.; Xu, Z.; et al. Enhanced photovoltage for inverted planar heterojunction perovskite solar cells. *Science* **2018**, *360*, 1442–1446. [CrossRef]
38. Chen, C.-P.; Huang, C.-Y.; Chuang, S.-C. Highly thermal stable and efficient organic photovoltaic cells with crosslinked networks appending open-cage fullerenes as additives. *Adv. Funct. Mater.* **2015**, *25*, 207–213. [CrossRef]
39. Murata, M.; Morinaka, Y.; Murata, Y.; Yoshikawa, O.; Sagawa, T.; Yoshikawa, S. Modification of the σ-framework of [60]fullerene for bulk-heterojunction solar cells. *Chem. Commun.* **2011**, *47*, 7335–7337. [CrossRef]
40. Chen, C.-P.; Lin, Y.-W.; Horng, J.-C.; Chuang, S.-C. Open-cage fullerenes as n-type materials in organic photovoltaics: Relevance of frontier energy levels, carrier mobility and morphology of different sizable open-cage fullerenes with power conversion efficiency in devices. *Adv. Energy Mater.* **2011**, *1*, 776–780. [CrossRef]
41. Artigas, A.; Pla-Quintana, A.; Lledó, A.; Roglans, A.; Solà, M. Expeditious preparation of open-cage fullerenes by Rhodium(I)-catalyzed [2+2+2] cycloaddition of diynes and C60: An experimental and theoretical study. *Chem. Eur. J.* **2018**, *24*, 10653–10661. [CrossRef]
42. Artigas, A.; Lledó, A.; Pla-Quintana, A.; Roglans, A.; Solà, M. Cover feature: A computational study of the intermolecular [2+2+2] cycloaddition of acetylene and C60 catalyzed by wilkinson's catalyst. *Chem. Eur. J.* **2017**, *23*, 14977. [CrossRef]
43. Closs, G.L.; Gautam, P.; Zhang, D.; Krusic, P.J.; Hill, S.A.; Wasserman, E. Steady-state and time-resolved direct detection EPR spectra of fullerene triplets in liquid solution and glassy matrixes: evidence for a dynamic Jahn-Teller effect in triplet C60. *J. Phys. Chem.* **1992**, *96*, 5228–5231. [CrossRef]
44. Sun, Q.J.; Wang, H.Q.; Yang, C.H.; Li, Y.F. Synthesis and electroluminescence of novel copolymers containing crown ether spacers. *J. Mater. Chem.* **2003**, *13*, 800–806. [CrossRef]
45. Liang, P.-W.; Liao, C.-Y.; Chueh, C.-C.; Zuo, F.; Williams, S.T.; Xin, X.-K.; Lin, J.; Jen, A.K.Y. Additive enhanced crystallization of solution-processed perovskite for highly efficient planar-heterojunction solar cells. *Adv. Mater.* **2014**, *26*, 3748–3754. [CrossRef]

46. Wu, C.-G.; Chiang, C.-H.; Chang, S.H. A perovskite cell with a record-high-Voc of 1.61 V based on solvent annealed $CH_3NH_3PbBr_3$/ICBA active layer. *Nanoscale* **2016**, *8*, 4077–4085. [CrossRef]
47. Chen, S.; Hou, Y.; Chen, H.; Richter, M.; Guo, F.; Kahmann, S.; Tang, X.; Stubhan, T.; Zhang, H.; Li, N.; et al. Exploring the limiting open-circuit voltage and the voltage loss mechanism in planar ch3nh3pbbr3 perovskite solar cells. *Adv. Energy Mater.* **2016**, *6*, 1600132. [CrossRef]

© 2019 by the authors. Licensee MDPI, Basel, Switzerland. This article is an open access article distributed under the terms and conditions of the Creative Commons Attribution (CC BY) license (http://creativecommons.org/licenses/by/4.0/).

Chapter 6. A Rh-catalyzed cycloisomerization/Diels-Alder cascade reaction of 1,5-bisallenes for the synthesis of polycyclic heterocycles

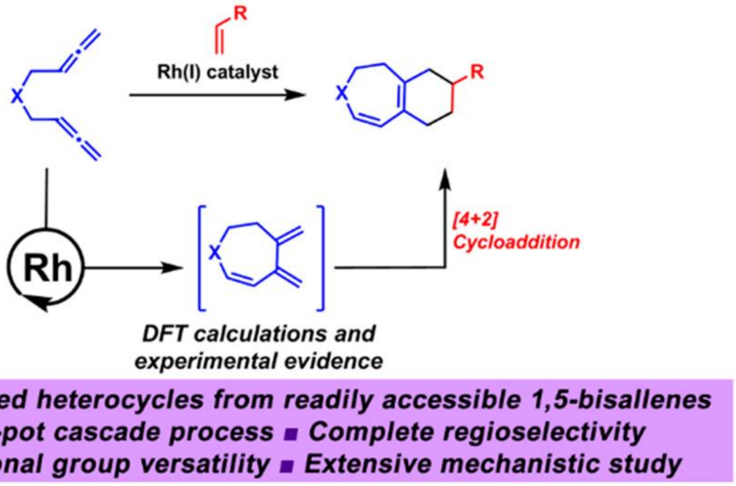
R
Rh(I) catalyst
X
R
Rh
X
[4+2] Cycloaddition
DFT calculations and experimental evidence
■7-membered heterocycles from readily accessible 1,5-bisallenes
■ One-pot cascade process ■ Complete regioselectivity
■ Functional group versatility ■ Extensive mechanistic study

Published in: *Org. Lett.* **2019**, *21*, 6608.

A**bstract:** A novel methodology to transform bisallenes into a variety of polycyclic derivatives employing rhodium(I) catalysis has been developed. This transformation encompasses an intramolecular Rh-catalyzed cycloisomerization of bisallenes **1** to deliver a reactive cycloheptadiene, which concomitantly undergoes a regioselective [4 + 2] cycloaddition with alkenes. A complete mechanistic study of this transformation has been undertaken including DFT calculations. Overall, the methodology presented here constitutes a new and straightforward entry to polycyclic dihydroazepine and dihydrooxepine derivatives employing catalytic methods.

Reproduced with permission from:

Artigas, A.; Vila, J.; Lledó, A.; Solà, M.; Pla-Quintana, A.; Roglans, A. A Rh-Catalyzed Cycloisomerization/Diels–Alder Cascade Reaction of 1,5-Bisallenes for the Synthesis of Polycyclic Heterocycles. *Org. Lett.* **2019**, *21*, 6608. © 2019 American Chemical Society.

OL Organic Letters

Letter

Cite This: *Org. Lett.* 2019, 21, 6608−6613

pubs.acs.org/OrgLett

A Rh-Catalyzed Cycloisomerization/Diels−Alder Cascade Reaction of 1,5-Bisallenes for the Synthesis of Polycyclic Heterocycles

Albert Artigas, Jordi Vila, Agustí Lledó, Miquel Solà,* Anna Pla-Quintana, and Anna Roglans*

Institut de Química Computacional i Catàlisi (IQCC) and Departament de Química, Universitat de Girona (UdG), Facultat de Ciències, C/Maria Aurèlia Capmany, 69, 17003-Girona, Catalunya, Spain

Supporting Information

ABSTRACT: A novel methodology to transform bisallenes into a variety of polycyclic derivatives employing rhodium(I) catalysis has been developed. This transformation encompasses an intramolecular Rh-catalyzed cycloisomerization of bisallenes **1** to deliver a reactive cycloheptadiene, which concomitantly undergoes a regioselective [4 + 2] cycloaddition with alkenes. A complete mechanistic study of this transformation has been undertaken including DFT calculations. Overall, the methodology presented here constitutes a new and straightforward entry to polycyclic dihydroazepine and dihydrooxepine derivatives employing catalytic methods.

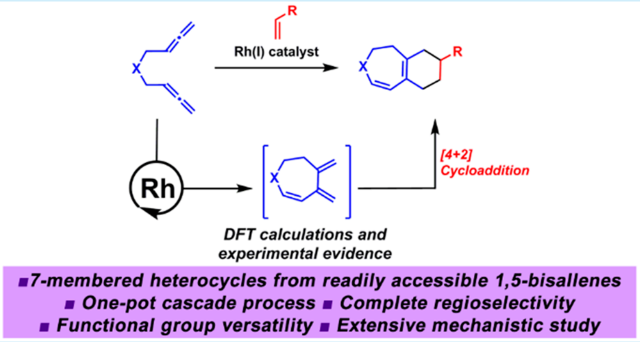
R
Rh(I) catalyst
X
R
Rh
X
[4+2] Cycloaddition
DFT calculations and experimental evidence
■ 7-membered heterocycles from readily accessible 1,5-bisallenes
■ One-pot cascade process ■ Complete regioselectivity
■ Functional group versatility ■ Extensive mechanistic study

Downloaded via UNIVERSITAT DE GIRONA on October 8, 2019 at 07:22:43 (UTC).
See https://pubs.acs.org/sharingguidelines for options on how to legitimately share published articles.

Transition-metal catalyzed cyclization reactions of unsaturated compounds have enormous synthetic potential for the preparation of a wide range of carbocyclic and heterocyclic scaffolds in a single step with perfect atom economy.[1] Among the different unsaturated substrates available, increasing attention has been focused toward the use of allenes, which have now become an established member of the synthetic arsenal for cyclization reactions and related processes.[2] Given that allenes are cumulated systems with two contiguous carbon−carbon double bonds, the control of the chemoselectivity—i.e., which of the two double bonds reacts—makes the construction of various products from one single substrate possible. The available chemical space is obviously increased when two allene moieties are involved.

When 1,5-bisallenes are treated under catalysis by transition metals, products with 5-, 6-, or 7-membered rings can be obtained. Palladium, platinum, and gold favor carbocyclization processes. Under palladium catalysis, 5-membered rings have been obtained by the groups of Ma, Yu, and Kang.[3] More recently, Bäckvall and co-workers described the formation of 7-membered rings.[4] A similar trend was observed using platinum, which allowed the synthesis of products featuring 5-[5] and 7-membered[6] rings. An unexpected example of a rare [2 + 2] cycloaddition of bisallenes has been described using *N*-heterocyclic carbene gold(I) catalysis to deliver 6-membered rings.[7]

On the other hand, rhodium-promoted cyclizations of 1,5-bisallenes are postulated to proceed via oxidative cyclization. Ma and co-workers[8] described a 2-fold cyclization of terminal bisallene under rhodium catalysis. The mechanism was postulated to be a [2 + 2 + 2] cycloaddition followed by a Diels−Alder reaction. The initial oxidative coupling can involve either the two internal double bonds or an internal and an external double bond of the two allene moieties, affording 5-membered rhodacycles fused to either 5- or 6-membered rings, respectively (Scheme 1a). The same group[9]

Scheme 1. Previous Studies in Rh(I)-Catalyzed Cyclization Reactions of 1,5-Bisallenes

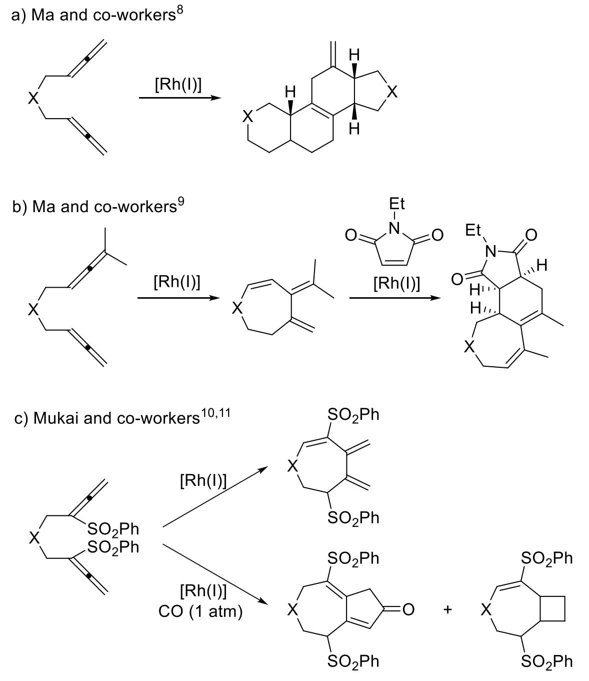
a) Ma and co-workers[8]
X
[Rh(I)]
H
H
X
X
H
b) Ma and co-workers[9]
X
[Rh(I)]
X
Et
N
O
O
[Rh(I)]
Et
N
O
O
H
H
H
X
c) Mukai and co-workers[10,11]
X
SO_2Ph
SO_2Ph
[Rh(I)]
X
SO_2Ph
SO_2Ph
[Rh(I)]
CO (1 atm)
X
SO_2Ph
SO_2Ph
O
+
X
SO_2Ph
SO_2Ph

Received: June 13, 2019
Published: July 11, 2019

ACS Publications © 2019 American Chemical Society

DOI: 10.1021/acs.orglett.9b02032
Org. Lett. 2019, 21, 6608−6613

described the synthesis of seven-membered trienes via Rh-catalyzed cycloisomerization of 1,5-bisallenes with substituents at the terminal positions (Scheme 1b). When these dienes were treated with *N*-ethyl maleimide under rhodium catalysis, the expected [4 + 2] adduct was not obtained, but rather a product derived from an initial isomerization of the double bonds followed by Diels–Alder cycloaddition. Mukai and co-workers[10] also managed to isolate an exocyclic diene when the initial bisallene was terminal although these bisallenes had the particularity of having two SO_2Ph groups at the internal carbon atom of the allene (Scheme 1c). Carbonylative [2 + 2 + 1] cycloadditions have been described by the groups of Mukai[10,11] (Scheme 1c) and Chung,[12] although this latter group used cobalt/rhodium heterobimetallic nanoparticles. In both cases, the authors postulated that the external double bonds of both allenes were involved in the oxidative cyclization step, affording a seven-membered scaffold. In Mukai's studies, a [2 + 2] cycloadduct without CO incorporation was usually obtained as by-product.

Azepine- and oxepine-containing fused ring systems are found in some pharmacologically active compounds and in natural products,[13] and their efficient synthesis is still highly challenging. Therefore, developing cycloaddition reactions of bisallenes with a third unsaturation being able to control the formation of a seven-membered ring is highly desirable. To the best of our knowledge, the Pauson–Khand-type reaction developed by Mukai[11] is the only example of such a process reported to date. Given these precedents, and based on our previous experience with Rh-catalyzed cycloaddition reactions involving allenes,[14] we envisaged developing a cycloaddition reaction between 1,5-bisallenes and alkenes with the aim of controlling the reaction toward the synthesis of fused seven-six-membered bicyclic systems.

We started by studying the cycloaddition of *N*-tosyl-tethered bisallene **1a** and ethyl acrylate **2a** (see Table 1) using 10% mol of cationic rhodium complex $[Rh(cod)_2]BF_4$ with (*R*)-BINAP in THF/CH_2Cl_2 (4:1). Two different compounds were obtained: compound **3aa**, with a 4-aza-bicyclo[5.4.0]undeca-1(7),2-diene skeleton, and the seven-membered cross-conjugated triene **4a**. When the bulky phosphine DTBM-Segphos was used, the yield of **3aa** was improved to 65%, and the yield of triene **4a** was reduced to 5%. However, **5a**, originating from the cycloisomerization of the bisallene, was obtained in 15% yield.[15] Lowering the temperature to 40 °C avoided the formation of **4a**, resulting in our optimized set of conditions (see the Supporting Information (SI) for the complete optimization study).

Table 1. Optimization of the Rhodium(I)-Catalyzed Cycloaddition of Bisallene 1a with Alkene 2a[a]

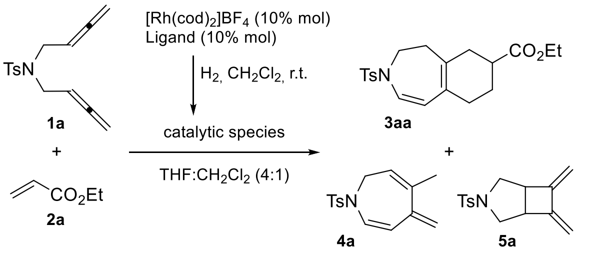

entry	ligand	temp (°C)	reaction time (h)	yield (%) **3aa**/**4a**/**5a**
1	(*R*)-BINAP	65	4	49/45/–
2	(*R*)-DTBM-SegPhos	65	4	65/05/15
3	(*R*)-DTBM-SegPhos	40	16	60/–/15

[a] Reaction conditions: 0.18 mmol of **1a** ([**1a**] = 9 mM), 50 equiv of **2a**, 10% mol of Rh catalyst in 20 mL of THF/CH_2Cl_2 (4:1) at the indicated temperature and time. The 10% mol mixture of $[Rh(cod)_2]BF_4$ and phosphine was treated with hydrogen in dichloromethane (CH_2Cl_2) solution for catalyst activation prior to substrate addition.

Having established the optimum reaction conditions, the scope of the reaction was then evaluated, as shown in Figure 1.

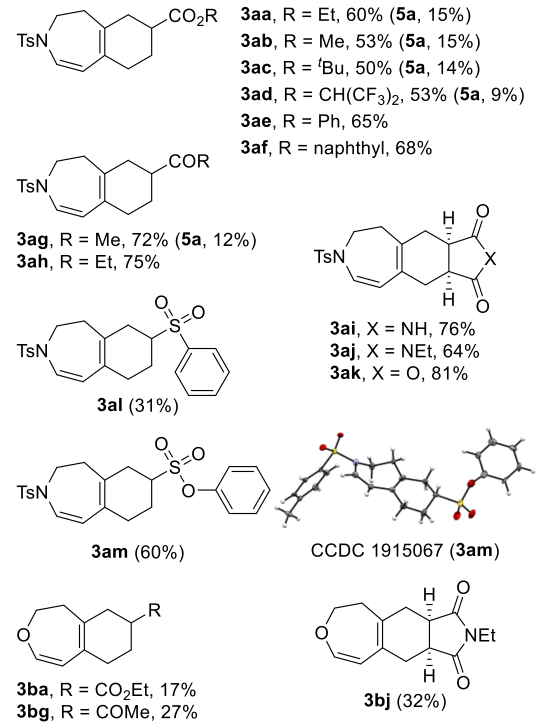

Figure 1. Scope of the cycloaddition of bisallenes **1** with alkenes **2**.

Overall, the reaction proceeds in good to moderate yields with a wide range of alkenes. Reactions involving alkyl and aryl acrylates (**2a**–**2f**) deliver products in yields ranging between 50% and 68%. Vinyl alkyl ketones **2g** and **2h** also produced the corresponding cycloadducts in 72% and 75% yields, respectively. In some cases, byproduct **5a** was also formed and separated from the desired product by column chromatography.[16] Disubstituted cyclic alkenes, such as maleimide (**2i**), *N*-ethyl maleimide (**2j**), and maleic anhydride (**2k**), underwent the cycloaddition reaction efficiently to produce derivatives **3ai**, **3aj**, and **3ak** in excellent yields and avoiding the formation of byproduct **5a**. The use of phenyl vinyl sulfone (**2l**) and phenyl vinyl sulfonate (**2m**) afforded derivatives **3al** and **3am** in 31% and 60% yields, respectively, and, again, no traces of **5a**. In addition, two 1 mmol scale reactions using ethyl acrylate **2a** and vinyl methyl ketone **2g** were performed, affording a 69% yield of **3aa** (15% yield of **5a**) and a 77% yield of **3ag** (14% yield of **5a**), respectively. Single crystal X-ray diffraction analysis of compound **3am** (CCDC 1915067) allowed us to unambiguously establish the structure of the cycloadduct obtained.[17]

To extend the methodology to other 1,5-bisallenes, oxygen-tethered bisallene **1b** was prepared and reacted with three different alkenes: ethyl acrylate **2a**, methyl vinyl ketone **2g**, and

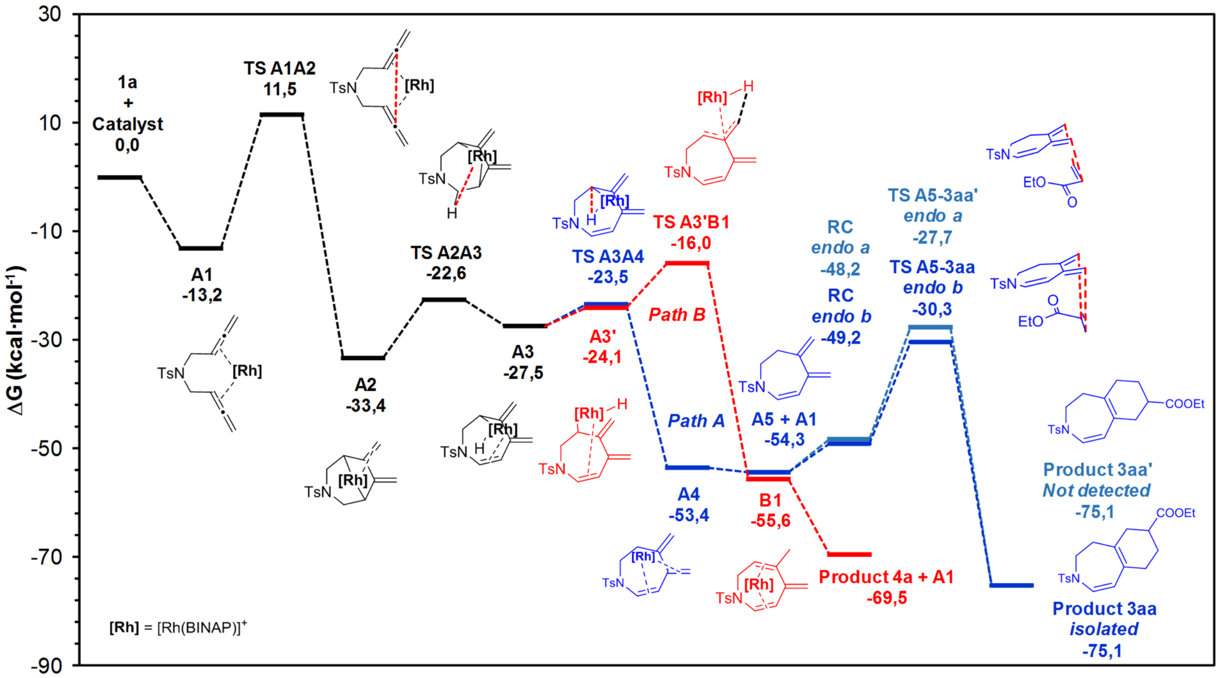

Figure 2. Gibbs energy profile for the tandem cycloisomerization/Diels–Alder cycloaddition (Path A, blue) leading to product **3aa** and cycloisomerization reaction (Path B, red) leading to product **4a**. RC = Reactant complex.

N-ethylmaleimide **2j** affording the corresponding derivatives **3ba**, **3bg**, and **3bj** in moderate yields ranging from 17% to 32%.

Since a stereogenic center was generated in derivatives **3**, the enantiomeric excess was measured in all cases, but no enantioinduction was observed regardless of the substrate or the ligand used. This result is commensurate with the mechanism proposed for this transformation (*vide infra*).

To gain further understanding of the reaction mechanism, we completed our study by evaluating computationally the process that transforms **1a** into **3aa**. The Gibbs energy profile computed at 313.15 K and 1 atm with the M06L-D3/cc-pVTZ-PP/SMD(76% THF, 24% CH_2Cl_2)[18]//B3LYP-D3/cc-pVDZ-PP method is depicted in Figure 2, and the catalytic cycle is shown in Figure 3 and the molecular structures of the TSs in Figure S4. To reduce the computational effort required, BINAP was chosen as the model phosphine ligand instead of the optimal ligand (*R*)-DTBM-Segphos (see SI for a complete description of the computational methods).

The reaction starts with η^4-coordination of $[Rh(BINAP)]^+$ to the two internal double bonds of 1,5-bisallene **1a** to form the square-planar 16-electron intermediate **A1**. This process is exergonic by 13.2 kcal/mol. Upon coordination, intermediate **A1** readily experiences oxidative coupling at the central carbon atoms of both allene moieties to deliver intermediate **A2**, a rhodabicyclo[3.2.1]octane complex featuring two contiguous exocyclic methylene groups. This first step has a Gibbs energy barrier of 24.7 kcal/mol through **TS A1A2** and is exergonic by 20.2 kcal/mol. Intermediate **A2** is an 18-electron species and shows a distorted octahedral geometry in which one of the O atoms of the tosyl group occupies one of the six positions (d_{Rh-O}= 2.231 Å) and one of the two exocyclic double bonds is η^2-coordinated to the Rh center (d_{Rh-C} = 2.196 and 2.132 Å). The fact that internal bonds in allenes are more reactive than their external counterparts has already been reported in previous studies by our group.[14a,d] An alternative mechanism for this transformation by which a bisallylic rhodacyclopentane intermediate resulted from the initial oxidative coupling was proposed by Ma[9] and by Mukai,[10] although no mechanistic studies were reported. Our computational calculations seem to contradict this proposal, although care should be taken when comparing these two transformations owing to the different substitution patterns of the bisallene precursors involved.

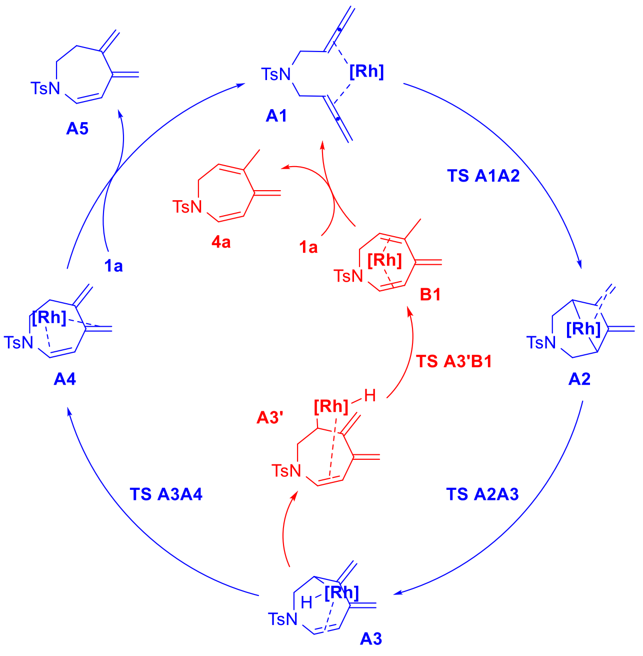

Figure 3. Catalytic cycle for the two Rh(I)-catalyzed tandem cycloisomerization reactions of 1,5-bisallene **1a** leading to intermediate **A5** (Path A, blue) and product **4a** (Path B, red).

A2 is converted into intermediate **A3** through a β-hydride elimination mechanism. This process is slightly endergonic by 5.9 kcal/mol and has a Gibbs energy barrier of 10.8 kcal/mol

(**TS A2A3**). The Rh center in intermediate **A3** is η^2-coordinated to the newly formed C═C bond and presents a distorted tetrahedral geometry. Reductive elimination from intermediate **A3** to form **A4** has to surmount a barrier of 4.0 kcal/mol (**TS A3A4**) and releases 25.9 kcal/mol. Subsequent release of the initial Rh(I) complex leads to triene intermediate **A5**, completing the catalytic cycle (Path A in Figures 2 and 3). Alternatively, intermediate **A3** can experience a rearrangement with a rotation through the C−Rh bond that approaches the hydride coordinated to Rh to one of the C═C exocyclic double bonds giving **A3′** (Path B in Figures 2 and 3). Reductive elimination through **TS A3′B1** has a cost of 8.1 kcal/mol and is exergonic by 31.5 kcal/mol. This alternative mechanism provides a rational explanation for the formation of compound **4a**.

On the other hand (Path A in Figure 2), the formation of intermediate **A5** is followed by [4 + 2] cycloaddition with ethyl acrylate **2a** to deliver compound **3aa**. The formation of the desired reaction product **3aa** has an overall reaction energy (ΔG_r) of −75.1 kcal/mol. Importantly, the regiochemistry of the reaction can also be explained by our computed reaction mechanism. While "*endo a*" approximation of the dienophile (i.e., **TS A5−3aa′**) has a Gibbs energy barrier of 26.6 kcal/mol, the "*endo b*" approximation (i.e., **TS A5−3aa**) has a lower cost of 24.0 kcal/mol. Such a difference in energy ($\Delta\Delta G^\ddagger = 2.6$ kcal/mol) accounts for the selective formation of the actual reaction product **3aa**.

It has not escaped our attention that, in the same way that intermediate **A5** does, intermediates **A2**, **A3**, and **A4** are ripe to experience [4 + 2] cycloaddition with ethyl acrylate **2a** before β-hydride elimination, reductive elimination or catalyst release takes place, respectively. Considering this, we computed all potential reaction paths leading to reaction product **3aa** (see Figures S5, S6, and S7 in the SI). We found that all alternative reaction mechanisms analyzed have higher barriers or do not explain the observed regioselectivity.

In summary, the reaction mechanisms leading to compounds **A5** and **4a** (paths A and B in Figure 2) have an energetic span between the turnover frequency (TOF) determining intermediate (TDI, **A1**) and TOF determining transition state (TDTS, **TS A1A2**) of 24.7 kcal/mol.[19] Once formed, intermediate **A5** reacts with ethyl acrylate **2a** through a regioselective catalyst-free Diels−Alder cycloaddition to provide compound **3aa**.

With the aim of fully validating the proposed reaction mechanism, we completed our study by performing additional experiments. First, the involvement of reaction byproduct **5a** as a reaction intermediate of the catalytic cycle was ruled out by heating a mixture of this compound and ethyl acrylate **2a** in the absence and presence (Schemes S4 and S5) of the rhodium catalytic mixture. In both cases, only starting materials were recovered. Computational calculations are again in good agreement with the experiments (see Figure S8 in the SI).

Finally, in an attempt to isolate intermediate **A5**, we performed the reaction in the absence of a dienophile (Scheme 2). Even though **A5** could not be obtained as a stable reaction product, we found indirect evidence of its formation. Homodimer **6a** was isolated in 58% yield, indicating that it is a promiscuous intermediate acting as both the diene and the dienophile in Diels−Alder reactions. Remarkably, only one out of the four possible isomers of the dimer was obtained. This last finding not only gives an experimental confirmation of our computational results, but opens new avenues for the preparation of complex spirocyclic compounds in a straightforward and selective manner starting from 1,5-bisallenes. The isolation by Ma and co-workers[8] of another homodimer of **1a** (Scheme 1a), when a different catalytic system was employed, is worth noting and highlights the importance of the coordination environment in favoring disparate mechanistic outcomes.

Scheme 2. Additional Mechanistic Experiments Performed

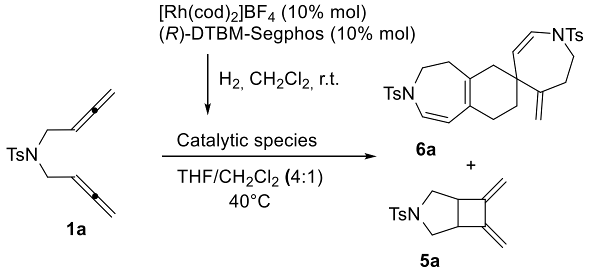
[Rh(cod)$_2$]BF$_4$ (10% mol)
(*R*)-DTBM-Segphos (10% mol)
H$_2$, CH$_2$Cl$_2$, r.t.
Catalytic species
THF/CH$_2$Cl$_2$ (4:1)
40°C
TsN
1a
TsN
NTs
6a
+
TsN
5a

A related work by Breit and co-workers[20] was described during the preparation of this manuscript, reporting on a rhodium-catalyzed cycloisomerization of 1,6-allenenes to afford six-membered ring exocyclic 1,3-dienes and further tandem Diels−Alder reaction. Our allene/allene/alkene triad of unsaturated partners offers a much complex mechanistic scenario as exemplified by our mechanistic study, and therefore a commensurate potential for developing new reactivity manifolds.

In conclusion, we have developed an efficient cascade process based on an intramolecular Rh-catalyzed cycloisomerization of 1,5-bisallenes (**1**) leading to a nonisolable cycloheptadiene intermediate followed by a regioselective Diels−Alder cycloaddition with alkenes (**2**). The new process affords a variety of polycyclic heterocycles **3** containing dihydroazepine- and dihydrooxepine-fused ring systems. DFT calculations show that the reaction leading to **3aa** from **1a** takes place through an oxidative coupling of the rhodium at the central carbon atoms of both allenes followed by a β-hydride elimination to form intermediate **A3** and reductive elimination to give intermediate **A5**. An uncatalyzed and regioselective Diels−Alder cycloaddition to **A5** generates the final product.

■ ASSOCIATED CONTENT

Ⓢ Supporting Information

The Supporting Information is available free of charge on the ACS Publications website at DOI: 10.1021/acs.orglett.9b02032.

Experimental procedures, optimization of the reaction, compound characterization data, crystallographic data and computational data (PDF)

Accession Codes

CCDC 1915067 contains the supplementary crystallographic data for this paper. These data can be obtained free of charge via www.ccdc.cam.ac.uk/data_request/cif, or by emailing data_request@ccdc.cam.ac.uk, or by contacting The Cambridge Crystallographic Data Centre, 12 Union Road, Cambridge CB2 1EZ, UK; fax: +44 1223 336033.

■ AUTHOR INFORMATION

Corresponding Authors

*E-mail: miquel.sola@udg.edu.

*E-mail: anna.roglans@udg.edu.

ORCID

Albert Artigas: 0000-0002-7351-0066
Agustí Lledó: 0000-0003-3681-6688
Miquel Solà: 0000-0002-1917-7450
Anna Pla-Quintana: 0000-0003-2545-9048
Anna Roglans: 0000-0002-7943-5706

Notes

The authors declare no competing financial interest.

■ ACKNOWLEDGMENTS

We are grateful for the financial support by the Spanish Ministry of Economy and Competitivity (MINECO) (Projects CTQ2017-85341-P and CTQ2017-83587-P, FI predoctoral grant to A.A., RyC Contract RYC2012-11112 to A.L.), the Generalitat de Catalunya (Project 2017-SGR-39, Xarxa de Referència en Química Teòrica i Computacional, ICREA Academia 2014 prize for M.S.), and UdG for an IF predoctoral grant to J.V.

■ REFERENCES

(1) For selected reviews, see: (a) Kotha, S.; Lahiri, K.; Sreevani, G. Design and synthesis of aromatics through [2 + 2 + 2] cyclotrimerization. *Synlett* **2018**, *29*, 2342−2361. (b) Yamamoto, Y. Recent topics of Cp*RuCl-catalyzed annulation reactions. *Tetrahedron Lett.* **2017**, *58*, 3787−3794. (c) Neuhaus, J. D.; Willis, M. C. Homogeneous rhodium(I)-catalysis in *de novo* heterocycle synthesis. *Org. Biomol. Chem.* **2016**, *14*, 4986−5000. (d) Omae, I. Characteristic reactions of group 9 transition metal compounds in organic synthesis. *Appl. Organomet. Chem.* **2009**, *23*, 91−107. (e) Michelet, V.; Toullec, P. Y.; Genêt, J.-P. Cycloisomerization of 1,*n*-enynes: challenging metal-catalyzed rearrangements and mechanistic insights. *Angew. Chem., Int. Ed.* **2008**, *47*, 4268−4315.

(2) For selected and recent reviews, see: (a) Lledó, A.; Pla-Quintana, A.; Roglans, A. Allenes, versatile unsaturated motifs in transition-metal-catalysed [2 + 2 + 2] cycloaddition reactions. *Chem. Soc. Rev.* **2016**, *45*, 2010−2023. (b) Alcaide, B.; Almendros, P.; Aragoncillo, C. Cyclization reactions of bis(allenes) for the synthesis of polycarbo-(hetero)cycles. *Chem. Soc. Rev.* **2014**, *43*, 3106−3135. (c) Kitagaki, S.; Inagaki, F.; Mukai, C. [2 + 2 + 1] Cyclization of allenes. *Chem. Soc. Rev.* **2014**, *43*, 2956−2978. (d) López, F.; Mascareñas, J. L. [4 + 2] and [4 + 3] Catalytic cycloadditions of allenes. *Chem. Soc. Rev.* **2014**, *43*, 2904−2915. (e) Ye, J.; Ma, S. Palladium-catalyzed cyclization reactions of allenes in the presence of unsaturated carbon-carbon bonds. *Acc. Chem. Res.* **2014**, *47*, 989−1000. (f) López, F.; Mascareñas, J. L. Allenes as three-carbon units in catalytic cycloadditions: new opportunities with transition-metal catalysts. *Chem. - Eur. J.* **2011**, *17*, 418−428. (g) Aubert, C.; Fensterbank, L.; Garcia, P.; Malacria, M.; Simonneau, A. Transition metal catalyzed cycloisomerizations of 1,n-allenynes and allenenes. *Chem. Rev.* **2011**, *111*, 1954−1993. (h) Chen, G.; Jiang, X.; Fu, C.; Ma, S. The diversified reactivities of 1,5-bisallenes. *Chem. Lett.* **2010**, *39*, 78−81.

(3) (a) Jiang, X.; Cheng, X.; Ma, S. Controllable [2 + 2] cycloadditions of 1,5-bisallenyl-substituted compounds. *Angew. Chem., Int. Ed.* **2006**, *45*, 8009−8013. (b) Hong, Y.-T.; Yoon, S.-K.; Kang, S.-K.; Yu, C.-M. A stereoselective carbocyclization of bis(allenes) with germylstannane catalyzed by palladium complexes. *Eur. J. Org. Chem.* **2004**, *2004*, 4628−4635. (c) Kang, S. K.; Baik, T. G.; Kulak, A. N.; Ha, Y. H.; Lim, Y.; Park, J. Palladium-catalyzed carbocyclization/silastannylation and distannylation of bis(allenes). *J. Am. Chem. Soc.* **2000**, *122*, 11529−11530.

(4) (a) Zhu, C.; Yang, B.; Qiu, Y.; Bäckvall, J.-E. Highly selective construction of seven-membered carbocycles by olefin-assisted palladium-catalyzed oxidative carbocyclization-alkoxycarbonylation of bisallenes. *Angew. Chem., Int. Ed.* **2016**, *55*, 14405−14408. (b) Zhu, C.; Yang, B.; Mai, B. K.; Palazzotto, S.; Qiu, Y.; Gudmundsson, A.; Ricke, A.; Himo, F.; Bäckvall, J.-E. Highly selective palladium-catalyzed hydroborylative carbocyclization of bisallenes to seven-membered rings. *J. Am. Chem. Soc.* **2018**, *140*, 14324−14333.

(5) Lim, Y. N.; Kim, H.-T.; Yoon, H.-S.; Jang, H.-Y. Regio- and stereoselective reductive cyclization of 1,5-bisallenes under hydrogenation conditions. *Bull. Korean Chem. Soc.* **2011**, *32*, 3117−3119.

(6) Quirós, M. T.; Hurtado-Rodrigo, C.; Muñoz, M. P. Nucleophile dependent formation of 6-and 7-membered *N*-heterocycles by platinum-catalysed cyclisation of 1,5-bisallenes. *Org. Biomol. Chem.* **2017**, *15*, 6731−6737.

(7) Kim, S. M.; Park, J. H.; Kang, Y. K.; Chung, Y. K. *N*-heterocyclic carbene gold(I) catalyzed transformation of *N*-tethered 1,5-bisallenes to 6,7-dimethylene-3-azabicyclo[3.1.1]heptanes. *Angew. Chem., Int. Ed.* **2009**, *48*, 4532−4535.

(8) (a) Ma, S.; Lu, P.; Lu, L.; Hou, H.; Wei, J.; He, Q.; Gu, Z.; Jiang, X.; Jin, X. What can a metal catalyst do with allenes? One-step formation of steroid scaffolds from readily available starting materials. *Angew. Chem., Int. Ed.* **2005**, *44*, 5275−5278. (b) Ma, S.; Lu, L. Rh^{I}-catalyzed bimolecular cyclization between two different 1,5-bisallenes: a combinatorial one-step approach to heterosteroids and mechanistic implications. *Chem. - Asian J.* **2007**, *2*, 199−204. (c) Lu, P.; Ma, S. Rh-catalyzed triple allene approach to bicycle[4.4.0]decene derivatives and its application for the stepwise synthesis of steroid-like tetracyclic skeletons. *Org. Lett.* **2007**, *9*, 5319−5321.

(9) (a) Lu, P.; Ma, S. Observation of new cycloisomerization pattern of 1,5-bisallenes. catalyst and substituent effects. *Org. Lett.* **2007**, *9*, 2095−2097. (b) Lu, P.; Kuang, J.; Ma, S. Carbon-carbon double-bond isomerization and Diels-Alder reaction of dimethyl 5-methylene-4-isopropylidene-2-cycloheptene-1,1-dicarboxylate with dienophiles. *Synlett* **2010**, *2010*, 227−230.

(10) Kawamura, T.; Inagaki, F.; Narita, S.; Takahashi, Y.; Hirata, S.; Kitagaki, S.; Mukai, C. Rhodium(I)-catalyzed intramolecular carbonylative [2 + 2 + 1] cycloadditions and cycloisomerizations of bis(sulfonylallene)s. *Chem. - Eur. J.* **2010**, *16*, 5173−5183.

(11) Inagaki, F.; Narita, S.; Hasegawa, T.; Kitagaki, S.; Mukai, C. Rhodium(I)-catalyzed intramolecular carbonylative [2 + 2 + 1] cycloaddition of bis(allene)s: bicyclo[6.3.0]undecadienones and bicyclo[5.3.0]decadienones. *Angew. Chem., Int. Ed.* **2009**, *48*, 2007−2011.

(12) Park, J. H.; Kim, E.; Kim, H.-M.; Choi, S. Y.; Chung, Y. K. Cobalt/rhodium heterobimetallic nanoparticle-catalyzed carbonylative [2 + 2 + 1] cycloaddition of allenes and bisallenes to Pauson-Khand-type reaction products. *Chem. Commun.* **2008**, 2388−2390.

(13) For selected reviews, see: (a) Meyer, A. G.; Bissember, A. C.; Hyland, C. J. T.; Williams, C. C.; Szabo, M.; Abel, S.-A. G.; Bird, M. J.; Hyland, I. K.; Pham, H. Seven-membered rings, chapter 7. *Prog. Heterocycl. Chem.* **2018**, *30*, 493−550. (b) Nguyen, T. V.; Hartmann, J. M.; Enders, D. Recent synthetic strategies to access seven-membered carbocycles in natural product synthesis. *Synthesis* **2013**, *45*, 845−873. (c) Riley, D. L.; van Otterlo, W. A. L. Oxepines and azepines, Chapter 15. *Heterocycles in Natural Product Synthesis*; Wiley-VCH: Weinheim, Germany, 2011. (d) Kantorowski, E. J.; Kurth, M. J. Expansion to seven-membered rings. *Tetrahedron* **2000**, *56*, 4317−4353. (e) Liu, J.-h.; Steigel, A.; Reininger, E.; Bauer, R. Two new prenylated 3-benzoxepin derivatives as cyclooxygenase inhibitors from *Perilla frutescens* var. *acuta*. *J. Nat. Prod.* **2000**, *63*, 403−405. Selected and recent studies based on the synthesis of benzo[*d*]azepine derivatives: (f) Jiang, B.; Liu, J.-X.; Wei, Y.; Shi, M. Nickel-catalyzed synthesis of benzo[*b*]naphthol[1,2-*d*]azepine via intramolecular radical tandem cyclization of alkyl bromide-tethered alkylidenecyclopropanes. *Org. Lett.* **2018**, *20*, 6229−6233. (g) Nayak, M.; Kang, Y. K.; Kim, I. Altering the cyclization modes: temperature-dependent intramolecular 7-*endo-dig* vs 6-*endo-dig* electrophilic ring closures. *Org. Lett.* **2017**, *19*, 1474−1477. (h) Adamovskyi, M. I.; Ryabukhin, S. V.; Sibgatulin, D. A.; Rusanov, E.; Grygorenko, O. O. Beyond the five and six: evaluation of seven-membered cyclic anhydrides in the Castagnoli-Cushman reaction. *Org. Lett.* **2017**, *19*, 130−133.

(14) (a) Cassú, D.; Parella, T.; Solà, M.; Pla-Quintana, A.; Roglans, A. Rhodium-catalyzed [2 + 2 + 2] cycloaddition reactions of linear allene−ene−ynes to afford fused tricyclic scaffolds: insights into the mechanism. *Chem. - Eur. J.* **2017**, *23*, 14889−14899. (b) Haraburda, E.; Fernández, M.; Gifreu, A.; Garcia, J.; Parella, T.; Pla-Quintana, A.; Roglans, A. Chiral induction in intramolecular Rhodium-catalyzed [2 + 2 + 2] cycloadditions of optically active allene−ene/yne−allene substrates. *Adv. Synth. Catal.* **2017**, *359*, 506−512. (c) Haraburda, E.; Lledó, A.; Roglans, A.; Pla-Quintana, A. Dehydrogenative [2 + 2 + 2] cycloaddition of cyano-yne-allene substrates: convenient access to 2,6-naphthyridine scaffolds. *Org. Lett.* **2015**, *17*, 2882−2885. (d) Haraburda, E.; Torres, Ò.; Parella, T.; Solà, M.; Pla-Quintana, A. Stereoselective Rhodium-catalysed [2 + 2 + 2] cycloaddition of linear allene−ene/yne−allene substrates: reactivity and theoretical mechanistic studies. *Chem. - Eur. J.* **2014**, *20*, 5034−5045. For a review, see: (e) Pla-Quintana, A.; Roglans, A. Chiral induction in [2 + 2 + 2] cycloaddition reactions. *Asian J. Org. Chem.* **2018**, *7*, 1706−1718.

(15) Compound **5a** was synthesized by Ma and co-workers [see ref 3a] through a palladium(0)-catalyzed [2 + 2] cycloaddition of bisallene **1a**.

(16) The formation or absence of product **5a** is surprising (especially comparing **3ag** and **3ah**) and points to a delicate balance of reaction rates among the multistep processes leading to products **3** and **5**.

(17) The thermal ellipsoids in the ORTEP plot of the X-ray structure of **3am** are drawn at 50% probability.

(18) (76% THF, 24% CH_2Cl_2) is equivalent to a 4:1 v/v ratio of THF/CH_2Cl_2.

(19) (a) Kozuch, S.; Shaik, S. Kinetic-quantum chemical model for catalytic cycles: the Haber-Bosch process and the effect of reagent concentration. *J. Phys. Chem. A* **2008**, *112*, 6032−6041. (b) Kozuch, S.; Shaik, S. How to conceptualize catalytic cycles? The energetic span model. *Acc. Chem. Res.* **2011**, *44*, 101−110.

(20) Zhou, Y.; Nikbakht, A.; Bauer, F.; Breit, B. Rhodium catalyzed cycloisomerization and tandem Diels-Alder reaction for facile access to diverse bicyclic and tricyclic heterocycles. *Chem. Sci.* **2019**, *10*, 4805−4810.

Chapter 7. Regioselectivity in Diels–Alder cycloadditions of $^{\#6094}C_{68}$ fullerene with a triplet ground state

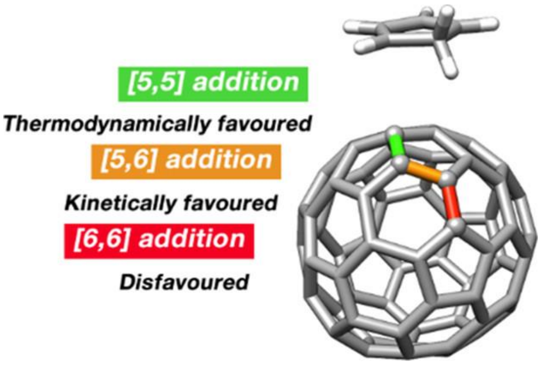

Published in: *J. Org. Chem.* **2019**, 84, 9017.

Abstract: To achieve full control on the regioselectivity of chemical additions to fullerenes is a major goal in the field of reactivity of carbon nanostructures. In this work, we computationally analyze the regioselectivity of the Diels–Alder (DA) reaction of cyclopentadiene to the hollow non-isolated pentagon rule (IPR) $^{\#6094}C_{68}$ fullerene, which possesses a triplet ground state. Our aim is to check whether the typically favored [6,6]-addition in fullerenes can be shifted to the [5,6] bonds in $^{\#6094}C_{68}$ due to the change in the ground state. Our results show that the [5,5] adduct is the thermodynamic reaction product, whereas the kinetic product is the [5,6] bond of type F, adjacent to a pentalene unit. As compared to the singlet state, in the triplet state, the Gibbs barrier for the attack to the [5,6] bond of $^{\#6094}C_{68}$ is reduced by about 5 kcal·mol^{-1}, the DA cycloaddition becoming more regioselective. Our energy decomposition analysis shows that the change of regioselectivity in the DA reaction of hollow fullerenes from the usual [6,6] bond to the [5,6] bond in $^{\#6094}C_{68}$ is driven by higher stabilizing orbital interactions in the latter bond favored by the spin density accumulation around the two pentalene units of the cage. The findings of this investigation complement those of earlier studies on regioselectivity of IPR fullerenes and endohedral metallofullerenes.

Reproduced with permission from:

Artigas, A.; Fernández, I.; Solà, M. Regioselectivity in Diels–Alder Cycloadditions of $^{\#6094}C_{68}$ Fullerene with a Triplet Ground State. *J. Org. Chem.* **2019**, *84*, 9017. © 2019 American Chemical Society.

JOC The Journal of Organic Chemistry
Article
Cite This: J. Org. Chem. 2019, 84, 9017−9024
pubs.acs.org/joc

Downloaded via UNIVERSITAT DE GIRONA on October 8, 2019 at 07:40:33 (UTC).
See https://pubs.acs.org/sharingguidelines for options on how to legitimately share published articles.

Regioselectivity in Diels−Alder Cycloadditions of $^{\#6094}C_{68}$ Fullerene with a Triplet Ground State

Albert Artigas,[†] Israel Fernández,*,[‡] and Miquel Solà*,[†]

[†]Institut de Química Computacional i Catàlisi (IQCC) and Departament de Química, Universitat de Girona, C/Maria Aurèlia Capmany 69, 17003 Girona, Catalonia, Spain

[‡]Departamento de Química Orgánica I and Centro de Innovación en Química Avanzada (ORFEO-CINQA), Facultad de Ciencias Químicas, Universidad Complutense de Madrid, 28040 Madrid, Spain

Supporting Information

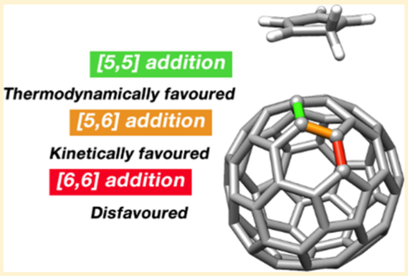

ABSTRACT: To achieve full control on the regioselectivity of chemical additions to fullerenes is a major goal in the field of reactivity of carbon nanostructures. In this work, we computationally analyze the regioselectivity of the Diels−Alder (DA) reaction of cyclopentadiene to the hollow nonisolated pentagon rule (IPR) $^{\#6094}C_{68}$ fullerene, which possesses a triplet ground state. Our aim is to check whether the typically favored [6,6]-addition in fullerenes can be shifted to the [5,6] bonds in $^{\#6094}C_{68}$ due to the change in the ground state. Our results show that the [5,5] adduct is the thermodynamic reaction product, whereas the kinetic product is the [5,6] bond of type F, adjacent to a pentalene unit. As compared to the singlet state, in the triplet state, the Gibbs barrier for the attack to the [5,6] bond of $^{\#6094}C_{68}$ is reduced by about 5 kcal·mol^{-1}, the DA cycloaddition becoming more regioselective. Our energy decomposition analysis shows that the change of regioselectivity in the DA reaction of hollow fullerenes from the usual [6,6] bond to the [5,6] bond in $^{\#6094}C_{68}$ is driven by higher stabilizing orbital interactions in the latter bond favored by the spin density accumulation around the two pentalene units of the cage. The findings of this investigation complement those of earlier studies on regioselectivity of IPR fullerenes and endohedral metallofullerenes.

1. INTRODUCTION

Fullerenes are hollow cage molecules formed exclusively by carbon atoms arranged in a variable number of hexagons and twelve pentagons.[1−3] Since the discovery of C_{60},[4] many different hollow fullerenes have been reported. The great majority follow the so-called isolated pentagon rule (IPR) formulated by Kroto.[5] This rule states that fullerenes with isolated pentagons are preferred over those containing adjacent five-membered rings (5-MRs). The reason behind this preference is that bonds shared by two pentagons (pentalene units) increase the local strain affording less-stable molecules. Indeed, the pentagonal adjacency penalty rule quantifies the destabilization produced by adjacent pentagon pairs (APPs) in 19−24 kcal·mol^{-1} per APP.[6] Stabilization of non-IPR fullerene molecules[7] can be achieved by releasing the strain generated by fused 5-MRs through exohedral functionalization like in $C_{50}Cl_{10}$[8] or by inclusion of metal clusters in endohedral metallofullerenes (EMFs) such as $Sc_2@C_{66}$[9] or $Sc_3N@C_{68}$.[10,11] Non-IPR fullerenes are expected to be more reactive than their IPR counterparts. In 2012, the non-IPR fullerene $^{\#6094}C_{68}$ was produced and captured as a chloride $C_{68}Cl_8$.[12] $^{\#6094}C_{68}$ cannot be isolated in the bulk and, therefore, this elusive cage is just an intermediate that can be captured by chlorination. Interestingly, $^{\#6094}C_{68}$ is one of the few hollow nonfunctionalized fullerenes that have a triplet ground state.[13] The stability of the triplet ground state of $^{\#6094}C_{68}$ is attributed to the aromatic character of this electronic state[13] as compared to the antiaromatic character of its singlet state.[12] The singlet−triplet splitting energy in $^{\#6094}C_{68}$ was calculated to be ca. 8 kcal·mol^{-1}.[13]

Fullerenes obeying the IPR have two different types of C−C bonds: the [6,6] bonds in the ring junctions between two 6-MRs and the [5,6] bonds in the connection between a hexagon and a pentagon. For non-IPR species, one has to also consider the presence of [5,5] bonds (see Scheme 1 for the different bond types). The [6,6] bonds are more reactive than the [5,6] bonds in IPR hollow fullerenes, while [5,6] additions are more

Scheme 1. Classification of the Different Bond Types That Are Present in Fullerene $^{\#6094}C_{68}$

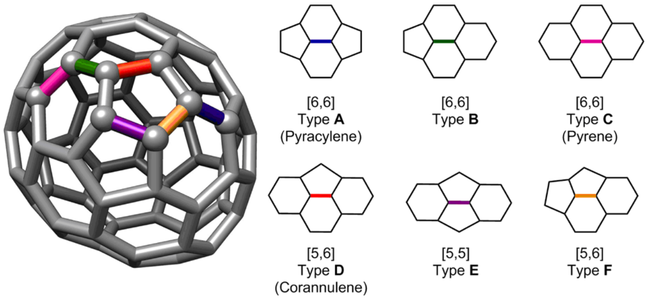

Received: April 3, 2019
Published: June 17, 2019

ACS Publications © 2019 American Chemical Society

DOI: 10.1021/acs.joc.9b00921

common in EMFs.[14,15] From a synthetic point of view, it would be desirable to have control on the regioselectivity of the exohedral cycloadditions to fullerenes.[1,16] Several years ago, some of us found that successive reductions of C_{60} ($C_{60}{}^{-q}$, $q = 0-6$) modify the regioselectivity of the Diels−Alder (DA) additions, from the usual [6,6] addition in neutral species to addition of the [5,6] bond when the number of electrons added to C_{60} was higher than four.[17] This modification of the regioselectivity was explained through the local aromaticity changes in the 5- and 6-MRs of the fullerene in the reduction process. Electrons added to the cage accumulate in the 5-MRs that gain the cyclopentadienyl anion character, increasing their aromaticity significantly. In this situation, addition to a [5,6] bond of type D ($[5,6]_D$), which involves breaking the aromaticity of a unique 5-MR, becomes more favorable than addition to a [6,6] bond of type A that destroys the aromaticity of two 5-MRs. Unfortunately, experimental proof of this change of reactivity was not possible because of the difficulties associated with generating cycloadducts from highly negatively charged fullerenes like $C_{60}{}^{-5}$ or $C_{60}{}^{-6}$. More recently, some of us reported that the regioselectivity of the DA cycloaddition changes from [6,6] to [5,6] addition when the spin of the fullerenic cage is increased.[18] Indeed, for the triplet C_{60}, the most favored addition is already the [5,6] addition. Not only for the triplet, but also for high spin states, the most favored product is the [5,6] adduct, whereas in the ground state it is the [6,6] product. As before, the origin of this change in the regioselectivity is connected to the local aromatic character of the molecular cage. In open-shell C_{60}, the spin density accumulates in the 5-MRs that may become more aromatic by getting more triplet cyclopentadienyl cation character. Again, addition to a $[5,6]_D$ bond, which involves breaking the aromaticity of a unique 5-MR, is favored over addition to a $[6,6]_A$ bond that cancels the aromaticity of two 5-MRs. Despite computations predicting a change of regioselectivity when moving from S_0 to T_1, the experimental results showed that the DA cycloaddition between isoindene and photoexcited $^3C_{60}$ also generates the [6,6] adduct instead of the predicted [5,6] one.[18] By analyzing the reaction in more detail, we computationally found that in the T_1 state the reaction goes through an intersystem crossing (ISC) to reach the S_0 state. When this happens, the reaction ends up in the ground state therefore affording the expected [6,6] product.

Taking into account that the triplet C_{60} yields the [6,6] product due to the occurrence of an ISC and as such ISC is not expected to occur in $^{\#6094}C_{68}$ because this system has already a T_0 ground state, we thought that $^{\#6094}C_{68}$ could be one of the few hollow nonfunctionalized fullerenic cages that prefers [5,6] over the [6,6] addition in DA reactions. To check this hypothesis, we have computationally studied all possible additions to $^{\#6094}C_{68}$ (see Figure 1 for all different bonds of $^{\#6094}C_{68}$). For the most stable products, we have also located the corresponding transition states. We anticipate here that our results show that for $^{\#6094}C_{68}$ the most reactive [5,6] bond reacts much faster than the most reactive [6,6] bond. It is worth noting that the DA cycloaddition to C_{68} has been studied before.[19] However, the cage considered was that of $^{\#6140}C_{68}$ that has a singlet ground state. For this non-IPR fullerene, the [5,5] bond was reported to be the most favored thermodynamically, whereas kinetically the most reactive bond was a [5,6] bond of the F type next to the pentalene unit.[19]

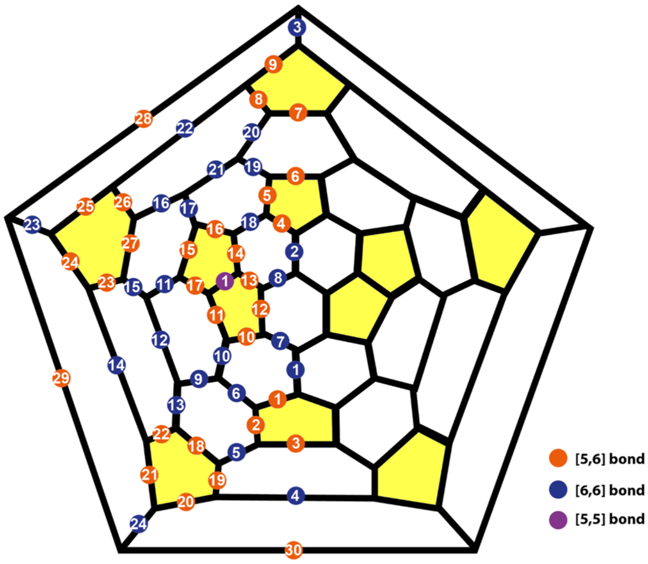

Figure 1. Schlegel diagram of $^{\#6094}C_{68}$ with labels considered in this work for all different bonds.

2. COMPUTATIONAL DETAILS

All geometry optimizations were performed with the Gaussian 09 package[20] by using the UB3LYP hybrid density functional[21,22] with the D3 Grimme's corrections for dispersion[23] and the 6-31G(d,p) basis set[24] without symmetry constraints. Analytical Hessians were computed to confirm that the optimized structures are indeed minima (zero imaginary frequencies) or transition states (one imaginary frequency). $\langle S^2 \rangle$ values computed at the UB3LYP/6-31G(d,p) values were analyzed for all stationary points of the [5,5], $[5,6]_D$, $[5,6]_F$, and [6,6] studied reaction paths to assess the extent of spin contamination (see Table S2 in the Supporting Information). For the triplet state species, only two $\langle S^2 \rangle$ values, corresponding to the biradical intermediate and the transition state (TS) of the first step in the [6,6] path, were found to have a $\langle S^2 \rangle$ value that was a little bit higher than 10% of the expected $\langle S^2 \rangle = 2$. To analyze the effect of the basis set on the optimized geometries, intermediates, and TS for [5,5] and $[5,6]_F$ paths were re-optimized with the 6-311G(d,p) basis set. Superimposed geometries and root-mean-square deviation values (Å) are reported in Figure S9 in the Supporting Information. No significant changes were found in any of the recomputed geometries.

The attacks to the most reactive [5,5], [5,6], and [6,6] bonds were discussed by means of the activation strain model (ASM)[25−29] of reactivity at the UM06-2X-D3/def2-TZVPP[30]//UB3LYP-D3/6-31G(d,p) level of theory. In the ASM, the bonding energy is made up of two major components (eq 1)

$$\Delta E(\zeta) = \Delta E_{\mathrm{strain}}(\zeta) + \Delta E_{\mathrm{int}}(\zeta) \tag{1}$$

In this formula, ζ is the intrinsic reaction coordinate. The strain energy (also known as distortion energy), $\Delta E_{\mathrm{strain}}(\zeta)$, is the amount of energy required to deform the separated fragments from their equilibrium structure to the geometry that they have at position ζ of the reaction coordinate. The interaction energy $\Delta E_{\mathrm{int}}(\zeta)$ corresponds to the actual energy change when the prepared fragments are combined to form the overall molecule at position ζ of the reaction coordinate.

DOI: 10.1021/acs.joc.9b00921
J. Org. Chem. 2019, 84, 9017−9024

Table 1. Predicted Reaction Energies (ΔE_R, kcal·mol^{-1}, UB3LYP-D3/6-31G(d,p) Level) for the DA Reaction of Cyclopentadiene Over All Nonequivalent Bonds of $^{\#6094}C_{68}$

[6,6] isomers				[5,6] isomers			
Bond[a]	**Spin**	**Bond type**[b]	**ΔE$_R$ (kcal·mol^{-1})**	**Bond**[a]	**Spin**	**Bond type**[b]	**ΔE$_R$ (kcal·mol^{-1})**
1	1	B	-0.3	**1**	0	D	-13.5
2	1	B	-12.9	**2**	1	D	-4.3
3	1	A	-19.8	**3**	0	D	5.5
4	1	A	-19.2	**4**	0	D	-16.5
5	1	A	-15.4	**5**	0	D	-1.5
6	1	B	-6.6	**6**	1	D	-4.9
7	1	B	-4.0	**7**	1	D	-3.7
8	1	B	0.0	**8**	0	D	-2.9
9	1	C	11.4	**9**	0	D	-0.7
10	0	B	-1.7	**10**	0	D	-16.8
11	1	B	4.9	**11**	0	F	-23.3
12	0	C	13.3	**12**	1	D	-15.3
13	1	B	-7.9	**13**	0	F	-31.2
14	1	A	-11.2	**14**	0	F	-20.9
15	1	B	0.2	**15**	1	D	-9.8
16	1	B	-1.2	**16**	0	D	-6.6
17	1	B	-4.9	**17**	0	F	-21.6
18	1	A	-11.0	**18**	1	D	0.1
19	1	B	2.2	**19**	1	D	6.3
20	1	B	0.6	**20**	1	D	3.8
21	1	C	22.9	**21**	1	D	6.1
22	1	A	-12.8	**22**	1	D	0.9
23	1	A	-16.0	**23**	1	D	2.0
24	1	A	-14.5	**24**	1	D	7.1
				25	1	D	2.4
				26	0	D	-3.6
				27	1	D	-6.2
				28	1	D	2.4
				29	1	D	4.8
				30	1	D	3.2

[5,5] isomers			
Bond[a]	**Spin**	**Bond type**[b]	**ΔE$_R$ (kcal·mol^{-1})**
1	0	E	-38.5

[a] For bond numbering, see Figure 1. [b] For bond types, see Scheme 1.

The $\Delta E_{\mathrm{int}}(\zeta)$ term can be further decomposed in the framework of the Kohn–Sham molecular orbital model by using the so-called energy decomposition analysis (EDA) method.[31−34] Within this methodology, the interaction energy is decomposed into the following chemically meaningful contributions (eq 2)

$$\Delta E_{\mathrm{int}}(\zeta) = \Delta E_{\mathrm{elstat}}(\zeta) + \Delta E_{\mathrm{Pauli}}(\zeta) + \Delta E_{\mathrm{orb}}(\zeta) + \Delta E_{\mathrm{disp}}(\zeta) \tag{2}$$

The term $\Delta E_{\mathrm{elstat}}(\zeta)$ corresponds to the classical electrostatic interaction between the unperturbed charge distributions of the prepared (i.e., distorted) fragments and is usually attractive. The Pauli repulsion $\Delta E_{\mathrm{Pauli}}(\zeta)$ comprises the destabilizing interactions between occupied molecular orbitals and it is

Scheme 2. General Mechanism of the DA Cycloaddition Involving $^{\#6094}C_{68}$ and Cyclopentadiene

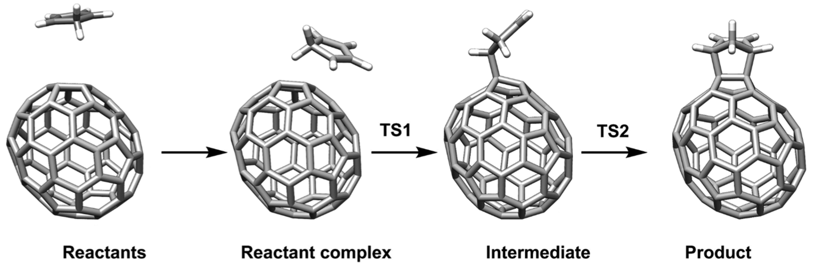

responsible for the steric repulsion. The orbital interaction $\Delta E_{orb}(\zeta)$ accounts for bond pair formation, charge transfer, and polarization, whereas the $\Delta E_{disp}(\zeta)$ term takes into account the interactions that are due to dispersion forces. Finally, the origins of the orbital interactions were analyzed quantitatively by using the NOCV (natural orbital for chemical valence) extension of the EDA method.[35] All the EDA–NOCV calculations were performed with the ADF program[36] at the UM06-2X-D3/TZ2P level using the optimized UB3LYP-D3/6-31G(d,p) geometries. Therefore, this level is denoted as the UM06-2X-D3/TZ2P//UB3LYP-D3/6-31G-(d,p) level of theory. In EDA, open-shell fragments were treated with spin-unrestricted formalism but, for technical reasons, spin polarization was not included. This error causes the studied bond to become, in the order of a few kcal·mol^{-1}, too strong without affecting trends. DLPNO-CCSD/def2-TZVP//UB3LYP/6-31G(d,p) single-point energy calculations[37] with the def2-TZVP/C auxiliary basis set and the RIJCOSX approximation for the HF step using the def2-TZVP/J auxiliary basis set were performed with the ORCA 4.0.0.2 program.[38] The energy barriers obtained at this level of theory show the same reactivity trends as obtained at the UB3LYP-D3 and UM06-2X-D3 levels of theory and confirm the reliability of the results found with these two latter functionals. For instance, the difference in energy barriers for the [5,5]/[5,6] and [6,6] first attack (vide infra) are $\Delta\Delta E^{\ddagger}_{\text{DPLNO-CC}}$ = 6.1 kcal·mol^{-1}, $\Delta\Delta E^{\ddagger}_{\text{UM06-2X-D3}}$ = 9.4 kcal·mol^{-1}, and $\Delta\Delta E^{\ddagger}_{\text{UB3LYP-D3}}$ = 12.6 kcal·mol^{-1} in favor of the [5,5]/[5,6] path. T_1 diagnostic[39] values obtained from DLPNO-CC calculations were in all the cases smaller than 0.02, indicating the single reference character of the species studied.

3. RESULTS AND DISCUSSION

In this section, we discuss first the thermodynamics of the DA cycloadditions of cyclopentadiene (Cp) on all different bonds of $^{\#6094}C_{68}$, second, we study the kinetics of the most exothermic additions and, finally, we provide a rationale for the energy barriers of the most kinetically favored attacks with the ASM of reactivity combined with the EDA–NOCV method.

3.1. Thermodynamics of the DA Cycloadditions.

The reaction energies obtained at the UB3LYP-D3/6-31G(d,p) level for the DA addition of the cyclopentadiene over all 55 nonequivalent bonds of $^{\#6094}C_{68}$ (see Figure 1) are listed in Table 1. It is important to remark that the reaction energies presented in Table 1 are relative energies with respect to Cp and $^{\#6094}C_{68}$ when they are infinitely separated. Table 1 also contains the spin state of the final product. In most of the additions, the most stable product has a triplet ground state. However, in some particular cases, the final most stable product has a singlet ground state instead. For all unsymmetrical isomers, both the endo and exo approaches were considered. Table 1 contains the reaction energy of the most favored approach, whereas Table S1 lists the reaction energy of all possible attacks.

As can be seen, in general, the studied DA cycloaddition is not a very exothermic reaction. In fact, 20 attacks out of 55 are endothermic. The less reactive bonds are those in the ring junctions involving three or four 6-MRS (bond types B, C, and D), which contain the less pyramidalized C atoms. On the other hand, all additions to $[6,6]_A$ and $[5,6]_F$ bonds are exothermic. In general, cycloadditions at the [5,6] bonds are somewhat more exothermic than the [6,6] ones with average exothermicities of −5.3 and −4.3 kcal·mol^{-1}, respectively. The most favored thermodynamic product is that obtained from the addition attack on the [5,5] bond **1** (ΔE_R = −38.5 kcal·mol^{-1}) followed by the $[5,6]_F$ bond **13** of F type (ΔE_R = −31.2 kcal·mol^{-1}). The most exothermic attack to a $[6,6]_A$ bond corresponds to type A bond **3** (ΔE_R = −19.8 kcal·mol^{-1}). Finally, bond **4** is the most thermodynamically favored addition to bonds of the D type. The Bell–Evans–Polanyi plots of several DA cycloadditions to fullerenes, EMFs, and polycyclic aromatic hydrocarbons show a good linear relationship between reaction energies and energy barriers.[40−44] For this reason, we analyzed the complete reaction pathway only for the most exothermic attacks of cyclopentadiene over $^{\#6094}C_{68}$, that is, additions to the $[5,5]_E$ bond, $[5,6]_F$ bond **13** adjacent to a pentalene unit, $[6,6]_A$ bond **3**, and $[5,6]_D$ bond **4**. The results are discussed in the next subsection.

3.2. Kinetic Behavior of the DA Cycloadditions.

Scheme 2 presents a general overview of the reaction mechanism and Table 2 summarizes the reaction energies (ΔG_R, kcal·mol^{-1}) and energy barriers ($\Delta G^{\ddagger}$, kcal·mol^{-1}) for the most reactive bond of each type. As shown in Scheme 2, DA cycloadditions to these systems occur stepwise because of the triplet ground state of $^{\#6094}C_{68}$, which sharply contrasts

Table 2. Reaction Energies (ΔG_R, kcal·mol^{-1}) and Energy Barriers ($\Delta G^{\ddagger}$, kcal·mol^{-1}) for the DA Reaction of Cyclopentadiene Over the Most Reactive Bonds of $^{\#6094}C_{68}$ in Its Triplet Ground State[a]

cycloaddition	ΔG_R	$\Delta G^{\ddagger}$	$\Delta G^{\ddagger}_{\text{concerted}}$
[5,5]	−18.6	11.3	18.2
$[6,6]_A$	−2.0	25.0	27.0
$[5,6]_D$	−1.1	17.2	20.4
$[5,6]_F$	−12.6	11.3	16.1

[a] $\Delta G^{\ddagger}_{\text{concerted}}$ refers to the barriers of the DA cycloaddition of cyclopentadiene to $^{\#6094}C_{68}$ in its singlet closed-shell state.

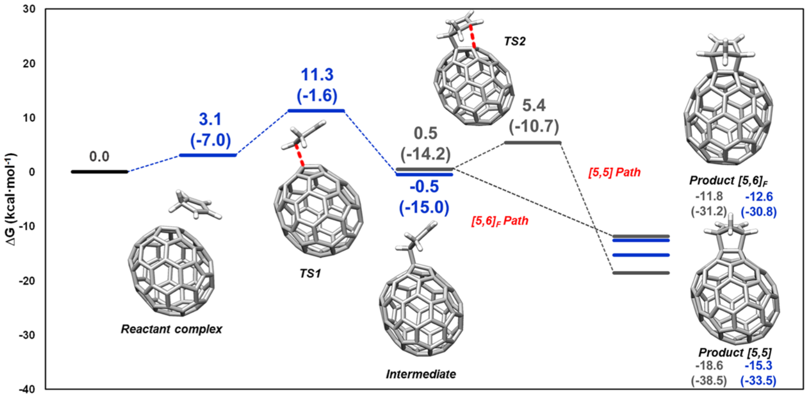

Figure 2. UB3LYP-D3/6-31G(d,p) Gibbs energy profile for the [5,5] and $[5,6]_F$ paths. Electronic relative energies are given within parenthesis. All energies are relative energies to infinitely separated reactants and are given in kcal·mol^{-1}. Blue color refers to triplet state structures.

with most DA cycloadditions to fullerenes and EMFs that proceed in a concerted manner.[15,45,46]

The reaction path leading to the $[6,6]_A$ adduct **3** (see Figure S1 in the Supporting Information) takes place entirely in the triplet state. It is slightly exergonic by 2 kcal·mol^{-1} and has an energy barrier of 25 kcal·mol^{-1} (Table 2). Overall, the $[6,6]_A$ adduct is the least favored among the most reactive bonds studied, both kinetically and thermodynamically. The reaction paths leading to the $[5,6]_F$ and [5,5] products are identical until the first addition takes place (Figure 2). For these $[5,6]_F$ and [5,5] reaction paths, the initial attack of the cyclopentadiene moiety takes place on C44 of $^{\#6094}C_{68}$ (see Scheme S1 in the Supporting Information and Figure 4 for atom labels) leading to the formation of a diradical intermediate. This process is exergonic by 0.5 kcal·mol^{-1} and has a Gibbs energy barrier of 11.3 kcal·mol^{-1}. It is worth mentioning that in the regioselective chlorination of $^{\#6094}C_{68}$, the first addition of Cl to $^{\#6094}C_{68}$ also occurs at the same C44.[13] The intermediate formed in this first step, which has a triplet ground state, evolves to the final $[5,6]_F$ and [5,5] products via a second addition that takes place through an ISC. Such ISC is expected to be very efficient given that it is known that $^1C_{60}$ can undergo ISC to $^3C_{60}$ with very high quantum yields.[47] For the [5,5] bond, the second addition is exergonic by 18.1 kcal·mol^{-1} and has an energy barrier of 5.9 kcal·mol^{-1} (see Figure S3). It is worth mentioning here that the resulting [5,5] adduct has a singlet ground state. For the $[5,6]_F$ path, the second addition is an almost barrier-less process (to reach the ISC from the triplet intermediate has a cost of less than 1 kcal·mol^{-1}, see Figure S2 in the Supporting Information), and is exergonic by 12.1 kcal·mol^{-1}. Before reaching the final adduct, there is another ISC from the singlet to the triplet state, so the final regioisomer has a triplet state with a very low singlet−triplet energy gap of only 0.8 kcal·mol^{-1}. From our computational results, we conclude that the [5,5] adduct is the thermodynamic reaction product while the kinetic product is the $[5,6]_F$ one. Anyhow, our calculations firmly confirm our initial hypothesis, that is $^{\#6094}C_{68}$ is one of the few hollow nonfunctionalized fullerenic cages that prefers [5,6] over the [6,6] addition in DA reactions. We have also analyzed the cycloaddition reaction on the most favored $[5,6]_D$ bond (Table 1). This latter bond appears to be more reactive than the $[6,6]_A$ analyzed but still much less than its [5,5] and $[5,6]_F$ counterparts. Furthermore, the geometries of the transition states (TSs) for the initial attack, which is the rate determining step of the entire process, are shown in Figure 3. As can be seen, the C−C bond length of the bond being formed ranges from 1.95 to 2.16 Å, with the more exergonic attacks having earlier TSs. Finally, we evaluated the effect of temperature on the regioselectivity by recomputing the Gibbs energy profile of [5,5] and $[5,6]_F$ paths at 373 K (see Figure S8 in the Supporting Information). No significant changes were observed with the increase in temperature.

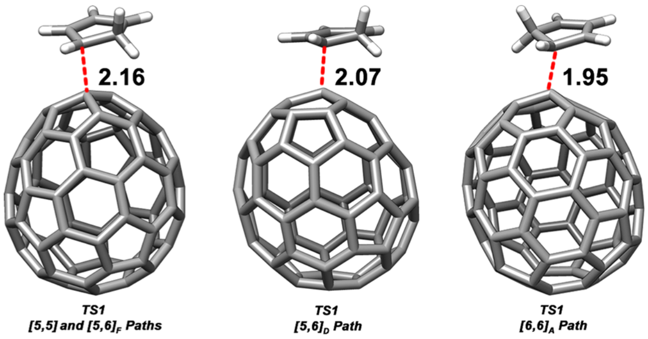

Figure 3. Optimized geometries of the transition state for the initial attack of cyclopentadiene to the most reactive (a) $[6,6]_A$ bond, (b) $[5,6]_F$ and $[5,6]_D$ bond, and (c) [5,5] bond. Distances are given in Angstroms (Å).

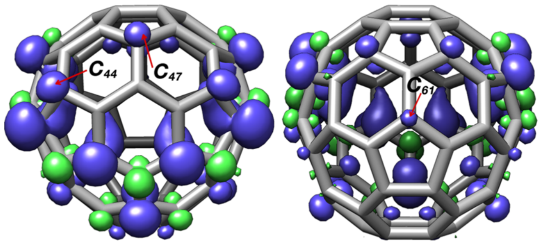

Figure 4. Excess of spin density in $^{\#6094}C_{68}$. Isosurface value of 0.004 au. By convention excess α spin density in blue is termed positive. C44, C47, and C61 indicated with an arrow.

Such a difference in reactivity between [5,5] and $[5,6]_F$ bonds (attack to C44 carbon) on one side and $[5,6]_D$ bond (attack to C47 carbon) on the other side may be attributed in part to the higher degree of pyramidalization of the [5,5] and $[5,6]_F$, the latter being clearly influenced by the adjacency to a pentalene unit (see Scheme 1). Indeed, the pyramidalization angles[48,49] of C44, C47, and C61 are 16.1°, 11.9°, and 11.9°, respectively. However, it is also important to look at the excess of α spin density (Figure 4) showing C44 with larger lobes of

DOI: 10.1021/acs.joc.9b00921
J. Org. Chem. 2019, 84, 9017−9024

spin density than C61 and C47 involved in the $[6,6]_A$ and $[5,6]_D$ attacks, respectively. We have also analyzed the DA cycloaddition of cyclopentadiene to $^{\#6094}C_{68}$ in its singlet closed-shell state to analyze the effect of changing from the triplet to the singlet state on the reactivity. As can be seen in Table 2, the Gibbs energy barriers for the singlet closed-shell state are 2−7 kcal·mol^{-1} higher than those of the stepwise reaction mechanism, but the regioselectivity remains more or less the same. The most affected attacks are the [5,5] and $[5,6]_F$ with Gibbs energy barriers reduced by 7 and 5 kcal·mol^{-1}, respectively. Therefore, the triplet state favors particularly the reactivity of these two bonds and almost does not modify the reactivity of the $[6,6]_A$ bond. The higher degree of pyramidalization of the [5,5] and $[5,6]_F$ bonds better explains the higher reactivity of these bonds. The effect of the open-shell electronic structure is therefore important but not decisive. This result is in line with the fact that for the singlet $^{\#6140}C_{68}$, the [5,5] bond was reported to be the most favored thermodynamically, whereas kinetically the most reactive bond was a $[5,6]_F$ adjacent to the pentalene unit.[19]

3.3. Understanding the Different Reactivity Trends.

In this last subsection, we applied the ASM of reactivity to quantitatively understand the origin of the different reactivity of the [5,5], $[5,6]_F$, and $[6,6]_A$ most reactive bonds of $^{\#6094}C_{68}$. We applied the ASM to the initial attack, which is the rate determining step, from the reactant complex to TS1 (see Scheme 2). [5,5] and $[5,6]_F$ cycloadditions share the same initial attack. Figure 5 shows the computed activation strain diagrams for the $[5,5]/[5,6]_F$ and $[6,6]_A$ cycloadditions from the reactant complex up to the respective TS1s along the intrinsic reaction coordinate projected onto the forming C···C bond distance. As can be seen, for the $[6,6]_A$ cycloaddition, the strain energy is significantly less destabilizing than in the $[5,5]/[5,6]_F$ attacks from the beginning of the process up to the corresponding transition state region. Therefore, the ΔE_{strain} is not at all responsible for the higher barrier computed for the $[6,6]_A$-pathway. At variance, the interaction energy is clearly much stronger for the addition on the $[5,5]/[5,6]_F$ attacks than on the [6,6]-bond along the entire reaction coordinate. This highly stabilizing interaction between the reactants is able to offset the higher destabilizing effect of the ΔE_{strain}, which is then translated into the computed lower barrier for the process involving the $[5,5]/[5,6]_F$ bonds.

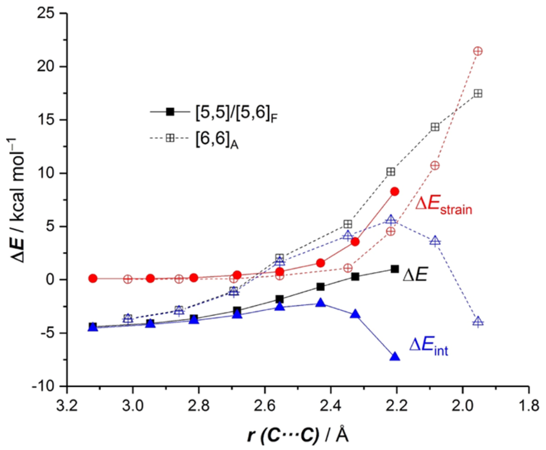

Figure 5. Comparative activation-strain diagrams of the DA cycloaddition reactions between cyclopentadiene and the $[5,5]/[5,6]_F$ (solid lines) and $[6,6]_A$ (dashed lines) bonds of $^{\#6094}C_{68}$ along the intrinsic reaction coordinate projected onto the forming C···C bond distance. All data were computed at the UM06-2X-D3/def2-TZVPP//UB3LYP-D3/6-31G(d,p).

Further quantitative insight into the factors making the interaction between reactants weaker for the $[6,6]_A$ cycloaddition can be achieved by means of the EDA method. Figure 6 shows the evolution of the different contributions to the total interaction energy along the reaction coordinate for the $[5,5]/[5,6]_F$ and $[6,6]_A$ cycloadditions. The $\Delta E_{elstat}(\zeta)$ and $\Delta E_{disp}(\zeta)$ terms are almost identical for the two attacks and therefore are not decisive for the higher interaction computed for the process involving the $[5,5]/[5,6]_F$ bonds. In contrast, the $[5,5]/[5,6]_F$ addition clearly benefits from much stronger orbital interactions (ΔE_{orb}) and also, from a less destabilizing Pauli repulsion (albeit to a less extent). For instance, at the same C···C forming bond length of 2.2 Å, and for the $[5,5]/[5,6]_F$ and $[6,6]_A$, respectively, the computed ΔE_{elstat} is −32.4 and −34.4 kcal·mol^{-1}, ΔE_{Pauli} 57.6 and 63.9 kcal·mol^{-1}, ΔE_{disp} −5.7 and −6.0 kcal·mol^{-1}, whereas ΔE_{orb} is −38.8 and −29.3 kcal·mol^{-1}. The higher Pauli repulsion for the [6,6] attack can be attributed to the close proximity of the CH_2 group of the cyclopentadiene to the C_{68} cage in the TS (2.716 Å for [6,6] TS1 and 2.777 Å for [5,6] TS1). Therefore, it can be concluded that the stronger orbital interactions between the deformed reactants of the $[5,5]/[5,6]_F$ cycloaddition mainly constitute the origin of the lower barrier computed for this attack.

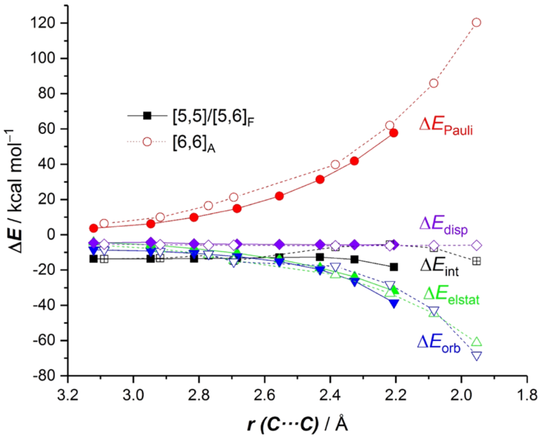

Figure 6. Comparative EDA of the DA cycloaddition reactions between cyclopentadiene and the $[5,5]/[5,6]_F$ (solid line) and $[6,6]_A$ (dashed line) bonds of $^{\#6094}C_{68}$ along the intrinsic reaction coordinate projected onto the forming C···C bond distance. All data were computed at the UM06-2X-D3/TZ2P//UB3LYP-D3/6-31G(d,p).

Finally, the ΔE_{orb} term has been further partitioned by using the EDA−NOCV procedure. This approach suggests that the main orbital interaction corresponds to the π(diene) → π_{SOMO}(fullerene) (see Figure 7, charge flow is red → blue) that leads to the formation of a new C−C bond and the accumulation of excess density in the cyclopentadiene. Interestingly, this dominant orbital interaction is much stronger for the $[5,5]/[5,6]_F$ attack than for the $[6,6]_A$ one, as clearly viewed from the associated stabilizing deformation energies ($\Delta E(\rho_1)$) computed at the same consistent C···C bond forming distance of 2.2 Å (see Figure 7). We attribute the observed difference to the large contribution of C44 to the SOMO of $^{\#6094}C_{68}$ and to the larger spin density on this C

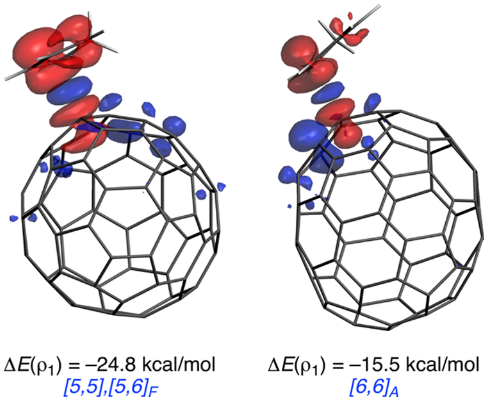
$\Delta E(\rho_1) = -24.8$ kcal/mol
[5,5],[5,6]$_F$
$\Delta E(\rho_1) = -15.5$ kcal/mol
[6,6]$_A$

Figure 7. Plot of the deformation densities ($\Delta\rho$) of the pairwise orbital interactions between cyclopentadiene and the [5,5]/[5,6]$_F$ and [6,6]$_A$ bonds of $^{\#6094}C_{68}$ and associated stabilization energies ($\Delta E(\rho_1)$, in kcal·mol^{-1}). The color code of the charge flow is red → blue. All data computed at the UM06-2X-D3/TZ2P//UB3LYP-D3/6-31G(d,p).

atom (see above), which is translated into a significantly higher $\langle\pi(\text{diene})-\pi_{\text{SOMO}}(\text{fullerene})\rangle$ molecular orbital overlap computed for the process involving the [5,5]/[5,6]$_F$ bond (S = 0.081 vs 0.030). As a consequence of this stronger orbital interaction, the total interaction energy between the deformed reactants is also stronger for the [5,5]/[5,6]$_F$ approach, which ultimately results in the predicted [5,6] regioselectivity.

4. CONCLUSIONS

We have studied the regioselectivity of the DA cycloaddition of cyclopentadiene to $^{\#6094}C_{68}$ in its triplet ground state. We have shown that $^{\#6094}C_{68}$ is one of the first reported hollow nonfunctionalized fullerene that favors the cycloaddition to [5,6] instead of the typically preferred [6,6] bond. Our results indicate that the [5,5] adduct is the thermodynamic reaction product, whereas the kinetic product is the [5,6]$_F$ one. This change of regioselectivity in the DA reaction of hollow fullerenes from the usual [6,6] bond to the [5,6] bond in $^{\#6094}C_{68}$ is driven by the more stabilizing orbital interaction favored by the spin density accumulation around the pentalene region of the cage.

Our results highlight important differences in the regioselectivity of DA cycloaddition of IPR and non-IPR fullerenes. For IPR fullerenes, the [6,6] addition is preferred in the singlet closed-shell state,[45] whereas in the triplet state the preferred attack takes place on the [5,6] bond.[18] For non-IPR fullerenes, the [5,5] adduct is the thermodynamic reaction product and the [5,6]$_F$ adduct is the one obtained under kinetic control, irrespective of the electronic state being a singlet[19] or a triplet. However, we have found that in the triplet state the regioselectivity in favor of the [5,5] and [5,6]$_F$ attacks is enhanced by 5−7 kcal·mol^{-1}. The findings of this research provide additional insights into the problem of the regioselectivity in fullerenes and EMFs, which, in our opinion, may be useful for the experimental generation of unusual fullerene derivatives.

■ ASSOCIATED CONTENT

Ⓢ Supporting Information

The Supporting Information is available free of charge on the ACS Publications website at DOI: 10.1021/acs.joc.9b00921.

Schlegel diagram with labeling of the atoms, reaction energies for all possible attacks, Gibbs energy profiles for attacks to bonds **1**, **3**, **4**, and **13**, and linear transits from the diradical intermediate to the reaction product for the studied [5,5], [5,6]$_D$, and [5,6]$_F$ attacks, and Cartesian *xyz* coordinates for all optimized reactants, intermediates, transition states, and products (PDF)

■ AUTHOR INFORMATION

Corresponding Authors

*E-mail: israel@quim.ucm.es (I.F.).
*E-mail: miquel.sola@udg.edu (M.S.).

ORCID

Albert Artigas: 0000-0002-7351-0066
Israel Fernández: 0000-0002-0186-9774
Miquel Solà: 0000-0002-1917-7450

Notes

The authors declare no competing financial interest.

■ ACKNOWLEDGMENTS

Financial support was provided by the Spanish Ministerio de Economía y Competitividad (MINECO) and FEDER (grants CTQ2016-78205-P and CTQ2016-81797-REDC to I.F. and CTQ2017-85341-P to M.S.), and Catalan DIUE (projects 2017SGR39, ICREA Academia 2014 prize, and XRQTC to M.S.). The FEDER grant UNGI10-4E-801 has also funded this research. A.A. acknowledges the MINECO and the European Social Fund (ESF) for a FPI grant.

■ REFERENCES

(1) Hirsch, A.; Brettreich, M. *Fullerenes: Chemistry and Reactions*; John Wiley & Sons: Weinheim, 2004.

(2) Fowler, P. W.; Manolopoulos, D. E. *An Atlas of Fullerenes*; Clarendon Press: Oxford, 1995.

(3) *Chemistry of Nanocarbons*; Akasaka, T., Wudl, F., Nagase, S., Eds.; John Wiley & Sons: Chichester, 2010.

(4) Kroto, H. W.; Heath, J. R.; O'Brien, S. C.; Curl, R. F.; Smalley, R. E. C_{60}—Buckminsterfullerene. *Nature* **1985**, *318*, 162−163.

(5) Kroto, H. W. The stability of the fullerenes C_n, with n = 24, 28, 32, 36, 50, 60 and 70. *Nature* **1987**, *329*, 529−531.

(6) Albertazzi, E.; Domene, C.; Fowler, P. W.; Heine, G.; Van Alsenoy, C.; Zerbetto, F.; Zerbetto, F. Pentagon adjacency as a determinant of fullerene stability. *Phys. Chem. Chem. Phys.* **1999**, *1*, 2913−2918.

(7) Tan, Y.-Z.; Xie, S.-Y.; Huang, R.-B.; Zheng, L.-S. The stabilization of fused-pentagon fullerene molecules. *Nat. Chem.* **2009**, *1*, 450−460.

(8) Xie, S.-Y.; Gao, F.; Lu, X.; Huang, R.-B.; Wang, C.-R.; Zhang, X.; Liu, M.-L.; Deng, S.-L.; Zheng, L.-S. Capturing the Labile Fullerene[50] as $C_{50}Cl_{10}$. *Science* **2004**, *304*, 699.

(9) Wang, C.-R.; Kai, T.; Tomiyama, T.; Yoshida, T.; Kobayashi, Y.; Nishibori, E.; Takata, M.; Sakata, M.; Shinohara, H. C_{66} fullerene encaging a scandium dimer. *Nature* **2000**, *408*, 426−427.

(10) Olmstead, M. M.; Lee, H. M.; Duchamp, J. C.; Stevenson, S.; Marciu, D.; Dorn, H. C.; Balch, A. L. $Sc_3N@C_{68}$: Folded Pentalene Coordination in an Endohedral Fullerene that Does Not Obey the Isolated Pentagon Rule. *Angew. Chem., Int. Ed.* **2003**, *42*, 900−903.

(11) Cai, T.; Xu, L.; Shu, C.; Reid, J. E.; Gibson, H. W.; Dorn, H. C. Synthesis and Characterization of a Non-IPR Fullerene Derivative: $Sc_3N@C_{68}[C(COOC_2H_5)_2]$. *J. Phys. Chem. C* **2008**, *112*, 19203−19208.

(12) Amsharov, K. Y.; Ziegler, K.; Mueller, A.; Jansen, M. Capturing the Antiaromatic $^{\#6094}C_{68}$ Carbon Cage in the Radio-Frequency Furnace. *Chem.—Eur. J.* **2012**, *18*, 9289−9293.

(13) Dang, J.-S.; Zheng, J.-J.; Wang, W.-W.; Zhao, X. Open-Shell Triplet Character of $^{\#6094}C_{68}$: Spherical Aromaticity, Thermodynamic Stability, and Regioselective Chlorination. *Inorg. Chem.* **2013**, *52*, 4762−4764.

(14) Jin, P.; Li, Y.; Magagula, S.; Chen, Z. Exohedral functionalization of endohedral metallofullerenes: Interplay between inside and outside. *Coord. Chem. Rev.* **2019**, *388*, 406−439.

(15) Osuna, S.; Swart, M.; Solà, M. The reactivity of endohedral fullerenes. What can be learnt from computational studies? *Phys. Chem. Chem. Phys.* **2011**, *13*, 3585−3603.

(16) Hirsch, A. *The Chemistry of Fullerenes*; Thieme: Sttutgart, Germany, 1994.

(17) Garcia-Borràs, M.; Osuna, S.; Swart, M.; Luis, J. M.; Solà, M. Electrochemical control of the regioselectivity in the exohedral functionalization of C_{60}: the role of aromaticity. *Chem. Commun.* **2013**, *49*, 1220−1222.

(18) El Bakouri, O.; Garcia-Borràs, M.; Girón, R. M.; Filippone, S.; Martín, N.; Solà, M. On the regioselectivity of the Diels−Alder cycloaddition to C_{60} in high spin states. *Phys. Chem. Chem. Phys.* **2018**, *20*, 11577−11585.

(19) Yang, T.; Zhao, X.; Nagase, S.; Akasaka, T. Diels−Alder Reaction on Free C_{68} Fullerene and Endohedral $Sc_3N@C_{68}$ Fullerene Violating the Isolated Pentagon Rule: Importance of Pentagon Adjacency. *Chem.—Asian J.* **2014**, *9*, 2604−2611.

(20) Frisch, M. J.; Trucks, G. W.; Schlegel, H. B.; Scuseria, G. E.; Robb, M. A.; Cheeseman, J. R.; Scalmani, G.; Barone, V.; Mennucci, B.; Petersson, G. A.; Nakatsuji, H.; Caricato, M.; Li, X.; Hratchian, H. P.; Izmaylov, A. F.; Bloino, J.; Zheng, G.; Sonnenberg, J. L.; Hada, M.; Ehara, M.; Toyota, K.; Fukuda, R.; Hasegawa, J.; Ishida, M.; Nakajima, T.; Honda, Y.; Kitao, O.; Nakai, H.; Vreven, T.; Montgomery, J. A., Jr.; Peralta, J. E.; Ogliaro, F.; Bearpark, M.; Heyd, J. J.; Brothers, E.; Kudin, K. N.; Staroverov, V. N.; Kobayashi, R.; Normand, J.; Raghavachari, K.; Rendell, A.; Burant, J. C.; Iyengar, S. S.; Tomasi, J.; Cossi, M.; Rega, N.; Millam, J. M.; Klene, M.; Knox, J. E.; Cross, J. B.; Bakken, V.; Adamo, C.; Jaramillo, J.; Gomperts, R.; Stratmann, R. E.; Yazyev, O.; Austin, A. J.; Cammi, R.; Pomelli, C.; Ochterski, J. W.; Martin, R. L.; Morokuma, K.; Zakrzewski, V. G.; Voth, G. A.; Salvador, P.; Dannenberg, J. J.; Dapprich, S.; Daniels, A. D.; Farkas, O.; Foresman, J. B.; Ortiz, J. V.; Cioslowski, J.; Fox, D. J. *Gaussian 09*, revision D.01; Gaussian, Inc.: Wallingford, CT, 2009.

(21) Becke, A. D. Density-functional thermochemistry. III. The role of exact exchange. *J. Chem. Phys.* **1993**, *98*, 5648−5652.

(22) Lee, C.; Yang, W.; Parr, R. G. Development of the Colle-Salvetti correlation-energy formula into a functional of the electron density. *Phys. Rev. B: Condens. Matter Mater. Phys.* **1988**, *37*, 785−789.

(23) Grimme, S.; Antony, J.; Ehrlich, S.; Krieg, H. A consistent and accurate ab initio parametrization of density functional dispersion correction (DFT-D) for the 94 elements H-Pu. *J. Chem. Phys.* **2010**, *132*, 154104.

(24) Frisch, M. J.; Pople, J. A.; Binkley, J. S. Self-consistent molecular orbital methods 25. Supplementary functions for Gaussian basis sets. *J. Chem. Phys.* **1984**, *80*, 3265−3269.

(25) Bickelhaupt, F. M.; Baerends, E. J. In *Reviews in Computational Chemistry*; Lipkowitz, K. B., Boyd, D. B., Eds.; Wiley-VCH: New York, 2000; Vol. *15*, pp 1−86.

(26) Fernández, I.; Bickelhaupt, F. M. The activation strain model and molecular orbital theory: understanding and designing chemical reactions. *Chem. Soc. Rev.* **2014**, *43*, 4953−4967.

(27) Bickelhaupt, F. M.; Houk, K. N. Analyzing Reaction Rates with the Distortion/Interaction-Activation Strain Model. *Angew. Chem., Int. Ed.* **2017**, *56*, 10070−10086.

(28) Wolters, L. P.; Bickelhaupt, F. M. The activation strain model and molecular orbital theory. *Wiley Interdiscip. Rev.: Comput. Mol. Sci.* **2015**, *5*, 324−343.

(29) Fernández, I. Understanding the Reactivity of Fullerenes Through the Activation Strain Model. *Eur. J. Org. Chem.* **2018**, 1394−1402.

(30) Weigend, F.; Ahlrichs, R. Balanced basis sets of split valence, triple zeta valence and quadruple zeta valence quality for H to Rn: Design and assessment of accuracy. *Phys. Chem. Chem. Phys.* **2005**, *7*, 3297−3305.

(31) Kitaura, K.; Morokuma, K. A New Energy Decomposition Scheme for Molecular Interactions within the Hartree-Fock Approximation. *Int. J. Quantum Chem.* **1976**, *10*, 325−340.

(32) Morokuma, K. Why do molecules interact? The origin of electron donor-acceptor complexes, hydrogen bonding and proton affinity. *Acc. Chem. Res.* **1977**, *10*, 294−300.

(33) Ziegler, T.; Rauk, A. On the calculation of Bonding Energies by the Hartree-Fock-Slater Method. *Theor. Chim. Acta* **1977**, *46*, 1−10.

(34) Hopffgarten, M. v.; Frenking, G. Energy decomposition analysis. *Wiley Interdiscip. Rev.: Comput. Mol. Sci.* **2012**, *2*, 43−62.

(35) Mitoraj, M. P.; Michalak, A.; Ziegler, T. A Combined Charge and Energy Decomposition Scheme for Bond Analysis. *J. Chem. Theory Comput.* **2009**, *5*, 962−975.

(36) te Velde, G.; Bickelhaupt, F. M.; Baerends, E. J.; Fonseca Guerra, C.; van Gisbergen, S. J. A.; Snijders, J. G.; Ziegler, T. Chemistry with ADF. *J. Comput. Chem.* **2001**, *22*, 931−967.

(37) Neese, F.; Wennmohs, F.; Hansen, A. Efficient and accurate local approximations to coupled-electron pair approaches: An attempt to revive the pair natural orbital method. *J. Chem. Phys.* **2009**, *130*, 114108.

(38) Neese, F. The ORCA program system. *Wiley Interdiscip. Rev.: Comput. Mol. Sci.* **2012**, *2*, 73−78.

(39) Lee, T. J.; Taylor, P. R. A diagnostic for determining the quality of single-reference electron correlation methods. *Int. J. Quantum Chem.* **2009**, *36*, 199−207.

(40) Garcia-Borràs, M.; Romero-Rivera, A.; Osuna, S.; Luis, J. M.; Swart, M.; Solà, M. The Frozen Cage Model: A Computationally Low-Cost Tool for Predicting the Exohedral Regioselectivity of Cycloaddition Reactions Involving Endohedral Metallofullerenes. *J. Chem. Theory Comput.* **2012**, *8*, 1671−1683.

(41) Fernández, I.; Solà, M.; Bickelhaupt, F. M. Origin of Reactivity Trends of Noble Gas Endohedral Fullerenes $Ng_2@C_{60}$ (Ng = He to Xe). *J. Chem. Theory Comput.* **2014**, *10*, 3863−3870.

(42) García-Rodeja, Y.; Solà, M.; Bickelhaupt, F. M.; Fernández, I. Reactivity and Selectivity of Bowl-Shaped Polycyclic Aromatic Hydrocarbons: Relationship to C_{60}. *Chem.—Eur. J.* **2016**, *22*, 1368−1378.

(43) García-Rodeja, Y.; Solà, M.; Fernández, I. Understanding the Reactivity of Planar Polycyclic Aromatic Hydrocarbons: Towards the Graphene Limit. *Chem.—Eur. J.* **2016**, *22*, 10572−10580.

(44) García-Rodeja, Y.; Solà, M.; Bickelhaupt, F. M.; Fernández, I. Understanding the Reactivity of Ion-Encapsulated Fullerenes. *Chem.—Eur. J.* **2017**, *23*, 11030−11036.

(45) Fernández, I.; Solà, M.; Bickelhaupt, F. M. Why Do Cycloaddition Reactions Involving C_{60} Prefer [6,6] over [5,6] Bonds? *Chem.—Eur. J.* **2013**, *19*, 7416−7422.

(46) Garcia-Borràs, M.; Osuna, S.; Luis, J. M.; Swart, M.; Solà, M. A Complete Guide on the Influence of Metal Clusters in the Diels−Alder Regioselectivity of I_h-C_{80} Endohedral Metallofullerenes. *Chem.—Eur. J.* **2013**, *19*, 14931−14940.

(47) Hung, R. R.; Grabowski, J. J. A precise determination of the triplet energy of carbon (C_{60}) by photoacoustic calorimetry. *J. Phys. Chem.* **1991**, *95*, 6073−6075.

(48) Haddon, R. C. POAV3 program. QCPE 508/QCMP 044, *QCPE Bull.*. **1988**, *8*, 8.

(49) Haddon, R. C. Measure of nonplanarity in conjugated organic molecules: which structurally characterized molecule displays the highest degree of pyramidalization? *J. Am. Chem. Soc.* **1990**, *112*, 3385−3389.

Chapter 8. Results and Discussion

A general perspective of the work presented in chapters 3-7 is given in the following sections. In order to avoid redundancy, only the most important results will be presented, together with some additional data that was omitted in the publications or was included as supplementary material. Moreover, the content corresponding to each separate research article will be discussed here as a whole, so the reader can better perceive the coherence of the work developed. In the same way as in chapter 2, the content has been divided in three sections. Section 1 provides a summarized discussion of the results reported in Chapters 3, 4 and 5 and encompasses all the work related to the [2+2+2] cycloaddition reaction of C_{60} and alkynes, from computational studies to practical applications. In section 2, we describe a novel catalytic methodology to access 7-membered fused heterocycles starting from 1,5-bisallenes and alkenes. The mechanism of the process was also studied by DFT calculations. As stated in chapter 2, this methodology was developed with the ultimate goal of fullerene functionalization. In this regard, successful preliminary results obtained with C_{60} not included in the publication corresponding to chapter 6 can be found here. Finally, a computational study on the reactivity of fullerene $^{\#6094}C_{68}$ is reported in section 3.

Note: compound numbering is coherent in each subsection and may differ from that employed in the original publications.

Section 1: Rh(I) catalyzed [2+2+2] cycloadditions of fullerenes and alkynes

1.1. A computational study of the intermolecular [2+2+2] cycloaddition of acetylene and C_{60} catalyzed by Wilkinson's complex

At the onset of the present thesis, the rhodium-catalyzed [2+2+2] cycloaddition of fullerene C_{60} and two alkynes was studied by computational means. While two examples of such processes had been previously reported in the literature using stoichiometric amounts of Ni(0) [162] and Pd(0) [164] complexes (see subsection 2.3.5 and references cited therein), the ability of rhodium complexes to promote or catalyze the reaction remained unexplored. Moreover, the reaction mechanism was not assessed either experimentally or computationally in any of these two reports. Taking these precedents into account, the two main goals of this first project were:

1. To provide a mechanistic pathway for the formation of 1,3-cyclohexene derivatives of C_{60} by reaction of the fullerene with two alkynes catalyzed by a transition metal.
2. To computationally analyze the feasibility to functionalize fullerenes *via* a Rh-catalyzed reaction prior to experimental investigation of the process.

To accomplish this goal, a reaction model consisting of two acetylene molecules, one molecule of C_{60} and Wilkinson's complex [RhCl(PPh_3)$_3$] was selected to study the process (**Scheme 8.1**). With this model at hand, we analyzed all potential reaction pathways that transform a C_{60} molecule into a 1,3-cyclohexadiene derivative. All computational calculations were performed at the M06L-D3/cc-pVTZ//B3LYP-D3/cc-pVDZ level of theory in gas phase, at 298.15 K and 1 atm. We considered three possible active catalysts, namely [RhCl(PPh_3)$_2$], [RhCl(PPh_3)] and [RhCl]. Although it is well-known that C_{60} is selectively functionalized at the [6,6] junctions when subjected to cycloaddition reactions, we investigated the reaction pathways leading to a [6,6] and a [5,6] cycloadducts. As expected, the [6,6]-fused 1,3-cyclohexadiene-C_{60} derivative is favored both kinetically and thermodynamically. Only the most relevant reactions paths will be discussed here. Further results can be found in the supplementary material (**Figures S1-7**).

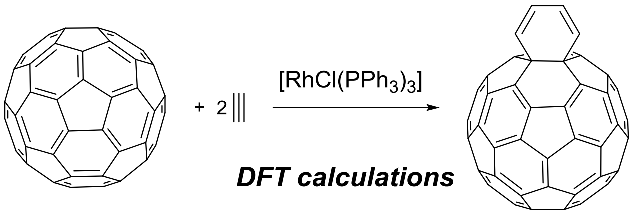

Scheme 8.1. Simplified reaction model used to study the [2+2+2] cycloaddition of C_{60} and 2 alkynes.

After activation of the catalyst through the substitution of a triphenylphosphine (PPh_3) ligand of Wilkinson's complex by one acetylene molecule, intermediate **A2** enters the catalytic cycle. This initial process is endergonic by 15.0 kcal/mol. From **A2**, we considered two possible mechanisms. In path A pathways (red path in **Figure 8.1**), coordination of a second acetylene molecule forms **A3**, an 18-electron species in which the two PPh_3 ligands occupy axial positions of the trigonal bipyramid (tbp). Subsequent interconversion to intermediate **A3'** *via* a Berry pseudorotation [399,400] of the tbp and oxidative coupling through **TS A3'A4** yields rhodacyclopentadiene intermediate **A4**. Formation of **A4** from **A3** releases 11.0 kcal/mol and has a Gibbs energy barrier of 22.4 kcal/mol. For path A, the oxidative coupling step was found to be rate-determining. Thus, in this case **A3** is the turnover frequency (TOF)-determining intermediate (TDI) and **TS A3'A4** is the TOF-determining TS (TDTS).

Alternatively (blue path in **Figure 8.1**), intermediate **A2** coordinates to a C_{60} molecule to give **B3**. In this case, the axial positions are occupied by Cl and acetylene. Oxidative coupling from intermediate **B3** through **TS B3B4** to form the 16-electron rhodacyclopentane species **B4** has an energy barrier of 21.0 kcal/mol and is exergonic by 13.0 kcal/mol. Contrary to path A, in this case the oxidative coupling is not the rate-determining step (rds), since the insertion step (see below) has a larger Gibbs energy barrier.

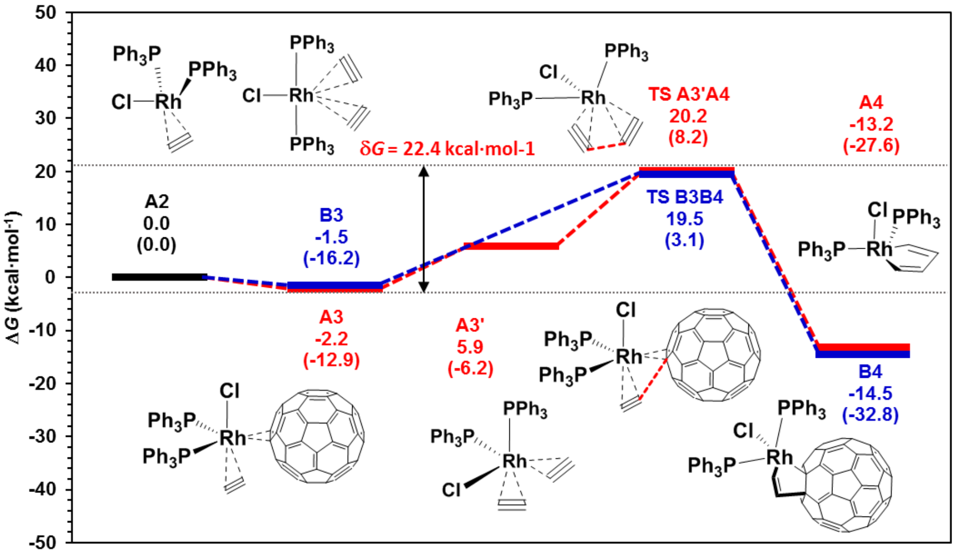

Figure 8.1. M06L-D3/cc-pVTZ-PP//B3LYP-D3/cc-pVDZ Gibbs energy profile for the oxidative coupling step (Red = path A; Blue = path B). Energies in parentheses are electronic energies.

In path A (red path in **Figure 8.2**), intermediate **A4** loses one PPh_3 ligand to form **A5** in a process that has a cost of 14.6 kcal/mol. After this, coordination of a C_{60} molecule results in intermediate **A6** by releasing 21.6 kcal/mol. The Schore mechanism is then operative in the insertion of a [6,6] bond into the Rh–C bond of intermediate **A6**. Consequently, rhodacycloheptatriene intermediate **A7** is formed through **TS A6A7**. This step has a Gibbs energy barrier of 6.7 kcal/mol and is exergonic by 12.4 kcal/mol. Additionally, we considered an alternative mechanism involving [4+2] cycloaddition between the C_{60} and the rhodacyclopentadiene moieties of **A6** to form intermediate **C7** (see Path C in **Figure S5-6** in the supplementary material). However, this process has a larger barrier of 24.7 kcal/mol.

In path B (blue path in **Figure 8.2**), coordination of an acetylene molecule to intermediate **B4** leads to intermediate **B5**, which is destabilized by 15.9 kcal/mol. Subsequently, loss of one phosphine and Rh–C insertion again by the Schore mechanism leads again to rhodacycloheptatriene intermediate **A7**. Formation of **A7** through **TS B6A7** has a small barrier of 6.3 kcal/mol and releases 44.2 kcal/mol. Interestingly, the insertion step is rate-determining for the case of path B, since the energetic span from the TDI (**B4**) to the TDTS (**TS B6A7**) is 26.1 kcal/mol. From these results one should expect path A to be much more favorable.

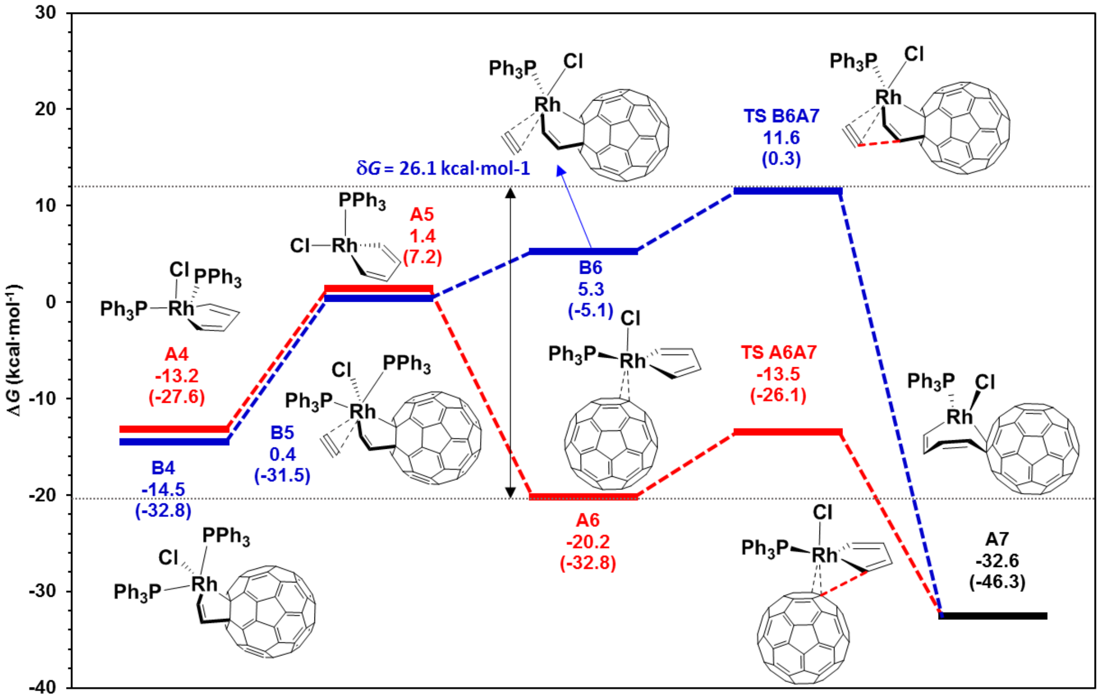

Figure 8.2. M06L-D3/cc-pVTZ-PP//B3LYP-D3/cc-pVDZ Gibbs energy profile for the insertion steps (Red = path A; Blue = path B). Energies in parentheses are electronic energies.

Paths A and B merge in intermediate **A7** and share a common reaction path until intermediate **A11 (Figure 8.3)**. Reductive elimination occurs in **A7** to generate intermediate **A8.** This step is slightly exergonic by 1.6 kcal/mol and takes place through a Gibbs energy barrier of 15.2 kcal/mol. **A8** accepts a PPh_3 ligand to form intermediate **A9**. Finally, release of the reaction product and recovery of intermediate **A2** by coordination of a new acetylene molecule completes the catalytic cycle. Taken together, the results show that the Wilkinson's complex-catalyzed [2+2+2] cycloaddition reaction of C_{60} and two acetylene molecules is exergonic by 51.6 kcal/mol and has a Gibbs energy barrier of 22.4 kcal/mol.

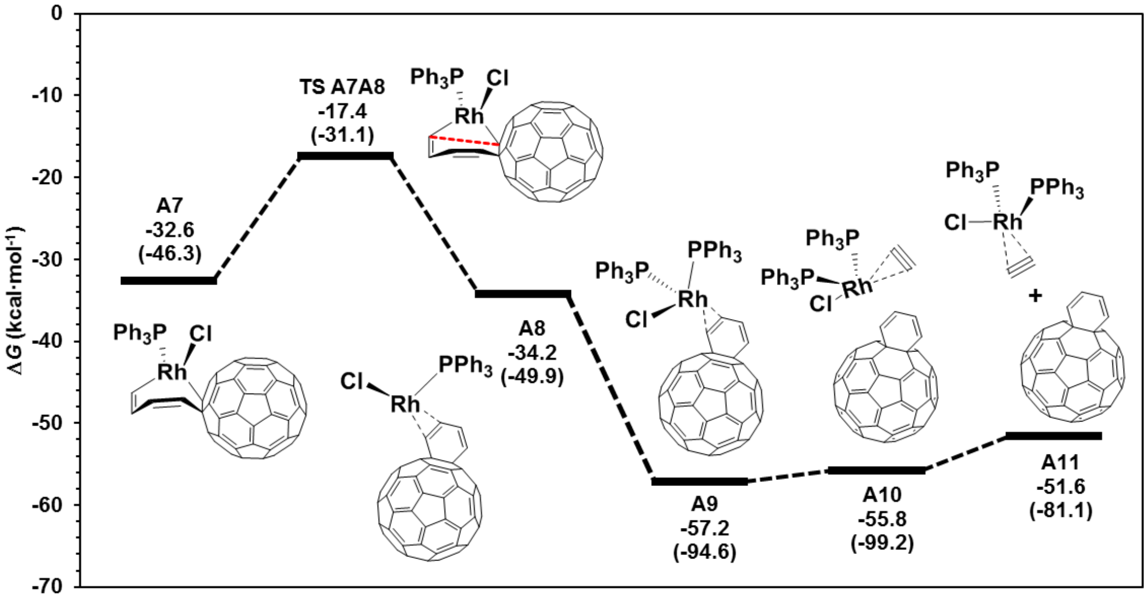

Figure 8.3. M06L-D3/cc-pVTZ-PP//B3LYP-D3/cc-pVDZ Gibbs energy profile for the reductive elimination step and product release. Energies in parentheses are electronic energies.

For comparison purposes, we re-computed the [2+2+2] cycloaddition of three acetylene molecules catalyzed by Wilkinson's complex (**Figure 8.4**). Though this reaction was already studied in our group some years ago [256], dispersion effects were not considered in that report.

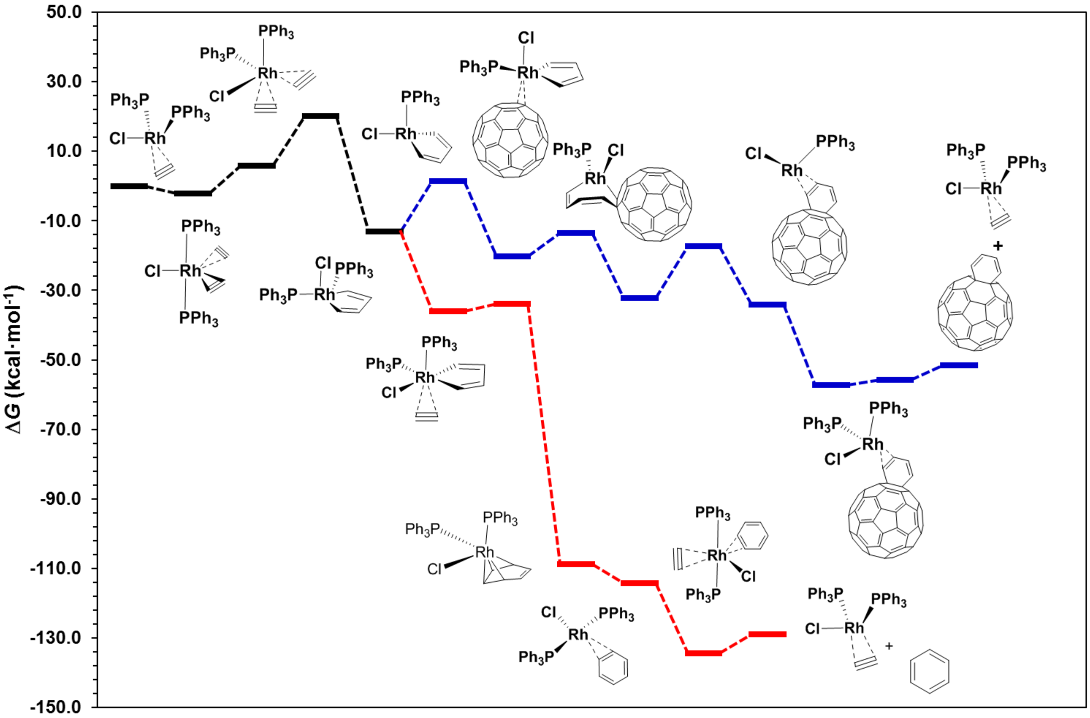

Figure 8.4. M06L-D3/cc-pVTZ-PP//B3LYP-D3 Gibbs energy profiles for the [2+2+2] cycloaddition reaction catalyzed by Wilkinson's complex of (a) C_{60} and to acetylene molecules, and (b) three acetylene molecules. Blue = C_{60} path; Red = acetylene cyclotrimerization path.

Comparing both reaction mechanisms, one can easily conclude that benzene formation is clearly favored over formation of a cyclohexadiene-fused C_{60} derivative. Indeed, coordination of a third acetylene molecule to intermediate **A4** and subsequent steps are considerably more exergonic and have negligible reaction barriers.

However, computations showed that the reaction involving C_{60} is also a feasible process. In conclusion, when performing the reaction experimentally, formation of arene byproducts must be expected and it should be avoided to some extent by properly tuning the reaction conditions to switch the selectivity towards C_{60}. In view of these preliminary computational results obtained with Wilkinson's complex, changing to other Rh(I) catalytic systems would be an obvious approach to start with.

Finally, additional calculations were performed in order to evaluate the impact of solvent effects in the reaction mechanism (**Figure 8.5**). With this in mind, path A was re-computed adding solvent corrections using the SMD continuum solvent model, considering toluene as the solvent at the same level of theory used for gas phase calculations. The results revealed that solvent effects have a minimal impact on the Gibbs energy barriers. The most important changes were observed in the dissociation of PPh_3 ligand in intermediate **A4**, which is favored by 5 kcal/mol. Moreover, the last steps of the reaction, corresponding to release of the reaction product, are better described when solvent effects are taken into account.

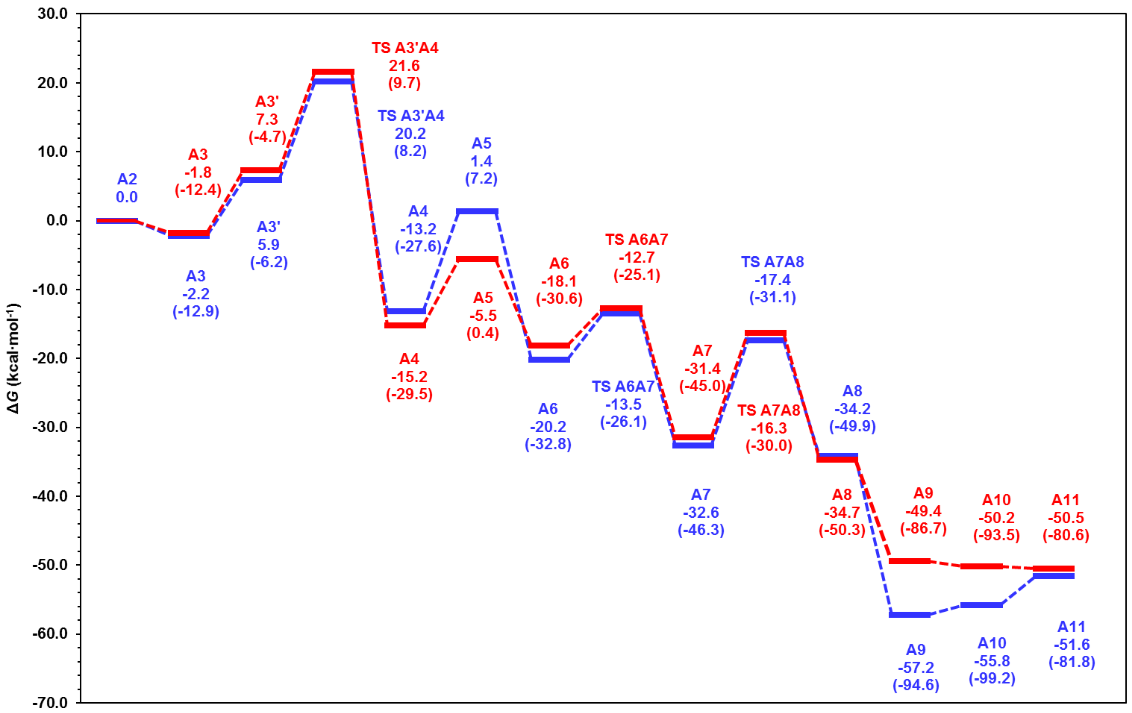

Figure 8.5. M06L-D3/cc-pVTZ-PP//B3LYP-D3 Gibbs energy profile for the [2+2+2] cycloaddition reaction of C_{60} and to acetylene molecules catalyzed by Wilkinson's complex. Gas phase vs. toluene solution (SMD). Blue = gas phase. Red = solvent = toluene. Energies in parentheses are electronic energies.

1.2. Expeditious preparation of open-cage fullerenes by rhodium(I)-catalyzed [2+2+2] cycloaddition of diynes and C_{60}: an experimental and theoretical study

The results obtained in our DFT study of the [2+2+2] cycloaddition of C_{60} and two acetylene molecules catalyzed by Wilkinson's complex prompted us to study the process experimentally with the aim of developing a catalytic version of the reaction using a Rh(I) complex as the catalyst and a series of diynes as alkyne-containing reaction partners.

In line with our initial predictions, the reaction of N-Ts tethered diyne **1a** and C_{60} in the presence of either 10 mol% or stoichiometric amounts of $[RhCl(PPh_3)_3]$ did not afford the desired cycloadduct. Although it was not isolated, we reasoned that a homocoupling product resulting from cyclotrimerization reaction of diyne **1a** with itself (**Figure 8.6**) must have been operative.

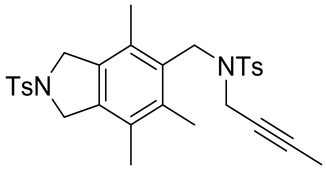

Figure 8.6. Structure of homocoupled **1a**.

We then moved to a combination of cationic Rh(I) complex $[Rh(cod)_2]BF_4$ with diverse diphosphine ligands. Indeed, such catalytic systems have been successfully used in the [2+2+2] cycloaddition reaction of diynes and diverse alkenes (see section 2 of the introduction and references cited therein). In a first attempt, we employed a 10 mol% 1:1 mixture of $[Rh(cod)_2]BF_4$ and BINAP as a benchmark catalytic system. This mixture was dissolved in CH_2Cl_2, treated with H_2(g) for 30 min, concentrated, re-dissolved in *o*-DCB and incorporated *via* syringe to a preheated *o*-DCB solution of C_{60} and **1a** (1 equivalent). The reaction mixture was stirred in *o*-DCB, at 90 ºC for 4h. Under these conditions, a dark brown solid could be isolated as a single reaction product after purification by column chromatography. The molecular formula of the obtained product was determined by electrospray ionization HRMS to be $C_{75}H_{17}NO_2S$, confirming the formation of a monoadduct in a 20% yield. Then, NMR spectroscopy experiments were used to establish its exact structure. Both ^{1}H and ^{13}C NMR spectra showed that the new compound had C_s symmetry, rather than the C_{2v} symmetry expected for a 1,3-cyclohexadiene derivative of C_{60} (**Figure 8.7**). Careful analysis of NMR data revealed an unexpected outcome: the product that had been formed in the reaction was actually bis(fulleroid) **2a**. Further evidence of the identity of **2a** was provided by its UV-vis spectrum. Likewise, as for previously reported fulleroids or bis(fulleroids), **2a** is purple in solution, accounting for the conserved 60 π-conjugated system of the parent fullerene.

As already discussed in section 1 of the introduction, the synthesis of open-cage bis(fulleroid) derivatives starting from 1,3-cyclohexadiene derivatives of C_{60} and C_{70} has already been described [161–170]. However, in previously reported examples, photochemical reaction conditions were necessary in order to promote the formal [4+4]/retro-[2+2+2] reaction mechanism that ultimately leads to the open-cage structure. As a paradigmatic example, very similar 1,3-cyclohexadiene derivatives reported by Cheng years ago required UV (λ = 350 nm) irradiation for 2 h to arrange into the corresponding bis(fulleroids) [162]. Since in our case the reaction mixture was not irradiated –note that even when performing the reaction in the dark, the 1,3-cyclohexadiene-fused compound could not be isolated– an alternative mechanistic pathway had to be postulated. As discussed below, we were able to provide a rational explanation for this transformation on the basis of DFT calculations (see below).

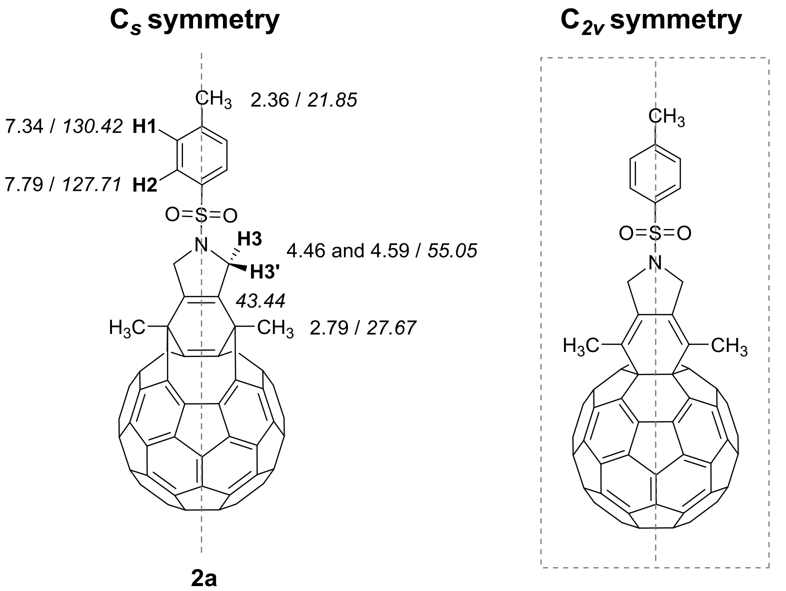
Cs symmetry
C2v symmetry
CH3 2.36 / 21.85
7.34 / 130.42 H1
7.79 / 127.71 H2
O=S=O
N
H3
H3'
4.46 and 4.59 / 55.05
43.44
H3C
CH3 2.79 / 27.67
CH3
O=S=O
N
H3C
CH3

2a
Bis(fulleroid)
(Obtained)

Cyclohexadiene derivative
(Never detected)

Figure 8.7. Structure of a) obtained bis(fulleroid) **2a**, and b) expected 1,3-cyclohexadiene product. Selected ^{1}H and ^{13}C (*in italics*) NMR chemical shifts of **2a**.

With these results at hand, we proceeded to optimize the reaction conditions (**Table 8.1**) The catalytic activity of several cationic Rh(I)/phosphine complexes was surveyed. We analyzed also the influence of temperature, MW heating, reaction time and concentration of substrates on the reaction outcome. Eventually, we came up with an optimized set of conditions: using 10% mol of a 1:1 $[Rh(cod)_2]BF_4$/Tol-BINAP mixture, heating at 90 ºC for 4h, working at a low concentration ($[C_{60}]$ = 1.4 mM) and employing 5 equivalents of diyne **1a**, the desired product **2a** was obtained in a 52% yield.

Table 8.1. Rh(I)-catalyzed [2+2+2] cycloaddition of C_{60} with diyne **1a**: Optimization of reaction parameters.

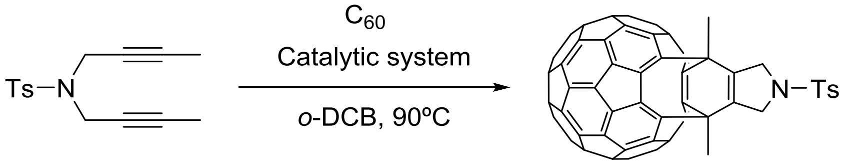
Ts–N
C60
Catalytic system
o-DCB, 90ºC
N–Ts

1a **2a**

Entry	Catalytic system	Ratio (mol) C_{60}/**1a**	**[C_{60}]** (mM)	Yield of **2a** (%)
1	$[Rh(PPh_3)_3Cl]$	1:1	7	0
2	$[Rh(cod)_2BF_4]$/BINAP	1:1	7	20
3	$[Rh(cod)_2BF_4]$/Tol-BINAP	1:1	7	28
4	$[Rh(cod)_2BF_4]$/Tol-BINAP	1:1	7	43
5	$[Rh(cod)_2BF_4]$/Tol-BINAP	1:5	1.4	52

Having established the optimum reaction conditions, we proceeded to evaluate the scope of the process (**Figure 8.8**). First, a series of sulfonamide tethered bis(fulleroids) **2b-g** bearing distinct functional groups were synthetized with moderate to good yields. Additionally, we prepared malonate-tethered bis(fulleroid) **2h**.

Unfortunately, methylene and oxygen-tethered diynes did not afford the desired reaction products **2i-j**. The substitution pattern of the triple bonds was found to have a dramatic influence on the reaction outcome. Diynes exhibiting phenyl or carboxylate terminal groups only afforded traces of the corresponding products. The same results were obtained when changing to terminal diynes. Only products **2k** and **2o**, keeping one of the two alkynes unsubstituted, could be obtained with very low isolated yields. Together with the desired products, homocoupling products were obtained.

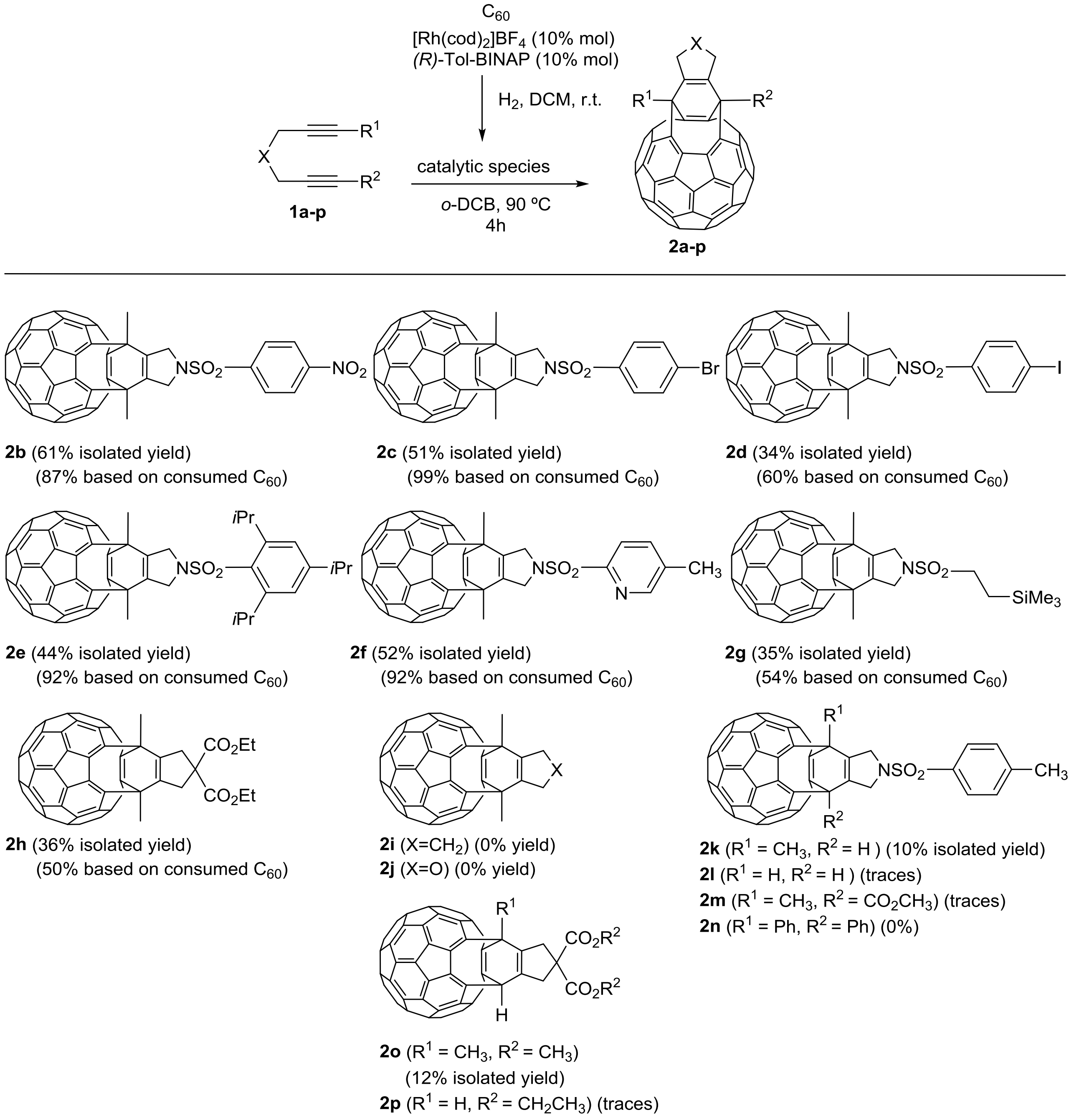

2b (61% isolated yield)
(87% based on consumed C_{60})

2c (51% isolated yield)
(99% based on consumed C_{60})

2d (34% isolated yield)
(60% based on consumed C_{60})

2e (44% isolated yield)
(92% based on consumed C_{60})

2f (52% isolated yield)
(92% based on consumed C_{60})

2g (35% isolated yield)
(54% based on consumed C_{60})

2h (36% isolated yield)
(50% based on consumed C_{60})

2i ($X=CH_2$) (0% yield)
2j (X=O) (0% yield)

2k ($R^1 = CH_3$, $R^2 = H$) (10% isolated yield)
2l ($R^1 = H$, $R^2 = H$) (traces)
2m ($R^1 = CH_3$, $R^2 = CO_2CH_3$) (traces)
2n ($R^1 = Ph$, $R^2 = Ph$) (0%)

2o ($R^1 = CH_3$, $R^2 = CH_3$)
(12% isolated yield)
2p ($R^1 = H$, $R^2 = CH_2CH_3$) (traces)

Figure 8.8. Scope of the Rh(I)-catalyzed [2+2+2] cycloaddition of C_{60} with diynes. Reaction conditions: 0.07 mmol of C_{60}, 5 equivalents of diyne **1**, 10% mol of Rh catalyst in 50 mL of o-dichlorobenzene (*o*-DCB) at 90 °C for 4h. The 10% mol mixture of $[Rh(cod)_2]BF_4$ and Tol-BINAP was treated with hydrogen in dichloromethane (DCM) solution for catalyst activation prior to substrate addition.

Further functionalization of the products obtained was achieved by subjecting bis(fulleroid) **2d** to standard Suzuki-Miyaura reaction conditions (**Scheme 8.2a**). Initially, **2d** was reacted with aryl boronic acid **3a** in the presence of 10% mol of $Pd(PPh_3)_4$, 2.5 equivalents of Cs_2CO_3 in a 9:1 toluene/H_2O mixture heating at 100 ºC for 4 h. Following this synthetic strategy we were able to prepare compounds **4b** and **4c**, both bearing interesting moieties for their potential use in the field of PV. For the case of **4c**, we isolated dehalogenated bis(fulleroid) **S3** (see supplementary material) together with the desired cross-coupling product. We also managed to expand the 8-membered hole of **2a** by simply exposing a $CDCl_3$ solution of this compound to sunlight and air (**Scheme 8.2b**). After 5 h, only open-cage dicarbonyl compound **5** resulting from oxidative photocleavage was detected by NMR spectroscopy and HRMS.

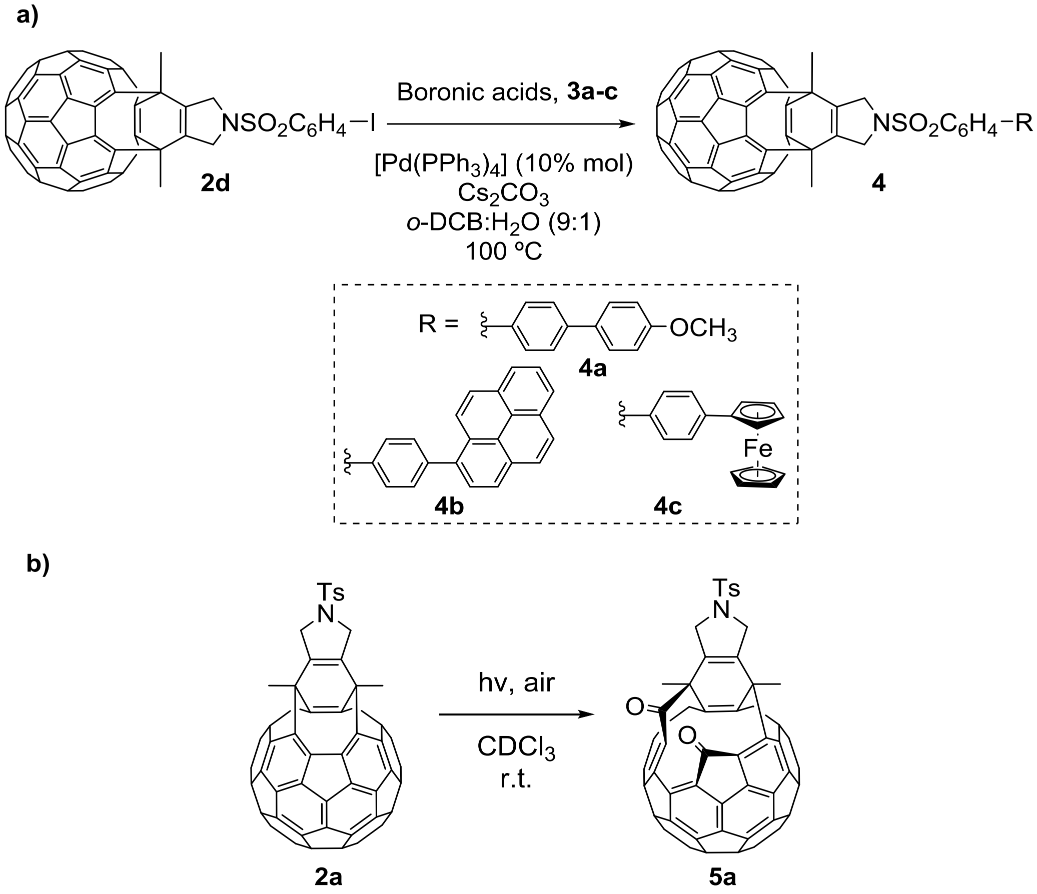

Scheme 8.2. Further functionalization of bis(fulleroids) **2**.

The electrochemical behavior of compounds **2a**, **4b**, **4c** and **5** was assessed by CV experiments (**Table 8.2**). All compounds showed two fully reversible reduction waves under the experimental conditions used, corresponding to two sequential one-electron reductions. For compounds **2a**, **4b** and **4c** covalent modification of the fullerene cage results in a cathodic shift with respect to C_{60}. Conversely, compound **5a** is more easily reduced than C_{60} and exhibits a redox behavior comparable to other previously reported open-cage dicarbonyl derivatives [187].

Table 8.2. Redox potentials of fulleroids **2a**, **4b**, **4c**, **5a** and C_{60}. E½ in V vs Fc/Fc+, 0.2 mM C_{60}/**2a/4b-c/5a** and 0.1 M $Bu_4N^+ClO_4$- in o-dichlorobenzene, SCE reference electrode, Pt working electrode, Pt wire auxiliary electrode, scan rate 50 mV.s-1, 25 °C).

Entry	Compound	E^1_{red}	E^2_{red}	E^3_{red}
1	C_{60}	-1.109	-1.514	-2.009
2	**2a**	-1.213	-1.626	
3	**4b**	-1.228	-1.633	
4	**4c**	-1.211	-1.594	
5	**5a**	-0.987	-1.370	

With the aim of understanding the formation of bis(fulleroid) products **2** the we completed our study by computationally investigating the reaction mechanism. DFT calculations were performed at the M06-D3/cc-pVTZ//B3LYP-D3/cc-pVDZ 363.15 K level of theory at 363.15 K and 1 atm in *o*-DCB (SMD) using a simplified model of the Rh(I) catalyst (see **Figure S7** in the supplementary material) . The results obtained revealed that the first steps of the reaction (from **A0** to **A5**) correspond to the classic [2+2+2] cycloaddition reaction mechanism (**Figure 8.9**), almost identic to the already discussed mechanism in the previous subsection for a reaction model of C_{60}, two acetylene molecules and Wilkinson's complex. The only difference found is that involvement of rhodabicylic intermediate **A5** instead of a rhodacycloheptadiene intermediate (see alternative path through **A5'** in **Figure S8** in the supplementary material). An alternative path B involving oxidative coupling between the diyne and a [6,6] bond of C_{60} leads again to a less favorable reaction path (see **Figure S9** in the supplementary material).

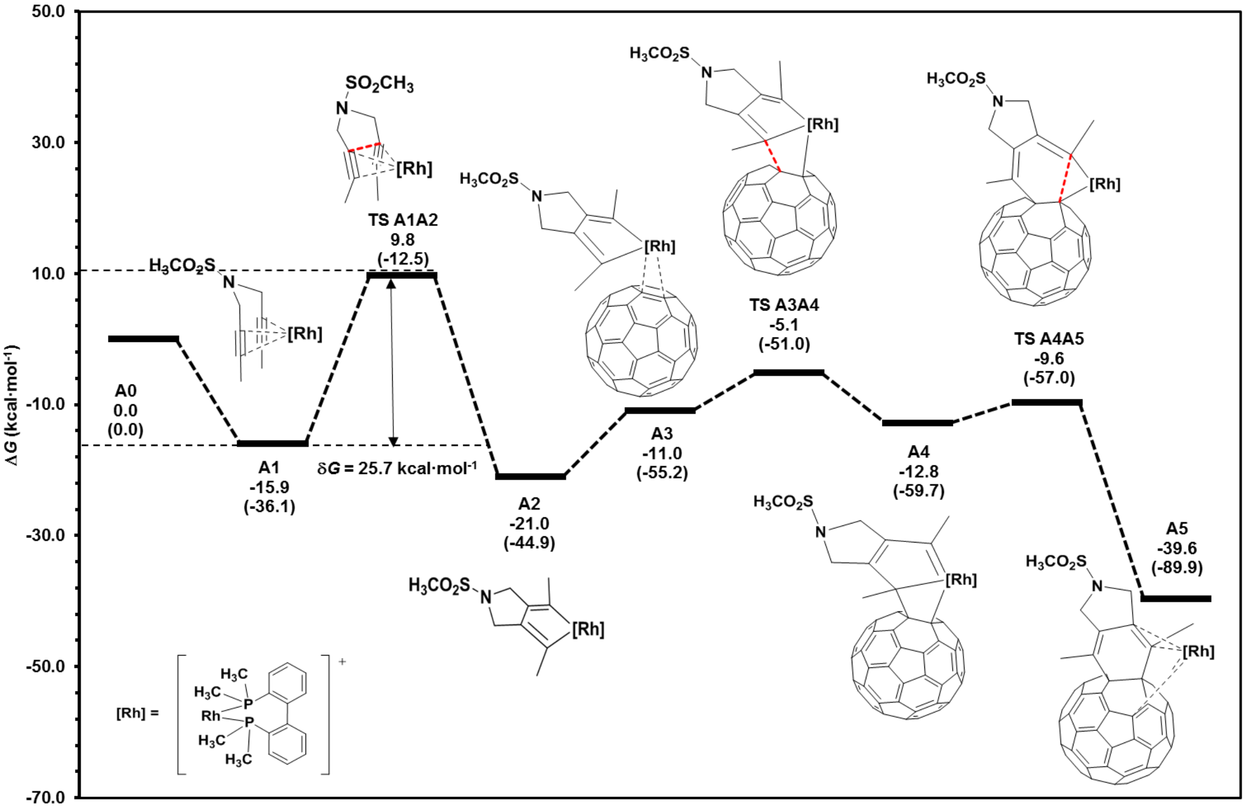

Figure 8.9. M06-D3/cc-pVTZ-PP//B3LYP-D3/cc-pVDZ Gibbs energy profile for the [2+2+2] cycloaddition of model diyne and C_{60}. Energies in parentheses are electronic energies.

However, this reaction mechanism does not explain the formation of the actual reaction bis(fulleroid) product. With this in mind, we explored different scenarios to elucidate the cage-opening mechanism. First, we considered the [4+4]/retro-[2+2+2] sequence in isolated 1,3-cyclohexadiene adduct (**Figure 8.10**). The results demonstrated that this reaction is only possible in the first triplet excited state. The same conclusions were obtained when evaluating an alternative di-π-methane rearrangement mechanism (**Figure 8.11**).

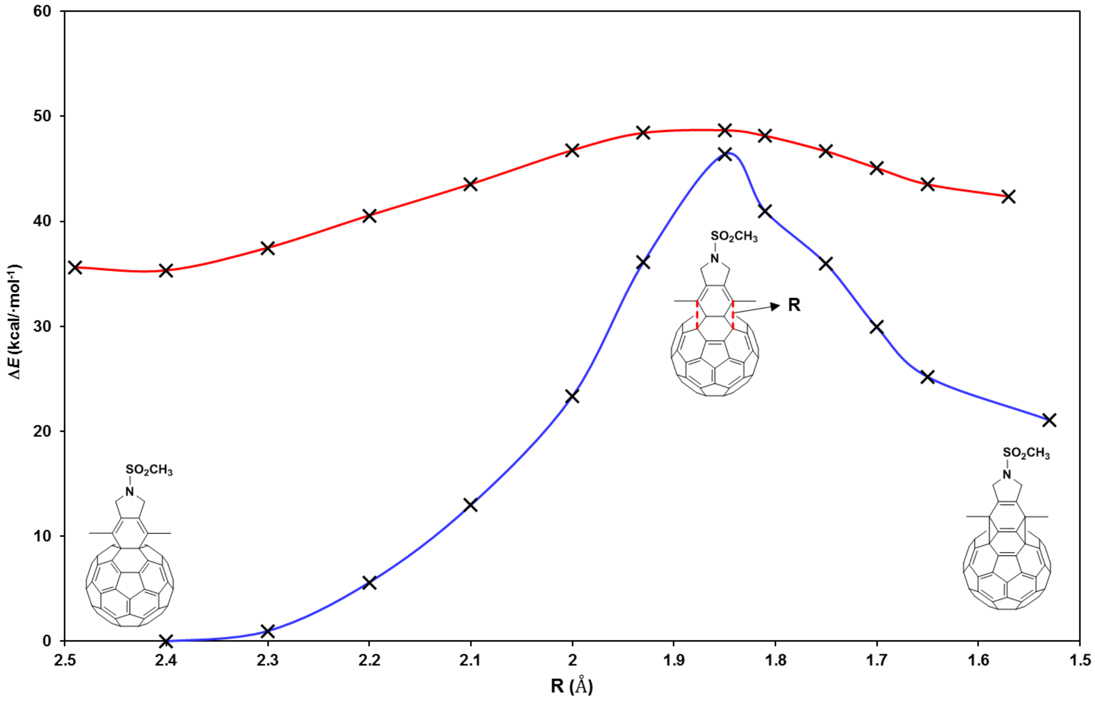

Figure 8.10. B3LYP-D3/cc-pVDZ-PP relaxed scan for the [4+4] cycloaddition. Blue = singlet state. Red = triplet state.

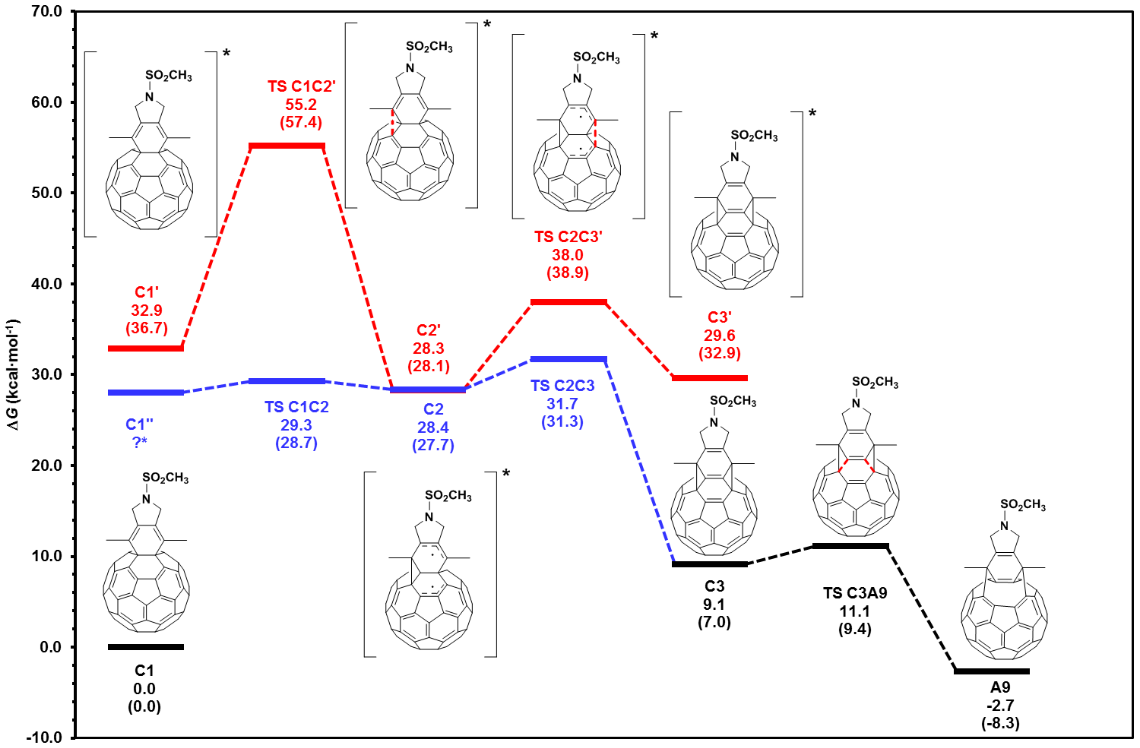

Figure 8.11. M06/cc-pVTZ-PP//B3LYP-D3/ccpVDZ Gibbs energy profile for the di-p-methane rearrangement. Energies in parentheses are electronic energies. Blue = open-shell singlet. Red = triplet state. Black = singlet state. *Not calculated. We estimate the energy of intermediate C1'' is similar to the one of the triplet state partner C1'.

Once these two mechanisms were ruled out, we considered a third scenario: our hypothesis at this point was that the Rh(I) catalyst employed in the reaction was playing a role not only in the [2+2+2] cycloaddition steps, but also in the steps required for the double [5,6] bond scission that lead to the reaction product. Thus, we investigated the Rh(I)-catalyzed process that transforms intermediate **A5** into **A9** (**Figure 8.12**). Intermediate **A5** experiences a di-π-methane rearrangement to provide bis(methanofullerene) intermediate **A7**. This process is accessible in the singlet ground state thanks to the participation of the Rh(I) complex. After this, retro-[2+2+2] cycloaddition and release of the catalyst by substitution with a new diyne molecule closes the catalytic cycle. Alternatively, release of the catalyst can take place in intermediate **A8**, since final retro-[2+2+2] step is also feasible from the isolated bis(methanofullerene). The overall process has an energetic span between the TDI **A1** and TDTS **TS A1A2** of 25.7 kcal/mol and is exergonic by 51.2 kcal/mol.

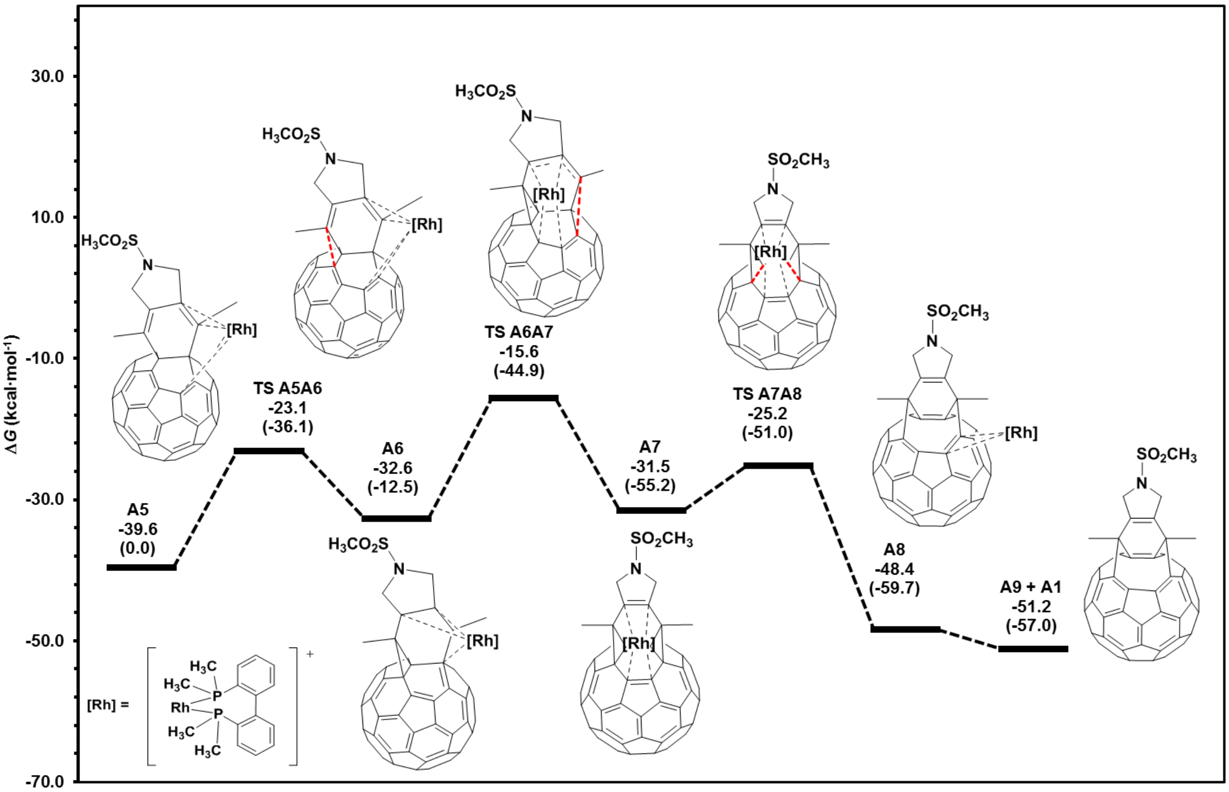

Figure 8.12. M06-D3/cc-pVTZ-PP//B3LYP-D3/cc-pVDZ Gibbs energy profile for the Rh-catalyzed cage-opening di-π-methane rearrangement. Energies in parentheses are electronic energies.

1.3. Enhanced open-circuit voltage in perovskite solar cells with open-cage [60]Fullerene derivatives as electron-transporting materials

Fullerene derivatives are, so far, the n-type materials of choice in PSCs with an inverted (p-i-n) planar structure (see subsection 1.8.3 in chapter 1 and references cited therein). Besides acting as efficient ETLs, fullerenes have proved effective as additives or interfacial modification layers due to their ability to passivate the charge traps at the surface of thin films and to assist ohmic contact at the ETL-metal electrode interface. Moreover, they can improve device stability by acting as a barrier for moisture and can serve as a template for high quality crystal growth. Most of the fullerene-based PSCs reported in the literature rely on the use of $PC_{61}BM$ or $PC_{71}BM$ as the ETL, since they benefit from high electron mobility and crystalline packing. However, many studies report on the introduction of other derivatives as a strategy to further improve both the performance and stability of PSCs. While most of the compounds reported are structurally related surrogates of $PC_{61}BM$ and $PC_{71}BM$, obtained by analogous cyclopropanation reactions, other synthetic derivatives resulting from other reactions (*e.g.* [3+2] and [4+2] cycloadditions) have also been successfully incorporated [214,218–220].

As a third goal in this first section we attempted to incorporate open-cage dicarbonyl fullerene derivatives **5a-c** as the ETLs in PSCs with a p-i-n structure (**Scheme 8.3**). This work was done in collaboration with the group of Prof. Echegoyen as a result of a research stay of three months in his laboratories at the University of Texas at El Paso (UTEP). In this collaborative project, the author contributed to the synthesis of the fullerene derivatives tested.

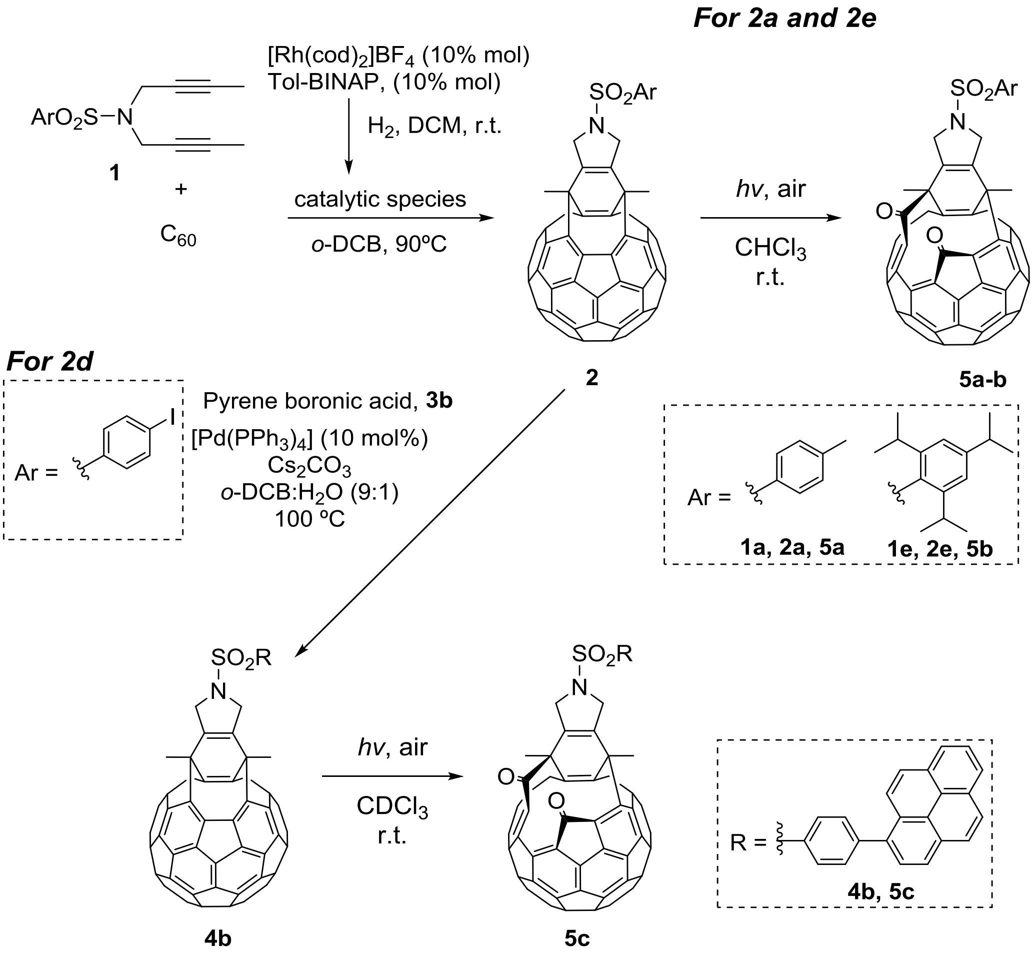
For 2a and 2e
[Rh(cod)2]BF4 (10% mol)
Tol-BINAP, (10% mol)
H2, DCM, r.t.
catalytic species
o-DCB, 90ºC
ArO2S–N
1
+
C60
SO2Ar
N
2
hv, air
CHCl3
r.t.
O
5a-b
For 2d
Ar =
I
Pyrene boronic acid, 3b
[Pd(PPh3)4] (10 mol%)
Cs2CO3
o-DCB:H2O (9:1)
100 ºC
1a, 2a, 5a
1e, 2e, 5b
SO2R
4b
hv, air
CDCl3
r.t.
5c
R =
4b, 5c

Scheme 8.3. Synthesis of the three open-cage dicarbonyl derivatives incorporated in PSCs.

Compounds **5a-c** were prepared according to our synthetic protocol, which encompasses a Rh(I)-catalyzed cycloaddition reaction followed by oxygenative photocleavage of the obtained open-cage derivatives. For the case compound of **5c**, an additional step involving Suzuki-Miyaura cross-coupling of bis(fulleroid) **2d** with pyrene boronic acid **3c** was required. Open-cage fullerene **5a** displays a N-Ts functionality and was selected as a benchmark compound. Compound **5b** has improved solubility provided by the presence of 3 isopropyl functional groups in its aryl moiety. Since it has been reported that fullerene derivatives with enhanced solubilities present improved passivation ability at the grain boundaries of the perovskite layer [401], we expected this feature to be beneficial in terms of device performance. Finally, **5c** was chosen to test the influence of the pyrene light-harvesting fragment. Control devices based on $PC_{61}BM$ were used as the control.

The HOMO/LUMO levels of compounds **5a-c** (**Figure 8.13a**) were estimated from UV-Vis and CV experiments (see **Figure S10-11**). Overall, their photophysical and electrochemical properties were found to be close to those of $PC_{61}BM$. These results prompted as to move on and test the performance of **5a-c** as ETLs in PSCs. First, electrical conductivities were measured by recording *J-V* curves for electron only devices with a structure ITO/Al/Fullerene/Al. Similar values in the range of 2.8–4.8 x 10^{-4} $cm^2V^{-1}s^{-1}$ were obtained. Next, passivation ability was assessed on the basis of photoluminescence (PL) (**Figure 8.13b**) and time-resolved photoluminescence (TR-PL) experiments of the perovskite with and without the incorporation of **5a-c** and $PC_{61}BM$. Best results were obtained for compound **5a**. These results contradict our initial hypothesis about the enhanced passivation ability of **5b**. Nonetheless, this outcome may be reasoned in terms of the low crystallinity of compound **5b**. It has been postulated that this crystalline ETLs reduce energy disorder and that this has a beneficial impact on the passivation of charge traps [402]. The low solubility of **5c** in chlorobenzene (**Figure S12**) prevented the formation of good quality films and, therefore, this compound exhibited significantly worse performance. TR-PL also showed faster decays for compounds **5a** and **5b (Figure S13)**, indicating higher inhibition of charge recombination processes.

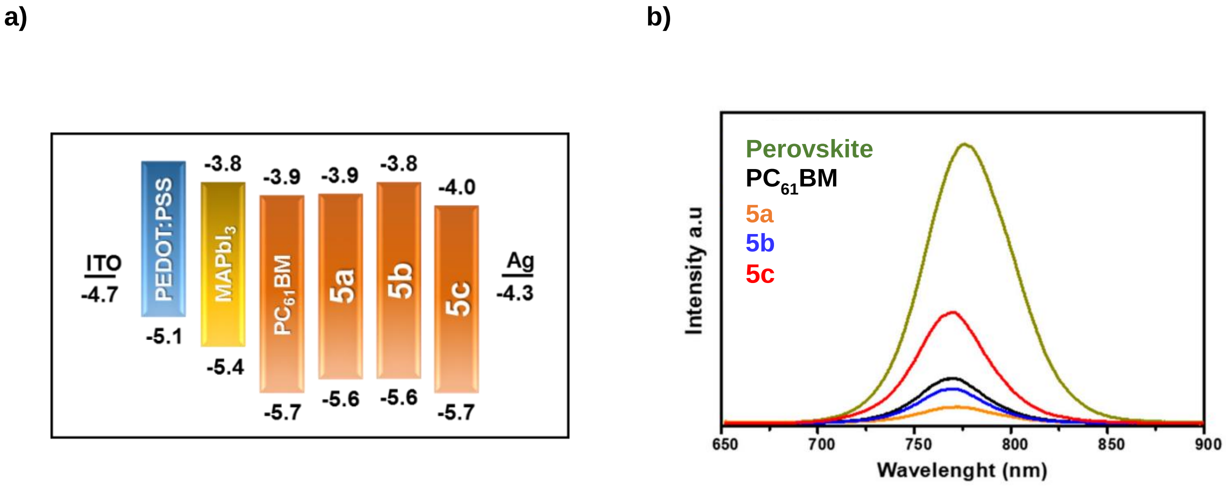

Figure 8.13. (a) Representation of HOMO/LUMO energy levels estimated from CV and UV-vis experiments (eV). (b) PL spectra of perovskite and perovskite/ETL films.

Compounds **5a-c** and $PC_{61}BM$ were incorporated in devices with an ITO/PEDOT:PSS/perovskite/fullerene/Ag structure. **5a** and **5b** showed PCE values of up to 16.92% and 16.37%, respectively. Also, high V_{oc} values of 1.01 V for **5a** and 0.97 V for **5b** were obtained (**Figure 8.14**). By its part, control devices based on $PC_{61}BM$ showed 16.22% PCE and 0.92 V_{oc}. This significant improvement of V_{oc} values was attributed to the higher LUMO levels as compared with $PC_{61}BM$. Again, the low solubility of **2c** prevented us from obtaining good quality devices. This fact explains the poor performance of this compound. Finally, devices fabricated with **5a** and **5b** exhibited comparable stability to the ones incorporating $PC_{61}BM$ (**Figure S14**) and negligible hysteresis (**Figure S15**).

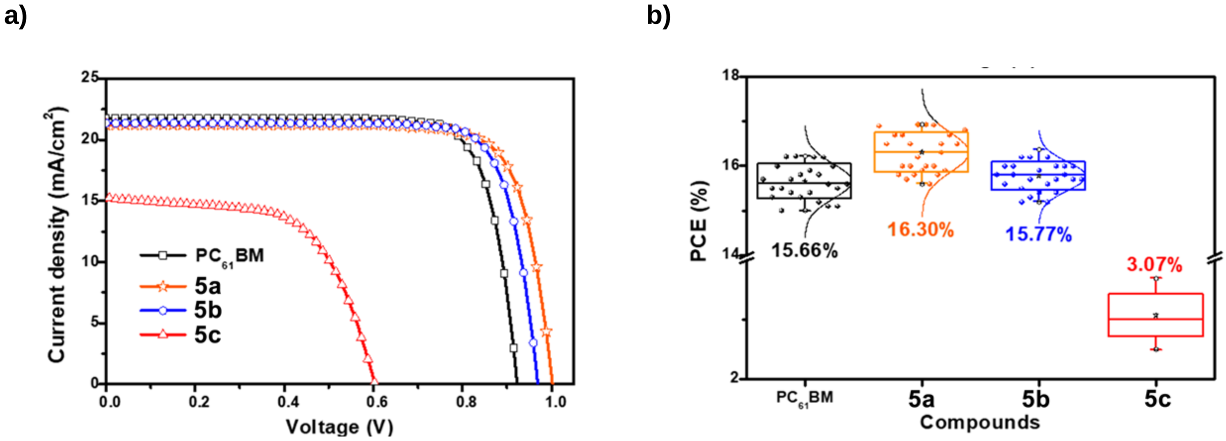

Figure 8.14. (a) *J-V* curves of devices incorporationg open-cage dicarbonyl derivatives **5a-c** and PC$_{61}$BM. (b) PCE measured for 25 independent cells, average values and representation of the standard deviation (SD).

In conclusion, this work disclosed the ability of open-cage derivatives to behave as the ETLs in PSCs. Compounds with appropriate solubility offered better performances than PC$_{61}$BM thanks to enhanced V_{oc} values, which in turn are explained by higher LUMO levels. This preliminary account opens the door to develop new derivatives with superior performances based on our straightforward synthetic methodology.

To summarize, in this first section we have studied the Rh(I)-catalyzed [2+2+2] cycloaddition of C$_{60}$ with alkynes. In the first project, we analyzed computationally all possible reaction paths that lead to a cyclohexadiene-fused fullerene derivative starting from C$_{60}$ and acetylene. We concluded that, although it is a feasible process, the formation of benzene by alkyne cyclotrimerization is clearly more favorable. The preliminary computational results obtained guided the study the reaction in the laboratory. Eventually, we came up with a catalytic protocol to prepare open-cage bis(fulleroids) starting from C$_{60}$ and a series of diynes. Combination of experiments and theory was key to understand the mechanism underlying the cage-opening steps of the reaction. Finally, we prepared three open-cage dicarbonylic C$_{60}$ derivatives by oxygenative photocleavage of three different bis(fulleroids). These compounds were successfully incorporated as the ETLs in PSCs.

Section 2: A Rh-catalyzed cycloisomerization/Diels-Alder cascade reaction of 1,5-bisallenes for the synthesis of polycyclic heterocycles and the functionalization of fullerenes

Our research group has investigated the participation of several functional groups in Rh(I)-catalyzed [2+2+2] cycloaddition reactions (see section 2 in chapter 1 and references cited therein). Specifically for the last years, we have focused on the use of allene-containing molecules. Recently, in the context of this doctoral thesis, we turned our attention to the chemistry of 1,5-bisallenes. When treated under transition metal catalysis, this class of compounds experience diversified transformations, yielding products with 5- [328,329], 6- [330] or 7-membered [331,332] rings. However, most of the reactions reported consist of cycloisomerization reactions or homocoupling reactions of the starting bisallene products. Cyclization reactions of bisallenes incorporating a third unsaturated partner are scarce [322–325,333].

With these precedents in mind, our starting goal was to develop a synthetic methodology based on Rh(I) catalysis involving 1,5-bisallenes and fullerenes as the unsaturated partners in an analogous process to that described in chapter 4 and section 1 of the present chapter. Since there were no precedents of such process employing simple alkenes, we decided to set a previous objective before addressing the more challenging goal of fullerene functionalization. Consequently, ethyl acrylate **2a** was chosen as a model compound to initially investigate the reaction. Our initial hypothesis was that after oxidative coupling, one, two or three of rhodacyclopentane intermediates **I**, **II** and **III** would result. Subsequent insertion of the alkene and reductive elimination would afford products **A**, **B** and **C**, respectively (**Scheme 8.4**).

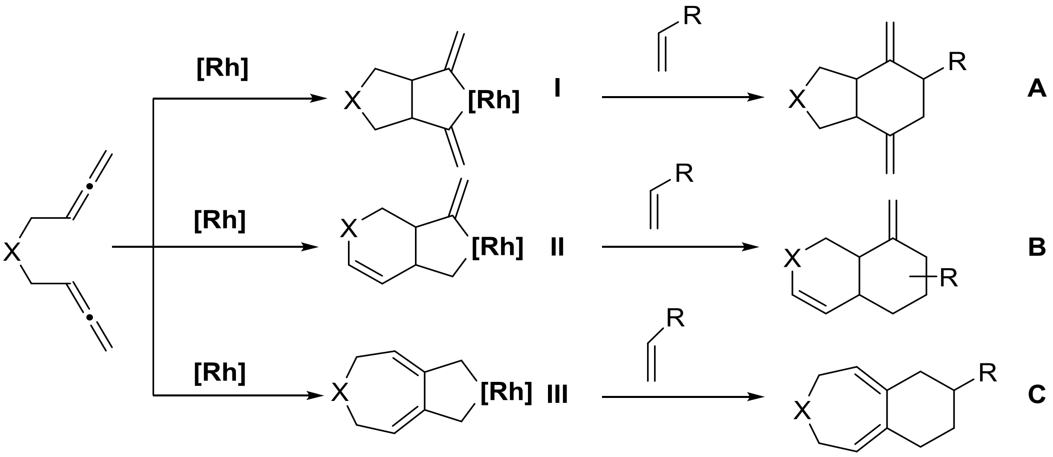

Scheme 8.4. Simplified mechanistic pathway for the [2+2+2] cycloaddition of 1,5-bisallenes and an alkene.

After some experimentation, we eventually found that heating a mixture of N-Ts bisallene **1a** and ethyl acrylate **2a** in the presence of a 10 mol % 1:1 $[Rh(cod)_2]BF_4$/Tol-BINAP mixture led to the formation of benzazepine product **3aa** in a 30% yield and with complete regioselectivity (entry **1** in **Table 8.3**). Remarkably, we observed that under these reaction conditions, the formation of a product displaying a 7-MR was favored. Azepine- and oxepine-containing fused ring systems are found in some pharmacologically active compounds and in natural products [403–410] and their efficient synthesis is in general highly challenging. Therefore, developing cycloaddition reactions of bisallenes with a third unsaturation being able to control the formation of a 7-MR is desirable. Together with **3aa**, a novel cycloisomerisation product **4a** was also formed in a 29% yield.

Table 8.3. Rh(I)-catalyzed cycloaddition of **1a** with ethyl acrylate **2a**. Optimization of reaction parameters.

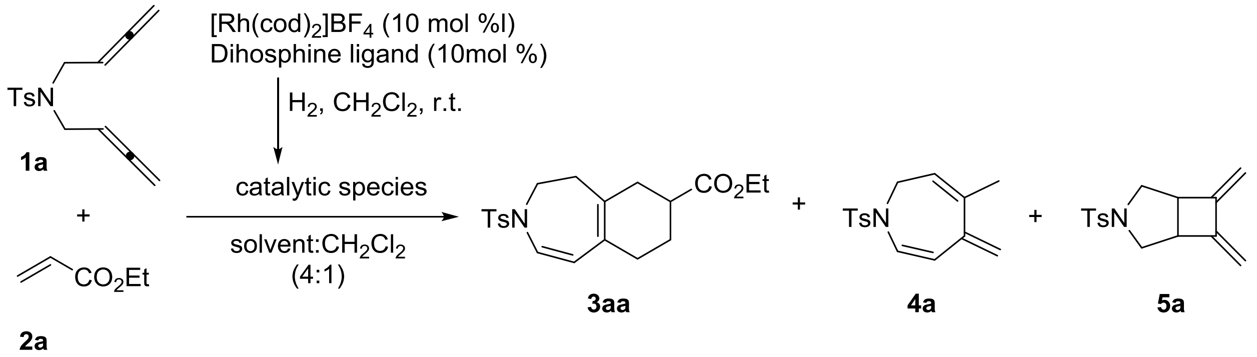
[Rh(cod)2]BF4 (10 mol %l)
Dihosphine ligand (10mol %)
H2, CH2Cl2, r.t.
catalytic species
solvent:CH2Cl2
(4:1)
TsN
1a
+
CO2Et
2a
TsN
CO2Et
3aa
+
TsN
4a
+
TsN
5a

Entry	Ligand	Solvent	[**1a**] (mM)	Temperature (ºC)	**1a**:**2a** ratio	Yield of **3aa** / **4a** / **5a** (%)
1	(*R*)-BINAP	Toluene	18	65	1:10	30 / 29 / -
2	(*R*)-BINAP	THF	18	65	1:10	46 / 39 / -
3	(*R*)-BINAP	THF	9	65	1:50	49 / 45 / -
4	(*R*)-DTBM-Segphos	THF	9	65	1:50	65 / 5 / 15
5	(*R*)-DTBM-Segphos	THF	9	40	1:50	60 / - / 15

However, careful analysis of the reaction product made us realize that the compound formed was not exactly the anticipated [2+2+2] reaction product (structure C in **Scheme 8.4**), but a closely related isomer. Conversely, we saw that the position of the double bonds in the seven-membered moiety was analogous to other compounds already reported by Ma and Mukai. Following this observation, we changed our hypothesis to propose an alternative mechanism of the reaction, that would proceed as follows: the Rh(I) complex would promote the transformation of **1a** into a triene intermediate with two exocyclic double bonds, which in turn would react with a dienophile *via* a DA cycloaddition reaction, leading to the final product. This is, to the best of our knowledge, the second case of a one-pot controlled formation of a 7-membered bisallene cycloisomer followed by reaction with another unsaturated partner. The first one was reported some years ago by Mukai and consists of a [2+2+1] carbonylative reaction [333].

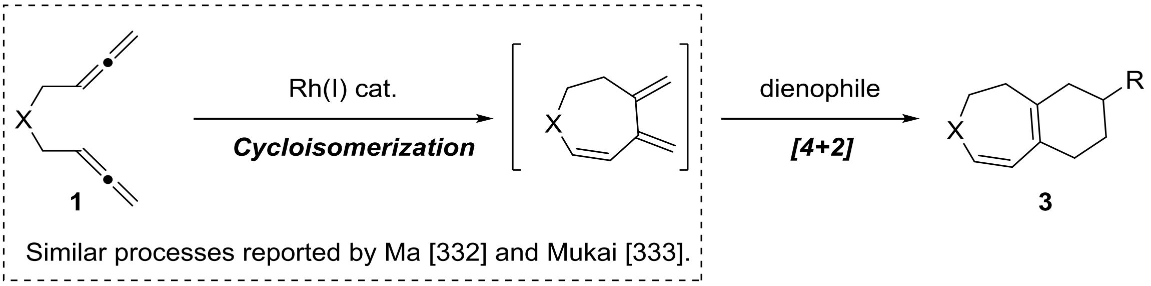
X
1
Rh(I) cat.
Cycloisomerization
X
dienophile
[4+2]
X
R
3
Similar processes reported by Ma [332] and Mukai [333].

Scheme 8.5. Proposed reaction mechanism for the transformation of bisallene **1** into reaction product **3**.

We then proceeded to optimize the reaction conditions in order to increase the overall yield and selectivity towards the formation of **3aa** (see **Table 8.3** and **Table S1** in the supplementary material). Using (*R*)-DTBM-

Segphos as a ligand, a mixture of THF and DCM as a solvent and heating at 40 ºC, the desired product was obtained in a 60% isolated yield. We also managed to get rid of the undesired cycloisomerization byproduct under these conditions. In turn, another product (**5a**) originated from [2+2] cycloaddition of the internal double bonds of the **1a** was obtained in 15% yield.

With an established set of conditions at hand, the scope of the reaction was evaluated (**Figure 8.15**). Overall, the reaction proceeds with good to moderate yields with a wide range of alkenes. Also oxepine compounds could be obtained starting from an *O*-tethered bisallene, though in considerably lower yields. As observed later during the computational study of the reaction, interaction of the oxygen atoms in the sulfonamide with the Rh center of the catalyst might result in beneficial effects for the outcome of the reaction. Single crystal X-ray diffraction analysis of compound **3am** (CCDC 1915067) allowed us to unambiguously establish the structure of the cycloadducts obtained.

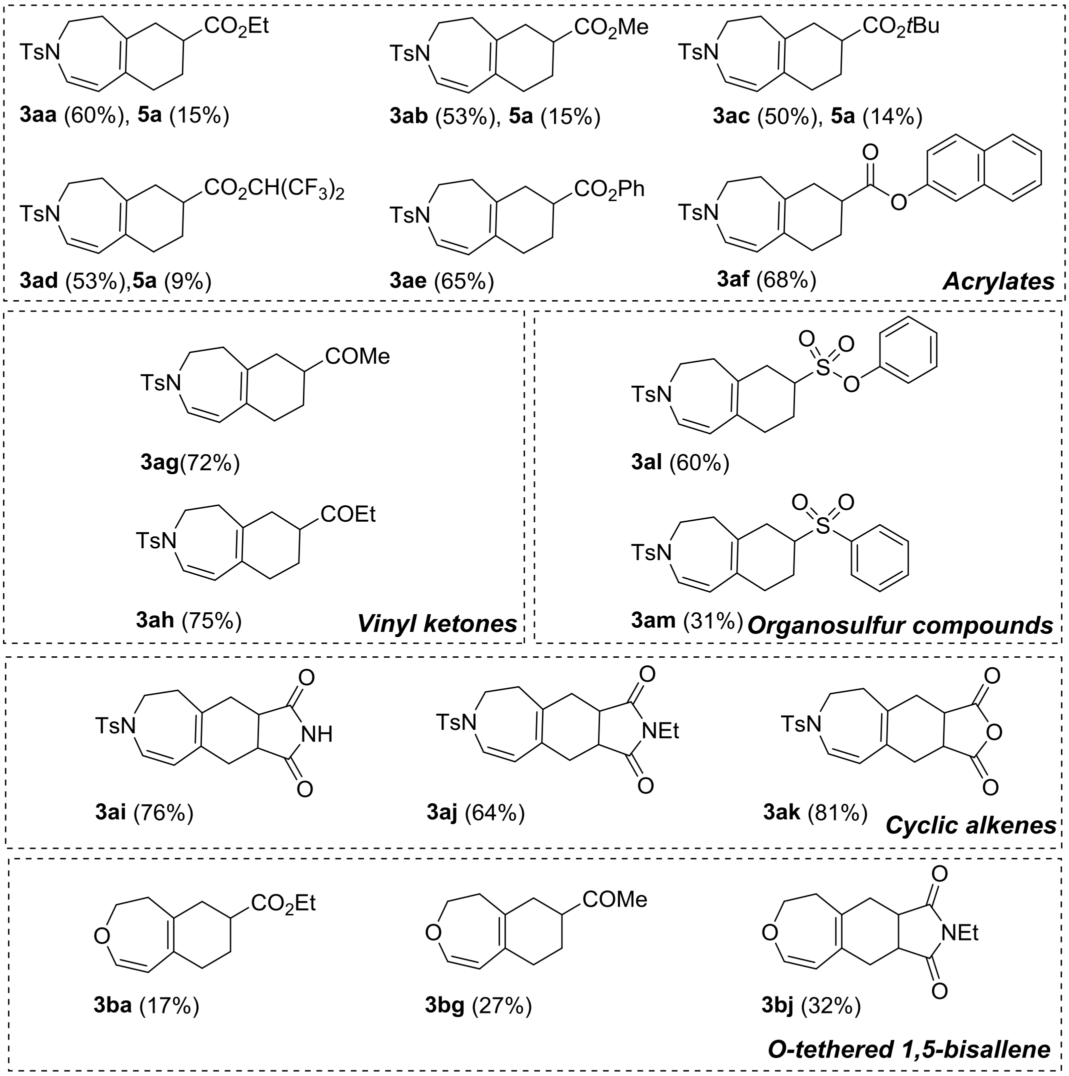
3aa (60%), **5a** (15%)
3ab (53%), **5a** (15%)
3ac (50%), **5a** (14%)
3ad (53%),**5a** (9%)
3ae (65%)
3af (68%)
Acrylates
3ag(72%)
3ah (75%)
Vinyl ketones
3al (60%)
3am (31%)
Organosulfur compounds
3ai (76%)
3aj (64%)
3ak (81%)
Cyclic alkenes
3ba (17%)
3bg (27%)
3bj (32%)
O-tethered 1,5-bisallene

Figure 8.15. Scope of the cycloaddition of 1,5-bisallenes **1** and alkenes **2**.

Since a stereogenic center was generated in derivatives **3**, the enantiomeric excess was measured in all cases, but no enantioinduction was observed regardless of the substrate or the ligand used (**Figure 8.16**). This result is commensurate with the mechanism proposed for this transformation.

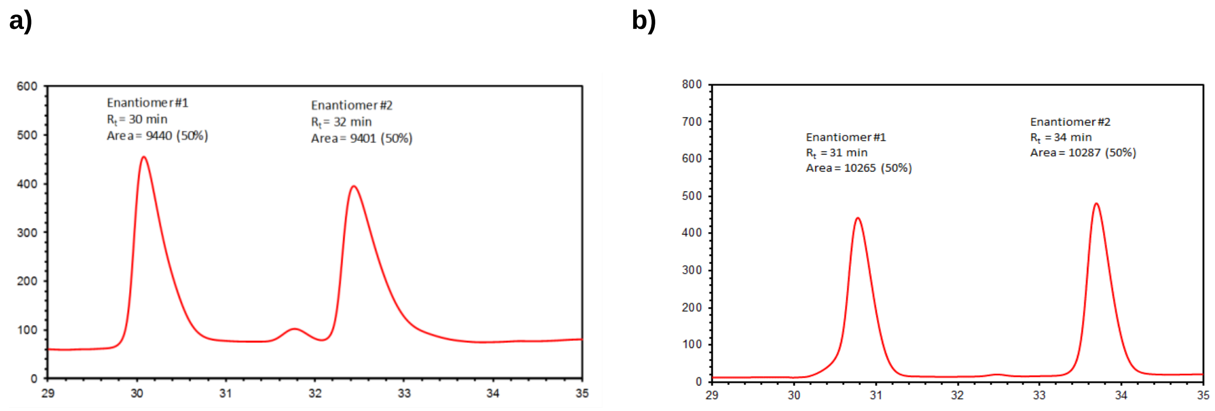

Figure 8.16. HPLC trace of compound **3aa** obtained (a) using (±)-BINAP as a diphosphine ligand and (b) under optimal conditions, using (*R*)-DTBM-Segphos as a phosphine ligand. Conditions: Chiralpak IA column (4.6 x 250 mm, 5 µm); 1 mL/min flow rate; 100% hexane → 20% 2-propanol in hexane; 40 min.; λ= 254 nm.

To confirm our proposed reaction mechanism, we completed our study by evaluating computationally the process that transforms the bisallene into the reaction product. Calculations at the M06L-D3/cc-pVTZ-PP//B3LYP-D3/cc-pVDZ-PP level of theory, at 313.15 K and 1 atm in a 76:24 (mol) mixture of THF/CH_2Cl_2 allowed us to propose the mechanism depicted in **Figure 8.17**.

The reaction starts with η^4-coordination of $[Rh(BINAP)]^+$ to the two internal double bonds of 1,5-bisallene **1a** to form the square-planar 16-electron intermediate **A1**. This process is exergonic by 13.2 kcal/mol. Upon coordination, intermediate **A1** readily experiences oxidative coupling at the central carbon atoms of both allene moieties to deliver intermediate **A2**, a rhodabicyclo[3.2.1]octane complex featuring two contiguous exocyclic methylene groups. This first step has a Gibbs energy barrier of 24.7 kcal/mol through **TS A1A2** and is exergonic by 20.2 kcal/mol. **A2** is then converted into intermediate **A3** through a β-hydride elimination mechanism. This process is slightly endergonic by 5.9 kcal/mol and has a Gibbs energy barrier of 10.8 kcal/mol (**TS A2A3**). Reductive elimination from intermediate **A3** to form **A4** has to surmount a barrier of 4.0 kcal/mol (**TS A3A4**) and releases 25.9 kcal/mol. Subsequent release of the initial Rh(I) complex leads to triene intermediate **A5**, completing the catalytic cycle (Path A in **Figure 8.17**). Alternatively, intermediate **A3** can experience a rearrangement with a rotation through the C–Rh bond that approaches the hydride coordinated to Rh to one of the C═C exocyclic double bonds giving **A3′** (Path B in **Figure 8.17**). Reductive elimination through **TS A3′B1** has a cost of 8.1 kcal/mol and is exergonic by 31.5 kcal/mol. This alternative mechanism provides a rational explanation for the formation of compound **4a**. On the other hand, the formation of intermediate **A5** is followed by [4+2] cycloaddition with ethyl acrylate **2a** to deliver compound **3aa**. The formation of the desired reaction product **3aa** has an overall reaction energy ($\Delta G r$) of −75.1 kcal/mol. Importantly, the regiochemistry of the reaction can also be explained by our computed reaction mechanism. While "endo a" approximation of the dienophile (*i.e.* **TS A5–3aa′**) has a Gibbs energy barrier of 26.6 kcal/mol, "endo b" approximation (*i.e.*, **TS A5–3aa**) has a lower cost of 24.0 kcal/mol. Such a difference in energy ($\Delta\Delta G^\ddagger$ = 2.6 kcal/mol) accounts for the selective formation of the actual reaction product **3aa**.

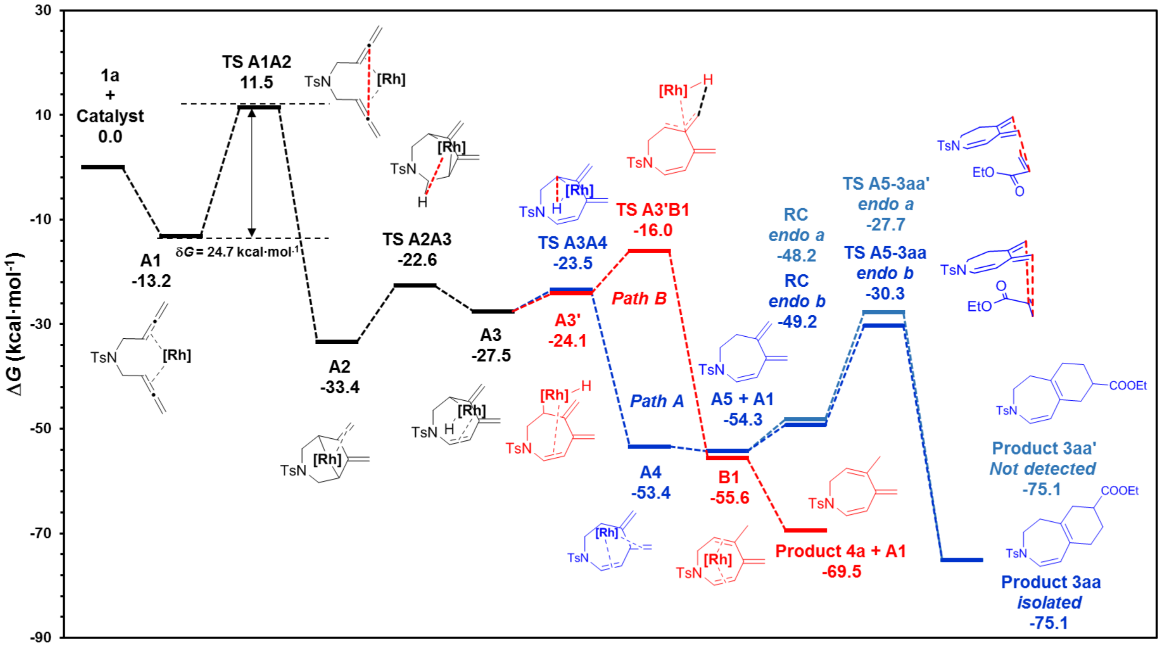

Figure 8.17. M06L-D3/cc-pVTZ-PP/SMD(76% THF, 24% CH_2Cl_2)//B3LYP-D3/cc-pVDZ-PP Gibbs energy profile for the tandem cycloisomerization/DA cycloaddition leading to product **3aa** (Path A) and cycloisomerization reaction leading to product **4a** (Path B). RC = reactant complex.

Alternative reaction pathways involving DA cycloadditions from intermediates **A2** (**Figure 8.18**), **A3** (**Figure 8.19**) and **A4** (**Figure 8.20**) can be found were also computed. However, all alternative mechanisms computed have higher barriers or do not explain the observed regioselectivity. In summary, the reaction mechanisms leading to compounds **A5** and **4a** have an energetic span between the TDI (**A1**) and TOF (**TS A1A2**) of 24.7 kcal/mol. Once formed, intermediate **A5** reacts with ethyl acrylate **2a** through a regioselective catalyst-free DA cycloaddition to provide compound **3aa**.

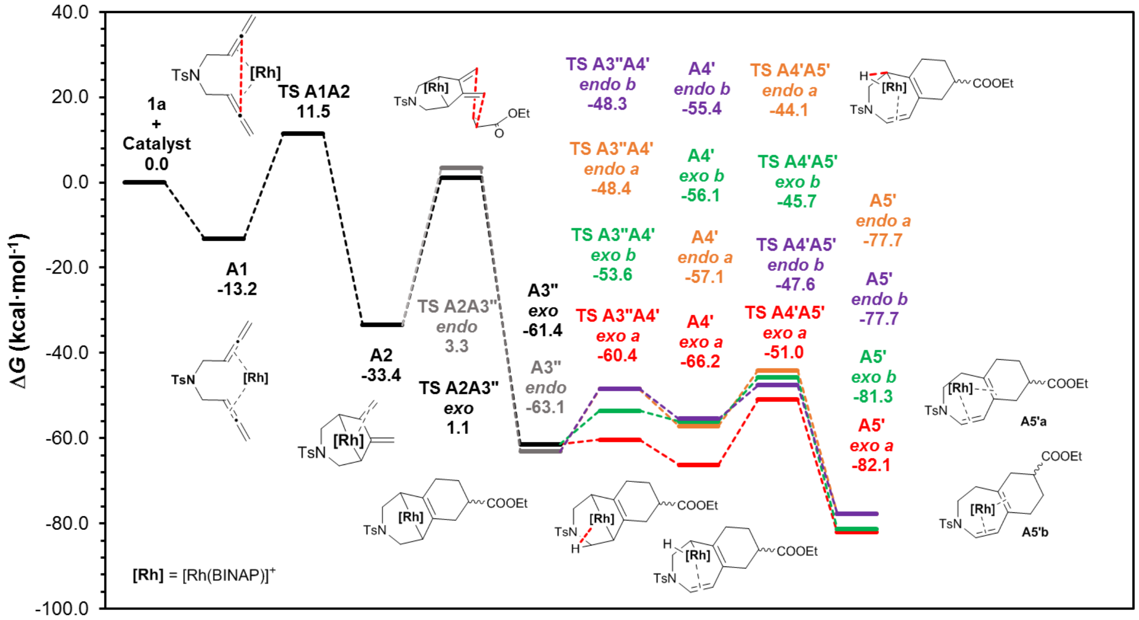

Figure 8.18. M06L-D3/cc-pVTZ-PP/SMD(76% THF, 24% CH_2Cl_2)//B3LYP-D3/cc-pVDZ-PP Gibbs energy profile for the tandem cycloisomerization/DA cycloaddition leading to product **3aa** (DA cycloaddition involving **A2**).

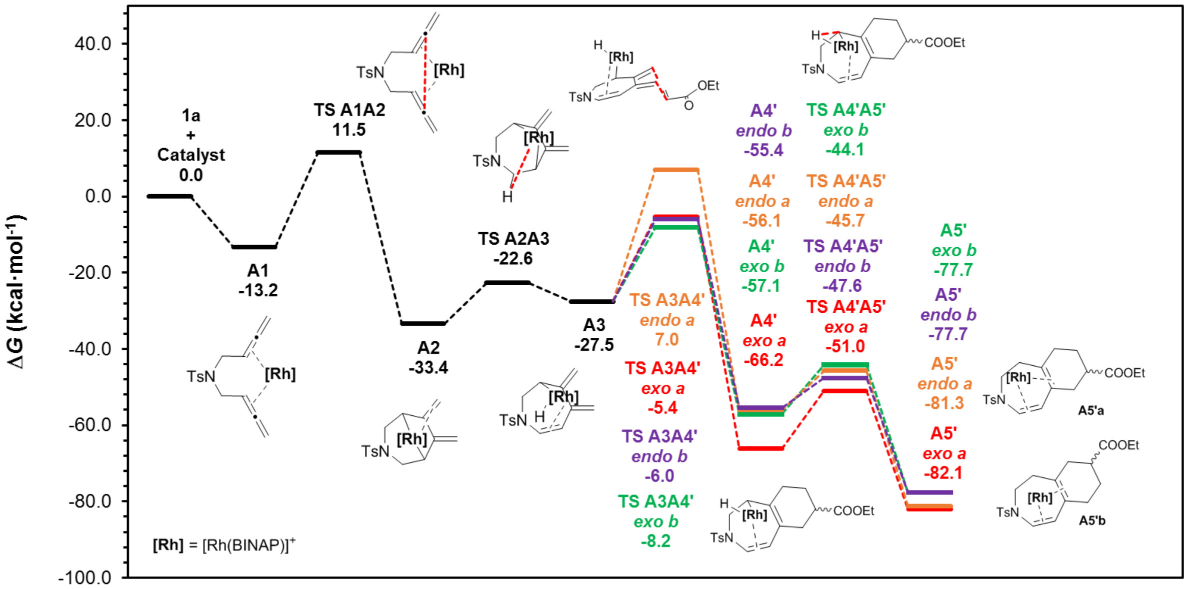

Figure 8.19. M06L-D3/cc-pVTZ-PP/SMD(76% THF, 24% CH_2Cl_2)//B3LYP-D3/cc-pVDZ-PP Gibbs energy profile for the tandem cycloisomerization/DA cycloaddition leading to product **3aa** (DA cycloaddition involving **A3**).

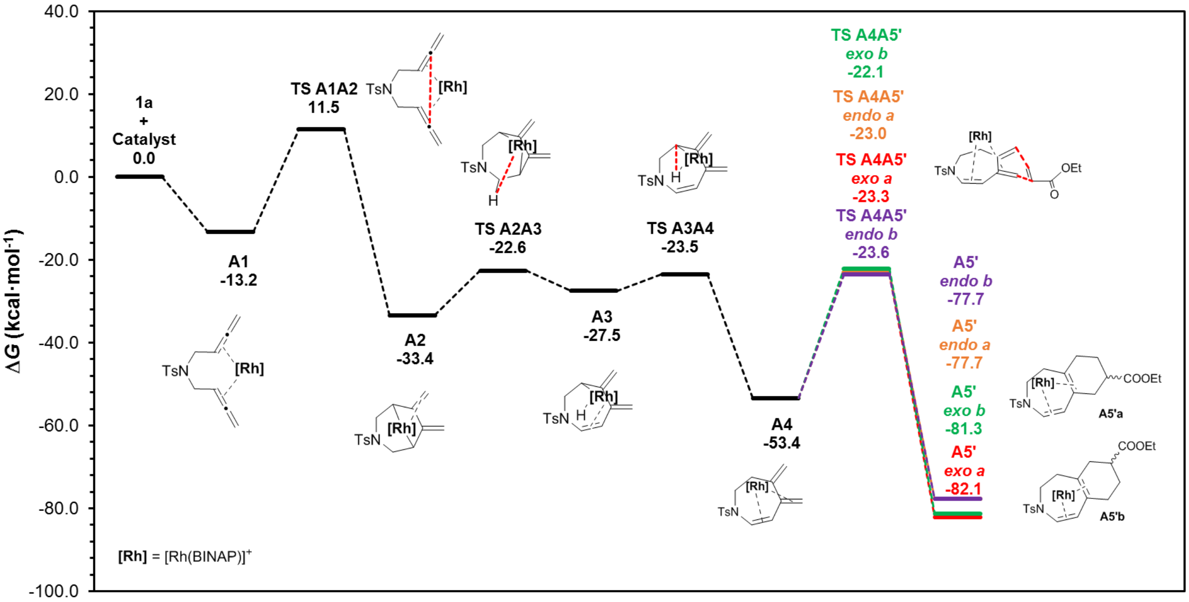

Figure 8.20. M06L-D3/cc-pVTZ-PP/SMD(76% THF, 24% CH_2Cl_2)//B3LYP-D3/cc-pVDZ-PP Gibbs energy profile for the tandem cycloisomerization/DA cycloaddition leading to product **3aa** (DA cycloaddition involving **A4**).

Further evidence of the mechanism was provided by additional calculations, which ruled out the involvement of **5a** (**Figure 8.21**). Intermediate **C1** has to surmount a Gibbs energy barrier of 52.1 kcal/mol (**TS C1A2**) in order to be transformed into **A2**. The backward process is not energetically feasible either (**TS A2C1**, $\Delta G^{\ddagger}$ = 45.3 kcal/mol). These results show that the byproduct **5a** must be formed by a completely independent mechanism involving a Rh(I)-catalyzed [2+2] cycloaddition of the internal C–C double bonds of **1a**. Likewise, heating a mixture of **5a** and ethyl acrylate **2a** in the presence and absence of the catalytic system provided only unreacted starting materials.

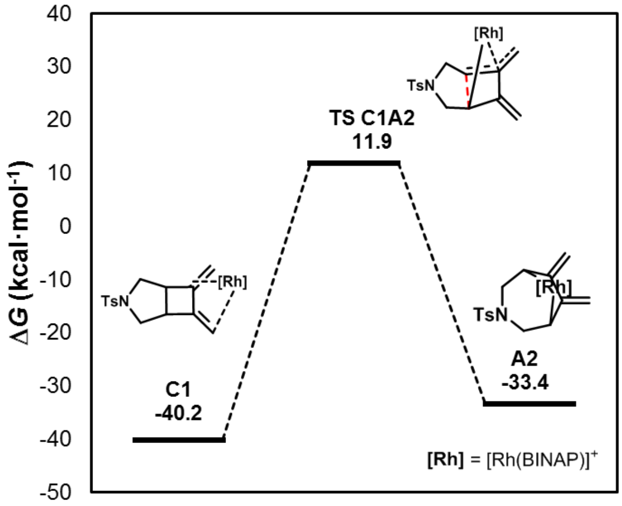

Figure 8.21. M06L-D3/cc-pVTZ-PP/SMD(76% THF, 24% CH_2Cl_2)//B3LYP-D3/cc-pVDZ-PP Gibbs energy profile for the transformation of intermediate **C1** into intermediate **A2** catalysed by $[Rh(BINAP)]^+$.

We then performed the reaction in absence of an alkene (**Scheme 8.6**) in an attempt to isolate intermediate **A5.** Under these reaction conditions, we managed to isolate compound **6a**, which forms as a result of DA reaction of **A5** with itself behaving as both the diene and the dienophile. The results not only confirm the mechanism, but also provide a straightforward methodology to form spirocyclic compounds in a completely regioselective manner.

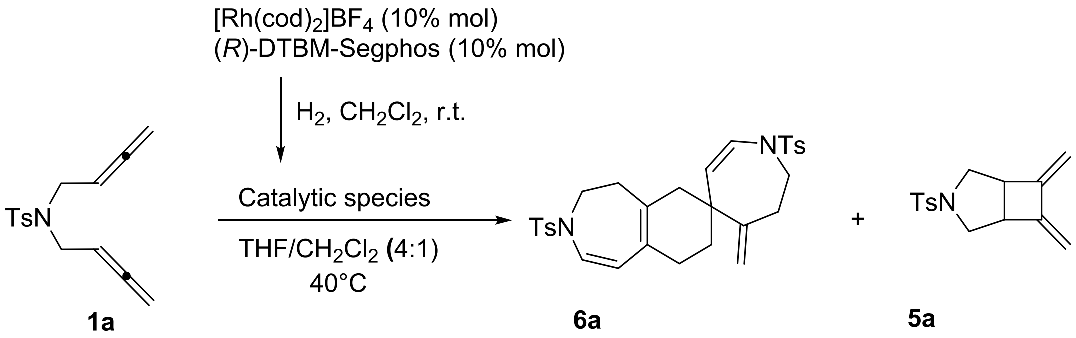

Scheme 8.6. Isolation of **6a** in mechanistic experiments indirectly reveal the formation of a triene intermediate **A5**.

Once the above discussed methodology was established, we moved on to undertake the final goal of fullerene functionalization. We reasoned that, after proper adjustment of the reaction conditions, the scope of our recently developed reaction could be easily expanded to include C_{60}. This was based on two facts: first, we have just shown that the last mechanistic step of the reaction consists of a DA cycloaddition reaction between intermediate **A5** and an electron deficient alkene. Second, we have repeatedly discussed along this thesis the ability of fullerenes to efficiently participate as dienophiles in such kind of reactions with a broad range of dienic substrates.

The optimized set of conditions employed for simple alkenes was adapted in a first explorative experiment. In order to achieve proper solubility of C_{60} in the reaction mixture, the solvent was changed to *o*-DCB. The optimal [Rh(cod)$_2$]BF$_4$/(*R*)-DTBM-Segphos was used as the catalytic system and 2 equivalents of 1,5-bisallene **1a** were added (entry **1** in **Table 8.4**).

Table 8.4. Rh(I)-catalyzed cycloaddition of **1a** with C$_{60}$: Optimization of reaction parameters.

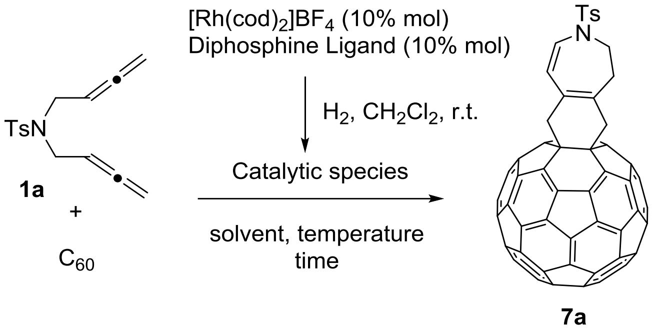

Entry	Dihosphine ligand	Ratio C$_{60}$:**1a**	Solvent	[C$_{60}$] (mM)	Temperature (ºC)	Time (min)	Yield (%)
1	(*R*)-DTBM-segphos	1:2	o-DCB	1.4	180	30	0[a]
2	(*R*)-DTBM-segphos	1.1:1	o-DCB	1.4	180	10	<5
3	(*R*)-DTBM-segphos	1.1:1	o-DCB	1.4	90	20	56
4	(*R*)-BINAP	1.1:1	o-DCB	1.4	90	240	42
5	(*R*)-H$_8$-BINAP	1.1:1	o-DCB	1.4	90	240	42[d]
6	(*R*)-Tol-BINAP	1.1:1	o-DCB	1.4	90	240	20[d]
7	(*R*)-DTBM-segphos	1.1:1	o-DCB	2.8	90	20	30

The reaction mixture was heated at reflux and turned from purple to dark brown after approximately 10 min, at which point the formation of a reaction product was observable by TLC (CH$_2$Cl$_2$), together with unreacted C$_{60}$. Repeated monitoring after 30 minutes of reaction did not show either the product or unreacted fullerene. Conversely, complete retention at the bottom of the TLC plate was observed. At this point, we rationalized that an excess of **1a** in the reaction mixture may promote the formation of polyadducts. Then, we repeated the reaction employing a slight excess of C$_{60}$ and reducing the reaction time to 10 min. Direct subjection of the reaction mixture to a chromatographic column previously packed with CS$_2$ and subsequent elution with toluene resulted in the isolation of small amounts of a dark brown solid, whose structure was initially assigned to monoadduct **7a** based on UV-Vis and ESI-HRMS experiments. We then analyzed the effect of the temperature on the reaction outcome. Heating the reaction mixture at 90 ºC and carefully monitoring the reaction progress allowed us to obtain the reaction product in 56% isolated yield after purification by column chromatography. The identity of **7a** was unambiguously confirmed this time by 1D and 2D NMR experiments. With these results at hand, we surveyed the activity of three additional diphosphine ligands. All of them turned out to be less effective and required longer reaction times. Furthermore, undetermined impurities were observed in the ^{1}H NMR spectra. Doubling the concentration of substrates in the reaction mixture was found to be detrimental in terms of reaction yield.

The stability of **7a** towards light and air was assessed by exposing a $CDCl_3$ mixture to sunlight in an open NMR tube. Repeated analysis by ^1H NMR resulted in significant decrease in intensity of all the signals corresponding to the product, accompanied by the appearance of new sets of complex undetermined signals. In addition, ESI-HRMS analysis showed a strong peak corresponding to M+Na+32 m/z. These results are commensurate with unspecific oxidation of **7a**, a process that may occur as a result of light-promoted reaction with $^1O_2$. The fact that fullerenes and their derivatives are efficient $^1O_2$ synthesizers is well precedented (see subsection 1.5 in chapter 1 and references cited therein).

Further work regarding fullerene functionalization by the Rh(I)-catalyzed cycloisomerization/DA cascade reactions of 1,5-bisallenes with fullerenes will be developed by other researchers in our group, in the context of their respective doctoral thesis.

As a summary, in this section we have described the development of a novel catalytic methodology to transform 1,5-bisallenes into a series of polycyclic heterocycles. As shown by DFT calculations, the process encompasses a Rh(I)-catalyzed cycloisomerization reaction of bisallenes **1** and subsequent DA reaction of the resulting triene intermediates with alkenes **2**. Furthermore, this synthetic protocol has been adapted to allow fullerene functionalization.

Section 3: Regioselectivity in Diels–Alder cycloadditions of $^{\#6094}C_{68}$ fullerene with a triplet ground state

Our group has been dedicated to the computational study of the regioselectivity of chemical reactions involving fullerenes and EMFs for many years. Within this context, one of the objectives of the present thesis was to study the regioselectivity in DA cycloadditions of fullerene $^{\#6094}C_{68}$. This fullerene cannot be isolated after production in the arc reactor, but indirect evidence of its formation was obtained for the first time in 2012 by an *in situ* chlorination reaction that gave octachloride derivative $C_{68}Cl_{18}$. Fullerene $^{\#6094}C_{68}$ has two main peculiarities: it is one of the few hollow fullerenes with a non-IPR cage and one of the few hollow non-functionalized fullerenes with a triplet ground (T_0) state [25,26].

Our group studied recently the DA reactions of C_{60} at high spin states. From computational results, it was predicted that for the triplet and higher spin states the regioselectivity of DA cycloadditions was reversed to favor the formation of [5,6] adducts. However, experimental results showed that the reaction of C_{60} with isoindene and photoexcited $^3C_{60}$ delivered only the [6,6] adducts. Careful analysis of the reaction mechanism showed that in the T_1 state the reaction proceeds through and ISC to reach the singlet (S_0) ground state [411]. Taking this precedent into account, and assuming that such an ISC is not expected to be operative in $^{\#6094}C_{68}$ due to its T_0 state, we hypothesized that this fullerene could favor [5,6] additions over [6,6] additions (**Scheme 8.7**).

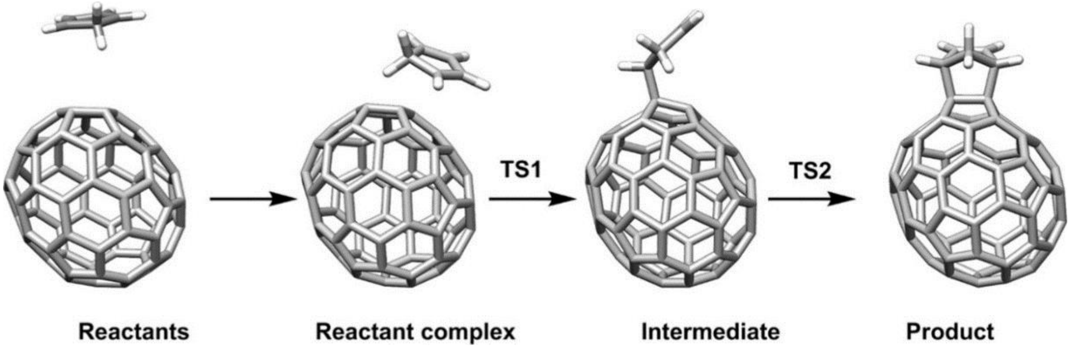

Scheme 8.7. General stepwise mechanism for the DA cycloaddition involving $^{\#6094}C_{68}$ and cyclopentadiene.

As a first approach to check our hypothesis, we computed the structure and reaction energies (ΔE_R) of all possible DA adducts over all 55 nonequivalent bonds. Overall, $^{\#6094}C_{68}$ has 24 [6,6] bonds (8 type A, 13 type B and 3 type C), 30 [5,6] bonds (26 type and 4 type F) and 1 type E [5,5] bond. For the most stable adducts of each type, we computed the corresponding intermediates and transition states comprising the whole reaction mechanism**,** which proceeds *via* a stepwise radicalary mechanism.

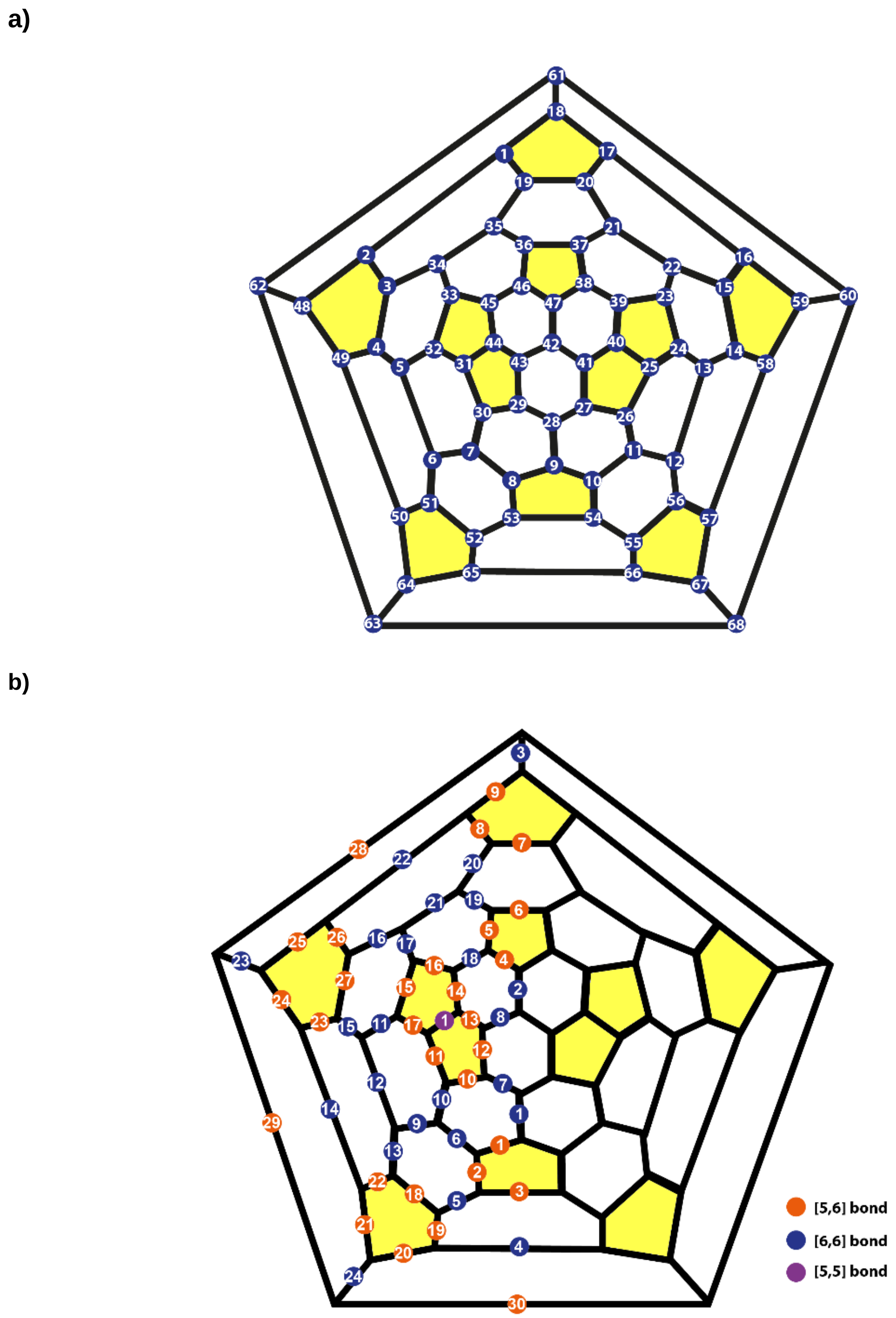

Figure 8.22. Schlegel diagrams of fullerene $^{\#6094}C_{68}$ showing (a) arbitrary atom numbering and (b) arbitrary bond numbering.

Calculations at the UB3LYP/6-31G (d,p) level of theory showed that, in general, the DA cycloaddition on $^{\#6094}C_{68}$ is not a very exothermic reaction. In fact, 20 out of 55 additions are endothermic. The most favored addition takes place at the [5,5] bond (**1**), followed by the addition at one $[5,6]_F$ bond (**13**). The best [6,6] addition takes place at type A bond **3**. The reaction involving type D [5,6] bond **4** was also considered. In general, reactions where B, C and D bonds are involved are less favorable, with 20 additions being endothermic ($\Delta E_R > 0$).

The $[5,6]_F$ and [5,5] reaction paths are identical until the first addition in C44. This process is exergonic by 0.5 kcal/mol and has to surmount a Gibbs energy barrier of 11.3 kcal/mol. The intermediate formed in this first step, which has a triplet ground state, can evolve either to the final $[5,6]_F$ or [5,5] products *via* a second addition that involves a ISC. For the [5,5] bond, the second addition is exergonic by 18.1 kcal/mol and has an energy barrier of 5.9 kcal/mol. For the $[5,6]_F$ path, the second addition is an almost barrier-less process and is exergonic by 12.1 kcal/mol. Before reaching the final adduct, there is another ISC from the singlet to the triplet state, so that the final regioisomer has a triplet state with a very low singlet–triplet energy gap of only 0.8 kcal/mol. From our computational results, we conclude that the [5,5] adduct is the thermodynamic reaction product while the kinetic product is the $[5,6]_F$ one.

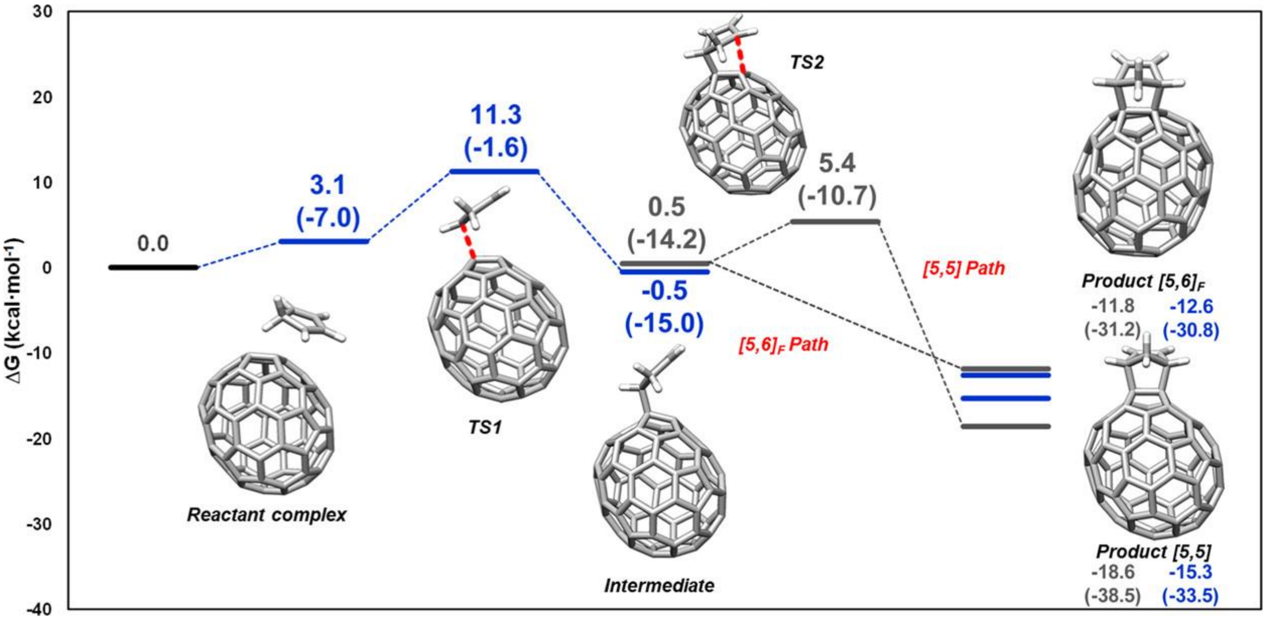

Figure 8.23. UB3LYP-D3/6-31G(d,p) Gibbs energy profile for the [5,5] and $[5,6]_F$ paths. Electronic energies given in parentheses.

The additions involving a $[6,6]_A$ and $[5,6]_D$ bonds are considerably less favored both kinetically and thermodynamically. Such a difference can be attributed to the higher degree of pyramidalization of C44 compared to C47. Indeed, C44 is clearly influenced by the pentalene unit. Also, the reactivity is governed by the distribution of excess spin density, showing larger lobes at C44 as compared with C61 and C46, involved in $[6,6]_A$ and $[5,6]_D$ attacks respectively. However, we found the influence of pyramidalization better explains the reactivity of the different bonds, since the concerted additions computed at the singlet state showed the same reactivity trends. The effect of the open-shell electronic structure is therefore important, but not decisive.

To get further insight into the reactivity trends, we compared the reactivity of the $[5,5]/[5,6]_F$ and [6,6] on the basis of the ASM. EDA calculations performed at the UM06-2X-D3/TZVP//UB3LYP-D3/6-31G(d,p) level of theory revealed that the more stabilizing orbital interactions, favored by the spin density accumulation around the pentalene region of the cage, are responsible for the particular reactivity of $^{\#6094}C_{68}$ (**Figure 8.24**). This last part of the work was done in collaboration with Dr. Israel Fernández at the Universidad Complutense de Madrid (UCM).

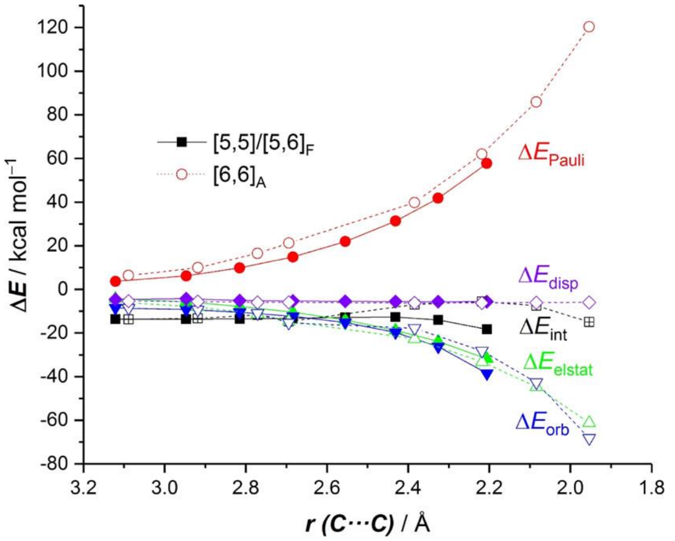

Figure 8.24. Comparative EDA of the [5,5]/$[5,6]_\mathrm{F}$ and [6,6] attacks computed at the UM06-2X-D3/TZVP//UB3LYP-D3/6-31G(d,p) level of theory.

As a summary, in this section we have studied the regioselectivity of elusive fullerene $^{\#6094}C_{68}$. We have shown that $^{\#6094}C_{68}$ is one of the first reported hollow nonfunctionalized fullerene that favors the cycloaddition to [5,6] instead of the typically preferred [6,6] bond. Our results indicate that the [5,5] adduct is the thermodynamic reaction product, whereas the kinetic product is the $[5,6]_\mathrm{F}$ one. This change of regioselectivity in the DA reaction of hollow fullerenes from the usual [6,6] bond to the [5,6] bond in $^{\#6094}C_{68}$ is driven by the more stabilizing orbital interaction favored by the spin density accumulation around the pentalene region of the cage.

Finally, as a conclusive remark for the whole thesis, we have combined experiments and theory to study the reactivity of fullerenes. Two new synthetic methods based on Rh(I) catalysis have been developed and their mechanisms were thoroughly elucidated using quantum chemical calculations. In addition, some of the compounds prepared have been successfully used as the ETLs in PSCs. The regioselectivity of DA cycloadditions involving $^{\#6094}C_{68}$ and cyclopentadiene has been studied by computational means. The results obtained in this last project have contributed to the fundamental understanding of the factors that govern fullerene reactivity.

Chapter 9. Conclusions

Section 1: Rh(I) catalyzed [2+2+2] cycloadditions of fullerenes and alkynes

The first goal we proposed in this thesis was to study computationally the mechanism of the [2+2+2] cycloaddition of C_{60} and two acetylene molecules catalyzed by Wilkinson's complex. After carefully analyzing all potential reaction pathways we concluded that:

- The [2+2+2] cycloaddition reaction of C_{60} and two acetylene molecules to form a cyclohexadiene ring fused to a [6,6] bond of C_{60}, catalyzed by Wilkinson's complex constitutes a feasible process both kinetically and thermodynamically.
- The lowest energy reaction pathway involves oxidative addition of the two acetylene molecules followed by insertion of C_{60} into a Rh−C bond of the rhodacyclopentadiene intermediate formed. Nonetheless, alternative feasible reaction pathways have been considered and could also be operative.
- As expected for a cycloaddition reaction involving C_{60}, the process considered takes place selectively at the [6,6] junctions.
- The formation of the cyclohexadiene-fused fullerene derivative has to compete with acetylene cyclotrimerization, which has been found to be a more favorable competing process. However, proper tuning of the reaction conditions may favor the formation of the desired product over benzene.

Based on the results obtained in chapter 3 and relying on previous numerous precedents of Rh(I)-catalyzed [2+2+2] cycloadditions developed within our research group we envisaged the development of a catalytic version of the [2+2+2] cycloaddition reaction between diynes and fullerene C_{60}. A thorough experimental and computational study into the reaction lead to the following conclusions:

- The synthetic protocol developed is catalytic in rhodium and provides a variety of bis(fulleroids) with good to moderate yields.
- Further functionalization of the compounds obtained has been accomplished by a Pd-catalyzed cross-coupling reaction with three different aryl boronic acids
- Reaction of the synthesized bis(fulleroids) with oxygen and air easily allows photooxygenative cleavage leading to open-cage dicarbonylic fullerene derivatives exhibiting a 12-membered hole.
- DFT calculations showed that the reaction takes place through a Rh-catalyzed [2+2+2] cycloaddition to yield a cyclohexadiene-fused C_{60} intermediate. This intermediate evolves to the final bis(fulleroid) product through a Rh-catalyzed di-π-methane rearrangement pathway followed by a retro-[2+2+2] cycloaddition.

In chapter 5, we set the goal of incorporating three different open-cage dicarbonylic fullerene derivatives as the ETMs in PSCs with a planar inverted (p-i-n) configuration. Synthesis of the fullerene derivatives followed by construction and testing of photovoltaic devices allowed us to conclude:

- For those compounds with appropriate solubility, the resulting PSCs offered performances rivaling or even superior to those of analogous cells employing the $PC_{61}BM$ reference. High V_{oc} values exceeding 1.0 V were recorded in one case. The good result obtained are explained by high passivation ability and high LUMO values of the compounds tested.

- PSCs based on open-cage fullerene derivatives showed negligible hysteretic behavior.
- This preliminary account opens the door to develop new derivatives with superior performances based on our straightforward synthetic methodology.

Section 2: A Rh-catalyzed cycloisomerization/Diels-Alder cascade reaction of 1,5-bisallenes for the synthesis of polycyclic heterocycles and the functionalization of fullerenes

In the context of the last project developed in this thesis, we developed a novel reaction protocol to transform 1,5-bisallenes into a series of dihydroazepine- and dihydrooxepine-fused ring systems. The results provided by experimental and computational data allowed us to derive the following conclusions:

- The process developed gives access to a series of polycyclic heterocycles containing dihydroazepine moieties that were obtained with good to moderate yields. Also dihydrooxepine-containing compounds could be prepared, though in much lower yields.
- Oxidative coupling at the central bonds of the 1,5-bisallene leads to the formation of a rhodabicyclo[3.2.1]octane intermediate exhibiting two exocyclic bonds. Subsequent β-hydride elimination, followed by catalyst release yields a triene intermediate that ultimately experiences a regioselective DA cycloaddition providing the observed reaction products. Our mechanistic proposal was supported by performing additional experiments.
- The reaction was successfully applied to the functionalization of C_{60}.

Section 3: Regioselectivity in Diels–Alder cycloadditions of $^{\#6094}C_{68}$ fullerene with a triplet ground state

The regioselectivity of the DA cycloaddition between fullerene $^{\#6094}C_{68}$ and cyclopentadiene was studied as described in chapter 7. We showed that:

- Fullerene $^{\#6094}C_{68}$ is one of the first reported hollow non-functionalized fullerene that favors the cycloaddition to a [5,6] instead of the typically preferred [6,6] bond.
- Our results indicate that the [5,5] adduct is the thermodynamic reaction product, whereas the kinetic product is the $[5,6]_F$ one.
- The observed reactivity trends can be explained by more stabilizing orbital interactions. This is, in turn favored by spin density accumulation around the pentalene units of the fullerene cage.

References

(1) IUPAC. *Compendium of Chemical Terminology*, 2nd Ed. (the "Gold Book"). Compiled by A. D. McNaught and A. Wilkinson. Blackwell Scientific Publications, Oxford (1997). XML on-Line Corrected Version: Http://Goldbook.Iupac.Org (2006-2019) Created by M. Nic, J. Jir.

(2) Kroto, H. W.; Heath, J. R.; O'Brien, S. C.; Curl, R. F.; Smalley, R. E. C_{60}: Buckminsterfullerene. *Nature* **1985**, *318*, 162.

(3) Krueger, A. *Carbon Materials and Nanotechnology*; Wiley, 2010.

(4) Georgakilas, V.; Perman, J. A.; Tucek, J.; Zboril, R. Broad Family of Carbon Nanoallotropes: Classification, Chemistry, and Applications of Fullerenes, Carbon Dots, Nanotubes, Graphene, Nanodiamonds, and Combined Superstructures. *Chem. Rev.* **2015**, *115*, 4744.

(5) Ugarte, D. Curling and Closure of Graphitic Networks under Electron-Beam Irradiation. *Nature* **1992**, *359*, 707.

(6) Iijima, S. Helical Microtubules of Graphitic Carbon. *Nature* **1991**, *354*, 56.

(7) Iijima, S.; Yudasaka, M.; Yamada, R.; Bandow, S.; Suenaga, K.; Kokai, F.; Takahashi, K. Nano-Aggregates of Single-Walled Graphitic Carbon Nano-Horns. *Chem. Phys. Lett.* **1999**, *309*, 165.

(8) Novoselov, K. S.; Geim, A. K.; Morozov, S. V.; Jiang, D.; Zhang, Y.; Dubonos, S. V.; Grigorieva, I. V.; Firsov, A. A. Electric Field in Atomically Thin Carbon Films. *Science* **2004**, *306*, 666.

(9) Smith, B. W.; Monthioux, M.; Luzzi, D. E. Encapsulated C_{60} in Carbon Nanotubes. *Nature* **1998**, *396*, 323.

(10) Yang, Z.; Ren, J.; Zhang, Z.; Chen, X.; Guan, G.; Qiu, L.; Zhang, Y.; Peng, H. Recent Advancement of Nanostructured Carbon for Energy Applications. *Chem. Rev.* **2015**, *115*, 5159.

(11) Baptista, F. R.; Belhout, S. A.; Giordani, S.; Quinn, S. J. Recent Developments in Carbon Nanomaterial Sensors. *Chem. Soc. Rev.* **2015**, *44*, 4433.

(12) Ahn, E. C.; Wong, H.-S. P.; Pop, E. Carbon Nanomaterials for Non-Volatile Memories. *Nat. Rev. Mater.* **2018**, *3*, 18009.

(13) Mauter, M. S.; Elimelech, M. Environmental Applications of Carbon-Based Nanomaterials. *Environ. Sci. Technol.* **2008**, *42*, 5843.

(14) Loh, K. P.; Ho, D.; Chiu, G. N. C.; Leong, D. T.; Pastorin, G.; Chow, E. K.-H. Clinical Applications of Carbon Nanomaterials in Diagnostics and Therapy. *Adv. Mater.* **2018**, *30*, 1802368.

(15) Kaiser, K.; Scriven, L. M.; Schulz, F.; Gawel, P.; Gross, L.; Anderson, H. L. An Sp-Hybridized Molecular Carbon Allotrope, Cyclo[18]Carbon. *Science* **2019**, *365*, 1299.

(16) Goldberg, M. A. Class of Multi-Symmetric Polyhedra. *Tohoku Math. Journal, First Ser.* **1937**, *43*, 104.

(17) Euler, L. Theorematum Quorundam Ad Numeros Primos Spectantium Demonstratio. *Comment. Acad. Sci. Petropolitanae* **1741**, *8*, 141.

(18) Bowers, M. T.; Kemper, P. R.; Von Helden, G.; Van Koppen, P. A. M. Gas-Phase Ion Chromatography: Transition Metal State Selection and Carbon Cluster Formation. *Science* **1993**, *260*, 1446.

(19) Powell, W. H.; Cozzi, F.; Moss, G. P.; Thilgen, C.; Hwu, R. J.-R.; Yerin, A. Nomenclature for the C_{60}-I_h and C_{70}-D_{5h} Fullerenes (IUPAC Recommendations 2002). *Pure Appl. Chem.* **2002**, *74*, 629.

(20) Fowler, P.; Manolopoulos, D. E. *An Atlas of Fullerenes*; Dover Publications, 2006.

(21) Schwerdtfeger, P.; Wirz, L. N.; Avery, J. The Topology of Fullerenes. *WIRES Comput. Mol. Sci.* **2015**, *5*, 96.

(22) Kroto, H. W. The Stability of the Fullerenes Cn, with n = 24, 28, 32, 36, 50, 60 and 70. *Nature* **1987**, *329*, 529.

(23) Albertazzi, E.; Domene, C.; Fowler, P. W.; Heine, T.; Seifert, G.; Van Alsenoy, C.; Zerbetto, F. Pentagon Adjacency as a Determinant of Fullerene Stability. *Phys. Chem. Chem. Phys.* **1999**, *1*, 2913.

(24) Tan, Y.-Z.; Xie, S.-Y.; Huang, R.-B.; Zheng, L.-S. The Stabilization of Fused-Pentagon Fullerene Molecules. *Nat. Chem.* **2009**, *1*, 450.

(25) Amsharov, K. Y.; Ziegler, K.; Mueller, A.; Jansen, M. Capturing the Antiaromatic $^{\#6094}C_{68}$ Carbon Cage in the Radio-Frequency Furnace. *Chem. Eur. J.* **2012**, *18*, 9289.

(26) Dang, J.-S.; Zheng, J.-J.; Wang, W.-W.; Zhao, X. Open-Shell Triplet Character of $^{\#6094}C_{68}$: Spherical Aromaticity, Thermodynamic Stability, and Regioselective Chlorination. *Inorg. Chem.* **2013**, *52*, 4762.

(27) Heath, J. R.; O'Brien, S. C.; Liu, Q. Z. Y.; Curl, R. F.; Tittel, F. K.; Smalley, R. E.; Kroto, H. W. Lanthanum Complexes of Spheroidal Carbon Shells. *J. Am. Chem. Soc.* **1985**, *107*, 7779.

(28) Chai, Y.; Guo, T.; Jin, C.; Haufler, R. E.; Chibante, L. P. F.; Fure, J.; Wang, L.; Alford, J. M.; Smalley, R. E. Fullerenes with Metals Inside. *J. Phys. Chem.* **1991**, *95*, 7564.

(29) Ghiassi, K. B.; Olmstead, M. M.; Balch, A. L. Gadolinium-Containing Endohedral Fullerenes: Structures and Function as Magnetic Resonance Imaging (MRI) Agents. *J. Chem. Soc. Dalt. Trans.* **2014**, *43*, 7346.

(30) Lu, X.; Echegoyen, L.; Balch, A. L.; Nagase, S.; Akasaka, T.; Echegoyen. *Endohedral Metallofullerenes: Basics and Applications*; CRC Press, 2014.

(31) Popov, A. A.; Yang, S.; Dunsch, L. Endohedral Fullerenes. *Chem. Rev.* **2013**, *113*, 5989.

(32) Yang, S.; Wei, T.; Jin, F. When Metal Clusters Meet Carbon Cages: Endohedral Clusterfullerenes.

Chem. Soc. Rev. **2017**, *46*, 5005.

(33) Chaur, M. N.; Melin, F.; Ortiz, A. L.; Echegoyen, L. Chemical, Electrochemical, and Structural Properties of Endohedral Metallofullerenes. *Angew. Chem. Int. Ed.* **2009**, *48*, 7514.

(34) Krätschmer, W.; Lamb, L. D.; Fostiropoulos, K.; Huffman, D. R. Solid C_{60}: A New Form of Carbon. *Nature* **1990**, *347*, 354.

(35) Haufler, R. E.; Conceicao, J.; Chibante, L. P. F.; Chai, Y.; Byrne, N. E.; Flanagan, S.; Haley, M. M.; O’Brien, S. C.; Pan, C.; Xiao, Z.; Billups, W. E.; Ciufolini, M. A; Hauge, R. H.; Margrave, L.J.; Curl, R. F.; Smalley, R. E. Efficient Production of C_{60} (Buckminsterfullerene), $C_{60}H_{36}$, and the Solvated Buckide Ion. *J. Phys. Chem.* **1990**, *94*, 8634.

(36) Hirsch, A.; Brettreich, M. *Fullerenes: Chemistry and Reactions*; Wiley-VCH, 2005.

(37) Langa De La Puente, F.; Nierengarten, J.-F. *Fullerenes*; Nanoscience & Nanotechnology Series; The Royal Society of Chemistry, 2011.

(38) Diederich, F.; Ettl, R.; Rubin, Y.; Whetten, R. L.; Beck, R.; Alvarez, M.; Anz, S.; Sensharma, D.; Wudl, F.; Khemani, K. C.; Koch, A. The Higher Fullerenes: Isolation and Characterization of C_{76}, C_{84}, C_{90}, C_{94}, and $C_{70}O$, an Oxide of D_{5h}-C_{70}. *Science* **1991**, *252*, 548.

(39) Stevenson, S.; Rice, G.; Glass, T.; Harich, K.; Cromer, F.; Jordan, M. R.; Craft, J.; Hadju, E.; Bible, R.; Olmstead, M. M.; Maitra, K.; Fisher, A.J.; Balch, A. L.; Dorn, H. C. Small-Bandgap Endohedral Metallofullerenes in High Yield and Purity. *Nature* **1999**, *401*, 55.

(40) Howard, J. B.; McKinnon, J. T.; Makarovsky, Y.; Lafleur, A. L.; Johnson, M. E. Fullerenes C_{60} and C_{70} in Flames. *Nature* **1991**, *352*, 139.

(41) Thilgen, C.; Diederich, F. Structural Aspects of Fullerene Chemistry: A Journey through Fullerene Chirality. *Chem. Rev.* **2006**, *106*, 5049.

(42) Liu, S.; Lu, Y.-J.; Kappes, M. M.; Ibers, J. A. The Structure of the C_{60} Molecule: X-Ray Crystal Structure Determination of a Twin at 110 K. *Science* **2006**, *254*, 408.

(43) McKenzie, D. R.; Davis, C. A.; Cockayne, D. J. H.; Muller, D. A.; Vassallo, A. M. The Structure of the C_{70} Molecule. *Nature* **1992**, *355*, 622.

(44) Ajie, H.; Alvarez, M. M.; Anz, S. J.; Beck, R. D.; Diederich, F.; Fostiropoulos, K.; Huffman, D. R.; Krätschmer, W.; Rubin, Y.; Schriver, K. E.;Sensharma, D.; Whetten, R. L. Characterization of the Soluble All-Carbon Molecules C_{60} and C_{70}. *J. Phys. Chem.* **1990**, *94*, 8630.

(45) Leach, S.; Vervloet, M.; Desprès, A.; Bréheret, E.; Hare, J. P.; John Dennis, T.; Kroto, H. W.; Taylor, R.; Walton, D. R. M. Electronic Spectra and Transitions of the Fullerene C_{60}. *Chem. Phys.* **1992**, *160*, 451.

(46) Arbogast, J. W.; Darmanyan, A. P.; Foote, C. S.; Diederich, F. N.; Whetten, R. L.; Rubin, Y.; Alvarez, M. M.; Anz, S. J. Photophysical Properties of Sixty Atom Carbon Molecule (C_{60}). *J. Phys. Chem.* **1991**, *95*, 11.

(47) Osuna, S.; Swart , M.; Solà, M. On the Mechanism of Action of Fullerene Derivatives in Superoxide Dismutation. *Chem. Eur. J.* **2010**, *16*, 3207.

(48) Tzirakis, M. D.; Orfanopoulos, M. Radical Reactions of Fullerenes: From Synthetic Organic Chemistry to Materials Science and Biology. *Chem. Rev.* **2013**, *113*, 5262.

(49) Reed, C. A.; Bolskar, R. D. Discrete Fulleride Anions and Fullerenium Cations. *Chem. Rev.* **2000**, *100*, 1075.

(50) Xie, Q.; Pérez-Cordero, E.; Echegoyen, L. Electrochemical Detection of C_{60}^{6-} and C_{70}^{6-}: Enhanced Stability of Fullerides in Solution. *J. Am. Chem. Soc.* **1992**, *114*, 3978.

(51) Wudl, F. The Chemical Properties of Buckminsterfullerene (C_{60}) and the Birth and Infancy of Fulleroids. *Acc. Chem. Res.* **1992**, *25*, 157.

(52) Montellano, A.; Mateo-Alonso, A.; Prato, M. Materials Chemistry of Fullerene C_{60} Derivatives. *J. Mater. Chem.* **2011**, *21*, 1305.

(53) Prato, M. [60]Fullerene Chemistry for Materials Science Applications. *J. Mater. Chem.* **1997**, *7*, 1097.

(54) Troshin, P. A.; Lyubovskaya, R. N. Organic Chemistry of Fullerenes: The Major Reactions, Types of Fullerene Derivatives and Prospects for Practical Use. *Russ. Chem. Rev.* **2008**, *77*, 323.

(55) Haddon, R. C. Chemistry of the Fullerenes: The Manifestation of Strain in a Class of Continuous Aromatic Molecules. *Science* **1993**, *261*, 1545.

(56) Allemand, P. M.; Srdanov, G.; Koch, A.; Khemani, K.; Wudl, F.; Rubin, Y.; Diederich, F.; Alvarez, M. M.; Anz, S. J.; Whetten, R. L. The Unusual Electron Spin Resonance of Fullerene C_{60} Anion Radical. *J. Am. Chem. Soc.* **1991**, *113*, 2780.

(57) Caron, C.; Subramanian, R.; D'Souza, F.; Kim, J.; Kutner, W.; Jones, M. T.; Kadish, K. M. Selective Electrosynthesis of Dimethylfullerene [$(CH_3)_2C_{60}$]: A Novel Method for the Controlled Functionalization of Fullerenes. *J. Am. Chem. Soc.* **1993**, *115*, 8505.

(58) Liu, H.-W.; Xu, H.; Shao, G.; Wang, G.-W. Zinc-Mediated Reductive Cyclization of [60]Fullerene with Enones and Subsequent Dehydration under Solvent-Free and Ball-Milling Conditions. *Org. Lett.* **2019**, *21*, 2625.

(59) Hebard, A. F.; Rosseinsky, M. J.; Haddon, R. C.; Murphy, D. W.; Glarum, S. H.; Palstra, T. T. M.; Ramirez, A. P.; Kortan, A. R. Superconductivity at 18 K in Potassium-Doped C_{60}. *Nature* **1991**, *350*, 600.

(60) Xie, Q.; Arias, F.; Echegoyen, L. Electrochemically-Reversible, Single-Electron Oxidation of C_{60} and C_{70}. *J. Am. Chem. Soc.* **1993**, *115*, 9818.

(61) Lin, H.-S.; Matsuo, Y. Functionalization of [60]Fullerene through Fullerene Cation Intermediates. *Chem. Commun.* **2018**, *54*, 11244.

(62) Iwashita, A.; Matsuo, Y.; Nakamura, E. $AlCl_3$-Mediated Mono-, Di-, and Trihydroarylation of [60]Fullerene. *Angew. Chem. Int. Ed.* **2007**, *46*, 3513.

(63) Hashiguchi, M.; Obata, N.; Maruyama, M.; Yeo, K. S.; Ueno, T.; Ikebe, T.; Takahashi, I.; Matsuo, Y. $FeCl_3$-Mediated Synthesis of Fullerenyl Esters as Low-LUMO Acceptors for Organic Photovoltaic Devices. *Org. Lett.* **2012**, *14*, 3276.

(64) Matsuo, Y.; Yu, Y.; Yang, X.-Y.; Ueno, H.; Okada, H.; Shibuya, H.; Choi, Y. S.; Jin, Y. W. Synthesis of Benzothieno[60]Fullerenes Through Fullerenyl Cation Intermediates. *J. Org. Chem.* **2019**, acs. joc.9b00549.

(65) Bingel, C. Cyclopropanierung von Fullerenen. *Chem. Ber.* **1993**, *126*, 1957.

(66) Camps, X.; Hirsch, A. Efficient Cyclopropanation of C_{60} Starting from Malonates. *J. Chem. Soc. Perkin Trans. 1* **1997**, *11*, 1595.

(67) Mori, S.; Nambo, M.; Chi, L. C.; Bouffard, J.; Itami, K. A. Bench-Stable Pd Catalyst for the Hydroarylation of Fullerene with Boronic Acids. *Org. Lett.* **2008**, *10*, 4609.

(68) Nambo, M.; Itami, K. Palladium-Catalyzed Carbon-Carbon Bond Formation and Cleavage of Organo(Hydro)Fullerenes. *Chem. Eur. J.* **2009**, *15*, 4760.

(69) Nambo, M.; Noyori, R.; Itami, K. Rh-Catalyzed Arylation and Alkenylation of C_{60} Using Organoboron Compounds. *J. Am. Chem. Soc.* **2007**, *129*, 8080.

(70) Martínez, J. P.; Solà, M.; Poater, A. On the Reaction Mechanism of the Rhodium-Catalyzed Arylation of Fullerene (C_{60}) with Organoboron Compounds in the Presence of Water. *ChemistryOpen* **2015**, *4*, 774.

(71) Matsuo, Y.; Nakamura, E. Selective Multiaddition of Organocopper Reagents to Fullerenes. *Chem. Rev.* **2008**, *108*, 3016.

(72) Nakamura, E. Bucky Ferrocene and Ruthenocene: Serendipity and Discoveries. *J. Organomet. Chem.* **2004**, *689*, 4630.

(73) Sawamura, M.; Kuninobu, Y.; Toganoh, M.; Matsuo, Y.; Yamanaka, M.; Nakamura, E. Hybrid of Ferrocene and Fullerene. *J. Am. Chem. Soc.* **2002**, *124*, 9354.

(74) Prato, M.; Li, Q. C.; Wudl, F.; Lucchini, V. Addition of Azides to Fullerene C_{60}: Synthesis of Azafulleroids. *J. Am. Chem. Soc.* **1993**, *115*, 1148.

(75) Akasaka, T.; Ando, W.; Kobayashi, K.; Nagase, S. Reaction of C_{60} with Silylene, the First Fullerene Silirane Derivative. *J. Am. Chem. Soc.* **1993**, *115*, 1605.

(76) Yamada, M.; Akasaka, T.; Nagase, S. Carbene Additions to Fullerenes. *Chem. Rev.* **2013**, *113*, 7209.

(77) Diederich, F.; Isaacs, L.; Philp, D. Syntheses, Structures, and Properties of Methanofullerenes. *Chem. Soc. Rev.* **1994**, *23*, 243.

(78) Cases, M.; Duran, M.; Mestres, J.; Martín, N.; Solà, M. Mechanism of the Addition Reaction of Alkyl Azides to [60]Fullerene and the Subsequent N_2 Extrusion to Form Monoimino-[60]Fullerenes. *J. Org. Chem.* **2001**, *66*, 433.

(79) Nakahodo, T.; Okada, M.; Morita, H.; Yoshimura, T.; Ishitsuka, M. O.; Tsuchiya, T.; Maeda, Y.; Fujihara, H.; Akasaka, T.; Gao, X.; Nagase, S. [2+1] Cycloaddition of Nitrene onto C_{60} Revisited: Interconversion between an Aziridinofullerene and an Azafulleroid. *Angew. Chem. Int. Ed.* **2008**, *47*, 1298.

(80) Hummelen, J. C.; Knight, B. W.; LePeq, F.; Wudl, F.; Yao, J.; Wilkins, C. L. Preparation and Characterization of Fulleroid and Methanofullerene Derivatives. *J. Org. Chem.* **1995**, *60*, 532.

(81) Clarke, T. M.; Durrant, J. R. Charge Photogeneration in Organic Solar Cells. *Chem. Rev.* **2010**, *110*, 6736.

(82) Pellicciari, R.; Annibali, D.; Costantino, G.; Marinozzi, M.; Natalini, B. Dirhodium(II) Tetraacetate-Mediated Decomposition of Ethyl Diazoacetate and Ethyl Diazomalonate in the Presence of Fullerene. A New Procedure for the Selective Synthesis of [6-6]-Closed Methanofullerenes. *Synlett* **1997**, 1196.

(83) Tuktarov, A. R.; Khuzin, A. A.; Popod'ko, N. R.; Dzhemilev, U. M. Cycloaddition of Diazothioates to [60]Fullerene. *Tetrahedron Lett.* **2012**, *53*, 3123.

(84) Tuktarov, A. R.; Korolev, V. V.; Tulyabaev, A. R.; Popod'ko, N. R.; Khalilov, L. M.; Dzhemilev, U. M. Synthesis of Optically Active Spiro Homo- and Methanofullerenes. *Tetrahedron Lett.* **2011**, *52*, 834.

(85) Tuktarov, A. R.; Akhmetov, A. R.; Khalilov, L. M.; Dzhemilev, U. M. Cycloaddition of Diazoketones to [60]Fullerene in the Presence of the Catalytic System $Pd(acac)_2$—PPh_3—Et_3Al. *Russ. Chem. Bull.* **2010**, *59*, 611.

(86) Maggini, M.; Scorrano, G.; Prato, M. Addition of Azomethine Ylides to C_{60}: Synthesis, Characterization, and Functionalization of Fullerene Pyrrolidines. *J. Am. Chem. Soc.* **1993**, *115*, 9798.

(87) Prato, M.; Maggini, M. Fulleropyrrolidines: A Family of Full-Fledged Fullerene Derivatives. *Acc. Chem. Res.* **1998**, *31*, 519.

(88) Delgado, J. L.; Martín, N.; de la Cruz, P.; Langa, F. Pyrazolinofullerenes: A Less Known Type of Highly Versatile Fullerene Derivatives. *Chem. Soc. Rev.* **2011**, *40*, 5232.

(89) Maroto, E. E.; Izquierdo, M.; Reboredo, S.; Marco-Martínez, J.; Filippone, S.; Martín, N. Chiral Fullerenes from Asymmetric Catalysis. *Acc. Chem. Res.* **2014**, *47*, 2660.

(90) Filippone, S.; Maroto, E. E.; Martín-Domenech, Á.; Suarez, M.; Martín, N. An Efficient Approach to Chiral Fullerene Derivatives by Catalytic Enantioselective 1,3-Dipolar Cycloadditions. *Nat. Chem.* **2009**, *1*, 578.

(91) Marco-Martínez, J.; Reboredo, S.; Izquierdo, M.; Marcos, V.; López, J. L.; Filippone, S.; Martín, N. Enantioselective Cycloaddition of Münchnones onto [60]Fullerene: Organocatalysis versus Metal Catalysis. *J. Am. Chem. Soc.* **2014**, *136*, 2897.

(92) Hoke, S. H.; Molstad, J.; Dilettato, D.; Jay, M. J.; Carlson, D.; Kahr, B.; Cooks, R. G. Reaction of Fullerenes and Benzyne. *J. Org. Chem.* **1992**, *57*, 5069.

(93) Ueda, M.; Sakaguchi, T.; Hayama, M.; Nakagawa, T.; Matsuo, Y.; Munechika, A.; Yoshida, S.; Yasuda, H.; Ryu, I. Regio- and Stereo-Selective Intermolecular [2+2] Cycloaddition of Allenol Esters with C_{60} Leading to Alkylidenecyclobutane-Annulated Fullerenes. *Chem. Commun.* **2016**, *52*, 13175.

(94) Yamada, M.; Ochi, R.; Yamamoto, Y.; Okada, S.; Maeda, Y. Transition-Metal-Catalyzed Divergent Functionalization of [60]Fullerene with Propargylic Esters. *Org. Biomol. Chem.* **2017**, *15*, 8499.

(95) Schlueter, J. A.; Seaman, J. M.; Taha, S.; Cohen, H.; Lykke, K. R.; Wang, H. H.; Williams, J. M. Synthesis, Purification, and Characterization of the 1 : 1 Addition Product of C_{60} and Anthracene. *J. Chem. Soc. Chem. Commun.* **1993**, 972.

(96) Kräutler, B.; Müller, T.; Maynollo, J.; Gruber, K.; Kratky, C.; Ochsenbein, P.; Schwarzenbach, D.; Bürgi, H.-B. A Topochemically Controlled, Regiospecific Fullerene Bisfunctionalization. *Angew. Chem. Int. Ed.* **1996**, *35*, 1204.

(97) Schwenninger, R.; Muller, T.; Krautler, B. Concise Route to Symmetric Multiadducts of [60]Fullerene: Preparation of an Equatorial Tetraadduct by Orthogonal Transposition. *J. Am. Chem. Soc.* **1997**, *119*, 9317.

(98) Belik, P.; Gügel, A.; Spickermann, J.; Müllen, K. Reaction of Buckminsterfullerene with *Ortho* - Quinodimethane: A New Access to Stable C_{60} Derivatives. *Angew. Chem. Int. Ed.* **1993**, *32*, 78.

(99) Muraoka, T.; Asaji, H.; Yamamoto, Y.; Matsuda, I.; Itoh, K. Rhodium-Catalyzed Silylative Carbocyclization on C_{60}. *Chem. Commun.* **2000**, 199.

(100) Martín, N.; Altable, M.; Filippone, S.; Martín-Domenech, Á.; Poater, A.; Solà, M. Regioselective Intramolecular Pauson-Khand Reactions of C_{60}: An Electrochemical Study and Theoretical Underpinning. *Chem. Eur. J.* **2005**, *11*, 2716.

(101) Martín, N.; Altable, M.; Filippone, S.; Martín-Domenech, Á. Highly Efficient Pauson–Khand Reaction with C_{60}: Regioselective Synthesis of Unprecedented *Cis-1* Biscycloadducts. *Chem. Commun.* **2004**, *4*,

1338.

(102) Zhou, D. B.; Wang, G. W. Synthesis of [60]Fullerene-Fused Spiroindanes by Palladium-Catalyzed Oxidative Annulation of [60]Fullerene with 2-Aryl Cyclic 1,3-Dicarbonyl Compounds. *Org. Lett.* **2016**, *18*, 2616.

(103) Zhou, D. B.; Wang, G. W. Palladium-Catalyzed Decarboxylative Annulation of 2-Arylbenzoic Acids with [60]Fullerene via C-H Bond Activation. *Org. Lett.* **2015**, *17*, 1260.

(104) Zhai, W. Q.; Peng, R. F.; Jin, B.; Wang, G. W. Synthesis of [60]Fullerene-Fused Tetrahydrobenzooxepine and Isochroman Derivatives via Hydroxyl-Directed C-H Activation/C-O Cyclization. *Org. Lett.* **2014**, *16*, 1638.

(105) Chen, C. P.; Luo, C.; Ting, C.; Chuang, S. C. Organic Photovoltaics Incorporating Fulleroisoquinolinones as N-Type Materials. *Chem. Commun.* **2011**, *47*, 1845.

(106) Zhou, D. B.; Wang, G. W. Synthesis of [60]Fullerene-Fused Tetralones via Palladium-Catalyzed Ketone-Directed sp^2 C–H Activation and sp^3 C–H Functionalization. *Adv. Synth. Catal.* **2016**, *358*, 1548.

(107) Yan, Y. T.; Gao, W.; Jin, B.; Shan, D. S.; Peng, R. F.; Chu, S. J. Palladium-Catalyzed Reaction of [60]Fullerene with Aroyl Compounds via Enolate-Mediated sp^2 C-H Bond Activation and Hydroxylation. *J. Org. Chem.* **2018**, *83*, 672.

(108) Rajeshkumar, V.; Chan, F.-W.; Chuang, S.-C. Palladium-Catalyzed and Hybrid Acids-Assisted Synthesis of [60]Fulleroazepines in One Pot under Mild Conditions: Annulation of N-Sulfonyl-2-Aminobiaryls with [60]Fullerene through Sequential C-H Bond Activation, C-C and C-N Bond Formation. *Adv. Synth. Catal.* **2012**, *354*, 2473.

(109) Chuang, S. C.; Rajeshkumar, V.; Cheng, C. A.; Deng, J. C.; Wang, G. W. Annulation of Benzamides with [60]Fullerene through Palladium(II)-Catalyzed C-H Bond Activation. *J. Org. Chem.* **2011**, *76*, 1599.

(110) Hashikawa, Y.; Murata, M.; Wakamiya, A.; Murata, Y. Palladium-Catalyzed Cyclization: Regioselectivity and Structure of Arene-Fused C_{60} Derivatives. *J. Am. Chem. Soc.* **2017**, *139*, 16350.

(111) Morton, J. R.; Preston, K. F.; Krusic, P. J.; Hill, S. A.; Wasserman, E. ESR Studies of the Reaction of Alkyl Radicals with Fullerene (C_{60}). *J. Phys. Chem.* **1992**, *96*, 3576.

(112) Beuerle, F.; Lebovitz, R.; Hirsch, A. Antioxidant Properties of Water-Soluble Fullerene Derivatives. In *Medicinal chemistry and pharmacological potential of fullerenes and carbon nanotubes*, Springer, 2008.

(113) Wang, G.-W.; Li, F.-B. Transition Metal Salt-Mediated Radical Reactions of [60]Fullerene. *Curr. Org. Chem.* **2012**, *16*, 1109.

(114) He, C.-L.; Liu, R.; Li, D.-D.; Zhu, S.-E.; Wang, G.-W. Synthesis and Functionalization of [60]Fullerene-Fused Imidazolines. *Org. Lett.* **2013**, *15*, 1532.

(115) Zhai, W.-Q.; Jiang, S.-P.; Peng, R.-F.; Jin, B.; Wang, G.-W. Facile Access to Novel [60]Fullerenyl Diethers and [60]Fullerene–Sugar Conjugates via Annulation of Diol Moieties. *Org. Lett.* **2015**, *17*, 1862.

(116) Liu, T.-X.; Zhang, Z.; Liu, Q.; Zhang, P.; Jia, P.; Zhang, Z.; Zhang, G. Synthesis of [60]Fullerene-Fused Tetrahydroazepinones and Azepinonimines via $Cu(OAc)_2$ -Promoted N-Heteroannulation Reaction. *Org. Lett.* **2014**, *16*, 1020.

(117) Li, C.; Zhang, D.; Zhang, X.; Wu, S.; Gao, X. Manganese(III)-Mediated Free Radical Reactions of [60]Fullerene with β-Dicarbonyl Compounds. *Org. Biomol. Chem.* **2004**, *2*, 3464.

(118) Martin, N.; Nierengarten, J.-F. *Supramolecular Chemistry of Fullerenes and Carbon Nanotubes*; Wiley-VCH, 2012.

(119) Vidal, S.; Izquierdo, M.; Filippone, S.; Fernández, I.; Akin, S.; Seo, J.-Y.; Zakeeruddin, S. M.; Grätzel, M.; Martín, N. Site-Selective Synthesis of β-[70]PCBM-like Fullerenes: Efficient Application in Perovskite Solar Cells. *Chem. Eur. J.* **2019**, *25*, 3224.

(120) Kiely, A. F.; Haddon, R. C.; Meier, M. S.; Selegue, J. P.; Brock, C. P.; Patrick, B. O.; Wang, G. W.; Chen, Y. The First Structurally Characterized Homofullerene (Fulleroid). *J. Am. Chem Soc.* **1999**, *121*, 7971.

(121) Herrmann, A.; Diederich, F.; Thilgen, C.; Meer, H.-U. Ter; Müller, W. H. Chemistry of the Higher Fullerenes: Preparative Isolation of C_{76} by HPLC and Synthesis, Separation, and Characterization of Diels-Alder Monoadducts of C_{70} and C_{76}. *Helv. Chim. Acta* **1994**, *77*, 1689.

(122) Castro, E.; Zavala, G.; Seetharaman, S.; D'Souza, F.; Echegoyen, L. Impact of Fullerene Derivative Isomeric Purity on the Performance of Inverted Planar Perovskite Solar Cells. *J. Mater. Chem. A* **2017**, *5*, 19485.

(123) Yang, W. W.; Li, Z. J.; Li, S. H.; Wu, S. L.; Shi, Z.; Gao, X. Reductive Activation of C_{70} Equatorial Carbons and Structurally Characterized C_{70} δ-Adduct with Closed [5,6]-Ring Fusion. *J. Org. Chem.* **2017**, *82*, 9253.

(124) Meier, M. S.; Wang, G. W.; Haddon, R. C.; Brock, C. P.; Lloyd, M. A.; Selegue, J. P. Benzyne Adds across a Closed 5-6 Ring Fusion in C_{70}: Evidence for Bond Delocalization in Fullerenes. *J. Am. Chem. Soc.* **1998**, *120*, 2337.

(125) Liosi, K.; Romero-Rivera, A.; Semivrazhskaya, O.; Caniglia, C. D.; Garcia-Borràs, M.; Trapp, N.; Osuna, S.; Yamakoshi, Y. Site-Selectivity of Prato Additions to C_{70} : Experimental and Theoretical Studies of a New Thermodynamic Product at the Dd -[5,6]-Junction. *Org. Lett.* **2019**, *21*, 5162.

(126) Tian, C.; Castro, E.; Wang, T.; Betancourt-Solis, G.; Rodriguez, G.; Echegoyen, L. Improved Performance and Stability of Inverted Planar Perovskite Solar Cells Using Fulleropyrrolidine Layers. *ACS Appl. Mater. Interfaces* **2016**, *8*, 31426.

(127) Umeyama, T.; Imahori, H. Isomer Effects of Fullerene Derivatives on Organic Photovoltaics and Perovskite Solar Cells. *Acc. Chem. Res.* **2019**, *52,* 2046.

(128) Akasaka, T.; Kato, T.; Kobayashi, K.; Nagase, S.; Yamamoto, K.; Funasaka, H.; Takahashi, T. Exohedral Adducts of La@C82. *Nature* **1995**, *374*, 600

(129) Garcia-Borràs, M.; Osuna, S.; Swart, M.; Luis, J. M.; Echegoyen, L.; Solà, M. Aromaticity as the Driving Force for the Stability of Non-IPR Endohedral Metallofullerene Bingel–Hirsch Adducts. *Chem. Commun.* **2013**, *49*, 8767.

(130) Garcia-Borràs, M.; Osuna, S.; Luis, J. M.; Swart, M.; Solà, M. A Complete Guide on the Influence of Metal Clusters in the Diels-Alder Regioselectivity of I_h-C_{80} Endohedral Metallofullerenes. *Chem. Eur. J.* **2013**, *19*, 14931.

(131) Garcia-Borràs, M.; Osuna, S.; Swart, M.; Luis, J. M.; Solà, M. Maximum Aromaticity as a Guiding Principle for the Most Suitable Hosting Cages in Endohedral Metallofullerenes. *Angew. Chem. Int. Ed.* **2013**, *125*, 9445.

(132) Garcia-Borràs, M.; Cerõn, M. R.; Osuna, S.; Izquierdo, M.; Luis, J. M.; Echegoyen, L.; Solà, M. The Regioselectivity of Bingel-Hirsch Cycloadditions on Isolated Pentagon Rule Endohedral Metallofullerenes. *Angew. Chem. Int. Ed.* **2016**, *55*, 2374.

(133) Garcia-Borràs, M.; Romero-Rivera, A.; Osuna, S.; Luis, J. M.; Swart, M.; Solà, M. The Frozen Cage Model: A Computationally Low-Cost Tool for Predicting the Exohedral Regioselectivity of Cycloaddition Reactions Involving Endohedral Metallofullerenes. *J. Chem. Theory Comput.* **2012**, *8*, 1671.

(134) Garcia-Borràs, M.; Luis, J. M.; Swart, M.; Solà, M. Diels-Alder and Retro-Diels-Alder Cycloadditions of (1,2,3,4,5-Pentamethyl) Cyclopentadiene to La@C_{2v}-C_{82}: Regioselectivity and Product Stability. *Chem. Eur. J.* **2013**, *19*, 4468.

(135) Garcia-Borràs, M.; Osuna, S.; Luis, J. M.; Swart, M.; Solà, M. The Exohedral Diels-Alder Reactivity of the Titanium Carbide Endohedral Metallofullerene Ti_2C_2@D_{3h}-C_{78}: Comparison with D_{3h}-C_{78} and M_3N@D_{3h}-C_{78} (M=Sc and Y) Reactivity. *Chem. Eur. J.* **2012**, *18*, 7141.

(136) Garcia-Borràs, M.; Luis, J. M.; Solà, M.; Osuna, S. The Key Role of Aromaticity in the Structure and Reactivity of C_{60} and Endohedral Metallofullerenes. *Inorganica Chim. Acta* **2017**, *468*, 38.

(137) Osuna, S.; Rodríguez-Fortea, A.; Poblet, J. M.; Solà, M.; Swart, M. Product Formation in the Prato Reaction on Sc_3N@D_{5h}-C_{80}: Preference for [5,6]-Bonds, and Not Pyracylenic Bonds. *Chem. Commun.* **2012**, *48*, 2486.

(138) Garcia-Borràs, M.; Osuna, S.; Luis, J. M.; Swart, M.; Solà, M. The Role of Aromaticity in Determining the Molecular Structure and Reactivity of (Endohedral Metallo)Fullerenes. *Chem. Soc. Rev.* **2014**, *43*, 5089.

(139) Osuna, S.; Swart, M.; Solà, M. The Reactivity of Endohedral Fullerenes. What Can Be Learnt from Computational Studies? *Phys. Chem. Chem. Phys.* **2011**, *13*, 3585.

(140) Kordatos, K.; Bosi, S.; Da Ros, T.; Zambon, A.; Lucchini, V.; Prato, M. Isolation and Characterization of All Eight Bisadducts of Fulleropyrrolidine Derivatives. *J. Org. Chem.* **2001**, *66*, 2802.

(141) Hirsch, A.; Lamparth, I.; Karfunkel, H. R. Fullerene Chemistry in Three Dimensions: Isolation of Seven Regioisomeric Bisadducts and Chiral Trisadducts of C_{60} and Di(Ethoxycarbonyl)Methylene. *Angew. Chem. Int. Ed.* **1994**, *33*, 437.

(142) Yan, W.; Seifermann, S. M.; Pierrat, P.; Bräse, S. Synthesis of Highly Functionalized C_{60} Fullerene Derivatives and Their Applications in Material and Life Sciences. *Org. Biomol. Chem* **2015**, *13*, 25.

(143) Krusic, P. J.; Wasserman, E.; Keizer, P. N.; Morton, J. R.; Preston, K. F. Radical Reactions of C_{60}. *Science* **1991**, *254*, 1183.

(144) Grösser, T.; Prato, M.; Lucchini, V.; Hirsch, A.; Wudl, F. Ring Expansion of the Fullerene Core by Highly Regioselective Formation of Diazafulleroids. *Angew. Chem. Int. Ed.* **1995**, *34*, 1343.

(145) Li, H.; Haque, S. A.; Kitaygorodskiy, A.; Meziani, M. J.; Torres-Castillo, M.; Sun, Y. P. Alternatively Modified Bingel Reaction for Efficient Syntheses of C_{60} Hexakis-Adducts. *Org. Lett.* **2006**, *8*, 5641.

(146) Diederich, F.; Kessinger, R. Templated Regioselective and Stereoselective Synthesis in Fullerene Chemistry. *Acc. Chem. Res.* **1999**, *32*, 537.

(147) Lamparth, I.; Maichle–Mössmer, C.; Hirsch, A. Reversible Template-Directed Activation of Equatorial Double Bonds of the Fullerene Framework: Regioselective Direct Synthesis, Crystal Structure, and Aromatic Properties of $T_hC_{66}(COOEt)_{12}$. *Angew. Chem. Int. Ed.* **1995**, *34*, 1607.

(148) Castro, E.; Azmani, K.; Garcia, A. H.; Aghabali, A.; Liu, S.; Metta-Magana, A. J.; Olmstead, M. M.; Rodríguez-Fortea, A.; Poblet, J. M.; Echegoyen, L. Unusual C_{2h}-Symmetric Trans-1-(Bis-Pyrrolidine)-Tetra-Malonate Hexa-Adducts of C_{60}: The Unexpected Regio- and Stereocontrol Mediated by Malonate–Pyrrolidine Interaction. *Chem. Eur. J.* **2017**, *23*, 15937.

(149) Cerón, M. R.; Castro, E.; Neti, V. S. P. K.; Dunk, P. W.; Echegoyen, L. A. Regiochemically Controlled Synthesis of a β-4-B′ [70]Fullerene Bis-Adduct. *J. Org. Chem.* **2017**, *82*, 893.

(150) Thilgen, C.; Sergeyev, S.; Diederich, F. Spacer-Controlled Multiple Functionalization of Fullerenes. In *Templates in chemistry I*, Springer, 2012.

(151) Thilgen, C.; Diederich, F. Tether-Directed Remote Functionalization of Fullerenes C_{60} and C_{70}. *Comptes Rendus Chimie* **2006**, *9*, 868.

(152) Zhou, Z.; Wilson, S. Tether-Directed Multiple Functionalization of Fullerene[60]. *Curr. Org. Chem.* **2005**, *9*, 789.

(153) Schick, G.; Jarrosson, T.; Rubin, Y. Formation of an Effective Opening within the Fullerene Core of C_{60} by an Unusual Reaction Sequence. *Angew. Chem. Int. Ed.* **1999**, *38*, 2360.

(154) Martín, N.; Altable, M.; Filippone, S.; Martín-Domenech, A.; Güell, M.; Solà, M. Thermal [2+2] Intramolecular Cycloadditions of Fuller-1,6-Enynes. *Angew. Chem. Int. Ed.* **2006**, *45*, 1439.

(155) Nierengarten, J.-F.; Habicher, T.; Kessinger, R.; Cardullo, F.; Diederich, F.; Gramlich, V.; Gisselbrecht, J.-P.; Boudon, C.; Gross, M. Macrocyclization on the Fullerene Core: Direct Regio- and Diastereoselective Multi-Functionalization of [60]Fullerene, and Synthesis of Fullerene-Dendrimer Derivatives. *Helv. Chim. Acta* **1997**, *80*, 2238.

(156) Isaacs, L.; Haldimann, R. F.; Diederich, F. Tether-Directed Remote Functionalization of Buckminsterfullerene: Regiospecific Hexaadduct Formation. *Angew. Chem. Int. Ed.* **1994**, *33*, 2339.

(157) Vougioukalakis, G. C.; Roubelakis, M. M.; Orfanopoulos, M. Open-Cage Fullerenes: Towards the Construction of Nanosized Molecular Containers. *Chem. Soc. Rev.* **2010**, *39*, 817.

(158) Wudl, F. The Chemical Properties of Buckminsterfullerene (C_{60}) and the Birth and Infancy of Fulleroids. *Acc. Chem. Res.* **1992**, *25*, 157.

(159) Hummeler, J. C.; Wudl, F.; Prato, M. There Is a Hole in My Bucky. *J. Am. Chem. Soc.* **1995**, *117*, 7003.

(160) Hachiya, H.; Kabe, Y. Production of a 15-Membered Ring Orifice in Open-Cage Fullerenes by Double Photooxygenation of Azafulleroid. *Chem. Lett.* **2009**, *38*, 372.

(161) Arce, M.-J.; Viado, A. L.; An, Y.-Z.; Khan, S. I.; Rubin, Y. Triple Scission of a Six-Membered Ring on the Surface of C_{60} via Consecutive Pericyclic Reactions and Oxidative Cobalt Insertion. *J. Am. Chem. Soc.* **1996**, *118*, 3775.

(162) Hsiao, T. Y.; Santhosh, K. C.; Liou, K. F.; Cheng, C. H. Nickel-Promoted First Ene-Diyne Cycloaddition Reaction on C_{60}: Synthesis and Photochemistry of the Fullerene Derivatives. *J. Am. Chem. Soc.* **1998**, *120*, 12232.

(163) Qian, W.; Bartberger, M. D.; Pastor, S. J.; Houk, K. N.; Wilkins, C. L.; Rubin, Y. C_{62} , a Non-Classical Fullerene Incorporating a Four-Membered Ring. *J. Am. Chem. Soc.* **2000**, *122*, 8333.

(164) Inoue, H.; Yamaguchi, H.; Suzuki, T.; Akasaka, T.; Murata, S. A Novel and Practical Synthesis of Alkoxycarbonyl-Substituted Bis(Fulleroid). *Synlett* **2000**, 1178.

(165) Murata, Y.; Murata, M.; Komatsu, K. The Reaction of Fullerene C_{60} with 4,6-Dimethyl-1,2,3-Triazine: Formation of an Open-Cage Fullerene Derivative. *J. Org. Chem.* **2001**, *66*, 8187.

(166) Qian, W.; Rubin, Y. Convergent, Regioselective Synthesis of Tetrakisfulleroids from C_{60}. *J. Org.*

Chem. **2002**, *67*, 7683.

(167) Iwamatsu, S.; Vijayalakshmi, P. S.; Hamajima, M.; Suresh, C. H.; Koga, N.; Suzuki, T.; Murata, S. A Novel Photorearrangement of a Cyclohexadiene Derivative of C_{60}. *Org. Lett.* **2002**, *4*, 1217.

(168) Suresh, C. H.; Vijayalakshmi, P. S.; Iwamatsu, S. I.; Murata, S.; Koga, N. Rearrangement of the Cyclohexadiene Derivatives of C_{60} to Bis(Fulleroid) and Bis(Methano)Fullerene: Structure, Stability, and Mechanism. *J. Org. Chem.* **2003**, *68*, 3522.

(169) Murata, Y.; Murata, M.; Komatsu, K. Synthesis, Structure, and Properties of Novel Open-Cage Fullerenes Having Heteroatom(s) on the Rim of the Orifice. *Chem. Eur. J.* **2003**, *9*, 1600.

(170) Qian, W.; Chuang, S. C.; Amador, R. B.; Jarrosson, T.; Sander, M.; Pieniazek, S.; Khan, S. I.; Rubin, Y. Synthesis of Stable Derivatives of C_{62}: The First Nonclassical Fullerene Incorporating a Four-Membered Ring. *J. Am. Chem. Soc.* **2003**, *125*, 2066.

(171) Inoue, H.; Yamaguchi, H.; Iwamatsu, S.; Uozaki, T.; Suzuki, T.; Akasaka, T.; Nagase, S.; Murata, S. Photooxygenative Partial Ring Cleavage of Bis(Fulleroid): Synthesis of a Novel Fullerene Derivative with a 12-Membered Ring. *Tetrahedron Lett.* **2001**, *42*, 895.

(172) Huang, S.; Xiao, Z.; Wang, F.; Gan, L.; Zhang, X.; Hu, X.; Zhang, S.; Lu, M.; Pan, Q.; Xu, L. Selective Preparation of Oxygen-Rich [60]Fullerene Derivatives by Stepwise Addition of Tert -Butylperoxy Radical and Further Functionalization of the Fullerene Mixed Peroxides. *J. Org. Chem.* **2004**, *69*, 2442.

(173) Gan, L. Molecular Containers Derived from [60]Fullerene through Peroxide Chemistry. *Acc. Chem. Res.* **2019**, *52*, 1793.

(174) Xiao, Z.; Yao, J.; Yang, D.; Wang, F.; Huang, S.; Gan, L.; Jia, Z.; Jiang, Z.; Yang, X.; Zheng, B.; Yuan, G.; Zhang, S.; Wang, Z. Synthesis of [59]Fullerenones through Peroxide-Mediated Stepwise Cleavage of Fullerene Skeleton Bonds and X-Ray Structures of Their Water-Encapsulated Open-Cage Complexes. *J. Am. Chem. Soc.* **2007**, *129*, 16149.

(175) Xu, L.; Ren, H.; Liang, S.; Sun, J.; Liu, Y.; Gan, L. Release of the Water Molecule Encapsulated Inside an Open-Cage Fullerene through Hydrogen Bonding Mediated by Hydrogen Fluoride. *Chem. Eur. J.* **2015**, *21*, 13539.

(176) Murata, Y.; Murata, M.; Komatsu, K. 100% Encapsulation of a Hydrogen Molecule into an Open-Cage Fullerene Derivative and Gas-Phase Generation of $H_2@C_{60}$. *J. Am. Chem. Soc.* **2003**, *125*, 7152.

(177) Xu, L.; Liang, S.; Sun, J.; Gan, L. Open-Cage Fullerene with a Stopper Acts as a Molecular Vial for a Single Water Molecule. *Org. Chem. Front.* **2015**, *2*, 1500.

(178) Komatsu, K.; Murata, M.; Murata, Y. Encapsulation of Molecular Hydrogen in Fullerene C_{60} by Organic Synthesis. *Science* **2005**, *307*, 238.

(179) Kurotobi, K.; Murata, Y. A Single Molecule of Water Encapsulated in Fullerene C_{60}. *Science* **2011**,

333, 613.

(180) Murata, Y.; Maeda, S.; Murata, M.; Komatsu, K. Encapsulation and Dynamic Behavior of Two H_2 Molecules in an Open-Cage C_{70}. *J. Am. Chem. Soc.* **2008**, *130*, 6702.

(181) Zhang, R.; Murata, M.; Aharen, T.; Wakamiya, A.; Shimoaka, T.; Hasegawa, T.; Murata, Y. Synthesis of a Distinct Water Dimer inside Fullerene C_{70}. *Nat. Chem.* **2016**, *8*, 435.

(182) Bloodworth, S.; Sitinova, G.; Alom, S.; Vidal, S.; Bacanu, G. R.; Elliott, S. J.; Light, M. E.; Herniman, J. M.; Langley, G. J.; Levitt, M. H.; Whitby, R. J. First Synthesis and Characterization of $CH_4@C_{60}$. *Angew. Chem. Int. Ed.* **2019**, *58*, 5038.

(183) Krachmalnicoff, A.; Bounds, R.; Mamone, S.; Alom, S.; Concistrè, M.; Meier, B.; Kouřil, K.; Light, M. E.; Johnson, M. R.; Rols, S.; et al. The Dipolar Endofullerene $HF@C_{60}$. *Nat. Chem.* **2016**, *8*, 953.

(184) Iwamatsu, S.; Stanisky, C. M.; Cross, R. J.; Saunders, M.; Mizorogi, N.; Nagase, S.; Murata, S. Carbon Monoxide Inside an Open-Cage Fullerene. *Angew. Chem. Int. Ed.* **2006**, *45*, 5337.

(185) Chen, C.-P.; Lin, Y.-W.; Horng, J.-C.; Chuang, S.-C. Open-Cage Fullerenes as n-Type Materials in Organic Photovoltaics: Relevance of Frontier Energy Levels, Carrier Mobility and Morphology of Different Sizable Open-Cage Fullerenes with Power Conversion Efficiency in Devices. *Adv. Energy Mater.* **2011**, *1*, 776.

(186) Chen, C.-P.; Huang, C.-Y.; Chuang, S.-C. Highly Thermal Stable and Efficient Organic Photovoltaic Cells with Crosslinked Networks Appending Open-Cage Fullerenes as Additives. *Adv. Funct. Mater.* **2015**, *25*, 207.

(187) Murata, M.; Morinaka, Y.; Murata, Y.; Yoshikawa, O.; Sagawa, T.; Yoshikawa, S. Modification of the σ-Framework of [60]Fullerene for Bulk-Heterojunction Solar Cells. *Chem. Commun.* **2011**, *47*, 7335.

(188) Gan, L.; Zhou, Z.; Xin, N. Synthesis of Metal Complexes with an Open-Cage Fullerene as the Ligand. *Chem. Eur. J.* **2018**, *24*, 451.

(189) Maroto, E. E.; Mateos, J.; Garcia-Borràs, M.; Osuna, S.; Filippone, S.; Herranz, M. Á.; Murata, Y.; Solà, M.; Martín, N. Enantiospecific *Cis–Trans* Isomerization in Chiral Fulleropyrrolidines: Hydrogen-Bonding Assistance in the Carbanion Stabilization in $H_2O@C_{60}$. *J. Am. Chem. Soc.* **2015**, *137*, 1190.

(190) Vidal, S.; Izquierdo, M.; Alom, S.; Garcia-Borràs, M.; Filippone, S.; Osuna, S.; Solà, M.; Whitby, R. J.; Martín, N. Effect of Incarcerated HF on the Exohedral Chemical Reactivity of $HF@C_{60}$. *Chem. Commun.* **2017**, *53*, 10993.

(191) Panwar, N.; Soehartono, A. M.; Chan, K. K.; Zeng, S.; Xu, G.; Qu, J.; Coquet, P.; Yong, K.-T.; Chen, X. Nanocarbons for Biology and Medicine: Sensing, Imaging, and Drug Delivery. *Chem. Rev.* **2019**, *119*, 9559.

(192) Castro, E.; Garcia, A. H.; Zavala, G.; Echegoyen, L. Fullerenes in Biology and Medicine. *J. Mater.*

Chem. B **2017**, *5*, 6523.

(193) Sijbesma, R.; Srdanov, G.; Wudl, F.; Castoro, J. A.; Wilkins, C.; Friedman, S. H.; DeCamp, D. L.; Kenyon, G. L. Synthesis of a Fullerene Derivative for the Inhibition of HIV Enzymes. *J. Am. Chem. Soc.* **1993**, *115*, 6510.

(194) Martinez, Z. S.; Castro, E.; Seong, C.-S.; Cerón, M. R.; Echegoyen, L.; Llano, M. Fullerene Derivatives Strongly Inhibit HIV-1 Replication by Affecting Virus Maturation without Impairing Protease Activity. *Antimicrob. Agents Chemother.* **2016**, *60*, 5731.

(195) Muñoz, A.; Sigwalt, D.; Illescas, B. M.; Luczkowiak, J.; Rodríguez-Pérez, L.; Nierengarten, I.; Holler, M.; Remy, J.-S.; Buffet, K.; Vincent, S. P.; Rojo, J.; Delgado, R.; Nierengarten, J.-F.; Martín, N. Synthesis of Giant Globular Multivalent Glycofullerenes as Potent Inhibitors in a Model of Ebola Virus Infection. *Nat. Chem.* **2016**, *8*, 50.

(196) Ramos-Soriano, J.; Reina, J. J.; Illescas, B. M.; de la Cruz, N.; Rodríguez-Pérez, L.; Lasala, F.; Rojo, J.; Delgado, R.; Martín, N. Synthesis of Highly Efficient Multivalent Disaccharide/[60]Fullerene Nanoballs for Emergent Viruses. *J. Am. Chem. Soc.* **2019**, *141*, 15403.

(197) Jiao, Q.; Li, L.; Mu, Q.; Zhang, Q. Immunomodulation of Nanoparticles in Nanomedicine Applications. *Biomed Res. Int.* **2014**, *2014*, 1.

(198) Kazemzadeh, H.; Mozafari, M. Fullerene-Based Delivery Systems. *Drug Discov. Today* **2019**, *24*, 898.

(199) European Comission. The Commission calls for a climate neutral Europe by 2050. https://europa.eu/rapid/press-release_IP-18-6543_en.htm (accessed Jul 30, 2019).

(200) Haase, F.; Hollemann, C.; Schäfer, S.; Merkle, A.; Rienäcker, M.; Krügener, J.; Brendel, R.; Peibst, R. Laser Contact Openings for Local Poly-Si-Metal Contacts Enabling 26.1%-Efficient POLO-IBC Solar Cells. *Sol. Energy Mater. Sol. Cells* **2018**, *186*, 184.

(201) Marinova, N.; Valero, S.; Delgado, J. L. Organic and Perovskite Solar Cells: Working Principles, Materials and Interfaces. *J. Colloid Interface Sci.* **2017**, *488*, 373.

(202) Mazzio, K. A.; Luscombe, C. K. The Future of Organic Photovoltaics. *Chem. Soc. Rev.* **2015**, *44*, 78.

(203) Rafique, S.; Abdullah, S. M.; Sulaiman, K.; Iwamoto, M. Fundamentals of Bulk Heterojunction Organic Solar Cells: An Overview of Stability/Degradation Issues and Strategies for Improvement. *Renew. Sustain. Energy Rev.* **2018**, *84*, 43.

(204) Li, C. Z.; Yip, H. L.; Jen, A. K.-Y. Functional Fullerenes for Organic Photovoltaics. *J. Mater. Chem.* **2012**, *22*, 4161.

(205) Collavini, S.; Delgado, J. L. Fullerenes: The Stars of Photovoltaics. *Sustain. Energy Fuels* **2018**, *2*, 2480.

(206) Cheng, P.; Li, G.; Zhan, X.; Yang, Y. Next-Generation Organic Photovoltaics Based on Non-Fullerene Acceptors. *Nat. Photonics* **2018**, *12*, 131.

(207) Cui, Y.; Yao, H.; Zhang, J.; Zhang, T.; Wang, Y.; Hong, L.; Xian, K.; Xu, B.; Zhang, S.; Peng, J.; Wei, Z.; Gao, F.; Hou, J. Over 16% Efficiency Organic Photovoltaic Cells Enabled by a Chlorinated Acceptor with Increased Open-Circuit Voltages. *Nat. Commun.* **2019**, *10*, 2515.

(208) Segura, J. L.; Martín, N.; Guldi, D. M. Materials for Organic Solar Cells: The C_{60} /π-Conjugated Oligomer Approach. *Chem. Soc. Rev.* **2005**, *34*, 31.

(209) Yu, G.; Gao, J.; Hummelen, J. C.; Wudl, F.; Heeger, A. J. Polymer Photovoltaic Cells: Enhanced Efficiencies via a Network of Internal Donor-Acceptor Heterojunctions. *Science* **1995**, *270*, 1789.

(210) Kojima, A.; Teshima, K.; Shirai, Y.; Miyasaka, T. Organometal Halide Perovskites as Visible-Light Sensitizers for Photovoltaic Cells. *J. Am. Chem. Soc.* **2009**, *131*, 6050.

(211) Hagfeldt, A.; Boschloo, G.; Sun, L.; Kloo, L.; Pettersson, H. Dye-Sensitized Solar Cells. *Chem. Rev.* **2010**, *110*, 6595.

(212) NREL. Best Research-Cell Efficiency Chart https://www.nrel.gov/pv/cell-efficiency.html (accessed Sep 18, 2019).

(213) Huang, F.; Li, M.; Siffalovic, P.; Cao, G.; Tian, J. From Scalable Solution Fabrication of Perovskite Films towards Commercialization of Solar Cells. *Energy Environ. Sci.* **2019**, *12*, 518.

(214) Castro, E.; Murillo, J.; Fernandez-Delgado, O.; Echegoyen, L. Progress in Fullerene-Based Hybrid Perovskite Solar Cells. *J. Mater. Chem. C* **2018**, *6*, 2635.

(215) Cui, P.; Wei, D.; Ji, J.; Huang, H.; Jia, E.; Dou, S.; Wang, T.; Wang, W.; Li, M. Planar p–n Homojunction Perovskite Solar Cells with Efficiency Exceeding 21.3%. *Nat. Energy* **2019**, *4*, 150.

(216) Liu, T.; Chen, K.; Hu, Q.; Zhu, R.; Gong, Q. Inverted Perovskite Solar Cells: Progresses and Perspectives. *Adv. Energy Mater.* **2016**, *6*, 1600457.

(217) Kim, H.; Lim, K.-G.; Lee, T.-W. Planar Heterojunction Organometal Halide Perovskite Solar Cells: Roles of Interfacial Layers. *Energy Environ. Sci.* **2016**, *9*, 12.

(218) Deng, L.-L.; Xie, S.-Y.; Gao, F. Fullerene-Based Materials for Photovoltaic Applications: Toward Efficient, Hysteresis-Free, and Stable Perovskite Solar Cells. *Adv. Electron. Mater.* **2018**, *4*, 1700435.

(219) Gatti, T.; Menna, E.; Meneghetti, M.; Maggini, M.; Petrozza, A.; Lamberti, F. The Renaissance of Fullerenes with Perovskite Solar Cells. *Nano Energy*. **2017**, *41*, 84.

(220) Fang, Y.; Bi, C.; Wang, D.; Huang, J. The Functions of Fullerenes in Hybrid Perovskite Solar Cells. *ACS Energy Lett.* **2017**, *2*, 782.

(221) Fernandez-Delgado, O.; Castro, E.; Ganivet, C. R.; Fosnacht, K.; Liu, F.; Mates, T.; Liu, Y.; Wu, X.;

Echegoyen, L. Variation of Interfacial Interactions in $PC_{61}BM$-like Electron-Transporting Compounds for Perovskite Solar Cells. *ACS Appl. Mater. Interfaces* **2019**, *11*, 34408.

(222) Yang, D.; Zhang, X.; Wang, K.; Wu, C.; Yang, R.; Hou, Y.; Jiang, Y.; Liu, S.; Priya, S. Stable Efficiency Exceeding 20.6% for Inverted Perovskite Solar Cells through Polymer-Optimized PCBM Electron-Transport Layers. *Nano Lett.* **2019**, *19*, 3313.

(223) Bates, R. *Organic Synthesis Using Transition Metals*; Wiley, 2012.

(224) Beller, M., Bolm, C. *Transition Metals for Organic Synthesis*; Wiley, 2004.

(225) Tanaka, K. *Transition-Metal-Mediated Aromatic Ring Construction*; Wiley, 2013.

(226) Tanaka, K. Transition Metal-Mediated Aromatic Ring Construction. In *Arene Chemistry*, Wiley, 2015.

(227) Lautens, M.; Klute, W.; Tam, W. Transition Metal-Mediated Cycloaddition Reactions. *Chem. Rev.* **1996**, *96*, 49.

(228) Bertholet, M. C. R. A thermally induced oligomerization of acetylene. *Held. Seances. Acad. Sci.* **1866**, 905.

(229) Reppe, W.; Schlichting, O.; Klager, K.; Toepel, T. Cyclisierende Polymerisation von Acetylen I Über Cyclooctatetraen. *Justus Liebigs Ann. Chem.* **1948**, *560*, 1.

(230) Broere, D.; Ruijter, E. Recent Advances in Transition-Metal-Catalyzed [2+2+2]-Cyclo(Co)Trimerization Reactions. *Synthesis* **2012**, *44*, 2639.

(231) Hua, R.; Victoria A. Abrenica, M.; Wang, P. Cycloaddition of Alkynes: Atom-Economic Protocols for Constructing Six-Membered Cycles. *Curr. Org. Chem.* **2011**, *15*, 712.

(232) Domínguez, G.; Pérez-Castells, J. Recent Advances in [2+2+2] Cycloaddition Reactions. *Chem. Soc. Rev.* **2011**, *40*, 3430.

(233) Chopade, P. R.; Louie, J. [2+2+2] Cycloaddition Reactions Catalyzed by Transition Metal Complexes. *Adv. Synth. Catal.* **2006**, *348*, 2307.

(234) Shibata, Y.; Tanaka, K. Rhodium-Catalyzed [2+2+2] Cycloaddition of Alkynes for the Synthesis of Substituted Benzenes: Catalysts, Reaction Scope, and Synthetic Applications. *Synthesis* **2012**, *44*, 323.

(235) Weding, N.; Hapke, M. Preparation and Synthetic Applications of Alkene Complexes of Group 9 Transition Metals in [2+2+2] Cycloaddition Reactions. *Chem. Soc. Rev.* **2011**, *40*, 4525.

(236) Tanaka, K. Cationic Rhodium(I)/BINAP-Type Bisphosphine Complexes: Versatile New Catalysts for Highly Chemo-, Regio-, and Enantioselective [2+2+2] Cycloadditions. *Synlett* **2007**, *13*, 1977.

(237) Gandon, V.; Aubert, C.; Malacria, M. Recent Progress in Cobalt-Mediated [2 + 2 + 2] Cycloaddition Reactions. *Chem. Commun.* **2006**, 2209.

(238) Babazadeh, M.; Soleimani-Amiri, S.; Vessally, E.; Hosseinian, A.; Edjlali, L. Transition Metal-Catalyzed [2 + 2 + 2] Cycloaddition of Nitrogen-Linked 1,6-Diynes: A Straightforward Route to Fused Pyrrolidine Systems. *RSC Adv.* **2017**, *7*, 43716.

(239) Lledó, A.; Pla-Quintana, A.; Roglans, A. Allenes, Versatile Unsaturated Motifs in Transition-Metal-Catalysed [2+2+2] Cycloaddition Reactions. *Chem. Soc. Rev.* **2016**, *45*, 2010.

(240) Domínguez, G.; Pérez-Castells, J. Alkenes in [2+2+2] Cycloadditions. *Chem. Eur. J.* **2016**, *22*, 6720.

(241) Tanaka, K. Rhodium-Catalyzed [2+2+2] Cycloaddition for the Synthesis of Substituted Pyridines, Pyridones, and Thiopyranimines. *Heterocycles* **2012**, *85*, 1017.

(242) Pla-Quintana, A.; Roglans, A.; Pla-Quintana, A.; Roglans, A. [2+2+2] Cycloaddition Reactions of Macrocyclic Systems Catalyzed by Transition Metals. A Review. *Molecules* **2010**, *15*, 9230.

(243) Heller, B.; Hapke, M. The Fascinating Construction of Pyridine Ring Systems by Transition Metal-Catalysed [2 + 2 + 2] Cycloaddition Reactions. *Chem. Soc. Rev.* **2007**, *36*, 1085.

(244) Yamamoto, Y. Recent Advances in Intramolecular Alkyne Cyclotrimerization and Its Applications. *Curr. Org. Chem.* **2005**, *9*, 503.

(245) Varela, J. A.; Saá, C. Construction of Pyridine Rings by Metal-Mediated [2 + 2 + 2] Cycloaddition. *Chem. Rev.* **2003**, *103*, 3787.

(246) Pla-Quintana, A.; Roglans, A. Chiral Induction in [2+2+2] Cycloaddition Reactions. *Asian J. Org. Chem.* **2018**, *7*, 1706.

(247) Amatore, M.; Aubert, C. Recent Advances in Stereoselective [2+2+2] Cycloadditions. *Eur. J. Org. Chem.* **2015**, 265.

(248) Galan, B. R.; Rovis, T. Beyond Reppe: Building Substituted Arenes by [2+2+2] Cycloadditions of Alkynes. *Angew. Chem. Int. Ed.* **2009**, *48*, 2830.

(249) Shibata, T.; Tsuchikama, K. Recent Advances in Enantioselective [2+2+2] Cycloaddition. *Org. Biomol. Chem.* **2008**, *6*, 1317.

(250) Saito, S.; Yamamoto, Y. Recent Advances in the Transition-Metal-Catalyzed Regioselective Approaches to Polysubstituted Benzene Derivatives. *Chem. Rev.* **2000**, *100*, 2901.

(251) Kotha, S.; Brahmachary, E.; Lahiri, K. Transition Metal Catalyzed [2+2+2] Cycloaddition and Application in Organic Synthesis. *Eur. J. Org. Chem.* **2005**, 4741.

(252) Kotha, S.; Lahiri, K.; Sreevani, G. Design and Synthesis of Aromatics through [2+2+2] Cyclotrimerization. *Synlett* **2018**, *29*, 2342.

(253) Parera, M.; Dachs, A.; Solà, M.; Pla-Quintana, A.; Roglans, A. Direct Detection of Key Intermediates in Rhodium(I)-Catalyzed [2+2+2] Cycloadditions of Alkynes by ESI-MS. *Chem. Eur. J.* **2012**, *18*,

13097.

(254) Dachs, A.; Torrent, A.; Pla-Quintana, A.; Roglans, A.; Jutand, A. Rates and Mechanism of Rhodium-Catalyzed [2+2+2] Cycloaddition of Bisalkynes and a Monoalkyne. *Organometallics* **2009**, *28*, 6036.

(255) Orian, L.; van Stralen, J. N. P.; Bickelhaupt, F. M. Cyclotrimerization Reactions Catalyzed by Rhodium(I) Half-Sandwich Complexes: A Mechanistic Density Functional Study. *Organometallics* **2007**, *26*, 3816.

(256) Dachs, A.; Osuna, S.; Roglans, A.; Solà, M. Density Functional Study of the [2+2+2] Cyclotrimerization of Acetylene Catalyzed by Wilkinson's Catalyst, $RhCl(PPh_3)_3$. *Organometallics* **2010**, *29*, 562.

(257) Schore, N. E. Transition-Metal-Mediated Cycloaddition Reactions of Alkynes in Organic Synthesis. *Chem. Rev.* **1988**, *88*, 1081.

(258) Torres, Ò.; Roglans, A.; Pla-Quintana, A.; Luis, J. M.; Solà, M. Computational Insight into Wilkinson's Complex Catalyzed [2 + 2 + 2] Cycloaddition Mechanism Leading to Pyridine Formation. *J. Organomet. Chem.* **2014**, *768*, 15.

(259) Funk, R. L.; Vollhardt, K. P. C. Transition-Metal-Catalyzed Alkyne Cyclizations. A Cobalt-Mediated Total Synthesis of Dl-Estrone. *J. Am. Chem. Soc.* **1980**, *102*, 5253.

(260) Anderson, E. A.; Alexanian, E. J.; Sorensen, E. J. Synthesis of the Furanosteroidal Antibiotic Viridin. *Angew. Chem. Int. Ed.* **2004**, *43*, 1998.

(261) Torrent, A.; González, I.; Pla-Quintana, A.; Roglans, A.; Moreno-Mañas, M.; Parella, T.; Benet-Buchholz, J. Transition Metal-Mediated Intramolecular [2+2+2] Cycloisomerizations of Cyclic Triynes and Enediynes. *J. Org. Chem.* **2005**, *70*, 2033.

(262) Dachs, A.; Torrent, A.; Roglans, A.; Parella, T.; Osuna, S.; Solà, M. Rhodium(I)-Catalysed Intramolecular [2+2+2] Cyclotrimerisations of 15-, 20- and 25-Membered Azamacrocycles: Experimental and Theoretical Mechanistic Studies. *Chem. Eur. J.* **2009**, *15*, 5289.

(263) González, I.; Bouquillon, S.; Roglans, A.; Muzart, J. Palladium and Rhodium-Catalyzed Intramolecular [2+2+2] Cycloisomerizations in Molten Tetrabutylammonium Bromide. *Tetrahedron Lett.* **2007**, *48*, 6425.

(264) Garcia, L.; Pla-Quintana, A.; Roglans, A. Synthesis of Non-Proteinogenic Phenylalanine Derivatives by Rhodium-Catalyzed [2+2+2] Cycloaddition Reactions. *Org. Biomol. Chem.* **2009**, *7*, 5020.

(265) González, I.; Pla-Quintana, A.; Roglans, A. Rhodium N-Heterocyclic Carbene Complexes as Effective Catalysts for [2+2+2]-Cycloaddition Reactions. *Synlett* **2009**, 2844.

(266) Brun, S.; Parera, M.; Pla-Quintana, A.; Roglans, A.; León, T.; Achard, T.; Solà, J.; Verdaguer, X.; Riera, A. Chiral N-Phosphino Sulfinamide Ligands in Rhodium(I)-Catalyzed [2+2+2] Cycloaddition

Reactions. *Tetrahedron* **2010**, *66*, 9032.

(267) Tanaka, K.; Shirasaka, K. Highly Chemo- and Regioselective Intermolecular Cyclotrimerization of Alkynes Catalyzed by Cationic Rhodium(I)/Modified BINAP Complexes. *Org. Lett.* **2003**, *5*, 4697.

(268) Nishigaki, S.; Shibata, Y.; Tanaka, K. Rhodium-Catalyzed Chemo- and Regioselective Intermolecular Cross-Cyclotrimerization of Nonactivated Terminal and Internal Alkynes. *J. Org. Chem.* **2017**, *82*, 11117.

(269) Hara, H.; Hirano, M.; Tanaka, K. Liquid Enol Ethers and Acetates as Gaseous Alkyne Equivalents in Rh-Catalyzed Chemo- and Regioselective Formal Cross-Alkyne Cyclotrimerization. *Org. Lett.* **2008**, *10*, 2537.

(270) Tanaka, K.; Hara, H.; Nishida, G.; Hirano, M. Synthesis of Perfluoroalkylated Benzenes and Pyridines through Cationic Rh(I)/Modified BINAP-Catalyzed Chemo- and Regioselective [2 + 2 + 2] Cycloaddition. *Org. Lett.* **2007**, *9*, 1907.

(271) Torres, Ò.; Fernàndez, M.; Díaz-Jiménez, À.; Pla-Quintana, A.; Roglans, A.; Solà, M. Examining the Factors That Govern the Regioselectivity in Rhodium-Catalyzed Alkyne Cyclotrimerization. *Organometallics* **2019**, *38*, 2853.

(272) Miyauchi, Y.; Johmoto, K.; Yasuda, N.; Uekusa, H.; Fujii, S.; Kiguchi, M.; Ito, H.; Itami, K.; Tanaka, K. Concise Synthesis and Facile Nanotube Assembly of a Symmetrically Multifunctionalized Cycloparaphenylene. *Chem. Eur. J.* **2015**, *21*, 18900.

(273) Nishigaki, S.; Fukui, M.; Sugiyama, H.; Uekusa, H.; Kawauchi, S.; Shibata, Y.; Tanaka, K. Synthesis, Structures, and Photophysical Properties of Alternating Donor–Acceptor Cycloparaphenylenes. *Chem. Eur. J.* **2017**, *23*, 7227.

(274) Hayase, N.; Miyauchi, Y.; Aida, Y.; Sugiyama, H.; Uekusa, H.; Shibata, Y.; Tanaka, K. Synthesis of [8]Cycloparaphenylene-Octacarboxylates via Rh-Catalyzed Stepwise Cross-Alkyne Cyclotrimerization. *Org. Lett.* **2017**, *19*, 2993.

(275) Hayase, N.; Sugiyama, H.; Uekusa, H.; Shibata, Y.; Tanaka, K. Rhodium-Catalyzed Synthesis, Crystal Structures, and Photophysical Properties of [6]Cycloparaphenylene Tetracarboxylates. *Org. Lett.* **2019**, *21*, 3895.

(276) Nishigaki, S.; Shibata, Y.; Nakajima, A.; Okajima, H.; Masumoto, Y.; Osawa, T.; Muranaka, A.; Sugiyama, H.; Horikawa, A.; Uekusa, H.; et al. Synthesis of Belt- and Möbius-Shaped Cycloparaphenylenes by Rhodium-Catalyzed Alkyne Cyclotrimerization. *J. Am. Chem. Soc.* **2019**, *141*, 14955.

(277) Hayase, N.; Nogami, J.; Shibata, Y.; Tanaka, K. Synthesis of A Highly Strained Spherical Carbon Nanocage via Regioselective Alkyne Cyclotrimerization. *Angew. Chem. Int. Ed.* **2019**, *58*, 9439.

(278) Dötz, F.; Brand, J. D.; Ito, S.; Gherghel, L.; Müllen, K. Synthesis of Large Polycyclic Aromatic Hydrocarbons: Variation of Size and Periphery. *J. Am. Chem. Soc.* **2000**, *122*, 7707.

(279) Cioni, P.; Diversi, P.; Ingrosso, G.; Lucherini, A.; Ronca, P. Rhodium-Catalyzed Synthesis of Pyridines from Alkynes and Nitriles. *J. Mol. Catal.* **1987**, *40*, 337.

(280) Tanaka, K.; Suzuki, N.; Nishida, G. Cationic Rhodium(I)/Modified-BINAP Catalyzed [2+2+2] Cycloaddition of Alkynes with Nitriles. *Eur. J. Org. Chem.* **2006**, 3917.

(281) Komine, Y.; Tanaka, K. Rhodium-Catalyzed Complete Regioselective Intermolecular Cross-Cyclotrimerization of Aryl Ethynyl Ethers and Nitriles or Isocyanates at Room Temperature. *Org. Lett.* **2010**, *12*, 1312.

(282) Kashima, K.; Teraoka, K.; Uekusa, H.; Shibata, Y.; Tanaka, K. Rhodium-Catalyzed Atroposelective [2 + 2 + 2] Cycloaddition of *Ortho* -Substituted Phenyl Diynes with Nitriles: Effect of *Ortho* Substituents on Regio- and Enantioselectivity. *Org. Lett.* **2016**, *18*, 2170.

(283) Garcia, L.; Pla-Quintana, A.; Roglans, A.; Parella, T. Microwave-Enhanced Rhodium-Catalyzed [2+2+2] Cycloaddition Reactions To Afford Highly Functionalized Pyridines and Bipyridines. *Eur. J. Org. Chem.* **2010**, 3407.

(284) Wada, A.; Noguchi, K.; Hirano, M.; Tanaka, K. Enantioselective Synthesis of C_2-Symmetric Spirobipyridine Ligands through Cationic Rh(I)/Modified-BINAP- Catalyzed Double [2 + 2 + 2] Cycloaddition. *Org. Lett.* **2007**, *9*, 1295.

(285) Preetz, A.; Drexler, H.-J.; Schulz, S.; Heller, D. BINAP: Rhodium–Diolefin Complexes in Asymmetric Hydrogenation. *Tetrehedron: Asymmetry* **2010**, *21*, 1226.

(286) Osborn, J. A.; Schrock, R. R. Preparation and Properties of Some Cationic Complexes of Rhodium(I) and Rhodium(III). *J. Am. Chem. Soc.* **1971**, *93*, 2397.

(287) Thiel, I.; Horstmann, M.; Jungk, P.; Keller, S.; Fischer, F.; Drexler, H.-J.; Heller, D.; Hapke, M. Insight into the Activation of In Situ Generated Chiral Rh^I Catalysts and Their Application in Cyclotrimerizations. *Chem. Eur. J.* **2017**, *23*, 17048.

(288) Shibata, T.; Arai, Y.; Tahara, Y. Enantioselective Construction of Quaternary Carbon Centers by Catalytic [2 + 2 + 2] Cycloaddition of 1,6-Enynes and Alkynes. *Org. Lett.* **2005**, *7*, 4955.

(289) Tsuchikama, K.; Kuwata, Y.; Shibata, T. Highly Enantioselective Construction of a Chiral Spirocyclic Structure by the [2 + 2 + 2] Cycloaddition of Diynes and Exo-Methylene Cyclic Compounds. *J. Am. Chem. Soc.* **2006**, *128*, 13686.

(290) Masutomi, K.; Sakiyama, N.; Noguchi, K.; Tanaka, K. Rhodium-Catalyzed Regio-, Diastereo-, and Enantioselective [2+2+2] Cycloaddition of 1,6-Enynes with Acrylamides. *Angew. Chem. Int. Ed.* **2012**, *51*, 13031.

(291) Ueda, H.; Masutomi, K.; Shibata, Y.; Tanaka, K. Rhodium-Catalyzed Asymmetric [2 + 2 + 2] Cyclization of 1,6-Enynes with Aliphatic and Aromatic Alkenes. *Org. Lett.* **2017**, *19*, 2913.

(292) Aida, Y.; Sugiyama, H.; Uekusa, H.; Shibata, Y.; Tanaka, K. Rhodium-Catalyzed Asymmetric [2 + 2 + 2] Cycloaddition of α,ω-Diynes with Unsymmetrical 1,2-Disubstituted Alkenes. *Org. Lett.* **2016**, *18*, 2672.

(293) Aida, Y.; Shibata, Y.; Tanaka, K. Rhodium-Catalyzed Asymmetric [2 + 2 + 2] Cycloaddition of Unsymmetrical α,ω-Diynes with Acenaphthylene. *J. Org. Chem.* **2018**, *83*, 2617.

(294) Fernández, M.; Parera, M.; Parella, T.; Lledó, A.; Le Bras, J.; Muzart, J.; Pla-Quintana, A.; Roglans, A. Rhodium-Catalyzed [2+2+2] Cycloadditions of Diynes with Morita-Baylis-Hillman Adducts: A Stereoselective Entry to Densely Functionalized Cyclohexadiene Scaffolds. *Adv. Synth. Catal.* **2016**, *358*, 1848.

(295) Hara, J.; Ishida, M.; Kobayashi, M.; Noguchi, K.; Tanaka, K. Highly Chemo-, Regio-, and Enantioselective Rhodium-Catalyzed Cross-Cyclotrimerization of Two Different Alkynes with Alkenes. *Angew. Chem. Int. Ed.* **2014**, *53*, 2956.

(296) Brun, S.; Garcia, L.; González, I.; Torrent, A.; Dachs, A.; Pla-Quintana, A.; Parella, T.; Roglans, A. Fused Tetracycles with a Benzene or Cyclohexadiene Core: [2 + 2 + 2] Cycloadditions on Macrocyclic Systems. *Chem. Commun.* **2008**, 4339.

(297) Dachs, A.; Roglans, A.; Solà, M. $RhCl(PPh_3)_3$ -Catalyzed Intramolecular Cycloaddition of Enediynes: The Nature of the Tether and Substituents Controls the Reaction Mechanism. *Organometallics* **2011**, *30*, 3151.

(298) Shibata, T.; Kurokawa, H.; Kanda, K. Enantioselective Intramolecular [2+2+2] Cycloaddition of Enediynes for the Synthesis of Chiral Cyclohexa-1,3-Dienes. *J. Org. Chem.* **2007**, *72*, 6521.

(299) Dachs, A.; Pla-Quintana, A.; Parella, T.; Solà, M.; Roglans, A. Intramolecular [2+2+2] Cycloaddition Reactions of Yne-Ene-Yne and Yne-Yne-Ene Enediynes Catalysed by Rh(I): Experimental and Theoretical Mechanistic Studies. *Chem. Eur. J.* **2011**, *17*, 14493.

(300) León, T.; Parera, M.; Roglans, A.; Riera, A.; Verdaguer, X. P-Stereogenic Secondary Iminophosphorane Ligands and Their Rhodium(I) Complexes: Taking Advantage of NH/PH Tautomerism. *Angew. Chem. Int. Ed.* **2012**, *51*, 6951.

(301) Tanaka, K. Catalytic Enantioselective Synthesis of Planar Chiral Cyclophanes. *Bull. Chem. Soc. Jpn.* **2018**, *91*, 187.

(302) Tanaka, K.; Kimura, Y.; Murayama, K. Enantioselective Helicene Synthesis by Rhodium-Catalyzed [2+2+2] Cycloadditions. *Bull. Chem. Soc. Jpn.* **2015**, *88*, 375.

(303) Tanaka, K. Transition-Metal-Catalyzed Enantioselective [2+2+2] Cycloadditions for the Synthesis of

Axially Chiral Biaryls. *Chem. Asian J.* **2009**, *4*, 508.

(304) Garcia, L.; Roglans, A.; Laurent, R.; Majoral, J.-P.; Pla-Quintana, A.; Caminade, A.-M. Dendritic Phosphoramidite Ligands for Rh-Catalyzed [2+2+2] Cycloaddition Reactions: Unprecedented Enhancement of Enantiodiscrimination. *Chem. Commun.* **2012**, *48*, 9248.

(305) Huang, X.; Ma, S. Allenation of Terminal Alkynes with Aldehydes and Ketones. *Acc. Chem. Res.* **2019**, *52*, 1301.

(306) Yu, S.; Ma, S. How Easy Are the Syntheses of Allenes? *Chem. Commun.* **2011**, *47*, 5384.

(307) Yu, S.; Ma, S. Allenes in Catalytic Asymmetric Synthesis and Natural Product Syntheses. *Angew. Chem. Int. Ed.* **2012**, *51*, 3074.

(308) Ma, S. Transition-Metal-Catalyzed Reactions of Allenes. *Pure Appl. Chem.* **2006**, *78*, 197.

(309) Hoffmann-Röder, A.; Krause, N. Synthesis and Properties of Allenic Natural Products and Pharmaceuticals. *Angew. Chem. Int. Ed.* **2004**, *43*, 1196.

(310) Benson, R. E.; Lindsey, R. V. Chemistry of Allene. I. Cyclopolymerization. Synthesis and Chemistry of 1,2,4-and 1,3,5-Trimethylenecyclohexane and 1,3,5,7-Tetramethylenecycloöctane. *J. Am. Chem. Soc.* **1959**, *81*, 4247.

(311) Benson, R. E.; Lindsey, R. V. Chemistry of Allene. II. Reaction of Allene with Acetylenes. *J. Am. Chem. Soc.* **1959**, *81*, 4250.

(312) Petit, M.; Aubert, C.; Malacria, M. Cobalt(I)-Mediated [2 + 2 + 2] Cyclization of Allenediynes toward a Diastereoselective Approach to 11-Aryl Steroid Skeletons. *Org. Lett.* **2004**, *6*, 3937.

(313) Petit, M.; Aubert, C.; Malacria, M. Diastereoselective Approach to 11-Aryl Steroid Skeletons through a Cobalt(I)-Mediated [2+2+2] Cyclization of Allenediynes. *Tetrahedron* **2006**, *62*, 10582.

(314) Saito, N.; Ichimaru, T.; Sato, Y. Ruthenium-Catalyzed Intramolecular [2+2+2] Cyclization of Allene-Yne-Enes: Construction of Fused-Tricyclic Skeletons. *Chem. Asian J.* **2012**, *7*, 1521.

(315) Ohta, Y.; Yasuda, S.; Yokogawa, Y.; Kurokawa, K.; Mukai, C. Stereospecific and Stereoselective Rhodium(I)-Catalyzed Intramolecular [2+2+2] Cycloaddition of Allene-Ene-Ynes: Construction of Bicyclo[4.1.0]Heptenes. *Angew. Chem. Int. Ed.* **2015**, *54*, 1240.

(316) Haraburda, E.; Torres, Ò.; Parella, T.; Solà, M.; Pla-Quintana, A. Stereoselective Rhodium-Catalysed [2+2+2] Cycloaddition of Linear Allene-Ene/Yne-Allene Substrates: Reactivity and Theoretical Mechanistic Studies. *Chem. Eur. J.* **2014**, *20*, 5034.

(317) Haraburda, E.; Fernández, M.; Gifreu, A.; Garcia, J.; Parella, T.; Pla-Quintana, A.; Roglans, A. Chiral Induction in Intramolecular Rhodium-Catalyzed [2+2+2] Cycloadditions of Optically Active Allene-Ene/Yne-Allene Substrates. *Adv. Synth. Catal.* **2017**, *359*, 506.

(318) Cassú, D.; Parella, T.; Solà, M.; Pla-Quintana, A.; Roglans, A. Rhodium-Catalyzed [2+2+2] Cycloaddition Reactions of Linear Allene-Ene-Ynes to Afford Fused Tricyclic Scaffolds: Insights into the Mechanism. *Chem. Eur. J.* **2017**, *23*, 14889.

(319) Haraburda, E.; Lledó, A.; Roglans, A.; Pla-Quintana, A. Dehydrogenative [2 + 2 + 2] Cycloaddition of Cyano-Yne-Allene Substrates: Convenient Access to 2,6-Naphthyridine Scaffolds. *Org. Lett.* **2015**, *17*, 2882.

(320) Brusoe, A. T.; Edwankar, R. V.; Alexanian, E. J. Enantioselective Intermolecular [2+2+2] Cycloadditions of Ene–Allenes with Allenoates. *Org. Lett.* **2012**, *14*, 6096.

(321) Noucti, N. N.; Alexanian, E. J. Stereoselective Nickel-Catalyzed [2+2+2] Cycloadditions and Alkenylative Cyclizations of Ene-Allenes and Alkenes. *Angew. Chem. Int. Ed.* **2013**, *52*, 8424.

(322) Ma, S.; Lu, P.; Lu, L.; Hou, H.; Wei, J.; He, Q.; Gu, Z.; Jiang, X.; Jin, X. What Can a Metal Catalyst Do with Allenes? One-Step Formation of Steroid Scaffolds from Readily Available Starting Materials. *Angew. Chem. Int. Ed.* **2005**, *117*, 5409.

(323) Ma, S.; Lu, L. Rh(I)-Catalyzed Bimolecular Cyclization between Two Different 1,5-Bisallenes: A Combinatorial One-Step Approach to Heterosteroids and Mechanistic Implications. *Chem. Asian J.* **2007**, *2*, 199.

(324) Lu, P.; Ma, S. Rh-Catalyzed Triple Allene Approach to Bicyclo[4.4.0]Decene Derivatives and Its Application for the Stepwise Synthesis of Steroid-like Tetracyclic Skeletons. *Org. Lett.* **2007**, *9*, 5319.

(325) Shu, W.; Jia, G.; Ma, S. Palladium-Catalyzed Three-Component Cascade Cyclization Reaction of Bisallenes with Propargylic Carbonates and Organoboronic Acids: Efficient Construction of Cis-Fused Bicyelo[4.3.0]Nonenes. *Angew. Chem. Int. Ed.* **2009**, *48*, 2788.

(326) Chen, G.; Jiang, X.; Fu, C.; Ma, S. The Diversified Reactivities of 1,5-Bisallenes. *Chem. Lett.* **2010**, *39*, 78.

(327) Alcaide, B.; Almendros, P.; Aragoncillo, C. Cyclization Reactions of Bis(Allenes) for the Synthesis of Polycarbo(Hetero)Cycles. *Chem. Soc. Rev.* **2014**, *43*, 3106.

(328) Jiang, X.; Cheng, X.; Ma, S. Controllable [2+2] Cycloadditions of 1,5-Bisallenyl-Substituted Compounds. *Angew. Chem. Int. Ed.* **2006**, *45*, 8009.

(329) Lim, Y.-N.; Kim, H.-T.; Yoon, H.-S.; Jang, H.-Y. Regio- and Stereoselective Reductive Cyclization of 1,5-Bisallenes under Hydrogenation Conditions. *Bull. Korean Chem. Soc.* **2011**, *32*, 3117.

(330) Kim, S. M.; Park, J. H.; Kang, Y. K.; Chung, Y. K. N-Heterocyclic Carbene Gold(I) Catalyzed Transformation of N-Tethered 1,5-Bisallenes to 6,7-Dimethylene-3-Azabicyclo[3.1.1]Heptanes. *Angew. Chem. Int. Ed.* **2009**, *48*, 4532.

(331) Lu, P.; Ma, S. Observation of New Cycloisomerization Pattern of 1,5-Bisallenes. Catalyst and

Substituent Effects. *Org. Lett.* **2007**, *9*, 2095.

(332) Kawamura, T.; Inagaki, F.; Narita, S.; Takahashi, Y.; Hirata, S.; Kitagaki, S.; Mukai, C. Rhodium(I)-Catalyzed Intramolecular Carbonylative [2+2+1] Cycloadditions and Cycloisomerizations of Bis(Sulfonylallene)s. *Chem. Eur. J.* **2010**, *16*, 5173.

(333) Inagaki, F.; Narita, S.; Hasegawa, T.; Kitagaki, S.; Mukai, C. Rhodium(I)-Catalyzed Intramolecular Carbonylative [2+2+1] Cycloaddition of Bis(Allene)s: Bicyclo[6.3.0]Undecadienones and Bicyclo[5.3.0]Decadienones. *Angew. Chem. Int. Ed.* **2009**, *48*, 2007.

(334) Liou, K.-F.; Cheng, C.-H. Cyclotrimerization of Alkynes with [60]Fullerene in the Presence of Tricyclohexylphosphine. *J. Chem. Soc. Chem. Commun.* **1995**, 1603.

(335) Yu, R. T.; Rovis, T. Enantioselective Rhodium-Catalyzed [2+2+2] Cycloaddition of Alkenyl Isocyanates and Terminal Alkynes: Application to the Total Synthesis of (+)-Lasubine II. *J. Am. Chem. Soc.* **2006**, *128*, 12370.

(336) Alvarez, S.; Medina, S.; Domínguez, G.; Pérez-Castells, J. [2+2+2] Cyclotrimerization of Alkynes and Isocyanates/Isothiocyanates Catalyzed by Ruthenium–Alkylidene Complexes. *J. Org. Chem.* **2013**, *78*, 9995.

(337) Ishii, M.; Mori, F.; Tanaka, K. Rhodium-Catalyzed [2+2+2] Cycloaddition of Diynes with Carbodiimides and Carbon Dioxide under Ambient Conditions. *Chem. Eur. J.* **2014**, *20*, 2169.

(338) Yamamoto, Y.; Takagishi, H.; Itoh, K. Ruthenium-Catalyzed Cycloaddition of 1,6-Diynes with Isothiocyanates and Carbon Disulfide: First Transition-Metal Catalyzed [2+2 +2] Cocyclotrimerization Involving C=S Double Bond. *J. Am. Chem. Soc.* **2002**, *124*, 28.

(339) Ishida, M.; Shibata, Y.; Noguchi, K.; Tanaka, K. Rhodium-Catalyzed Asymmetric [2+2+2] Cyclization of 1,6-Enynes and Aldehydes. *Chem. Eur. J.* **2011**, *17*, 12578.

(340) Nakajima, K.; Takata, S.; Sakata, K.; Nishibayashi, Y. Synthesis of Phosphabenzenes by an Iron-Catalyzed [2+2+2] Cycloaddition Reaction of Diynes with Phosphaalkynes. *Angew. Chem. Int. Ed.* **2015**, *54*, 7597.

(341) Hoshimoto, Y.; Ohata, T.; Ohashi, M.; Ogoshi, S. Nickel-Catalyzed Synthesis of *N* -Aryl-1,2-Dihydropyridines by [2+2+2] Cycloaddition of Imines with Alkynes through T-Shaped 14-Electron Aza-Nickelacycle Key Intermediates. *Chem. Eur. J.* **2014**, *20*, 4105.

(342) Schäfer, M.; Beattie, N. A.; Geetharani, K.; Schäfer, J.; Ewing, W. C.; Krahfuß, M.; Hörl, C.; Dewhurst, R. D.; Macgregor, S. A.; Lambert, C.; Braunschweig, H. Synthesis of Functionalized 1,4-Azaborinines by the Cyclization of Di- *Tert* -Butyliminoborane and Alkynes. *J. Am. Chem. Soc.* **2016**, *138*, 8212.

(343) Tsang, A. S.-K.; Sanhueza, I. A.; Schoenebeck, F. Combining Experimental and Computational Studies to Understand and Predict Reactivities of Relevance to Homogeneous Catalysis. *Chem. Eur. J.* **2014**,

20, 16432.

(344) Cheng, G.-J.; Zhang, X.; Chung, L. W.; Xu, L.; Wu, Y.-D. Computational Organic Chemistry: Bridging Theory and Experiment in Establishing the Mechanisms of Chemical Reactions. *J. Am. Chem. Soc.* **2015**, *137*, 1706.

(345) Arrieta, A.; de la Torre, M.; de Cózar, A.; Sierra, M.; Cossío, F. Computational Chemistry; A Useful Tool for the Chemical Synthesis of Complex Molecules, Heterocycles and Catalysts. *Synlett* **2013**, *24*, 535.

(346) Szabo, A.; Ostlund, N. S. *Modern Quantum Chemistry : Introduction to Advanced Electronic Structure Theory*; Dover Publications, 1996.

(347) Levine, I. N. *Quantum Chemistry*, PHI Learning, 2014.

(348) Jensen, F. *Introduction to Computational Chemistry*; John Wiley & Sons, 2007.

(349) Cramer, C. J. *Essentials of Computational Chemistry : Theories and Models*; Wiley, 2004.

(350) Koch, W.; Holthausen, M. C. *A Chemist's Guide to Density Functional Theory*; Wiley, 2001.

(351) Foresman, J. B.; Frisch, Ae. *Exploring Chemistry with Electronic Structure Methods,* Gaussian Inc., 2015.

(352) Bachrach, S. M. *Computational Organic Chemistry*; Wiley, 2007.

(353) Andrés Bort, J.; Bertran Rusca, J.; *Theoretical and Computational Chemistry : Foundations, Methods and Techniques*; Publicacions de la Universitat Jaume I, 2007.

(354) Gaussian 09, Revision E.01, Frisch, M. J.; Trucks, G. W.; Schlegel, H. B.; Scuseria, G. E.; Robb, M. A.; Cheeseman, J. R.; Scalmani, G.; Barone, V.; Mennucci, B.; Petersson, G. A.; Nakatsuji, H.; Caricato, M.; Li, X.; Hratchian, H. P.; Izmaylov, A. F.; Bloino, J.; Zheng, G.; Sonnenberg, J. L.; Hada, M.; Ehara, M.; Toyota, K.; Fukuda, R.; Hasegawa, J.; Ishida, M.; Nakajima, T.; Honda, Y.; Kitao, O.; Nakai, H.; Vreven, T.; Montgomery, J. A., Jr.; Peralta, J. E.; Ogliaro, F.; Bearpark, M.; Heyd, J. J.; Brothers, E.; Kudin, K. N.; Staroverov, V. N.; Kobayashi, R.; Normand, J.; Raghavachari, K.; Rendell, A.; Burant, J. C.; Iyengar, S. S.; Tomasi, J.; Cossi, M.; Rega, N.; Millam, J. M.; Klene, M.; Knox, J. E.; Cross, J. B.; Bakken, V.; Adamo, C.; Jaramillo, J.; Gomperts, R.; Stratmann, R. E.; Yazyev, O.; Austin, A. J.; Cammi, R.; Pomelli, C.; Ochterski, J. W.; Martin, R. L.; Morokuma, K.; Zakrzewski, V. G.; Voth, G. A.; Salvador, P.; Dannenberg, J. J.; Dapprich, S.; Daniels, A. D.; Farkas, Ö.; Foresman, J. B.; Ortiz, J. V.; Cioslowski, J.; Fox, D. J. Gaussian, Inc., Wallingford CT, 2009.

(355) Hohenberg, P.; Kohn, W. Inhomogeneous Electron Gas. *Phys. Rev.* **1964**, *136*, B864.

(356) Kohn, W.; Sham, L. J. Self-Consistent Equations Including Exchange and Correlation Effects. *Phys. Rev.* **1965**, *140*, 1133.

(357) Slater, J. C. A Simplification of the Hartree-Fock Method. *Phys. Rev.* **1951**, *81*, 385.

(358) Vosko, S. H.; Wilk, L.; Nusair, M. Accurate Spin-Dependent Electron Liquid Correlation Energies for Local Spin Density Calculations: A Critical Analysis. *Can. J. Phys.* **1980**, *58*, 1200.

(359) Becke, A. D. Density-Functional Exchange-Energy Approximation with Correct Asymptotic Behavior. *Phys. Rev. A* **1988**, *38*, 3098.

(360) Miehlich, B.; Savin, A.; Stoll, H.; Preuss, H. Results Obtained with the Correlation Energy Density Functionals of Becke and Lee, Yang and Parr. *Chem. Phys. Lett.* **1989**, *157*, 200.

(361) Lee, C.; Yang, W.; Parr, R. G. Development of the Colle-Salvetti Correlation-Energy Formula into a Functional of the Electron Density. *Phys. Rev. B* **1988**, *37*, 785.

(362) Perdew, J. P.; Chevary, J. A.; Vosko, S. H.; Jackson, K. A.; Pederson, M. R.; Singh, D. J.; Fiolhais, C. Atoms, Molecules, Solids, and Surfaces: Applications of the Generalized Gradient Approximation for Exchange and Correlation. *Phys. Rev. B* **1992**, *46*, 6671.

(363) Zhao, Y.; Truhlar, D. G. A New Local Density Functional for Main-Group Thermochemistry, Transition Metal Bonding, Thermochemical Kinetics, and Noncovalent Interactions. *J. Chem. Phys.* **2006**, *125*, 194101.

(364) Becke, A. D. Density-functional Thermochemistry. III. The Role of Exact Exchange. *J. Chem. Phys.* **1993**, *98*, 5648.

(365) Mardirossian, N.; Head-Gordon, M. Thirty Years of Density Functional Theory in Computational Chemistry: An Overview and Extensive Assessment of 200 Density Functionals. *Mol. Phys.* **2017**, *115*, 2315.

(366) Perdew, J. P.; Schmidt, K. Jacob's Ladder of Density Functional Approximations for the Exchange-Correlation Energy. *AIP Conference Proceedings* **2001**; *577*, 1.

(367) Schlegel, H. B. Geometry Optimization. *WIRES Comput. Mol. Sci.* **2011**, *1*, 790.

(368) Li, X.; Frisch, M. J. Energy-Represented Direct Inversion in the Iterative Subspace within a Hybrid Geometry Optimization Method. *J. Chem. Theory Comput.* **2006**, *2*, 835.

(369) Bofill, J. M. Updated Hessian Matrix and the Restricted Step Method for Locating Transition Structures. *J. Comput. Chem.* **1994**, *15*, 1.

(370) Bofill, J. M. Remarks on the Updated Hessian Matrix Methods. *Int. J. Quantum Chem.* **2003**, *94*, 324.

(371) Halgren, T. A.; Lipscomb, W. N. The Synchronous-Transit Method for Determining Reaction Pathways and Locating Molecular Transition States. *Chem. Phys. Lett.* **1977**, *49*, 225.

(372) Fukui, K. The Path of Chemical Reactions - the IRC Approach. *Acc. Chem. Res.* **1981**, *14*, 363.

(373) Hratchian, H. P.; Schlegel, H. B. Using Hessian Updating To Increase the Efficiency of a Hessian Based Predictor-Corrector Reaction Path Following Method. *J. Chem. Theory Comput.* **2005**, *1*, 61.

(374) Hratchian, H. P.; Schlegel, H. B. Accurate Reaction Paths Using a Hessian Based Predictor–Corrector Integrator. *J. Chem. Phys.* **2004**, *120*, 9918.

(375) Atkins, P.; De Paula, J. *The Elements of Physical Chemistry*, 3rd ed.; Oxford University Press: Oxford, 2006.

(376) Joseph W. Ochterski. Thermochemistry in Gaussian https://gaussian.com/thermo/ (accessed Sep 13, 2019).

(377) Kozuch, S.; Shaik, S. How to Conceptualize Catalytic Cycles? The Energetic Span Model. *Acc. Chem. Res.* **2011**, *44*, 101.

(378) Cundari, T. R.; Benson, M. T.; Lutz, M. L.; Sommerer, S. O. Effective Core Potential Approaches to the Chemistry of the Heavier Elements; John Wiley & Sons, Ltd, 2007; pp 145–202.

(379) Mennucci, B. Polarizable Continuum Model. *WIRES Comput. Mol. Sci.* **2012**, *2*, 386.

(380) Marenich, A. V.; Cramer, C. J.; Truhlar, D. G. Universal Solvation Model Based on Solute Electron Density and on a Continuum Model of the Solvent Defined by the Bulk Dielectric Constant and Atomic Surface Tensions. *J. Phys. Chem. B* **2009**, *113*, 6378.

(381) Grimme, S. Density Functional Theory with London Dispersion Corrections. *WIRES Comput. Mol. Sci.* **2011**, *1*, 211.

(382) Goerigk, L.; Kruse, H.; Grimme, S. Benchmarking Density Functional Methods against the S66 and S66x8 Datasets for Non-Covalent Interactions. *ChemPhysChem* **2011**, *12*, 3421.

(383) Luo, S.; Zhao, Y.; Truhlar, D. G. Validation of Electronic Structure Methods for Isomerization Reactions of Large Organic Molecules. *Phys. Chem. Chem. Phys.* **2011**, *13*, 13683.

(384) Goerigk, L.; Grimme, S. A Thorough Benchmark of Density Functional Methods for General Main Group Thermochemistry, Kinetics, and Noncovalent Interactions. *Phys. Chem. Chem. Phys.* **2011**, *13*, 6670.

(385) Grimme, S. Supramolecular Binding Thermodynamics by Dispersion-Corrected Density Functional Theory. *Chem. Eur. J.* **2012**, *18*, 9955.

(386) Grimme, S.; Hansen, A.; Brandenburg, J. G.; Bannwarth, C. Dispersion-Corrected Mean-Field Electronic Structure Methods. *Chem. Rev.* **2016**, *116*, 5105.

(387) Goerigk, L.; Hansen, A.; Bauer, C.; Ehrlich, S.; Najibi, A.; Grimme, S. A Look at the Density Functional Theory Zoo with the Advanced GMTKN55 Database for General Main Group Thermochemistry, Kinetics and Noncovalent Interactions. *Phys. Chem. Chem. Phys.* **2017**, *19*, 32184.

(388) Grimme, S.; Antony, J.; Ehrlich, S.; Krieg, H. A Consistent and Accurate *Ab Initio* Parametrization of Density Functional Dispersion Correction (DFT-D) for the 94 Elements H-Pu. *J. Chem. Phys.* **2010**, *132*, 154104.

(389) Grimme, S.; Ehrlich, S.; Goerigk, L. Effect of the Damping Function in Dispersion Corrected Density Functional Theory. *J. Comput. Chem.* **2011**, *32*, 1456.

(390) Osuna, S.; Swart, M.; Solà, M. Dispersion Corrections Essential for the Study of Chemical Reactivity in Fullerenes. *J. Phys. Chem. A* **2011**, *115,* 3491.

(391) Fernández, I.; Bickelhaupt, F. M. The Activation Strain Model and Molecular Orbital Theory: Understanding and Designing Chemical Reactions. *Chem. Soc. Rev.* **2014**, *43*, 4953.

(392) Hopffgarten, M. von; Frenking, G. Energy Decomposition Analysis. *WIRES Comput. Mol. Sci.* **2012**, *2*, 43.

(393) Frenking, G.; Matthias Bickelhaupt, F. The EDA Perspective of Chemical Bonding. In *The Chemical Bond*; Wiley, 2014.

(394) Zhao, Y.; Truhlar, D. G. The M06 Suite of Density Functionals for Main Group Thermochemistry, Thermochemical Kinetics, Noncovalent Interactions, Excited States, and Transition Elements: Two New Functionals and Systematic Testing of Four M06-Class Functionals and 12 Other Functionals. *Theor. Chem. Acc.* **2008**, *120*, 215.

(395) Dunning, T. H. Gaussian Basis Sets for Use in Correlated Molecular Calculations. I. The Atoms Boron through Neon and Hydrogen. *J. Chem. Phys.* **1989**, *90*, 1007.

(396) Frisch, M. J.; Pople, J. A.; Binkley, J. S. Self-consistent Molecular Orbital Methods 25. Supplementary Functions for Gaussian Basis Sets. *J. Chem. Phys.* **1984**, *80*, 3265.

(397) Peterson, K. A.; Figgen, D.; Dolg, M.; Stoll, H. Energy-Consistent Relativistic Pseudopotentials and Correlation Consistent Basis Sets for the 4d Elements Y–Pd. *J. Chem. Phys.* **2007**, *126*, 124101.

(398) te Velde, G.; Bickelhaupt, F. M.; Baerends, E. J.; Fonseca Guerra, C.; van Gisbergen, S. J. A.; Snijders, J. G.; Ziegler, T. Chemistry with ADF. *J. Comput. Chem.* **2001**, *22*, 931.

(399) Koga, N.; Jin, S. Q.; Morokuma, K. Rearrangement through Berry Pseudorotation and Olefin Insertion of D8 Five-Coordinate Rh(H)(C_2H_4)$(CO)_2$(PH_3). An Ab Initio MO Study. *J. Am. Chem. Soc.* **1988***, 110,* 3417.

(400) Brown, J. M.; Kent, A. G. Structural Characterisation in Solution of Intermediates in Rhodium-Catalysed Hydroformylation and Their Interconversion Pathways. *J. Chem. Soc. Perkin Trans. 2* **1987**, 1597.

(401) Tian, C.; Castro, E.; Betancourt-Solis, G.; Nan, Z.; Fernandez-Delgado, O.; Jankuru, S.; Echegoyen, L. Fullerene Derivative with a Branched Alkyl Chain Exhibits Enhanced Charge Extraction and Stability

in Inverted Planar Perovskite Solar Cells. *New J. Chem.* **2018**, *42*, 2896.

(402) Khadka, D. B.; Shirai, Y.; Yanagida, M.; Noda, T.; Miyano, K. Tailoring the Open-Circuit Voltage Deficit of Wide-Band-Gap Perovskite Solar Cells Using Alkyl Chain-Substituted Fullerene Derivatives. *ACS Appl. Mater. Interfaces* **2018**, *10*, 22074.

(403) Kantorowski, E. J.; Kurth, M. J. Expansion to Seven-Membered Rings. *Tetrahedron* **2000**, *56*, 4317.

(404) Riley, D. L.; van Otterlo, W. A. L. Oxepines and Azepines. In *Heterocycles in Natural Product Synthesis*; Wiley-VCH Verlag GmbH & Co. KGaA: Weinheim, Germany, 2011; pp 535–568.

(405) Nguyen, T.; Hartmann, J.; Enders, D. Recent Synthetic Strategies to Access Seven-Membered Carbocycles in Natural Product Synthesis. *Synthesis* **2013**, *45*, 845.

(406) Meyer, A. G.; Bissember, A. C.; Hyland, C. J. T.; Williams, C. C.; Szabo, M.; Abel, S.-A. G.; Bird, M. J.; Hyland, I. K.; Pham, H. Seven-Membered Rings. *Prog. Heterocycl. Chem.* **2018**, *30*, 493.

(407) Liu, J. H.; Steigel, A.; Reininger, E.; Bauer, R. Two New Prenylated 3-Benzoxepin Derivatives as Cyclooxygenase Inhibitors from *Perilla frutescens* var. *acuta*. *J. Nat. Prod.* **2000**, *63*, 403.

(408) Nayak, M.; Kang, Y. K.; Kim, I. Altering the Cyclization Modes: Temperature-Dependent Intramolecular 7- *Endo-Dig* vs 6- *Endo-Dig* Electrophilic Ring Closures. *Org. Lett.* **2017**, *19*, 1474.

(409) Adamovskyi, M. I.; Ryabukhin, S. V.; Sibgatulin, D. A.; Rusanov, E.; Grygorenko, O. O. Beyond the Five and Six: Evaluation of Seven-Membered Cyclic Anhydrides in the Castagnoli–Cushman Reaction. *Org. Lett.* **2017**, *19*, 130.

(410) Jiang, B.; Liu, J.-X.; Wei, Y.; Shi, M. Nickel-Catalyzed Synthesis of Benzo[*b*]Naphtho[1,2-*d*]Azepine via Intramolecular Radical Tandem Cyclization of Alkyl Bromide-Tethered Alkylidenecyclopropanes. *Org. Lett.* **2018**, *20*, 6229.

(411) El Bakouri, O.; Garcia-Borràs, M.; Girón, R. M.; Filippone, S.; Martín, N.; Solà, M. On the Regioselectivity of the Diels–Alder Cycloaddition to C_{60} in High Spin States. *Phys. Chem. Chem. Phys.* **2018**, *20*, 11577.

(412) Sylvester, K. T.; Chirik, P. J. Iron-Catalyzed, Hydrogen-Mediated Reductive Cyclization of 1,6-Enynes and Diynes: Evidence for Bis(Imino)Pyridine Ligand Participation. *J. Am. Chem. Soc.* **2009**, *131*, 8772.

(413) Richard, V.; Mé, A.; Ipouck, L.; Mé, D. S.; Gaillard, S.; Whitby, R. J.; Witulski, B.; Renaud, J.-L. Iron(II)-Catalysed [2+2+2] Cycloaddition for Pyridine Ring Construction. *Chem. Commun* **2014**, *50*, 593.

(414) Bednářová, E.; Colacino, E.; Lamaty, F.; Kotora, M. A Ruthenium Complex-Catalyzed Cyclotrimerization of Halodiynes with Nitriles. Synthesis of 2- and 3-Halopyridines. *Adv. Synth. Catal.* **2016**, *358*, 1916.

(415) Hashmi, A. S. K.; Häffner, T.; Rudolph, M.; Rominger, F. Gold Catalysis: Domino Reaction of En-Diynes to Highly Substituted Phenols. *Chem. Eur. J.* **2011**, *17*, 8195.

(416) Kang, S.-K.; Baik, T.-G.; Kulak, A. N.; Ha, Y.-H.; Lim, Y.; Park, J. Palladium-Catalyzed Carbocyclization/Silastannylation and Distannylation of Bis(Allenes). *J. Am. Chem. Soc.* **2000**, *122*, 11529.

Supplementary material

Supplementary digital material

The material listed below is attached to this thesis as digital supplementary material in *.pdf* format:

- A digital copy of this manuscript.
  Files: ***taar1de11.pdf***
- A digital copy of the research article and supporting information corresponding to chapter 3.
  Files: ***taar2de11.pdf*** and ***taar3de11.pdf***
- A digital copy of the research article and supporting information corresponding to chapter 4.
  Files: ***taar4de11.pdf*** and ***taar5de11.pdf***
- A digital copy of the research article and supporting information corresponding to chapter 5.
  Files: ***taar6de11.pdf*** and ***taar7de11.pdf***
- A digital copy of the research article and supporting information corresponding to chapter 6.
  Files: ***taar8de11.pdf*** and ***taar9de11.pdf***
- A digital copy of the research article and supporting information corresponding to chapter 7.
  Files: ***taar10de11.pdf*** and ***taar11de11.pdf***

Selected output files corresponding to computational calculations in chapters 3, 4, 6 and 7 are provided through the following links to the *ioChem-BD* quantum chemistry repository:

- **Chapter 3:**
  https://iochem.udg.edu:8443/browse/handle/100/854
- **Chapter 4:**
  https://iochem.udg.edu:8443/browse/handle/100/1060
- **Chapter 6:**
  https://iochem.udg.edu:8443/browse/handle/100/660
- **Chapter 7:**
  https://iochem.udg.edu:8443/browse/handle/100/816

Supplementary material for chapter 3

Figure S1. M06L-D3/cc-pVTZ//B3LYP/cc-pVDZ Gibbs energy profile for the C_{60} acetylene [2+2+2] cycloaddition catalyzed by Wilkinson's complex. Path A involving [6,6] bond. Electronic energies (Δ*E*) shown in parentheses. Blue: 1 PPh_3; Red = 0 PPh_3. Structures shown for the lowest energy path.

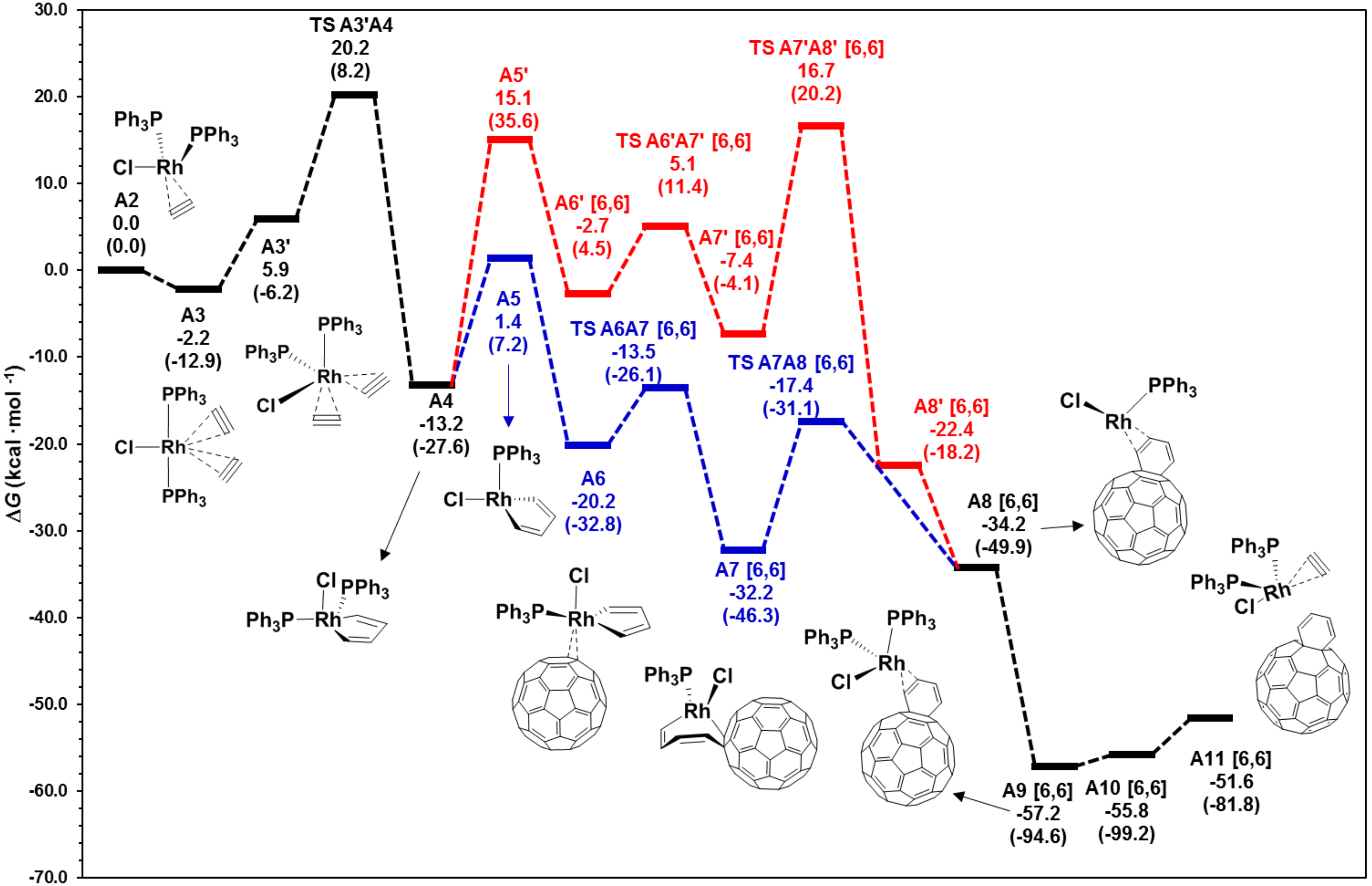

Figure S2. M06L-D3/cc-pVTZ//B3LYP/cc-pVDZ Gibbs energy profile for the C_{60} acetylene [2+2+2] cycloaddition catalyzed by Wilkinson's complex. Path A involving [5,6] bond. Electronic energies (Δ*E*) shown in parentheses. Blue: 1 PPh_3; Red = 0 PPh_3. Structures shown for the lowest energy path.

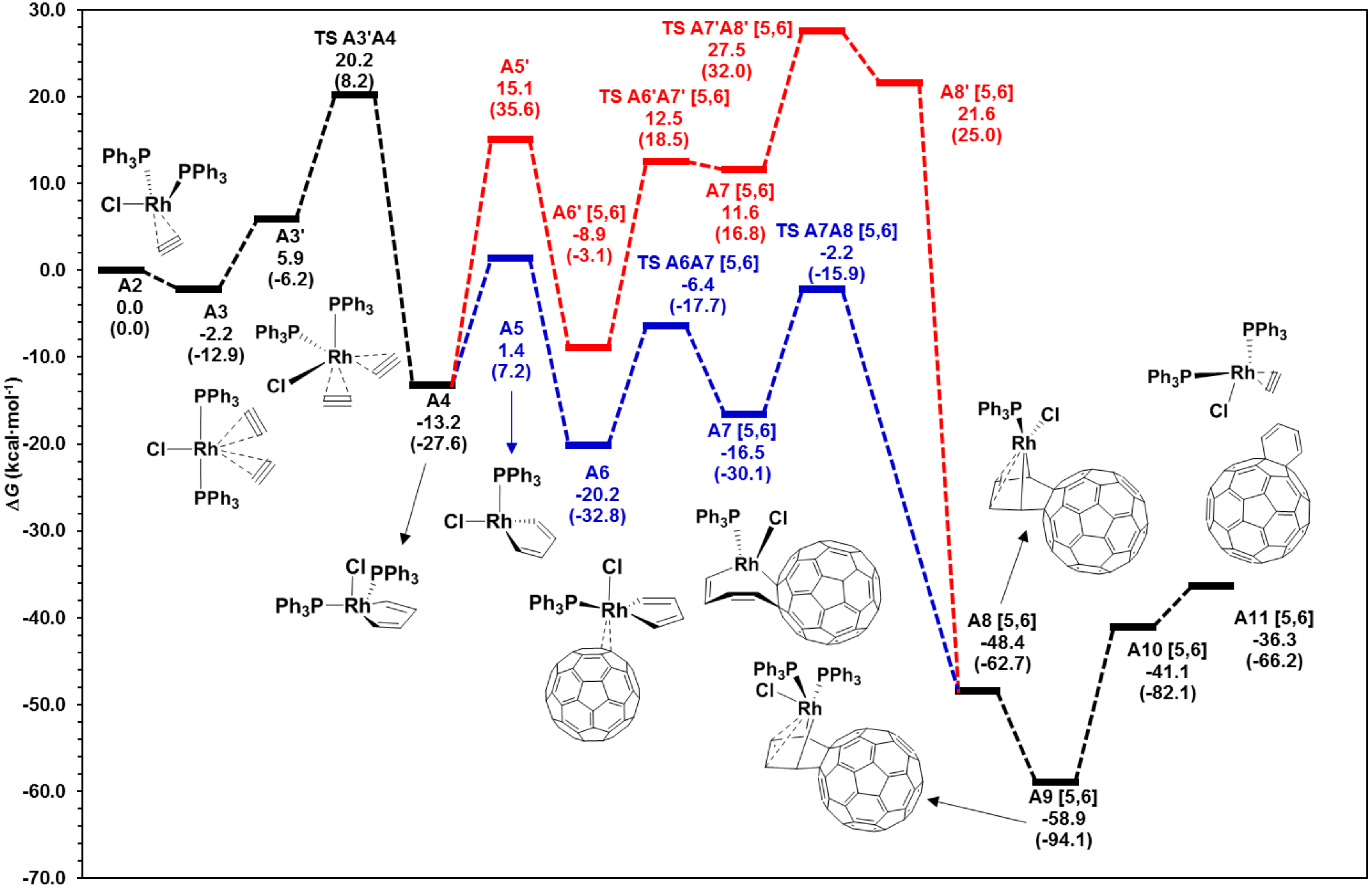

Figure S3. M06L-D3/cc-pVTZ//B3LYP/cc-pVDZ Gibbs energy profile for the C_{60} acetylene [2+2+2] cycloaddition catalyzed by Wilkinson's complex. Path B involving [6,6] bond. Electronic energies (Δ*E*) shown in parentheses. Green = 2 PPh_3; Blue: 1 PPh_3; Red = 0 PPh_3. Structures shown for the lowest energy path.

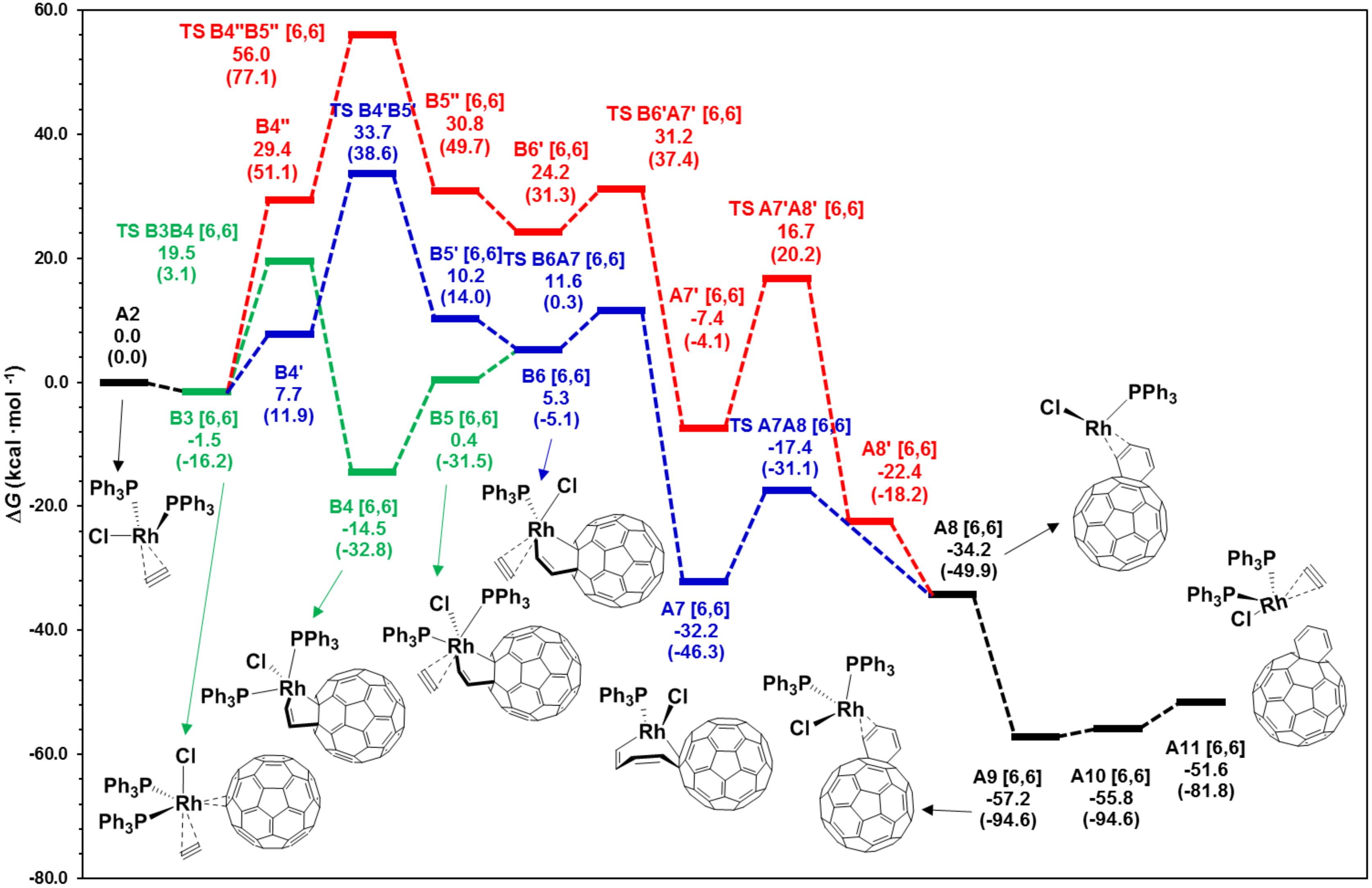

Figure S4. M06L-D3/cc-pVTZ//B3LYP/cc-pVDZ Gibbs energy profile for the C_{60} acetylene [2+2+2] cycloaddition catalyzed by Wilkinson's complex. Path B involving [5,6] bond. Electronic energies (Δ*E*) shown in parentheses. Green = 2 PPh_3 Blue: 1 PPh_3; Red = 0 PPh_3. Structures shown for the lowest energy path.

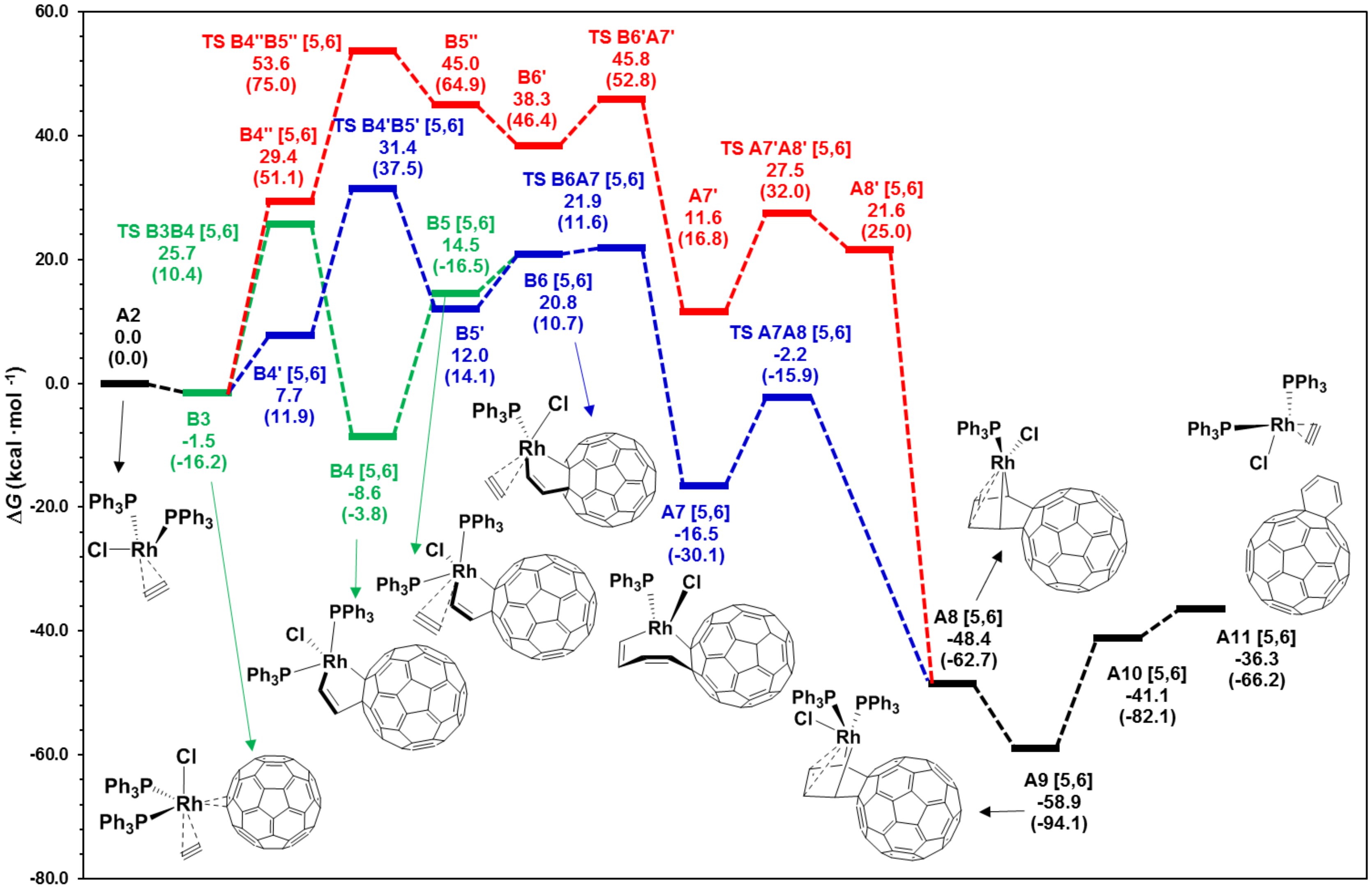

Figure S5. M06L-D3/cc-pVTZ//B3LYP/cc-pVDZ Gibbs energy profile for the C_{60} acetylene [2+2+2] cycloaddition catalyzed by Wilkinson's complex. Path C involving [6,6] bond. Electronic energies (Δ*E*) shown in parentheses. Blue: 1 PPh_3; Red = 0 PPh_3. Structures shown for the lowest energy path.

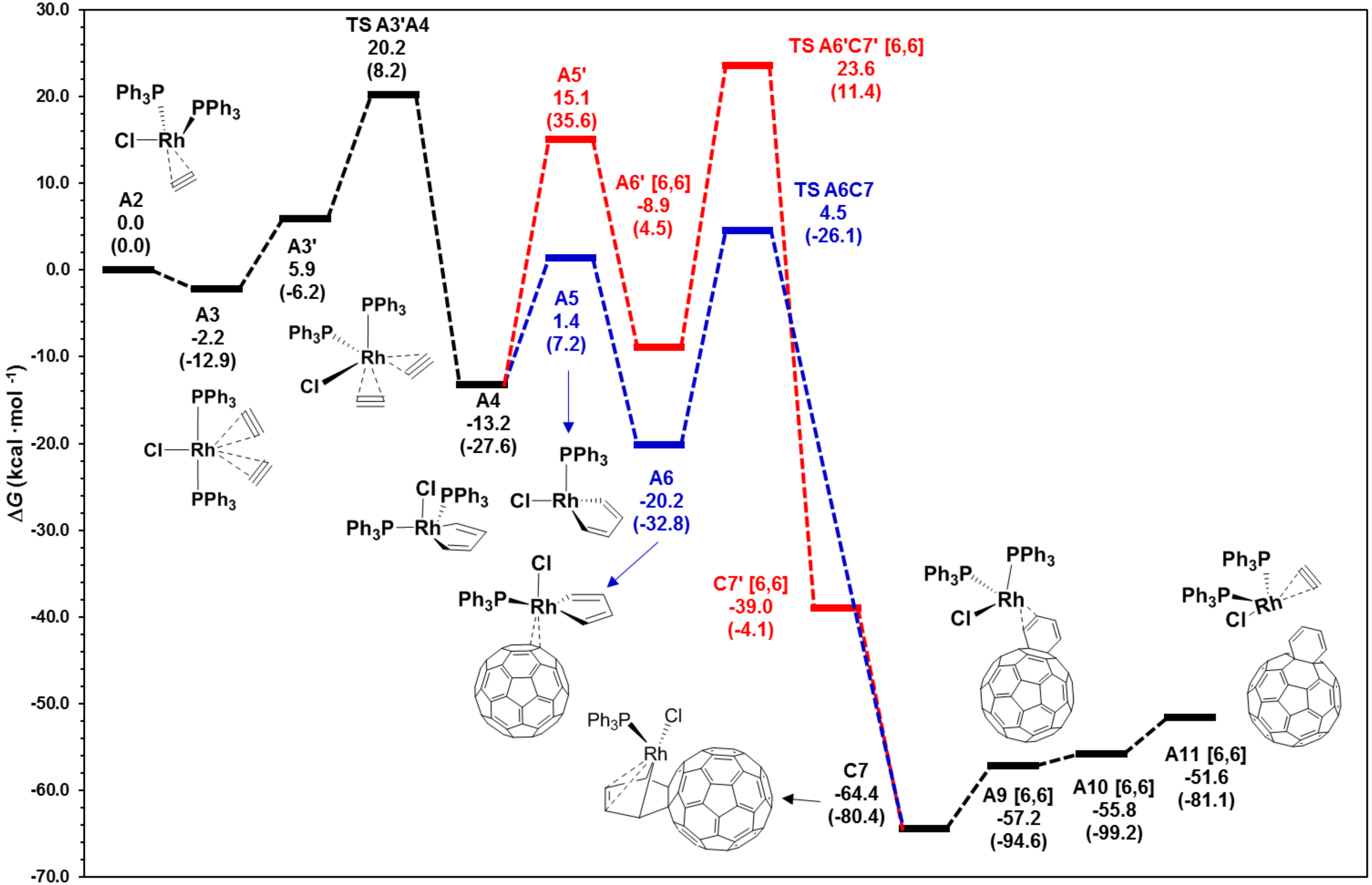

Figure S6. M06L-D3/cc-pVTZ//B3LYP/cc-pVDZ Gibbs energy profile for the C_{60} acetylene [2+2+2] cycloaddition catalyzed by Wilkinson's complex. Path C involving [5,6] bond. Electronic energies (Δ*E*) shown in parentheses. Blue: 1 PPh_3; Red = 0 PPh_3. Structures shown for the lowest energy path.

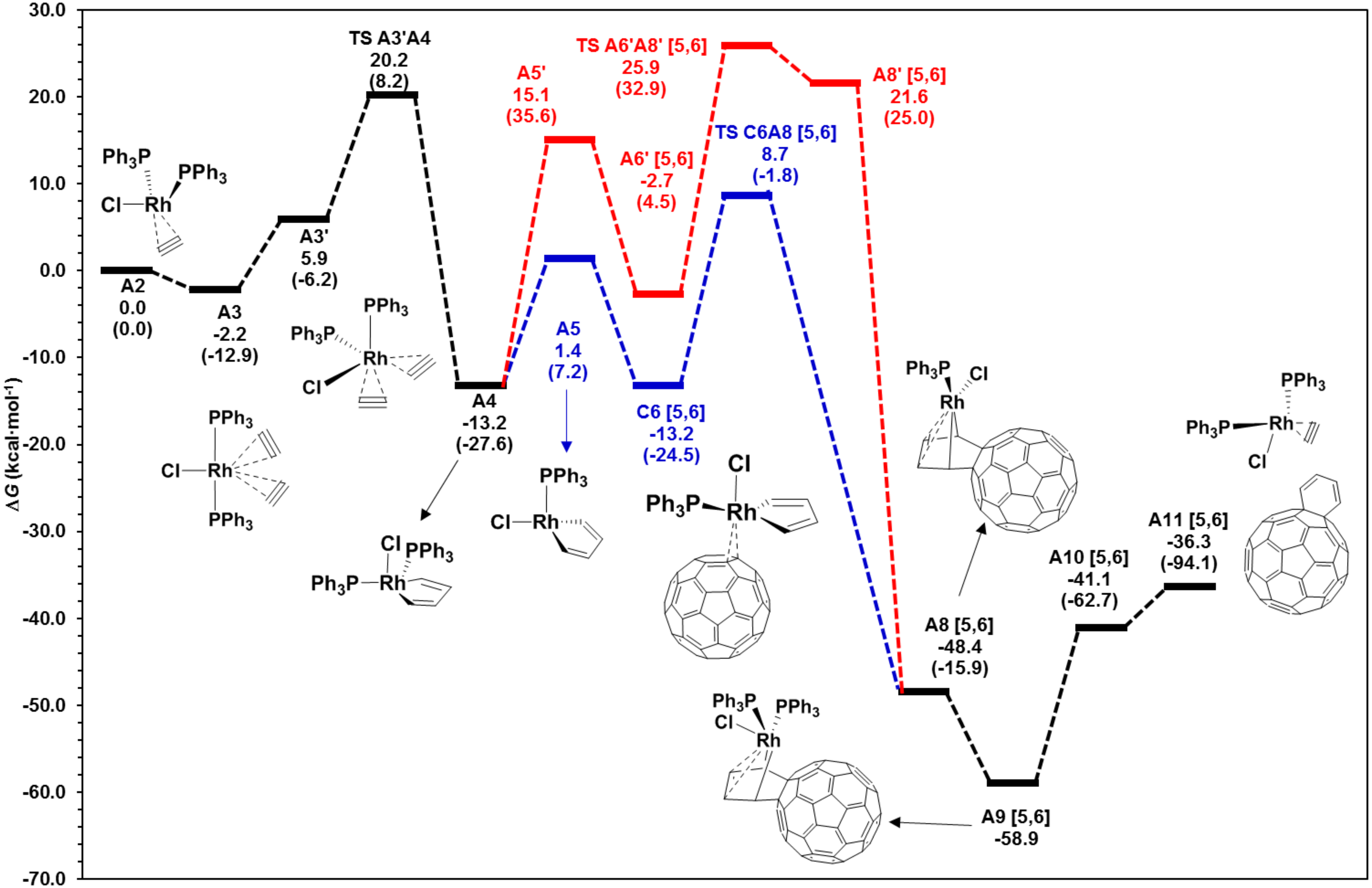

Figure S7. M06L-D3/cc-pVTZ//B3LYP/cc-pVDZ Gibbs energy profile for the acetylene cyclotrimerization catalyzed by Wilkinson's complex. Electronic energies (Δ*E*) shown in parentheses. Green = 2 PPh_3 Blue: 1 PPh_3; Red = 0 PPh_3. Structures shown for the lowest energy path.

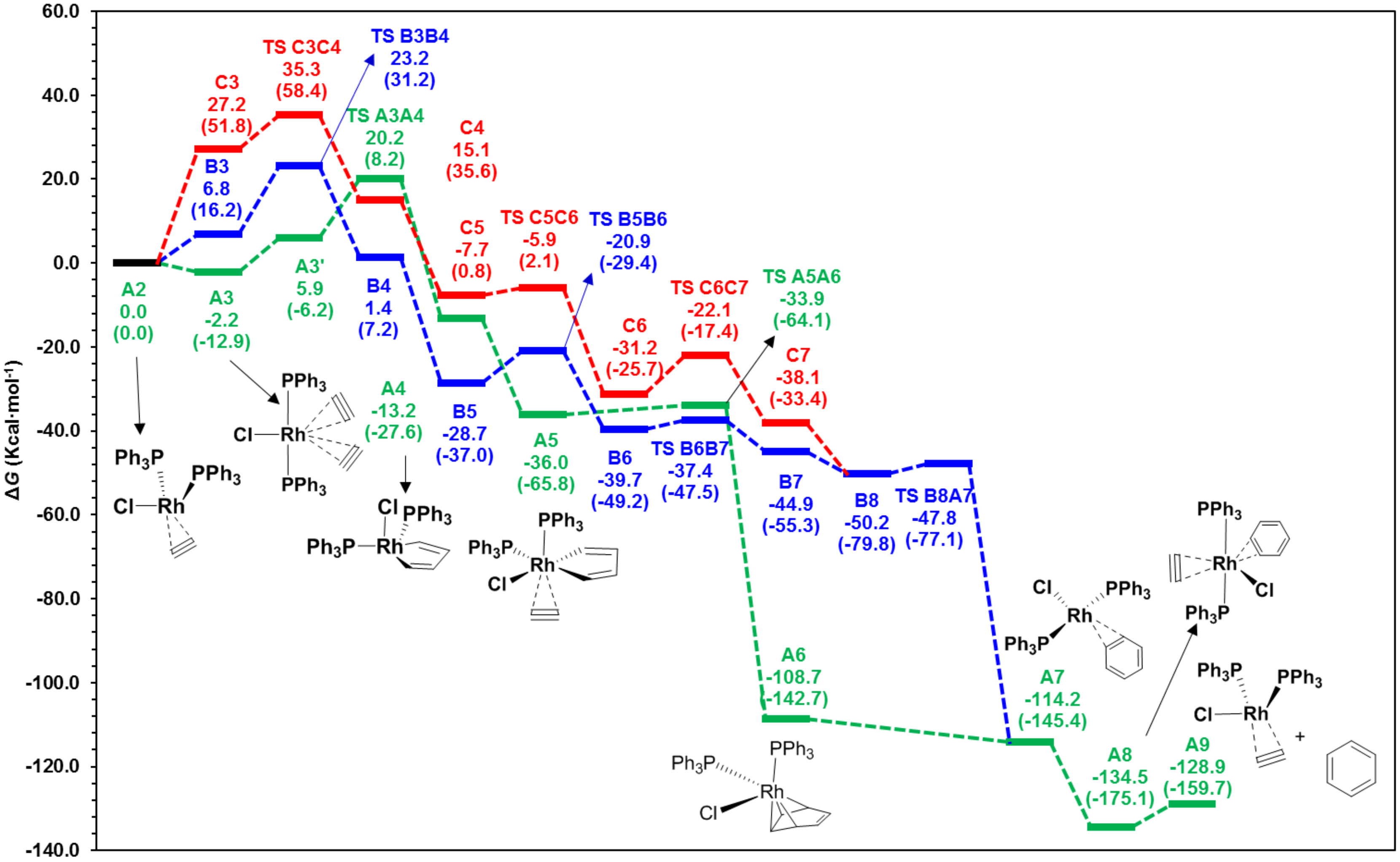

Supplementary material for chapter 4

Scheme S1. Synthesis of diynes **1d** and **1e**.

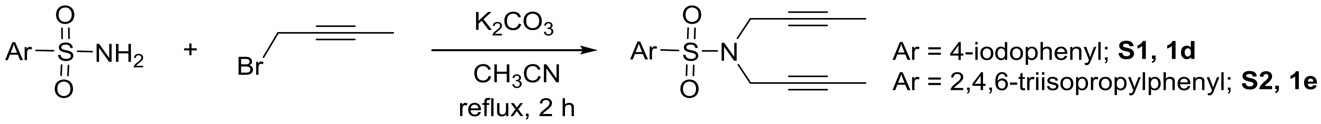
K2CO3
CH3CN
reflux, 2 h
Ar
Br
Ar = 4-iodophenyl; S1, 1d
Ar = 2,4,6-triisopropylphenyl; S2, 1e

In a round-bottom flask equipped with a reflux condenser and a magnetic stirrer, a suspension of the corresponding sulfonamide, **S1-S2** (1 equivalent) and K_2CO_3 (5 equivalents) was stirred in acetonitrile and heated to 80ºC. 1-bromo-2-butyne (2.1 equivalents) was then added dropwise to the reaction mixture and stirred at 80ºC for 2h until completion (TLC monitoring). The reaction mixture was then allowed to cool to room temperature, the solids were filtered off and the filtrate was concentrated to dryness and purified by column chromatography.

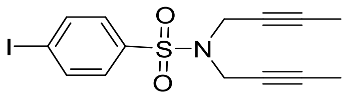

Compound 1d was obtained from 4-iodobenzenesulfonamide **S1** (2.00 g, 7.07 mmol) following the general procedure. Purification by column chromatography (SiO_2, 40–63 µm, CH_2Cl_2/hexanes 1:1) afforded compound **1d** (2.55 g, 93% yield) as a pale yellow solid.

MW ($C_{14}H_{14}INO_2S$): 387.24 g/mol; **Rf**: 0.44 (CH_2Cl_2/hexanes 1:1); **M.p**: 105-106ºC; **IR (ATR) ν (cm^{-1})**: 2912, 1565, 1336, 1154; **^{1}H NMR (400 MHz, $CDCl_3$) δ (ppm)**: 1.65 (t, *J* = 2.4 Hz, 6H), 4.06 (q, *J* = 2.4 Hz, 4H), 7.53 (d, *J* = 8.8 Hz, 2H), 7.85 (d, *J* = 8.8 Hz, 2H); **^{13}C NMR (101 MHz, $CDCl_3$) δ (ppm)**: 3.5, 36.9, 71.5, 82.1, 100.2, 129.4, 138.0, 138.4; **EA:** calculated for [$C_{14}H_{14}INO_2S$]: C, 43.42; H, 3.64; N, 3.62; found: C, 43.63 and 43.64; H, 3.39 and 3.50; N, 3.62 and 3.65.

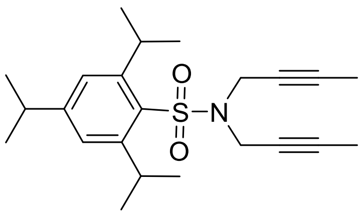

Compound 1e was obtained from 2,4,6-triisopropylbenzensulfonamide **S2** (2.00 g, 7.05 mmol), following the general procedure. Purification by column chromatography (SiO_2, 40–63 µm, hexanes/AcOEt 20:1) afforded compound **1e** (2.32 g, 85% yield) as a colourless solid.

MW ($C_{23}H_{33}NO_2S$): 387.58 g/mol; **Rf**: 0.40 (CH_2Cl_2/hexanes 1:1); **M.p**: 147-148ºC; **IR (ATR) ν (cm^{-1})**: 2952, 1598, 1315, 1151; **^{1}H NMR (400 MHz, $CDCl_3$) δ (ppm)**: 1.24 (d, *J* = 6.8 Hz, 12H), 1.25 (d, *J* = 6.8 Hz, 6H), 1.78 (t, *J* = 2.2 Hz, 6H), 2.89 (sept, *J* = 6.8 Hz, 1H), 4.04 (q, *J* = 2.2 Hz, 4H), 4.10 (hept, *J* = 6.8 Hz, 2H), 7.15 (s, 2H); **^{13}C NMR (101 MHz, $CDCl_3$) δ (ppm)**: 3.7, 23.7, 24.9, 29.4, 34.3, 35.3, 72.7, 81.2, 124.0, 130.8, 151.8, 153.3; **EA**: calculated for [$C_{23}H_{33}NO_2S$]: C, 71.28; H, 8.58; N, 3.61; found: C, 71.15 and 71.10; H, 8.52 and 8.44; N, 4.28 and 4.05.

Scheme S2.Synthesis of bis(fulleroids) **2a-h**, **2k** and **2o**.

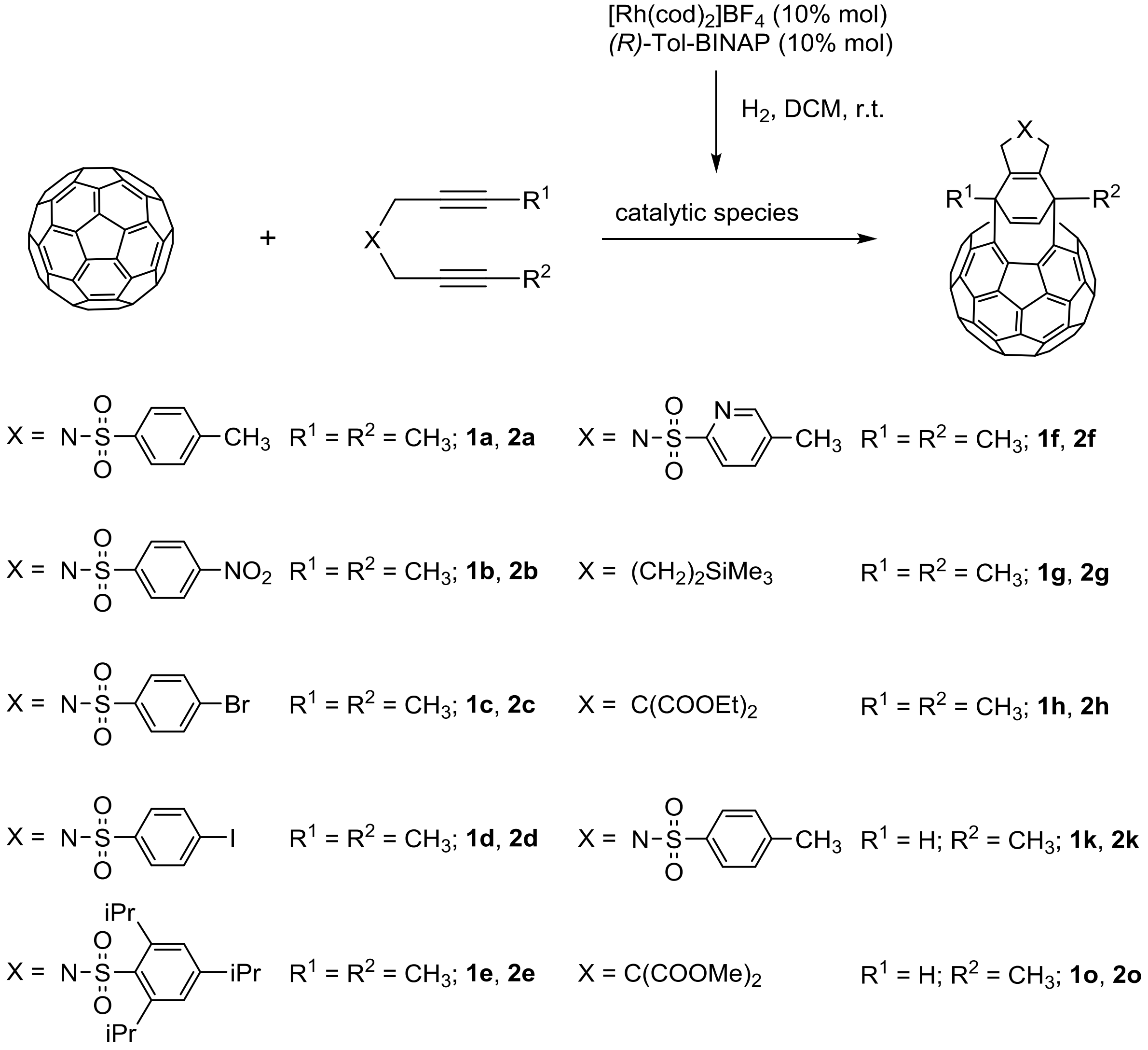
[Rh(cod)2]BF4 (10% mol)
(R)-Tol-BINAP (10% mol)
H2, DCM, r.t.
catalytic species
+
X
R1
R2
X = N-SO2-C6H4-CH3 R1 = R2 = CH3; 1a, 2a
X = N-SO2-C6H4-NO2 R1 = R2 = CH3; 1b, 2b
X = N-SO2-C6H4-Br R1 = R2 = CH3; 1c, 2c
X = N-SO2-C6H4-I R1 = R2 = CH3; 1d, 2d
X = N-SO2-C6H2(iPr)3 R1 = R2 = CH3; 1e, 2e
X = N-SO2-pyridyl-CH3 R1 = R2 = CH3; 1f, 2f
X = (CH2)2SiMe3 R1 = R2 = CH3; 1g, 2g
X = C(COOEt)2 R1 = R2 = CH3; 1h, 2h
X = N-SO2-C6H4-CH3 R1 = H; R2 = CH3; 1k, 2k
X = C(COOMe)2 R1 = H; R2 = CH3; 1o, 2o

In a 10 mL capped vial in an inert atmosphere, a solution of $[Rh(cod)_2]BF_4$ (0.1 equivalents) and *(R)*-Tol-BINAP (0.1 equivalents) in anhydrous CH_2Cl_2 (4 mL) was prepared. Hydrogen gas was bubbled into the catalyst solution for 30 min before it was concentrated to dryness, dissolved in anhydrous *o*-DCB and introduced into a solution of C_{60} (1 equivalent) and the corresponding diyne, **1a-h , k, o** (5 equivalents) in anhydrous *o*-DCB (1.4 mM), preheated to 90 °C. The resulting mixture was stirred at 90 °C for 4h. It was then allowed to cool down to room temperature, concentrated to dryness and purified by column chromatography.

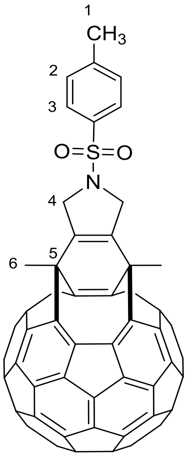

Compound 2a was obtained from C$_{60}$ (50 mg, 0.07 mmol) and diyne **1a** [294] (96 mg, 0.35 mmol), following the general procedure. Purification by column chromatography (SiO$_2$, 40–63 µm, toluene) afforded unreacted C$_{60}$ (25 mg) and **2a** (36 mg, 52% yield, 98% yield based on consumed C$_{60}$) as a dark brown solid. The analytical samples were prepared by washing **2a** with *n*-pentane (3 x 2 mL).

MW ($C_{75}H_{17}NO_2S$): 996.03 g/mol; **Rf**: 0.66 (CH_2Cl_2); **IR (ATR) *ν* (cm^{-1})**: 2916, 1326, 1157; **^{1}H NMR (400 MHz, CDCl$_3$) δ (ppm):** 2.36 (s, 3H, H**1**), 2.79 (s, 6H, H**6**), 4.42-4.50 (m, 2H, H**4**), 4.50-4.62 (m, 2H, H**4’**), 7.34 (d, *J* = 8.0 Hz, 2H, H**2**), 7.79 (d, *J* = 8.0 Hz, 2H, H**3**); **^{13}C NMR (101 MHz, CDCl$_3$) □ (ppm)**: 21.8 (C**1**), 27.7 (C**6**), 43.4 (C**5**), 55.0 (C**4**), 126.3, 127.7 (C**3**), 130.4 (C**2**), 133.7, 134.9, 135.0, 135.9, 136.9, 137.4, 137.7, 137.9, 138.6, 140.0, 140.3, 140.7, 141.3, 141.4, 143.5, 143.6, 143.9, 144.0, 144.1, 144.2, 144.22, 144.3, 144.5, 144.6, 144.8, 144.9, 145.0, 145.5, 145.8, 145.9, 149.6, 150.2 (two overlapping carbons); **UV-vis (CHCl$_3$) λ$_{max}$ (nm):** 264, 330, 518; **ESI-HRMS (*m/z*)** calcd for [M+Na]$^+$ = 1018.0872; found 1018.0878.

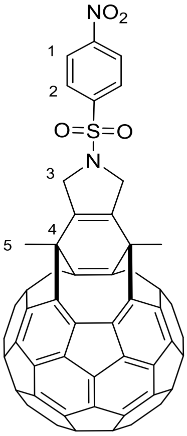

Compound 2b was obtained from C$_{60}$ (100 mg, 0.14 mmol) and diyne **1b** [294] (215 mg, 0.70 mmol), following the general procedure. Purification by column chromatography (SiO$_2$, 40–63 µm, toluene) afforded unreacted C$_{60}$ (32 mg) and **2b** (87 mg, 61% yield, 87% yield based on consumed C$_{60}$) as a dark brown solid. The analytical samples were prepared by washing with *n*-pentane (3 x 2 mL).

MW ($C_{74}H_{14}O_4N_2S$): 1027.00 g/mol; **Rf**: 0.70 (CH_2Cl_2); **IR (ATR) *ν* (cm^{-1})**: 2913, 1343, 1162; **^{1}H NMR (400 MHz, *o*-DCB-d$_4$) δ (ppm)**: 2.67 (s, 6H, H**5**), 4.45-4.60 (m, 4H, H**3**), 7.95 (d, *J* = 8.8 Hz, 2H, H**1**/H**2**), 8.12 (d, *J* = 8.8 Hz, 2H, H**1**/H**2**); **^{13}C NMR (101 MHz, *o*-DCB-d$_4$) δ (ppm)**: 27.3 (C**5**), 43.2 (C**4**), 55.0 (C**3**), 124.5 (C**1**/C**2**), 128.5 (C**1**/C**2**), 134.6, 134.9, 135.9, 136.5, 137.0, 137.2, 137.6, 138.2, 139.7, 140.2, 140.4, 140.8, 141.1, 142.6, 143.2, 143.3, 143.3, 143.5, 143.6, 143.8, 143.8, 143.9, 144.3, 144.4, 144.4, 144.5, 144.6, 145.1, 145.5, 145.6, 148.9, 149.8, 150.1 (two overlapping carbons) **ESI-HRMS (*m/z*)** calcd for [M+Na]$^+$ = 1049.0566; found 1049.0546.

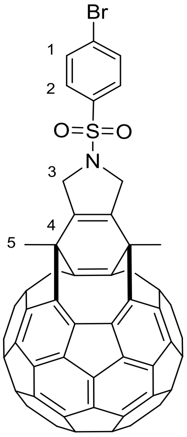

Compound 2c was obtained from C_{60} (50 mg, 0.07 mmol) and diyne **1c** [294] (119 mg, 0.70 mmol), following the general procedure. Purification by column chromatography (SiO_2, 40–63 µm, toluene) afforded unreacted C_{60} (24 mg) and **2c** (38 mg, 51% yield, 99% yield based on consumed C_{60}) as a dark brown solid. The analytical samples were prepared by washing with *n*-pentane (3 x 2 mL).

MW ($C_{74}H_{14}BrO_2NS$): 1060.90 g/mol; **Rf**: 0.76 (CH_2Cl_2); **IR (ATR) *ν* (cm^{-1})**: 2931, 1342, 1161; **^{1}H NMR (400 MHz, *o*-DCB-d$_4$) δ (ppm)**: 2.65 (s, 6H, H**5**), 4.42-4.58 (m, 4H, H**3**), 7.47 (d, *J* = 8.5 Hz, 2H, H**1**/H**2**), 7.71 (d, *J* = 8.5 Hz, 2H, H**1**/H**2**); **^{13}C NMR (101 MHz, *o*-DCB-d$_4$) □ (ppm)**: 27.3 (C**5**), 43.2 (C**4**), 54.9 (C**3**), 129.0 (C**1**/C**2**), 132.8 (C**1**/C**2**), 134.7, 134.9, 135.9, 136.1, 136.5, 137.0, 137.5, 137.6, 138.2, 139.7, 140.2, 140.5, 141.0, 141.1, 143.3, 143.3, 143.4, 143.5, 143.6, 143.8, 143.88, 143.9, 144.3, 144.4, 144.5, 144.6, 144.7, 145.2, 145.5, 145.6, 149.6, 150.0 (three overlapping carbons); **ESI-HRMS (*m/z*)** calcd for $[M+Na]^+$ = 1081.9821-1083.9806; found 1081.9797-1083.9794.

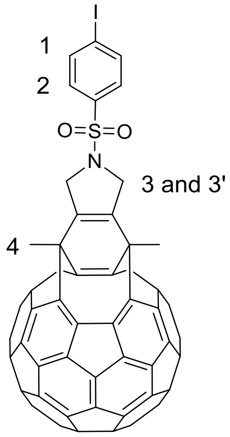

Compound 2d was obtained from C_{60} (100 mg, 0.14 mmol) and diyne **S-3c** (135 mg, 0.35 mmol), following the general procedure. Purification by column chromatography (SiO_2, 40–63 µm, toluene) afforded **2d** (60 mg, 39% yield) as a dark brown solid. The analytical samples were prepared by washing with CH_3OH (3 x 2 mL) and *n*-pentane (3 x 2 mL).

MW ($C_{74}H_{14}IO_2NS$): 1107.90 g/mol; **Rf**: 0.74; (CH_2Cl_2); **^{1}H NMR: (400 MHz, *o*-DCB-d$_4$/CS$_2$) δ (ppm)**: (s, 2.61, 3H, H**4**), 4.31-4.41 (m, 2H, H**3**), 4.42-4.47 (m, 2H, H**3'**), 7.66 (d, *J* = 8.5 Hz, 2H, H**2**), 7.79 (d, *J* = 8.5 Hz, 2H, H**1**); **ESI-HRMS (m/z):** calcd for $[M+Na]^+$ = 1129.9682; found: 1129.9662.

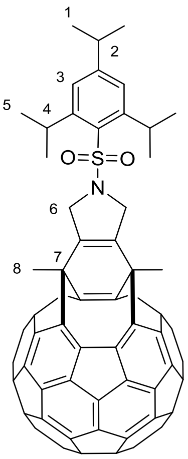

Compound 2e was obtained from C_{60} (50 mg, 0.07 mmol) and diyne **1e** (136 mg, 0.35 mmol), following the general procedure. Purification by column chromatography (SiO_2, 40–63 μm, toluene) afforded unreacted C_{60} (25 mg) and **2e** (34 mg, 44% yield, 92% yield based on consumed C_{60}) as a dark brown solid. The analytical samples were prepared by washing with *n*-pentane (3 x 2 mL) and CH_3OH (3 x 2 mL).

MW ($C_{83}H_{33}NO_2S$): 1108.24 g/mol; **Rf**: 0.84 (CH_2Cl_2); **IR (ATR)** $\boldsymbol{\nu}$ **(cm^{-1})**: 2916, 1314, 1151; **^{1}H NMR (400 MHz, $CDCl_3$) δ (ppm)**: 1.27 (d, *J* = 6.8 Hz, 6H), 1.31 (d, *J* = 6.8 Hz, 12H), 2.83 (s, 6H, H**8**), 2.93 (m, 1H, H**2**), 4.25-4.32 (m, 4H, H**6**), 4.67-4.72 (m, 2H, H**4**), 7.21 (s, 2H, H**3**); **^{13}C NMR (101 MHz, $CDCl_3$) δ (ppm)**: 23.7 (C**1**/C**5**), 24.9 (C**1**/C**5**), 27.7 (C**8**), 29.6 (C**4**), 34.3 (C**2**), 43.6 (C**7**), 53.2 (C**6**), 124.1 (C**3**), 124.2, 126.3, 131.2, 134.8, 135.1, 136.0, 136.9, 137.4, 137.9, 138.0, 138.7, 140.0, 140.4, 140.7, 141.3, 141.8, 143.6, 143.7, 143.9, 144.0, 144.1, 144.2, 144.3, 144.6, 144.8, 144.9, 145.1, 145.5, 145.8, 145.9, 150.7, 151.5, 153.5 (three overlapping carbons); **ESI-HRMS (*m/z*)** calcd for $[M+Na]^+$ = 1130.2124; found 1130.2097.

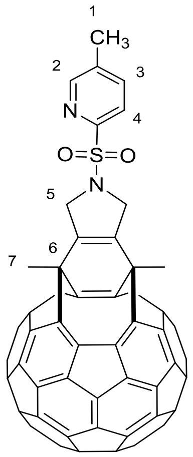

Compound 2f was obtained from C_{60} (50 mg, 0.07 mmol) and diyne **1f** [294] (97 mg, 0.35 mmol), following the general procedure. Purification by column chromatography (SiO_2, 40–63 μm, toluene) afforded unreacted C_{60} (24 mg) and **2f** (36 mg, 52% yield, 92% yield based on consumed C_{60}) as a dark brown solid. The analytical samples were prepared by washing with *n*-pentane (3 x 2 mL) and CH_3OH (3 x 2 mL).

MW ($C_{74}H_{16}N_2O_2S$): 997.01 g/mol; **Rf**: 0.40 (CH_2Cl_2); **IR (ATR)** $\boldsymbol{\nu}$ **(cm^{-1})**: 2917, 1342, 1168; **^{1}H NMR (400 MHz, $CDCl_3$) δ (ppm)**: 2.35 (s, 3H, H**1**), 2.80 (s, 6H, H**7**), 4.73 (s, 4H, H**5**), 7.70 (m, 1H, H**3**), 7.92 (d, *J* = 8.0 Hz, 1H, H**4**), 8.59 (m, 1H, H**2**); **^{13}C NMR (101 MHz, $CDCl_3$) δ (ppm)**: 18.9 (C**1**), 27.7 (C**7**), 43.5 (C**6**), 55.8 (C**5**), 123.2 (C**3**/C**4**), 126.3, 134.8, 134.9, 135.9, 136.8, 137.4, 137.7, 137.8, 137.9, 138.2 (C**3**/C**4**), 138.7, 140.0, 140.4, 140.7, 141.2, 141.4, 143.5, 143.6, 143.7, 143.9, 144.0, 144.1, 144.2, 144.23, 144.3, 144.6, 144.8, 145.0, 145.5, 145.8, 145.9, 149.3, 150.5, 151.2 (C**2**), 153.5 (two overlapping carbons); **ESI-HRMS (*m/z*)** calcd for $[M+Na]^+$ = 1019.0825; found 1019.0853.

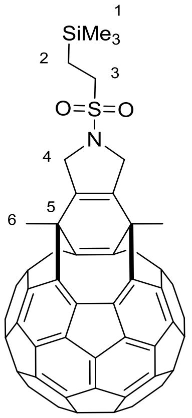

Compound 2g was obtained from C_{60} (100 mg, 0.14 mmol) and diyne **1g** [264] (215 mg, 0.70 mmol), following the general procedure. Purification by column chromatography (SiO_2, 40–63 µm, toluene) afforded unreacted C_{60} (36 mg) and **2g** (51 mg, 35% yield, 54% yield based on consumed C_{60}) as a dark brown solid. The analytical samples were prepared by washing with *n*-pentane (3 x 2 mL).

MW ($C_{73}H_{23}NO_2SSi$): 1006.14 g/mol; **Rf**: 0.64 (CH_2Cl_2); **IR (ATR) ν (cm^{-1})**: 2916, 1326, 1141; **^{1}H NMR: (400 MHz, $CDCl_3$) δ (ppm)**: 0.09 (s, 9H, H**1**), 1.10-1.17 (m, 2H, H**2**), 2.87 (s, 6H, H**6**), 3.00-3.10 (m, 2H, H**3**), 4.52-4.59 (m, 2H, H**4**), 4.65-4.73 (m, 2H, H**4’**); **^{13}C NMR (101 MHz, $CDCl_3$) δ (ppm)**: -1.7 (C**1**), 10.3 (C**2**), 27.9 (C**6**), 43.6 (C**5**), 46.8 (C**3**), 54.9 (C**4**), 126.3, 135.1, 135.2, 136.1, 136.9, 137.4, 137.8, 137.9, 138.7, 140.0, 140.5, 140.8, 141.3, 141.5, 143.6, 143.7, 143.9, 144.0, 144.1, 144.2, 144.3, 144.7, 144.8, 144.83, 144.9, 145.1, 145.5, 145.9, 145.95, 149.6, 150.5 (two overlapping carbons); **ESI-HRMS (*m/z*)** calcd for [M+Na]$^+$ = 1028.1111; found 1028.1111.

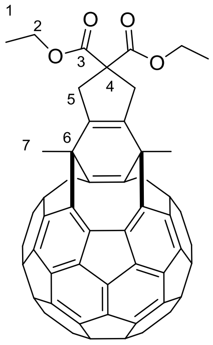

Compound 2h was obtained from C_{60} (100 mg, 0.14 mmol) and diyne **1h** [412] (185 mg, 0.70 mmol), following the general procedure. Purification by column chromatography (SiO_2, 40–63µm, toluene) afforded unreacted C_{60} (16 mg) and **2h** (25 mg, 36% yield, 50% yield based on consumed C_{60}) as a dark brown solid. The analytical samples were prepared by washing with *n*-pentane (3 x 2 mL).

MW ($C_{75}H_{20}O_4$): 984.98 g/mol; **Rf**: 0.70 (CH_2Cl_2); **IR (ATR) ν (cm^{-1})**: 2926, 1723; **^{1}H NMR (400 MHz, $CDCl_3$) δ (ppm)**: 1.29 (t, *J* = 7.0 Hz, 3H, H**1**), 1.34 (t, *J* = 7.0 Hz, 3H, H**1’**), 2.89 (s, 6H, H**7**), 3.32-3.52 (m, 4H, H**5**), 4.26 (q, *J* = 7.0 Hz, 2H, H**2**), 4.31 (q, *J* = 7.0 Hz, 2H, H**2’**); **^{13}C NMR (101 MHz, $CDCl_3$) δ (ppm)**: 14.2 (C**1**), 14.3 (C**1’**) 28.3 (C**7**), 40.4 (C**5**), 44.5 (C**6**), 58.4 (C**4**), 62.1 (C**2**), 126.7, 135.2, 135.9, 136.6, 136.9, 137.3, 137.8, 139.0, 139.2, 140.1, 140.3, 140.7, 141.1, 142.0, 143.5, 143.6, 143.7, 143.8, 144.0, 144.1, 144.2, 144.5, 144.6, 144.7, 144.8, 145.4, 145.9, 146.0, 149.9, 151.8, 171.6 (C**3**), 171.9 (C**3’**) (three overlapping carbons); **ESI-HRMS (m/z)** calcd for [M+Na]$^+$ = 10007.1254; found 1007.1229.

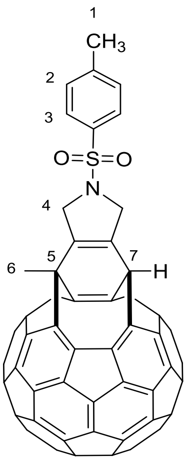

Compound 2k was obtained from C_{60} (50 mg, 0.07 mmol) and diyne **1k**[413] (91 mg, 0.35 mmol), following the general procedure. Purification by column chromatography (SiO_2, 40–63 μm, toluene) afforded **2k** (7 mg, 10% yield) as a dark brown solid. The analytical samples were prepared by washing with *n*-pentane (3 x 2 mL).

MW ($C_{74}H_{15}O_2NS$): 982.00 g/mol; **Rf**: 0.60 (CH_2Cl_2); **IR (ATR) ν (cm^{-1})**: 2914, 1341, 1157; **^{1}H NMR (400 MHz, $CDCl_3$) δ (ppm)**: 2.37 (s, 3H, H**1**), 2.77 (s, 3H, H**6**), 4.50-4.64 (m, 4H, H**4**), 6.50 (broad s, 1H, H**7**), 7.34 (d, *J* = 8.0 Hz, 2H, H**2**), 7.81 (d, *J* = 8.0 Hz, 2H, H3); **^{13}C NMR (101 MHz, $CDCl_3$) δ (ppm)**: 21.8 (C**1**), 27.4 (C**6**), 41.7 (C**7**), 43.9 (C**5**), 54.9 (C**4**), 55.9 (C**4'**), 127.7 (C**3**), 127.8, 130.4 (C**2**), 131.5, 133.8, 133.9, 134.2, 135.2, 135.3, 135.7, 136.5, 136.8, 136.9, 137.0, 137.5, 138.5, 140.1, 140.2, 140.3, 140.6, 140.7, 140.8, 140.9, 141.0, 141.2, 141.6, 143.5, 143.56, 143.6, 143.7, 143.8, 143.88, 143.9, 144.0, 144.1, 144.17, 144.2, 144.3, 144.4, 144.5, 144.6, 144.65, 144.7, 144.8, 144.9, 145.0, 145.5, 145.6, 145.7, 145.77, 145.8, 149.5, 151.7 (13 overlapping carbons); **ESI-HRMS (*m/z*)** calcd for $[M+Na]^+$ = 1004.0716; found 1004.0714.

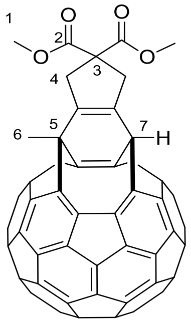

Compound 2o was obtained from C_{60} (50 mg, 0.07 mmol) and diyne **1o** [414] (78 mg, 0.35 mmol), following the general procedure. Purification by column chromatography (SiO_2, 40–63 μm, toluene) afforded **2o** (8 mg, 12% yield) as a dark brown solid. The analytical samples were prepared by washing with *n*-pentane (3 x 2 mL).

MW ($C_{72}H_{14}O_4$): 942.90 g/mol; **Rf**: 0.68 (CH_2Cl_2); **IR (ATR) ν (cm^{-1})**: 2916, 1727; **^{1}H NMR (400 MHz, $CDCl_3$) δ (ppm)**: 2.87 (s, 3H, H**6**), 3.39 (m, 1H, H**4**), 3.51-3.57 (m, 3H, H**4**,H**4'**), 3.82 (s, 3H, H**1**), 3.87 (s, 3H, H**1'**), 6.59 (broad s, 1H, H**7**); **^{13}C NMR (101 MHz; $CDCl_3$) □ (ppm)**: 27.9 (C**6**), 40.3 (C**1**), 41.8 (C**1'**), 43.6 (C**7**), 44.8 (C**5**), 53.2 (C**4**), 53.3 (C**4'**), 58.8 (C**3**), 125.6, 127.9, 133.1, 134.4, 135.0, 135.2, 135.4, 135.5, 136.7, 136.8, 137.3, 137.6, 138.1, 138.9, 139.2, 140.1, 140.2, 140.4, 140.5, 140.6, 140.7, 140.77, 140.8, 140.9, 141.3, 141.35, 141.37, 143.4, 143.5, 143.55, 143.6, 143.64, 143.7, 143.8, 143.9, 143.93, 143.94, 144.0, 144.1, 144.16, 144.2, 144.24, 144.27, 144.3, 144.4, 144.5, 144.57, 144.6, 144.8, 145.0, 145.5, 145.57, 145.59, 145.6, 145.7, 146.9, 149.6, 153.0, 171.9, 172.2 (four overlapping carbons); **ESI-HRMS (*m/z*)** calcd for $[M+Na]^+$ = 965.0784; found 965.0793.

Scheme S3. Synthesis of compounds **4a-c** by Suzuki-Miyaura cross-coupling

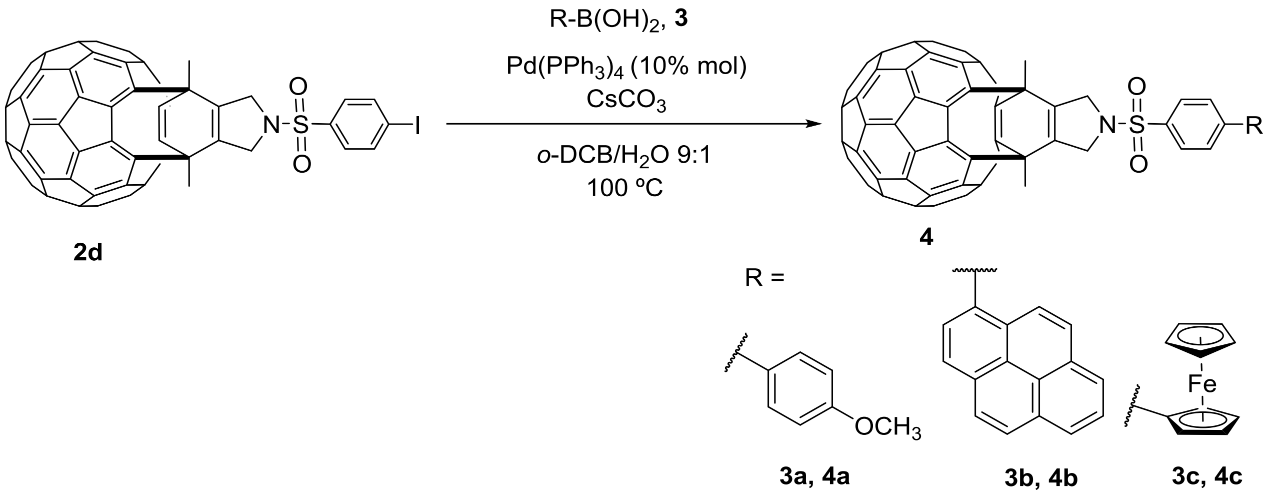

In a two-necked round-bottom flask, equipped with a reflux condenser and a magnetic stirrer, a suspension of iodo fulleroid derivative **2d**, the corresponding boronic acid **3** (2 equivalents), $CsCO_3$ (2.5 equivalents) and $Pd(PPh_3)_4$ (0.1 equivalents) was prepared in a mixture of 1,2-dichlorobenzene and water (9:1, 5.4 mM) under a stream of nitrogen gas. The resulting mixture was heated at 100 ºC and stirred in an inert atmosphere for 2–4 hours (TLC monitoring). The reaction mixture was then allowed to cool to room temperature, concentrated to dryness and purified by column chromatography.

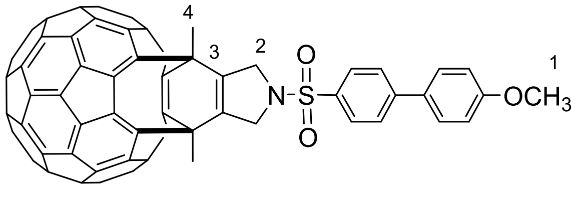

Compound 4a was obtained from **2d** (60 mg, 0.054 mmol) and **3a** (16 mg, 0.11 mmol), following the general procedure. Purification by column chromatography (SiO_2, 40–63 µm, CH_2Cl_2/hexanes 7:3) afforded compound **4a** (38 mg, 63% yield) as a dark brown solid.

MW ($C_{81}H_{21}O_3NS$): 1088.12 g/mol; **Rf**: 0.60 (CH_2Cl_2) **IR (ATR) *ν* (cm^{-1})**: 2917, 1341, 1157; **^{1}H NMR (400 MHz, CDCl$_3$) δ (ppm)**: 2.80 (s, 6H, H**4**), 3.87 (s, 3H, H**1**), 4.47-4.52 (m, 2H, H**2**), 4.60-4.67 (m, 2H, H**2’**), 6.93 (d, *J* = 8.4 Hz, 2H), 7.45 (d, *J* = 8.4 Hz, 2H), 7.71 (d, *J* = 8.0 Hz, 2H), 7.93 (d, *J* = 8.4 Hz, 2H); **^{13}C NMR (101 MHz, CDCl$_3$) δ (ppm)**: 27.6 (C**4**), 43.4 (C**3**), 55.2 (C**2**), 55.7 (C**1**), 114.7 (C**Ar**), 126.2, 127.5 (C**Ar**), 128.2 (C**Ar**), 128.3 (C**Ar**), 131.3, 134.0, 134.9, 134.93, 135.9, 136.8, 137.4, 137.6, 137.9, 138.5, 139.9, 140.1, 140.7, 141.2, 141.3, 143.4, 143.5, 143.54, 143.8, 143.9, 144.1, 144.18, 144.2, 144.24, 144.6, 144.8, 144.9, 145.4, 145.6, 145.8, 145.9, 149.5, 150.1, 160.4 (two overlapping carbons); **ESI-HRMS (*m/z*)** calcd for $[M+Na]^+$ = 1110.1134; found 1110.1109.

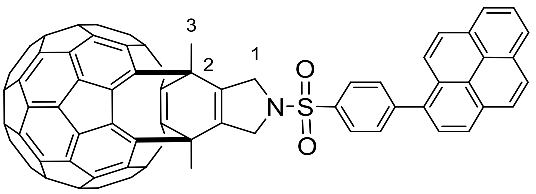

Compound 4b was obtained from **2d** (60 mg, 0.054 mmol) and **3b** (27 mg, 0.11 mmol), following the general procedure. Purification by column chromatography (SiO_2, 40–63 µm, CH_2Cl_2/hexanes 7:3) afforded compound **4b** (49 mg, 75% yield) as a dark brown solid.

MW ($C_{90}H_{23}NO_2S$): 1181.14 g/mol; **Rf**: 0.72 (CH_2Cl_2); **IR (ATR) ν (cm^{-1})**: 2922, 1341, 1159; **^{1}H NMR (400 MHz, CDCl$_3$) δ (ppm)**: 2.86 (s, 6H, H**3**), 4.57-4.65 (m, 2H, H**1**), 4.70-4.76 (m, 2H, H**1**'), 7.83-8.24 (m, 13H); **^{13}C NMR (101 MHz, CDCl$_3$) δ (ppm)**: 27.8 (C**3**), 43.5 (C**2**), 55.1 (C**1**), 124.4, 124.8, 124.9, 125.1, 125.4, 125.7, 126.3, 126.4, 127.4, 127.5, 127.8, 128.2, 128.3, 128.4, 130.9, 131.4, 131.6, 131.7, 134.9, 135.0, 135.3, 135.8, 136.0, 136.8, 137.4, 137.7, 137.9, 138.6, 139.9, 140.5, 140.7, 141.3, 141.33, 143.5, 143.55, 143.6, 143.8, 143.9, 144.1, 144.2, 144.25, 144.6, 144.7, 144.8, 145.0, 145.5, 145.8, 145.9, 146.5, 149.5, 150.4 (two overlapping carbons); **ESI-HRMS (*m/z*)** calcd for [M+Na]$^+$ = 1204.1342; found 1204.1364.

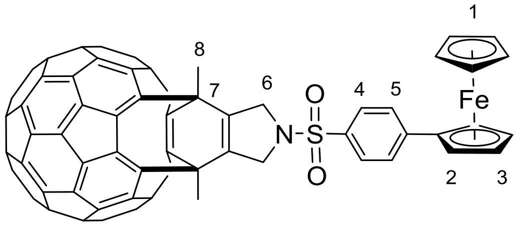

Compound 4c was obtained from **2d** (37 mg, 0.030 mmol) and **3c** (14 mg, 0.060 mmol), following the general procedure. Purification by column chromatography (SiO_2, 40–63 µm, toluene) afforded compound **4c** (5 mg, 14% yield) as a dark brown solid and byproduct **S3** (3 mg, 11 % yield) as a dark brown solid.

MW ($C_{84}H_{23}FeNO_2S$) 1166.02 g/mol; **Rf**: 0.60 (CH_2Cl_2); **IR (ATR) ν (cm^{-1})**: 2915, 1337, 1159; **^{1}H NMR (400 MHz, CDCl$_3$) δ (ppm)**: 2.79 (s, 6H, H**8**), 4.02 (s, 5H, H**1**), 4.38 (t, *J* = 2.0 Hz, 2H, H**2**/**3**), 4.22-4.49 (m, 2H, H**6**), 4.59 (t, *J* = 2.0 Hz, 2H, H**2**/**3**), 4.60-4.65 (m, 2H, H**6'**), 7.56 (d, *J* = 8.0 Hz, 2H, H**4**/H**5**), 7.78 (d, *J* = 8.4 Hz, 2H, H**4**/H5); **^{13}C NMR (101 MHz, CDCl$_3$) δ (ppm)**: 27.7 (C**8**), 43.4 (C**7**), 55.2 (C**6**), 67.1 (C**2**/**3**), 69.9 (C**1**), 70.4 (C**2**/**3**), 125.4, 126.2, 126.8 (C**4**/**5**), 127.5, 127.7 (C**4**/**5**), 128.3, 129.2, 129.7, 132.8, 134.9, 135.9, 136.8, 137.3, 137.6, 137.8, 138.5, 139.9, 140.1, 140.7, 141.2, 141.4, 143.4, 143.5, 143.8, 143.9, 144.0, 144.1, 144.2, 144.5, 144.7, 144.8, 144.9, 145.4, 145.8, 146.3, 150.0 (two overlapping carbons); **ESI-HRMS (*m/z*)** calcd for [M]$^+$ = 1165.0796; found 1165.0787.

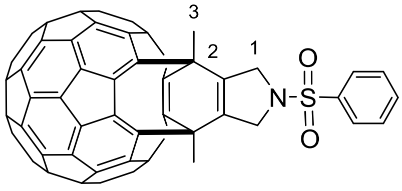

S3

MW ($C_{74}H_{15}NO_2S$): 981.99 g/mol; **Rf**: 0.64 (CH_2Cl_2); **IR (ATR) ν (cm^{-1})**: 2917, 1339, 1156; **^{1}H NMR (400 MHz, $CDCl_3$) δ (ppm)**: 2.79 (s, 6H, H**3**), 4.45-4.4.50 (m, 2H, H**1**), 4.58-4.62 (m, 2H, H**1'**), 7.55-7.7.62 (m, 3H), 7.90-7.93 (m, 2H); **^{13}C NMR (101 MHz, $CDCl_3$) δ (ppm)**: 27.7 (C**3**), 43.4 (C**2**), 55.0 (C**1**), 126.3 (C**Ar**), 127.5 (C**Ar**), 129.7 (C**Ar**), 133.5, 134.9, 135.1, 135.9, 136.7, 136.8, 137.4, 137.6, 137.9, 138.0, 138.6, 140.00, 140.3, 140.8, 141.3, 141.4, 143.5, 143.6, 143.9, 144.0, 144.1, 144.2, 144.3, 144.6, 144.8, 144.9, 145.0, 145.5, 145.8, 145.9, 149.6, 150.1 (two overlapping carbons); **ESI-HRMS (*m/z*)** calcd for $[M+Na]^+ = 1004.0716$; found 1004.0711.

Scheme S4. Oxidative photocleavage of fulleroid derivative **2a**.

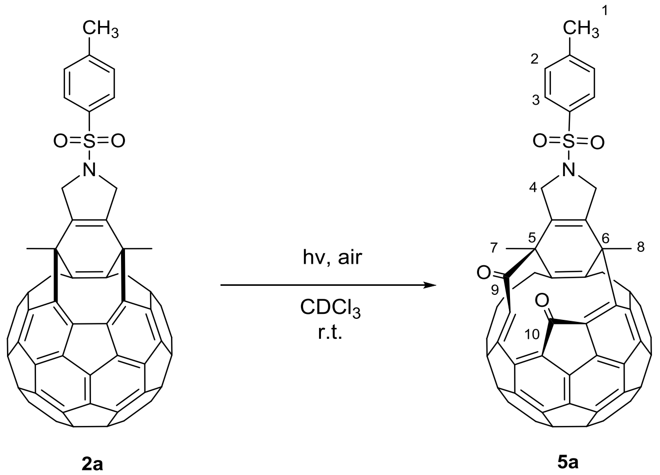

A solution of **2a** (5 mg, 0.005 mmol) in $CDCl_3$ (0.6 mL) was prepared in an NMR tube and exposed to sunlight and air for 5 hours, after which only compound **5** was detected by NMR and ESI-HRMS analysis.

MW ($C_{75}H_{17}NO_4S$): 1028.02 g/mol; **Rf**: 0.40 (CH_2Cl_2); **IR (ATR) ν (cm^{-1})**: 2919, 1734, 1682, 1339, 1155; **^{1}H NMR (400 MHz, $CDCl_3$) δ (ppm)**: 2.21 (s, 3H, H**7**), 2.46 (s, 3H, H**1**), 2.57 (s, 3H, H**8**), 4.90-5.00 (m, 3H, H**4**), 5.54 (m, 1H, H**4'**), 7.47 (d, *J* = 8.0 Hz, 2H, H**2**), 8.10 (d, *J* = 8.4 Hz, 2H, H**3**); **^{13}C NMR (101 MHz, $CDCl_3$) δ (ppm)**: 21.8 (C**1**), 31.7 (C**7/8**), 31.9 (C**7/8**), 42.7 (C**6**), 51.7 (C**5**), 54.8 (C**4**), 56.5 (C**4'**), 128.0 (C**3**), 130.0 (C**2**), 130.9, 131.2, 131.4, 132.2, 133.3, 133.4, 134.6, 135.1, 135.8, 135.9, 136.0, 136.3, 136.8, 137.7, 138.0, 139.1, 139.8, 139.9, 140.2, 140.25, 140.5, 140.6, 140.7, 141.1, 141.3, 141.9, 142.1, 142.5, 142.9, 143.1, 143.6, 144.2, 144.3, 144.6, 144.8, 145.0, 145.3, 145.33, 145.6, 145.8, 145.9, 145.91, 145.92, 145.96, 146.0, 146.1, 146.2, 146.3, 146.6, 147.1, 147.6, 147.8, 147.9, 148.9, 150.0, 150.1, 154.5, 191.5 (C**10**), 201.5 (C**9**) (five overlapping carbons); **UV-vis ($CHCl_3$) λ_{max} (nm):** 256, 324; **ESI-HRMS (*m/z*)** calcd for $[M+Na]^+ = 1050.0770$; found 1050.0770.

Figure S7. M06-D3/cc-pVTZ-PP//B3LYP-D3/cc-pVDZ-PP Gibbs energy profile for the transformation of **A1** into **A2** through **TS A1A2**. Comparison between dimethylphosphine vs diphenylphosphine models.

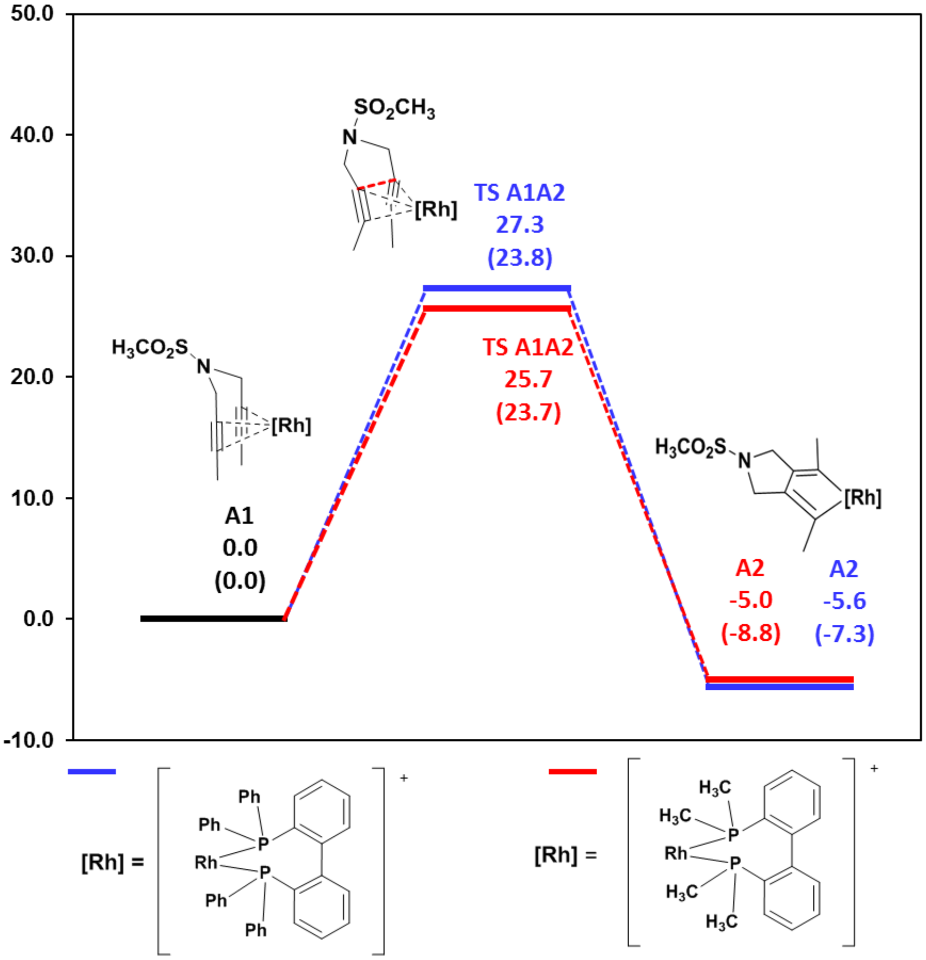

Figure S8. M06-D3/cc-pVTZ-PP//B3LYP-D3/cc-pVDZ-PP Gibbs energy profile for alternative Path A.

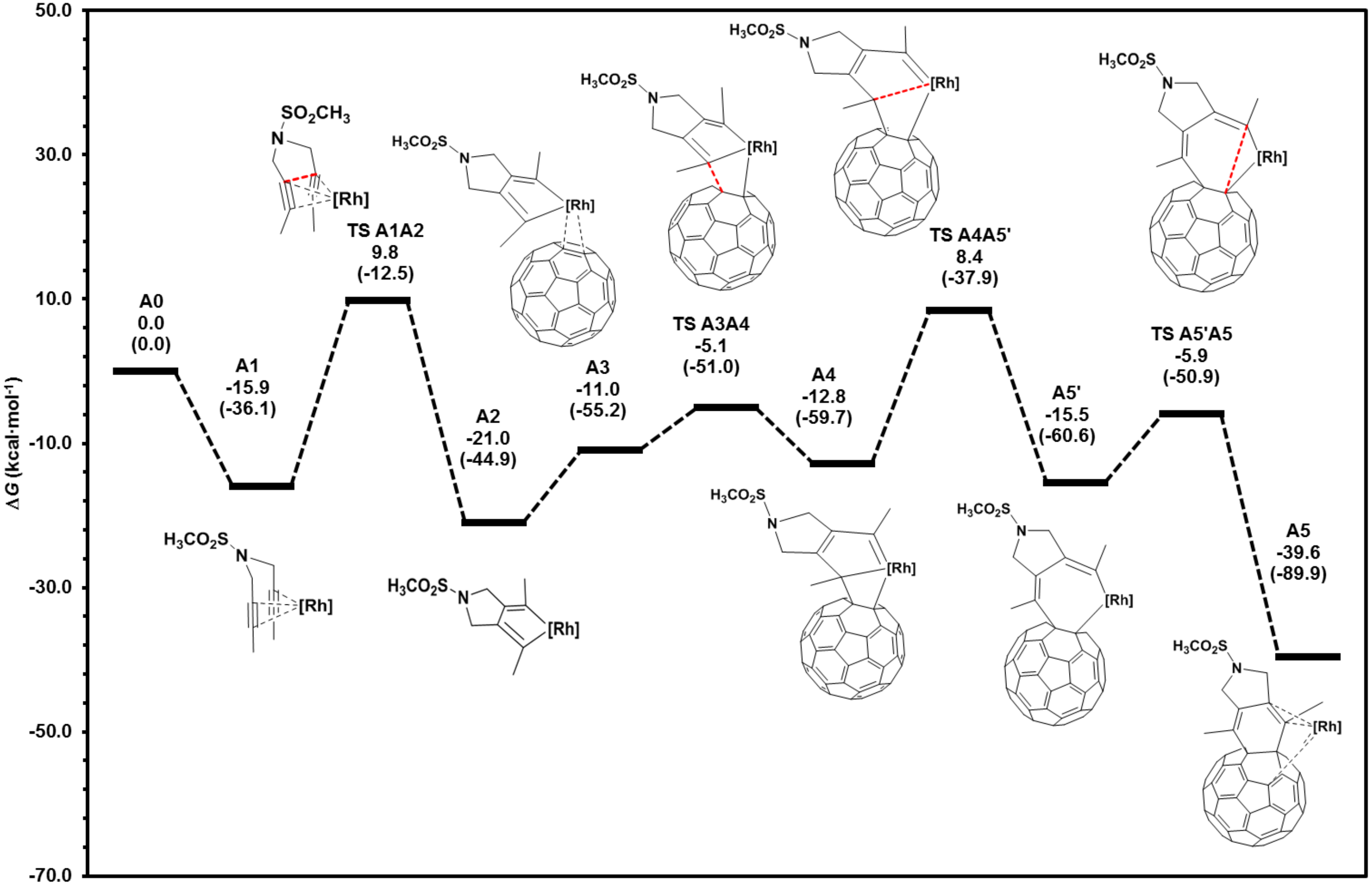

Figure S9. M06-D3/cc-pVTZ-PP//B3LYP-D3/cc-pVDZ-PP Gibbs energy profile for path B.

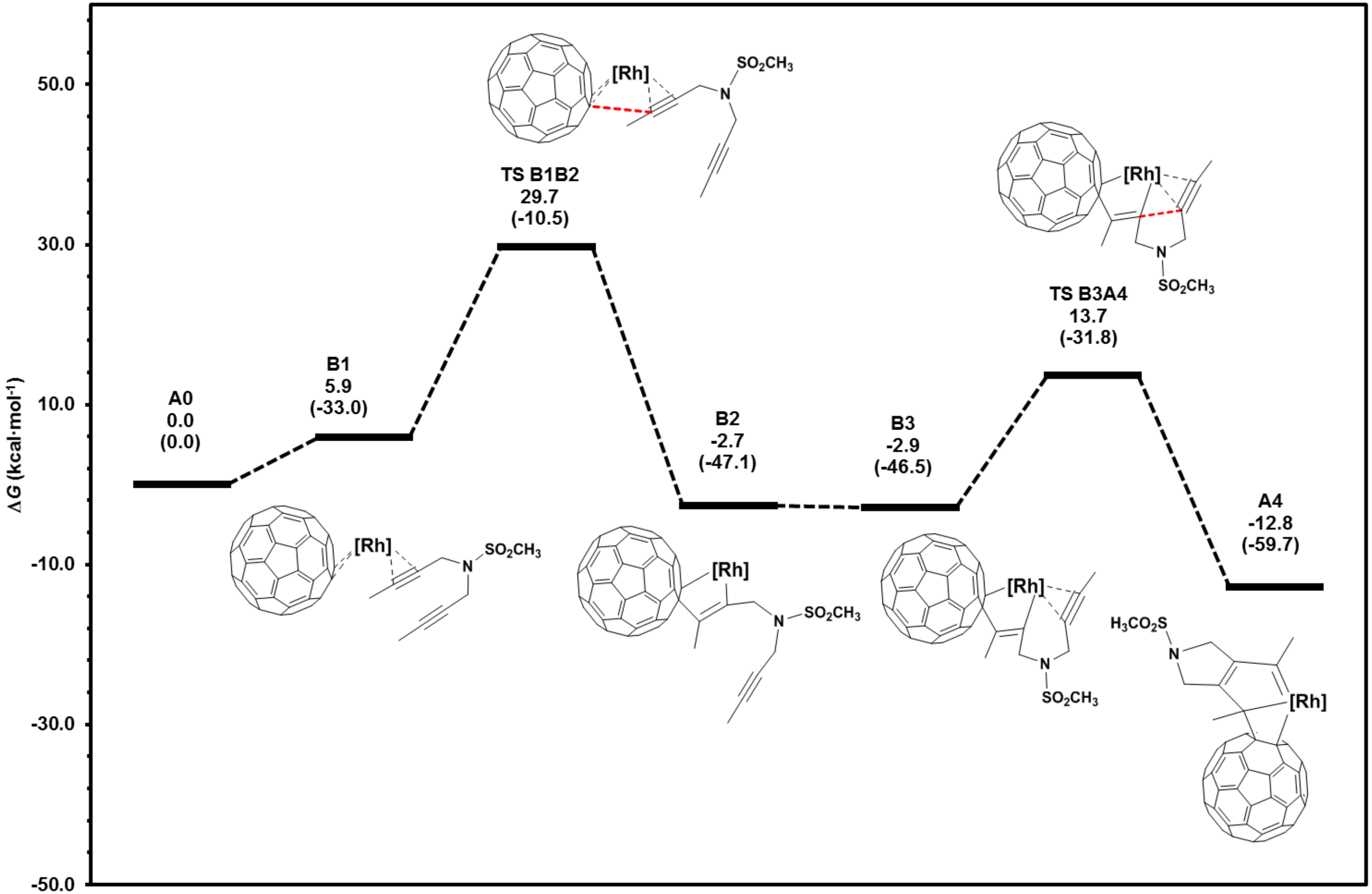

Supplementary material for chapter 5

Scheme S5. Oxidative photocleavage of compounds **2a**, **2e** and **4b**.

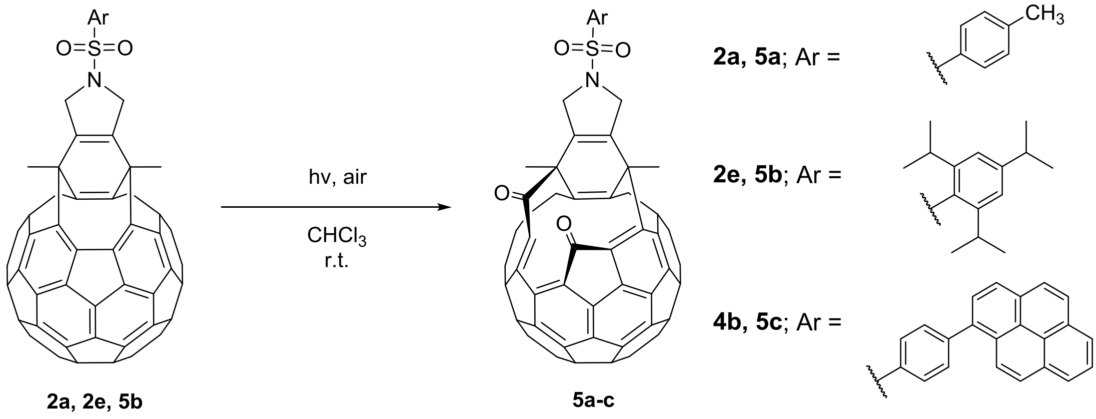

A solution of the corresponding C_{60} derivative **2a**, **2e** and **4b** in $CHCl_3$ (5 mL) was prepared in a vial and exposed to sunlight and air for 5 h. The resulting solution was concentrated under reduced pressure and purified by column chromatography to afford the corresponding dicarbonylic C_{60} derivative **5a-c** as a dark brown solid.

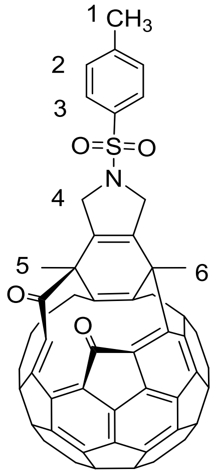

5a was obtained from **2a** (71 mg, 0.07 mmol) following the general procedure. Purification by column chromatography (silica gel, 40–63μm, hexanes/CH_2Cl_2) afforded **5a** (66 mg, 92%) as a dark brown solid. The analytical samples were prepared by washing with CH_3OH (3 x 2 mL) and *n*-pentane (3 x 2 mL).

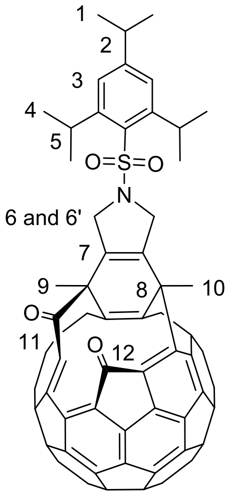

5b was obtained from **2e** (34 mg, 0.031 mmol) following the general procedure. Purification by column chromatography (SiO_2, 40–63μm, hexanes/CH_2Cl_2 1:1) afforded **5b** (31 mg, 89% yield) as a dark brown solid. The analytical samples were prepared by washing with CH_3OH (3 x 2 mL) and *n*-pentane (3 x 2 mL).

MW ($C_{83}H_{33}NO_4S$): 1140.24 g/mol; **Rf**: 0.80 (CH_2Cl_2); **IR (ATR) ν (cm^{-1})**: 2925, 1740, 1687 1318, 1152; **^{1}H NMR (400 MHz, CDCl$_3$) δ (ppm)**: 1.36 (d, *J* = 6.8, 6H, H**1**), 1.45 (d, *J* = 6.8, 6H, H**4**), 1.46 (d, *J* = 6.8, 6H, H**4'**), 2.26 (s, 3H, H**9**), 2.64 (s, 3H, H**10**), 3.02 (sept, *J* = 6.8, 1H, H**2**), 4.62 (sept, *J* = 6.8, 2H, H**5**), 4.93-5.04 (m, 3H, H**6**), 5.56-5.51 (m, 1H, H**6'**), 7.34 (s, 2H, H**3**); **^{13}C NMR (101 MHz, CDCl$_3$) δ (ppm)**: 23.8 (C**1**), 25.3 (C**4**), 29.9 (C**5**), 31.8 (C**9**), 32.0 (C**10**), 34.4 (C**2**), 42.9 (C**8**), 51.8 (C**8'**), 53.9 (C**6**), 55.3 (C**6'**), 124.2 (C**3**), 131.0, 131.4, 131.5, 131.8, 132.4, 133.3, 133.4, 134.7, 135.8, 136.0, 136.2, 136.3, 136.4, 136.9, 137.7, 138.0, 139.1, 139.9, 140.0, 140.3, 140.3, 140.5, 140.6, 140.7, 141.1, 141.3, 141.9, 142.1, 142.5, 142.9, 143.0, 143.1, 144.2, 144.3, 144.6, 144.8, 145.2, 145.3, 145.5, 145.6, 145.8, 145.9, 145.9, 145.9, 146.0, 146.0, 146.2, 146.2, 146.4, 146.6, 147.1, 147.6, 147.9, 147.9, 147.9, 148.9, 150.1, 150.3, 151.7, 153.2, 154.6, 191.6, 201.7 (two overlapping carbons); **UV-vis (CHCl$_3$) λ$_{max}$:** 421, 450, 510, 610 and 670 nm; **ESI-HRMS (*m/z*)** calcd for [M+Na]$^+$ = 1162.2028; found 1162.2005.

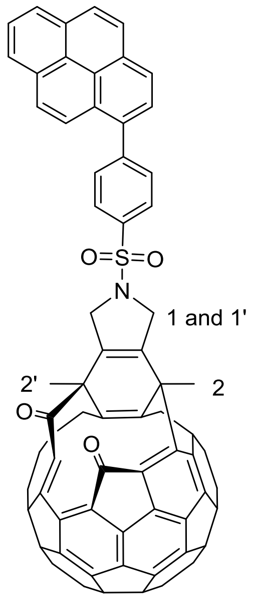

5c was obtained from **5c** (49 mg, 0.041 mmol) following the general procedure. Purification by column chromatography (silica gel, 40–63μm, hexanes/CH_2Cl_2) afforded **4b** (49 mg, 98% yield) as a dark brown solid. The analytical samples were prepared by washing with CH_3OH (3 x 2 mL) and *n*-pentane (3 x 2 mL).

MW ($C_{90}H_{23}NO_4S$): 1214.24 g/mol; **Rf**: 0.50 (CH_2Cl_2); **IR (ATR) ν (cm^{-1})**: 2916, 1727, 1372, 1157; **^{1}H NMR (400 MHz, CDCl$_3$) δ (ppm)**: 2.27 (s, 3H, H**2**), 2.64 (s, 3H, H**2'**), 5.00 – 5.11 (m, 3H, H**1**), 5.65 – 5.72 (m, 1H, H**1'**), 7.80 (d, *J* = 9.2 Hz, 1H, H**Ar**), 7.93 – 8.21 (m, 10H, H**Ar**) 8.45 (d, *J* = 7.9 Hz, 2H, H**Ar**); **UV-vis (CHCl$_3$) λ$_{max}$:** 421, 450, 510, 610 and 670 nm; **: ESI-HRMS (*m/z*)** calcd for [M+Na]$^+$ = 1236.1245; found 1236.1240.

Figure S10. Absorption spectra of compounds **5a-c** and $PC_{61}BM$.

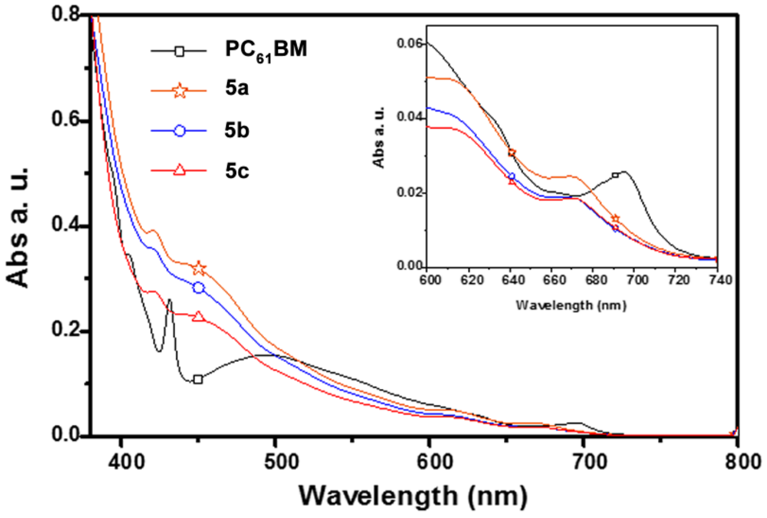

Figure S11. CV of compounds **5a-c.** Conditions: 0.1 mM C_{60}/**2a/4b-c/5a** and 0.05 M $Bu_4N^+PF_6$- in o-dichlorobenzene, silver wire pseudo-reference reference electrode, 1 mm glassy carbon disk working electrode, Pt wire auxiliary electrode, scan rate 100 mV.s^{-1}, 25 °C**.**

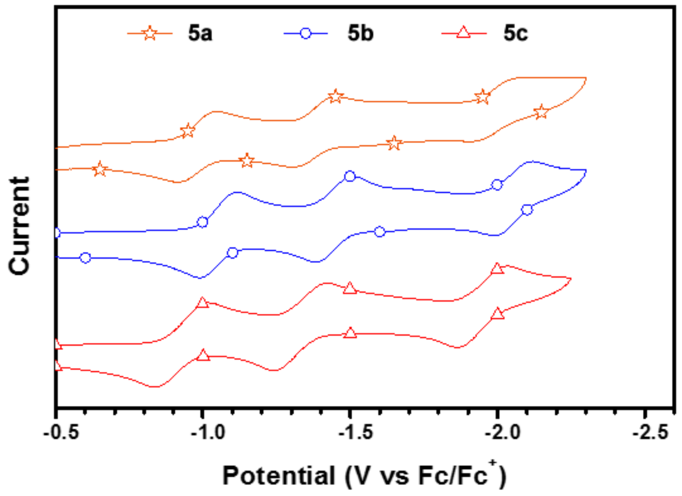

Figure S12. Chlorobenzene solutions (20 mg/ml) of **5a-b** and $PC_{61}BM$. **5c** dissolves only partially in chlorobenzene

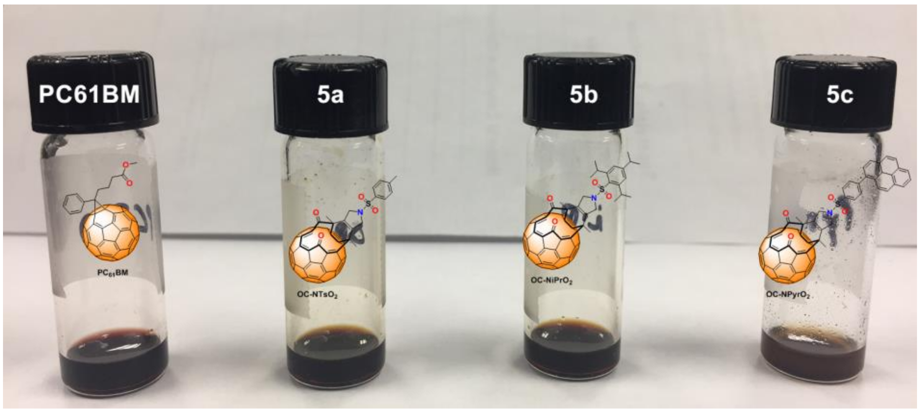

Figure S13. TR-PL of perovskite, perovskite/compounds **2a-c** and perovskite/$PC_{61}BM$ films.

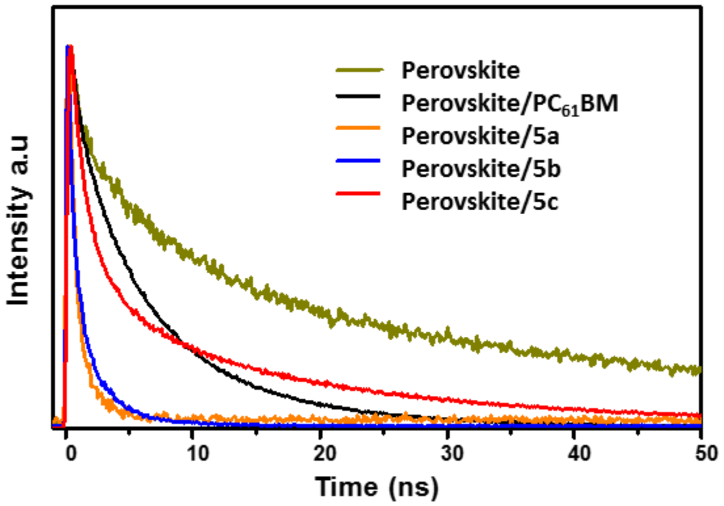

Figure S14. Stability of 5a-c and $PC_{61}BM$ devices.

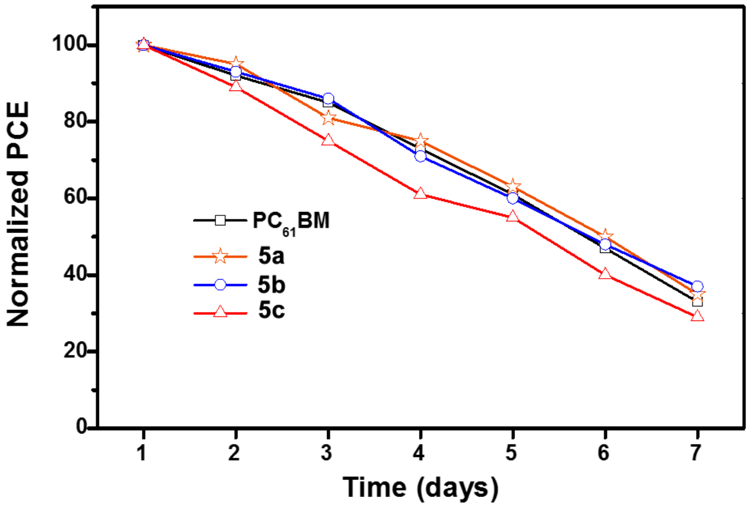

Figure S15. *J-V* curves of the inverted PSCs based on **2a,b** with respect to forward and reverse scan directions (the scanning rate was 100 mV/s).

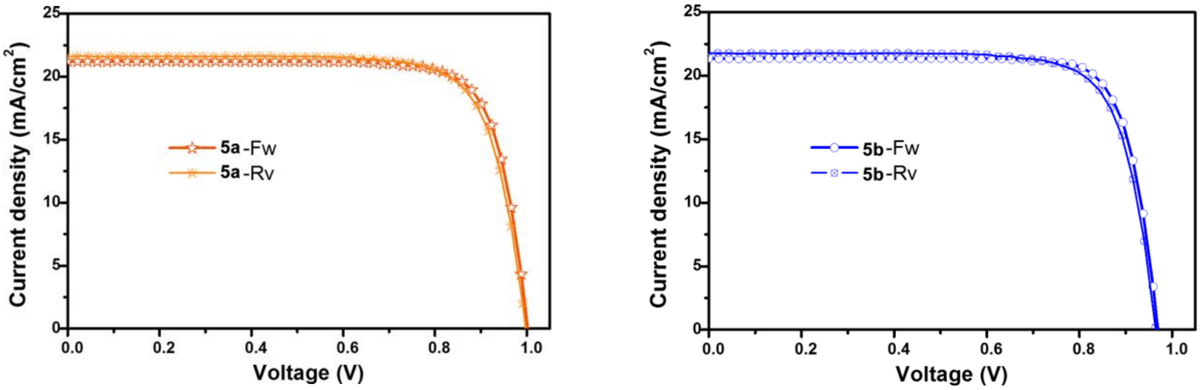

Supplementary material for chapter 6

Scheme S6. Synthesis of diyne **S4**.

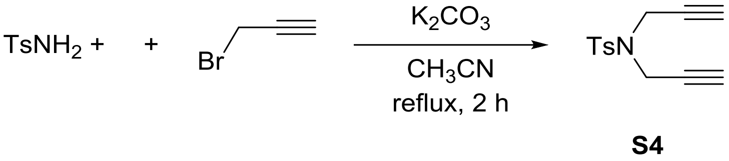

In a 100 mL round-bottom flask equipped with a reflux condenser and a magnetic stirrer, a mixture of 4-methylbenzenesulfonamide (1 g, 5.84 mmol), K_2CO_3 (4.80 g, 34.73 mmol) and propargyl bromide (1.45 mL, 80 % in toluene, 1.60 mg, 13.42 mmol) in acetonitrile (60 mL) was stirred at 80 °C for 2 h until completion (TLC monitoring). The reaction mixture was allowed to cool to room temperature, the solids were filtered off and the filtrate was concentrated under reduced pressure to provide a yellowish oil which was purified by column chromatography (SiO_2, 40–60 μm, Hexanes/CH_2Cl_2 1:1 v/v) to afford diyne **S4** (1.33 g, 92% yield), as a colourless solid.

MW ($C_{13}H_{13}NO_2S$): 247.3 g/mol; **Rf**: 0.33 (Hexanes/CH_2Cl_2 1:1); **^{1}H NMR (400 MHz, CDCl$_3$) δ (ppm)**: 2.14 (t, *J* = 2.4 Hz, 2H), 2.41 (s, 3H), 4.15 (d, *J* = 2.4 Hz, 4H), 7.28 (d, *J* = 8.4 Hz, 2H), 7.70 (d, *J* = 8.4 Hz, 2H); **^{13}C NMR (101 MHz, CDCl$_3$) δ (ppm)**: 21.67, 36.27, 74.17, 76.24, 127.96, 129.67, 135.22, 144.11.; **ESI-MS (m/z):** $[M+H]^+$ = 248.0. Spectral data in accordance with literature values [415]

Scheme S7. Synthesis of bisallenes **1a-b**.

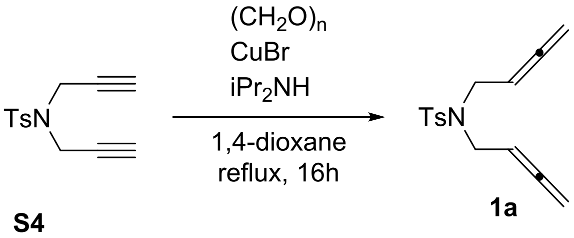

In a 250 mL round-bottom flask equipped with a reflux condenser and a magnetic stirrer, a suspension of diyne **S4** (6 g, 24.26 mmol), paraformaldehyde (3.64 g, 121.3 mmol) and CuBr (3.48 g, 24.26 mmol) in 1,4-dioxane (100 mL) was stirred and heated at reflux. Diisopropylamine (13.60 mL, 9.82 g, 97.04 mmol) was then added and the resulting mixture was stirred at reflux for 16 h until completion (TLC monitoring). The reaction mixture was allowed to cool to room temperature, filtered through a Celite pad and concentrated under reduced pressure. The resulting brown oil was mixed with Et_2O (200 mL) and water (100 mL) and the mixture was acidified to pH=2 with HCl 6M. The Et_2O/water layers were decanted from solid residues, the Et_2O layer was separated and the water layer was extracted with Et_2O (3 x 100 mL). The combined organic extracts were washed with water and brine, dried over anhydrous Na_2SO_4 and concentrated under reduced pressure. The crude product was purified by column chromatography (SiO_2, 40–60 μm, Hexanes/EtOAc 95:5 v/v) to afford bisallene **1a** (4.10 g, 61% yield) as a colorless solid.

MW ($C_{15}H_{17}NO_2S$): 275.4 g/mol; **Rf**: 0.50 (hexanes/EtOAc 8:2); **^{1}H NMR (400 MHz, $CDCl_3$) δ (ppm)**: 2.41 (s, 3H), 3.89 (dt, *J* = 6.8, 2.4 Hz, 4H), 4.70 (dt, *J* = 6.8, 2.4 Hz, 4H), 4.93 (quint., *J* = 6.8 Hz, 2H), 7.29 (d, *J* = 8.4, 2H), 7.69 (d, *J* = 8.4 Hz, 2H); **^{13}C NMR (101 MHz, $CDCl_3$) δ (ppm)**: 21.61, 45.77, 76.27, 85.75, 127.27, 129.79, 137.66, 143.40, 209.78; **ESI-MS (m/z):** $[M+Na]^+$: 298.0. Spectral data in accordance with literature values [412].

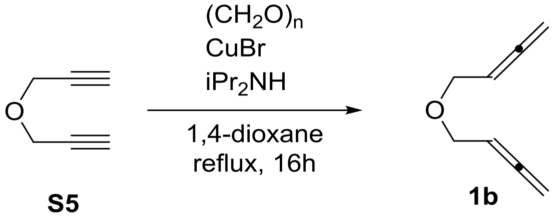

In a round-bottom flask equipped with a reflux condenser and a magnetic stirrer, a suspension of commercially available diyne **S5** (1.50 g, 15.96 mmol), paraformaldehyde (2.40 g, 80 mmol) and CuBr (2.30 g, 16.03 mmol) in 1,4-dioxane (60 mL) was stirred and heated at reflux. Diisopropylamine (9 mL, 6.48 g, 64 mmol) was then added and the resulting mixture was stirred for 16 h at reflux until completion (TLC monitoring). The reaction mixture was allowed to cool to room temperature, filtered through a Celite pad and concentrated under reduced pressure. The resulting brown oil was mixed with Et_2O (120 mL) and water (60 mL) and the mixture was acidified to pH=2 with HCl 6M. The Et_2O/water layers were decanted from any residues, the Et_2O layer was separated and the water layer was extracted with Et_2O (3 x 60 mL). The combined organic extracts were washed with water and brine, dried over anhydrous Na_2SO_4 and concentrated under reduced pressure. The crude product was purified by column chromatography (SiO_2, 40–60 μm, Hexanes/EtOAc 95:5 v/v) to provide bisallene **1b** (394 mg, 20% yield) as a yellowish oil.

MW ($C_8H_{10}O$): 122.2 g/mol; **Rf**: 0.67 (hexanes/EtOAc 8:2); **IR (ATR) *ν* (cm^{-1})**: 2920, 2854, 1953, 1450, 1357, 1318, 1251, 1077; **^{1}H NMR (400 MHz, $CDCl_3$) δ (ppm)**: 4.03 (dt, *J* = 6.8, 2.4 Hz, 4H), 4.78 (dt, *J* = 6.8, 2.4 Hz, 4H), 5.23 (quint, *J* = 6.8 Hz, 2H); **^{13}C NMR (101 MHz, $CDCl_3$) δ (ppm)**: 67.68, 75.78, 87.67, 209.49.

Table S1. Optimization of the Rh(I)-catalyzed cycloaddition of bisallene **1a** with alkene **2a**.

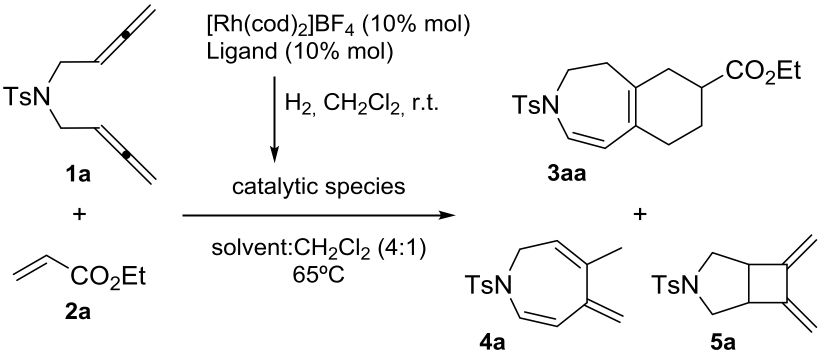

Entry	Ligand	Solvent	[**1a**] (mM)	Temperature (ºC)	**1a**:**2a** ratio	Yield of **3aa** / **4a** / **5a** (%)
1	(*R*)-BINAP	Toluene	18	65	1:10	30 / 29 / -
2	(*R*)-BINAP	DCE	18	65	1:10	- / - / -
3	(*R*)-BINAP	Acetonitrile	18	65	1:10	29 / 18 / -
4	(*R*)-BINAP	1,4-Dioxane	18	65	1:10	42 / 53 / -
5	(*R*)-BINAP	EtOH	18	65	1:10	18 / 24 / -
6	(*R*)-BINAP	THF	18	65	1:10	46 / 39 / -
7	(*R*)-BINAP	THF	18	65	1:50	45 / 45 / -
8	(*R*)-BINAP	THF	9	65	1:10	46 / 52 / -
9	(*R*)-BINAP	THF	9	65	1:50	49 / 45 / -
10	(*R*)-Tol-BINAP	THF	9	65	1:50	54 / 44 / -
11	(*R*)-H_8-BINAP	THF	9	65	1:50	54 / 38 / -
12	(*R*)-Monophos	THF	9	65	1:50	26 / 18 / -
13	BIPHEP	THF	9	65	1:50	- / 37 / -
14	(*R*)-DTBM-Segphos	THF	9	65	1:50	65 / 5 / 15
15	(*R*)-DTBM-Segphos	THF	9	40	1:50	60 / - / 15
16[b]	(*R*)-DTBM-Segphos	THF	9	40	1:50	44 / - / 15
17[c]	-	THF	9	40	1:50	- / - / -
18	-	THF	9	40	1:50	- / - / -

Reaction conditions: 0.09 mmol of **1a**, 10-50 equivalents of **2a**, 10% mol of Rh catalyst in 10-20 mL of solvent:CH_2Cl_2 (4:1) at 65ºC for 4h or 40ºC for 16h. The 10% mol mixture of $[Rh(cod)_2]BF_4$ and phosphine was treated with hydrogen in dichloromethane (CH_2Cl_2) solution for catalyst activation prior to substrate addition. b The reaction was run with 5% mol of $[Rh(cod)_2]BF_4$ and 5% mol of ligand. c The reaction was run without $[Rh(cod)_2]BF_4$.

Scheme S8. General procedure for the synthesis of product **3aa.**

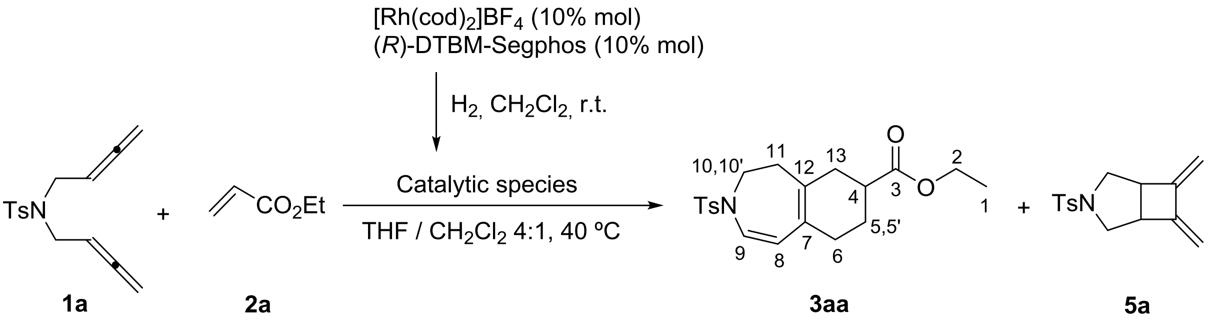

In a 10 mL capped vial, a mixture of [Rh(cod)$_2$]BF$_4$ (7.4 mg, 0.018 mmol) and (*R*)-DTBM-Segphos (23.6 mg, 0.020 mmol) was purged with nitrogen and dissolved in anhydrous CH$_2$Cl$_2$ (4 mL). Hydrogen gas was bubbled into the catalyst solution and the mixture was stirred for 30 min. The resulting mixture was concentrated to dryness under a stream of nitrogen, dissolved again in anhydrous CH$_2$Cl$_2$ (4 mL) and transferred via syringe into a solution of bisallene **1a** (50 mg, 0.18 mmol, 1 equiv.) and ethyl acrylate **2a** (1.0 mL, 9.00 mmol, 50 equiv.) in anhydrous THF (16 mL) preheated to 40 °C and under inert atmosphere. The resulting mixture was stirred at 40 ºC for 16h. The solvent was removed under reduced pressure and the crude reaction mixture was purified by column chromatography on silica gel using hexane/EtOAc mixtures as the eluent (98:2 to 95:5 v/v). Concentration under reduced pressure afforded compound **5a** (7.7 mg, 15% yield) as a colourless solid, and **3aa** (40.2 mg, 60% yield) as a pale yellow oil (in order of elution).

3aa: **MW** ($C_{20}H_{25}NO_4S$): 375.48 g/mol; **Rf**: 0.49 (Hexane/EtOAc 8:2); **IR (ATR) *ν* (cm^{-1})**: 2924, 1724, 1344, 1161; **^{1}H NMR (400 MHz, CDCl$_3$) δ (ppm):** 1.22 (t, *J* = 7.1, 3H, H**1**), 1.51 - 1.62 (m, 1H, H**5/5'**), 1.90 - 1.97 (m, 1H, H**5**/H**5'**), 2.05 - 2.13 (m, 2H, H**11**), 2.10 - 2.17 (m, 2H, H**6**), 2.15 - 2.33 (m, 2H, H**13**), 2.38 - 2.47 (m, 1H, H**4**), 2.42 (s, 3H, CH$_3$-**Ar**), 3.47 (ddd, *J* = 13.4, 6.1, 3.0 Hz, 1H, H**10/10'**), 3.64 - 3.71 (m, 1H, H**10**/H**10'**), 4.11 (q, *J* = 7.1 Hz, 2H, H**2**), 4.86 (d, *J* = 10.3 Hz, 1H, H**8**), 6.66 (d, *J* = 10.3 Hz, 1H, H**9**), 7.30 (d, *J* = 8.2 Hz, 2H, CH-**Ar**), 7.66 (d, *J* = 8.2 Hz, 2H, CH-**Ar**); **^{13}C NMR (101 MHz, CDCl$_3$) δ (ppm):** 14.35 (C**1**), 21.70 (CH$_3$-**Ar**), 25.41 (C**5**), 30.91 (C**6**), 34.59 (C**13**), 36.32 (C**11**), 39.52 (C**4**), 47.08 (C**10**), 60.49 (C**2**), 110.58 (C**8**), 124.74 (C**9**), 126.11 (C**7**), 127.18 (CH-**Ar**), 130.01 (CH-**Ar**), 133.54 (C**12**), 135.72 (C-**Ar**), 143.96 (C-**Ar)**, 175.57 (C**3**); **ESI-HRMS (*m/z*)** calcd for [M+Na]$^+$ = 398.1397; found 398.1405.

5a: **MW** ($C_{15}H_{17}NO_2S$): 275.4 g/mol; **Rf**: 0.35 (Hexane/EtOAc 8:2); **^{1}H NMR (400 MHz, CDCl$_3$) δ(ppm):** 2.43 (s, 3H), 2.75 (dd, *J* = 9.6, 6.0 Hz, 2H), 3.28 - 3.34 (m, 2H), 3.62 (d, *J* = 9.6 Hz, 2H), 4.80 (s, 2H), 5.22 (s, 2H), 7.31 (d, *J* = 8.3 Hz, 2H), 7.68 (d, *J* = 8.3 Hz, 2H); **^{13}C NMR (101 MHz, CDCl$_3$) δ (ppm):** 21.68, 44.81, 53.49, 105.69, 128.24, 129.61, 132.28, 143.68, 149.15; **ESI-MS (*m/z*)** [M+H]$^+$ = 275.1. Spectral data in accordance with literature values.[416]

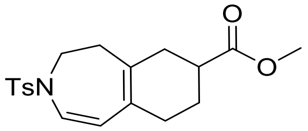

Compound 3ab was obtained from bisallene **1a** (52 mg, 0.19 mmol) and methyl acrylate (0.84 mL, 9.3 mmol), following the general procedure. Purification by column chromatography (silica gel, 40–63 µm, Hexanes/EtOAc) provided **5a** (7.7 mg, 15% yield) as a colourless solid and **3ab** (36 mg, 53% yield) as a yellow oil.

MW ($C_{19}H_{23}NO_4S$): 361.46 g/mol **Rf**: 0.31 (Hexane/EtOAc 8:2); **IR (ATR) ν (cm^{-1})**: 2924, 1727, 1341, 1158; **^{1}H NMR (400 MHz, CDCl$_3$) δ (ppm):** 1.51 - 1.63 (m, 1H), 1.91 - 1.98 (m, 1H), 2.06 - 2.33 (m, 6H), 2.40 - 2.50 (m, 1H), 2.42 (s, 3H), 3.48 (ddd, *J* = 13.4, 6.2, 3.0 Hz, 1H), 3.66 (s, 3H), 3.63 - 3.71 (m, 1H), 4.86 (d, *J* = 10.3 Hz, 1H), 6.66 (d, *J* = 10.3 Hz, 1H), 7.31 (d, *J* = 8.3 Hz, 2H), 7.66 (d, *J* = 8.3 Hz, 2H); **^{13}C NMR (101 MHz, CDCl$_3$) δ (ppm)**: 21.70, 25.40, 30.90, 34.58, 36.33, 39.42, 47.08, 51.82, 110.52, 124.82, 126.15, 127.20, 130.02, 133.44, 135.76, 143.97, 176.00; **ESI-HRMS (*m/z*)** calcd for [M+Na]$^+$ = 384.1240; found 384.1236.

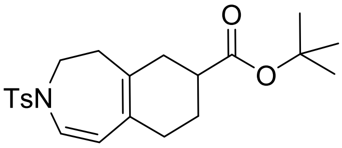

Compound 3ac was obtained from bisallene **1a** (49.6 mg, 0.18 mmol) and tert-butyl acrylate (1.36 mL, 98%, 9.1 mmol), following the general procedure. Purification by column chromatography (silica gel, 40–63 µm, Hexanes/EtOAc) provided **5a** (7.1 mg, 14 %yield) as a colourless solid and **3ac** (36.6 mg, 50% yield) as a pale yellow oil.

MW ($C_{22}H_{29}NO_4S$): 403.54 g/mol; **Rf**: 0.36 (Hexane/EtOAc 9:1); **IR (ATR) ν (cm^{-1})**: 2924, 1719, 1343, 1149; **^{1}H NMR (400 MHz, CDCl$_3$) δ (ppm):** 1.41 (s, 9H), 1.48 - 1.59 (m, 1H), 1.85 - 1.94 (m, 1H), 2.08 - 2.27 (m, 6H), 2.29 - 2.38 (m, 1H), 2.42 (s, 3H), 3.48 (ddd, J = 13.4, 6.1, 2.9 Hz, 1H), 3.63 - 3.71 (m, 1H), 4.86 (d, J = 10.3 Hz, 1H), 6.66 (d, J = 10.3 Hz, 1H), 7.30 (d, J = 8.4, 2H), 7.66 (d, J = 8.4 Hz, 2H); **^{13}C NMR (101 MHz, CDCl$_3$) δ (ppm)**: 21.72, 25.48, 28.20, 30.95, 34.74, 36.35, 40.43, 47.12, 80.24, 110.73, 124.65, 126.09, 127.21, 130.02, 133.82, 135.78, 143.95, 174.99; **ESI-HRMS (*m/z*)** calcd for [M+Na]$^+$ = 426.1710; found 426.1712.

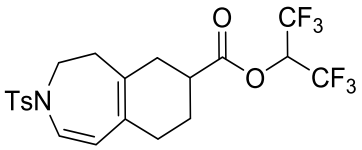

Compound 3ad was obtained from bisallene **1a** (51.8 mg, 0.19 mmol) and 1,1,1,3,3,3-hexafluoroisopropyl acrylate (1.55 mL, 99%, 9.2 mmol), following the general procedure. Purification by column chromatography (silica gel, 40–63 µm, Hexanes/EtOAc) provided **3ad** (49.3 mg, 53% yield) as a yellowish oil and **5a** (4.3 mg, 8% yield) as a colourless solid.

MW ($C_{21}H_{21}F_6NO_4S$): 497.45 g/mol; **Rf**: 0.40 (Hexane/EtOAc 9:1); **IR (ATR) ν (cm^{-1})**: 2926, 1772, 1349, 1197, 1163; **^{1}H NMR (400 MHz, CDCl$_3$) δ (ppm):** 1.65 - 1.77 (m, 1H), 1.98 - 2.06 (m, 1H), 2.11 - 2.40 (m, 6H), 2.45 (s, 3H), 2.67 - 2.76 (m, 1H), 3.52 (ddd, J = 13.6, 6.4, 2.9 Hz, 1H), 3.66 - 3.74 (m, 1H), 4.88 (d, J = 10.3 Hz, 1H), 5.76 (hept, $^3J_{H-F}$ = 6.1 Hz, 1H), 6.72 (d, J = 10.3 Hz, 1H), 7.34 (d, J = 8.4 Hz, 2H), 7.69 (d, J = 8.4 Hz, 2H); **^{13}C NMR (101 MHz, CDCl$_3$) δ (ppm)**: 21.71, 24.92, 30.28, 33.89, 36.21, 38.89, 47.00, 66.51 (quint, $^2J_{C-F}$ = 34.7), 110.11, 120.53 (q, $^1J_{C-F}$ = 283.3) 125.27, 126.37, 127.22, 130.06, 132.29, 135.66, 144.08, 172.16; **ESI-HRMS (*m/z*)** calcd for [M+Na]$^+$ = 520.0988; found 520.1001.

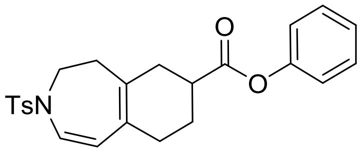

Compound 3ae was obtained from bis(allene) **1a** (50.2 mg, 0.18 mmol) and phenyl acrylate (1.25 mL, 9.1 mmol), following the general procedure. Purification by column chromatography (silica gel, 40–63 µm, Hexanes/EtOAc 98:2 to 90:10) provided **3ae** (50.4 mg, 65% yield) as a pale yellow oil.

MW ($C_{24}H_{25}NO_4S$): 423.53 g/mol; **Rf**: 0.24 (Hexane/EtOAc 9:1); **IR (ATR) ν (cm^{-1})**: 2923, 1748, 1340, 1157; **^{1}H NMR (400 MHz, CDCl$_3$) δ (ppm):** 1.69 - 1.80 (m, 1H), 2.07 - 2.18 (m, 3H), 2.19 - 2.27 (m, 2H), 2.30 - 2.49 (m, 2H), 2.42 (s, 3H), 2.68 - 2.77 (m, 1H), 3.51 (ddd, J = 13.4, 6.2, 2.9 Hz, 1H), 3.67 - 3.74 (m, 1H), 4.90 (d, J = 10.3 Hz, 1H), 6.70 (d, J = 10.3 Hz, 1H), 7.04 (dd, J = 8.6, 1.2 Hz, 2H), 7.19 - 7.24 (m, 1H), 7.31 (d, J = 8.4 Hz, 2H), 7.32 - 7.41 (m, 2H), 7.67 (d, J = 8.4 Hz, 2H); **^{13}C NMR (101 MHz, CDCl$_3$) δ (ppm)**: 21.72, 25.39, 30.78, 34.45, 36.35, 39.61, 47.09, 110.45, 121.58, 124.97, 125.92, 126.26, 127.21, 129.55, 130.05, 133.21, 135.73, 144.02, 150.86, 174.04; **ESI-HRMS (*m/z*)** calcd for [M+Na]$^+$ = 446.1397; found 446.1397.

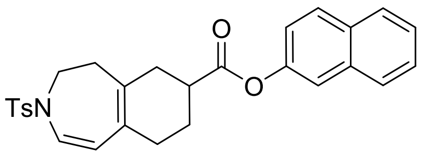

Compound 3af was obtained from bisallene **1a** (49.9 mg, 0.18 mmol) and naphtyl acrylate (909 mg, 4.6 mmol), following the general procedure. Purification by column chromatography (silica gel, 40–63 µm, Hexanes/EtOAc 98:2 to 90:10) provided **3af** (58 mg, 68% yield) as a pale yellow solid.

MW ($C_{28}H_{27}NO_4S$): 473.59 g/mol; **Rf**: 0.34 (Hexane/EtOAc 8:2); **MP (°C):** 144 - 146 (Hexane/EtOAc 9:1); **IR (ATR) *ν* (cm^{-1})**: 2921, 1745, 1345, 1161; **^{1}H NMR (400 MHz, CDCl$_3$) δ (ppm):** 1.73 - 1.86 (m, 1H), 2.12 - 2.30 (m, 5H), 2.34 - 2.54 (m, 2H), 2.42 (s, 3H), 2.74 - 2.82 (m, 1H), 3.53 (ddd, *J* = 13.4, 6.3, 2.9 Hz, 1H), 3.68 - 3.76 (m, 1H), 4.91 (d, *J* = 10.3 Hz, 1H), 6.71 (d, *J* = 10.3 Hz, 1H), 7.18 (dd, *J* = 8.9, 2.3 Hz, 1H), 7.32 (d, *J* = 8.3 Hz, 2H), 7.43 - 7.53 (m, 3H), 7.68 (d, *J* = 8.3 Hz, 2H), 7.79 (dd, *J* = 7.1, 2.1 Hz, 1H), 7.82 - 7.86 (m, 2H); **^{13}C NMR (101 MHz, CDCl$_3$) δ (ppm)**: 21.72, 25.45, 30.83, 34.50, 36.37, 39.70, 47.10, 110.44, 118.53, 121.15, 125.01, 125.83, 126.29, 126.72, 127.21, 127.72, 127.90, 129.53, 130.05, 131.55, 133.20, 133.87, 135.73, 144.02, 148.50, 174.21; **ESI-HRMS (*m/z*)** calcd for [M+Na]$^+$ = 496.1553; found 496.1547.

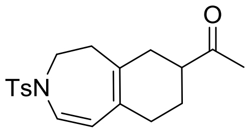

Compound 3ag was obtained from bisallene **1a** (49.5 mg, 0.18 mmol) and 3-buten-2-one (0.74 mL, 99%, 9.0 mmol), following the general procedure. Purification by column chromatography (silica gel, 40–63 µm, Hexanes/EtOAc 98:2 to 90:10) provided **5a** (5.8 mg, 12% yield) as a colourless solid and **3ag** (45 mg, 72% yield) as a yellowish oil.

MW ($C_{19}H_{23}NO_3S$): 345.46 g/mol; **Rf**: 0.17 (Hexane/EtOAc 8:2); **IR (ATR) *ν* (cm^{-1})**: 2921, 1703, 1342, 1160; **^{1}H NMR (400 MHz, CDCl$_3$) δ (ppm):** 1.41 - 1.50 (m, 1H), 1.89 - 1.96 (m, 1H), 2.04 - 2.27 (m, 6H), 2.14 (s, 3H), 2.41 (s, 3H), 2.44 - 2.53 (m, 1H), 3.46 (ddd, *J* = 13.5, 6.8, 2.3 Hz, 1H), 3.64 - 3.72 (m, 1H), 4.85 (d, *J* = 10.3 Hz, 1H), 6.66 (d, *J* = 10.3 Hz, 1H), 7.30 (d, *J* = 8.3 Hz, 2H), 7.65 (d, *J* = 8.3 Hz, 2H); **^{13}C NMR (101 MHz, CDCl$_3$) δ (ppm)**: 21.69, 25.04, 28.16, 31.20, 33.77, 36.40, 47.05, 47.39, 110.46, 124.78, 126.10, 127.17, 130.01, 133.61, 135.70, 143.98, 211.19; **ESI-HRMS (*m/z*)** calcd for [M+Na]$^+$ = 368.1291; found 368.1294.

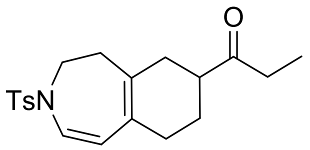

Compound 3ah was obtained from bisallene **1a** (50 mg, 0.18 mmol) and 1-penten-3-one (0.93 mL, 97%, 9.1 mmol), following the general procedure. Purification by column chromatography (silica gel, 40–63 μm, Hexanes/EtOAc 98:2 to 90:10) provided **3ah** (48.8 mg, 75% yield) as a yellowish oil.

MW ($C_{20}H_{25}NO_3S$): 359.48 g/mol; **Rf**: 0.29 (Hexane/EtOAc 8:2); **IR (ATR) ν (cm^{-1})**: 2924, 1704, 1342, 1160; **^{1}H NMR (400 MHz, CDCl$_3$) δ (ppm):** 1.03 (t, *J* = 7.3 Hz, 3H), 1.40 - 1.52 (m, 1H), 1.83 - 1.93 (m, 1H), 2.01 - 2.30 (m, 6H), 2.37 - 2.56 (m, 3H), 2.42 (s, 3H), 3.47 (ddd, *J* = 13.4, 7.1, 2.2 Hz, 1H), 3.65 – 3.74 (m, 1H), 4.86 (d, *J* = 10.3 Hz, 1H), 6.66 (d, *J* = 10.3 Hz, 1H), 7.31 (d, *J* = 8.4 Hz, 2H), 7.66 (d, *J* = 8.4 Hz, 2H); **^{13}C NMR (101 MHz, CDCl$_3$) δ (ppm)**: 7.91, 21.72, 25.30, 31.30, 34.08, 34.10, 36.45, 46.47, 47.08, 110.53, 124.78, 126.08, 127.21, 130.03, 133.82, 135.76, 143.99, 213.86; **ESI-HRMS (*m/z*)** calcd for [M+Na]$^+$ = 382.1447; found 382.1447.

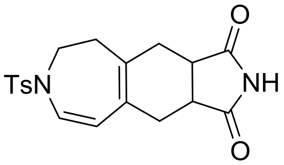

Compound 3ai was obtained from bisallene **1a** (50 mg, 0.18 mmol) and maleimide (88 mg, 0.91 mmol), following the general procedure. Purification by column chromatography (silica gel, 40–63 μm, hexanes/EtOAc 8:2 to 1:1) provided **3ai** (51 mg, 76% yield) as a pale yellow solid.

MW ($C_{19}H_{20}N_2O_4S$): 372.44 g/mol; **Rf**: 0.24 (Hexane/EtOAc 1:1); **MP (°C)**: 221 - 223 (Hexane/EtOAc 1:1); **IR (ATR) ν (cm^{-1})**: 3220, 2924, 1775, 1699, 1331, 1157; **^{1}H NMR (400 MHz, CDCl$_3$) δ (ppm):** 2.25 - 2.35 (m, 4H), 2.42 (s, 3H), 2.44 - 2.56 (m, 2H), 3.02 - 3.12 (m, 2H), 3.41 - 3.57 (m, 2H), 4.97 (d, *J* = 9.9 Hz, 1H), 6.65 (d, *J* = 9.9 Hz, 1H), 7.31 (d, *J* = 8.3 Hz, 2H), 7.64 (d, *J* = 8.3 Hz, 2H), 8.06 (s, 1H); **^{13}C NMR (101 MHz, CDCl$_3$) δ (ppm)**: 21.72, 31.95, 32.17, 38.10, 40.89, 41.00, 46.51, 110.13, 126.84, 127.18, 127.42, 130.10, 135.16, 135.66, 144.22, 179.60, 179.78; **ESI-HRMS (*m/z*)** calcd for [M+Na]$^+$ = 395.1036; found 395.1043.

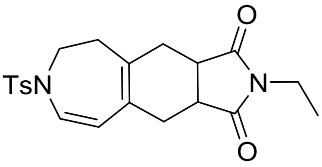

Compound 3aj was obtained from bisallene **1a** (49.8 mg, 0.18 mmol) and N-ethylmaleimide (603 mg, 4.8 mmol), following the general procedure. Purification by column chromatography (silica gel, 40–63 μm, Hexanes/EtOAc 8:2 to 1:1) provided **3aj** (46.5 mg, 64% yield) as a pale yellow solid.

MW ($C_{21}H_{24}N_2O_4S$): 400.49 g/mol; **Rf**: 0.37 (Hexane/EtOAc 1:1); **MP (°C):** 140 - 141 (Hexane/EtOAc 1:1); **IR (ATR) *ν* (cm^{-1})**: 2913, 1764, 1687, 1334, 1160; **^{1}H NMR (400 MHz, CDCl$_3$) δ (ppm):** 0.90 (t, *J* = 7.2 Hz, 3H), 2.14 - 2.36 (m, 4H), 2.41 (s, 3H), 2.47 - 2.58 (m, 2H), 2.94 - 3.04 (m, 2H), 3.39 (d, *J* = 7.2 Hz, 2H), 3.38 - 3.45 (m, 1H), 3.51 (ddd, *J* = 13.7, 6.9, 1.7 Hz, 1H), 4.96 (d, *J* = 10.0 Hz, 1H), 6.63 (d, *J* = 10.0 Hz, 1H), 7.28 (d, *J* = 8.3 Hz, 2H), 7.61 (d, *J* = 8.3 Hz, 2H); **^{13}C NMR (101 MHz, CDCl$_3$) δ (ppm)**: 13.24, 21.69, 32.30, 32.55, 33.81, 37.94, 39.63, 39.71, 46.39, 110.14, 126.55, 127.14, 127.44, 130.04, 135.18, 135.59, 144.11, 179.43, 179.74; **ESI-HRMS (*m/z*)** calcd for [M+Na]$^+$ = 423.1349; found 423.1348.

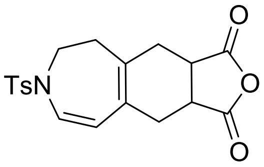

Compound 3ak was obtained from bisallene **1a** (49.6 mg, 0.18 mmol) and maleic anhydride (446 mg, 4.5 mmol), following the general procedure. Purification by column chromatography (silica gel, 40–63 µm, Hexanes/EtOAc 8:2 to 1:1) provided **3ak** (54.8 mg, 81% yield) as a yellow solid.

MW ($C_{19}H_{19}NO_5S$): 373.42 g/mol; **Rf**: 0.46 (Hexane/EtOAc 1:1); **MP (°C):** 156 - 157 (Hexane/EtOAc 1:1); **IR (ATR) *ν* (cm^{-1})**: 2919, 1841, 1769, 1348, 1159; **^{1}H NMR (400 MHz, CDCl$_3$) δ (ppm):** 2.17 - 2.26 (m, 1H), 2.31 - 2.41 (m, 3H), 2.44 (s, 3H), 2.50 - 2.62 (m, 2H), 3.27 - 3.38 (m, 2H), 3.49 - 3.55 (m, 2H), 4.98 (d, *J* = 10 Hz, 1H), 6.71 (d, *J* = 10 Hz, 1H), 7.32 (d, *J* = 8.4 Hz, 2H), 7.63 (d, *J* = 8.4 Hz, 2H); **^{13}C NMR (101 MHz, CDCl$_3$) δ (ppm)**: 21.73, 32.07, 32.20, 37.97, 40.26, 40.33, 46.30, 109.70, 127.09, 127.67, 127.76, 130.22, 134.93, 135.51, 144.49, 173.80, 174.09; **ESI-HRMS (*m/z*)** calcd for [M+Na]$^+$ = 396.0876; found 396.0876.

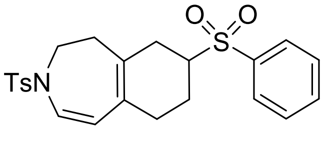

Compound 3al was obtained from bisallene **1a** (50.1 mg, 0.18 mmol) and phenyl vinyl sulfone (828 mg, 4.9 mmol), following the general procedure. Purification by column chromatography (silica gel, 40–63 µm, Hexanes/EtOAc 98:2 to 90:10) provided **3al** (24.7 mg, 31% yield) as a pale yellow solid.

MW ($C_{23}H_{25}NO_4S_2$): 443.58 g/mol; **Rf**: 0.29 (Hexane/EtOAc 7:3); **MP (°C):** 104 - 109 (dec.), (Hexane/EtOAc 9:1); **IR (ATR) ν (cm^{-1})**: 2923, 1343, 1302, 1160, 1143; **^{1}H NMR (400 MHz, CDCl$_3$) δ (ppm):** 1.37 - 1.50 (m, 1H), 1.92 - 2.15 (m, 6H), 2.20 - 2.28 (m, 1H), 2.32 (s, 3H), 2.91 - 3.01 (m, 1H), 3.34 (ddd, *J* = 13.6, 7.0, 2.3 Hz, 1H), 3.50 - 3.57 (m, 1H), 4.71 (d, *J* = 10.3 Hz, 1H), 6.57 (d, *J* = 10.3 Hz, 1H), 7.20 (d, *J* = 8.4 Hz, 2H), 7.43 - 7.50 (m, 2H), 7.51 - 7.59 (m, 3H), 7.72 – 7.81 (m, 2H); **^{13}C NMR (101 MHz, CDCl$_3$) δ (ppm)**: 21.73, 22.19, 30.83, 31.29, 36.21, 46.87, 60.18, 109.54, 125.61, 126.45, 127.20, 129.08, 129.32, 130.09, 131.46, 133.93, 135.56, 137.27, 144.16; **ESI-HRMS (*m/z*)** calcd for [M+Na]$^+$ = 466.1117; found 466.1117.

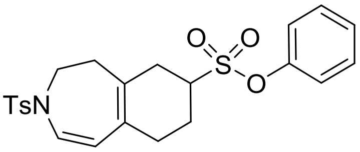

Compound 3am was obtained from bisallene **1a** (50.3 mg, 0.18 mmol) and phenyl vinyl sulfonate (1,0 g 5.4 mmol), following the general procedure. Purification by column chromatography (silica gel, 40–63 µm, Hexanes/EtOAc 98:2 to 90:10) provided **3am** (50.2 mg, 60% yield) as a colourless solid.

MW ($C_{23}H_{25}NO_5S_2$): 459.57 g/mol; **Rf**: 0.48 (Hexane/EtOAc 7:3); **MP (°C):** 125 - 126 (Hexane/EtOAc 9:1); **IR (ATR) ν (cm^{-1})**: 2919, 1364, 1341, 1159, 1143; **^{1}H NMR (400 MHz, CDCl$_3$) δ (ppm):** 1.78 - 1.92 (m, 1H), 2.08 - 2.24 (m, 2H), 2.30 (d, *J* = 7.6 Hz, 2H), 2.34 - 2.41 (m, 1H), 2.43 (s, 3H), 2.47 - 2.55 (m, 1H), 2.58 - 2.69 (m, 1H), 3.29 - 3.40 (m, 1H), 3.49 (ddd, *J* = 13.6, 7.0, 2.3 Hz, 1H), 3.67 - 3.75 (m, 1H), 4.87 (d, *J* = 10.3 Hz, 1H), 6.73 (d, *J* = 10.3 Hz, 1H), 7.21 -7.25 (m, 2H), 7.27 - 7.30 (m, 1H), 7.32 (d, *J* = 8.3 Hz, 2H), 7.36 - 7.42 (m, 2H), 7.66 (d, *J* = 8.3 Hz, 2H); **^{13}C NMR (101 MHz, CDCl$_3$) δ (ppm)**: 21.74, 23.21, 30.59, 32.10, 36.18, 46.89, 56.81, 109.39, 122.09, 125.88, 126.55, 127.22, 127.25, 130.09, 130.12, 131.06, 135.56, 144.21, 149.05; **ESI-HRMS (*m/z*)** calcd for [M+Na]$^+$ = 482.1066; found 482.1078.

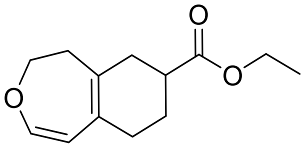

Compound 3ba was obtained from bisallene **1b** (23.4 mg, 0.19 mmol) and ethyl acrylate (1.0 mL, 99%, 9.1 mmol), following the general procedure. Purification by column chromatography (silica gel, 40–63 µm, Hexanes/EtOAc 99:1) provided **3ba** (7.2 mg, 17% yield) as a pale yellow oil.

MW ($C_{13}H_{18}O_3$): 222.28 g/mol; **Rf**: 0.61(Hexane/EtOAc 9:1); **IR (ATR) ν (cm^{-1})**: 2924, 1729; **^{1}H NMR (400 MHz, $CDCl_3$) δ (ppm):** 1.26 (t, *J* = 7.1 Hz, 3H), 1.57 - 1.69 (m, 1H), 1.95 - 2.02 (m, 1H), 2.08 - 2.20 (m, 2H), 2.22 - 2.44 (m, 3H), 2.45 - 2.54 (m, 2H), 4.07 - 4.22 (m, 2H), 4.14 (q, *J* = 7.1 Hz, 2H), 4.57 (d, *J* = 7.9 Hz, 1H), 6.26 (d, *J* = 7.9 Hz, 1H) ; **^{13}C NMR (101 MHz, $CDCl_3$) δ (ppm)**: 14.40, 25.54, 30.72, 34.27, 38.90, 39.77, 60.49, 70.09, 105.83, 126.20, 131.98, 145.02, 175.86; **ESI-HRMS (*m/z*)** calcd for $[M+Na]^+$ = 245.1148; found 245.1146.

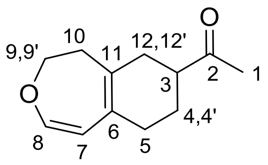

Compound 3bg was obtained from bisallene **1b** (23.4 mg, 0.19 mmol) and 3-buten-2-one (0.74, 99%, mL, 9.0 mmol), following the general procedure. Purification by column chromatography (silica gel, 40–63 µm, Hexanes/EtOAc 98:2) provided **3bg** (10.0 mg, 27% yield) as a pale yellow oil.

MW ($C_{12}H_{16}O_2$): 192.26 g/mol; **Rf**: 0.49 (Hexane/EtOAc 8:2); **IR (ATR) ν (cm^{-1})**: 2923, 1704; **^{1}H NMR (400 MHz, $CDCl_3$) δ (ppm):** 1.44 - 1.57 (m, 1H, H**4**/H**4’**), 1.92 - 2.01 (m, 1H, H**4**/H**4’**), 2.09 - 2.22 (m, 3H, H**5**, H**12**/H**12’**), 2.18 (s, 3H, H**1**), 2.23 - 2.34 (m, 1H, H**12**/H**12’**), 2.36 - 2.50 (m, 2H, H**10**), 2.50 - 2.60 (m, 1H, H**3**), 4.11 (ddd, *J* = 10.9, 6.8, 1.6 Hz, 1H, H**9**/H**9’**), 4.18 (ddd, *J* = 10.9, 5.9, 2.0 Hz, 1H, H**9**/H**9’**), 4.57 (d, *J* = 7.8 Hz, 1H, H**7**), 6.26 (d, *J* = 7.8 Hz, 1H, H**8**) ; **^{13}C NMR (101 MHz, $CDCl_3$) δ (ppm)**: 25.13 (C**4**), 28.21 (C**1**), 31.00 (C**5**), 33.51 (C**12**), 38.96 (C**10**), 47.70 (C**3**), 70.05 (C**9**), 105.73 (C**7**), 126.23 (C**6**), 132.01 (C**11**), 145.08 (C**8**), 211.52 (C**2**); **ESI-HRMS (*m/z*)** calcd for $[M+Na]^+$ = 215.1043; found 215.1037.

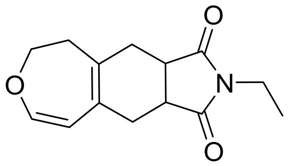

Compound 3bj was obtained from bisallene **1b** (23.4 mg, 0.19 mmol) and N-ethylmaleimide (580 mg, 4.6 mmol), following the general procedure. Purification by column chromatography (silica gel, 40–63 µm, Hexanes/EtOAc 95:5 to 80:20) provided **3bj** (15.0 mg, 32% yield) as a pale yellow oil.

MW ($C_{14}H_{17}NO_3$): 247.29 g/mol; **Rf**: 0.21(Hexane/EtOAc 8:2); **IR (ATR) ν (cm^{-1})**: 2922, 1763, 1684; **^{1}H NMR (400 MHz, $CDCl_3$) δ (ppm):** 1.07 (t, *J* = 7.2 Hz, 3H), 2.27 - 2.38 (m, 2H), 2.47 - 2.63 (m, 4H), 2.99 - 3.06 (m, 2H), 3.48 (q, *J* = 7.2 Hz, 2H), 4.00 (ddd, *J* = 11.2, 6.2, 2.1 Hz, 1H), 4.09 (ddd, *J* = 11.2, 6.1, 2.2 Hz, 1H), 4.68 (d, *J* = 7.6 Hz, 1H), 6.25 (d, *J* = 7.6 Hz, 1H); **^{13}C NMR (101 MHz, $CDCl_3$) δ (ppm)**: 13.34, 31.83, 31.89, 33.90, 39.76, 39.79, 40.00, 69.63, 105.85, 127.48, 133.53, 147.04, 179.71, 180.02; **ESI-HRMS (*m/z*)** calcd for $[M+Na]^+$ = 270.1101; found 270.1107.

Compound 4a

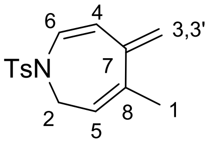

MW ($C_{15}H_{17}NO_2S$): 275.4 g/mol; **Rf**: 0.50 (Hexanes/EtOAc 8:2); **IR (ATR) ν (cm^{-1})**: 2921, 2852, 1456, 1337, 1158, 1090; **^{1}H NMR (400 MHz, CDCl$_3$) δ(ppm):** 1.76 (s, 3H, H**1**), 2.41 (s, 3H, CH$_3$-**Ar**), 3.95 (d, *J* = 7.2 Hz, 2H, H**2**), 5.02 (s, 1H, H**3**/H**3'**), 5.09 (s, 1H, H**3**/H**3'**), 5.37 (d, *J* = 10.4 Hz, 1H, H**4**), 5.55 (t, *J* = 7.2 Hz, 1H, H**5**), 6.52 (d, *J* = 10.4, 1H, H**6**), 7.28 (d, *J* = 8.4 Hz, 2H, H-**Ar**), 7.66 (d, *J* = 8.4, 2H, H-**Ar**); **^{13}C NMR (101 MHz, CDCl$_3$) δ (ppm)**: 21.64 (CH$_3$-**Ar**), 23.01 (C**1**), 45.60 (C**2**), 113.72 (C**4**), 117.68 (C**3**), 120.91 (C**5**), 127.01 (C**6**),127.13 (CH-**Ar**), 129.83 (CH-**Ar**), 136.24 (C-**Ar**), 142.06 (C**7**), 143.46 (C**8**), 143.90 (C-**Ar**); **ESI-HRMS (*m/z*)** calcd for [M+Na]$^+$ = 298.0872; found: 298.0875.

Scheme S9. Mechanistic experiments using compound **5a** and ethyl acrylate **2a**

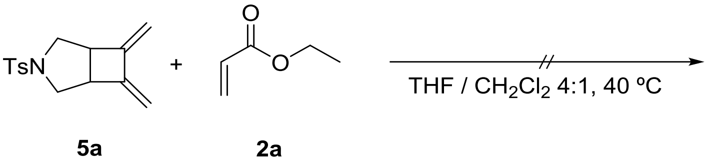

In a 25 mL round-bottom flask equipped with a magnetic stirrer and an inert atmosphere, a solution of **5a** (15 mg, 0.055 mmol) and ethyl acrylate **2a** (0.3 mL, 275 mg, 2.75 mmol) in a 4:1 mixture of THF/CH$_2$Cl$_2$ (6 mL) was stirred at 40 °C for 16h. The solvent and ethyl acrylate **2a** were removed under reduced pressure. ^{1}H NMR analysis of the crude product revealed the presence of unaltered starting material **5a**.

Scheme S10. Mechanistic experiments using compound **5a**, ethyl acrylate **2a** and Rh(I) catalyst

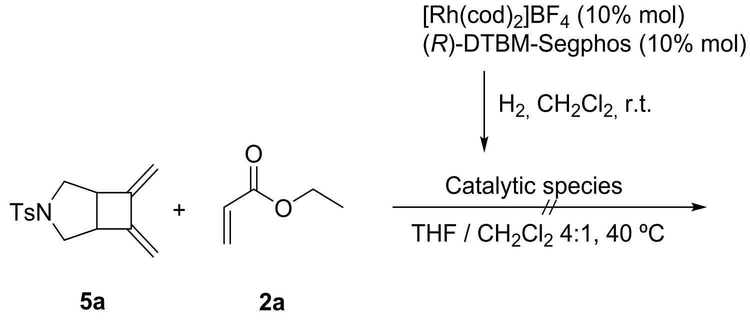
[Rh(cod)2]BF4 (10% mol)
(R)-DTBM-Segphos (10% mol)
H2, CH2Cl2, r.t.
Catalytic species
THF / CH2Cl2 4:1, 40 ºC
TsN
O
O
+
5a
2a

In a 10 mL capped vial, a mixture of [Rh(cod)$_2$]BF$_4$ (4.26 mg, 0.010 mmol) and *(R)*-DTBM-Segphos (12.4 mg, 0.011 mmol) was purged with nitrogen and dissolved in anhydrous CH$_2$Cl$_2$ (4 mL). Hydrogen gas was bubbled into the catalyst solution for 30 min. The resulting mixture was concentrated to dryness, dissolved again in anhydrous CH$_2$Cl$_2$ (2 mL) and transferred via syringe into a 40 °C preheated solution of **5a** (29 mg, 0.11 mmol) and ethyl acrylate **2a** (0.6 mL, 550 mg, 5.33 mmol) in anhydrous THF (10 mL) and under inert atmosphere. The resulting mixture was stirred at 40 °C for 16h. The solvent and ethyl acrylate **2a** were removed under reduced pressure and the crude reaction mixture was filtered through a short silica gel pad (Hexanes/EtOAc 8:2 v/v). ^{1}H NMR analysis of the crude product revealed the presence of unaltered starting material **5a**.

Scheme S6. Mechanistic experiments using compound **1a** and Rh(I) catalyst

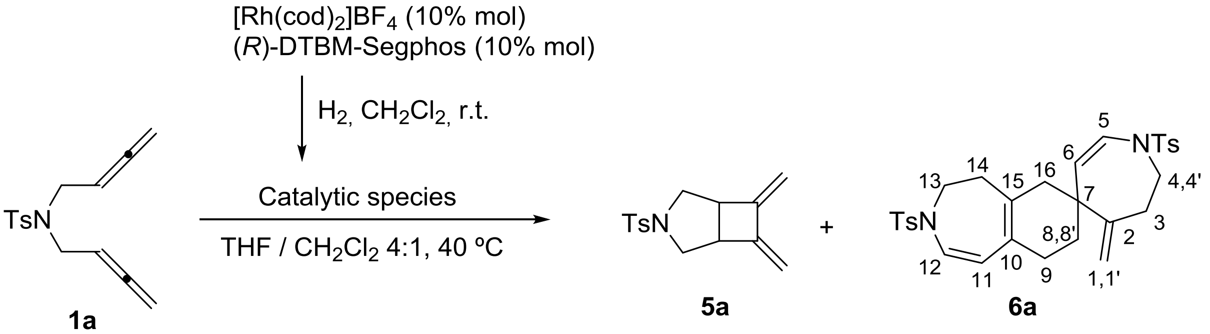
[Rh(cod)2]BF4 (10% mol)
(R)-DTBM-Segphos (10% mol)
H2, CH2Cl2, r.t.
Catalytic species
THF / CH2Cl2 4:1, 40 ºC
TsN
1a
TsN
+
5a
TsN
NTs
5
6
4,4'
16
14
13
15
7
3
8,8'
2
12
10
11
9
1,1'
6a

In a 10 mL capped vial, a mixture of [Rh(cod)$_2$]BF$_4$ (7.4 mg, 0.018 mmol) and *(R)*-DTBM-Segphos (23.6 mg, 0.020 mmol) was purged with nitrogen and dissolved in anhydrous CH$_2$Cl$_2$ (4 mL). Hydrogen gas was bubbled into the catalyst solution and the mixture was stirred for 30 min. The resulting mixture was concentrated to dryness, dissolved again in anhydrous CH$_2$Cl$_2$ (4 mL) and transferred via syringe into a preheated solution to 40 °C of bisallene **1a** (48.4 mg, 0.18 mmol) in anhydrous THF (16 mL) and under inert atmosphere. The resulting mixture was stirred at 40 °C for 16 h. The solvent was removed under reduced pressure and the crude reaction mixture was purified by column chromatography on silica gel using hexane/EtOAc mixtures as the eluent (95:5 to 90:10 v/v), affording first, compound **5a** (5.5 mg, 12% yield) as a colourless solid, and second, **6a** (28.3 mg, 58% yield) as a pale yellow solid.

6a: **MW** ($C_{30}H_{34}N_2O_4S_2$): 550.73 g/mol; **Rf**: 0.26 (Hexane/EtOAc 8:2); **MP (°C):** 87-92 (dec); **IR (ATR) ν (cm^{-1})**: 2921, 1336, 1156; **^{1}H NMR (400 MHz, CDCl$_3$) δ (ppm):** 1.46 - 1.55 (m, 1H, H**8**/H**8’**), 1.56 - 1.66 (m, 1H, H**8**/H**8’**), 1.93 - 2.20 (m, 6H, H**9**, H**14**, H**16**), 2.42 (s, 3H, CH_3-**Ar**), 2.42 (s, 3H, CH_3-**Ar**), 2.43 - 2.55 (m, 2H, H**3**), 3.38 - 3.48 (m, 1H, H**4**/H**4’**), 3.49 - 3.66 (m, 3H, H**4**/H**4’**,H**13**), 4.52 (s, 1H, H**1**/H**1’**), 4.63 (s, 1H, H**1**/H**1’**), 4.71 (d, *J* = 9.5 Hz, 1H, H**6**), 4.84 (d, *J* = 10.3 Hz, 1H, H**11**), 6.27 (d, *J* = 9.5 Hz, 1H, H**5**), 6.64 (d, *J* = 10.3 Hz, 1H, H**12**), 7.28 (d, *J* = 8.2 Hz, 2H, CH-**Ar**), 7.31 (d, *J* = 8.2 Hz, 2H, CH-**Ar**), 7.66 (m, 4H, CH-**Ar**); **^{13}C NMR (101 MHz, CDCl$_3$) δ (ppm)**: 21.67 (CH_3-**Ar**), 21.71 (CH_3-**Ar**), 29.10 (C**9**), 32.71 (C**8**), 34.74 (C**3**), 36.69 (C**14**), 42.46 (C**7**), 44.58 (C**16**), 47.03 (C**13**), 50.10 (C**4**), 110.59 (C**11**), 111.82 (C**1**), 122.64 (C**6**), 124.72 (C**12**), 125.67 (C**5**), 125.83 (C**10**), 127.18 (CH-**Ar**), 127.19 (CH-**Ar**), 129.78 (CH-**Ar**), 130.01 (CH-**Ar**), 132.95 (C**15**), 135.83 (C-**Ar**), 136.25 (C-**Ar**), 143.72 (C-**Ar**), 143.97(C-**Ar**), 149.30 (C**2**); **ESI-HRMS (*m/z*)** calcd for $[M+Na]^+$ = 573.1852; found 573.1836.

Scheme S11. Synthesis of **7a**

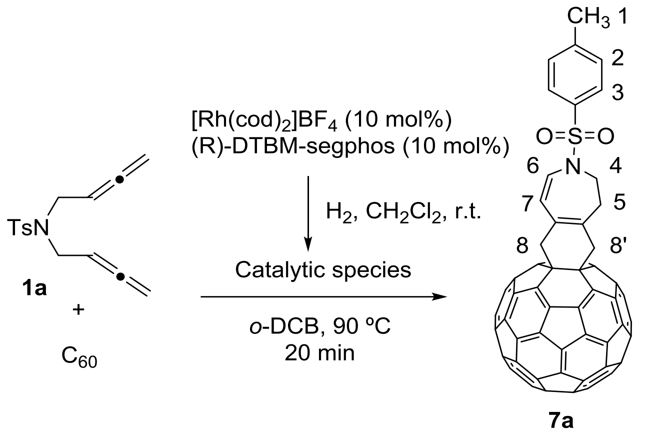

In a 10 mL capped vial in an inert atmosphere, a solution of $[Rh(cod)_2]BF_4$ (2.2 mg, 0.0054 mmol, 0.1 equivalents) and *(R)*-DTBM-Segphos (6.4 mg, 0.0054 mmol, 0.1 equivalents) in anhydrous CH_2Cl_2 (4 mL) was prepared. Hydrogen gas was bubbled into the catalyst solution for 30 min before it was concentrated to dryness, dissolved in anhydrous *o*-DCB and introduced into a solution of C_{60} (43.2 mg, 0.06 mmol, 1.1 equivalents) and the corresponding (15 mg, 0.054 mmol, 1 equivalent) in anhydrous *o*-DCB (1.4 mM), preheated to 90 °C. The resulting mixture was stirred at 90 °C for 20 min, allowed to cool down to room temperature and directly subjected to column chromatography on silica gel using CS_2 as the eluent to provide unreacted. Furthert elution with toluene gave compound **7a** (31 mg, 56%) as a dark brown solid.

MW ($C_{75}H_{17}NO_2S$): 996.03 g/mol; **Rf**: 0.5 (toluene); **IR (ATR) ν (cm^{-1})**: 3082, 1344, 1159; **^{1}H NMR (400 MHz, CDCl$_3$) δ (ppm):** 2.39 (s, 3H, H**1**), 2.86 (t, *J* = 4.8 Hz, 2H, H**5**), 3.97 (t, *J* = 4.8 Hz, 2H, H**4**), 3.93-4.16 (m, 4H, H**8**//H**8’**)**,** 5.57 (d, *J* = 9.6 Hz, 1H, H**7**), 6.97 (d, *J* = 9.6 Hz, 1H, H**6**), 7.35 (d, *J* = 8.1 Hz, 2H, H**Ar**), 7.78 (d, *J* = 8.1, 2H, H**Ar**); **^{13}C NMR (101 MHz, CDCl$_3$) δ (ppm):** 14.3, 35.9, 48.9, 57.4, 61.7, 62.1, 65.2, 77.2, 135.0, 140.3, 141.8, 142.2, 142.2, 142.3, 142.3, 142.5, 142.6, 142.7, 142.8, 143.3, 143.3, 143.7, 144.9, 144.9, 145.5, 145.6, 145.6, 145.6, 145.7, 146.0, 146.1, 146.4, 146.4, 146.6, 146.7, 146.7, 146.7, 147.8, 156.8; **UV-vis ($CHCl_3$) λ_{max}:** 437 nm; **ESI-HRMS (*m/z*)** calcd for $[M+Na]^+$ = 1018.0844; found 1018.0872.

Supplementary material for chapter 7

Table S2. UB3LYP/6-31G(d,p) reaction energies (Δ*E*r) of all possible $^{\#6094}C_{68}$-Cp adducts.

[6,6] ISOMERS					
ISOMER	#C INVOLVED	JUNCTION TYPE	*E*	Δ*E* (Hartree)	Δ*E* (kcal·mol^{-1})
1 (S = 0)	28 9	B	-2785.21802	0.014628373	9.2
1 (S = 1)	28 9	B	-2785.233088	-0.000439797	-0.3
2 (S = 0)	42 47	B	-2785.252070	-0.019421927	-12.2
2 (S = 1)	42 47	B	-2785.253129	-0.020480147	-12.9
3 (S = 0)	18 61	A	-2785.258682	-0.026033937	-16.3
3 (S = 1)	18 61	A	-2785.264227	-0.031578467	-19.8
4a (S = 0)	65 66	A	-2785.249735	-0.017086007	-10.7
4a (S = 1)	65 66	A	-2785.263416	-0.030767217	-19.3
4b (S = 0)	65 66	A	-2785.249814	-0.017165607	-10.8
4b (S = 1)	65 66	A	-2785.263244	-0.030595777	-19.2
5a (S = 0)	52 53	A	-2785.252113	-0.019464967	-12.2
5a (S = 1)	52 53	A	-2785.257024	-0.024375307	-15.3
5b (S = 0)	52 53	A	-2785.252569	-0.019920487	-12.5
5b (S = 1)	52 53	A	-2785.257129	-0.024480267	-15.4
6a (S = 0)	7 8	B	-2785.240014	-0.007365727	-4.6
6a (S = 1)	7 8	B	-2785.243208	-0.010559837	-6.6
6b (S = 0)	7 8	B	-2785.239185	-0.006536097	-4.1
6b (S = 1)	7 8	B	-2785.242712	-0.010063497	-6.3
7a (S = 0)	28 29	B	-2785.238351	-0.005702387	-3.6
7a (S = 1)	28 29	B	-2785.238957	-0.006308197	-4.0
7b (S = 0)	28 29	B	-2785.238523	-0.005874867	-3.7
7b (S = 1)	28 29	B	-2785.239037	-0.006388677	-4.0
8a (S = 0)	42 43	B	-2785.235404	0.00363307	2.3
8a (S = 1)	42 43	B	-2785.236294	0.0027435	1.7
8b (S = 0)	42 43	B	-2785.238523	0.00051438	0.3
8b (S = 1)	42 43	B	-2785.239037	-1.80000E-07	0.0
9a (S = 0)	6 7	C	-2785.212983	0.02605362	16.3
9a (S = 1)	6 7	C	-2785.220926	0.01811134	11.4
9b (S = 0)	6 7	C	-2785.213157	0.02588015	16.2
9b (S = 1)	6 7	C	-2785.220281	0.01875625	11.8
10a (S = 0)	7 30	B	-2785.24128	-0.00224311	-1.4
10a (S = 1)	7 30	B	-2785.236294	0.0027435	1.7
10b (S = 0)	7 30	B	-2785.241730	-0.00269335	-1.7
10b (S = 1)	7 30	B	-2785.234228	0.00480931	3.0
11a (S = 0)	5 32	B	-2785.225893	0.01314406	8.2
11a (S = 1)	5 32	B	-2785.23062	0.00841667	5.3
11b (S = 0)	5 32	B	-2785.226635	0.01240183	7.8
11b (S = 1)	5 32	B	-2785.231269	0.00776754	4.9
12a (S = 0)	5 6	C	-2785.217273	0.02176427	13.7
12a (S = 1)	5 6	C	-2785.215896	0.02314124	14.5
12b (S = 0)	5 6	C	-2785.217904	0.02113345	13.3
12b (S = 1)	5 6	C	-2785.216655	0.02238163	14.0
13a (S = 0)	6 51	B	-2785.248243	-0.00920554	-5.8
13a (S = 1)	6 51	B	-2785.251586	-0.01254914	-7.9
13b (S = 0)	6 51	B	-2785.248379	-0.00934231	-5.9
13b (S = 1)	6 51	B	-2785.251361	-0.01232374	-7.7
14a (S = 0)	49 50	A	-2785.24692	-0.00788258	-4.9
14a (S = 1)	49 50	A	-2785.256616	-0.01757887	-11.0
14b (S = 0)	49 50	A	-2785.246992	-0.00795498	-5.0
14b (S = 1)	49 50	A	-2785.256853	-0.01781649	-11.2
15a (S = 0)	4 5	B	-2785.226787	0.01225013	7.7
15a (S = 1)	4 5	B	-2785.238694	0.00034322	0.2
15b (S = 0)	4 5	B	-2785.226944	0.01209262	7.6
15b (S = 1)	4 5	B	-2785.237957	0.00107984	0.7

16a (S = 0)	3 34	B	-2785.229184	0.00985337	6.2
16a (S = 1)	3 34	B	-2785.240732	-0.00169451	-1.1
16b (S = 0)	3 34	B	-2785.229943	0.00909421	5.7
16b (S = 1)	3 34	B	-2785.240985	-0.00194787	-1.2
17a (S = 0)	33 34	B	-2785.241278	-0.00224066	-1.4
17a (S = 1)	33 34	B	-2785.246567	-0.00753024	-4.7
17b (S = 0)	33 34	B	-2785.241816	-0.00277908	-1.7
17b (S = 1)	33 34	B	-2785.246807	-0.00777002	-4.9
18a (S = 0)	45 46	A	-2785.252561	-0.01352406	-8.5
18a (S = 1)	45 46	A	-2785.255979	-0.01694211	-10.6
18b (S = 0)	45 46	A	-2785.252945	-0.01390793	-8.7
18b (S = 1)	45 46	A	-2785.256615	-0.0175777	-11.0
19a (S = 0)	35 36	B	-2785.232716	0.00632057	4.0
19a (S = 1)	35 36	B	-2785.235496	0.00354096	2.2
19b (S = 0)	35 36	B	-2785.231666	0.00737094	4.6
19b (S = 1)	35 36	B	-2785.234905	0.00413206	2.6
20a (S = 0)	19 35	B	-2785.231548	0.00748909	4.7
20a (S = 1)	19 35	B	-2785.238148	0.00088901	0.6
20b (S = 0)	19 35	B	-2785.231032	0.00800468	5.0
20b (S = 1)	19 35	B	-2785.237024	0.0020128	1.3
21 a (S = 0)	34 35	C	-2785.189547	0.04949045	31.1
21 a (S = 1)	34 35	C	-2785.202525	0.03651204	22.9
21b (S = 0)	34 35	C	-2785.189425	0.04961213	31.1
21b (S = 1)	34 35	C	-2785.202556	0.03648075	22.9
22a (S = 0)	1 2	A	-2785.250241	-0.01120377	-7.0
22a (S = 1)	1 2	A	-2785.259478	-0.02044099	-12.8
22b (S = 0)	1 2	A	-2785.249946	-0.01090893	-6.8
22b (S = 1)	1 2	A	-2785.258911	-0.01987404	-12.5
23a (S = 0)	48 62	A	-2785.254586	-0.01554853	-9.8
23a (S = 1)	48 62	A	-2785.264396	-0.02535868	-15.9
23b (S = 0)	48 62	A	-2785.254653	-0.01561647	-9.8
23b (S = 1)	48 62	A	-2785.264493	-0.02545556	-16.0
24a (S = 0)	63 64	A	-2785.248611	-0.00957419	-6.0
24a (S = 1)	63 64	A	-2785.262108	-0.02307068	-14.5
24b (S = 0)	63 64	A	-2785.248566	-0.00952876	-6.0
24b (S = 1)	63 64	A	-2785.262167	-0.02312996	-14.5

[5,6] ISOMERS					
ISOMER	# C INVOLVED	JUNCTION TYPE	*E*	Δ*E* (Hartree)	Δ*E* (kcal·mol^{-1})
1a (S = 0)	8 9	D	-2785.259483	-0.02044609	-12.8
1a (S = 1)	8 9	D	-2785.253054	-0.01401707	-8.8
1b (S = 0)	8 9	D	-2785.260553	-0.02151643	-13.5
1b (S = 1)	8 9	D	-2785.254756	-0.01571866	-9.9
2a (S = 0)	8 53	D	-2785.243154	-0.00411655	-2.6
2a (S = 1)	8 53	D	-2785.245131	-0.00609431	-3.8
2b (S = 0)	8 53	D	-2785.243432	-0.00439514	-2.8
2b (S = 1)	8 53	D	-2785.245877	-0.00684037	-4.3
3a (S = 0)	53 54	D	-2785.2303104	0.0087266	5.5
3a (S = 1)	53 54	D	-2785.2244256	0.01461142	9.2
3b (S = 0)	53 54	D	-2785.230095	0.00894245	5.6
3b (S = 1)	53 54	D	-2785.22417	0.0148674	9.3
4a (S = 0)	46 47	D	-2785.26534	-0.02630341	-16.5
4a (S = 1)	46 47	D	-2785.252685	-0.0136482	-8.6
4b (S = 0)	46 47	D	-2785.264653	-0.02561635	-16.1
4b (S = 1)	46 47	D	-2785.251459	-0.01242213	-7.8

5a (S = 0)	36 46	D	-2785.241432	-0.00239513	-1.5
5a (S = 1)	36 46	D	-2785.231826	0.00721103	4.5
5b (S = 0)	36 46	D	-2785.241332	-0.00229495	-1.4
5b (S = 1)	36 46	D	-2785.232789	0.00624809	3.9
6a (S = 0)	36 37	D	-2785.239337	-0.00030038	-0.2
6a (S = 1)	36 37	D	-2785.246895	-0.00785768	-4.9
6b (S = 0)	36 37	D	-2785.237458	0.00157863	1.0
6b (S = 1)	36 37	D	-2785.244458	-0.00542108	-3.4
7a (S = 0)	19 20	D	-2785.243567	-0.00452977	-2.8
7a (S = 1)	19 20	D	-2785.24492	-0.00588296	-3.7
7b (S = 0)	19 20	D	-2785.241409	-0.00237237	-1.5
7b (S = 1)	19 20	D	-2785.242584	-0.00354723	-2.2
8a (S = 0)	1 19	D	-2785.243644	-0.00460673	-2.9
8a (S = 1)	1 19	D	-2785.234736	0.00430135	2.7
8b (S = 0)	1 19	D	-2785.24276	-0.00372267	-2.3
8b (S = 1)	1 19	D	-2785.233668	0.0053695	3.4
9a (S = 0)	1 18	D	-2785.239431	-0.00039398	-0.2
9a (S = 1)	1 18	D	-2785.235724	0.00331266	2.1
9b (S = 0)	1 18	D	-2785.240111	-0.0010735	-0.7
9b (S = 1)	1 18	D	-2785.236723	0.00231403	1.5
10a (S = 0)	29 30	D	-2785.265834	-0.02679655	-16.8
10a (S = 1)	29 30	D	-2785.264587	-0.02554991	-16.0
10b (S = 0)	29 30	D	-2785.26443	-0.0253934	-15.9
10b (S = 1)	29 30	D	-2785.262903	-0.02386591	-15.0
11a (S = 0)	30 31	F	-2785.275429	-0.03639178	-22.8
11a (S = 1)	30 31	F	-2785.274133	-0.03509597	-22.0
11b (S = 0)	30 31	F	-2785.276211	-0.03717432	-23.3
11b (S = 1)	30 31	F	-2785.275315	-0.03627827	-22.8
12a (S = 0)	29 43	D	-2785.261874	-0.02283734	-14.3
12a (S = 1)	29 43	D	-2785.26192	-0.0228829	-14.4
12b (S = 0)	29 43	D	-2785.262346	-0.02330909	-14.6
12b (S = 1)	29 43	D	-2785.263396	-0.02435932	-15.3
13a (S = 0)	43 44	F	-2785.281602	-0.048953747	-30.7
13a (S = 1)	43 44	F	-2785.28033	-0.047681987	-29.9
13b (S = 0)	43 44	F	-2785.282388	-0.049739427	-31.2
13b (S = 1)	43 44	F	-2785.281677	-0.049028617	-30.8
14a (S = 0)	44 45	F	-2785.272267	-0.03323	-20.9
14a (S = 1)	44 45	F	-2785.263854	-0.02481716	-15.6
14b (S = 0)	44 45	F	-2785.271622	-0.03258452	-20.4
14b (S = 1)	44 45	F	-2785.262992	-0.02395546	-15.0
15a (S = 0)	32 33	D	-2785.253731	-0.01469351	-9.2
15a (S = 1)	32 33	D	-2785.254612	-0.01557505	-9.8
15b (S = 0)	32 33	D	-2785.251581	-0.01254375	-7.9
15b (S = 1)	32 33	D	-2785.252019	-0.01298194	-8.1
16a (S = 0)	33 45	D	-2785.249575	-0.01053805	-6.6
16a (S = 1)	33 45	D	-2785.245713	-0.00667581	-4.2
16b (S = 0)	33 45	D	-2785.250291	-0.01125366	-7.1
16b (S = 1)	33 45	D	-2785.246598	-0.00756113	-4.7
17a (S = 0)	31 32	F	-2785.272452	-0.03341456	-21.0

17a (S = 1)	31 32	F	-2785.267399	-0.02836237	-17.8
17b (S = 0)	31 32	F	-2785.273489	-0.03445222	-21.6
17b (S = 1)	31 32	F	-2785.2688	-0.02976282	-18.7
18a (S = 0)	51 52	D	-2785.22968	0.0093567	5.9
18a (S = 1)	51 52	D	-2785.237314	0.00172294	1.1
18b (S = 0)	51 52	D	-2785.229703	0.00933406	5.9
18b (S = 1)	51 52	D	-2785.238897	0.00014016	0.1
19a (S = 0)	52 65	D	-2785.218949	0.02008812	12.6
19a (S = 1)	52 65	D	-2785.228929	0.01010784	6.3
19b (S = 0)	52 65	D	-2785.218825	0.02021202	12.7
19b (S = 1)	52 65	D	-2785.228638	0.01039878	6.5
20a (S = 0)	64 65	D	-2785.219312	0.01972523	12.4
20a (S = 1)	64 65	D	-2785.231582	0.00745462	4.7
20b (S = 0)	64 65	D	-2785.220314	0.01872289	11.7
20b (S = 1)	64 65	D	-2785.232929	0.00610766	3.8
21a (S = 0)	50 64	D	-2785.219059	0.01997807	12.5
21a (S = 1)	50 64	D	-2785.228678	0.01035902	6.5
21b (S = 0)	50 64	D	-2785.219507	0.01953029	12.3
21b (S = 1)	50 64	D	-2785.22935	0.00968672	6.1
22a (S = 0)	50 51	D	-2785.231704	0.00733331	4.6
22a (S = 1)	50 51	D	-2785.237678	0.00135947	0.9
22b (S = 0)	50 51	D	-2785.230329	0.00870753	5.5
22b (S = 1)	50 51	D	-2785.236345	0.00269178	1.7
23a (S = 0)	4 49	D	-2785.226551	0.01248612	7.8
23a (S = 1)	4 49	D	-2785.235921	0.0031164	2.0
23b (S = 0)	4 49	D	-2785.226591	0.0124457	7.8
23b (S = 1)	4 49	D	-2785.235503	0.00353441	2.2
24a (S = 0)	48 49	D	-2785.224699	0.01433836	9.0
24a (S = 1)	48 49	D	-2785.227178	0.0118594	7.4
24b (S = 0)	48 49	D	-2785.225003	0.01403364	8.8
24b (S = 1)	48 49	D	-2785.227766	0.01127085	7.1
25a (S = 0)	2 48	D	-2785.224852	0.01418516	8.9
25a (S = 1)	2 48	D	-2785.234431	0.00460556	2.9
25b (S = 0)	2 48	D	-2785.225241	0.01379627	8.7
25b (S = 1)	2 48	D	-2785.23519	0.00384718	2.4
26a (S = 0)	2 3	D	-2785.243748	-0.0047113	-3.0
26a (S = 1)	2 3	D	-2785.243638	-0.00460133	-2.9
26b (S = 0)	2 3	D	-2785.244703	-0.00566646	-3.6
26b (S = 1)	2 3	D	-2785.244426	-0.00538908	-3.4
27a (S = 0)	3 4	D	-2785.240823	-0.00178601	-1.1
27a (S = 1)	3 4	D	-2785.246444	-0.00740745	-4.6
27b (S = 0)	3 4	D	-2785.24318	-0.0041429	-2.6
27b (S = 1)	3 4	D	-2785.248897	-0.00986012	-6.2
28a (S = 0)	61 62	D	-2785.227731	0.01130612	7.1
28a (S = 1)	61 62	D	-2785.235213	0.00382448	2.4
28b (S = 0)	61 62	D	-2785.226477	0.01256027	7.9
28b (S = 1)	61 62	D	-2785.235213	0.00382448	2.4
29a (S = 0)	62 63	D	-2785.22313	0.01590655	10.0
29a (S = 1)	62 63	D	-2785.231363	0.00767384	4.8

29b (S = 0)	62 63	D	-2785.222185	0.01685173	10.6
29b (S = 1)	62 63	D	-2785.230204	0.00883299	5.5
30a (S = 0)	63 68	D	-2785.222817	0.0162197	10.2
30a (S = 1)	63 68	D	-2785.234007	0.00503025	3.2
30b (S = 0)	63 38	D	-2785.22178	0.01725738	10.8
30b (S = 1)	63 68	D	-2785.233084	0.00595267	3.7

[5,5] ISOMERS					
ISOMER	# C INVOLVED	JUNCTION TYPE	*E*	Δ*E* (Hartree)	Δ*E* (kcal·mol^{-1})
1a (S = 0)	31 44	E	-2785.293944	-0.061295067	-38.5
1a (S = 1)	31 44	E	-2785.286092	-0.053443987	-33.5
1b (S = 0)	31 44	E	-2785.29347	-0.0544325	-34.2
1b (S = 1)	31 44	E	-2785.285866	-0.04682901	-29.4

Figure S 16. UB3LYP-D3/6-31G(d,p) Gibbs energy profile for the formation of adduct [6,6]. All energies are relative to infinitely separated reactants and are given in kcal·mol^{-1}.

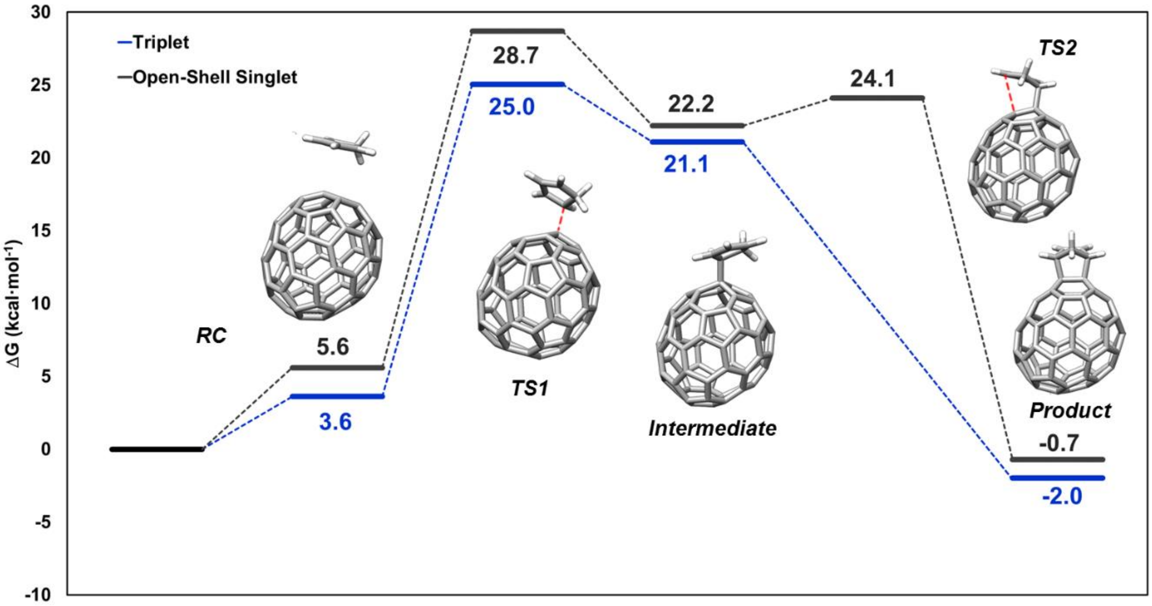

Figure S17. UB3LYP-D3/6-31G(d,p) Gibbs energy profile for the formation of adduct [5,6]F. All energies are relative to infinitely separated reactants and are given in kcal·mol^{-1}.

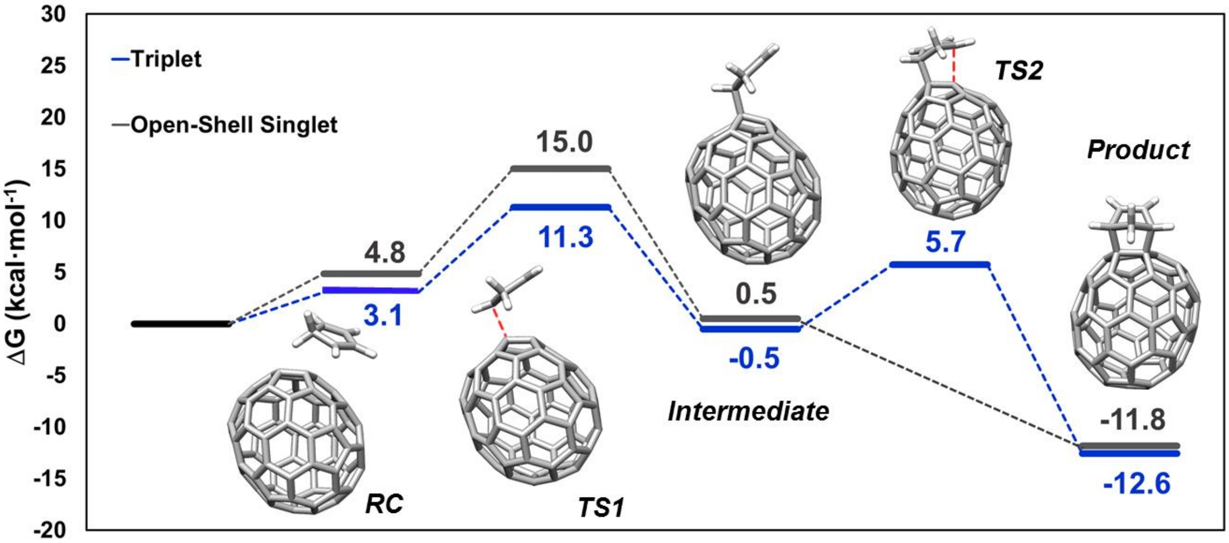

Figure S18. UB3LYP-D3/6-31G(d,p) Gibbs energy profile for the formation of adduct [5,5]. All energies are relative to infinitely separated reactants and are given in kcal·mol^{-1}.

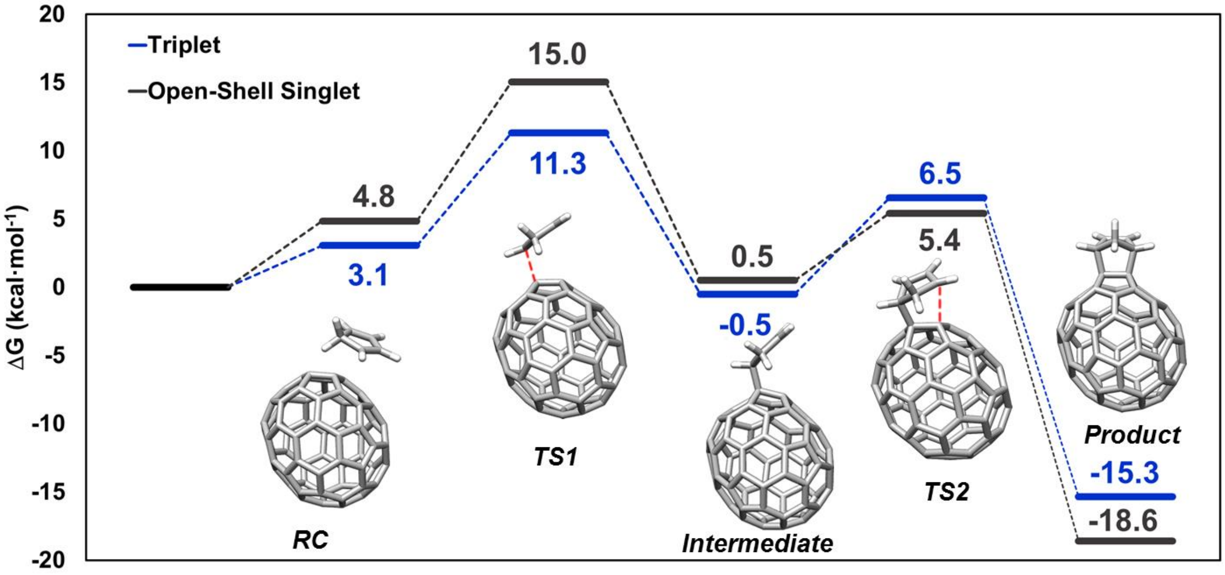

Figure S19. UB3LYP-D3/6-31G(d,p) Gibbs energy profile for the formation of adduct [5,6]D. All energies are relative to infinitely separated reactants and are given in kcal·mol^{-1}.

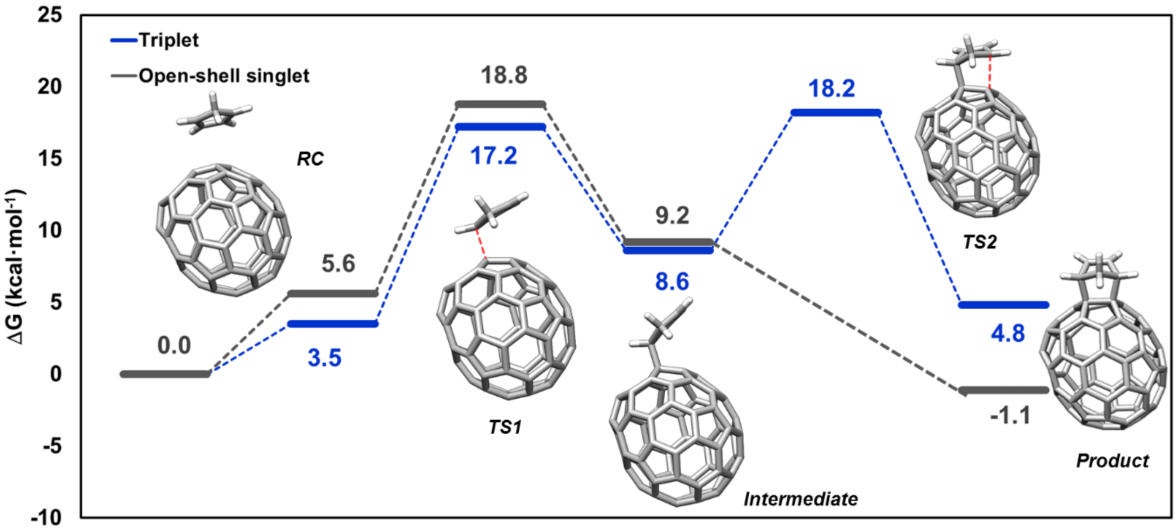

Figure S20. UB3LYP-D3/6-31G(d,p) Relaxed scan between biradical intermediate and reaction product (triplet state, path [6,6]).

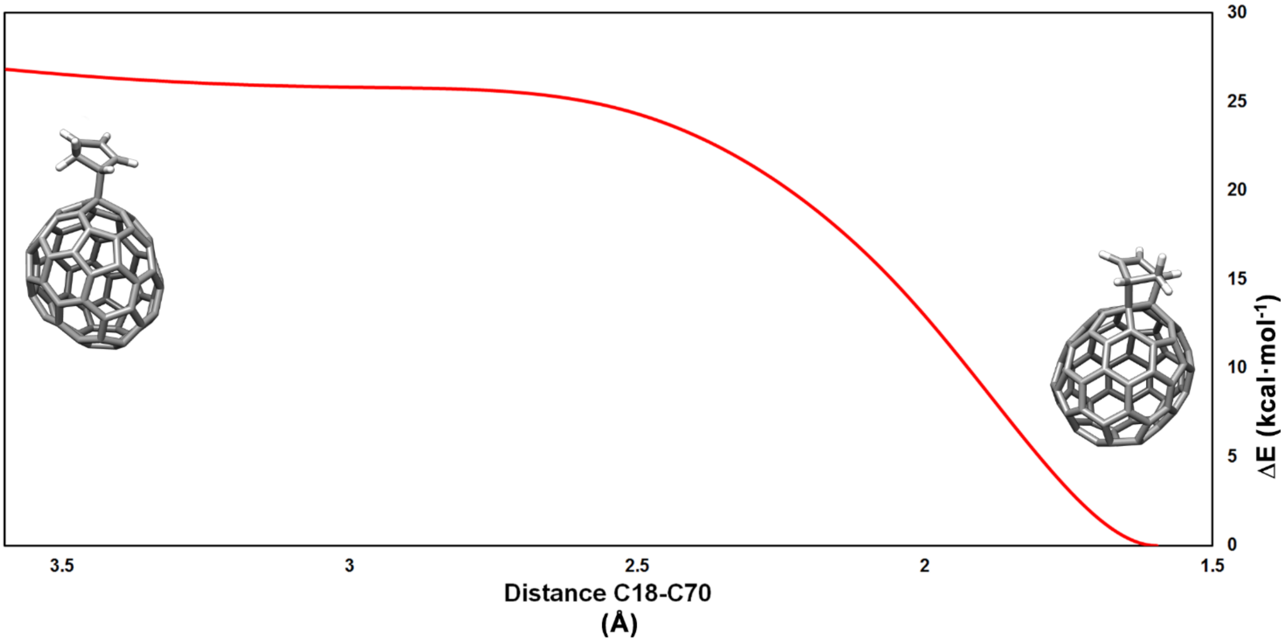

Figure S21. UB3LYP-D3/6-31G(d,p) Relaxed scan between biradical intermediate and reaction product (Open-shell singlet state, path $[5,6]_F$).

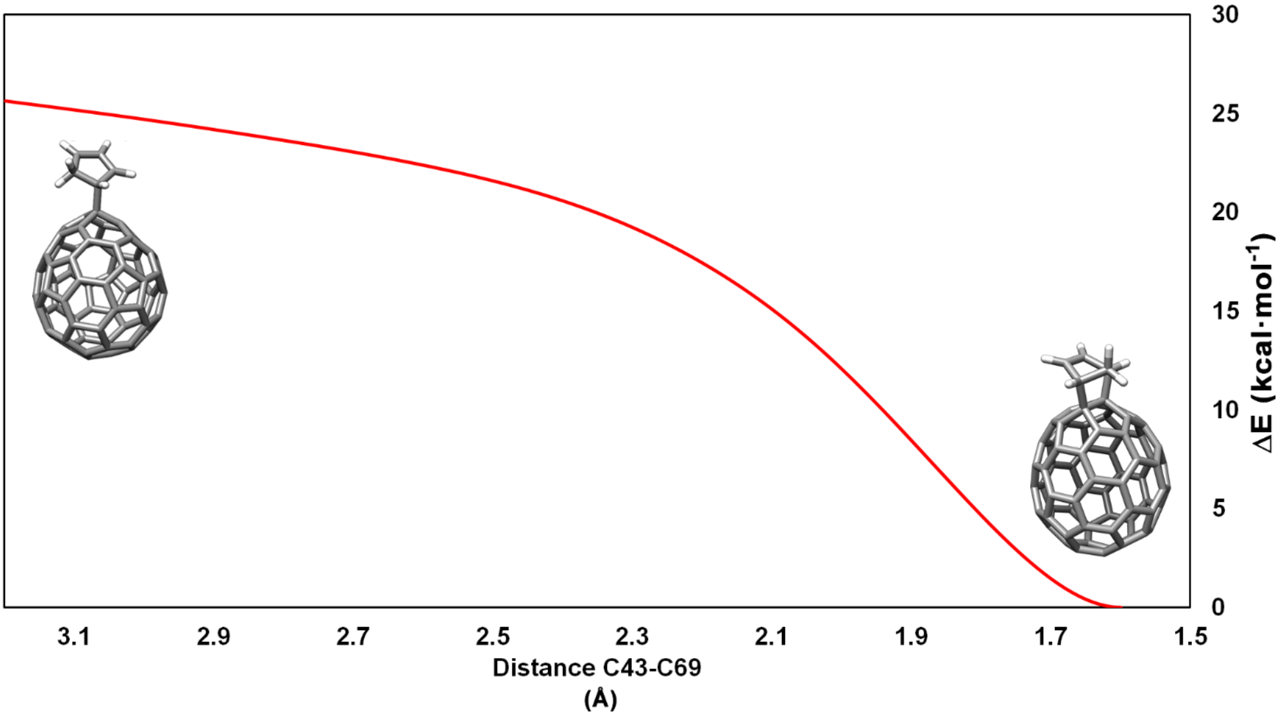

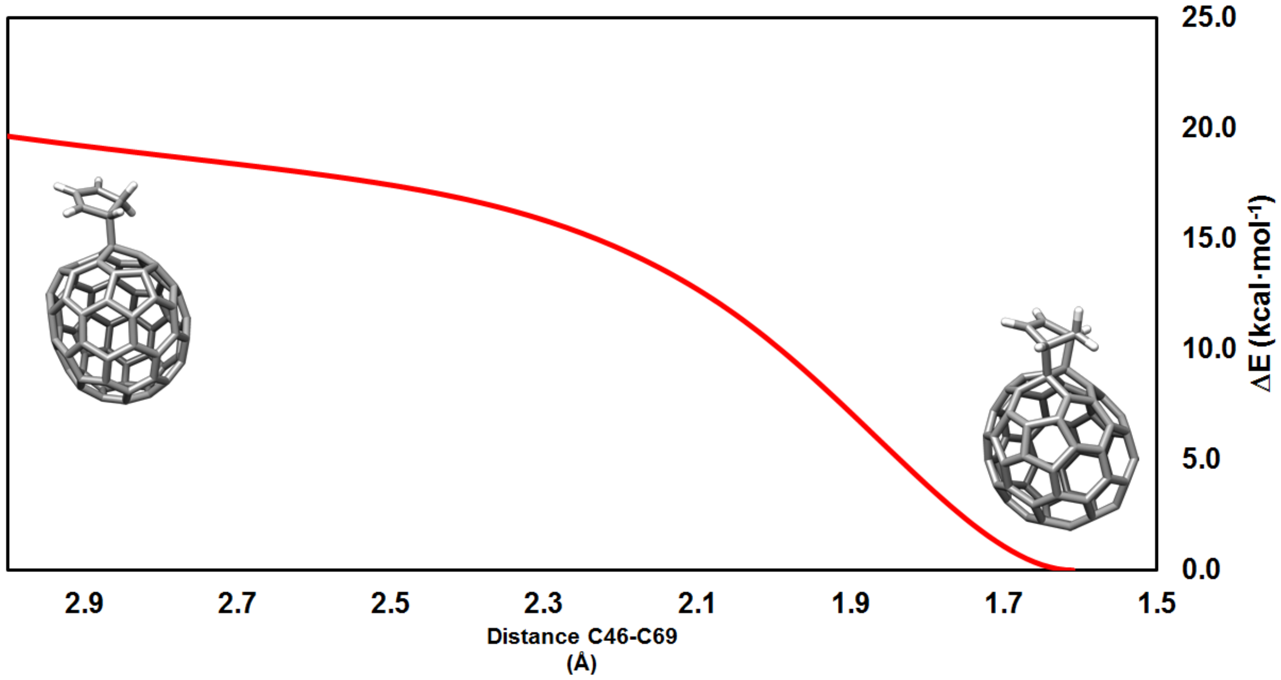Figure S22. UB3LYP-D3/6-31G(d,p) Relaxed scan between biradical intermediate and reaction product (Open-shell singlet state, path $[5,6]_D$).